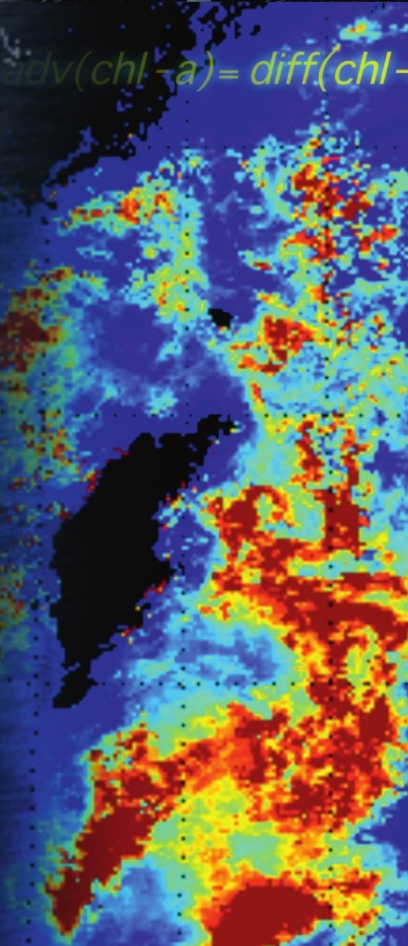
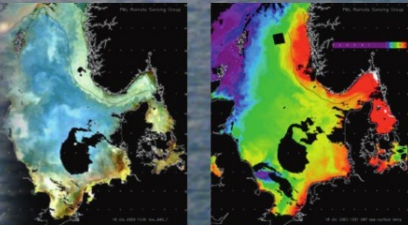




# MONITORING OF HARMFUL ALGAL BLOOMS



Springer



Lasse H. Pettersson  
Dmitry Pozdnyakov



# Monitoring of Harmful Algal Blooms

---

Lasse H. Pettersson and Dmitry Pozdnyakov

---

# Monitoring of Harmful Algal Blooms



Published in association with  
**Praxis Publishing**  
Chichester, UK



Lasse H. Pettersson  
Mohn–Sverdrup Center for Global Ocean Studies and Operational Oceanography at  
Nansen Environmental and Remote Sensing Center  
Bergen  
Norway

Professor Dmitry Pozdnyakov  
Nansen International Environmental and Remote Sensing Center  
St. Petersburg  
Russia

---

SPRINGER-PRAXIS BOOKS IN GEOPHYSICAL SCIENCES  
SUBJECT ADVISORY EDITOR: Philippe Blondel, C.Geol., F.G.S., Ph.D., M.Sc., F.I.O.A., Senior Scientist,  
Department of Physics, University of Bath, Bath, U.K.  
Published in association with the Nansen Centers in Bergen and St. Petersburg  
Nansen Center's Polar Series No. 6

---

ISBN 978-3-540-22892-9      ISBN 978-3-540-68209-7 (eBook)

DOI 10.1007/978-3-540-68209-7

Springer Heidelberg New York Dordrecht London

Library of Congress Control Number: 2011934509

© Springer-Verlag Berlin Heidelberg 2013

This work is subject to copyright. All rights are reserved by the Publisher, whether the whole or part of the material is concerned, specifically the rights of translation, reprinting, reuse of illustrations, recitation, broadcasting, reproduction on microfilms or in any other physical way, and transmission or information storage and retrieval, electronic adaptation, computer software, or by similar or dissimilar methodology now known or hereafter developed. Exempted from this legal reservation are brief excerpts in connection with reviews or scholarly analysis or material supplied specifically for the purpose of being entered and executed on a computer system, for exclusive use by the purchaser of the work. Duplication of this publication or parts thereof is permitted only under the provisions of the Copyright Law of the Publisher's location, in its current version, and permission for use must always be obtained from Springer. Permissions for use may be obtained through RightsLink at the Copyright Clearance Center. Violations are liable to prosecution under the respective Copyright Law.

The use of general descriptive names, registered names, trademarks, service marks, etc. in this publication does not imply, even in the absence of a specific statement, that such names are exempt from the relevant protective laws and regulations and therefore free for general use.

While the advice and information in this book are believed to be true and accurate at the date of publication, neither the authors nor the editors nor the publisher can accept any legal responsibility for any errors or omissions that may be made. The publisher makes no warranty, express or implied, with respect to the material contained herein.

Cover design: Jim Wilkie

Project management: OPS Ltd., Gt. Yarmouth, Norfolk, U.K.

Printed on acid-free paper

Springer is part of Springer Science+Business Media ([www.springer.com](http://www.springer.com))

# Contents

<b>Preface . . . . .</b>	ix
<b>Acknowledgments . . . . .</b>	xv
<b>About the authors . . . . .</b>	xvii
<b>List of figures . . . . .</b>	xix
<b>List of tables . . . . .</b>	xxv
<b>List of abbreviations and acronyms . . . . .</b>	xxvii
<b>1 Qualification, species variety, and consequences of harmful algal blooms (HABs) . . . . .</b>	1
1.1 Introduction . . . . .	1
1.2 Harmful algal bloom species qualification and variety . . . . .	3
1.3 Ecological aspects . . . . .	4
1.4 Food safety, health, and sanitary aspects . . . . .	9
1.5 Economic aspects . . . . .	20
1.6 Concluding remarks . . . . .	24
<b>2 Biology and ecology of harmful algal species . . . . .</b>	25
2.1 Role of hydrodynamics . . . . .	26
2.2 Role of biogeochemistry . . . . .	29
2.3 Role played by other factors . . . . .	31
2.4 Case studies . . . . .	32
2.4.1 <i>Chattonella</i> or <i>Pseudochattonella</i> spp. in the North Sea/ Skagerrak . . . . .	32
2.4.2 Cyanobacteria blooms in the Baltic Sea . . . . .	40
2.4.3 <i>Gymnodinium catenatum</i> blooms in the Galician Rías . . . . .	43

<b>3 Potential of remote sensing for identification, delineation, and monitoring of harmful algal blooms . . . . .</b>	<b>49</b>
3.1 Taxonomy and pigment composition of harmful algae . . . . .	50
3.2 Absorption and emission spectral features of pigments . . . . .	52
3.3 Inherent optical and apparent properties of natural waters . . . . .	61
3.4 Optical properties of the major color-producing agents (CPAs) in natural waters . . . . .	65
3.4.1 Absorption cross-sections of whole algal cells and pigments . . . . .	65
3.4.2 Backscattering cross-sections of algal cells . . . . .	68
3.4.3 Fluorescence cross-sections, $\phi_{php}^*(\lambda)$ of algal cells . . . . .	72
3.4.4 Optical impact of mucilage . . . . .	72
3.4.5 Absorption and backscattering cross-sections of suspended minerals and dissolved organic matter . . . . .	73
3.5 Harmful algae detection: methodologies . . . . .	80
3.5.1 Detection of expressions of pigment composition in harmful algae in absorption and water column reflectance spectra . . . . .	80
3.5.2 Detection of massive HABs through remote estimation of chl-a concentration/phytoplankton biomass levels . . . . .	95
3.6 Synergistic approaches for HAB detection and monitoring . . . . .	107
3.7 Closing remarks . . . . .	110
<b>4 Monitoring harmful algal blooms from space . . . . .</b>	<b>113</b>
4.1 Some case studies of bloom events in the world's oceans . . . . .	114
4.1.1 The North and Baltic Seas . . . . .	116
4.1.2 The Korean Southeast and East China Seas . . . . .	118
4.1.3 The Pearl River Estuary, China . . . . .	119
4.1.4 The Yellow Sea/Bohai Sea, China . . . . .	120
4.1.5 Vietnam coastal waters . . . . .	121
4.1.6 Moreton Bay, Australia . . . . .	121
4.1.7 The Gulf of Finland . . . . .	122
4.1.8 Lake Erie, U.S.A./Canada . . . . .	124
4.1.9 Norwegian coastal waters . . . . .	125
4.1.10 Applications of FLH data products for HAB monitoring	170
4.2 Role played by synergies between satellite EO data in HAB monitoring . . . . .	177
4.3 Near-real time surveillance of HABs . . . . .	188
4.3.1 Norwegian HAB-monitoring services . . . . .	188
4.3.2 British EO Data Acquisition and Analysis Service (NEODAAS) . . . . .	197
4.3.3 U.S. HAB monitoring system for the Gulf of Mexico . . . . .	199
4.4 Closing remarks . . . . .	200

<b>5 Integrated modeling and satellite monitoring of algal blooms . . . . .</b>	<b>203</b>
5.1 Marine/shelf sea ecosystem modeling: nature, capabilities, and limitations . . . . .	203
5.1.1 General characterization of marine ecosystem models . . . . .	203
5.1.2 Types of marine ecosystem models simulating algal blooms . . . . .	206
5.2 Global to regional model simulations: specific features . . . . .	211
5.2.1 General considerations . . . . .	211
5.2.2 Equatorial Pacific Ocean . . . . .	218
5.2.3 Subtropical and tropical waters . . . . .	220
5.2.4 Barcelona Harbor, the Mediterranean Sea . . . . .	222
5.2.5 European continental shelf waters . . . . .	225
5.3 Modeling HABs as an element of integrated marine monitoring . . . . .	236
5.3.1 HAB modeling for the North Sea and Skagerrak waters . . . . .	237
5.3.2 HAB modeling for the Baltic Sea . . . . .	247
5.3.3 HAB modeling in the Galician Rías . . . . .	255
5.4 Closing remarks . . . . .	261
<b>Afterword . . . . .</b>	<b>263</b>
<b>References . . . . .</b>	<b>269</b>
<b>Index . . . . .</b>	<b>299</b>

*To Margareth, Marikken, and Jonathan for their long-lasting support  
and patience—Lasse*

*To my daughter Irina and late mother Natalia whose love and  
dedication have made my life so rewarding—Dmitry*

# Preface

The term “algal bloom” is used to describe the temporal and spatial accumulation of phytoplankton—in general or a single species—in an aquatic environment. The phenomenon of water discoloration produced by harmful algal blooms is an intrinsic phenomenon of the Earth’s aquatic environments and is well known from history, however its incidence and proliferation throughout the world’s oceans remained relatively undiscovered and not understood until the last century.

However, during the last 40–50 years, this natural marine biological phenomenon has become increasingly frequent and widespread causing serious concern not solely in the scientific community but also to the authorities, fisheries, industry, and the public in general. The occurrence of such events, termed *harmful algal blooms* (HABs), began being reported by mass media as front-page news, due to their impact causing severe economic losses and damage, direct human health problems, and the image of a degrading marine and coastal environment. Technological development and in particular new monitoring techniques including satellite Earth observation (EO) have facilitated research advances.

The main motivation of this book resides in the role that the Nansen Environmental and Remote Sensing Center (NERSC) in Bergen played in the early initiation and further development of integrated satellite EO, *in situ* monitoring, and ocean ecosystem modeling methodologies not only to study scientifically, but also to reveal, monitor, and forecast algal blooms (HABs, in particular) as well as to develop tools for dissemination of the information to the relevant stakeholders, including applications related to fisheries and aquaculture (Pettersson, 1990; Stiansen *et al.*, 2002).

Back in the 1980s, a team of scientists at the Nansen Center led by Prof. Ola M. Johannessen started to tackle the highly challenging scientific task of developing physical oceanography into operational oceanography, or “weather forecasting” for the oceans, through combined development of satellite remote sensing, field



The harmful *Chrysochromulina polylepis* bloom in 1988 in Norwegian coastal waters got huge media attention that prompted headlines like “*The algae disaster*”, “*When the ocean dies*”, and “*The algae is thrown away*”. Courtesy: Bergens Tidende.

observations, and numerical ocean modeling (e.g., Johannessen and Pettersson, 1988).

Unexpectedly, in May–June 1988 the algae *Chrysochromulina polylepis* created a massive harmful bloom in a large part of southern coastal Norwegian waters, generating a range of environmental problems and causing severe losses of fish to the Norwegian aquaculture industry amounting to some €4 million (Johannessen and Pettersson, 1988; Dundas *et al.*, 1989; Johannessen *et al.*, 1989a, b). *Ad hoc* monitoring and forecasting activities were initiated by mobilizing public authorities, scientists, and other stakeholders. The Institute of Marine Research and the University of Bergen initiated dedicated ship surveillance cruises to the bloom area. Two aircraft from the Norwegian Pollution Authority (SFT) and the Swedish Coastguard equipped with side-looking airborne radar (SLAR) as well as infrared (IR) and ultraviolet (UV) airborne sensors—instrumentation intended for oil spill reconnaissance and not designed for HAB detection were used in daily reconnaissance. The *ad hoc* established team of scientists along with other experts were nevertheless successful in delineating the HAB areas of *C. polylepis* and providing valuable forecasts of bloom development in other areas, which could be used to take action to mitigate economic losses. Several aquaculture cages were towed away into less saline fjord areas to escape the bloom area (see photo on the book cover)

and reduce the losses of caged fish. The event received extensive TV and newspaper media attention and details on how the bloom developed were for the first time ever in Norway broadcast daily.

Early during the bloom it was determined that thermal fronts in marine waters were intimately related to off-coastal extension of the bloom, a finding that triggered the processing and use of AVHRR to delineate ocean temperature fronts. These IR satellite images (see [Figure 4.1](#)) provided daily information on the sea surface temperature (and, hence, advection of the *C. polyepis* area) in the meanders and small-scale eddies driven by the Norwegian Coastal Current (NCC). Even at this stage of HAB research, Johannessen and Pettersson (1988), Dundas *et al.* (1989), and Johannessen *et al.* (1989a, b) combined their spaceborne data with a two-layer quasi-geostrophic ocean model implemented at the Nansen Center (e.g., Haugan *et al.*, 1991) (see [Figure 4.3](#)) and demonstrated the use of this model to predict advection of the *C. polyepis* bloom.

In the wake of this event, discussions in Norway accelerated the establishment of a national pilot project for ocean monitoring and forecasting (HOV or Hav overvåkning og varsel; see, e.g., Johannessen and Pettersson, 1988). Thus, Norway at that time was an international forerunner in initiating and developing operational oceanography services by setting up and using a state-of-the-art observational ocean *in situ* network, satellite and airborne remote-sensing technologies, and comprehensive coupling of marine hydrodynamic and ecosystem modeling in near real-time monitoring and forecasting. During the last three decades the Nansen Center has taken great strides in this direction through research development of methodologies, synergistic applications of multi-sensor satellite data, and data assimilation in numerical ocean circulation and ecosystem models.

Accordingly, this book is focused on the relevant research activities at the Nansen Center; however, the authors have also pursued the goal of portraying the state of the art in HAB-related activities across the world.

Furthermore, studies have revealed that the detrimental effects of HAB events are multifaceted. They not only involve algal toxin action, but also the impact of factors like the high abundance of phytoplankton biomass, exudation of mucilage, alteration of biogeochemical status of the aquatic environment (e.g., depletion of dissolved oxygen), significant changes in the indigenous trophic/food web interactions, etc.

Numerous investigations have shown that the aftermath of HAB events is not only confined to the welfare status of the aquatic ecosystem, but propagates further affecting humans through toxic contamination of food, deteriorating sanitary conditions, and very significant economic losses.

Despite the extensive scientific knowledge that has already been built up, the reasons for such extensive proliferation and increased incidence of HABs throughout the world during recent decades remain unclear and, generally, are attributed to the combined action of natural ecosystem variability, anthropogenic impact, and climate change. Understandably, ranking the actual role of each of these mechanisms in generating HABs is difficult because they steadily enhance with time and, furthermore, are intimately interrelated in many ways.

In some coastal and off-shore regions of the world's oceans, HABs emerge on a regular basis, but the exact timing of their onset, location, actual extent, and duration may vary significantly from year to year. Bloom-triggering factors are often associated with physical, chemical, and biological conditions and their seasonal variation. At the same time, there are many areas in the oceans and seas where HABs originate unexpectedly or very irregularly. Such events may be brought about through invasive alien algae species being transported to a new geographical region by ballast water, for example.

Moreover, the nature of HABs proves to be complicated and again not well understood. For example, traditionally harmful algae do not always remain harmful and, *vice versa*, some blooms of phytoplankton species known as non-harmful turn out to be harmful under specific local conditions. The exact qualification of a HAB as a harmful/non-harmful bloom requires identification and monitoring using shipborne surveys, sampling, and sophisticated laboratory analyses.

The extent, frequency, spatial, and temporal dynamics of the HAB life cycle—as well as the nature of this phenomenon in conjunction with the associated challenges to aquatic environments and eventually to human society—are all factors that in concert warrant the necessity of developing an efficient integrated system of early detection and warning, monitoring, and prediction of HAB events, in order to take mitigatory actions.

In light of the above, remote-sensing surveillance (especially spaceborne and airborne) are instrumental in the early detection and further monitoring of HABs. This is prompted by such valuable attributes of satellite remote sensing as unrivaled high spatial coverage of oceanic/marine areas and high revisiting frequency (e.g., daily), which is of paramount importance when tackling the problem of HAB monitoring. But are these capabilities really sufficient for satellite remote sensing to be a reliable and complementary monitoring tool? If they are not, what are the limitations? Are such limitations of a current technical, methodological, or fundamental nature? What is required then to perform this challenging task? What complementary means need to be involved or need to be developed? What should an “ideal” monitoring system look like? What components should it encompass? What is already being done in this respect and what is to be done in the future?

This book has been conceived as an endeavor to explore the above suite of issues and is organized in five thematic chapters. To accommodate the above thrust, we begin by discussing in *Chapter 1* both the main criteria that attribute phytoplankton species and associated blooms to the category of harmful ones. Then we refer to HAB-driven detrimental effects. This is followed by characterization of the spatial distribution of occurrence of HAB events and associated specific toxic contamination throughout the world's oceans. Finally, we analyze the variety of consequences of HAB events from the perspectives of (i) aquatic system ecology, (ii) human ecology (health/food safety/sanitary conditions), and (iii) social economy (direct and indirect losses).

*Chapter 2* addresses the biology and ecology of harmful algal species. We examine the role of major factors favoring the occurrence of HABs, including ocean physics, biogeochemistry, weather conditions, climate change, and anthropo-

genic impact (e.g., eutrophication). This is followed by extensive illustrative material produced by a number of case studies conducted in the North and Baltic Seas as well as in the Galician Rias mostly as part of large-scale international research projects coordinated by the Nansen Center.

Based on the first two chapters reflecting the fundamentals of HABs as a hydrobiological phenomenon, *Chapter 3* opens the discussion of issues that are at the base of remote sensing of HABs. As an indirect method, remote sensing always deals with proxy variables. Therefore, in order to meet the challenge of efficient use of remote-sensing means for detection and monitoring of HABs, it is mandatory to identify the appropriate proxies. The latter should be related to in-water color-producing agents (CPAs) inherent in harmful (and also in non-harmful) algae and producing the effect of water discoloration. This choice is motivated by the present availability of satellite sensors operating in the visible range of the electromagnetic spectrum, which is fundamentally important since it is only visible radiation that appreciably penetrates the water column. In pursuit of this goal, we begin Chapter 3 by examining such proxies, which reside in the pigment composition inherent in the cells of various harmful algae species, cell absorption, and backscattering as well as light emission/fluorescence properties. The optical properties of other CPAs generally coexisting with algae in natural waters and also affecting the light signal are discussed as well. These sections are followed by an overview of the variety of methodological approaches suggested so far for remote detection, density assessment, and monitoring of HABs.

Because the presence of a HAB in the water column may also have some surface expressions such as anomalies in water surface temperature and roughness, we conclude Chapter 3 with a discussion of the prerequisites for synergistic use of satellite remote-sensing Earth observation (EO) means. Satellite sensors operating in the visible, infrared, and microwave spectral regions constitute such means, the latter two being the most appropriate tools to investigate the surface micro-layer structure of the ocean surface.

*Chapter 4* expands on the practical integrated monitoring of HABs using satellite EO information sources. First, we present the methodological approaches employed and the results of studies of identify HAB events. Although the literature on this issue is extremely extensive, the scope of this section does not allow us to review the entire range of such publications; instead, we only address the most recent ones to give ample examples from as wide a variety of marine/aquatic environments *throughout the world* as possible in order to better illustrate our discussions in Chapters 1 and 2.

Moreover, an important aim of this overview is to reveal the extent to which methodological approaches aimed at the identification of harmful algal species, as discussed in Chapter 3, have actually been realized in current integrated remote-sensing studies or services of HAB identification and monitoring.

Section 4.2 is devoted to the discussion of practical implementation of a synergistic approach to identification and monitoring of algal blooms, in general, and HABs, in particular. This is done to highlight the conditions under which this approach presents its virtues in full measure.

Chapter 4 concludes with an extensive section exemplifying a couple of integrated HAB monitoring systems using satellite EO data, which are presently operational and constitute a part of national services of HAB detection, surveillance, and early warning. The discussion in this section is predominantly based on the experience gained by Norway, as part of the European Commission and European Space Agency Global Monitoring for Environment and Security (GMES) system, as well as by the U.S.A., where there are already several services for this purpose.

*Chapter 5* provides a review of the presently available coupled ocean and marine ecosystem models developed for forecasting the development of the marine ecosystem, including (harmful) algal blooms. Again, the emphasis is on the ecological models used by the Norwegian HAB monitoring research community. This is done partly to make Chapter 4 comprehensive and partly to complete the description of the Norwegian HAB monitoring and prediction service.

Finally, the *Afterword* presents our vision of the present state of the art in integrated HAB monitoring and forecasting systems as well as the prospects of more sophisticated methodologies becoming available in the future and further improvements of logistic practices supporting such services due to the new satellite sensors scheduled for launch.

During the final editing of the manuscript one of our prime satellites supplying optical Earth observation data—the European Envisat satellite—has stopped sending data to Earth, after near 10 years of successful operation. Fortunately, for our purposes, optical ocean color data are available from other satellites and space agencies. These data are now being used more extensively by us while waiting for the European Sentinel satellites due for launch in the coming years. This event emphasizes the need for international cooperation, continuity, and backup solutions for sensors in order to support both research and operations using satellite Earth observation data.

This book is essentially a sharing of our experiences in the basic and practical research development of the methodologies, their validation, and implementation of HAB monitoring from space and model-based prediction of how such events are likely to unfold. Welcome to *Monitoring of Harmful Algal Blooms*.

*Lasse H. Pettersson*

*Dmitry Pozdnyakov*

May 2012

The Nansen Centers

Bergen, Norway/

St. Petersburg, Russia

## Acknowledgments

The authors express their profound gratitude to Prof. Ola M. Johannessen, Founding Director of the *Nansen Environmental and Remote Sensing Center in Bergen*, who initiated and pioneered HAB research at the Center, for his most valuable role in conceiving this book, general guidance, and encouragement at all stages of its preparation and publication.

The research and activities providing the foundation for this book are the result of teamwork at the Nansen Centers in Bergen and St. Petersburg, involving several scientists through many years. Particular thanks go to Prof. Johnny A. Johannessen, who has been the Research Director of this team since its early activities. Thanks go to current and former colleagues in Bergen and St. Petersburg Drs. Knut-Frode Dagestad, Dominique Durand, Øyvind Frette, Torill Hamre, Peter M. Haugan, Anton Korosov, Tor I. Olaussen, Annette Samuelsen, Morten Stette, and to former Ph.D. students Drs. Are Folkestad, Anton Lyaskovskiy, and Yunfei Wang and current Ph.D. students Evgeny Morozov and Dmitry Petrenko, who have co-authored publications and reports conducted jointly with us which are drawn upon and cited in this book. The authors acknowledge the contributions from our colleagues, and their material is properly cited in the book. Some of the research presented in this book was completed with support from the *Mohn–Sverdrup Center for Global Ocean Studies and Operational Oceanography* at the Nansen Center through a donation from Trond Mohn c/o Frank Mohn AS.

The authors are also grateful for the financial support provided by the European Commission under the project *Harmful Algae Bloom Initiation and Prediction (HABILE)*, contract number: EVK3-CT2001-00063. Some of the research conducted under this extensive project constitutes the content of this book and sincere thanks go to all the HABILE project participants, especially to Per Andersen, Francisco Figueras, Steve Groom, Bengt Karlson, Seppo Kaitala, Tørbjørn Lorentzen, Lars-Johan Naustvoll, Andreas Neuman, Tapani Stipa, Einar Svendsen, as well as the abovementioned colleagues at the Nansen Center

## xvi Acknowledgments

for their contributions to reports and publications cited or used in this book. Research projects funded by the Research Council of Norway, Norwegian Space Center, European Space Center, and INTAS (the International Association for the Promotion of Cooperation with Scientists from the Independent States of the Former Soviet Union) have contributed to the research basis for the content of this book. The Norwegian Government has granted the Nansen Center in Bergen annual basic funding from 2012 as a national environmental research institute. Covering a topic of high relevance, the final editing of the book manuscript is supported through this grant and thanks go to the Ministry of the Environment for their support.

The authors also acknowledge the contribution to Chapter 3 from Prof. Hartmut Grassl. The authors also thank Martin Miles for language editing and Tor I. Olaussen, Mohamed Babiker, and Dmitry Petrenko for their help with artwork preparation.

## About the authors

**Lasse H. Pettersson** (1957) is Leading Scientist and Director for International Cooperation at the Nansen Environmental and Remote Sensing Center (NERSC) in Bergen, Norway.

Scientifically, he leads the marine and coastal optical remote-sensing research at NERSC. He has more than 26 years of experience of research and applications of Earth Observation satellite data for marine and sea ice environmental and climate studies and applications.

He was the deputy project leader of the project “Climate and Environmental Changes in the Arctic—CECA”, elected the laureate for the EU DESCARTES research prize in 2005.

He is the author and co-author of 63 scientific referee publications, 6 books, and several thematic monographs, as well as teaching materials for universities and school classes. He has also co-authored more than 120 technical reports to clients/national and international agencies, as well as 30 popular science-related articles for the general public.

With university education in physical oceanography, his long-time primary research interests concern the monitoring of harmful algal blooms, water quality, and marine ecosystems. Given his expertise, he has been the primary coordinator of several multinational research and application projects funded by the European Commission, Research Council of Norway, Norwegian Space Center, European Space Agency (ESA), and industry.

He has been appointed a member of both the ESA Science Advisory Group (SAG) for the Medium Resolution Imaging Spectrometer (MERIS) sensor and the NASA SeaWiFS Science Team.

He has extensive experience in international scientific and educational cooperation; in particular, with Russia since 1992 and with India since 1998. He also holds the positions of Vice President at the Nansen International Environmental and Remote Sensing Center in St. Petersburg, Russia and the Nansen Environmental Research Center in Cochin, India.

**Dmitry V. Pozdnyakov** (1942), Ph.D., Prof. Dr. received his doctorate in physics in 1972 from the State University of St. Petersburg, Russia, where he conducted infrared studies simulating gas/aerosol interactions. His work revealed previously unknown sink mechanisms of climate-controlling gases, including the stratospheric ozone-depleting fluorocarbons.

He then accepted a lecturing post in the Division of Atmospheric Physics at the State University. As a Visiting Professor, he lectured in physics and atmospheric optics for five years at the University of Conakry, Guinea.

In 1983 he joined the Institute for Lake Research of the Russian (then U.S.S.R.) Academy of Sciences, where his research interests switched to limnological ecology and hydro-optics. He has developed bio-optical algorithms for remote sensing of water quality parameters utilizing passive spectrometric and active lidar techniques. His scientific team has remotely investigated the trophic status of nearly all the large lakes and water storage reservoirs in the European part of the former U.S.S.R.

He was awarded a D.Sc. degree in 1992, and in 1996 he became a full university professor. He has authored more than 200 scientific papers, brochures, and books published by Russian and international publishers, including CRC Press and Springer-Praxis.

He is a two-time (1992 and 2006) recipient of the Chandler–Misener Award presented by the International Association for the Great Lakes Research for his work, which is documented in a number of companion publications.

He currently holds the position of Research Director at the scientific foundation that is the Nansen International Environmental and Remote Sensing Center (NIERSC), and is Invited Professor at the Electrotechnical University, both in St. Petersburg. His research activities continue to be directed towards the optical properties and remote sensing of inland, coastal, and marine waters, which resulted in numerous publications addressing the American and European Great Lakes as well as the Baltic, Kara, and White Seas, and the North Atlantic.

# Figures

1.1	Presence of PSP toxins in 1993–2002 in European waters . . . . .	5
1.2	Presence of PSP toxins in 1993–2002 in North American waters . . . . .	6
1.3	Presence of DSP toxins in 1993–2002 in European waters . . . . .	7
1.4	Presence of ASP toxins in 1993–2002 in European waters . . . . .	8
1.5	Presence of ASP toxins in 1993–2002 in North American waters . . . . .	9
1.6	Presence of <i>Ciguatera</i> toxins in 1993–2002 in North American waters . . . . .	10
1.7	Presence of NSP toxins in 1993–2002 in North American waters . . . . .	11
1.8	Presence of cyanobacteria and other toxins in 1993–2002 in European waters . . . . .	12
1.9	Presence of DSP toxins in 1993–2002 in North American waters . . . . .	13
1.10	Reported areas suffering from toxins in 1993–2002 in European and North American waters . . . . .	16
1.11	Reported animal and plant mortalities in 1993–2002 in European and North American waters . . . . .	18
2.1	Time series of weekly averages of SST in the North Sea for the period January–May 1998 derived from the NOAA AVHRR sensor . . . . .	34
2.2	Measurements of <i>Pseudochartonella farcima</i> at Flødevigen Research Station (1986 to 2010) . . . . .	35
2.3	<i>Pseudochartonella</i> spp. abundance and timing of onset in the North Sea/Skagerrak/Kattegat area, during the period 1998 to 2002 . . . . .	36
2.4	Vertical profiles of <i>Pseudochartonella</i> aff. <i>verruculosa</i> and <i>Heterosigma</i> at Lyngør during the 2001 bloom . . . . .	38
2.5	<i>Pseudochartonella</i> spp. abundance vs. salinity in the North Sea/Skagerrak/Kattegat area during the period 1998–2003 . . . . .	39
2.6	<i>Pseudochartonella</i> spp. abundance vs. SST in the North Sea/Skagerrak/Kattegat area, during the period 1998–2003 . . . . .	39
2.7	<i>Pseudochartonella</i> spp. abundance vs. $\text{NO}_2 + \text{NO}_3$ concentration in the North Sea/Skagerrak/Kattegat area, during the period 1998–2003 . . . . .	40
2.8	Occurrence of cyanobacteria in relation to water temperature . . . . .	41
2.9	Occurrence of cyanobacteria in relation to salinity . . . . .	42
2.10	Occurrence of cyanobacteria in relation to DIN:DIP ratio . . . . .	42

xx Figures

<b>2.11</b>	Schematic representation of circulation in the Spanish Rías during upwelling and downwelling conditions and their typical off-shore SST conditions revealed in satellite images . . . . .	44
<b>2.12</b>	Time evolution of total phytoplankton and diatom abundance and total phytoplankton and dinoflagellate abundance in the surface waters of a sampled station in the Ría de Vigo in 1987–1988 . . . . .	45
<b>2.13</b>	Time evolution of temperature and mean abundance of diatoms, dinoflagellates, and the swimmer species <i>Karenia mikimotoi</i> in shelf waters in front of the Ría de Vigo in 2001–2002 . . . . .	45
<b>2.14</b>	Sequence showing the initiation and development of a <i>Gymnodinium catenatum</i> bloom in the Ría de Vigo in September–October 1993 . . . . .	46
<b>2.15</b>	Graph showing the possible long-term relationship between climate variability and PSP events caused by <i>Gymnodinium catenatum</i> in the Galician Rías Baixas during the years 1981 to 1998. . . . .	47
<b>3.1</b>	Absorption spectrum of <i>chl-a</i> in acetone . . . . .	54
<b>3.2</b>	<i>In vivo</i> absorption spectra of algal cells from several classes . . . . .	54
<b>3.3</b>	Absorption spectra of three <i>chl-c</i> in diethyl ether or acetone . . . . .	56
<b>3.4</b>	Absorption spectrum of $\alpha$ -carotene dissolved in acetone . . . . .	57
<b>3.5</b>	Absorption spectrum of diadinoxanthin dissolved in acetone. . . . .	58
<b>3.6</b>	Absorption spectrum of dinoxanthin dissolved in acetone . . . . .	58
<b>3.7</b>	Absorption spectrum of fucoxanthin dissolved in acetone . . . . .	59
<b>3.8</b>	Absorption spectrum of 19'-hexanoyloxyfucoxanthin dissolved in acetone . . . . .	59
<b>3.9</b>	Absorption spectrum of peridinin dissolved in acetone . . . . .	60
<b>3.10</b>	Absorption spectrum of zeaxanthin dissolved in acetone. . . . .	60
<b>3.11</b>	Absorption by biliproteins from blue-green algae . . . . .	61
<b>3.12</b>	Intercomparison of independent determinations of the absorption cross-section spectra for non-chlorophyllous matter. . . . .	74
<b>3.13</b>	Backscattering cross-section spectra for suspended minerals . . . . .	75
<b>3.14</b>	Absorption by phytoplankton, and second-derivative spectra . . . . .	86
<b>3.15</b>	Reflectance spectrum measured on June 14, 1995 and the fourth-derivative spectrum. . . . .	88
<b>3.16</b>	Flow diagram of the Nansen Centers' BOREALI. . . . .	105
<b>4.1</b>	Chlorophyll distribution in North Sea and Skagerrak region as retrieved by the MERIS, MODIS/Aqua, and SeaWiFS for February 23, March 9, and April 1, 2004. . . . .	116
<b>4.2</b>	Example SeaWiFS contrast-enhanced false-color composites of HABs . . . . .	117
<b>4.3</b>	Evolution of SST fields for the North Sea based on NOAA AVHRR data from April 28, May 15, May 21, May 22, and May 30, 1988 during an extensive <i>Chrysochromulina</i> bloom . . . . .	127
<b>4.4</b>	Summary of the observed algal front location during the <i>Chrysochromulina</i> bloom during its advance-and-retreat period in the Norwegian Coastal Current . . . . .	128
<b>4.5</b>	Modeled stream function in the upper layer predicted for June 1 during the <i>Chrysochromulina</i> bloom in 1988 . . . . .	129
<b>4.6</b>	The web page of the NERSC service providing near-real time access to satellite-based EO data products for monitoring of HAB events . . . . .	131
<b>4.7</b>	Daily images of the $C_{chl}$ concentrations during the early spring bloom in 2006 in the North Sea and Norwegian Coastal Current . . . . .	133
<b>4.8</b>	Seven-day composites of the $C_{chl}$ concentrations during the early spring bloom in 2006 in the North Sea and Norwegian Coastal Current . . . . .	133

<b>4.9</b>	Map of the key current circulation features in the North Sea . . . . .	135
<b>4.10</b>	Sequence of three SeaWiFS images resolving <i>chl-a</i> concentration and two SST images during the <i>Pseudochattonella</i> bloom in May 1998 . . . . .	137
<b>4.11</b>	Contour plot of the maximum <i>chl-a</i> values in 0 to 30-meter depth, based on data collected by <i>R/V Dannevig</i> and <i>Håkon Mosby</i> during the period May 9 to 19, 1998, and subsection of the SeaWiFS <i>chl-a</i> concentration image from May 15 resolving the instantaneous phytoplankton distribution in the same areas as mapped during 10 days by ship measurements . . . . .	138
<b>4.12</b>	Near-synoptic coverage of the AVHRR SST, ERS SAR image, and SeaWiFS <i>chl-a</i> distribution covering the western Skagerrak and Jutland Current on May 15, 1998 . . . . .	140
<b>4.13</b>	SeaWiFS <i>chl-a</i> pigment data for May 13–15, 1998; surface wind speed and direction for May 15 at noon . . . . .	141
<b>4.14</b>	Near-synoptic coverage of AVHRR SST, ERS-2 SAR backscatter, and SeaWiFS <i>chl-a</i> concentration on May 4, 2000 covering the Skagerrak region . . . . .	144
<b>4.15</b>	Extract from Figure 4.12 focusing on the West Jutland current, showing AVHRR SST at 05:54 UTC, 04:42 UTC, SeaWiFS <i>chl-a</i> concentration at 12:19 UTC, and ERS-2 SAR backscatter at 21:30 UTC on May 5, 2000 . . . . .	145
<b>4.16</b>	Reanalysis wind fields (from ECMWF) during May 4, 2000 . . . . .	146
<b>4.17</b>	Example of various sea surface features and phenomenon resolved in SAR radar and SeaWiFS <i>chl-a</i> data taken 9 hours apart on May 4, 2000 . . . . .	148
<b>4.18</b>	ECMWF wind field for the eastern North Sea, Radarsat ScanSAR image, and the corresponding AVHRR SST image . . . . .	151
<b>4.19</b>	SeaWiFS <i>chl-a</i> concentrations for March 25–27, 2001, and a mosaic of the two ERS-2 SAR scenes . . . . .	153
<b>4.20</b>	Wind field as retrieved from ERS-2 SAR using the CMOD-IFR2 algorithm and wind direction from the image spectra, and wind vectors overlaid on the SeaWiFS <i>chl-a</i> image, for comparison with the ECMWF . . . . .	155
<b>4.21</b>	ERS-2 SAR images overlaid on the SeaWiFS <i>chl-a</i> concentration distribution for March 27, 2001, shown with different opacity of the SAR image . . . . .	156
<b>4.22</b>	Satellite EO data for May 8 and 9, 2001, comparing <i>chl-a</i> , SST, and radar backscatter . . . . .	159
<b>4.23</b>	Monthly summary of <i>in situ</i> cell counts of the abundance of <i>Pseudochattonella</i> during the period January to June in 1998 and 1999 . . . . .	160
<b>4.24</b>	Monitoring of west Jutland Danish waters in April 2009 during the <i>Pseudochattonella</i> bloom . . . . .	163
<b>4.25</b>	A MERIS RGB image during cloud-free conditions over the Baltic and North Seas and spatial distribution of the <i>chl-a</i> concentration derived from the same satellite data . . . . .	164
<b>4.26</b>	Cloud-free conditions over major parts of the North Sea on May 19, 1999 . .	167
<b>4.27</b>	SeaWiFS ocean color image from July 16, 2003 covering major parts of the North Sea . . . . .	168
<b>4.28</b>	MERIS-based FLH values in Skagerrak for the eight dates in 2003 and 2004 .	173
<b>4.29</b>	Spatial pattern of the MERIS FLH product in Skagerrak for the eight dates specified in Table 4.3 . . . . .	174
<b>4.30</b>	Based on the data in Figure 4.25, <i>FLH</i> values are plotted versus NIVA FerryBox <i>in situ</i> $C_{chl}$ . . . . .	176
<b>4.31</b>	Statistical regression of the <i>FLH:chl</i> ratio as a function of temperature and PAR for the data set in Figure 4.27 . . . . .	176

## xxii Figures

<b>4.32</b>	Sensor synergies illustrated with EO images from June 5, 2006 illustrating the co-location of the ocean fronts in the Norwegian Coastal Current expressed in the gradients in $C_{chl}$ , SST, and AS . . . . .	179
<b>4.33</b>	An example of a cyanobacterial bloom in the Baltic Sea on July 25, 2005 . . . . .	181
<b>4.34</b>	Another example of a cyanobacterial bloom in the Baltic Sea on July 1, 2005 . . . . .	182
<b>4.35</b>	A meso-scale eddy during a cyanobacteria bloom in the Baltic Sea . . . . .	183
<b>4.36</b>	A coastal front in the southernmost part of the Baltic Sea . . . . .	184
<b>4.37</b>	A meso-scale eddy in the Baltic Sea . . . . .	186
<b>4.38</b>	Bathymetry of the Baltic Sea . . . . .	187
<b>4.39</b>	The generic chain for delivery of HAB monitoring and forecasting services developed at NERSC . . . . .	189
<b>4.40</b>	An example of the weekly AlgeInfo bulletin assessing the state of algae populations along the coasts of Norway . . . . .	190
<b>4.41</b>	An example of NIVA FerryBox observations acquired from several ships of opportunity in Norwegian coastal and off-shore waters. . . . .	191
<b>4.42</b>	Schematic of the various levels of data processing implemented in the near-real time processing of satellite EO data at the Nansen Center for use in monitoring of HAB events in coastal waters as well as other applications . . . . .	193
<b>4.43</b>	The sequence of data files generated for the time-averaging (binning) of MERIS data in the near-real time satellite Earth observation processing system in operation at the Nansen Center . . . . .	194
<b>4.44</b>	The suite of near-real time EO-based products available at <a href="http://hab.nerc.no">http://hab.nerc.no</a> on a daily basis . . . . .	195
<b>4.45</b>	Schematic view of synergies between different satellite EO data products exploited through combining products from various sensors and production chains in a common processing and analysis infrastructure . . . . .	196
<b>4.46</b>	Data from various distributed sources and services are integrated in a Web Map Service (WMS), in order to facilitate user access and interpretations . . . . .	197
<b>5.1</b>	Monthly average sea surface current vectors and current speed from the NERSC ToPAZ model system for January 2008 . . . . .	206
<b>5.2</b>	Qualitative comparison between the spatial distributions of <i>chl-a</i> concentration obtained from a SeaWiFS image taken over the White Sea in late May, June, and October, 2001, and the modeled phytoplankton biomass for the same time periods and year . . . . .	234
<b>5.3</b>	An illustration of the physical impact of the model grid size illustrated by the bottom topography maps for the coarse grid resolution NORWECOM model, and fine grid resolution . . . . .	238
<b>5.4</b>	Schematics of the main biochemical compartments and processes in the NORWECOM marine ecosystem model used at IMR, and the main compartments of the NORWECOM model version implemented at the Nansen Center . . . . .	240
<b>5.5</b>	Specific growth rate for <i>Chattonella</i> as a function of water salinity and temperature as parameterized in the NORWECOM model . . . . .	242
<b>5.6</b>	NORWECOM model simulations of surface currents and flagellate concentrations on March 21, 2001, and the satellite image from the same day . . . . .	244
<b>5.7</b>	NORWECOM model simulations of surface circulation and flagellate concentrations on March 29, and April 5, 2001 based on the assimilation of satellite observations from March 21. . . . .	246
<b>5.8</b>	NORWECOM model simulations of peak production of diatoms in 2000, 2001, and 2002 . . . . .	248

<b>5.9</b>	NORWECOM model simulations of annual depth-integrated production of <i>Chattonella</i> for 1998–2001 . . . . .	250
<b>5.10</b>	NORWECOM model simulations of the time series of <i>Chattonella</i> production at a location outside Lista for the years 1998–2001. . . . .	251
<b>5.11</b>	NORWECOM model simulations of the daily mean wind stress for a location outside Lista in the years 1998–2001 for the period March–May . . . . .	252
<b>5.12</b>	Temporal variability of the N/P ratio and cyanobacterial biomass derived from observations and from model simulations . . . . .	253
<b>5.13</b>	Temporal variability of water temperature and cyanobacterial biomass derived from observations and simulations . . . . .	254
<b>5.14</b>	Temporal variability of <i>Nodularia</i> biomass and vertical velocity in the water column. . . . .	254
<b>5.15</b>	Simulated summer distribution of <i>Nodularia</i> and <i>Aphanizomenon</i> for the Baltic Sea during summer . . . . .	256
<b>5.16</b>	Surface currents and salinity distribution during the upwelling episode on April 3, 2003 and the pronounced downwelling event on May 3, 2003 in the Galician Rías . . . . .	259
<b>5.17</b>	Transect along the ría's axis during the 2003 upwelling episode for nitrate, and total chlorophyll . . . . .	260
<b>5.18</b>	Transect along the ría's axis during the pronounced downwelling event for nitrate and total chlorophyll. . . . .	261
<b>A.1</b>	Concentrations of <i>chl-a</i> in coastal European waters during 2008 summer reported from <i>in situ</i> measurements, and retrieved from satellite data	265

# Tables

<b>1.1</b>	Types of algae proliferating into HABs . . . . .	14
<b>1.2</b>	Estimated annual economic losses from HABs in the United States . . . . .	23
<b>1.3</b>	Socio-economic effects from HABs in selected European marine waters . . . . .	23
<b>1.4</b>	Socio-economic impacts of HABs in European marine waters at the turn of the 21st century . . . . .	23
<b>2.1</b>	Summary of <i>Chattonella</i> blooms in the North Sea/Skagerrak and Kattegat during 1997–2009 . . . . .	33
<b>3.1</b>	Phytoplankton size classes vs. harmful algal divisions/classes . . . . .	52
<b>3.2</b>	Distribution of major and taxonomically significant pigments in harmful algae . . . . .	53
<b>3.3</b>	Mean characteristics of Gaussian bands and associated specific absorption coefficients of chlorophylls and carotenoids for Georges Bank waters . . . . .	69
<b>3.4</b>	Absorption peak locations and their interpretation in terms of associated pigments for subsurface waters of the English Channel . . . . .	87
<b>3.5</b>	Spectral values of the parameters $U$ , $S$ , and $a_2^*$ for mixed and diatom-dominated phytoplankton populations for the SeaWiFS wavelengths and their corresponding Raman wavelength . . . . .	98
<b>4.1</b>	Comparison of the spectral band locations of the MODIS and MERIS sensors in the visible and near-infrared spectral ranges, including an indication of their primary applications . . . . .	123
<b>4.2</b>	Overviews of HAB events in and around the North Sea where multiple EO satellite sensor data have been studied to assess the algal bloom situation . . . . .	132
<b>4.3</b>	Dates of synoptic acquisition of the MERIS RR and NIVA FerryBox data . . . . .	172
<b>4.4</b>	Flag designations used in MERIS products . . . . .	175
<b>4.5</b>	Detection capabilities and deficiencies using sensor synergy combining SAR, IR radiometry, passive microwaves, spectrometry, and altimetry for monitoring meso-scale dynamics and variability . . . . .	178
<b>5.1</b>	Examples of marine ecosystem models for the prediction of HABs developed before 1995 . . . . .	208

## Abbreviations and acronyms

AB	Algal Bloom
AD	Advection–Dispersion
Alg@line	HAB monitoring, research, and monitoring service
AOP(s)	Apparent Optical Property(ies)
ASAR	Advanced Synthetic Aperture Radar
ASP	Amnesic Shellfish Poisoning
AVHRR	Advanced Very High Resolution Radiometer
BEAM	Mosaic processor
BOREALI	Bio-Optical RETrieval ALgorithm
CASI	Compact Airborne Spectrographic Imager
CDOM	Chromophoric Dissolved Organic Matter
CFP	Ciguatera Fish Poisoning
COADS	Comprehensive Ocean–Atmosphere Data Set
COHERENS	Coupled Hydrodynamic Ecological Model for Regional Northwest European Shelf Seas
CPA(s)	Color Producing Agent(s)
CS	Consumer Surplus
CTP	Cyanobacterial Toxin Poisoning
CZCS	Coastal Zone Color Scanner
DAAC	Distributed Active Archive Center
DIMAP	DIgital MAPping
DIN	Dissolved Inorganic Nitrogen
DIP	Dissolved Inorganic Phosphorus
DISPRO	Prototype implementation of Data Integration System for Marine Pollution and Water Quality (DISMAR)
DOAS	Differential Optical Absorption Spectroscopy
DOM	Dissolved Organic Matter
DSA	Derivative Spectroscopy Analyses

DSP	Diarrheic Shellfish Poisoning
DSRS	Dundee Satellite Receiving Station
E&SE	Enclosed and Semi-Enclosed (marine systems)
ECMWF	European Centre for Medium-Range Weather Forecasts
ECOHAM	ECOlogical North Sea Model, HAMBurg
ELISE	Ecological modeling software
EM	Ecosystem Modeling
EnKF	Ensemble Kalman Filter
ENSO	El Niño Southern Oscillation
ENVISAT	ENVIronmental SATellite of ESA
EO	Earth Observation
ERDAS Imagine	Collection of software tools designed specifically to process imagery
ERS	European Remote Sensing satellite
ERSEM	European Regional Seas Ecosystem Model
ESA	European Space Agency
ESE	Enclosed and Semi-Enclosed (marine systems)
ESRI	Economic and Social Research Institute
ETM+	Enhanced Thematic Mapper
FD	Norwegian Directorate of Fisheries
FIMR	Finnish Institute for Marine Research
FLH	Fluorescence Line Height
FPCA	Forward Principal Component Analysis
FR	Fine Resolution (300 m pixels)
GEOSS	Global Earth Observation System of Systems
GeP&CO	Geochemistry, Phytoplankton, and Color of the Ocean
GHER	Geo-Hydrodynamics and Environmental Research model
GIS	Geographic Information System
GMES	Global Monitoring for Environmental Security (a European program)
GMT	Greenwich Mean Time
GOTM	General Ocean Turbulence Model
HAB	Harmful Algal Bloom
HABILE	Harmful Algal Bloom Initiation and Prediction in Large European Ecosystems (an EU Framework Program project, coordinated by NERSC)
HOT	Haze Optimization Transformation
HOV	Hav overvåkning og varsling (ocean monitoring and forecasting system)
HPLC	High Performance Liquid Chromatography
HYCOM	Hybrid Coordinate Ocean Model
IBM	Individual-Based Model
IIM	Instituto de Investigaciones Marinas (Vigo, Spain)

IMO	International Maritime Organization
IMR	Institute for Marine Research (Norway)
IOP(s)	Inherent Optical Property(ies)
IR	Infrared
ISPM	Inorganic Suspended Particulate Matter
JGOFS	Joint Global Ocean Flux Study
KPP	K-Profile Parameterization
L-M	Levenberg–Marquardt procedure
LANDSAT	LAND Monitoring SATellite
LMT	Levenberg–Marquardt Technique
LRI	Laboratoire de Recherche et Informatique (France)
LT	Lidar Technique
MATLAB	Software package with a wide spectrum of computational functions
MCI	Maximum Chlorophyll Index
MCSST	Multi-Channel Sea Surface Temperature (algorithm)
MERIS	MEdium Resolution Imaging Spectrometer
MLP	Multi-Layer Perceptron
MODIS	MODerate Resolution Imaging Spectroradiometer
MSD	Minimum Spectral Distance
MSE	Mean Square Error
N	Nitrogen
NAO	North Atlantic Oscillation
NASA	National Aeronautics and Space Administration
NCAR	National Center for Atmospheric Research
NCC	Norwegian Coastal Current
NCOF	National Center for Ocean Forecasting
NEODAAS	NERC Earth Observation Data Acquisition and Analysis Service
NERC	Natural Environment Research Council (U.K.)
NERSC	Nansen Environmental and Remote Sensing Center, Bergen, Norway
NIERSC	Nansen International Environmental and Remote Sensing Center, St. Petersburg, Russia
NIVA	Norwegian Institute for Water Research
NN	Neural Network
NOAA	National Oceanic and Atmospheric Administration
NORWECOM	Norwegian Ecological Model System
NPZD	Nutrient, Phytoplankton, Zooplankton, and Detritus (marine ecosystem model)
NRCS	Normalized Radar Cross Section
NRT	Near Real Time
NSP	Neurotoxic Shellfish Poisoning
NTU	Nephelometric Turbidity Unit
NW	North-West

xxx Abbreviations and acronyms

OC	Ocean Color
OC2	Ocean Chlorophyll algorithm 2
OCM	Ocean Color Monitor
OCR	Open Coastal Region
OCTS	Ocean Color and Temperature Scanner
OGC	Ocean General Circulation (model)
P	Phosphorus
PAR	Photosynthetically Active Radiation
PC	Phycocyanin Content
PCB	PolyChlorinated Biphenyl
PDO	Pacific Decadal Oscillation
PFT	Plankton Functional Type
PLS	Partial Least Squares
PML	Plymouth Marine Laboratory (U.K.)
POL-3DB	Proudman Oceanographic Laboratory three-dimensional block
POMS/MONCOZE	Princeton Ocean Model
ppm	parts per million
PRI	PRecision Image (format for ERS SAR satellite images)
PS	Producer Surplus
PSP	Paralytic Shellfish Poisoning
Quicksat	Micro-satellite
RADARSAT	Advanced Earth observation satellite with SAR onboard
RGB	Red–Green–Blue
rms	root mean square
ROI	Region Of Interest
ROMS	Regional Ocean Modeling System
RR	Rough Resolution (mode)
RSDAS	Remote Sensing Data Analysis Service
SAR	Synthetic Aperture Radar
ScanSAR	Scanning Synthetic Aperture Radar
SCIAMACHY	SCanning Imaging Absorption spectroMeter for Atmospheric CHartographY (satellite EO sensor)
SCOOP	SeCure Online Order Processing
SeaBAM	SeaWiFS Bio-Optical Algorithm Mini-Workshop
SeaDAS	SeaWiFS Data Analysis System
SeaWiFS	Sea-viewing Wide Field-of-view Sensor
SLC	Synechococcus-Like Cyanobacteria
SMHI	Swedish Meteorological and Hydrological Institute
SOOP	Ships Of Opportunity Program
SST	Sea Surface Temperature
SWAN	Simulating WAves Nearshore
TAO	Tropical Atmosphere Ocean experiment

TC	Tasseled Cap Transformation (method used in remote sensing)
TEP	Transparent Exopolymeric Particle
TIR	Thermal InfraRed
TOA	Top Of the Atmosphere
TSM	Total Suspended Matter
UMN	University of Minnesota
UTC	Coordinated Universal Time
UV	Ultraviolet (part of the spectrum)
VAT	Value Added Tax
VRS	Vibrational Raman Scattering
WFS	Web Feature Service
WMS	Web Map Service
WQP	Water Quality Property
WTP index	Willingness To Pay index
XML	Extensible Markup Language
YS	Yellow Substance

# 1

## Qualification, species variety, and consequences of harmful algal blooms (HABs)

### 1.1 INTRODUCTION

Life in marine, coastal, and inland water bodies is almost universally rooted in the biological conversion of light energy to chemical bond energy that is stored in the form of organic carbon compounds. This conversion, called photosynthesis, takes place in floating microalgae collectively called *phytoplankton*, and the associated organic matter generation is named *primary production*. This explains why phytoplankton is figuratively called the “grass of the aquatic environment”, being the primary source of the marine food web. It is indeed upon them that the indigenous aquatic organisms of higher trophic levels feed either directly or via an intricate system of food web interactions.

The composition and abundance of phytoplankton communities in marine and inland waters are determined by a wealth of factors, principal among which are nutrients and sunlight availability, as well as the hydrographic and other physical conditions in the water. Waters with low, moderate, high, and super-high content of nutrients are termed *oligotrophic*, *mesotrophic*, *eutrophic*, and *hypertrophic*, respectively. Accordingly, phytoplankton content generally increases from oligotrophic to hypertrophic conditions.

For each water body trophic type, some intrinsic compositions of phytoplankton types/species are characteristic of each vegetation season (i.e., spring, summer, and autumn). Temporal variations in phytoplankton abundance generally exhibit several maxima, their amplitude growing with the trophic status of the water body.

However, phytoplankton *abundance* is not a sole indicator of the trophic status of water bodies: the transition from oligotrophy to higher trophic levels, driven either by natural processes or anthropogenic forcing, is intrinsically associated with drastic changes in the *floristic composition* of the indigenous phytoplankton community. In combination with light availability, beneficial in-water thermal and hydrodynamic conditions as well as a calm wind/sea state, nutrient enrichment of

the aquatic environment (as a result of land/river runoff or water mass upwelling/advection, etc.) results in the occurrence of a massive development of phytoplankton in waters with a trophic status higher than oligotrophic. Such phenomena are called *algal blooms* and generally are due to an intensive growth of a certain group of algal species with one or several taxa being predominant (Petrova, 1990).

The term “algal bloom” is used to describe an accumulation in time and space of phytoplankton in general or a single species. There is no single definition to what can be called a bloom. The term “species-specific” is used to characterize abundance maxima going from rather slight increases in the abundance of a single species representing a maximum in time and space, to impressive large-scale multi-species phenomena representing several million cells/l or several 100 mg Chl-a/m<sup>3</sup>. Phytoplankton blooms can either be generated due to *in situ* growth or as the result of horizontal/vertical advection followed by accumulation or a combination of *in situ* growth and advection. A conceptual model of a bloom scenario consists of a succession of several phases in time.

**Phase 1.** “Pre-bloom” phase—The species is only present in very low concentrations in the pelagic zone or, alternatively, is present in the sediment in encysted form. To proceed to the next phase of bloom development, the cysts must germinate and the excysted specimens enter the pelagic water environment.

**Phase 2.** “Growth” phase—The species present in pelagic waters now enters the growth phase. The major parameters determining the growth rate at the cell level are the availability of light and inorganic nutrients, temperature, salinity, and in some cases turbulence. On the population level the population growth rate is a combination of the physiological growth process in combination with loss processes such as grazing, sedimentation (e.g., during encystment—vertical), and dispersion (horizontal and vertical).

**Phase 3.** “Bloom” phase—The species enters the bloom phase when it reaches a maximum concentration in time. This concentration or concentration level can be maintained for some time reaching from hours to months depending upon the bloom species. The maximum concentration can be regarded as a measure of the carrying capacity for the species in the specific system where the bloom occurs. Most often the bloom concentration is controlled by a combination of light availability and nutrient availability.

**Phase 4.** “Crash” or decay phase—The bloom is terminated during the bloom decline phase/crash phase. Decline of a bloom can be the result of increased grazing pressure, cease of growth due to lack of inorganic nutrients, encystment, interactions with bacteria and/or virus, and dispersion (e.g., due to a storm event). One or a combination of the abovementioned factors can cause the decay of the bloom.

The occurrence of algal blooms entails a general intensification of biological activity in the water body that is first and foremost related to zooplankton

grazing of algae, massive excretion of fecal pellets, bacterial decomposition of the latter and dead algal cells, generation of detritus, chemical and photochemical transformations of autochthonic organic matter, etc. The algal bloom areas not only become the main pastures for fish, but also the arena for developing detrimental processes of various gravity, such as rapid depletion of oxygen resulting in anoxic conditions in the euphotic zone (at least in its upper part) and egestion (excretion) of pernicious substances (sometimes toxic). In concert, they may lead to mortality of some aquatic organisms sensitive to such alterations of their habitat conditions.

Nevertheless, there are cases, which are progressively frequent throughout the world's oceans, where algal blooms are nearly *monospecific*. The outbreak of such algae is unusually intense, and produce really huge algal masses spread over large water areas. Such outbreaks, also called *harmful algal blooms*, are characterized by a wide variety of effects, including enhanced toxicity of water, water discoloration (produced by red tides, cyanobacterial blooms, and other species), clogging of fish gills by excessive algal biomass and mucilage, etc. This constitutes a wide spectrum of aftermath damage, the discussion of which follows this introduction.

## 1.2 HARMFUL ALGAL BLOOM SPECIES QUALIFICATION AND VARIETY

As mentioned briefly above, microscopic algae indigenous to the world's oceans are an indispensable/fundamental element of food web interactions inherent in aquatic ecosystems. They are food for herbivorous zooplankton, filter-feeding bivalve shellfish (such as oysters, mussels, scallops, clams), and the larvae of crustaceans and finfish. From this specific perspective, the enhanced development of microalgae (termed an "algal bloom") is natural, beneficial, and crucial for sustainability of living resources of marine and freshwater bodies (Pozdnyakov *et al.*, 1998), and, in the industrial epoch, is also advantageous for aquaculture.

However, in some cases outbreaks of microalgae can be *harmful*. Algal blooms qualify as harmful if they are associated with three general types of causative organisms producing (i) toxins, (ii) high biomass, and (iii) mucilage. To qualify as a harmful algal bloom (HAB) the species has to have characteristics of one or more of the above categories.

The abovementioned causative organisms are capable of triggering multifaceted and devastating ecological, health and sanitary, as well as economic impacts. Albeit highly detrimental, the impacts produced by these organisms remain limited in area and duration because of the unique capability of mother nature to combat such extreme bloom events. This is due to the ability of natural aquatic environments to restore the initial/intrinsic *status quo* through self-purification.

It should not be assumed that HABs are unprecedented modern phenomena intrinsically arising from contemporary anthropogenic influence or climate change. Indeed, perhaps the first mention of HABs, dating back to about 1000 years BC, can be found in the Bible "... all waters that were in the river were turned to blood. And the fish that was in the river died, and the river stank, and the Egyptians could not drink

*of the water of the river*" (Exodus 7: 20–21). This implies that in a strict sense harmful algae are completely natural phenomena, existing throughout recorded history. Being inherent to aquatic ecological systems, they play a specific role in the intricate system of natural hydrobiochemical interactions, and natural aquatic environments are intrinsically suitable to efficiently regulate this problem.

However, over recent decades, a worrisome trend in the steeply increasing incidence of HAB events in marine, coastal, and freshwater environments has been recorded throughout the world's oceans causing both water toxification (Figures 1.1–1.9, Anonymous, 2005a, b; for toxin-type abbreviations see Table 1.1) and discoloration, thus making the problem today one of the most pressing and challenging from the aforementioned perspectives.

Of the 4,000 species of extant marine microalgae/phytoplankton, some 300 species can at times proliferate in such huge numbers that they discolor the water surface (so-called "red tides"), while only about 80 species produce toxins (Sournia *et al.*, 1978; Dahl *et al.*, 1999; Hallegraeff, 2003). Mainly the phytoplankton is then a natural, crucial, and beneficial part of the marine food web, however a few species have toxic or harmful effects that need our attention to cope with.

Table 1.1 lists three major groups of HABs classified according to the nature of the detrimental effects they produce in aquatic ecology and, eventually, in humans.

### 1.3 ECOLOGICAL ASPECTS

The *ecological* impacts of HABs include mass mortalities of wild and farmed fish (the latter are particularly vulnerable and visible whereas wild fish often have the freedom to swim away from problem areas) and shellfish. They can also bring about human illness (respiratory or digestive tract problems, memory loss, seizures, lesions, and skin and eye irritation) and even death from consumption of contaminated shellfish or fish. HABs can be the cause of death of marine mammals (including such large animals as whales, sea lions, seals, otters, and dolphins) when receiving toxins through the food chain via contaminated zooplankton or fish. Poultry and wild seabirds (e.g., pelicans damaged by diatom domoic acid contained in anchovies), wild land animals and cattle (receiving drinking water contaminated by algal toxins) can also suffer and even die from HABs. The growing coastal tourism industry also suffers for direct or indirect impacts of HABs through people's selection of the "pure" recreation areas.

The harmfulness of HABs is not always directly associated with HAB high biomass: sometimes even low algal concentrations can cause serious detrimental effects given the high toxicity of the algae involved. On the other hand, only in rather exceptional cases does the water *per se* in bloom areas become toxic enough to present an appreciable danger for humans.

Importantly, the effects impairing aquatic ecology stem not only from trophic and respiratory mechanisms, but also from alterations of the subsurface light regime: light screening due to huge concentrations of HAB algae, release of exudates (including dissolved organic matter), formation of foam, relatively thin but highly dense

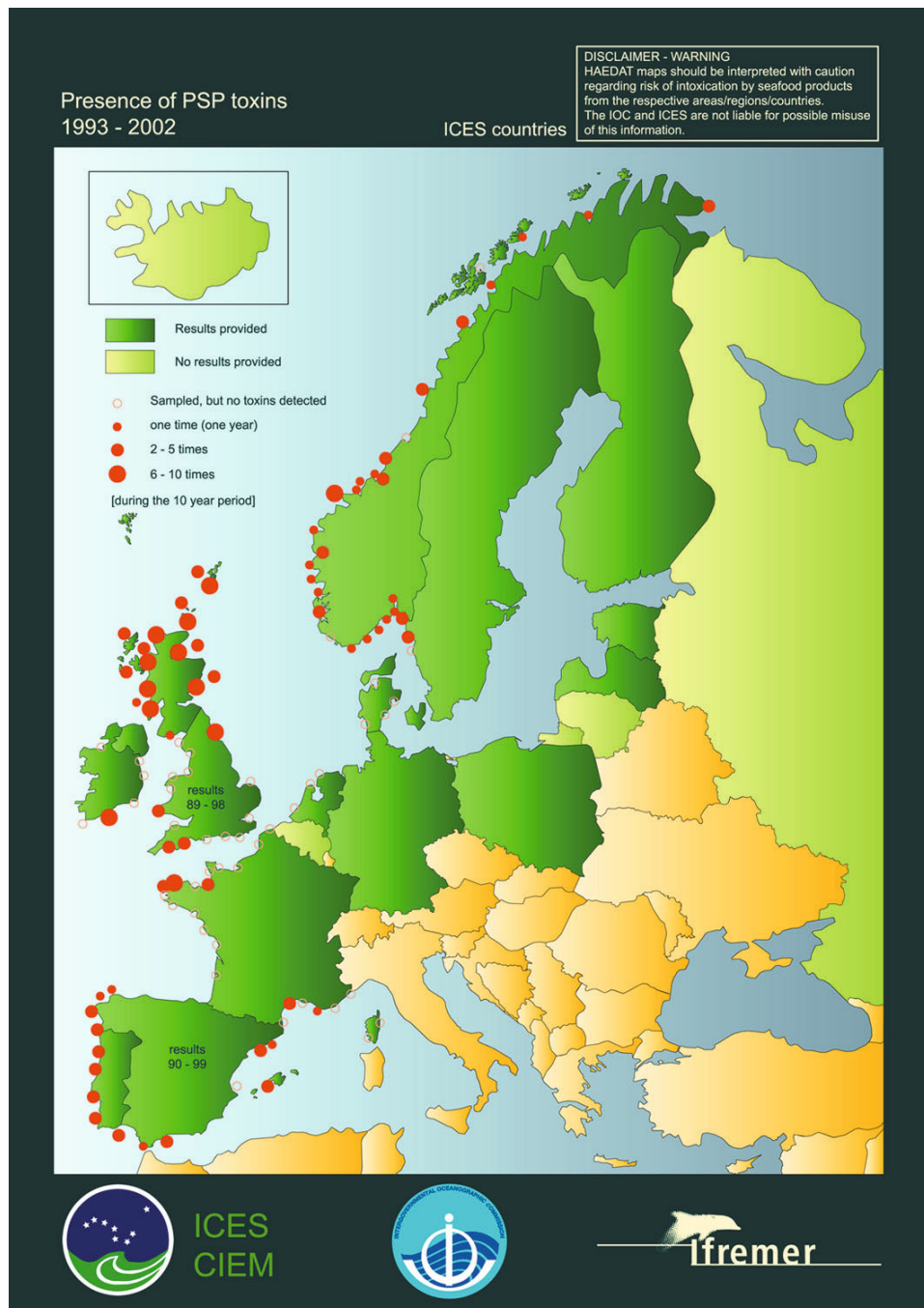


**Figure 1.1.** Presence of PSP toxins in 1993–2002 in European waters (<http://www.ifremer.fr/var/envlit/storage/documents/dossiers/ciem/Pdf/icesmaps.pdf>).

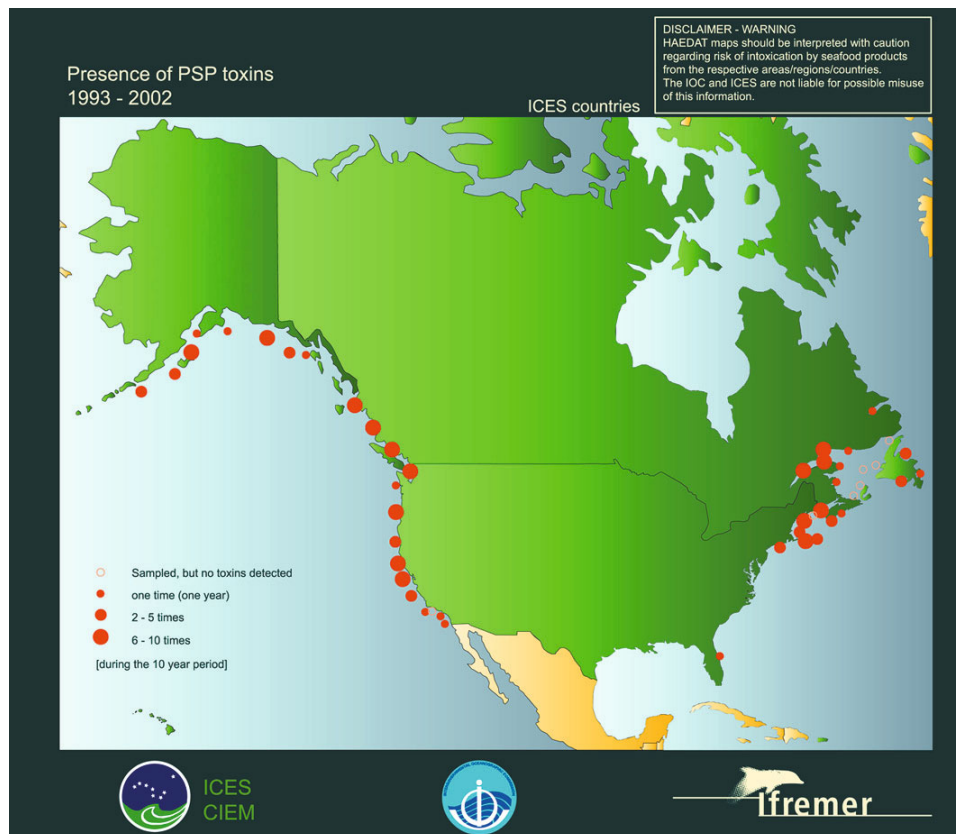


**Figure 1.2.** Presence of PSP toxins in 1993–2002 in North American waters (<http://wwz.ifremer.fr/var/envlit/storage/documents/dossiers/ciem/Pdf/icesmaps.pdf>).

films (at various depths within the euphotic zone), and scum on the water surface—all of these phenomena are bound to drastically reduce light availability in the water column and appreciably change its spectral composition (the aforementioned water discolouration).

This is highly consequential in terms of photosynthetic activity not only in phytoplankton but also in submerged aquatic vegetation and benthic communities. This constitutes an additional mechanism of HAB interference in water-dissolved oxygen and CO<sub>2</sub> regimes, inconveniencing and damaging coexisting hydro-flora and hydro-fauna. These forward propagating and feedback impacts are actually much more abundant, have more ramifications, and affect practically all levels of the aquatic ecosystem during both harmful and non-harmful algal blooms.

A combined effect of the above impacts of (H)ABs on the aquatic environment is thought to further lead to a loss in *biodiversity* as a result of removing the food web interactions of such species, for which altered living conditions become untenable.

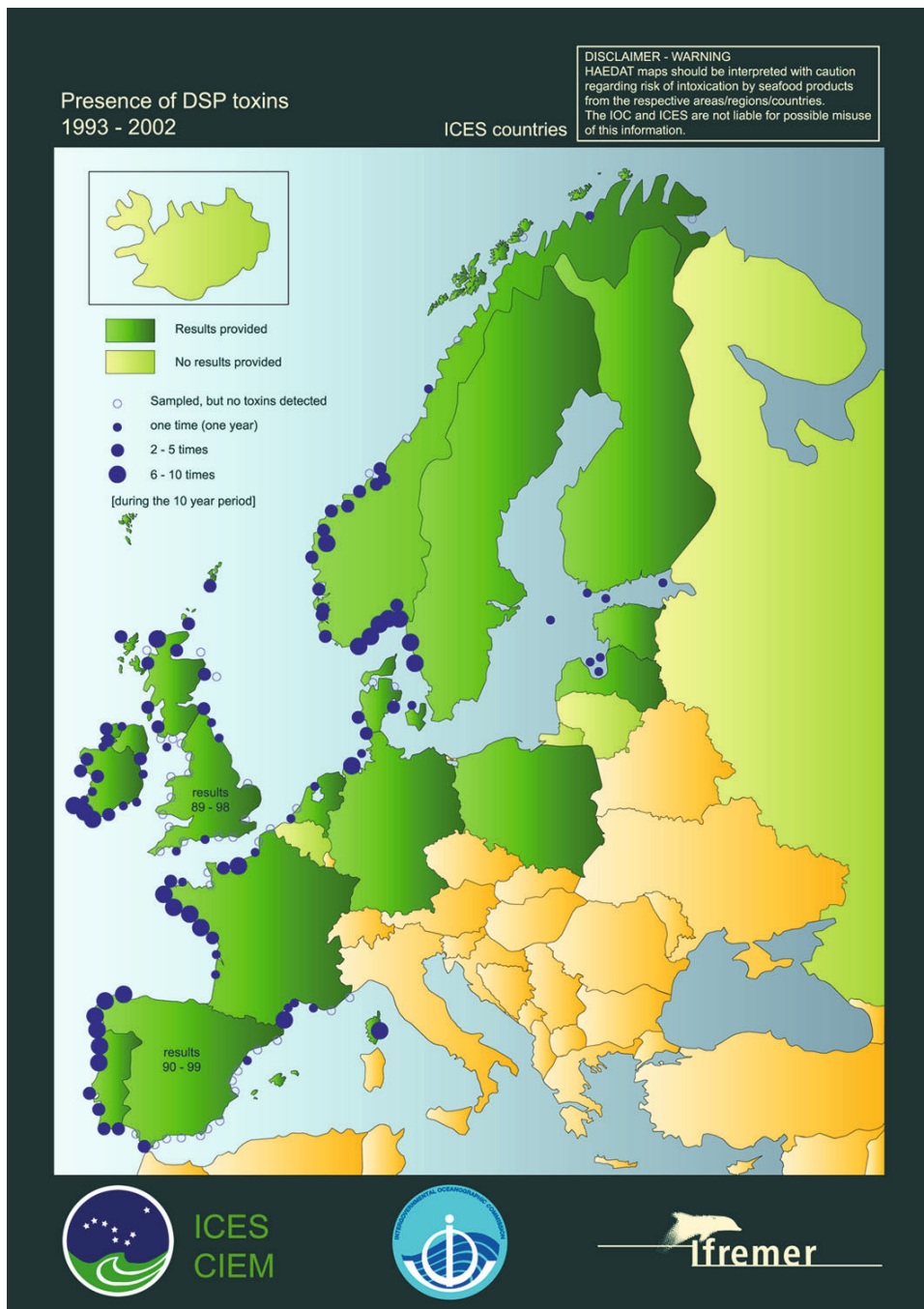
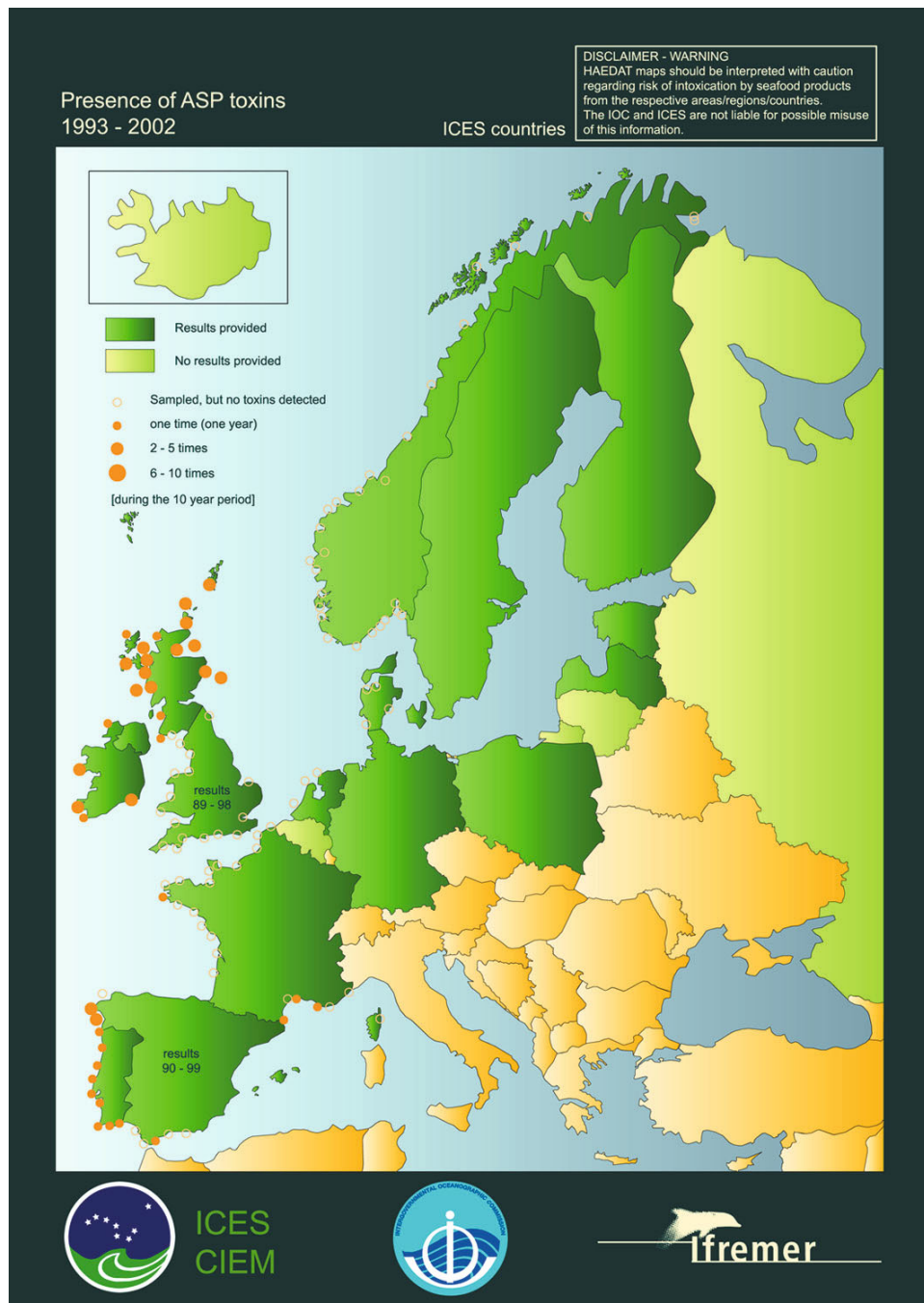
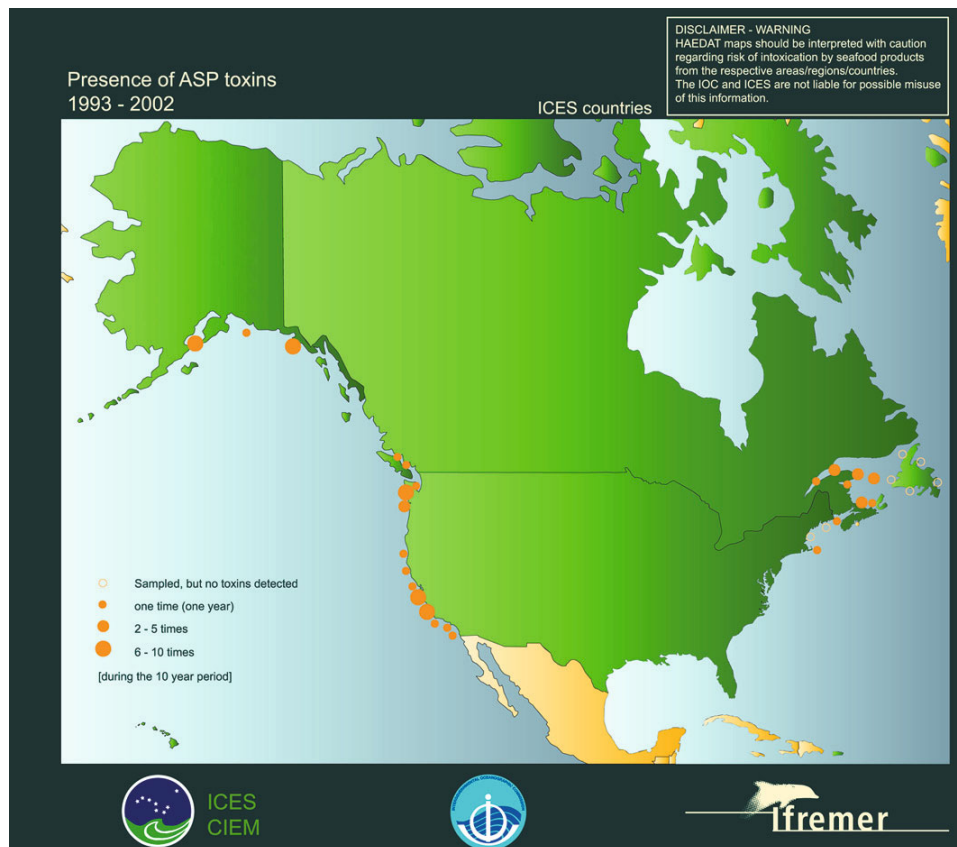


Figure 1.3. Presence of DSP toxins in 1993–2002 in European waters (<http://www.ifremer.fr/var/envlit/storage/documents/dossiers/ciem/Pdf/icesmaps.pdf>).



**Figure 1.4.** Presence of ASP toxins in 1993–2002 in European waters  
<http://www.ifremer.fr/var/envlit/storage/documents/dossiers/ciem/Pdf/icesmaps.pdf>)



**Figure 1.5.** Presence of ASP toxins in 1993–2002 in North American waters (<http://wwz.ifremer.fr/var/envlit/storage/documents/dossiers/ciem/Pdf/icesmaps.pdf>).

## 1.4 FOOD SAFETY, HEALTH, AND SANITARY ASPECTS

The *health and sanitary aspects* of HABs have already been partially mentioned. In this context, it is worth emphasizing that the consumption of food (not solely seafood, but also other foodstuffs that through food chain reactions become contaminated with toxic substances, see above) contaminated by algal toxins at low to moderate levels could mean longer term chronic exposure of the populace, with immediate or delayed health consequences (Anonymous, 2003b).

There is solid evidence (in support of previous reports such as Falconer, 2005) that cyanobacteria cells (such as *Microcystis aeruginosa* and *Anabaena flos aquae*) pass through drinking water filters after sudden increases in hydraulic loading rates (Dugan and Williams, 2006). Similar problems are encountered at drinking water treatment plants in Australia (Hoeger *et al.*, 2004), North America (Knappe *et al.*, 2004), Germany (Bernhardt, 2005), and many other countries. This toxin infiltration

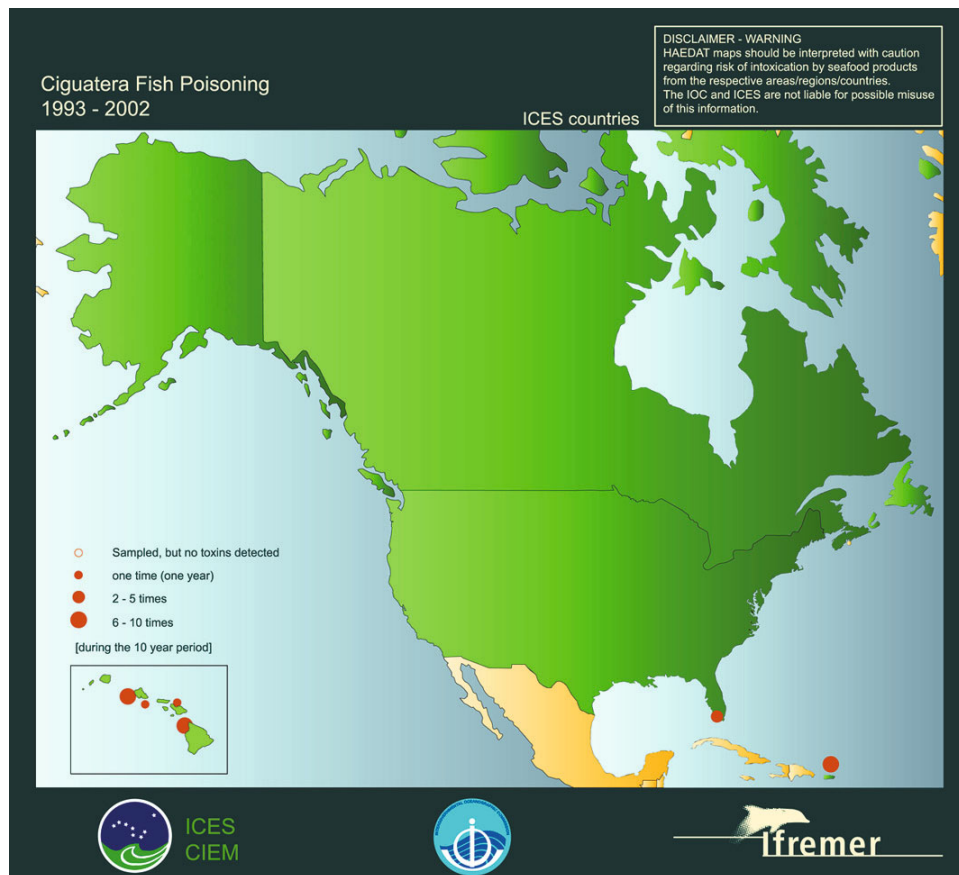


**Figure 1.6.** Presence of *Ciguatera* toxins in 1993–2002 in North American waters (<http://wwz.ifremer.fr/var/envlit/storage/documents/dossiers/ciem/Pdf/icesmaps.pdf>).

has been acknowledged as a serious sanitary and health threat requiring continuous monitoring and preventive/mitigating measures.

Foul-smelling masses of dead and decaying microalgae and extensive foam accumulations on beaches and shorelines create, in addition to recreation-related problems, serious sanitary problems, because of rapid development of pathogenic organisms and insects, the latter being carriers of harmful bacteria. In some countries the fish catch, when found untenable for consumption, ends up being dumped and provokes similar sanitary problems (Anonymous, 2003c).

Often associated with dinoflagellates (e.g., such floating algae as *Dinophysis fortii*, *D. acuminata*, *D. acuta*, *D. norvegica*, *D. mitra*, *D. rotundata*, and benthic *Prorocentrum lima*), diarrheic shellfish poisoning (DSP) causes serious problems for scallop, shellfish, and mussel fisheries. Ailment symptoms are frequently mistaken for bacterial gastric infections, so the problem may be far more widespread and

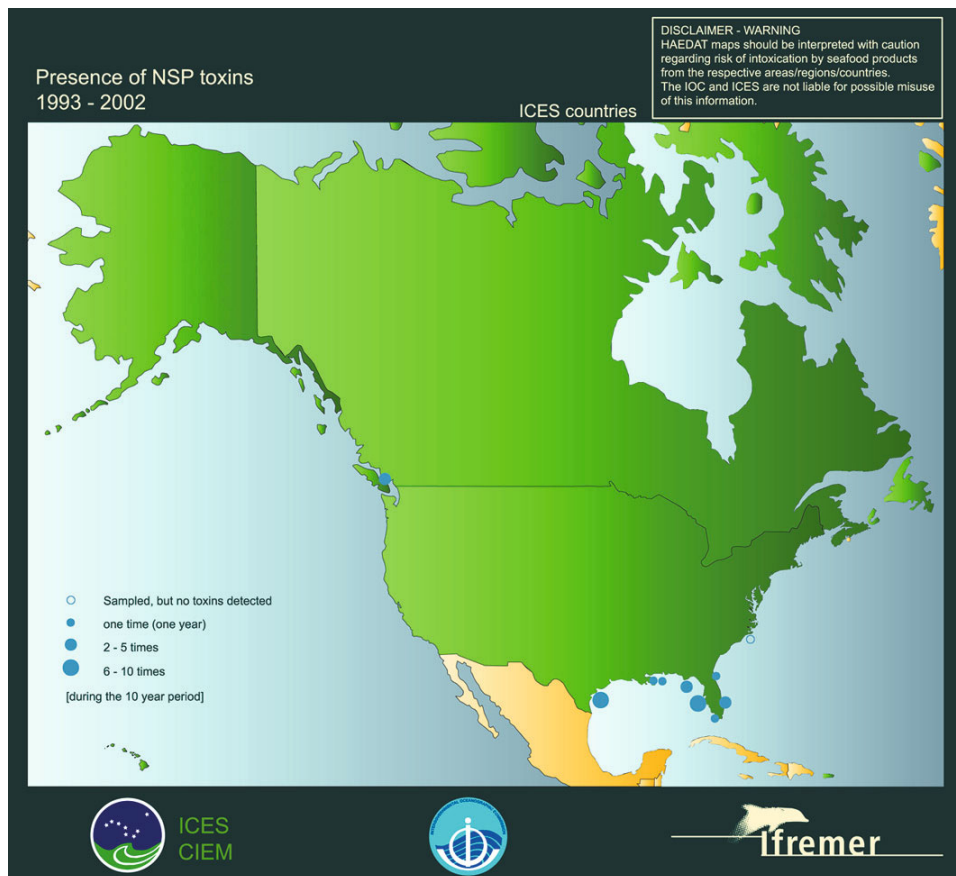


**Figure 1.7.** Presence of NSP toxins in 1993–2002 in North American waters (<http://wwz.ifremer.fr/var/envlit/storage/documents/dossiers/ciem/Pdf/icesmaps.pdf>).

serious than previously assumed. Some of the polyether toxins involved reportedly promote stomach tumors (for references see Anonymous, 1995). Shellfish containing more than 2 µg of okadaic acid and/or 1.8 µg of dinophysis toxin per gram of seafood are considered unfit for human consumption. The known distributions of *DSP* include Japan, Europe, Chile, Thailand, Canada (Nova Scotia), Australia (Tasmania), and New Zealand (see also Figures 1.3 and 1.9).

The first recognized case of *amnesic shellfish poisoning (ASP)* occurred in Canada, where it caused several deaths and more than 100 cases of acute health problems (such as abdominal cramps, vomiting, disorientation, and memory loss/amnesia) as a result of consumption of blue mussels. The causative toxins (e.g., domoic acid) is produced by diatoms (such as *Pseudonitzschia multiseries*, *P. pseudodelicatissima*, *P. australis*, *P. seriata*, and *P. delicatissima*).

Shellfish containing domoic acid in excess of 20 µg per gram of shellfish meat are considered unfit for human consumption. Reports of domoic acid in seafood

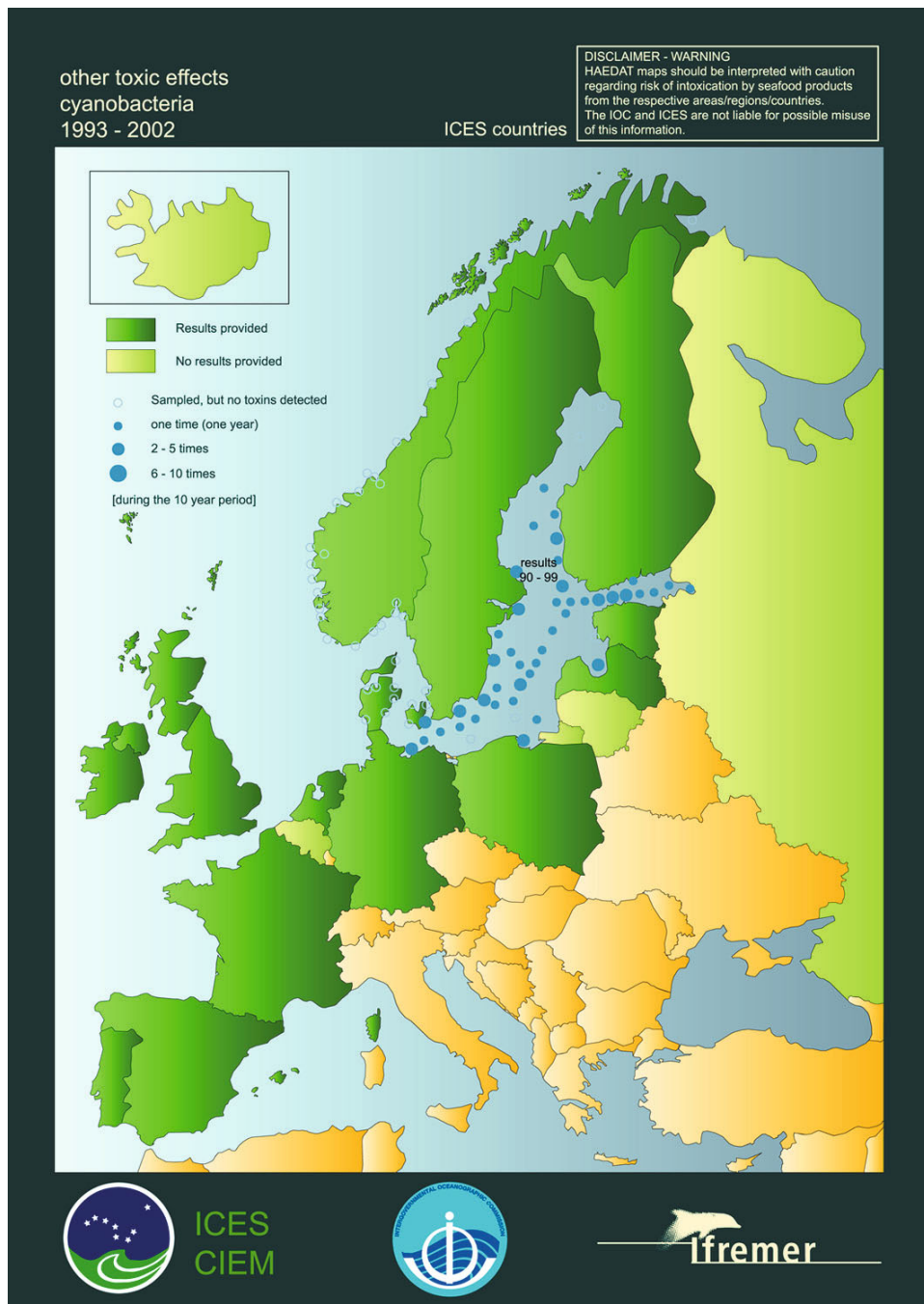


**Figure 1.8.** Presence of cyanobacteria and other toxins in 1993–2002 in European waters (<http://wwz.ifremer.fr/var/envlit/storage/documents/dossiers/ciem/Pdf/icesmaps.pdf>).



**Figure 1.9.** Presence of DSP toxins in 1993–2002 in North American waters (<http://wwz.ifremer.fr/var/envlit/storage/documents/dossiers/ciem/Pdf/icesmaps.pdf>).

products have come mostly from North America, Canada, and only marginally from Europe, Australia, Japan, and New Zealand (Figures 1.10 and 1.11).

Many food safety problems are associated with the ever-increasing utilization of coastal waters for agriculture. Interestingly, aquaculture sites can act as testbeds or bioassay systems, which due to continuous and thorough control of the health status of farmed organisms are efficient indicators of proliferation of harmful species/problem organisms not known to exist there before and producing either *PSP*, *DSP*, *NSP*, or *ASP* effects or damaging gills (such as caused by the diatoms *Chaetoceros convolutes* and *C. concavicornue*).

Caged fish death may equally be caused by capillary hemorrhage, dysfunctions of gas exchange at the gills, suffocation from mucus, and secondary infection of damaged tissue (Anonymous, 1995). Gill tissue is reported to be particularly vulnerable to fatty acids, which eventually destroy red blood cells. Such algal species as

**Table 1.1.** Types of algae proliferating into HABs (Anonymous, 1995).

<i>Major effect</i>	<i>Some responsible organisms</i>
<p>Species that produce basically harmless water discolorants, but, under exceptional conditions, capable of growing so dense that they cause indiscriminate killing of fish and invertebrates due to oxygen depletion</p>	<p>Dinoflagellates:  <i>Gonyaulax polygramma</i>  <i>Noctiluca scintillans</i>  <i>Scrippsiella trochoidea</i></p> <p>Cyanobacterium:  <i>Trichodesmium erythraeum</i></p>
<p>Species that produce potent toxins that can find their way through the food chain to humans, causing a variety of gastro-intestinal and neurological illnesses:</p> <p>(a) Paralytic shellfish poisoning (PSP)</p> <p>(b) Diarrheic shellfish poisoning (DSP)</p> <p>(c) Amnesic shellfish poisoning (ASP)</p> <p>(d) Ciguatera fish poisoning (CFP)</p> <p>(e) Neurotoxic shellfish poisoning (NSP)</p> <p>(f) Cyanobacterial toxin poisoning (CTP)</p>	<p>Dinoflagellates:  <i>Alexandrium acatenella</i>, <i>A. cohorticula</i>,  <i>A. fundyense</i>, <i>A. franterculus</i>, <i>A. minutum</i>,  <i>A. tamarensis</i>, <i>Gymnodinium catenatum</i>,  <i>Pyrodinium bahamense</i> var. <i>compressum</i></p> <p>Dinoflagellates:  <i>Dinophysis acuta</i>, <i>D. acuminata</i>, <i>D. fortii</i>,  <i>D. norvegica</i>, <i>D. mitra</i>, <i>D. rotundata</i>,  <i>Prorocentrum lima</i></p> <p>Diatoms:  <i>Pseudonitzschia multiseries</i>,  <i>P. pseudodelicatissima</i>, <i>P. australis</i></p> <p>Dinoflagellates:  <i>Gambierdiscus toxicus</i>, <i>Osteopsis</i> spp.,  <i>Prorocentrum</i> spp.</p> <p>Dinoflagellates:  <i>Gymnodinium breve</i>, <i>G. cf. breve</i></p> <p>Cyanobacteria:  <i>Anabaena circinalis</i>, <i>Microcystis aeruginosa</i>,  <i>Nodularia spumigena</i></p>
<p>Species that are non-toxic to humans, but harmful to fish and invertebrates by damaging (either mechanically or through production of hemolytic substances) or clogging their gills (also through production of mucilaginous substances that can also be toxic for aquatic animals)</p>	<p>Diatoms:  <i>Chaetoceros convolutes</i></p> <p>Dinoflagellates:  <i>Gymnodinium mikimotoi</i>,  <i>Prorocentrum minimum</i></p> <p>Prymnesiophytes:  <i>Chrysochromulina polylepis</i>,  <i>Prymnesium parvum</i>, <i>P. patelliferum</i>,</p> <p>Raphidophytes:  <i>Heterosigma carterae</i>, <i>Chattonella antiqua</i></p>

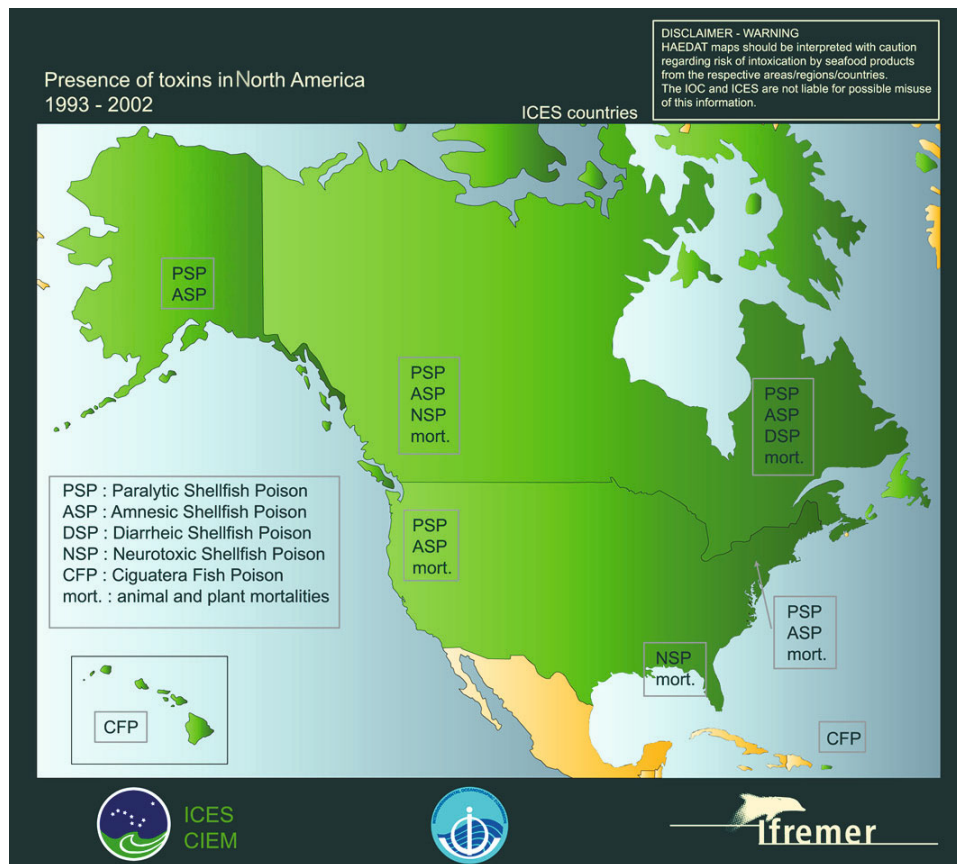
the Raphidophytes (e.g., *Heterosigma carterae* and *Chattonella antica*) and the Prymnesiophytes (e.g., *Chrysochromulina polylepis* and *Prymnesium parvum*) are implicated in this respect. The major problem in all the above cases resides in the fact that unhealthy caged fish are highly vulnerable to pathogenic bacteria and, having been supplied to consumers, can also cause human health problems, not readily associative with consumed cultured seafood. Such secondary causative relationships are often overlooked (for references see Anonymous, 1995). In addition, direct fish mortality is a major problem for the aquaculture industry.

*Ciguatera fish poisoning (CFP)* contaminates such fish as red bass, chinaman fish, moray eel, paddle tail, and some others as a result of benthic dinoflagellates such as *Gambierdiscus toxicus* and the like living not only in epiphytic association with seaweeds but also occurring in sediments and coral rubble. Although originally indigenous to tropical oceanic environments, there is evidence that the *CFP*-producing algae begin expanding mostly as a result of reef disturbance by more frequent and strong hurricanes, human (e.g., tourism) developments resulting in providing benthic substrate for these algae to grow (Sellner *et al.*, 2003). It appears reasonable to hypothesize that, with ongoing climate warming, the geography of habitats of *CFP*-implicated algae can expand to more northern latitudes.

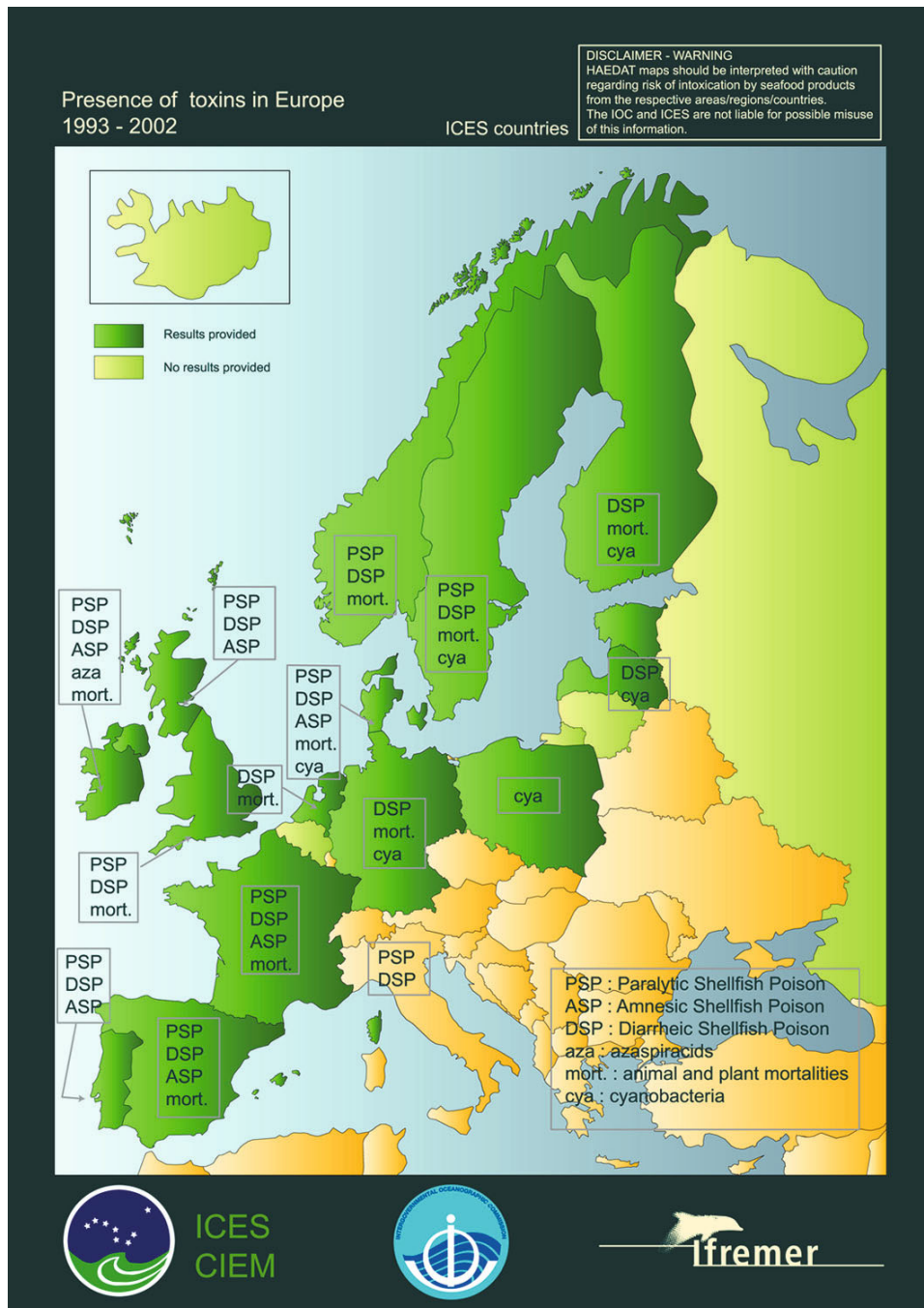
*Neurotoxic shellfish poisoning (NSP)* produced by the unarmored dinoflagellate *Gymnodinium breve* was mainly endemic to the Gulf of Mexico and the east coast of Florida, where “red tides” had been reported as early as the middle of the 19th century. One of the human health-impairing effects associated with such blooms is the generation of toxic aerosols formed by wave action and provoking respiratory asthma-like symptoms (for references see Anonymous, 1995). Later, red tides became common off the coast of North Carolina as a result of entrainment by the Gulf Stream. Surprisingly, in the early 1990s, an organism akin to *Gymnodinium breve* caused more than 180 human shellfish poisonings in New Zealand. It is conjectured that this algae used to be only a marginal taxon present in low concentrations, but has since developed into bloom proportions as a result of a triggering mechanism that has now been identified.

In previous decades, the *paralytic shellfish poisoning (PSP)* effects due to the dinoflagellate *Gymnodinium catenatum* were typical of ocean habitats at low latitudes in the Northern Hemisphere. In Europe, these algae were the source of human health problems that were almost exclusive to the Mediterranean and the Atlantic coast of Spain, Portugal, and Morocco. But there are serious reasons to expect that with the onset of favorable conditions (e.g., evolving global warming) this dinoflagellate can generate harmful blooms even in such a northern marine environment as the North Sea: fossil cysts of this species (which had survived the Little Ice Age) have recently been detected in bottom sediments within the region extending from the Danish coast and German Bight up to southern Scandinavia.

Another pathway of locally introduced HAB species is associated with increased ship transport and their discharge of ballast water in coastal areas, which is presently illegal and strictly regulated through international agreements within the International Maritime Organization (IMO). “Alien” algal/bacterial



**Figure 1.10.** Reported areas suffering from toxins in 1993–2002 in European (opposite page) and North American waters (<http://wwz.ifremer.fr/var/envlit/storage/documents/dossiers/ciem/Pdf/icesmaps.pdf>).



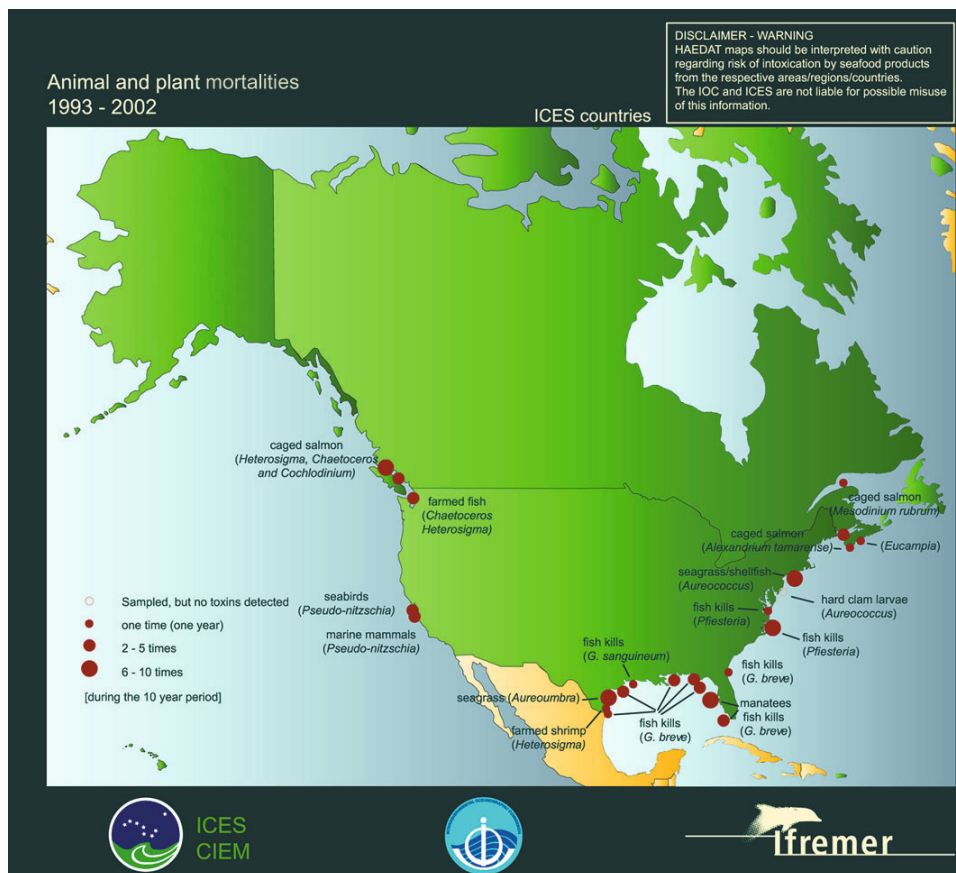
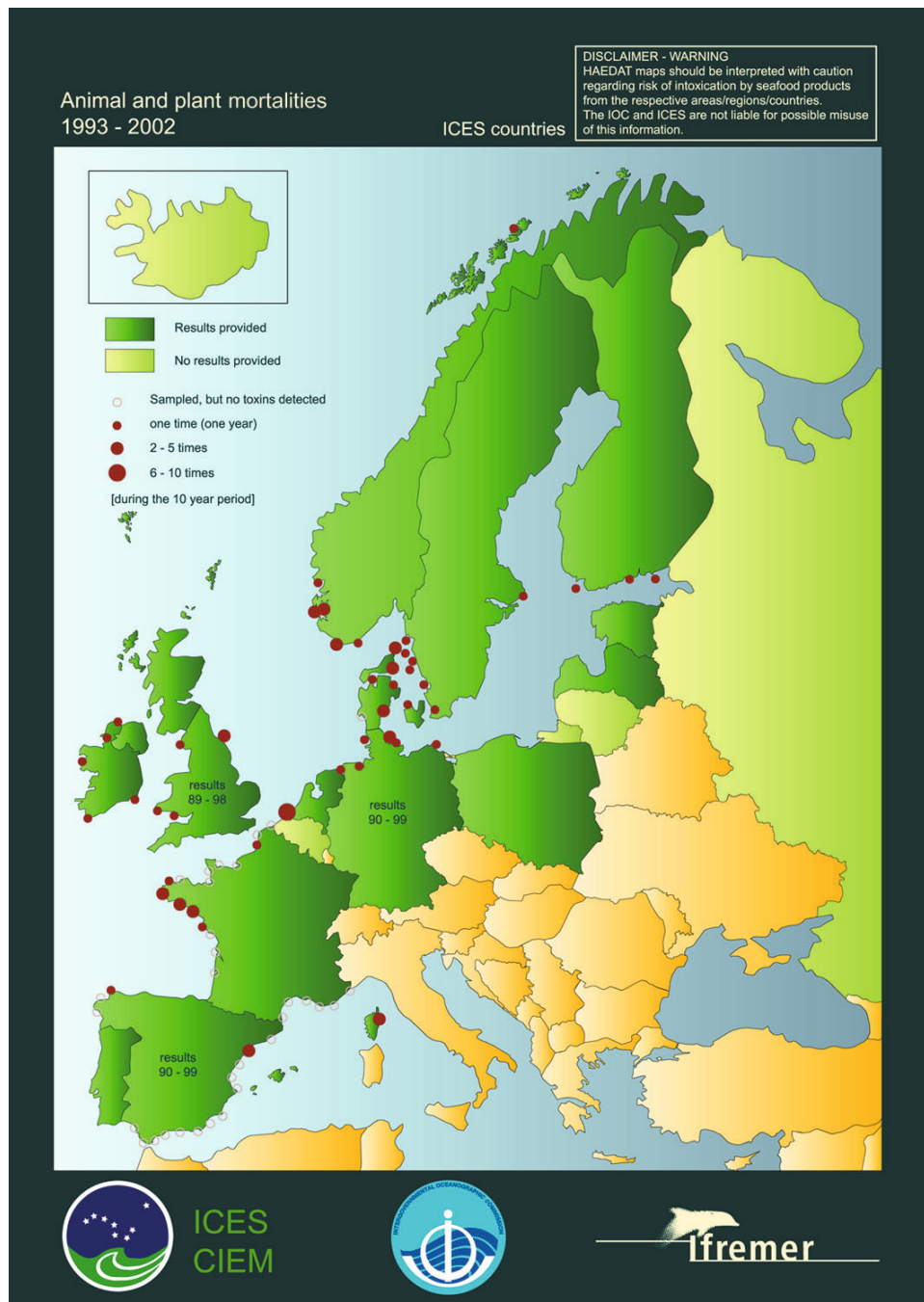


**Figure 1.11.** Reported animal and plant mortalities in 1993–2002 in European (opposite page) and North American waters (<http://wwz.ifremer.fr/var/envlit/storage/documents/dossiers/ciem/Pdf/icesmaps.pdf>).



species enter the ambient aquatic environment in discharged ballast water and, as newcomers, may well be immune to the local trophic interactions and begin to rapidly proliferate.

## 1.5 ECONOMIC ASPECTS

The *economic aspects* of HAB impacts on wild fishery, aquaculture, commercial tourism, and more generally human welfare are multifaceted and of major concern.

The welfare level of society at time  $t$ ,  $W$  is a sum of two principal components: namely, producers' and consumers' surplus,  $PS$  and  $CS$ , respectively. The change in economic welfare is accordingly the sum

$$\Delta W = \Delta PS + \Delta CS \quad (1.1)$$

where  $\Delta PS$  is a measure that expresses how much the input factors (i.e., labor and capital) *de facto* earn over or beyond the best alternative allocation of productive resources.  $\Delta CS$  is a measure that expresses the difference between what consumers are willing to pay for the good and what they actually pay for it in the market. Thus, the welfare changes induced by HABs can be assessed by estimating respective changes in economic welfare,  $\Delta W$ .

Lorentzen and Pettersson (2005) have shown through their analyses that when industry is a price-taker (i.e., taking price as a constant), a significant cost induced by a HAB event will reduce  $\Delta PS$ . However, when *aggregated* industry can in some way affect the market price, the net effect is ambiguous: on the one hand, the HAB event reduces the quantity supplied, and the reduction increases the market price. On the other hand, the HAB event increases production costs at any level of production. Thus, it appears impossible to conclude *a priori* whether the increased revenue effect is bigger or smaller than the increased production costs if the value of demand elasticity is not known. For instance, the shellfish industry can occasionally be stopped temporarily or even closed down because of shellfish poisoning, and harvesting of the shell can be postponed until the shell becomes poison-free, and income is not necessarily irretrievably lost, but postponed.

However, by all accounts the increased revenue must be too small to compensate for the negative cost and quantity effect. In situations where the industry has accumulated value during the production process, the loss equals the market value of the lost fish.

Nevertheless, a HAB event can also cause disease as a result of consumption of tainted seafood or contaminated drinking water. This is bound to induce a set of costs (e.g., medication and hospitalization costs, transportation costs, loss of worker productivity as a result of his/her absence from work). Leaving deaths out of account, a rough estimate of the economic costs of illness ( $C$ ) of  $n$  persons is a sum of two components:

$$C = \sum_{i=1}^n w_i t_i + \sum_{i=1}^n M_i \quad (1.2)$$

where  $w_i$  = sick person's wage rate per day (reflecting the market value including taxes such as VAT);

$t_i$  = number of work days lost by the sick person (assuming that this number is less than one year);

$M_i$  = costs of medical treatment for the sick person.

As an example, consider the case of socio-economic effects driven by *DSP* toxins in Norwegian waters. Through July to October 2002 between 200 and 300 persons were seriously poisoned by eating contaminated brown crabs (*Cancer pagurus*). The crabs had a high concentration of the *DSP* toxin as a result of their eating shellfish, which in turn had been feeding on toxic algae. According to statistical data, on average, the labor cost per hour in Norwegian industry was between about NOK180 (Norwegian kroner) and NOK200 in 2000. Assuming that the work day duration is 7.5 hours and 250 persons became ill over three days, the economic cost proved to be significant and amounts to  $C = 250 \cdot 180 \cdot 7.5 \cdot 3 \approx$  NOK 1,000,000 or about U.S.\$100,000.

In addition, immediately after the poisoning epidemic, sales of brown crabs dropped dramatically bringing about an inevitable reduction in fishermen's income, the latter proving to be much higher than costs associated with the economic costs. The cost of medical treatment was not reported, but presumably constituted between NOK180,000 and NOK200,000.

The market price is a monetary measure of what the marginal consumer is willing to pay for the good. However, there exist non-marketable goods that are not priced in the market; for example, the recreational value of a lake or a public area. Harmful algal blooms can cause damage to goods that are not sold in a market. We use the "willingness-to-pay" method in estimating the monetary value of non-marketable goods. In general, the monetary value of a good can be estimated from the consumer's willingness-to-pay (WTP). There are two approaches to ascertain this: directly asking people about their WTP and indirectly deriving the WTP by analyzing people's behavior when buying private goods. People's relationship with, and evaluation of, the environment has two aspects: a *use relation* and a *non-use relation*. The *use value* refers to situations where people physically use or have the intention of using the environment (e.g., the recreational value of fishing, bathing/swimming/surfing, boating, etc.). The *non-use* value refers to the (altruistic) value of preserving the environment for both present and future generations. Of course, the direct approach to deriving the WTP can estimate both *use* and *non-use* values.

Here is another example from Norway. Environmental studies based upon the WTP method started in the early 1980s. Strand (1981) analyzed the effects on people's welfare brought about by acid rain from the perspective of the damage done to water quality and recreational fishing. Estimating the WTP to avoid total extinction of freshwater fish in Norway over a period of 10 years, he worked out that the average WTP would be between about NOK1,700 to NOK2,750 per year per person older than 15 years.

During the period 1981–1991, 11 studies into the recreational value of freshwater and marine water angling have shown the average recreational value (*use value*) per

angling day to be about 185 NOK. According to two case studies of *non-use values* of freshwater fish stocks (Navrud, 1992), the WTP values varied between NOK120 and NOK48 depending on the study site location. These figures provide an insight into people's evaluation of the environment. However, it can be presumed that people's expectations for the quality of environment are presently much higher compared with those dating back to the early 1980s and 1990s (i.e., the time period of the cited studies).

During the last 15–20 years there have been several reports reflecting systematic assessments of the different effects induced by HABs. In 2001 there was a very significant vernal outbreak of *Chattonella* and *Heterosigma* in the Skagerrak. Salmon farmers lost about 1,100 tons of fish. Estimates of  $\Delta PS$  indicated that the loss in producers' surplus was NOK25,500,000 (given the market price of salmon, NOK25 per kilo, at that time).

The Norwegian Directorate for Fishery reported that the loss of farmed salmon due to harmful algae and/or jellyfish in 1999 was as high as 178,000 individuals. With the average weight of the fish of about 1.69 kg, and the average price NOK21.62/kg in that year, the estimated loss in producers' surplus was  $\Delta PS = \text{NOK}6,500,000$ . In 2001 the analogous loss for salmon constituted already NOK43,600,000. In 2002, this figure for trout was as high as NOK100,000,000. During 2004, the cumulative loss as a result of HAB for salmon and trout proved once again to be close to NOK40,000,000. It was reported that there was a huge loss of farmed salmon (about 650 tons) in June 2005 due to a *Heterosigma* bloom in southern Norway. Two plants were hit, and the associated loss,  $\Delta PS$ , was assessed at NOK13,000,000.

In May 1998, *Chattonella* spp. caused a loss of about 350 tons of farmed salmon in the area around Farsund and Flekkfjord in southern Norway. It was the first time that *Chattonella* had been registered in such high and harmful concentrations causing fish mortality. The economic loss,  $\Delta PS$ , was estimated at NOK12,800,000.

In the United States the annual economic impact from HABs during the 4-year period (1989–1992) has been assessed (Anderson, D. M. *et al.*, 2000) and grouped into four major impact categories: public health, commercial fishery, recreation and tourism, and monitoring and management cost. [Table 1.2](#) summarizes these results. Assessed *total* costs for this period is U.S.\$49,000,000 per year, with public health costs accounting for the largest portion.

The socio-economic effects of HABs in various European marine waters as revealed in the course of case studies are illustrated in [Table 1.3](#) (after Scatasta *et al.*, 2004).

Annually averaged costs driven by HABs across the entire European marine tract were even more significant ([Table 1.4](#)).

As illustrated in [Table 1.4](#), the greatest losses are associated with the tourism sector, followed by consumer losses in the mussel aquaculture sector. The country with the heaviest losses appears to be Spain closely followed by France and Italy (Norway was not included in the above study). It should also be pointed out that over 70% of the losses in the mussel sector are losses in consumer surpluses.

A final example comes from Asia. In China, during fall 1998, the largest HAB events occurred in the Bohai Sea, affecting an area of about 8,000 km<sup>2</sup> and caused

**Table 1.2.** Estimated annual economic losses from HABs in the United States (estimates are from the 1987–1992 period, reported in U.S.\$) (Anderson, D. M. *et al.*, 2000).

Loss category	Costs			
	Low	High	Average	% of total
Public health	18,493,825	24,912,544	22,202,597	45
Commercial fishery	13,400,691	25,265,896	18,407,948	37
Recreation/Tourism	—	29,304,357	6,630,415	13
Monitoring/Management	2,029,955	2,124,307	2,088,885	4
<i>Total</i>	<i>33,924,471</i>	<i>81,607,104</i>	<i>49,329,845</i>	<i>100</i>

**Table 1.3.** Socio-economic effects from HABs in selected European marine waters (Anderson, D. M. *et al.*, 2000).

Geographical region	Economic sector	Welfare effects due to HABs: $\Delta W = \Delta PS + \Delta CS$
Galicia (Spain)	Mussel aquaculture sector	Between €56m and €255m per year (based on case studies during the period 1989–1998)
Rimini (Italy)	Mussel aquaculture sector	€1.7m per year
Riccione (Italy)	Tourism sector	€0.9m to €4.8m per year
Galway (Ireland)	Tourism sector	€8.8m to €16.1m per year
North-Holland (The Netherlands)	Tourism sector	€9.6m to €16.8m per year
Hanko (Finland)	Tourism sector	€85,000 to €538,000 per year
La Pradet, Hyères, and Carqueiranne (France)	Tourism sector	€400,000 to €433,000 per year

**Table 1.4.** Socio-economic impacts of HABs in European marine waters at the turn of the 21st century (annually averaged, in €m) (Anderson, D. M. *et al.*, 2000).

Public health	Commercial fishery	Recreation and tourism (for 2000)	Monitoring and management	Total welfare effects $\Delta W = \Delta PS + \Delta CS$
0.12	158	687 <sup>a</sup>	19	864

<sup>a</sup>Assuming that about 40% of coastal visitors have experienced the impact of HABs.

the biggest economic loss by killing fish and seriously damaging aquaculture. The accumulated economic loss was assessed at about RMB1 billion (for references see Tang *et al.*, 2003, 2004).

These are but a few of the many examples that could be given, as HABs are reported not only from Europe, the U.S.A., and China, but also from India, Polynesia, Australia, the Middle East, and Latin America.

## 1.6 CONCLUDING REMARKS

The discussions in the above sections provide convincing evidence of the significant and highly harmful effects produced by HABs, from various perspectives ranging from aquatic ecology to human health and the socio-economic dimension. Given their possibly omnipresent and increasing occurrence throughout the world's oceans, the HAB phenomenon requires serious attention, more extensive and intensive investigations, and efficient monitoring, skillful forecasting, and possible development of effective mitigation actions.

A number of activities are presently underway. Operational systems have already been developed that are subject to continuous improvement as a result of satellite sensors and new pioneering methodological techniques (e.g., Robinson *et al.*, 2008). An *integrated* approach to operational HAB monitoring is presently acknowledged as a most promising way of tackling HAB problem management issues, which is our focus in Chapter 4.

It is clear that efficient and timely early detection of HABs and further surveillance of HAB spatial and temporal dynamics—in addition to fundamental studies of HABs *per se*, initiating/triggering mechanisms, and intrinsic and highly complicated pathways of interaction with the ambient environment—are urgently needed for prevention of the associated major damage discussed above. Because HABs are (i) synoptic-scale events and their occurrence is not necessarily repetitive (at least in terms of their intensity) and (ii) often temporally and spatially sporadic, the use of traditional shipborne observations/water sampling/laboratory analyses can hardly in isolation be considered an operational solution. Therefore, the integrated use of airborne and spaceborne sensors operating in the optical spectral region, *in situ* monitoring, and marine ecosystem prediction models are necessary for efficient management of HAB events in coastal waters.

Nevertheless, what remote-sensing methods in this respect are really capable of is not yet confidently established and remains debatable. In an attempt to better elucidate these issues, later chapters address the following subjects in detail: the optical properties of harmful algae (Chapter 3); the potential and inherent limitations of optical remote sensing of such phenomena (Chapter 4); and the development of operational algorithms and pilot practical applications (Chapter 5).

Before directly addressing these issues, however, we precede them by a dedicated chapter discussing the salient features of (H)ABs and the nature of internal and external forcing that controls their initiation, development, and eventual demise—see Chapter 2.

# 2

## Biology and ecology of harmful algal species

As discussed in Chapter 1, harmful algal bloom (HAB) problems are associated primarily with two general types of causative organisms: namely, toxin producers and high-biomass producers—some organisms have attributes of both groups. Importantly, toxin producers may lead to harmful consequences even when present in low cell concentrations (Sellner *et al.*, 2003) whereas the impact of algae of the second group only has ecological consequences when their proliferation attains exceptionally high levels (Glibert *et al.*, 2001).

It is acknowledged that the expression of HABs is a function of the physics and environmental controls acting on the HAB species, and from this perspective HABs must be considered as a *systematic–ecological* phenomenon.

There are a number of different and sometimes competing factors that promote preferable growth conditions for a specific group of HAB algae. These factors encompass the natural variability of hydrodynamics, light availability, nutrient loading, individual algal physiological and behavioral patterns, trophodynamic interactions/changes in the grazing community, anthropogenic eutrophication, and, allegedly, global change processes. Further, this combination of factors leads to specific HAB bloom events that, by and large, are generally *monospecific* (although in many cases what was formerly considered a single species is in fact a mixture of genetically similar strains of that species) (Anonymous, 1995).

In the context of the aquatic *ecosystem* approach, open coastal and basin-scale systems are generally those that are more likely controlled by meso-scale to large-scale physical processes as opposed to enclosed or semi-enclosed systems (Filatov *et al.*, 2005). Thus, understanding the dynamics of HABs in these dynamic systems may require close consideration of intimate interactions of in-water biophysical and geochemical processes, as well as external forcing stemming from either direct anthropogenic or climate change impacts/mechanisms.

## 2.1 ROLE OF HYDRODYNAMICS

Open coastal regions (OCRs) prone to HAB events often have narrow and steep upwelling-dominated regions, as is the case, for example, along the Pacific coast of the U.S.A. and the Atlantic coast of Spain and Portugal. The main function of upwelling movements is the migration of nutrient-rich deep waters into the euphotic zone and promoting conditions for intensive growth of algae there.

On the other hand, there are OCRs frequently or occasionally plagued by HABs where upwelling is *not* a dominant feature, as is found in the broad North Sea region such as Skagerrak and Kattegat (Johannessen *et al.*, 2006; Bratbak *et al.*, 2011) as well as in regions subject to buoyancy-driven currents moving, for example, along the Norwegian Atlantic Coast, the Louisiana–Texas coastline in the Gulf of Mexico (Anonymous, 2003b), and the east coast of Japan bathed by the Kuroshio Current (Anonymous, 1995).

Strong currents promote the origination of meso-scale circulation features such as eddies, which can be critical for algal bloom dynamics. Eddies can have various roles. They can promote algal bloom initiation and rapid growth of cell concentration due to accumulation resulting from retention as a result of circular movement of the water. At the same time, because of the latter, they can trap the bloom and prevent or control its advection to other areas and further development: under such circumstances, the algal mass can be doomed to rapid depletion of nutrients, extensive zooplankton grazing, and, ultimately, premature dwindling of the community population. For example, there were reports that a *Chattonella* bloom was trapped in meso-scale eddies within the Norwegian Coastal Current. This precluded its further spread and transportation along the coastline and resulted in a temporally geographical limitation of the impact of this HAB event on the aquatic environment (Pettersson *et al.*, 2005).

Other hydrodynamic features are also important. Convergence at fronts associated with upward vertical movements of significant water masses or invasion of river plumes may result in a spike of algal concentration enhancement or subduction of algal blooms beneath the surface, as was documented in 1992 for Spain in the vicinity of Prego (Anonymous, 2003b).

Tidal fronts, formed at the abutment of stratified offshore water and tidally mixed waters frequently become areas densely populated by algae (Pingree *et al.*, 1975). Algal accumulations at front systems are well documented for, *inter alia*, the western English Channel (Holligan, 1979), the mouth of the Gulf of Finland (Moisander *et al.*, 1997), Chesapeake Bay (Sellner *et al.*, 1991), and many other locations throughout the world's oceans (for further references see Sellner *et al.*, 2003).

Frontal jets and coastal currents are efficient in effecting the alongshore transport of algal blooms. This in turn is conducive to the initiation of either inshore or offshore blooms depending on the absence or presence of prominent coastal headlands. Thus, topography and shore geometry can significantly influence (H)AB dynamics.

Mesoscale water density stratification can cause subsurface transport of algal

blooms from one area to another *without any visible surface expressions* of this phenomenon. For instance, this frequently occurs in the Skagerrak region where one can observe a subsurface sinking of waters in the Jutland region and its further entrainment by currents along the coast of southern Norway.

It is now common knowledge that HABs are frequently organized into thin layers, not necessarily only at the water surface–atmosphere interface but also at certain depths; these are mainly in the *upper part* of the euphotic zone (e.g., Marcailou *et al.*, 2000). There are plenty of such reports in relation to *Alexandrium catenella*, *Dinophysis acuminata*, *Chaetoceros debilis*, and others (Anonymous, 2003b). Although there are thermohydrodynamic-based theories of this phenomenon, this issue remains presently unresolved.

In OCRs with shallow waters subjected to strong wind-driven vertical mixing, the algal cysts buried in bottom sediments can be brought back to surface layers and initiate a massive growth of the phytoplankton community. This process is regularly observed, for example, in connection with the winter rest of several algae cysts at the bottom and their activation during early spring blooms.

For OCRs, upwelling events are thus critically important for initiation and proliferation of HABs. These regions are subjected to strong seasonal cycling with intermittent infusions of nutrients from nutrient-rich deeper water layers.

Franks and Anderson (1992) highlighted the critical importance of upwelling and downwelling phenomena for toxic bloom initiation and development. The benthic environment in the Gulf of Maine has been shown to have an extended *Alexandrium tamarensense* cyst seabed located offshore at 150 m depth. Importantly, the cyst population proved to be 20 times denser than in shallow waters of the gulf. It has been found that during upwelling a combination of cysts migrating upward from the seabed and the surface-trapped plume of brackish water, originating from river runoff, causes the plume to thin vertically and extend offshore, blanketing the area above the seabed.

Growing from germinated cysts and tending to reach light-rich surface waters, the *A. tamarensense* cells end up inhabiting this thin surface layer. However, with the change of wind conditions and origination of downwelling movements at the shoreline, the developed algae are brought back to shore and eventually develop into an extensive bloom.

In those OCRs where upwelling is not typical, early spring algal blooms are supplied with nutrients through winter mixing with deeper layers as a result of spring overturn. Further, with the establishment of stratification, nutrient delivery proceeds through river input as well as tidal and wind-driven mixing.

Hydrodynamics are at the origin of the so-called coastal retention zones, which are different from those discussed above in relation to eddies: water circulation patterns can lead to formation of “reservations”—isolated water masses with specific chemical, biological, and thermohydrodynamic regimes. Such unique properties associated with a relatively long residence time within the retention zones favor rapid and massive development of algae, predominantly of toxic origin as a result of intrinsic biological mechanisms. The latter reside in (i) toxin accumulation from indigenous toxic algae, (ii) sexual cross-breeding effected by toxin egestions,

(iii) genetic modifications, spurring up the development of non-obligatory toxic species capable of developing their toxicity in the course of growth phases, and (iv) low consumption of algal cells by zooplankton as a result of grazing slowdown, etc. As a result, transport from these zones to other regions along the coast can initiate onset of a major bloom of toxic algae uncharacteristic of the local indigenous algal taxonomy (Fermín *et al.*, 1996).

*Enclosed* and *semi-enclosed* (ESE) marine systems offer suitable conditions not only to accommodate matter brought from land or with river runoff, but also from contiguous ocean waters. Although varying in location, size, bathymetry, and morphology, ESE marine systems have in common their susceptibility to bloom events. This is conditioned not only by shallowness and associated replenishment of nutrients from sediment resuspensions and restrictive circulation but also mostly by the delivery of nutrients through runoff from land and rivers and, generally to a lesser degree, atmospheric deposition.

The most important *physical* factor conditioning the initiation and proliferation of a HAB is the *stability* of the water column. The onset of thermal stratification (e.g., as a result of arrival of buoyant freshwater that prevents both vertical exchange of deep waters with the surface layers and, consequently, channeling of oxygen down to the depth) conditions favorable for establishing such convergent features as fronts may actively contribute to bloom initiation (for the reasons, see above).

Importantly, ESE marine systems are retentive not solely because of coastline features. In addition, features such as keys, islands, sandbanks, siltbanks, tidal fronts, etc. restrict hydrodynamic interaction with the open ocean, determining longer residence times not only in the inner but also outer parts of estuaries, fjords, or embayments. From this perspective, the Baltic Sea, which regularly experiences massive cyanobacteria blooms, is an example of an extreme case. Deep-water renewals occur there episodically on decadal scales.

Horizontal transport in a stratified ESE marine system is frequently driven not so much by river runoff, but by local circulation whose strength might be 10 times that of the streams of inflowing rivers.

On short timescales, it is wind-induced circulation that often prevails in determining to a large degree the intensity of upper-layer water exchange with neighboring water masses. However, this exchange is not solely a consequence of water transport by wind-driven currents, it is also one of gravitational force arising from water level differences between the ocean and the linked enclosed water body.

Intermittent, near-instantaneous inputs of freshwater from rivers into an ESE marine system and, conversely, dense saline waters from the contiguous oceanic area can be conducive to algae and other waterborne matter accumulation.

In smaller ESE marine systems this effect may be accentuated by stratified flow interactions with bottom relief, topographically steered river runoff fronts, or hydraulic controls.

In larger ESE marine systems, such as the Baltic Sea, the Coriolis effect plays the role of a retaining and sustaining factor: low-density brackish waters originating from river inflow are drawn to the sea shores while fronts, being fed with additional energy, become more sustainable. In the Baltic Sea, owing to its large dimensions,

strong meso-scale water movements, such as coastal jets, eddies, upwelling, and fronts control hydraulic interactions between shelf and pelagic waters. Thus, large ESE marine systems exhibit features of both ESE and OCR marine systems.

One of the striking phenomena revealed through the comparison of HAB events in ESE and OCR marine systems occurring under various geographic/climatic and biogeochemical conditions is that, notwithstanding sharp contrasts in incidence and extent, the key functional groups and species prove to be common.

At the same time, increasing evidence indicates that species once identified as harmless in some areas become harmful in other areas. For instance, *Prorocentrum minimum* and *Mesodinium rubrum* cause harmful blooms in the Chesapeake Bay (due to high toxic biomass and high non-toxic biomass, respectively) are indigenous components of the plankton community in the Baltic Sea, but they form blooms without harmful effects. Similarly, *Heterocapsa triquetra* and *H. rotundata* cause mahogany tides in Chesapeake Bay but they develop non-harmful blooms in the Baltic Sea (Anonymous, 2003b). These findings warrant the supposition that biogeochemical aspects might play a deciding role given similar types of marine systems (Kudela *et al.*, 2002).

In the open ocean, HAB proliferation in spring is determined principally by the timing of the shutdown of *convective overturning*, although episodic strong winds add to vertical mixing and can potentially affect the onset of stratification and can be at the basis of *interannual variations* in HAB bloom lifecycles: initiation, development, and demise.

In OCRs away from inputs of freshwater, stratification is controlled by competing solar insolation-induced water stratification, convective overturning, wind stress, and tidal-driven vertical mixing. As mentioned above, in tidally energetic regions, such as the shelf seas of northwestern Europe, tidal mixing prevails in determining the summer vertical water column structure.

## 2.2 ROLE OF BIOGEOCHEMISTRY

The hydrodynamic mechanisms determining HAB initiation, frequency of occurrence, and the vexing expansion across the world's oceans are generally closely related to biogeochemical processes (Holmedal and Utne, 2006). One of the numerous examples is cross-bay tilting of the pycnocline induced by winds shifting from calm/weak westerly winds to strong southerly winds along the axis of Chesapeake Bay drives subpycnocline remineralized nutrients into the euphotic zone, resulting in a bloom outbreak (Sellner *et al.*, 2003). Such phenomena are common along the western coasts of major continents bringing about similar nitrification effects, which spur up enhanced algal production and often harmful algal blooms.

Like all autotrophic algae, growth of autotrophic harmful algae requires some major conditions to be met: availability of nutrients, favorable water temperature, stable vertical stratification (Sharples *et al.*, 2006), and light—although for mixotrophic and, even more so, heterotrophic algae, light availability is optional.

Water column vertical mixing/stratification is controlled by water temperature and salinity, particularly in inshore areas subject to freshwater discharge, offshore currents, and upwelling.

HAB events often follow a period of intense rainfall and runoff—both of which enhance water column stratification and enclose in the upper layer the chemicals favorable to algal growth—followed thereafter by a period of intense solar illumination. It is believed that heavy rainfall can also contribute to coastal water nitrification through provision of some nutrients important for the development of a specific HAB event. For example, Graneli *et al.* (1993) assumed that selenium and cobalt have been partially responsible for blooms of *Chrysochromulina polylepis* in the Skagerrak and Kattegat.

The hydrochemical habitat of planktonic organisms is extremely complex and highly variable temporally, being subject to seasonal, regional, and long-term modifications. For example, seasonal variations of oxygen content in the water column, especially in bottom waters, are full of consequences for shallow poorly flushed coastal waters, at aquaculture sites, and in regions exhibiting environmental degradation.

The effects of hydrochemical conditions/habitat on HABs are thought to be twofold: (1) influencing predominant species selection and (2) promoting algal growth into a bloom. Marine harmful algae<sup>1</sup> are generally nitrogen-limited, although in inland water environments indigenous algae are generally phosphorus-limited. For diatoms, silica levels might also be a limiting factor.

Accordingly, there is growing evidence strongly indicating that HAB outbreaks occur with steadily increasing incidence and spatial extension in nutrient-rich waters (Andersen *et al.*, 2006). The importance of nitrification can be exemplified by well-documented long-term tendencies in escalation of blooms of *Phaeocystis pouchetti* in Dutch coastal waters, *Prorocentrum cordata* in the Black Sea, and there are numerous similar reports from other marine environments (for the Baltic Sea see for example Rönneberg and Bonsdorff, 2004).

In light of the above, coastal eutrophication is considered as one of the major forcing factors in HAB occurrences. Mass introduction of nutrients might proceed in a variety of pathways ranging from cattle/hog farm waste ponds, inefficient use of manure/fertilizers to waste disposal/sewage waters of municipal and industrial origin. However, this list is certainly not exhaustive. For example, huge amounts of nutrients can be dragged up from bottom sediments either due to civil engineering (e.g., dredging) or storm-induced scavenging of bottom sediments in harbors and bays, coastal zones, and even in shallow non-coastal areas. For instance, cyanobacterial pigments likely from the summer dominant taxa *Nodularia* and *Aphanizomenon*, remaining at very low levels in the Baltic Sea for the previous 7,000 years (Poutinen and Nikkilä, 2001) showed a dramatic increase in the 1960s, which is certainly due to the action of two conjoint factors: huge post-

<sup>1</sup> A possible exception is cyanobacteria, which can take up nitrogen from the atmosphere, but need the phosphorus available in the water column, as is the case of cyanobacteria blooms in the Baltic Sea.

World War accumulations of N and P in bottom sediments are recurrently returned (in mineralized form) to the euphotic zone as a result of strong storms typical of the wintertime and springtime.

Aquacultural production of shellfish and finfish generates large amounts of excretory products (feces, pseudofeces, and so on), which are rich in N and P and may also include toxins from the medication of caged fish. Particulates, either defecated matter or the decomposing flesh of dead fish, settle at the bottom and through remineralization yield N and P suitable for algae to feed on. Accordingly the licensing conditions for aquaculture sites may include limitations with respect to the allowed period of operations at one specific location.

However, along with the nutrition factor, the *life cycles* of algae might be very important in the context of the HAB problem (e.g., within the lifecycle of *Alexandrium* spp.). As was discussed above, during periods unfavorable for sustainable development, algae produce resting cysts that settle on the bottom and, after a dormancy term, can break open and release vegetative cells that ascend to the euphotic zone to initiate a spate of extensive algal bloom. Importantly, some diatoms and cyanobacteria are apt to also produce similar resting organisms (called spores and akinetes, respectively). This property gives dinoflagellates and such specific diatoms and cyanobacteria an important advantage over algal populations devoid of such an ability to persist under temporarily unfavorable conditions. Therefore, this may explain the abrupt and massive surging of one algal taxon that occurs in some cases when algae of other taxa remain peripheral in the outbreacking phytoplankton community.

## 2.3 ROLE PLAYED BY OTHER FACTORS

Meteorological events, atmosphere–ocean variability, and global change implications can reportedly provoke not only bloom formation but also large-scale alterations to the present state of the aquatic ecosystem. For example, the typical vernal *Mesodinium/Noctiluca* blooms in the waters of the northeast coastal zone of New Zealand gave way to summer *Raphidophytæ* and *Dinoflagellate* blooms. This succession is uncharacteristic and, in contrast with spring diatoms, summer dinoflagellates and diatoms outburst again in the fall. The revealed change in species succession order was associated with an El Niño that brought lower-than-normal water temperatures (Rhodes *et al.*, 2001).

The North Atlantic Oscillation (NAO) can also be implicated in HAB transportation and proliferation. This can be exemplified by a case recorded in Spain: the bloom initially “ignited” by upwelling-driven nutrification then spread over the northwestern coastal zone by NAO-conditioned alongshore winds (Fraga and Bakun, 1993). In the late 1980s, dedicated studies in Swedish fjords established that the positive phase NAO (i.e., milder winters and higher levels of salinity) were significantly correlated with the growth dynamics of *Dinophysis* species as well as *Chrysochromulina polylepis* and *Gymnodinium aureolum*.

The general mechanisms or processes leading to algal bloom formation, proliferation, and decay can be further specified through the results of a comparative study addressing three geographical regions in European waters: namely, the North Sea/Skagerrak, the Baltic Sea, and the Galician Rías (Pettersson *et al.*, 2005). These case studies provide evidence to support this book's thrust to advocate the importance of combining comprehensive monitoring of HABs with associated ecological modeling with the objective of establishing an efficient integrated system of early warning, detection, monitoring, and forecasting of HAB events. Accordingly, such model simulations have been accomplished for the three abovementioned cases and are presented in Chapter 5 along with a broader discussion of this issue.

## 2.4 CASE STUDIES

### 2.4.1 *Chattonella* or *Pseudochattonella* spp. in the North Sea/Skaggerak

During the period 1997–2002, three large blooms of the flagellate *Chattonella* aff. *verruculosa*<sup>2</sup> occurred in the North Sea/Skagerrak/Kattegat region, in 1998, 2000, and 2001. During the first and the last blooms, fish mortality was registered in fish farms along the southern coast of Norway. It is likely that the above pernicious species had been initially introduced, possibly for example through ballast water, to the area in 1998, and during the following years spread further across the area becoming today a well-established species in the region. A short chronicle of the major *Chattonella* bloom events affecting the waters of Norwegian concern is presented in [Table 2.1](#).

Our analyses of the *Chattonella* bloom occurrences in 1998, 2000, and 2001 match the above discussions in Sections 2.1–2.3 in the following way. The blooms were all observed in coastal water masses characterized by shallow water or a shallow pycnocline, relatively low salinity, and relatively high availability of nutrients due to runoff from land and regeneration of nutrients from the sediment. Distinct coastal water masses (revealed by their temperature signal) are characteristic of *Chattonella* bloom areas along the west coast of Denmark, the west coast of Sweden, and the south Norwegian coast ([Figure 2.1](#)).

The first bloom of *Chattonella* in the North Sea/Skagerrak/Kattegat area observed in 1998 was due to *Chattonella* aff. *verruculosa*. The bloom initially originated off the west coast of Denmark at the beginning of April, and further spread to cover the area extending from the German Bight, along the west coast of Denmark, to Sweden. In May it reached the southern coast of Norway and was advected northward to Boknafjord (Stavanger). The highest algal concentration was recorded off the west coast of Denmark.

This was the first registered large-scale evidence of a *Chattonella* bloom in the Skagerrak area. However, reanalysis of data from the Swedish west coast revealed

<sup>2</sup> Riisberg and Edvardsen (2008) have reclassified the *Chattonella verruculosa* bloom events in the waters discussed in this book to *Pseudochattonella verruculosa* (see also Section 4.1.9).

**Table 2.1.** Summary of *Chattonella* blooms in the North Sea/Skagerrak and Kattegat during 1997–2009.

1997	There was no large-scale <i>Chattonella</i> bloom, but a local bloom was observed in the Århus Bugt, Denmark.
1998	The first major <i>Chattonella</i> bloom year. The bloom originated off the west coast of Jutland and was transported northward along the west coast by the Jutland Current. The major part of the bloom patch was supposed to be advected from Denmark over to the southern part of Norway as a result of blockage in the eastward direction as a result of the Baltic outflow in the Kattegat. Part of the bloom might have spread to the Swedish west coast, crossing under the Baltic Outflow Current. Following transport to the southern part of Norway the bloom spread to the Swedish coast due to east/southeastern currents compensating the Baltic outflow at the surface.
1999	No <i>Chattonella</i> bloom reported.
2000	The second <i>Chattonella</i> bloom year. Occurred only in the North Sea. No further northward transport to the waters of the Swedish west coast and the southern part of Norway, which was presumably as a result of blockage of the Jutland Current south of Skagen.
2001	The third <i>Chattonella</i> bloom year. Developed mainly in the Kattegat/Skagerrak area, during early spring in cold water. Low algal concentrations in the North Sea: presumably because the bloom originated and developed in the Kattegat and successively in the Baltic Outflow Current with further transportation to the Norwegian coast.
2002	Late spring <i>Chattonella</i> blooms reported in warm water in April to May.
2004	Two major <i>Chattonella</i> blooms in the North Sea/Skagerrak region. The first in February and March in the Kattegat affected the Swedish west coast, however it was observed in very low concentrations in Norwegian waters. In April confined to the waters along the west coast of Denmark.
2006	Early spring <i>Chattonella</i> blooms reported in cold water in January to March.
2007	A <i>Chattonella</i> bloom in the Kattegat, but with no effects or reports from Norwegian waters.
2009	<i>Pseudochattonella farcima</i> bloom in west Jutland waters in April. Monitored by ship and satellite measurements and ocean modeling.

that *Chattonella* was already present there at low levels in 1990, a fact which, in all probability, has been overlooked in routine investigations (L. Edler, pers. commun.).

In late April 2000 a new bloom of *Chattonella* spp. was observed in the southern part of the west coast of Denmark. Between late April and mid-May, the bloom extended from the German Bight to Skagen (northern part of Jutland, Denmark). The entire duration of this HAB event was less than a month.

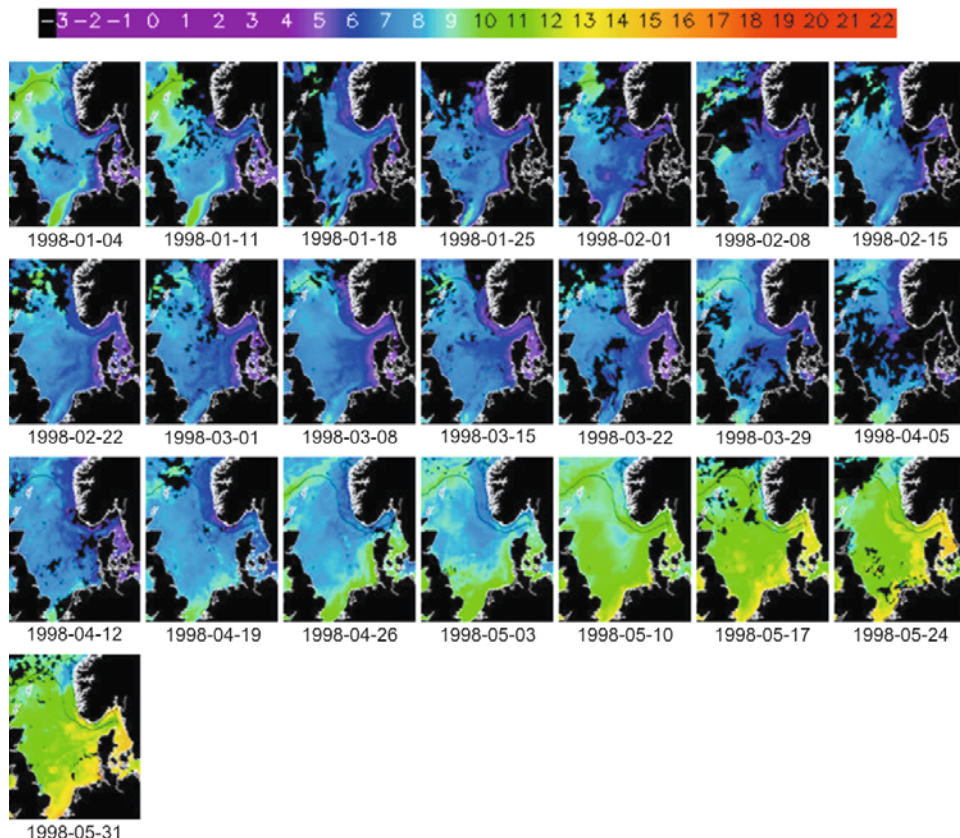


**Figure 2.1.** Time series of weekly averages of sea surface temperature (SST in °C) in the North Sea for the period January–May 1998 derived from the NOAA AVHRR sensor.

The last bloom of this case series occurred in the Skagerrak area in March–April 2001. The bloom was first observed off the Swedish west coast at the beginning of March, extending to the southern coast of Norway during the second half of March. At the beginning of April, the bloom covered the Swedish west coast and the southern coast of Norway up to Mandal (southern tip of Norway). The bloom disappeared from the area on or about April 20, and the total lifetime of this bloom was nearly two months.

*In situ* observations indicate that *Chattonella* takes about 2–3 weeks of growth to turn into a major bloom. During the pre-bloom/initiation period, nutrients were abundant, solar illumination was substantial (high-pressure periods over the North Sea), and winds were weak enough to minimize the advection of *Chattonella* cells and nutrients from the coastal waters out to the North Sea. It is evidenced that since 1998 to date, *Chattonella* is invariably present in the spring constituting an inherent constituent of the late spring phytoplankton community.

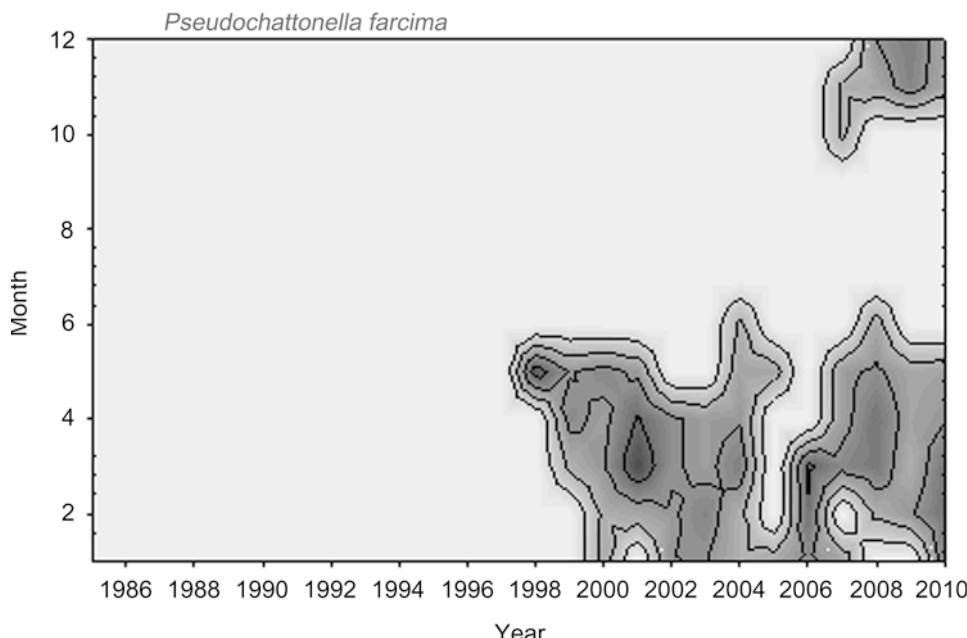


**Figure 2.2.** Measurements of *Pseudocharonella farcima* at Flødevigen Research Station (1986 to 2010), illustrating its abundance and the expanded seasonal (*y*-axis) intensity and increased frequency of occurrence during the most recent years. The data are log-transformed. Courtesy: Lars Johan Naustvoll, IMR.

The Institute of Marine Research in Flødevigen (Lars Johan Naustvoll, pers. commun.) has extensively studied *Pseudocharonella farcima* and monitored its abundance at its research station location since 1986. As indicated above, it is a species that proliferates in Norwegian waters during the spring and winter period and has done so predominantly since 1997, with some irregular interannual variations in bloom intensity. During recent years it has also been observed during December and to some extent in November (see Figure 2.2). The abundance of *Pseudocharonella farcima* seems to be a more regular and annual phenomenon in the Kattegat (eastern Danish waters) and farther south in the German Bight.

These studies of *Chattonella* bloom development confirmed the aforementioned worldwide observations in enclosed or semi-enclosed, as well as open, coastal marine ecosystems of HAB evolution in space and time: this process can largely be characterized as a four-stage process:

**Phase 1.** In the *pre-bloom* phase the species is present only in very low concentrations in either pelagic areas or in bottom sediments in encysted form. To proceed to the next phase of bloom development, the cysts undergo germination and encysted specimens enter the pelagic environment.

**Phase 2.** In the *growth phase*, as a result of light harvesting and uptake of nutrients (which need to be present in ample amounts), primary production increases very rapidly but is dependent on water temperature, salinity, and slight vertical mixing within the euphotic zone. At the population level, the growth rate is controlled by an algal physiological growth process in combination with loss processes such as zooplankton grazing and cyst sinking as well as dispersion/advection intervention.

**Phase 3.** The *bloom phase* is the period of algal maximum concentration; its duration varies, but is usually not in excess of a couple of months.

**Phase 4.** The *declining phase* begins when the dynamic balance between algal growth and loss shifts to the latter. This is the result of a number of factors such as prevailing grazing pressure, depletion of nutrients, encystment, intervention of bacteria and/or viruses, and dispersion (e.g., as a result of a storm event).

The *Chattonella* case study has revealed that, although the duration of blooms has not shown any tendency to increase or decrease, the onset of blooms occurred progressively earlier during the study period (Figure 2.3). To be more specific, the

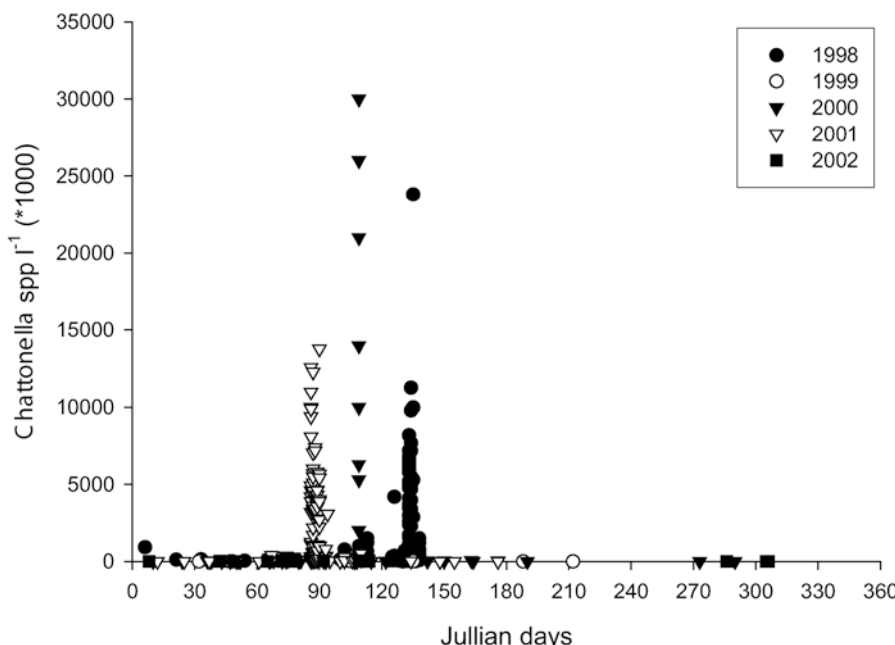


**Figure 2.3.** *Pseudochattonella* spp. abundance and timing of onset in the North Sea/Skagerrak/Kattegat area, during the period 1998 to 2002. Courtesy: L. J. Naustvoll, IMR.

2001 bloom started one month earlier than the other two blooms (Table 2.1). The bloom in 2001 occurred just after the early spring diatom bloom partly overlapping with the spring bloom, whereas the previous blooms occurred well after the spring bloom had completely disappeared. The bloom most likely started off the southern coast of the Swedish Kattegat and was entrained later on by the Baltic Outflow Current northward along the west coast of Sweden.

Regional ocean circulation modeling results indicate that there was a pronounced outflow from Kattegat to Skagerrak at the beginning of March 2001. At the time of the bloom apex, it covered the entire Swedish west coast and the Norwegian Skagerrak coast as far as Mandal. Incidentally, a *Chattonella* bloom was not reported from the Danish west coast in March 2001, but was observed there much later, in mid-April, when it was also reported along the Norwegian coast east of Lindesnes. Ocean circulation models for this area indicate that the bloom has been restricted due to the northeasterly winds and eddies formed in the Lindesnes area, which efficiently restricted further advection of the bloom northwestward along the Norwegian coast.

Studies of the vertical profiles of *Chattonella* blooms have indicated that algal cells were mainly accumulated in the upper few meters of the water column. During the bloom in 1998 *Chattonella* was observed down to 30 meters at the Danish Skagerrak coast. The highest abundance was observed in the upper 10 meters. More or less the same pattern was observed in 2001. A high abundance of *Chattonella* was observed above the halocline at most stations and the highest concentrations were found in the upper 5 meters (Figure 2.4). However, *Chattonella* may also be present as a subsurface maximum.

Regarding the aquatic environment parameters favorable for the massive growth of *Chattonella*, the following water salinity and temperature regimes were identified. *Chattonella* spp. were observed in waters with salinity ( $S$ , psu) levels between 12 psu and 35 psu (Figure 2.5), and preferably at  $20 \leq S \leq 34$  psu. These observations are backed up by experiments with the Norwegian strain of *Chattonella* aff. *verruculosa*, which showed positive growth within salinity  $S$  in the range 15–35 psu (Ref.).

Importantly, this species is found to be unable to grow at salinities less than 10 psu (D. Naustvoll, unpublished data). Therefore, there are reasons to presume that at least *Chattonella* aff. *verruculosa* cannot be responsible for major bloom events in Baltic Sea waters characterized by low salinity levels.

Nonetheless, *Chattonella* aff. *verruculosa* has an exemplary tolerance of broad (0–21°C) water temperature ( $T$ ) excursions (Figure 2.6) and can produce blooms in Scandinavian waters during the time period extending from late winter to early summer. Laboratory experiments indicate that this species has the highest growth rate at  $T \leq 10^\circ\text{C}$  (D. Naustvoll, unpublished data). Thus, this species qualifies as a cold-water organism.

Comparing the pre-spring bloom nutrient content variations during the studied period, it was found not unexpectedly that in 2002 and especially in 1998 there were exceptionally high concentrations of inorganic N near the coast, which by the mechanisms described in Sections 2.1–2.3 were subsequently drawn away from the

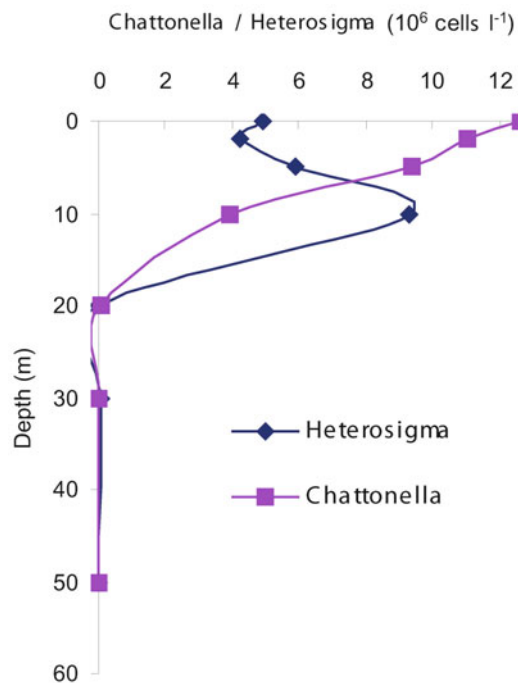


**Figure 2.4.** Vertical profiles of *Pseudochattonella* aff. *verruculosa* and *Heterosigma* at Lyngør during the 2001 bloom. The profile from this station was found to be typical of the coastal zone of southern Norway, except for stations heavily affected by freshwater runoff. Courtesy: L. J. Naustvoll, IMR.

immediate proximity to the coast. It conforms to the paradigm that *Chattonella* is predominantly nitrogen (N) limited. However, it is interesting to note that even though the highest biomass of *Chattonella* was registered in waters with rather high N concentrations, no clear relationship between the concentrations of inorganic N and *Chattonella* abundance has been found (Figure 2.7).

In contrast to N, the observed (rather moderate) concentrations of inorganic P showed significantly less interannual variability. The concentrations of dissolved silicate were rather high throughout the years 1998–2002 (although *Chattonella*, unlike diatoms, is known not to be silicate limited).

Analyses of the influence of meteorology and irradiance on *Chattonella* blooms have revealed that in 1998, 2000, and 2001 wind energy was low from mid April to mid May whereas during the same period in 1999 and 2002 it was definitely higher. Regarding insolation, in 1998 and 2000 there was a stable increase in down-welling irradiance from mid April to mid May, but in 1999 the irradiance was very low in early May, and in 2002 it was only at moderate levels in late April–early May. These data are consistent with what was pointed out in this respect in Sections 2.1–2.3.

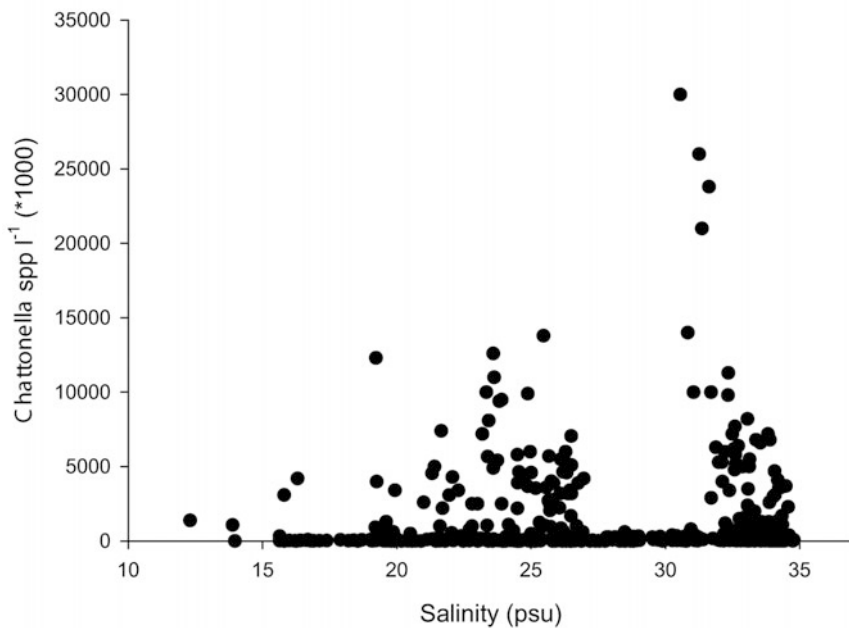


**Figure 2.5.** *Pseudochattonella* spp. abundance vs. salinity in the North Sea/Skagerrak/Kattegat area during the period 1998–2003. Courtesy: L. J. Naustvoll, IMR.

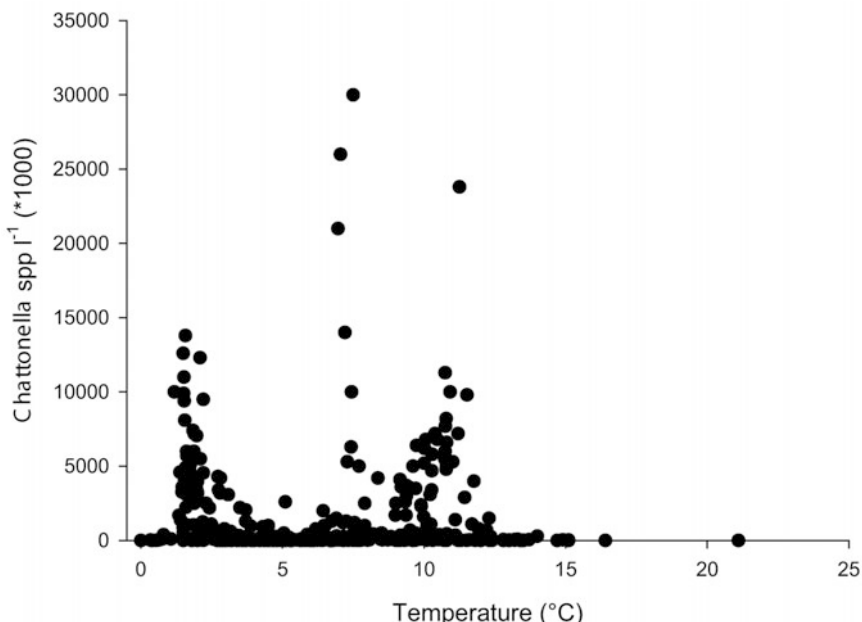


**Figure 2.6.** *Pseudochattonella* spp. abundance vs. sea surface temperature in the North Sea/Skagerrak/Kattegat area, during the period 1998–2003. Courtesy: L. J. Naustvoll, IMR.

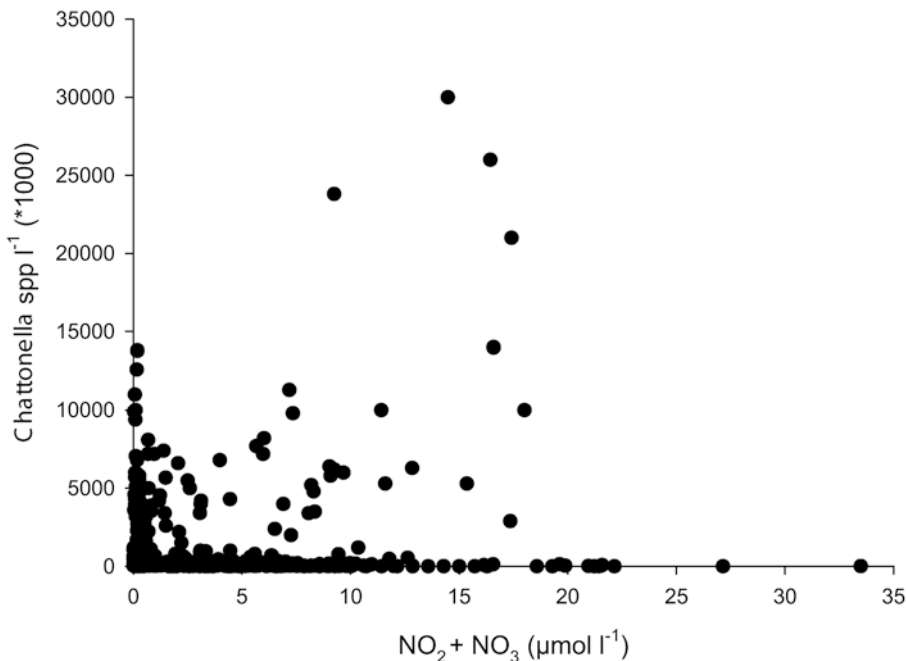


**Figure 2.7.** *Pseudochattonella* spp. abundance vs. NO<sub>2</sub> + NO<sub>3</sub> concentration (μmol L<sup>-1</sup>) in the North Sea/Skagerrak/Kattegat area, during the period 1998–2003. Courtesy: L. J. Naustvoll, IMR.

#### 2.4.2 Cyanobacteria blooms in the Baltic Sea

The Baltic Sea is among the largest seas with brackish water, with salinities ( $S$ ) ranging from almost freshwater in the Bay of Bothnia to 15 psu in the Belt Sea. The vertical profile of  $S$  exhibits strong variations; for example, in the Baltic proper  $S$  varies from 7 psu at the surface to 11 psu at the bottom.

The nutrient load in the Baltic Sea has increased since 1900 by a factor of 4 for N and a factor of 8 for P, turning this water body into a mesotrophic one. While the issue of nutrient limitation for pelagic algae in the Baltic Sea remains a subject of debate, a common concern is intensified eutrophication.

Salinity and temperature stratification, which develops in the Baltic Sea especially during summer, inhibits vertical mixing and hence cuts down the input of inorganic nutrients from below the thermocline to the surface; under such conditions, only cyanobacteria (as an alga capable of nitrogen uptake directly from the atmosphere) have the advantage of growing and generating summertime blooms, provided that enough P has been brought into the euphotic zone by vernal overturning and left after the preceding vernal bloom. Moreover, high internal phosphorus storage in cells is supposed to enable cyanobacteria to grow even under limiting external phosphate concentrations.

Thus, the triggering factors for cyanobacteria bloom initiation in the Baltic Sea are as discussed in Sections 2.1–2.3: namely, a stratified water column, calm weather (wind speed  $<5$  m/s), and high water temperature ( $>15^{\circ}\text{C}$ ) for 1–2 weeks.

Cyanobacteria occurrence in the Baltic Sea was evaluated according to the Finnish Alg@line data (for data description see Ruokanen *et al.* 2003) for the years 1997–2002. The data for the most common cyanobacteria species *Nodularia spumigena* Mertens and *Aphanizomenon flos-aquae* Ralfs (hereinafter referred to as *Nodularia* and *Aphanizomenon*) were analyzed in this case study.

Although there are various algal species capable of producing toxins in the Baltic Sea, the real damage is generally caused by frequent and vast blooms of *Nodularia* (Laamanen *et al.*, 2001). Also, the frequently occurring cyanobacteria species *Aphanizomenon* is considered as a serious nuisance for fishing and recreation.

Field data from the discussed case study indicate that these cyanobacteria species have different demands on their environment: *Aphanizomenon* prefers lower temperatures and salinities than *Nodularia* (Figures 2.8 and 2.9). *Aphanizomenon* also prefers a lower dissolved inorganic nitrogen (DIN):dissolved inorganic phosphorus (DIP) ratio (Figure 2.10). These different responses may be rooted in the different vertical, horizontal, and temporal distributions of the two genera in the Baltic Sea.

Different preferences in water *salinity*, *temperature*, and DIN/DIP ratio conditions determine seasonal and interannual variability in the spatial distributions of these two cyanobacteria species. After the vernal diatom bloom, cyanobacteria start to accumulate the intercellular phosphorus necessary for their later growth. In

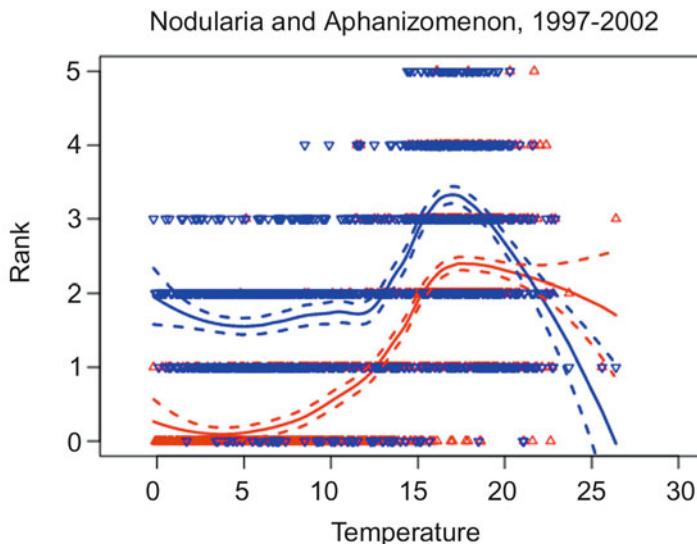


**Figure 2.8.** Occurrence of cyanobacteria in relation to water temperature. Red lines—*Nodularia*, blue lines—*Aphanizomenon*. Courtesy: S. Kaitala, FIMR.

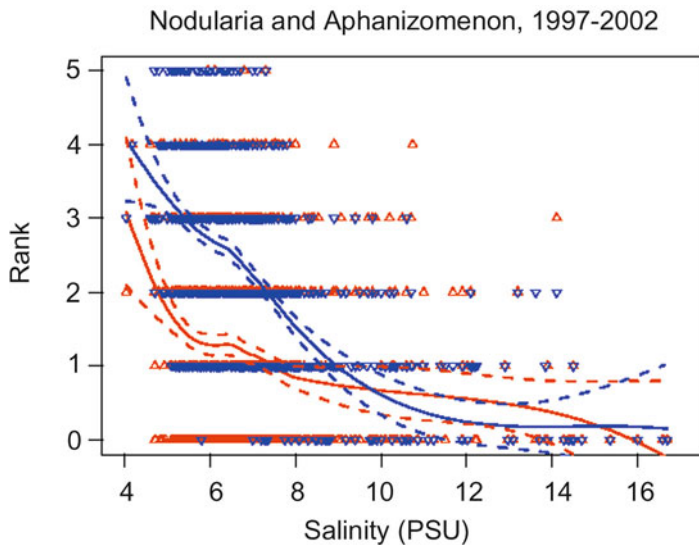


**Figure 2.9.** Occurrence of cyanobacteria in relation to salinity. Red lines—*Nodularia*, blue lines—*Aphanizomenon*. Courtesy: S. Kaitala, FIMR.

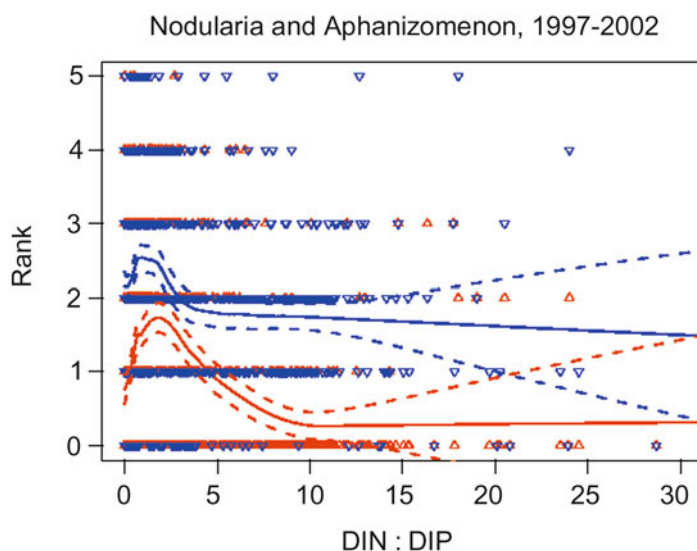


**Figure 2.10.** Occurrence of cyanobacteria in relation to DIN:DIP ratio. Red lines—*Nodularia*, blue lines—*Aphanizomenon*. Courtesy: S. Kaitala, FIMR.

June–July begins the major onset of the rapid buildup of *Aphanizomenon* accumulations, most expressed in the Gulf of Finland. However, by late spring, appreciable concentrations of *Aphanizomenon* can be found as a result of this species' better (than *Nodularia*) adaptation to low temperatures. The summertime increase in water temperature  $T$  in excess of 15°C causes a significant enhancement of *Nodularia* content.

The highest counts of *Nodularia* cells in most years were observed in the central Baltic Sea, where generally the highest sea surface temperature (SST) occurs. In the fall, the growth of *Nodularia* starts to ebb as a consequence of decreasing  $T$ , and by late December it has all but disappeared.

In winter, low water temperature and decreased incident solar radiation in combination with enhanced mixing drastically reduce phytoplankton concentrations, but not completely. During this period, a number of complex processes occur that are important for phytoplankton community resuscitation in the following year. First and foremost, nutrient mineralization in sediments and the late winter–early spring overturning of water masses lead to a replenishment of nutrients in the mixed layer. At the same time, water salinity invariably exhibits no seasonal cycle.

The frequent occurrences of massive outbreaks of *Nodularia* in the Baltic Sea in summer are spurred on by low DIN/DIP ratios (resulting from depletion of inorganic nitrogen). Such conditions, as discussed earlier in this section, promote the growth of cyanobacteria. Blooms of *Nodularia*, as a cyanobacterium species, are certainly partially the result of sufficient phosphate concentrations left after the spring bloom, but more strongly by warm and calm weather conditions, low wind, high water temperature, and strong stratification.

Interannual variations in *cyanobacteria* blooms are brought about by atmospheric (both physical and chemical) oceanic parameters that force excursions. The highest interannual variability is found in the Gulf of Finland whereas fluctuations in the southern and central Baltic Sea are comparatively small. In 1997 and 1998, in all three regions of the Baltic Sea lower SST and chlorophyll concentrations were observed in February compared with the time period 1998–2002. However, a rapid increase of  $T$  in 1997 caused fast growth of diatom phytoplankton in spring followed by *Aphanizomenon* and *Nodularia* blooms in summer.

### 2.4.3 *Gymnodinium catenatum* blooms in the Galician Rías

Blooms of dinoflagellates, often harmful, are relatively frequent in the Rías Baixas of Galicia in four bays along the northwestern Iberian Peninsula where seasonal upwelling–downwelling events are among the main oceanographic features (Figueiras *et al.*, 2002).

Study of these blooms has provided a coherent picture of HAB dynamics in the region. Seasonal upwelling on the northwestern Iberian shelf occurs on average between March and September when northerly winds are dominant, whereas downwelling motions prevail during the rest of the year owing to the predominance of southerly and westerly winds. Coastal upwelling and downwelling phenomena

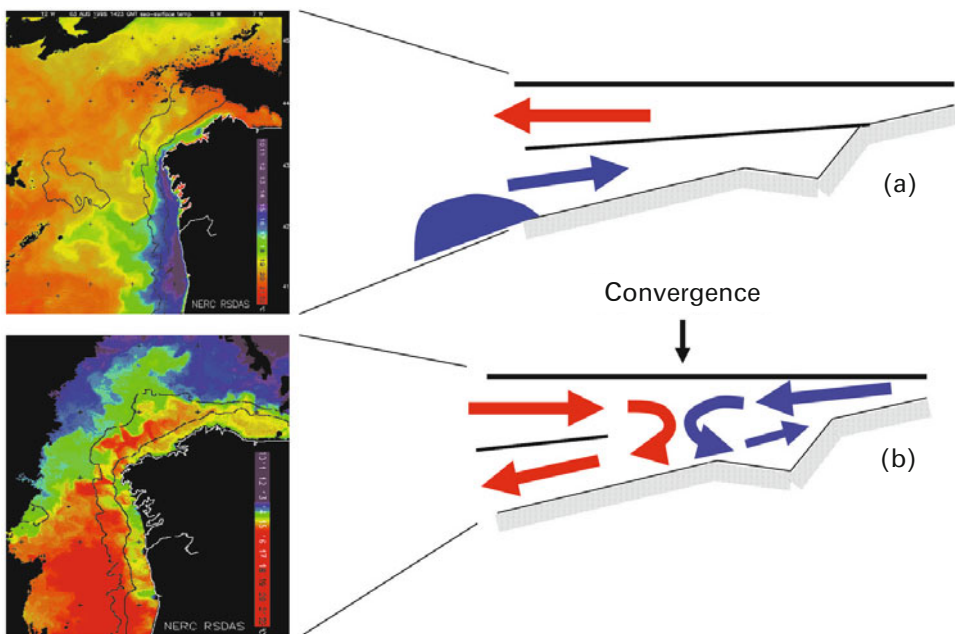


**Figure 2.11.** Schematic representation of circulation in the Spanish Rías during (a) upwelling and (b) downwelling conditions and their typical off-shore sea surface temperature (SST) conditions revealed in satellite images. Courtesy: F.G. Figueras, IIM.

greatly influence circulation in the rías (Figure 2.11) and hence the exchange processes between the rías and the adjacent shelf (Álvarez-Salgado *et al.*, 2000; Tilstone *et al.*, 2000). Upwelling forces two-layer density-induced positive circulation in the rías characterized by the outflow of surface waters and a compensating inflow of upwelled water at the bottom.

The transition to seasonal downwelling, which coincides with the rapid change to southerly winds, establishes a *reversal circulation*, during which surface coastal water enters the rías to develop a downwelling front at the location where it meets inner waters that are under higher continental influence. During this reversal circulation, the outflow towards the ocean in the outer circulation cell (Figure 2.10b) takes place at the *bottom layer*.

Reversal circulation modifies the distribution of algal assemblages along the rías and in the nearest shelf: under upwelling conditions, it is characterized by the predominance of diatoms in the inner waters as well as by higher concentrations of dinoflagellates towards the shelf (Tilstone *et al.*, 1994). Downwelling causes the advection of dinoflagellates to the interior of the rías and promotes their accumulation in the downwelling front (Fermín *et al.*, 1996). This accumulation occurs because the capability of dinoflagellates to swim vertically allows them to compensate for the downward velocity generated in this convergence. Diatoms, unable to counteract such downward velocity, are pushed down in the water column to be then exported towards the shelf by bottom outflow (Figure 2.12).

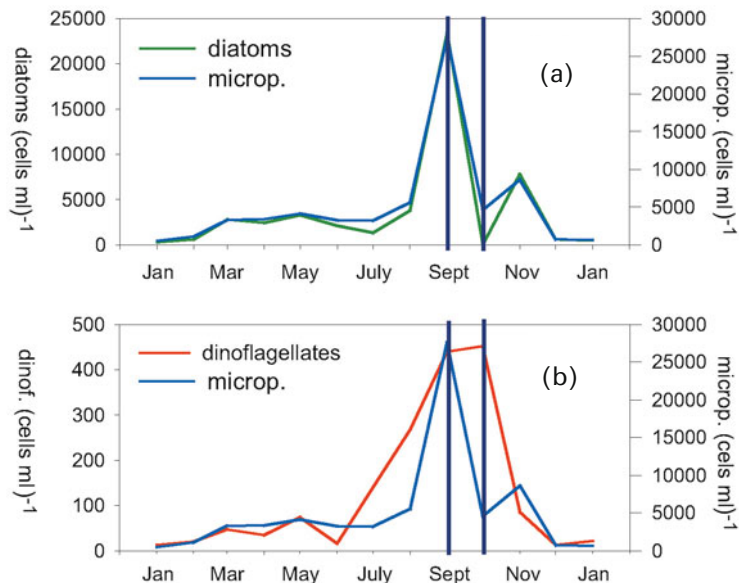


**Figure 2.12.** Time evolution of (a) total phytoplankton and diatom abundance and (b) total phytoplankton and dinoflagellate abundance in the surface waters of a sampled station in the Ría de Vigo in 1987–1988. Values in (a) and (b) are monthly averages. Vertical bars mark the autumn transition to downwelling. Courtesy: F.G. Figueras, IIM.

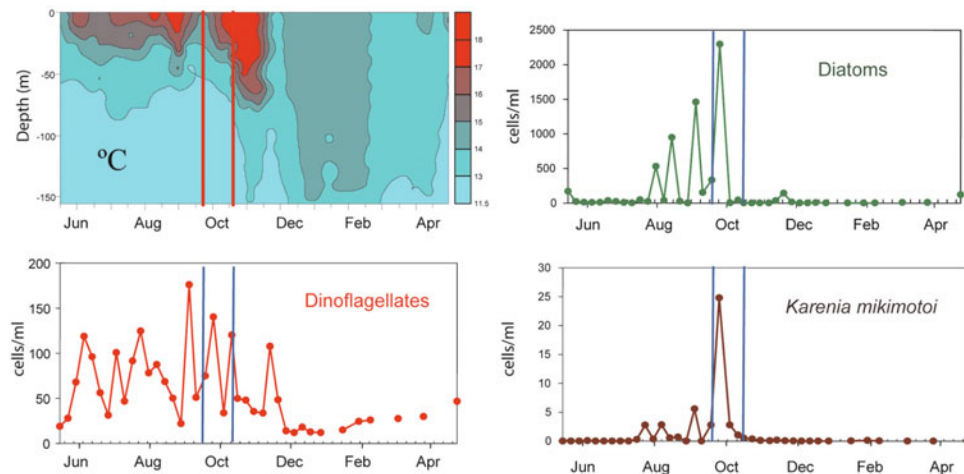


**Figure 2.13.** Time evolution (June to April) of temperature (upper left) and mean abundance (cells/ml) of diatoms, dinoflagellates, and the swimmer species *Karenia mikimotoi* in shelf waters in front of the Ría de Vigo in 2001–2002. Vertical bars mark the autumn downwelling transition. Courtesy: F. G. Figueras, IIM.

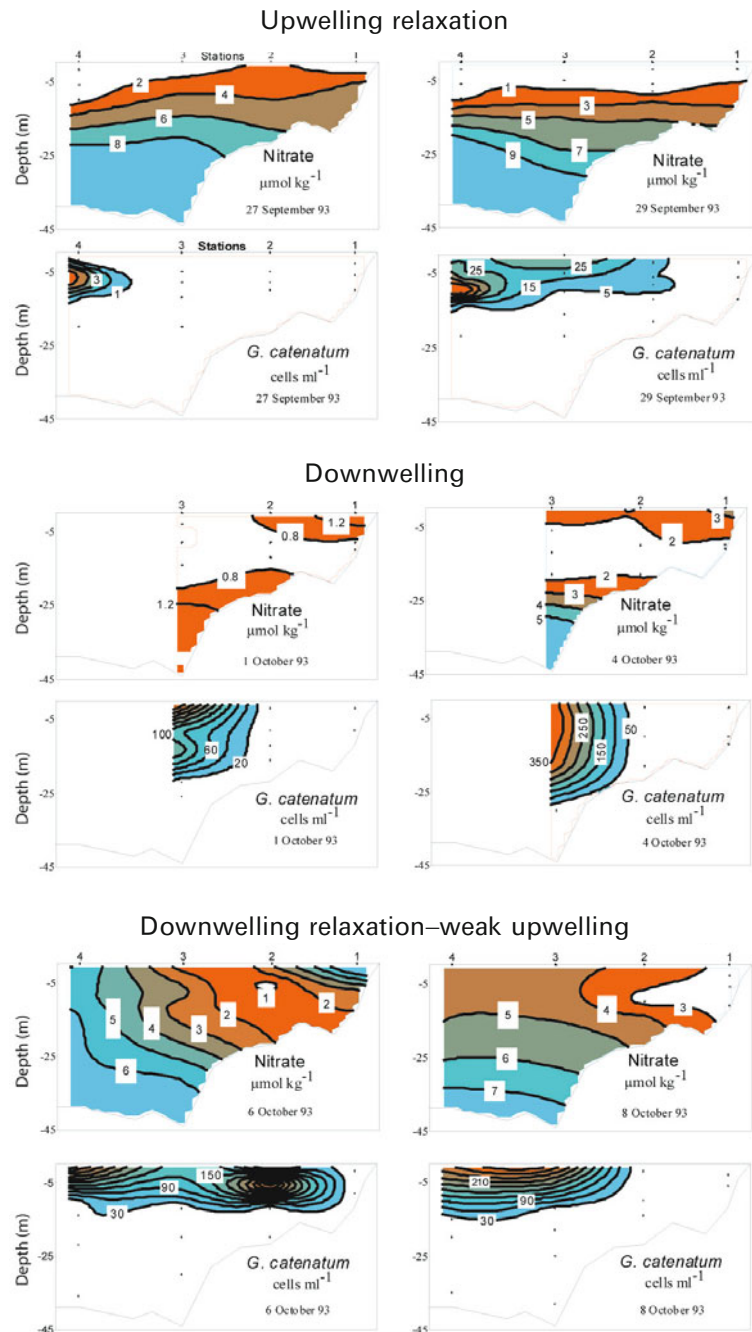


**Figure 2.14.** Sequence showing the initiation and development of a *Gymnodinium catenatum* bloom in the Ría de Vigo in September–October 1993. Nitrate distribution can be used as a tracer of upwelling/downwelling. Courtesy: F. G. Figueras, IIM.

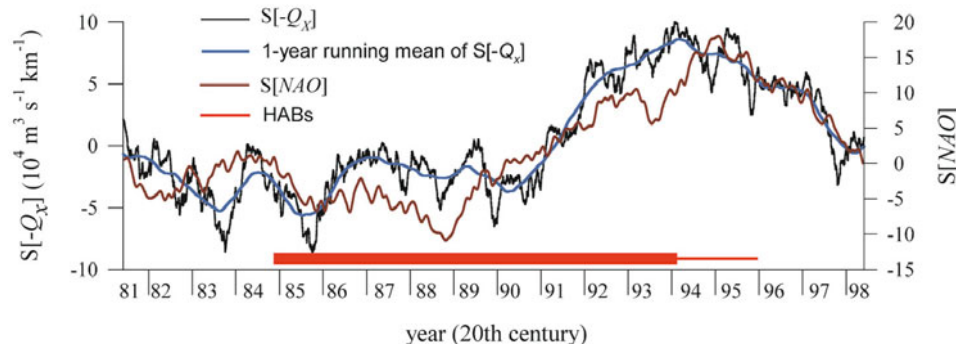


**Figure 2.15.** Graph showing the possible long-term relationship between climate variability and PSP events caused by *Gymnodinium catenatum* in the Galician Rías Baixas (NW Iberian Peninsula) during the years 1981 to 1998. Courtesy: F. G. Figueras, IIM.

This kind of HAB initiation has also been observed in a one-year-long record of data from a station on the shelf with a sampling frequency of once per week (Figure 2.13). Consequently, it can be assumed that autumn downwelling is the key oceanographic process for HAB initiation off the coast of Galicia in the northwestern Iberian Peninsula.

Regardless of which dinoflagellate species predominates as a consequence of downwelling, the actual development of the alga into a bloom also needs an appropriate nutrient supply, which is provided by the return of moderate upwelling conditions (Fermin *et al.*, 1996): strong upwelling enhances positive circulation and favors diatom growth (Figure 2.14). Large runoff during downwelling, another nutrient source for the surface layer, also enhances positive circulation and hence displacement of the downwelling front toward the shelf.

Therefore, the two processes—strong upwelling and runoff—tend to disperse dinoflagellates into shelf waters. Historical data also suggest that HAB episodes are related to long-term variability in upwelling (Figure 2.15), which in turn is connected with interannual climatic variations such as the North Atlantic Oscillation (NAO).

After this analysis of general mechanisms controlling the incidence, surficial extension, and variation of HABs brought about by a multitude of internal and external factors, which were further exemplified by a few case studies, we now turn to a discussion of harmful algal cellular properties, principally from the perspective of their optical attributes. The latter form the basis for remote monitoring of HABs. The approaches and methods used for this are elaborated in Chapter 4.

# 3

## Potential of remote sensing for identification, delineation, and monitoring of harmful algal blooms

The challenges to society and the impact of harmful algal blooms (HABs) on society justify intensive study and comprehensive monitoring of such events. When designing a monitoring strategy, several goals might be pursued, including *early warning*. Because HAB events are generally spatially extensive and heterogeneous as well as dynamic, satellite Earth observation is considered an important component of a monitoring system, provided that remote-sensing techniques are suited to this end. As an explicitly indirect method, remote sensing deals with *proxy* variables of biological ocean variables. These proxy variables can be (inexact) indicators of the occurrence of harmful algal species. In what follows we will analyze the present and future potential of remote-sensing methods for meeting the requirements of HAB early detection and dynamics surveillance in different aquatic environments.

An assessment of remote-sensing capabilities for these purposes requires first a discussion of the pigment compositions inherent in various harmful species (Section 3.1), as well as the absorption properties of the major types of pigments and their impact on the bulk absorption spectra of algal cells (Section 3.2). This is motivated by the major approach, which is based on the *passive optical* remote sensing of water. Only visible radiation penetrates the water column to any degree—in contrast to microwave and infrared radiation. Traveling through the aquatic medium, sunlight photons interact (through absorption as well as elastic and inelastic scattering) with the molecules encountered (i.e., the water itself and its dissolved or suspended constituents). This leads to alterations to the spectral composition in the propagating radiative flux (e.g., Pozdnyakov and Grassl, 2003). Due to backward scattering from optical heterogeneities inherent in the water, some of the downwelling photons become deflected and eventually directed to the water-air interface. Therefore, the backscattered flux emerging from beneath the water surface brings information towards the remotely located sensor on the inherent optical properties (IOPs) of the water column (Section 3.3). IOPs are additive in nature and encompass the

absorption and backscattering contributions from each of the substances co-existing in water.

Section 3.4 discusses the optical properties of the major color-producing agents. Knowledge of the absorption properties of phytoplankton cells and other indigenous water constituents such as suspended minerals and dissolved organic matter are thus needed for passive remote sensing. *Active optical* remote sensing is based on registering airborne laser-induced light emission (fluorescence) from natural fluorophores present in water; these are algal pigments and dissolved organic matter. Hence, the spectral emission spectra of these substances will also be discussed.

Section 3.5 presents methodologies for harmful algae detection using optical satellite Earth observation (EO) data sources. Given the intensity and bandwidth of the absorption and fluorescence bands of algal pigments, the requirements for spectral resolution of the registered optical signal can be assessed and compared to the present feasibilities of satellite and airborne sensors. Because the remotely sensed signal is inevitably contaminated by the optical influence of the intervening atmosphere between the ocean surface and the remote-sensing sensor (the so-called path radiance impact), atmospheric correction is needed. Together with the sensor's sensitivity and spectral resolution, the accuracy of the applied atmospheric correction eventually determines the degree to which HABs can be remotely detected.

The feasibility of optical remote sensing might be enhanced if concurrent satellite data in the infrared (IR) and microwave spectral regions are available. This is why such synergistic applications of satellite Earth observation data are discussed in Section 3.6. Finally, a discussion of the potential of forthcoming hyperspectral sensors and related methodologies concludes this chapter.

### 3.1 TAXONOMY AND PIGMENT COMPOSITION OF HARMFUL ALGAE

The taxonomic rankings used in physiology are sometimes confusing to the non-biologist. In this book, the following hierarchies are used, listed in decreasing rank: division (word ending in “-phyta”), class (word ending in “-phyceae”), order (word ending in “-ales”), family (word ending in “-aceae”), genus, and species. It is seen from Chapter 2 that the following divisions/classes, genera, and species are associated with *harmful algae*.

**Cyanophyta** (cyanobacteria or blue-green algae, coccoid unicells, filaments or colonies, blue-green, grey-green, or red) Cyanobacteria are mostly found in tropical and subtropical phytoplankton, but also in phytoplankton of brackish waters (e.g., in the Baltic Sea), estuaries, eutrophic freshwater lakes, and rivers. The ability to flourish in warm waters under high-light conditions has enabled them to produce blooms in inland and coastal habitats (e.g., *Nodularia spumigena*).

Cyanobacteria are known to cause most of the problems in freshwater environments, but marine animals, especially aquacultured fish, are also affected

(Anonymous, 1995). Although strains within species of *Anabaena*, *Aphanizomenon*, *Cylindrospermopsis*, *Microcystis*, *Nodularia*, *Nostoc*, and *Oscillatoria* are responsible for most toxic episodes, there are over 30 species of cyanobacteria that can be associated with toxic water blooms. For example, the species *Trichodesmium erythraeum* causes indiscriminate mortality of fish and invertebrates due to oxygen depletion.

**Dinophyta** (Dinoflagellates; *dinos* = whirling) This group of unicellular eukaryotic organisms (mostly reddish-brown in color) are termed “flagellates” because the majority, including the *toxic* species, can swim by means of a pair of whip-like flagella. Dinoflagellates occur in both saltwater and freshwater. The great majority of this protist group are photosynthetic (*Noctiluca* and some species of *Dinophysis* are the notable exceptions). Several subgroups of Dinoflagellates that frequently develop in the world oceans are known to be occasionally or invariably harmful: Gymnodinoids and Noctilucoids (e.g., *Amphidinium*, *Cochlodinium*, *Gymnodinium* genera), Peridinoids (*Peridinium* genus), Gonyaulacoids (e.g., *Alexandrium*, *Pyrodinium*, *Gonyaulax*, *Gambierdiscus*, *Ostreopsis*, *Ceratium* genera), Dinophysoids (*Dinophysis* genus), Prorocentroids (*Prorocentrum* genus).

Species such as *Gonyaulax polygramma*, *Noctiluca scintillans*, *Scripsiella trachoidea*, *Gymnodinium mikimotoi*, *Cochlodinium polykrikoides*, and some others, which produce basically harmless water discolorants, can under exceptional conditions grow so dense that they cause indiscriminate mortality of fish and invertebrates due to oxygen depletion (e.g., the well-known red tide phenomenon). *Pfiesteria* spp. are known to cause tumors and endanger public health (Anonymous, 2003e).

**Haptophytes** (Prymnesiophytes) These are gold to golden-brown flagellates that comprise a heterogeneous group of unicellular algae. The best known are the coccolithophorids, mainly temperate water forms (with the exception of *Emiliania huxleyi* and some others), which generate calcite scales on the cell surface. Presently only species of the genera *Prymnesium*, *Chrysosphaerulina*, and *Phaeocystis* (a cosmopolitan genus of foam-producing species) are generally recognized as potentially toxic. The species *Prymnesium parvum* and *P. patelliferum* cause the damaging or clogging of fish gills.

**Bacillariophyta** (diatoms) Diatoms, unicellular orange or brown (depending on the intensity of pigmentation) algae, are ubiquitous throughout the world's oceans and in all kinds of aquatic habitats. The genera and species dealt with here are those that are considered harmful due to (i) *mucilage* production (*Thalassiora*, *Coscinodiscus*, *Chaetoceros*), (ii) *physical damage* to fish gills (*Chaetoceros*), and (iii) *toxin* production (*Pseudonitzschia*).

**Raphidophyceae** (marine raphidophytes) These are small golden-brown flagellates that can pose a serious threat to finfish aquaculture due to both *physical clogging* of gills by mucus excretion as well as *gill damage by hemolytic substances*. The following

**Table 3.1.** Phytoplankton size classes vs. harmful algal divisions/classes (culled from Table 2.2 of Anonymous, 1997).

Algal class	<i>Microplankton</i> (20– $\geq$ 200 $\mu\text{m}$ )	<i>Nanoplankton</i> (2–20 $\mu\text{m}$ )	<i>Picoplankton</i> (0.2–2 $\mu\text{m}$ )
Cyanophyta	+	+	+
Dinophyta	+	+	–
Prymnesiophyceae	–	+	–
Bacillariophyta	+	+	–
Raphidophyceae	+	–	–

genera/species are most frequently associated in this connection: *Chattonella*, *Heterosigma*, *Olisthodiscus lutes*, *Fibrocaspa*.

This concise and inevitably incomplete list of algal classes/genera/species, which are ascribed to the category of harmful aquatic organisms, is explicitly indicative of the immense diversity of phytoplankton that need monitoring in the world's oceans (e.g., Johnsen *et al.*, 2011; Roy *et al.*, 2011). Their sizes are very variable (Table 3.1) and the pigment composition is complex (Table 3.2).

Table 3.2 does not include chlorophyll-*b* because it is not supported by more recent investigations. The dinoflagellate *Lepidodinium chlorophorum* (class Dinophyceae, order Gymnodiniaceae) (Elbrächter and Schnepf, 1996; Hansen *et al.*, 2007) is acknowledged as a harmful foam-producing species. *L. chlorophorum* cells excrete into water polysaccharides as transparent colloidal biopolymers, which further, through coagulation, yield transparent exopolymeric particles (TEPs). TEPs affect the rate of zooplankton uptake of phytoplankton, retain/accumulate bacteria and viruses, and thus accentuate the pathogenic background in the ambient aquatic environment. *L. chlorophorum* cells are green peridinin-containing plastids with a chlorophyll complex consisting of chlorophyll-*a* and chlorophyll-*b* pigments (Takishita *et al.*, 2008). Thus, Table 3.2 should also encapsulate chlorophyll-*b* as a taxonomically significant pigment in harmful algae.

### 3.2 ABSORPTION AND EMISSION SPECTRAL FEATURES OF PIGMENTS

#### *Chlorophylls (chl)*

Purified chl-*a* absorb at  $\sim$ 430 nm (blue, Soret) and  $\sim$ 660 nm (red). There are also inflexions at about 380, 410, 535, 590 and 615 nm (Figure 3.1). The emission/fluorescence band emerges at  $\sim$ 660 nm (for excitation at 430 nm). In living cells (Figure

**Table 3.2.** Distribution of major and taxonomically significant pigments in harmful algae (culled from Table 2.3 of Anonymous, 1997).

Pigment	Algal division/class				
	Cyanophyta	Dinophyta	Prymnesio-phyceae	Bacillario-phyta	Raphidophyceae
<b>Chlorophylls</b>					
<i>a</i>	●	●	●	●	●
<i>c</i> <sub>1</sub>				●	
<i>c</i> <sub>2</sub>		●	●	●	
<i>c</i> <sub>3</sub>			●		●
<b>Carotenes</b>					
<i>α</i>	+		+	<i>a</i>	+
<i>β</i>					
<b>Xanthophylls</b>					
Diadinoxanthin		●	●	●	●
Dinoxanthin		+			
Fucoxanthin			●	●	●
19'-Hexanoyloxy-fucoxanthin			●		
Peridinin					
Zeaxanthin	●	●			
<b>Biliproteins</b>					
Allophycocyanins	●				
Phycocyanins	●				
Phycoerythrins	●				

Code: ● = major pigment (>10%); + = minor pigment (1–10%) of total chlorophylls or carotenoids or biliproteins.

<sup>a</sup> Bacillariophyta also contain low amounts of β-carotene (Prezelin and Boczar, 1986).

3.2) the red band ratios of 2.5–2.7 are indicative of healthy algal cells, whereas very high ratios (5.6–7.5) indicate the presence of degradation products from senescent cells or detrital material. *In vivo*, the absorption maximum of *chl-b* centers at ~470 nm (Soohoo *et al.*, 1986; Hoepffner and Sathyendranath, 1993).

Figure 3.3 illustrates the absorption spectra of three *chl-c* pigments in organic solvents. *Chl-c*<sub>1</sub>, *c*<sub>2</sub>, *c*<sub>3</sub> display a strong absorption band at ~450 nm and two minor bands at ~580 and ~625 nm. The emission/fluorescence band for all three *chl-c* pigments is located at ~634 nm (for excitation at 450 nm).

### Carotenes

α-Carotene dissolved in acetone exhibits two major absorption bands at ~447 and 475 nm, as well as two inflexions at 422 and 334 nm (Figure 3.4). The absorption

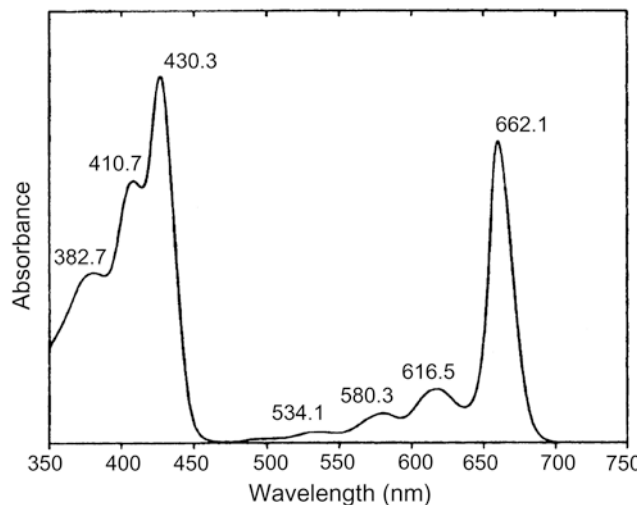


**Figure 3.1.** Absorption spectrum of *chl-a* in acetone (for references see Anonymous, 1997, p. 458).

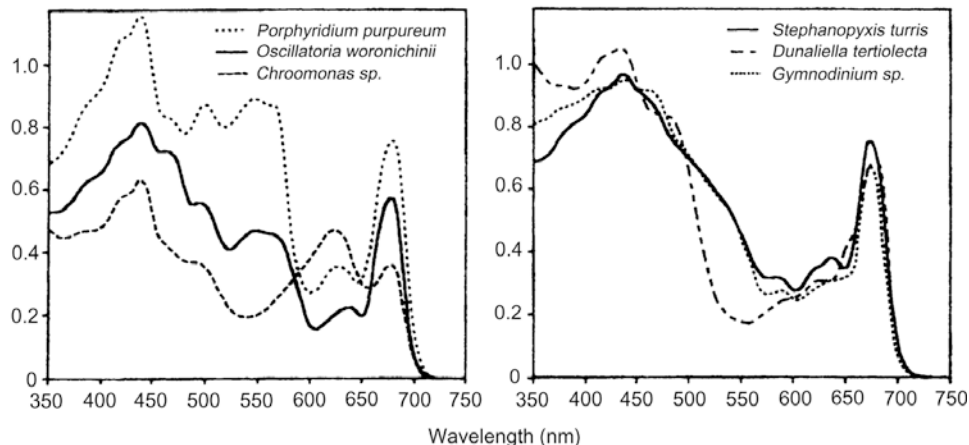


**Figure 3.2.** *In vivo* absorption spectra of algal cells from several classes, of which three are ascribed to harmful alga: Bacillariophyta (*Stephanopyxis turris*), Dinophyta (*Gymnodinium* sp.), and Cyanophyta (*Oscillatoria woronichinii*) (culled from Fig. 3.1, Anonymous, 1997, p. 88).

spectrum of  $\beta$ -carotene dissolved in acetone displays very similar signatures: absorption bands at 453 and 480 nm, and an inflection at 426 nm. Carotenoids and the xanthophylls discussed below are not fluorophores and, hence, do not fluoresce.

### Xanthophylls

There are two absorption bands in the absorption spectrum of diadinoxanthin dissolved in acetone: at 448 and 478 nm, with an inflection at 425 nm ([Figure 3.5](#)). Dinoxanthin dissolved in acetone exhibits two major absorption bands at ~442 and ~471 nm and an enhanced inflection at ~418 nm ([Figure 3.6](#)). The absorption spectrum of fucoxanthin dissolved in acetone displays a strong absorption band at ~446 nm and an inflection at ~468 nm ([Figure 3.7](#)). 19'-Hexanoyloxyfucoxanthin dissolved in acetone absorbs at ~444 and 470 nm, and there is an inflection at 420 nm ([Figure 3.8](#)). The absorption spectrum of peridinin dissolved in acetone ([Figure 3.9](#)) exhibits a single strong band at ~473 nm, and an inflection at 458 nm (when dissolved in *n*-hexane, peridinin displays two absorption bands at ~455 and 487 nm, the first of them being stronger). In the absorption spectrum of zeaxanthin dissolved in acetone there are two absorption bands at ~454 and ~481 nm and an inflection at 428 nm ([Figure 3.10](#)).

According to their function in the algal cell, fucoxanthin, 19'-hexanoyloxyfucoxanthin, and peridinin are ascribed to photosynthetically active carotenoids;  $\beta$ -carotene, zeaxanthin, diadinoxanthin are termed photoprotectant carotenoids (Lutz *et al.*, 1998).

### Biliproteins

Biliprotein chloroplast pigments are found only in certain algae: Rodophyta, Cryptophyta, and Cyanophyta. The red, blue, and purple biliproteins are called phycoerythrin, phycocyanin, and allophycocyanin, respectively ([Figure 3.11](#)). Phycoerythrin absorbs light over a broad range of the visible spectrum with one maximum for blue-greens and three maxima for red algae, all placed between 500 and 570 nm. Phycocyanin absorbs light at slightly longer wavelengths between 550 and 620 nm. Allophycocyanin is the longest wavelength-absorbing biliprotein. All three pigments exhibit enhanced absorption in the ultraviolet (<350 nm). The spectral features of the absorption of biliproteins for a variety of algal species have been reported (e.g., Anonymous, 1981; Kirk, 1983; Babichenko *et al.*, 1993, 1999; Lalli and Parsons, 1995; Vincent *et al.*, 2004).

Biliproteins are fluorophores. The fluorescent maxima for phycoerythrin, phycocyanin, and allophycocyanin are centered at 575, 635, and 660 nm with excitation at 565, 615, and 650 nm, respectively (Anonymous, 1981).

In addition to the above pigments, there are ultraviolet-absorbing/screening substances in cyanobacteria and phytoplankton. These are mycosporine-like amino acids and the cyanobacterial sheath pigment (Sinha *et al.*, 1998).

Homogeneous solutions of free *chl*, carotenoids, and biliproteins (as in organic solvents) are not found in photosynthetic cells: pigments function in photosynthesis only when associated with specific apoproteins such as *chl* and carotenoid-containing pigment–protein complexes.

The association with proteins modifies pigment spectra. Free *chl-a* absorb in the red part of the spectrum at about 660 nm ([Figure 3.1](#)), but associated with specific reaction center I and II apoproteins they absorb at 700 and at 680 nm.

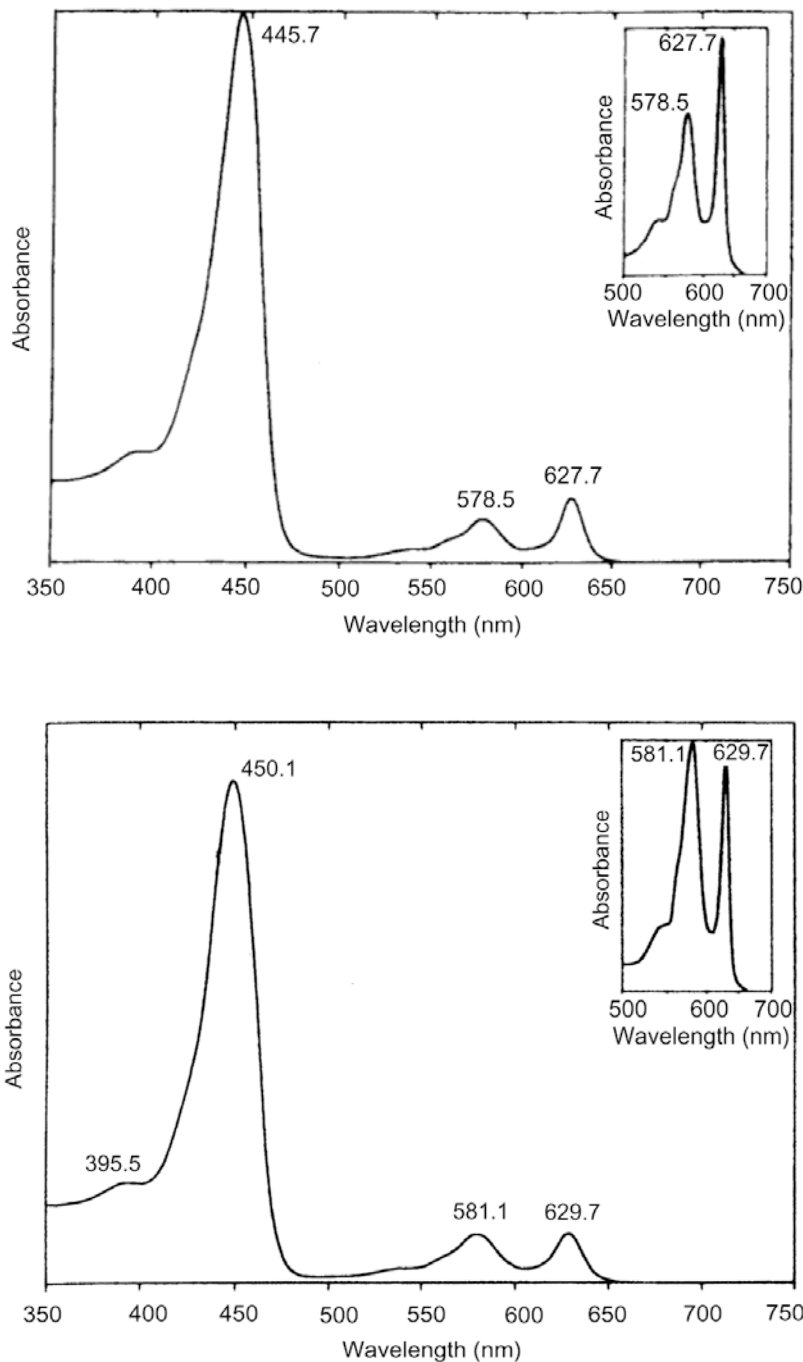


**Figure 3.3.** Absorption spectra of three *chl-c* in diethyl ether (*chl-c*<sub>1</sub>, *c*<sub>2</sub>) or acetone (*chl-c*<sub>3</sub>) (culled from Fig. 7.4, Anonymous, 1997, pp. 480, 482, 484).

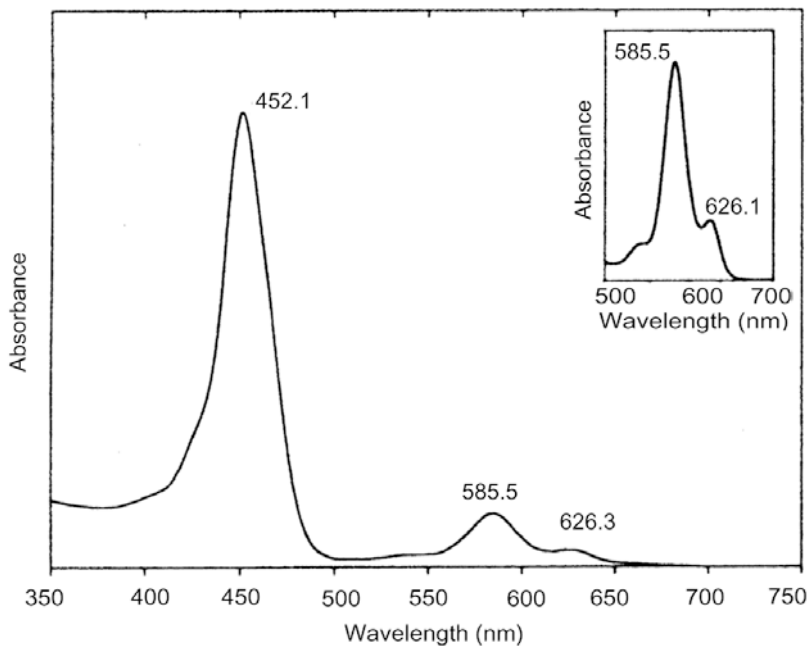
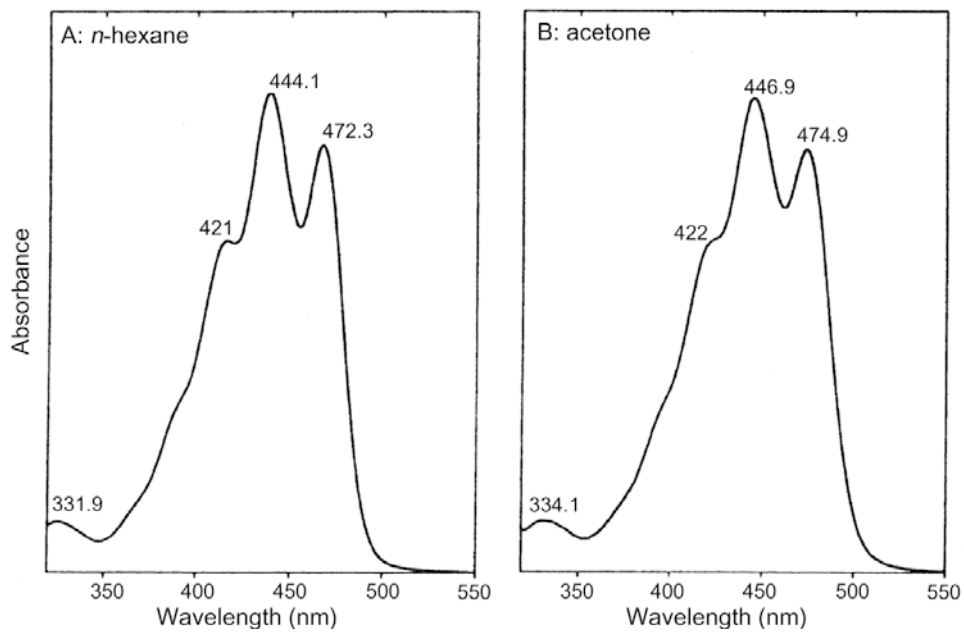
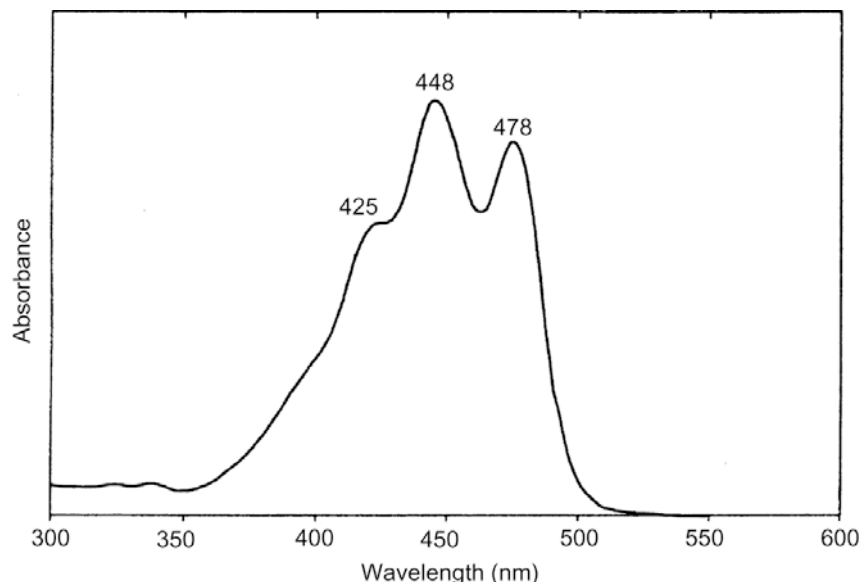
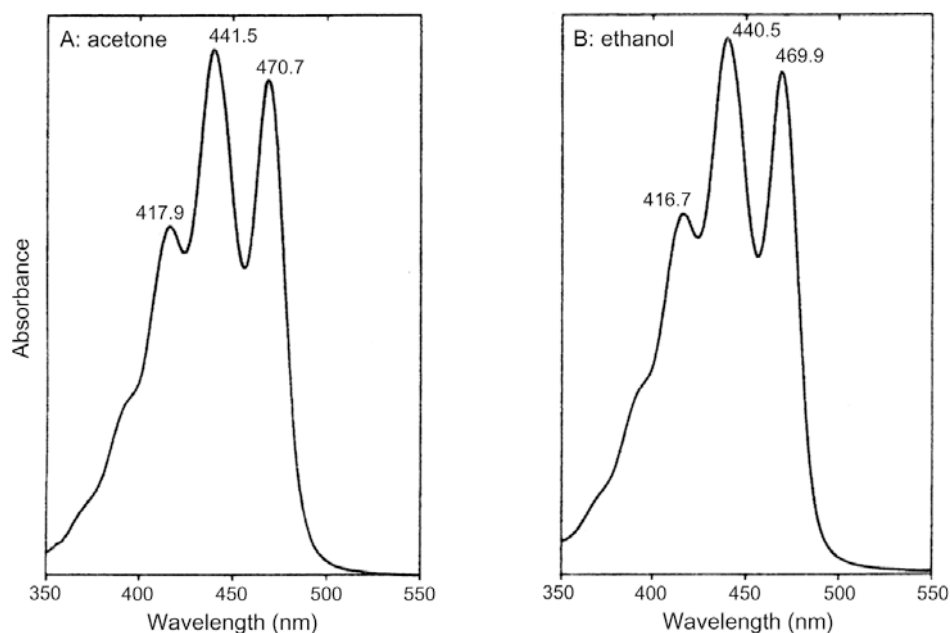


Figure 3.3 (cont.)

Figure 3.4. Absorption spectrum of  $\alpha$ -carotene dissolved in acetone (culled from Anonymous, 1997, p. 504).



**Figure 3.5.** Absorption spectrum of diadinoxanthin dissolved in acetone (culled from Anonymous, 1997, p. 516).



**Figure 3.6.** Absorption spectrum of dinoxanthin dissolved in acetone (culled from Anonymous, 1997, p. 520).

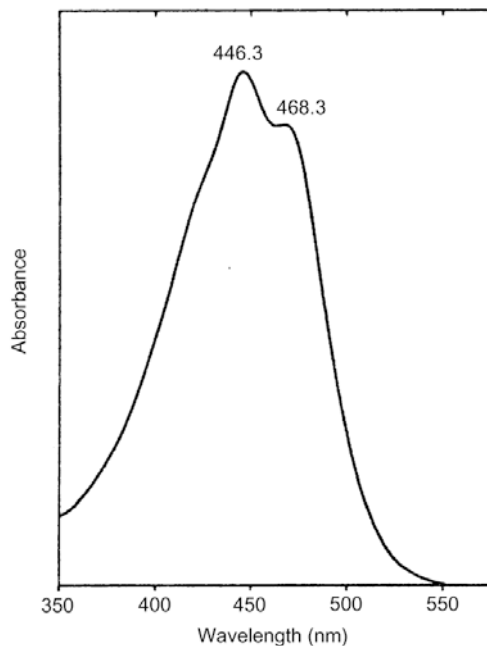


**Figure 3.7.** Absorption spectrum of fucoxanthin dissolved in acetone (culled from Anonymous, 1997, p. 526).

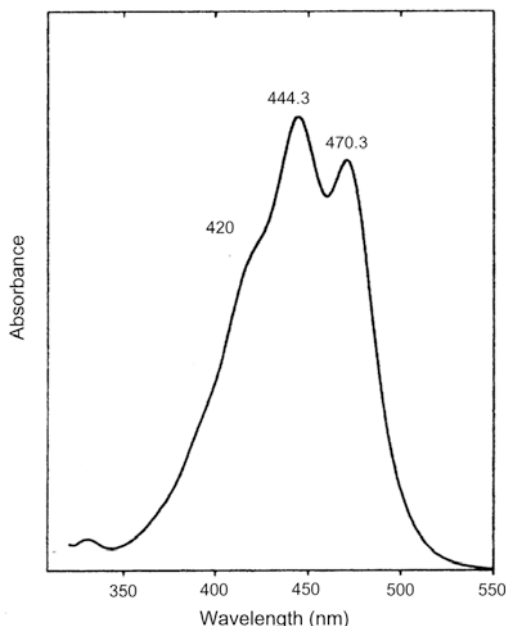


**Figure 3.8.** Absorption spectrum of 19'-hexanoyloxyfucoxanthin dissolved in acetone (culled from Anonymous, 1997, p. 528).

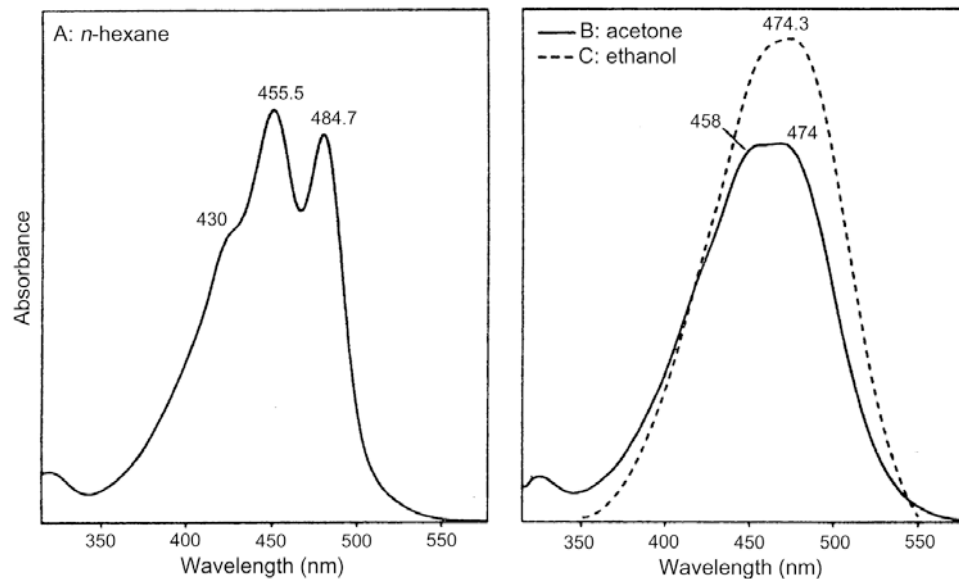


**Figure 3.9.** Absorption spectrum of peridinin dissolved in acetone (culled from Anonymous, 1997, p. 540).

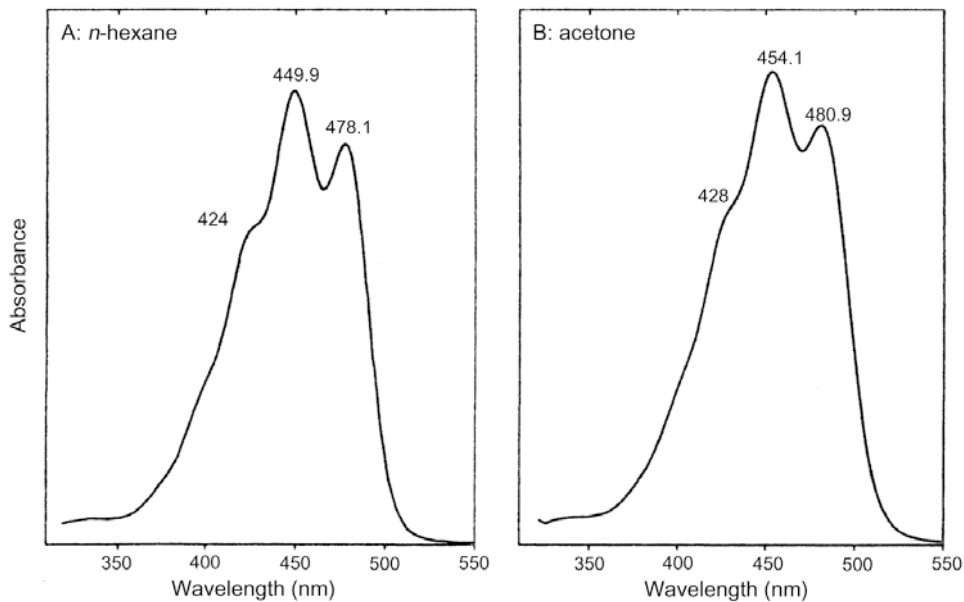


**Figure 3.10.** Absorption spectrum of zeaxanthin dissolved in acetone (culled from, Anonymous, 1997, p. 552).

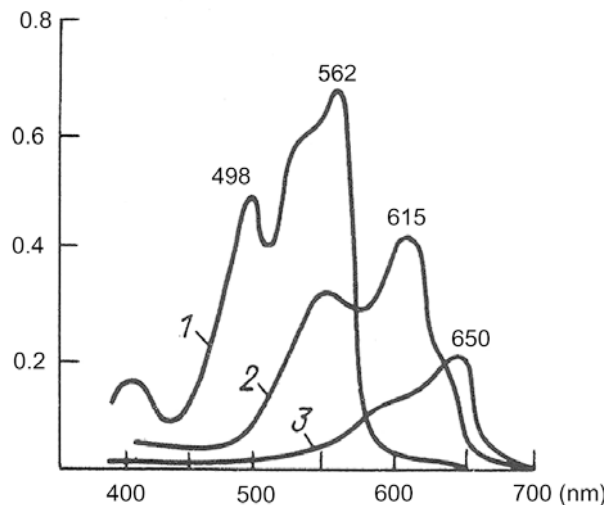


**Figure 3.11.** Absorption by biliproteins from blue-green algae: 1—phycoerythrin, 2—phycocyanin, 3—allophycocyanin (Kirk, 1983).

The modification of *chl* spectra by bonding with proteins is also reflected in *in vivo* spectra (Figure 3.2, for references see Anonymous, 1997). It is reported that phycocyanin *in vivo* fluoresces at 660 nm with excitation at 630 nm (Vincent *et al.*, 2004).

The relative content of pigments in living algae is variable, being influenced by a number of factors. The most consequential factors are nutrient limitation and irradiance (Henriksen *et al.*, 2002). Nutrient conditions also control the fluorescence intensity of algae (Babichenko *et al.*, 2001).

The absorption spectrum of living phytoplankton is not solely affected by pigment composition, community size structure also plays a part (Lohrenz *et al.*, 2003). The absorption and emission properties of algal pigments *in vitro* and *in vivo* can also be presented as specific (i.e., per unit concentration) characteristics (Bidigare and Ondrusek, 1990; Hoepffner and Sathyendranath, 1993; Ahn *et al.*, 1992; Sathyendranath *et al.*, 2001; for other references see Pozdnyakov and Grassl, 2003). As discussed hereafter, the corresponding *in vivo* quantities are important inputs to the methodologies of remote detection and mapping of harmful algal taxonomy.

### 3.3 INHERENT OPTICAL AND APPARENT PROPERTIES OF NATURAL WATERS

Open ocean waters—termed “case I” waters (Morel and Prieur, 1977)—are generally loaded only with indigenous phytoplankton and their *retinue*—that is, accompanying and co-varying products of their life cycles, as well as some microscopic organisms such as flagellates, bacteria, and viruses, which are also indigenous to oceanic waters (Sathyendranath, 2000). Therefore, spectral variations in the light

emerging from beneath the water surface must be proportional to the in-water concentrations of phytoplankton, or its proxy: the concentration of chlorophyll (*chl*) contained in algal cells.

However, waters in the coastal zone as well as inland waters, referred to as “case II” waters (Morel and Prieur, 1977) are characterized by optical properties that are influenced not only by the indigenous phytoplankton and the substances originating from the life cycle of phytoplankton, but also by other matters independent of phytoplankton (denoted herein as *chl*), notably inorganic/terrigenous particulate matter in suspension (*sm*) and dissolved organics (*doc*). Their content in the water column is often abundant enough to compete with phytoplankton in influencing the resultant optical properties of case II waters, thus rendering such waters optically very complex. The spectral variations of water-leaving light prove to be controlled not only by *chl*, but also other in-water color-producing agents (CPAs), mainly encompassing the water itself (i.e., H<sub>2</sub>O molecules) and *chl*, also *sm* and *doc* (Bukata *et al.*, 1995). These constituents are traditionally associated with the so-called non-scientific *water quality properties* (WQPs), although more substances contribute to these (Anonymous, 1992).

As mentioned above, while traveling through the water column, light becomes attenuated because of the interactions of photons (absorption and scattering) with aquatic constituents. Numerically, the attenuation of direct sunlight (as opposed to diffuse sky light) in the water body can be assessed—via the beam absorption coefficient  $a(\lambda)$ , beam scattering coefficient  $b(\lambda)$ , and beam attenuation coefficient  $c(\lambda)$ —with:

$$c(\lambda) \equiv a(\lambda) + b(\lambda), \quad (3.1)$$

where  $\lambda$  is the spectral wavelength of light propagating through the aquatic medium, and coefficients  $a, b, c$  are given in m<sup>-1</sup>.

Importantly, the values of the coefficients  $a(\lambda)$ ,  $b(\lambda)$ , and  $c(\lambda)$  are independent of the manner in which the medium under observation is being illuminated. Such optical properties, therefore, should be independent of the radiation distribution within this medium and entirely depend on the intrinsic physical/chemical attributes of water constituents. Accordingly, all three quantities  $a(\lambda)$ ,  $b(\lambda)$ , and  $c(\lambda)$  qualify as *inherent optical properties* (IOPs) of the medium.

It is noteworthy that inherent optical properties are *additive* in nature and result from the individual contributions of co-existing absorbing and/or scattering constituents indigenous to natural waters:

$$a = \sum_i^N a_i; \quad b = \sum_j^{N'} b_j, \quad (3.2)$$

where  $i = 1, 2, 3, \dots, N$ ;  $j = 1, 2, 3, \dots, N'$ ,  $N$  and  $N'$  are the total numbers of absorbing and scattering constituents co-existing in water.

The above additive expressions for  $a$ ,  $b$  (and also  $c$ ) can be further modified via introducing *specific* absorption  $a^*$  and *specific* scattering  $b^*$  coefficients (also referred

to as absorption and scattering *cross-sections*):

$$a = \sum_i^N C_i a_i^*; \quad b = \sum_j^{N'} C_j b_j^*, \quad (3.3)$$

where  $i, j, N$ , and  $N'$  are as above,  $C_i$  and  $C_j$  are the in-water concentrations of absorbing and scattering agents, respectively.

The angular distribution of the scattered light resulting from the aforementioned photon interactions is specified in terms of a *volume scattering function*,  $\beta(\theta, \phi)$ , where  $\theta$  is the sun zenith angle and  $\phi$  is the azimuthal angle.  $\beta(\theta, \phi)$  defines the ratio of scattered radiance in a direction  $(\theta, \phi)$  per unit scattering volume to the value of incident solar irradiance  $E$ . Assuming the independence of azimuth (which is a common approximation in the majority of natural waters), the angular dependence of the volume scattering function is generally confined to  $\theta$ . If normalized to the scattering coefficient  $b$ , the volume scattering function  $\beta(\theta)$  is named the *scattering phase function*,  $P(\theta)$ . In the case of an *isotropic* scattering medium, the phase function  $P$  is understandably equal to unity. Together with  $a, b, c, \beta(\theta, \phi)$ , and  $P(\theta)$  are also IOPs. Importantly, all IOPs are spectrally dependent, but for simplicity this dependence is omitted here.

Because light emerging from beneath the water surface (and eventually captured by a remote sensor) consists of photons reflected within the water column into the hemisphere facing the water-air interface, it is meaningful to single out the *back-scattering coefficient*,  $b_b = Bb$  along with the *forward scattering coefficient*,  $b_f = Fb$ , where  $B$  and  $F$  are the *backscattering* and *forward scattering probability*, respectively. Since all photons scattered by a unit volume are either scattered forward or backward, we get (Jerlov and Nielsen, 1974):

$$b_f + b_b = b. \quad (3.4)$$

Direct (sun) light propagation through the water column is accompanied by downward sky (*diffuse*) light. Irradiance beneath the air-water interface is attenuated as the light propagates downwards through the water column. Downwelling irradiance attenuation is described by the *irradiance attenuation coefficient*  $K_d(\lambda, z)$ , the logarithmic depth derivative of spectral irradiance at the subsurface depth  $z$ .

The intrinsic color of a water body is defined by spectral variations in *volume reflectance*  $R$  just beneath the water surface: the ratio of upwelling irradiance to downwelling irradiance at the same level within the water column. For  $z = k - 0$  the volume reflectance just beneath the surface is:

$$R(\lambda, -0) = \frac{E_u(\lambda, -0)}{E_d(\lambda, -0)}. \quad (3.5)$$

Both volume reflectance  $R$  and the irradiance attenuation coefficient  $K$  qualify as *apparent optical properties* (AOPs) and, unlike IOPs, they are dependent on the spatial distribution of incident (solar) radiation.

Numerous theoretical and field studies (Sathyendranath and Platt, 1997; Morel and Maritorena, 2001; Gordon, 2002, for other references see Pozdnyakov and

Grassl, 2003) have shown that  $R(\lambda, -0)$  is a function of bulk water absorption and backscattering coefficients,  $a$  and  $b_b$ , as well as solar zenith angle where  $\mu_0 = \cos(\theta'_0)$ , with  $\theta'_0$  being the in-water sun zenith refracted angle ( $\mu_0 = 0.858$  is taken for overcast conditions).

In the context of remote sensing in the optical spectrum, it is more appropriate to use the so-called remote-sensing reflectance,  $R_{rs}(\lambda, +0)$ , defined as the upwelling radiance leaving the water surface,  $L_u(\lambda, +0)$ , normalized by the downwelling irradiance,  $E_d(\lambda, +0)$ , just above the water surface. It has the dimension  $\text{sr}^{-1}$ . The downwelling irradiance ( $E_d(\lambda, +0)$ ) is the sum of diffuse  $E_{d,\text{sky}}(\lambda, +0)$  and direct  $E_{d,\text{sun}}(\lambda, \theta_0, +0)$  solar irradiance.

The remote sensing reflectance,  $R_{rs}(\lambda, +0)$ , which can be directly determined from atmospherically corrected satellite data, is closely related to the volume reflectance,  $R(\lambda, -0)$ , of the water body and, hence, to IOPs. For instance Jerome *et al.* (1996) found through Monte Carlo simulations that the *subsurface remote sensing reflectance*,  $R_{rsw}$ , can be related—for nadir view, flat water surface, a very wide range of in-water optical conditions (the backscattering probability varied between 0.0133 and 0.0440), sun zenith angles  $\theta_0$  from  $15^\circ$  to  $89^\circ$ —to inherent optical properties (IOPs) at high correlation (0.99) and an *rms* error of only 9% by:

$$\overline{R_{rsw}} = -0.00036 + 0.110(b_b/a) - 0.0447(b_b/a)^2. \quad (3.6)$$

For isotropic in-water and cardioidal incident radiance distribution (totally overcast skies) the subsurface remote-sensing reflectance is:

$$R_{rsw} = 1.045\overline{R_{rsw}}. \quad (3.7)$$

Therefore, through first retrieving  $R_{rs}(\lambda, +0)$  and then  $R_{rsw}$ —and based on the established relationships between  $R_{rsw}$ , bulk  $a$  and  $b_b$ , and partial concentrations of CPAs (eq. 3.3)—the latter can be remotely assessed given the spectral absorption and backscattering cross-sections  $a^*$  and  $b_b^*$  of the major CPAs. As such we first assume phytoplankton, suspended minerals, and dissolved organics, denoted herein as *chl*, *sm*, and *doc*. As indicated above, in the case of open ocean waters (case I waters), only *chl* and water *per se* essentially determine both  $a^*$  and  $b_b^*$ .

On the other hand, through the spectral composition of phytoplankton specific absorption,  $a_{chl}^*$  (which, due to its additive nature, is the sum of the specific absorptions of pigments inherent in indigenous algal cells), the spectrum of  $R_{rs}(\lambda, +0)$  may reflect the phytoplankton taxonomic structure or taxonomic identity in the area of observation.

In the case of HABs, which are often monospecific (earlier we mentioned that strictly speaking this is only the first approximation),  $R_{rs}(\lambda, +0)$  should reflect the contributions of chlorophylls, and, when appropriate, the carotenes, xanthophylls, and biliproteins present in the algae (Table 3.2). It is noteworthy that chlorophylls are always present in photosynthetic algae but, as indicated above, not all harmful algae are necessarily photosynthetic/autotrophic. Some of them (although constituting a minor part of HABs) are heterotrophic. Understandably, they only affect  $R_{rs}(\lambda, +0)$  through backscattering. Incidentally, the same refers to coccolithophores and also the coccoliths detached from them at the end of their algal life cycle.

Coccoliths remain suspended in the water after the algae that they belong to have died and sunk to depths beyond the surface water layer that can be detected by a remotely located sensor (e.g. Ackleson *et al.*, 1994; Johnsen *et al.*, 2009; Korosov *et al.*, 2009).

Therefore, in pursuit of the above-defined goal of HAB detection, it is necessary to consider the actual optical satellite Earth observation data presently available.

### 3.4 OPTICAL PROPERTIES OF THE MAJOR COLOR-PRODUCING AGENTS (CPAs) IN NATURAL WATERS

#### 3.4.1 Absorption cross-sections of whole algal cells and pigments

**Table 3.2** indicates that all *photosynthetic* harmful algae contain *chl-a*, and invariably (with the only exception of Cyanophyta) *chl-c<sub>2</sub>*, *chl-c<sub>1</sub>*, and *chl-c<sub>3</sub>* are found nearly solely in Bacillariophyta and Prymnesiophyceae, respectively. Hence, the presence or absence in the algal absorption spectrum of spectral signatures inherent in *chl-c<sub>2</sub>* and *chl-c<sub>3</sub>* might be a discriminative feature. The same refers to carotenoids and biliproteins. The latter are characteristic of Cyanophyta.

Estimations of *chl* spectral absorption cross-sections  $a_{chl}^*(\lambda)$  can be found in a wealth of publications (for references see Pozdnyakov and Grassl, 2003). Not infrequently, the reported  $a_{chl}^*(\lambda)$  values are only apparent quantities, because they reflect the cumulative effect of both intracellular pigment composition (including such auxiliary pigments as carotenes, xanthophylls, and biliproteins), and the size distribution of the cells, and as such they should instead be considered as absorption cross-sections of the *integral* algal cell,  $a_{php}^*(\lambda)$  (Bukata *et al.*, 1985; Kondratyev *et al.*, 1990; Hoepffner and Sathyendranath, 1992, 1993; Roesler and Perry, 1995):

$$a_{php}^* = \sum_{i=1}^n a_i^*(\lambda) C_i, \quad (3.8)$$

where  $n$  represents the total number of pigments considered,  $a_i^*(\lambda)$  is the specific absorption coefficient of the  $i$ th pigment at wavelength  $\lambda$ , and  $C_i$  is the concentration of the pigment.

These research results revealed rather broad ranges of the numerical values of such cross-sections, explicitly demonstrating that optical cross-sections are species dependent and, therefore, temporally and spatially variable. In addition, the optical properties of chlorophyll-bearing biota are subject to the effects of temperature, nitrogen, and light limitations. Using the marine diatom *Thalassiosira pseudonana* as an example, Stramski *et al.* (2002) found that the specific absorption of this alga increases under light limitation conditions, which is due to subsequent increase in the *chl-a* content of cells. At the same time, diatom specific absorption decreases due to a decrease in *chl-a* content as a result of temperature and nitrogen limitation.

However, the intercomparison given by Bukata *et al.* (1995) indicates (their Figure 5.1) that with very rare exceptions (e.g., the Sargasso Sea) the absorption cross-sections of phytoplankton  $a_{php}^*(\lambda)$  collected by different workers from the North Central Pacific, the California coast, the upwelling region off the coast of Peru, Lake Ladoga in northern Europe, and Lake Ontario in central North America, display similar spectral shapes. The data on  $a_{php}^*(\lambda)$  collected by Bukata *et al.* (1995) are further substantiated, both in terms of spectral signature and magnitude by the spectra of  $a_{php}^*(\lambda)$  for oceanic, marine, and coastal waters (Doerffer, 1992; Garver and Siegel, 1997).

Surprisingly, the spectra of  $a_{php}^*(\lambda)$  for Lake Ladoga and Lake Ontario are strikingly quantitatively close to each other (nearly identical), which indicates that both water bodies are characterized by optically and thus taxonomically comparable populations of chlorophyll-bearing biota.

Despite the limited data for inland waters, it should be noted that the two curves representing inland waters (curves 1 and 2 in Figure 5.1 of Bukata *et al.*, 1995) display larger absorption cross-section values at longer wavelengths than for oceanic and coastal waters. This is fully consistent with the data reported by Roesler and Perry (1995) for oceanic, fjord, coastal, and estuarine waters. This feature is also observable in the data from Lake Chilko (Gallie and Murtha, 1992), as well as from Gege (1998) and Gege *et al.* (2001). The latter workers investigated the spectral distribution of  $a_{php}^*(\lambda)$  for a wide variety of algal taxa, including the diatoms and dinoflagellates indigenous to Lake Constance (Germany). In all these cases, the intensity of the “red” absorption maximum was nearly comparable (but still inferior) to the height of the “blue” absorption band.

The position of the absorption bands as well as the spectral values of the specific absorption coefficients of photosynthetic pigments and, consequently, the spectral values of the specific absorption coefficient of phytoplankton reveal a spatial variability driven by a number of factors. In particular, the optical properties of algal cells are controlled by the water body’s trophic status since it largely determines, among other things, the taxonomic composition and size distribution of algal cells in the phytoplankton community.

Cirolli *et al.* (2002) found that, in general, when the phytoplankton abundance increases, larger size classes are added incrementally to the background of smaller cells. The spectral value of  $a_{php}^*(\lambda)$  proves to be very responsive to cell sizes, mostly due to pigment packaging and the concentration of accessory pigments. The smaller the algal species, the higher the peak values of  $a_{php}^*(\lambda = 450 \text{ nm})$ . For instance,  $a_{php}^*(\lambda = 450 \text{ nm})$  is about  $0.06 \text{ m}^2/\text{mg chl}$  for picoplankton (cells  $< 2 \mu\text{m}$ ), and it is *ca.* 0.04, 0.03, and  $0.01 \text{ m}^2/\text{mg chl}$  for ultraplankton (cells in the range  $2\text{--}5 \mu\text{m}$ ), nanoplankton (cells in the range  $5\text{--}20 \mu\text{m}$ ), and microplankton (cells  $> 20 \mu\text{m}$ ), respectively.

Earlier, according to the extensive studies conducted in various parts of the global ocean during various vegetation periods (April–October), at different depths ( $0\text{--}180 \text{ m}$ ), and in water masses of different trophic status ( $0.02 < C_{chl} < 25 \text{ mg/m}^3$ ) (Bricaud *et al.*, 1995; Allali *et al.*, 1997), the specific absorption coefficient of phytoplankton decreases with increasing chlorophyll concentration at all

wavelengths. Based on the analysis of more than 800 spectra of  $a_{php}^*(\lambda)$ , the following formulation has been suggested (Bricaud *et al.*, 1995):

$$a_{php}^*(\lambda) = A(\lambda)C_{chl}^{-B(\lambda)}, \quad (3.9)$$

where  $A$  and  $B$  are wavelength-dependent coefficients.  $a_{php}^*(\lambda)$  depends on  $C_{chl}$  most strongly in the blue and red part of the spectrum. An explanation of the  $a_{php}^*(\lambda)$  decline with increasing  $C_{chl}$  should obviously be sought in the interdependence between  $C_{chl}$  and the co-existing concentrations of accessory pigments: there is experimental evidence that the content in algal cells of such pigments as non-photosynthesizing carotenoids, *chl-b*, and divinyl *chl-b* is almost always higher in eutrophic rather than in mesotrophic and oligotrophic waters (Bidigare and Ondrusk, 1990).

In addition to variations in  $a_{php}^*(\lambda)$  driven by the trophic status of a water body, seasonal variations in  $a_{php}^*(\lambda)$  also prove to be essential (Kondratyev *et al.*, 1999; Sathyendranath *et al.*, 1999). This implies, strictly speaking, that the  $a_{php}^*(\lambda)$  spectral values to be included in a hydro-optical model of a water body should not only be trophic specific but also season specific.

Stramski *et al.* (2001) analyzed the importance of taking into account the detailed composition of the planktonic community for correct portrayal of the IOPs of a targeted water body: 18 planktonic components covering a size range from submicrometer viruses and heterotrophic bacteria to microplanktonic species with in-cell diameters of 30  $\mu\text{m}$  were involved. Stramski *et al.* showed that variations in the composition of a planktonic community might lead to significant variations in IOPs, although the chlorophyll concentration can remain unaltered.

Apart from the above factors impacting spectral variations in  $a_{php}^*(\lambda)$ , the presence of chlorophyll decomposition products in phytoplankton cells caused by oxygen hydrolysis also strongly influences  $a_{php}^*(\lambda)$ . The degradation of *chl-a* into *pheophytin* results in a displacement of the absorption maximum from 430 nm to *ca.* 415 nm, whereas the long-wavelength maximum at 664 nm transforms into a weaker band centered at *ca.* 667 nm. Weak acidification of the medium brings about a complete disappearance of the red absorption band. Therefore, any increase in the ratio of the blue to red absorption maximum in the spectral distribution of  $a_{php}^*(\lambda)$  may indicate the presence of “dead” or dying phytoplankton in considerable amounts (Sosik and Mitchell, 1995).

In some other studies (Bidigare *et al.*, 1989; Hoepffner and Sathyendranath, 1993)  $a_{php}^*(\lambda)$  is decomposed into components associated with the major photosynthetic pigments. These values, which were corrected for the packaging effect (Duygens, 1956), showed no significant dependence on algal species and, therefore, can be used to reconstruct the *in vivo* absorption spectrum if the concentrations of pigments are known. Conversely, knowing the absorption spectrum of an algal cell in the water, one can also use these individual pigment-associated absorption cross-sections to identify and evaluate indigenous intracellular pigments. A curve-fitting program used to this end decomposed the  $a_{php}^*(\lambda)$  spectrum into Gaussian

bands:

$$a_{php}(\lambda) = \sum_{j=1}^l C_j a_j^*(\lambda_{mj}) \exp \left[ \frac{(\lambda - \lambda_{mj})^2}{2\sigma_j^2} \right], \quad (3.10)$$

where  $\lambda_{mj}$  is the position of maximum absorption for the  $j$ th Gaussian band,  $\sigma_j$  determines the width of the peak,  $a_j^*(\lambda_{mj})$  is the specific absorption coefficient for the  $j$ th absorption band at  $\lambda_{mj}$  (the wavelength of maximum absorption), and  $C_j$  is the concentration of pigment responsible for the  $j$ th absorption band. Because a given pigment may be responsible for more than one absorption band,  $l$  in eq. (3.10) can be  $>n$  in eq. (3.9).

The initial values of half widths (equal to  $2.35\sigma$ ) and centers of maximum Gaussian absorption suggested by Hoepffner and Sathyendranath (1993) are the mean values obtained from cultures of three important phytoplankton groups: Bacillariophyceae, Haptophyceae, and Chlorophyceae; two of these are listed in Table 3.1 as being harmful algae. Table 3.3 illustrates the mean characteristics of the Gaussian bands and specific absorption coefficients of chlorophylls and carotenoids for Georges Bank waters (the western North Atlantic). In these waters, the phytoplankton community is dominated by large diatoms.

Table 3.3 indicates that the spectral values of the *chl-a* absorption cross-sections are consistently higher than those of carotenoids and only slightly in excess of those of *chl-c*; *chl-b* appears to be the most efficient light absorber compared to other chlorophylls. This naturally refers to the spectral ranges of respective absorption bands.

Bidigare *et al.* (1989) also report on the absorption cross-sections of *chl-a*, *chl-b*, *chl-c*, but separately on photoprotectant and photosynthetic carotenoids as well as on some biliproteins. The latter seem to be the least efficient light absorbers in comparison with other pigments inherent in harmful algae.

It is important to add that Babin and Stramski (2002) obtained experimental evidence indicating that phytoplankton cells in marine environments exhibit similar absorbance patterns in the *near-infrared* spectral region above 700 nm (i.e., a nearly flat spectrum with values very close to zero). This finding appears very significant for analyzing the spectral distribution of water-leaving radiance at these wavelengths. However, below 700 nm, the absorbance of aquatic particles collected *in situ* exhibit non-uniform spectral patterns with an appreciable enhancement centered at  $\sim 675$  nm, which is certainly due to the optical impact of biogeneous particles containing chlorophylloous pigments (Tassan and Ferrari, 2003).

### 3.4.2 Backscattering cross-sections of algal cells

In the backscattering cross-section spectra ( $b_{b_{php}}^*(\lambda)$ ) for phytoplankton from Lake Ladoga and Lake Ontario (Bukata *et al.*, 1995) two features are distinctly discernible (their Figure 5.3): a minimum at about 450 nm, which is followed by a broad maximum at about 550 nm. The minimum is a consequence of the scattering depression at the wavelengths of maximum absorption (430 to 650 nm). Phytoplankton

**Table 3.3.** Mean characteristics of Gaussian bands and associated specific absorption coefficients,  $m^2$  (mg pigment $^{-1}$ ), of chlorophylls and carotenoids for Georges Bank waters (from Hoepffner and Sathyendranath, 1993).

Parameters	Gaussian band number and associated pigment <sup>a</sup>												
	1 <i>chl-a</i>	2 <i>chl-a</i>	3 <i>chl-a</i>	4 <i>chl-c</i>	5 <i>chl-b</i>	6 carot.	7 <i>chl-c</i>	8 <i>chl-a</i>	9 <i>chl-c</i>	10 <i>chl-a</i>	11 <i>chl-b</i>	12 <i>chl-a</i>	13 <i>chl-a</i>
Half width, nm	43.7	21.8	32.8	28.2	37.9	46.6	50.3	46.4	40.1	28.5	23.4	25.6	34.0
Center, nm	382.3	411.8	435.2	462.8	466.2	489.3	535.6	586.1	621.6	640.7	653.0	675.7	700.2
Specific absorption coefficient	0.029	0.013	0.031	0.081	0.074	0.029	0.018	0.044	0.005	0.039	0.020	0.017	0.002

backscattering can be seen to have a similar behavior in data tabulated by Gregg *et al.* (1993) and in the modeling results reported by Gordon for oceanic waters (see [Figure 15](#) in Morel and Maritorena, 2001). Also, the spectra previously reported by Ahn *et al.* (1992) of phytoplankton backscattering cross-sections for a variety of algae species from Haptophyceae, Dinophyceae, Cyanophyceae, Chlorophyceae, and Cryptophyceae classes, ranging for different species between  $10^{-5}$  to  $10^{-3} \text{ m}^2 \text{ mg}^{-1}$  across the visible spectrum, display the same features of scattering depressions at wavelengths close to maximum absorptions.

For open ocean waters (i.e., case I waters), several parameterizations have been suggested to calculate *total particulate* backscattering. This implies that not only algal cells, but also bacteria, viruses, and other organic particles (i.e., detritus) constituting the phytoplankton retinue (whose abundance is proportional to  $C_{chl}$ ) are assumed to contribute to water column bulk backscattering. The following equation has been suggested by Sathyendranath *et al.* (2001):

$$b_b(\lambda, C) = 0.0407 \cdot C^{0.795} (600/\lambda)^{-n} (0.78 - 0.42 \log_{10} C), \quad (3.11)$$

with the value of  $n$  allowed to co-vary with  $C_{chl}$ :

$$n = \log_{10} C_{chl}. \quad (3.12)$$

Gordon and Morel (1993), Morel and Maritorena (2001), Morel *et al.* (2002), Maritorena *et al.* (2002) also suggested very similar expressions, which differed in the coefficients, however. Specific backscattering quantities can naturally be obtained from equations such as (3.11) for a number of characteristic ranges of *chl* concentrations. It should be underscored, however, that these are thoroughly generalized semi-analytical expressions suited to match the backscattering properties of the world oceans.

Available simultaneous data (see also Roesler and Perry, 1995) on phytoplankton absorption and backscattering coefficients, albeit very scarce, point to great natural variability in  $a_{php}^*(\lambda)$  and  $b_{b_{php}}^*(\lambda)$ . As an example, see Siegel *et al.* (1999), whose  $a_{php}^*(\lambda)$  values for the Pomeranian Bight and the Baltic Sea are between 2 and 10 times smaller than the  $a_{php}^*(\lambda)$  values illustrated in [Figure 5.1](#) of Bukata *et al.* (1995). This might be a consequence of the availability of nutrients and light, the vegetation season, taxonomic composition, phytoplankton size distribution as affected in addition by many other factors including nutrition and light availability, zooplankton grazing, bacterial decomposition rates, weather conditions, and vertical distribution conditioned by turbulent mixing (Carder *et al.*, 1999; Kondratyev *et al.*, 1999; Lohrentz *et al.*, 2003; Kim *et al.*, 2004).

By and large, the above data indicate that living algal cells exert relatively low influence on the backscattering processes of oceanic waters compared to other in-water constituents (see below). However, there is an important exception: coccolithophores, which are in the group of harmful algae (see the introduction to this chapter). Small marine Prymnesiophyte phytoplankton, coccolithophores, form external calcified scales (diameter  $\sim 2 \mu\text{m}$  and thickness 250 to 750 nm) called coccoliths. Coccoliths can form several layers and eventually detach. Of the coccolithophore species, *Emiliania huxleyi* is the most frequently occurring, and its

coccoliths can often be found from tropical to subtropical regions and farther north into regions with water temperatures about 0°C. Perhaps the most intriguing aspect of coccolithophores concerns the frequency and spatial extension of their blooms: 100 to 200 µm diameter coccolithophore blooms within temperate waters on an annual basis are observed. For instance, upwelling radiance measurements from the Coastal Zone Color Scanner (CZCS) as early as 1978 to 1986 frequently showed large mesoscale features that were sometimes characterized by complete saturation of band 3 (550 nm wavelength) of the CZCS. Balch *et al.* (1996) found empirically that the backscattering coefficient at  $\lambda = 546$  nm ( $b_b(546)$  in  $\text{m}^{-1}$ ) could be related statistically to the detached coccolith concentration ( $N_{cocco}$  in  $\text{mL}^{-1}$ ) through

$$b_b(546) = 1.35 \cdot 10^{-7} N_{cocco} + 3.06 \cdot 10^{-3}. \quad (3.13)$$

Also, it was established that the spectral variation of  $b_b$  could be approximated by

$$b_b(\lambda) \approx b_b(546) \cdot (546/\lambda), \quad (3.14)$$

where  $\lambda$  is wavelength in nm.

Following Gordon *et al.* (2001), Smyth *et al.* (2002b) modeled backscatter due to coccoliths with:

$$b_b(\lambda) = 10^6 N_{cocco} \cdot b_b^*(546)(\lambda/546)^{-1.35}, \quad (3.15)$$

where  $b_b^*(546)$  is equal to  $1.1 \times 10^{-13}$  (see also Voss *et al.*, 1998 and Balch *et al.*, 1999, although earlier Ackleson *et al.*, 1994 assessed the coccolith specific coefficients at 436 and 546 nm at  $8.18 \times 10^{-5}$  and  $5.92 \times 10^{-5} \text{ m}^2 \text{ mg}^{-1}$ , respectively, with the spectral dependence  $\sim 0.5507\lambda^{-1.45}$ ).

Balch *et al.* (1996) report statistical data on coccolithophore and coccolith concentrations observed in the central North Atlantic: the highest *E. huxleyi* coccolith and cell ( $\text{mL}^{-1}$ ) densities were  $\sim 10^6$  and  $10^4$ , respectively. These numbers are also substantiated by findings in, for example, the Ionian Sea (Malinverno *et al.*, 2003). Concentrations of up to  $3.2 \times 10^6$  cells  $\text{L}^{-1}$  and up to  $8.6 \times 10^7$  coccoliths  $\text{L}^{-1}$  have been reported from the Bay of Biscay (Lampert *et al.*, 2002). Tyrrell *et al.* (1999) earlier reported that the ratio of free coccoliths to cells can vary with typical ratios of 20–200. Assessed values of the coccolith backscattering coefficient  $b_b(\text{m}^{-1})$  at 436 and 546 nm varied (depending upon the coccolith concentration) at different stations between 0–0.08 and 0–0.06, respectively. According to the assessments made by Balch *et al.* (1996), the ratio  $b_b/(b_b + a)$  can reach 35% in the middle visible spectral range and the average calcite-specific scattering coefficient for 2 µm coccoliths was assessed at  $9.7 \times 10^{-3} \text{ m}^2 \cdot (\text{mg calcite})^{-1}$ . According to Holligan *et al.* (1983) the reflectance of water loaded with coccolithophores varied from 15% ( $\lambda = 430$  nm) to 10% ( $\lambda = 550$  nm) within a continental shelf edge. Ackleson *et al.* (1994) assessed the volume reflectance ( $\lambda = 443$  nm) of a water column within a coccolithophore bloom at 17% when the *E. huxleyi* cell abundance was  $10^4$  cells  $\text{L}^{-1}$ .

### 3.4.3 Fluorescence cross-sections, $\phi_{php}^*(\lambda)$ of algal cells

We discussed above the fluorescence of properties of individual pigments (chlorophylls and biliproteins) inherent in harmful algae. It was indicated that *chl-a* fluoresce at  $\sim 660$  nm (for excitation at 430 nm), whereas *chl-c* emit light at  $\sim 634$  nm (for excitation at 450 nm). The fluorescent maxima for phycoerythrin, phycocyanin, and allophycocyanin are centered at 575, 635, and 660 nm with excitation at 565, 615 and 650 nm, respectively.

Yentsch and Phinney (1985) showed that, while cyanobacteria, cryptomonads, and reds fluoresce at  $\sim 550$ – $560$  nm and  $\sim 660$  nm, the other species emit light exclusively in the red.

Ahn *et al.* (1992) studied the fluorescent properties of a number of algae, including those belonging to Haptophyceae, Dinophyceae, and Cyanophyceae (i.e., algal classes of harmful phytoplankton species). In conformity with the above it was found that Cyanophyceae fluoresce due to *chl-a* at 660–680 nm ( $\phi_{php}^* = 1 \times 10^3 \text{ m}^2 \text{ mg}^{-1}$ ) with a secondary emission band at  $\sim 700$ – $720$  nm ( $\phi_{php}^* = 0.4 \times 10^3 \text{ m}^2 \text{ mg}^{-1}$ ), but also due to biliproteins at 650 and 560–570 nm ( $\phi_{php}^* = 0.6 \times 10^3$  and  $0.7 \times 10^3 \text{ m}^2 \text{ mg}^{-1}$ ), respectively. Algae from Haptophyceae and Dinophyceae emit light at  $\sim 680$  nm and  $\sim 730$ – $740$  nm ( $\phi_{php}^* = 1.4 \times 10^3$  and  $0.03 \times 10^3 \text{ m}^2 \text{ mg}^{-1}$ , respectively).

It has been shown (Karabyshev, 1998) that fluorescence intensity in marine environments does not grow in strict proportionality to intracellular *chl* concentration, if the latter is above a threshold of about  $1$ – $2 \text{ mg m}^{-3}$ . Nutrient availability, temperature, and sun/sky illumination levels are known to significantly control algal fluorescence (Kondratyev *et al.*, 1999; Babichenko *et al.*, 2001).

Babichenko *et al.* (2001) found that, under different aquatic nitrogen conditions, the relationship between algal fluorescence and intracellular chlorophylous pigments was more complicated when other external factors (e.g., light, phosphorus, water temperature, etc.) were also taken into account. Evaluation of the pigment content of algae by fluorescence can underestimate the actual value in the stage of phytoplankton exponential growth due to lower fluorescence efficiency compared to that in the stationary phase of the life history of phytoplankton.

### 3.4.4 Optical impact of mucilage

Some algae—mostly Bacillariophyta (diatoms)—happen to be sources of harmful effects other than the aforementioned ones: toxicity, oxygen depletion, damaging/clogging gills, etc. (see introduction). These are represented by intense production of organic gelatinous material, which form suspended aggregates of varying sizes and shapes. The evolution of the phenomenon is thought to begin with small flocs of the order of millimeters, and end up with strings and sheets of a few centimeters or even clouds of the order of meters. This development sequence is initiated by abnormal exudation of polysaccharide chains by phytoplankton (in particular, some specific diatoms). The chains are followed by the formation of colloids and, then, through

aggregation, bigger assemblages. The most striking stage is their occasional presence at the surface as floating greyish to brownish strings and sheets.

These aggregations become suspended micro-ecosystems with their own particular composition in bacteria, phytoplanktonic algae, etc. The resulting biological activity, together with hydrodynamic forces, establishes a vertical distribution of mucilage in the water column.

Although some risk to human health may exist (linked in particular to possible concentrations of toxic allochthonous compounds), a major negative effect of this phenomenon is the damage caused to the tourism industry when floating mucilage concentrates near the coast and the visual and recreational effect that has.

Mucilage phenomena have been reported in the Adriatic Sea, among others. In the summer of 1989 abnormal production of mucilaginous matter occurred along the Italian coast south of the Po River delta (an area with one of the highest concentrations of tourists) and caused severe damage to the local economy (Tassan, 1993). This substance exhibited high reflectance that was almost equal in the two AVHRR spectral bands centered at 635 and 850 nm. These features contrast with clear water. Indeed, water *per se* (Pope and Fry, 1997) strongly absorbs in the red and, in particular, infrared domains.

When submerged, mucilage forms distinct layers associated with distinct subsurface maxima in the vertical distribution of both the apparent and inherent optical properties of the water column (Berthon *et al.*, 2000). These layers are characterized by a high value of light attenuation and a high value of the ratio of scattering-to-absorption coefficients *at all wavelengths*.

Surface reflectance ratios prove to be higher with regard to non-mucilage observations when the mucilage layers eventually transform into mucilaginous matter homogeneously distributed throughout the water column and, in particular, approaching the surface. However, the data set collected by Berthon *et al.* (2000) was very limited and the detection capability was based on small differences, such that the variance in non-mucilage water properties might have masked the properties of mucilage-contaminated water. The spatial resolution of Earth observation sensors may also impose practical limitations in this respect.

### 3.4.5 Absorption and backscattering cross-sections of suspended minerals and dissolved organic matter

As discussed above, in case II waters variations in the spectral composition of light emerging from beneath the water surface are not determined predominantly by phytoplankton (or their retinue), but by other CPAs present in the water masses, primarily suspended minerals (*sm*) and dissolved organics (*doc*). Therefore, the optical characteristics of both *sm* and *doc* need to be considered.

Interestingly, on some occasions the optical impact of *sm* and *doc* is also consequential for case I waters. There are reports (for references see Sathyendranath, 2000; Pozdnyakov and Grassl, 2003) explicitly indicating that, even in oceanic waters generally ascribed to the case I category, the influence of *doc* (of an endogenous

nature) and *sm* (atmospherically deposited particles) can be significant, the latter especially in the areas of influence of desert dust.

### 3.4.5.1 Suspended minerals (*sm*)

In coastal zones and inland water bodies, suspended sediment concentrations in surface waters can be rather high. A large portion of the *sm* coarse fraction is frequently found not only in the littoral but also pelagic zones of large lakes. The chemical composition of *sm* indicates that these particles are mainly composed of quartz, but there is also silica, clays, and calcites. These materials have low imaginary parts of the complex index of refraction ( $10^{-3}$ – $10^{-4}$ ), and their absorption increases towards the near UV spectral region and at wavelengths  $\lambda > 700$  nm (Kondratyev *et al.*, 1983).

There are very few published values for the absorption and backscattering cross-section spectra of suspended minerals— $a_{sm}^*(\lambda)$  and  $b_{b_{sm}}^*(\lambda)$ , respectively. Figure 3.12 (from Kondratyev *et al.*, 1999) is an intercomparison of absorption cross-section spectra obtained for *non-phytoplankton (non-chlorophyllous) matter* by several workers. The absorption cross-section spectra for Lake Ontario (Canada) and Lake Ladoga (northwestern Russia) (for references see Bukata *et al.*, 1995) and Lake Chilko (British Columbia) (Gallie and Murtha, 1992), and the Irish Sea (Bowers *et al.*, 1996) were determined for concentrations of *suspended minerals* in these inland water bodies and one marginal sea, and as such are directly comparable.

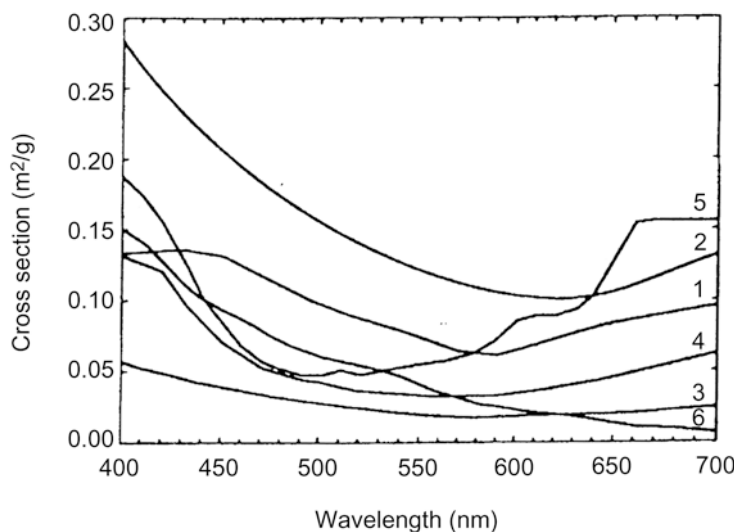


**Figure 3.12.** Intercomparison of independent determinations of the absorption cross-section spectra for non-chlorophyllous matter: 1—Bukata *et al.*, 1985; 2—Bukata *et al.*, 1981; 3—Gallie and Murtha, 1992; 4—Morel and Prieur, 1977; 5—Prieur and Sathyendranath, 1981; 6—Bowers *et al.* 1996 (Bukata *et al.*, 1995).

Suspended inorganic matter displays a distinct increase in absorption towards short wavelengths, a less pronounced increase in the red spectral interval, and a minimum in the range from 590 to 630 nm. Of all these determinations of  $a_{sm}^*(\lambda)$ , only the results from Lake Ladoga are numerous and thus statistically reliable because they were obtained from measurements during mid summer in three consecutive years, and a high level of coincidence between all three years' measurements has been found.

The  $a_{sm}^*(\lambda)$  values displayed in Figure 3.12 are in general compatible with the spectra reported by Morel and Prieur (1977) and Prieur and Sathyendranath (1981). However, in these papers the absorption cross-section spectra are for either “suspended and dissolved material apart from algae” or “non-chlorophyllous particles”, and hence include the effects of matter other than suspended minerals alone. The data collected by Roesler and Perry (1995) seem to come close to  $a_{sm}^*(\lambda)$ . Roesler and Perry also report that  $a_{sm}^*(\lambda)$  decreases steadily with increasing  $\lambda$ ; it also increases from oceanic to coastal and fresh waters. Babin and Stramski (2002) also found that absorption by aquatic suspended minerals and organic particulate matter are generally negligible in the near infrared.

In their model for case II waters, Sathyendranath *et al.* (1989) suggested that the backscattering coefficient of non-chlorophyllous particles follows a  $\lambda^{-n}$  law with small values of  $n$ : for case II waters  $n \approx 0$ . Figure 3.13 illustrates an intercomparison of the limited number of existing backscattering cross-section spectra specifically for

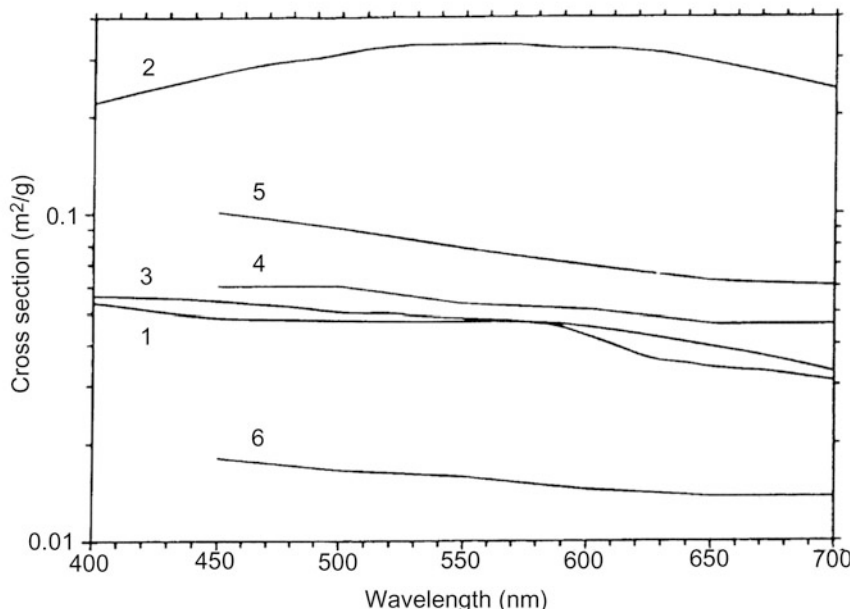


**Figure 3.13.** Backscattering cross-section spectra for suspended minerals. Data shown are from Bukata *et al.*, 1995 (curves 1 and 2); Gallie and Murtha, 1992 (curve 3), and Whitlock *et al.*, 1981 (curves 4, 5, and 6).

suspended minerals, once again from Lake Ontario, Lake Ladoga, Chilko Lake, and three rivers in Virginia. As seen, the  $b_{b_{sm}}^*$  spectra are nearly wavelength independent/non-selective:  $b_{b_{sm}}^*$  decreases only slowly with  $\lambda$ , which compares well with the data reported by Sathyendranath *et al.* (1989). The slight dependence of  $b_{b_{sm}}^*$  on  $\lambda$  has been parameterized by Whitte *et al.* (1982) by:

$$b_{b_{sm}}^* = A - B \cdot (10^{-5})\lambda, \quad (3.16)$$

with  $A = 0.0316$  and  $B = 0.844$ , respectively. However, these coefficients are not readily transferable to a wide variety of water bodies and should instead be considered as geographically area specific.

The value of  $b_{b_{sm}}^*$  over the entire visible spectrum (Figure 3.13 taken from Bukata *et al.*, 1995) varies strongly from 0.015 to  $0.3 \text{ m}^2/\text{g}$  with the highest values of  $b_{b_{sm}}^*$  stemming from the waters of Lake Ladoga. For the other inland waters,  $b_{b_{sm}}^*(\lambda)$  is confined to the interval  $0.04\text{--}0.10 \text{ m}^2/\text{g}$ , except for curve 6. The enhanced absorption of *sm* in Lake Ladoga is thought to be due to *sm* particulates being coated with colloidal *doc* (which is highly probable given the very high concentrations of *doc* in this water body— $8 \text{ g C/m}^3 \leq C_{\text{doc}} \leq 13 \text{ g C/m}^3$ —and a high fraction of *doc* residing in the water column is in a colloidal form). “Coating” of *sm* particles with organic colloidal matter in non-case I waters is amply evidenced through extensive studies conducted by Aponasenko *et al.* (1997) in a variety of natural waters. Indeed, *doc* is known to absorb stronger as  $\lambda$  decreases (see below), and within the spectral regions of strong absorption there is a decrease in specific scattering (this effect has already been discussed in relation to the backscattering spectral variations of chlorophyll).

Numerical simulations show that small (submicrometer) particles significantly contribute to the backscattering probability,  $B = b/b_b$  (Section 3.4; Risovic, 2002). This implies that *sm* backscattering cross-sections should account for such extra fine particulate matter. Accordingly, supporting *in situ* measurements need to be performed with filters that have very fine pores such that submicron mineral grains can also be retained. Experimental evidence of the importance of this issue has been reported by Pozdnyakov *et al.* (2003).

### 3.4.5.2 Dissolved organic matter (*doc*)

Dissolved organic matter (*doc*) concentrations are the consequence of either the photosynthetic activity of phytoplankton (autochthonic) or direct inputs of terrestrial matter (allochthonic). Of the total organic matter resulting from phytoplankton photosynthesis, up to 20% can be released to the ambient aquatic environment through *metabolic exudation/egestion* (Gorlenko *et al.*, 1974). These egesta are, in general, assimilated by bacterioplankton; however, in nutrient-limited waters, the phytoplankton themselves may compete with bacterioplankton for such egesta assimilation.

In fresh and brackish waters, *doc* is not conservative, instead it undergoes various biological and *photochemical* transformations (Bertilsson and Travnik, 2000) before residual *doc* is eventually discharged into the oceans. Solar radiation,

particularly in the ultraviolet, has the potential (especially in oligotrophic rather than eutrophic non-case I waters) to alter the spectral and molecular properties of (mostly allochthonous) *doc* and to promote its degradation, either directly through *photooxidation* or indirectly by increased *bioavailability* (see below).

Yellowness/brownishness is the characteristic hue of waters containing *doc* in large quantities, which is due to yellow and brown melanoids. These melanoids, however, comprise only a fraction ranging between 10 and 40% of aquatic *doc*.

Since allochthonous *doc* is generally absent from mid-oceanic (case I) waters, the aquatic humus in case I waters co-varies with phytoplankton (or its proxy, chlorophyll), keeping in mind that mid-oceanic waters are also nearly devoid of suspended minerals. Aquatic humus (*doc*) concentrations in oceanic waters are generally very low in the range 0.001–0.005 g C m<sup>−3</sup>. However, it should be pointed out that there are observations (Church *et al.*, 2002) indicating that a small fraction of annually produced organic matter in some locations of the world oceans can escape biological utilization on timescales of months to years. It has been conjectured that this might be the result of reorganization of the dynamics of the plankton community, bringing about significant alterations to the cycling of organic matter in the ecosystem. It is believed this can be driven by basin-scale climate variability.

The concentration or density of *doc* is usually given in grams of *carbon* per unit volume since carbon constitutes approximately *half* the *doc* by weight. Because of this, dissolved organic matter is designated herein by *doc* (where C stands for carbon). The concentration of *doc* in oceanic waters is about four orders of magnitude below the concentrations of dissolved salts. However, the optical impact of *doc* is stronger than that of dissolved salts. Although *doc* does not significantly impact on scattering within the water column, it considerably increases absorption. In inland and coastal waters, however, *doc* concentrations are often considerably higher: *doc* ranges from 1–2 g C m<sup>−3</sup> in oligo/mesotrophic waters to 20–25 g C m<sup>−3</sup> in hyper-eutrophic waters (Romankevich, 1977).

Absorption by *doc* decreases exponentially from short to long wavelengths in the visible spectrum. Observed *doc* absorption in the visible spectrum is a “tail” of electron transition absorption bands located in the ultraviolet (UV) part of the spectrum. The spectral dependence of the absorption coefficient  $\alpha_{ys}(\lambda)$  on the colored fraction of *doc* (the so-called *yellow* substance, *ys*) can be approximated well by a simple exponential function (Zepp and Schlotzhauer, 1981):

$$\alpha_{ys}(\lambda) = \alpha_{ys}(\lambda_0) \exp[-s(\lambda - \lambda_0)], \quad (3.17)$$

where *s* is a slope parameter that is assumed to be independent of wavelength  $\lambda$ . Values of *s* in marine systems range from 0.011 to 0.22 nm<sup>−1</sup>, whereas many freshwater environments, estuaries, and enclosed oceans exhibit even greater variability (for references see Kondratyev *et al.*, 1999). Humic substances, with their higher mass-specific absorption coefficients, prove to be removed from the water column more rapidly on entering marine waters from rivers that transport fulvic acids.

Hernes and Benner (2003) investigated the mechanisms and associated rates of sinks of terrigenous *doc* in marine systems. As a tracer, they used lignin, an aromatic compound, inherent in vascular plant sources. They found through incubation

experiments under laboratory conditions that *flocculation* and *microbial degradation*, as well as *photodegradation/bleaching* are the principal mechanisms of terrigenous *doc* removal in marine waters. Microbial degradation is clearly not as rapid as photo-oxidation in sunlit surface waters: photo-oxidation rates were three to fivefold greater than microbial degradation rates. However, microbial degradation occurs around the clock and throughout the water column. Therefore, the degradation of terrigenous dissolved organic matter is a competitive process between microbes and sunlight, with the importance of the individual process being dependent on light exposure.

Thus, the aforementioned constancy of the shape of the yellow substance absorption coefficient,  $a_{ys}(\lambda)$  vs.  $\lambda$  in eq. (3.17), for a given aquatic area enables the selection of a reference wavelength,  $\lambda_0$ , with which to compare the yellow substance concentrations of different waters. The selection of  $\lambda_0 = 400\text{ nm}$  is certainly appropriate since it represents the maximum  $a_{ys}$  in the visible spectrum. However,  $\lambda_0 = 440\text{ nm}$  as a reference wavelength is also frequently encountered in the literature.

However, standard spectrophotometric methods for determination of the abundance of the yellow substance/colored fraction of *doc* are laborious and susceptible to methodological biases. Automated liquid waveguide capillary cell approaches are believed to be much more promising in assuring higher accuracy and improving the spatial and temporal resolution of field data (Kirkpatrick *et al.*, 2003).

As indicated above, solar radiation can photo-bleach the chromophoric dissolved organic matter/yellow substance, but the associated changes in the shape of  $a_{ys}(\lambda)$  are poorly understood, particularly in the visible domain. Twardowski and Donaghy (2002) found in coastal fjords a drop in slope parameter,  $s$ , from  $0.0145\text{ nm}^{-1}$  in upper-surface waters to  $\sim 0.0138\text{ nm}^{-1}$ . Together with the rapid decline of  $a_{ys}(\lambda)$  with depth, this is thought to be evidence supporting the photo-degradation of chromophoric dissolved organic matter (CDOM). Laboratory experiments indicate that photo-degradation of CDOM shifts the absorption spectrum to shorter wavelengths by breaking up large humic complexes that are known to be responsible for the long-wavelength visible absorption of incident radiation. According to Blough and Green (1995), conjugated molecular systems absorb at lower energies/longer wavelengths as they increase in length. In relation to CDOM, it has indeed been shown that, when exposed to sunlight, high molecular weight *doc* and the average molecular weight fraction decrease rapidly (Allard *et al.*, 1994). Over long incubation periods ( $\approx 72$  hours) the value of  $s$  can increase up to  $0.0147\text{ nm}^{-1}$ . It is important to note that, notwithstanding the considerable loss in  $a_{ys}(\lambda)$  at longer wavelengths in magnitude, there is an even greater loss of yellow substance absorption at shorter wavelengths driven by photo-bleaching. Twardowski and Donaghy (2002) estimated that  $a_{ys}(412)$  can decrease in the top subsurface layers by  $0.03\text{ m}^{-1}$  due to photo-bleaching. Thus, the photo-bleaching/photo-degradation effect together with microbial decomposition can result in deeper penetration of light into the water column at all wavelengths (Whitehead *et al.*, 2000; Johannessen *et al.*, 2003).

Little attention has been given to the possible effects of *doc* on the scattering properties of natural waters. Although such neglect of the scattering from organic matter that resides in the water column is justified for true molecular solutions, there is sometimes a very substantial fraction of “dissolved” organic matter that is not in true molecular solution, but exists in colloidal form, which can impact the bulk scattering coefficient characterizing the optical properties of the water column.

More importantly, a certain, presumably small, fraction of *doc* can fluoresce with the emission maximum/maxima located in a wide spectral region extending from about 310 to 520 nm depending on the nature of *doc* and the excitation wavelength (Coble, 1994). For instance, when excited at 355 nm, *doc* fluoresce within a wide spectral band centered at  $\sim$ 425–430 nm (Barbini *et al.*, 2003). In water volume reflectance spectra, *doc* fluorescence is expressed with a maximum at 490–520 nm (Pozdnyakov and Grassl, 2003).

The data on fluorescence yield (which is the number of photons absorbed by the fluorophore normalized by the number of emitted/fluoresced photons of chromophoric dissolved organics) indicate strong dependence of  $\eta_{doc}$  on  $\lambda$ . Based on some river water data, its absolute magnitude varies from about 0.005–0.010 at  $\lambda = 250$  nm to 0.005–0.019 at  $\lambda = 470$  nm with the maximum value ranging from 0.007 to 0.028 at  $\lambda = 390$  nm (Green and Blough, 1994):

$\lambda$ , nm	310	330	350	370	390	410	430	450	470
$\eta_{doc} \cdot 10^4$	125	175	230	245	270	260	230	210	0

### 3.4.5.3 Air bubbles

In the upper layers of natural waters, trapped air bubbles are mainly generated by the injection of air by breaking waves. Also, air bubbles can originate from the life cycle of phytoplankton, and possibly, bacterioplankton. The refractive index of air bubbles *per se* is 0.75. The majority of air bubbles injected into the surface layers of natural waters are unstable. However, for oceanic air bubbles with long residence times, a bubble concentration of about  $10^5$  to  $10^6$  m $^{-3}$  and even as large as  $2.13 \times 10^7$  has been observed (for references see Yan *et al.*, 2002a). The size (radius,  $r$ ) of air bubbles varies from about 0.01 to about 350  $\mu\text{m}$ , following on average the bubble size distribution  $n(r) \sim r^4$  (Stramski, 1994). Bubbles are distributed within the top layer of the ocean, and observations indicate that the thickness of this layer can vary over a large range from 0.25 to 36 m. There is evidence (Yan *et al.*, 2002) that some bubble clouds could reach mean depths of about  $4H_s$ , where  $H_s$  is the significant wave height. But some bubble clouds can extend down to approximately  $6H_s$ : they are frequently observed at depths of 6 to 11 m and even down to 36 m (Wu, 1988). Given the bubble number density that has typically been reported from measurements in the sea (i.e., ranging, as we saw above, from about  $10^5$  to  $10^7$  cm $^{-3}$ ), the bubble population will significantly influence the scattering processes in the ocean, especially in oligotrophic waters.

Water bubbles can be covered with organic films composed mainly of proteins or lipids. The thickness of such coatings of bubbles in seawater has been estimated to range from 0.01  $\mu\text{m}$  for lipids to 1  $\mu\text{m}$  for proteins. The mean relative refractive index,  $n$ , of the coating substances ( $n \cong 1.20$  for proteins and  $n \cong 1.10$  for lipids) is quite different from that of clean water bubbles (see above). As shown by Zhang *et al.* (1998), this implies that coated bubbles scatter more strongly than clean bubbles. In any case, these air bubble-related scattering centers should also result in the attenuation of downwelling radiation because of absorption, as the imaginary part of the refractive index of coated bubbles lies between 0.001 and 0.006, which is similar to the mean imaginary index of the reflection of phytoplankton cells. The latter value is probably close to the maximum value for chlorophyll in the red absorption band (Morel, 1990). However, backscattered upwelling radiation is also increased. Both effects change volume reflectance, which then may be erroneously attributed to the presence of suspended organic or inorganic particulates.

According to Zhang *et al.* (1998), the mean scattering efficiency factor of bubbles is comparable to those of nanoplankton (2–20  $\mu\text{m}$ ) and microplankton (20–200  $\mu\text{m}$ ). However, for the *backscattering ratio/efficiency*, ranging from 0.02 for clean/uncoated bubbles to as high as 0.08 for bubbles with a 0.1  $\mu\text{m}$  thick protein cover, bubbles are at least one order of magnitude more efficient in backscattering than planktonic organisms. In general, the role of clean/coated bubbles in increasing/modifying the resultant volume reflectance will decrease as the concentration of phytoplankton and suspended minerals increases. However, this decreasing contribution will shrink with increasing  $\lambda$ . This is due to  $b_b$  being spectrally flat for both clean and coated bubbles (Zhang *et al.*, 1998), whereas it decreases with  $\lambda$  for seston (i.e., minute living organisms and particles of non-living matter).

The major difficulty in accounting for the optical influence of air bubbles, when analyzing the spectral composition of light emerging from beneath the water surface with the goal of identifying harmful algae and assessing their biomass, resides in the absence, to the best of our knowledge, of models reliably relating the driving parameter(s) (e.g., wind speed or/and phytoplankton concentration) to the total number of bubbles generated in top-layer water (Subramanian *et al.*, 2002).

## 3.5 HARMFUL ALGAE DETECTION: METHODOLOGIES

### 3.5.1 Detection of expressions of pigment composition in harmful algae in absorption and water column reflectance spectra

Kutser (2009) in his review paper points out that “recognition of bloom-forming phytoplankton at a species level based on their reflectance spectra requires uniqueness of spectral signatures of different species and sensors that are capable of detecting these differences.” Indeed, the number of spectral channels and the associated spectral resolution of, for example, SeaWiFS, MODIS, and MERIS (let alone LANDSAT, CZCS, AVHRR, SPOT, ASTER, and some others) are fre-

quently insufficient for such precise discrimination. However, several researchers have investigated the potential of the available satellite sensors from this perspective (e.g., Kutser, 2004; Ruiz-Verdu *et al.*, 2005; Simis *et al.*, 2005, 2007).

Therefore, Simis *et al.* (2005) suggested a semi-analytical band ratio-based algorithm for the identification and quantification of cyanobacterial phycocyanin (PC) in Spanish lake waters using only MERIS bands: the algorithm attributes the absorption signal derived from the 620 nm band to two absorption features that are dominant in cyanobacteria-rich waters: the PC absorption peak at ~615 nm and the shoulder at about 623–628 nm of the *chl-a* absorption peak. Subtraction of *chl*-inherent absorption in this spectral interval permits confident identification and quantification of the PC concentration. However, in waters rich in dissolved organic and inorganic suspended matter, the spectrometric influence of the latter needs to be taken into account, and Simis *et al.* (2007) had to suggest area-specific regression parameterizations to improve PC retrieval accuracy, and any translation of the Simis *et al.* (2005) algorithm to other inland waters requires modifications of the original regression expressions (Randolph *et al.*, 2008). The vulnerability of the Simis *et al.* (2005) algorithm is further accentuated by the influence of algae (other than the blue-green type) that co-exist in the phytoplankton community: the overestimation of PC may arise in the presence of *chl-a*, *chl-b*, and phaeophytin (Simis *et al.*, 2007). Therefore, an additional correction is required. Incidentally, Trees *et al.* (2000) advocate that—although the ratio of individual accessory pigments to *chl-a* can vary very significantly with changes in phytoplankton community composition and physiological state—there is a ubiquitous and remarkably stable relationship between total accessory pigments and *chl-a*. This also needs to be taken into consideration when developing retrieval algorithms based on the assumption of a rigorous relationship between *chl-a* and the accessory pigment used as a marker.

Subramanian *et al.* (2002) used a step-wise scheme that permitted areas of cyanobacteria *Trichodesmium* spp. blooms to be differentiated from neighboring areas dominated by endemic non-harmful algae. The procedure employs a reflectance model of this species developed earlier by Subramanian *et al.* (1999), absorption cross-sections of “other” co-existing phytoplankton species (Sathyendranath *et al.*, 1987), as well as absorption and backscattering parameterizations for other optically active components—that is, water *per se*, detritus, colored dissolved organic matter (CDOM)—suggested in the literature (for references see Subramanian *et al.*, 1999). A similar approach (but with the employment of another set of parameterizations and their original optical model of *Trichodesmium* spp.) has been developed by Westerberry *et al.* (2005) and Metsamaa *et al.* (2006).

As mentioned in Section 3.1, coccolithophores (class Prymnesiophyceae) are considered harmful algae because of their damaging or clogging effect on fish gills. In addition, these algae are thought to play an important climate-affecting role through their participation in the global carbon cycle. In this group of algae, *Emiliania huxleyi* is notable not only as an aquatic organism amply producing calcium carbonate and controlling ocean acidification rates, but also as a powerful

producer of dimethyl sulfide (DMS): the emission of this gas enhances the process of cloud formation, increases planet global albedo, and eventually changes global climate (Thierstein and Young, 2004).

Using the Gordon *et al.* (1988) algorithm Balch *et al.* (2005) suggested a 2-D algorithm simultaneously determining the concentration of *E. huxleyi chl-a* and coccoliths (see Section 3.4.2) in case I waters. The algorithm is based on combined analysis of normalized upwelling radiance at 550 and 440 nm, and operates robustly provided the chlorophyll concentrations are under a few milligrams per liter. The algorithm has been successfully applied to MODIS data and eventually embedded in the SeaDAS standard software package. However, the Balch *et al.* algorithm is not intended for situations where the *E. huxleyi bloom* is not monospecific, as it nearly invariably occurs in coastal or near-coastal waters.

In a satellite remote-sensing study of *E. huxleyi* blooms in the Bay of Biscay (France), where *E. huxleyi* blooms occur in the presence of some residual diatom masses, Korosov *et al.* (2009) compiled a model simulating the optical impact of *E. huxleyi*, detached coccoliths, and *co-existing diatoms* on upwelling radiance using the absorption and backscattering characteristics of the CPAs reported by Morel and Bricaud (1981); Bricaud *et al.* (1983); Balch *et al.* (1999); Pozdnyakov and Grassl (2003). The combined model was then used for processing Aqua MODIS images making use of the multivariate Levenberg–Marquardt technique (LMT). The results obtained with this processing tool permitted seasonal and spatial variations in *E. huxleyi* and diatom blooms across the bay to be revealed. In full conformity with the ecology of *E. huxleyi* (Lavender *et al.*, 2008), outbursts of this species revealed from MODIS data occur in areas that were previously the arena of massive growth of diatoms. The location of identified *E. huxleyi* blooms and their timing proved to be supported by reports on historical *in situ* observations in the Bay of Biscay (Lampert *et al.*, 2002).

Recently, Morozov *et al.* (2010) suggested an approach for detecting blooms of the dinoflagellate *Lepidodinium chlorophorum* (class Dinophyceae, order Gymnodinianaceae). Identified as harmful only recently (see Section 3.1), this species has attracted the attention of both aquatic ecologists and shellfish stakeholders, specifically on the French East Atlantic cost. The absence of data on the specific absorption and backscattering properties of *L. chlorophorum* does not preclude using LMT.

Nevertheless, the available *in situ* data set of *L. chlorophorum* cell number measurements was used to develop a dedicated neural network (NN) to be used for processing Aqua MODIS data. The output layer of the developed NN consisted of only one neuron. The values of subsurface remote-sensing reflectance,  $R_{rsw}(\lambda)$ , in channels 412, 443, 488, 531, 551 and 667 nm were fed into the input layer of neurons. These signals were further inverted in such a way that the output neuron number varied between 0 and 1. Here, 0 and 1 corresponded, respectively, to the absence and presence of *L. chlorophorum* blooming, whereas intermediate numbers were interpreted as pixels of the transition from blooming to non-blooming areas.

To enhance the efficiency of the NN procedure, the entire target area was

pre-processed (before training the NN emulator and further prior to its application) to sort out pixels that did not satisfy the following condition: the presence of a local minimum at the wavelength of the MODIS third channel (centered at 488 nm). This minimum (possibly of moderate to low amplitude) was expected to result from the long-wave wing of the absorption band of *chl-b* and the long-wave absorption band of peridinin (see Section 3.1). It is presumed that if the sought-for species is present within the analyzed pixel, but its portion is not predominant/very low in the phytoplankton community, then in the spectrum of  $R_{rsw}(\lambda)$  at  $\sim 488$  nm there should be no local inflection and the partial derivative  $\partial R_{rsw}(\lambda)/\partial \lambda$  is either invariant or not decreasing: such spectral features in  $R_{rsw}(\lambda)$  are routinely observable across the coastal zone of the Bay of Biscay when algal blooms are due to species whose pigments do include *chl-b*.

The algorithm was applied to multi-year MODIS images of the Bay of Biscay. In the processed images two types of areas were revealed where *L. chlorophorum* blooms occur either in some specific years or annually. However, the time series of retrievals obtained is unambiguously indicative that the frequency of such events along the East Atlantic French coastal zone has been increasing over the last decade.

By not addressing the issue of HAB detection explicitly, some workers (e.g., Hirata *et al.*, 2008; Nair *et al.*, 2008; and others) considered the possibility of identifying phytoplankton functional types from satellite ocean color. A phytoplankton functional group means “a group of species that, irrespective of phylogeny, share similar traits”, and all phytoplankton functional types can be classified along the following lines: (i) size and function, (ii) nitrogen fixers, (iii) silicifiers, (iv) calcifiers, (v) marine dimethyl sulfide (DMS) producers (Nair *et al.*, 2008).

Category (i) encompasses three size classes: picophytoplankton ( $0.2\text{--}2\ \mu\text{m}$ ), nanophytoplankton ( $2\text{--}20\ \mu\text{m}$ ), and microphytoplankton ( $>20\ \mu\text{m}$ ). The first class encompasses cyanobacteria (such as *Synechococcus* and *Prochlorococcus*) and green algae (such as *Ostereococcus*). The second class contains flagellate algae, protists, cyanobacteria, and photosynthetic autotrophic plankton. The third class is mostly composed of diatoms and dinoflagellates. Thus, it is clear that a size-based approach is inadequate from the perspective of unequivocal harmful algae identification.

Category (ii) includes cyanobacteria such as *Trichodesmium*, diazotrophic *Katagymneme* sp., and nitrogen-fixing species of the diatoms *Chaetoceros*, *Bacterastrum*, *Rhizosolenia*, *Hemiaulus* sp.

Category (iii) encapsulates four taxonomic groups: Chrysophyta, Silicoflagellates, Xanthophyta, and Bacillariophyta. The latter are the dominant silicifiers in marine ecosystems. Categories (iv) and (v) are coccolithophores.

Although algorithms have been developed (mostly regression area-specific expressions) to identify phytoplankton functional groups (for references see Ciotti and Bricaud, 2006; Devred *et al.*, 2006; Hirata *et al.*, 2008; Nair *et al.*, 2008), it is obvious that this approach is not particularly promising because four of the above categories, even if successfully identified from space, might not necessarily be composed of harmful algae.

### 3.5.1.1 Decomposition of absorption spectra

As discussed above, the absorption spectra of photosynthetic algae are characterized by a continuous envelope resulting from the spectra of the individual pigments inherent in the algal cell overlapping. While *chl-a* associated absorption bands are easily distinguishable due to the prevalence of *chl-a* in all types of algae, the contribution of accessory pigments is generally expressed as secondary bands or envelope inflexions (e.g., Hunter *et al.*, 2008). Although, the intrinsic contour of the absorption band has a Lorentzian shape, when measured by a spectrophotometer, the signal is transformed into a Gaussian curve. It was indicated above that (according to Hoepffner and Sathyendranath, 1993) the absorption spectra of monospecific algae can be presented as a summation of Gaussian bands simulating the absorbing properties of co-existing intracellular pigments (eq. 3.10). Derivative analysis (Bidigare *et al.*, 1989) is useful for resolving secondary peaks and shoulders produced by pigments present in the algae within overlapping absorption regions. The absorption maxima found by this method are located near or at the correct wavelength position. Therefore, the revealed absorption peaks may be objectively attributed to individual pigments.

The derivative of a curve is simply its slope at a given point. If the differentiation interval is very small, then the difference between successive values may be small compared to the noise. In contrast, a large differential interval can reduce the noise, but fine spectral features may be lost. The optimal differentiating interval depends on the level of noise in input data and the spectral bandwidth of the signal (Butler and Hopkins, 1970). In order to determine whether the inflection points in the original envelope represent a minimum or a maximum, the second derivative is calculated. The negative minima in the second derivative spectrum correspond to the maxima in the original spectrum. But, sometimes the second derivative fails to resolve all peaks, and derivatives of higher order are required.

Due to the fact that the observed spectrum is a summation of individual bands whose shape is basically Lorentzian but also reflects the Gaussian contribution, Aguirre-Gomez *et al.* (2001a) suggested modifying eq. (3.10) for  $a_{php}(\lambda)$  as follows:

$$a_{php} = \sum_{j=1}^l C_j [a_j^*(\lambda_{mj})G + \alpha_j^*(\lambda_{mj})L], \quad (3.18)$$

where

$$G = \exp\left(\frac{(\lambda - \lambda_{mj}^2)}{2\sigma_j^2}\right), \quad (3.19)$$

and

$$L = \left[1 + 4\left(\frac{(\lambda - \lambda_{mj})}{2\sigma_j^2}\right)\right]^{-1} \quad (3.20)$$

are the Gaussian and Lorentzian contributions to the absorption spectra of phytoplankton,  $a_j^*$  and  $\alpha_j^*$  are mean specific absorption coefficients for the  $j$ th

Gaussian and Lorentzian contributions, respectively, the other notations are as in eq. (3.10).

Thus, for example, the composition of the absorption spectrum of *Phaedactylum* (Bacillariophyta), the algae having the molar ratio of carotenoids (fucoxanthin and  $\beta$ -carotene in proportion 1:1) to chlorophylls ( $a + c$ ) of about 1:0.5, can be presented (Aguirre-Gomez *et al.*, 2001b) as:

$$a = 0.5[3chl-a + chl-(c_1 + c_2)] + (\text{fucoxanthin} + \beta\text{-carotene}). \quad (3.21)$$

Application of the above derivative approach to cultured *Phaedactylum* algae, whose pigment concentrations were determined by HPLC, resulted in a number of peaks that were further adjusted by taking into account the Gaussian and Lorentzian weights (the latter being only a small fraction of the former). Based on extensive research on spectroscopic expressions of chlorophyllous and auxiliary pigments in living cells, Aguirre-Gomez *et al.* (2001b) attributed the revealed peaks to *chl-a* and carotenoids (i.e., fucoxanthin and  $\beta$ -carotene) as well as to dinoxanthin, which is also inherent in Bacillariophyta (Table 3.2). The Guassian–Lorentzian approach has reportedly been successful in reproducing the input absorption spectrum.

Aguirre-Gomez *et al.* (2001a) report that extension of this approach to natural *monospecific* populations also produced acceptable results and provided for the identification of the major pigments inherent in the studied phytoplankton, although, naturally, it proved to be more difficult to obtain information from the absorption spectra of intact phytoplankton than from solvent-extracted pigments.

Extension of this methodology to remote sensing implies that it is the spectrum of remote-sensing reflectance,  $R_{rs}$ , that is to be analyzed to identify the individual pigments of phytoplankton and to finally attribute them to the indigenous type of algae. As was pointed out in Section 3.4,  $R_{rs}(+0, \lambda)$  is related to subsurface water volume reflectance  $R(-0, \lambda)$  (eq. 3.5) which, in turn, is a function of bulk absorption,  $a$ , and backscattering,  $b_b$ , coefficients of the aquatic medium:

$$R = R(a_w, a_{php}, a_{sm}, a_{doc}, b_{b_w}, b_{b_{php}}, b_{b_{sm}}, \lambda). \quad (3.22)$$

For the most general (case II water) situation, the major CPAs are water *per se*, phytoplankton, suspended minerals, and dissolved organic matter (although under specific situations, air bubbles, detritus, bacterioplankton, mucilage, and surfactants can significantly interfere). Thus, taking into account the above *major* CPAs, derivative reflectance spectra can be expressed as the rate of change of reflectance with wavelength,  $\lambda$ :

$$\begin{aligned} \frac{dR(\lambda)}{d\lambda} = & \frac{\partial R}{\partial \lambda} \cdot \frac{da_w}{d\lambda} + \frac{\partial R}{\partial a_{php}} \cdot \frac{\partial a_{php}}{\partial \lambda} + \frac{\partial R}{\partial a_{sm}} \cdot \frac{da_{sm}}{d\lambda} + \frac{\partial R}{\partial a_{doc}} \cdot \frac{da_{doc}}{d\lambda} \\ & + \frac{\partial R}{\partial b_{b_w}} \cdot \frac{db_{b_w}}{d\lambda} + \frac{\partial R}{\partial b_{b_{php}}} \cdot \frac{db_{b_{php}}}{d\lambda} + \frac{\partial R}{\partial b_{b_{sm}}} \cdot \frac{db_{b_{sm}}}{d\lambda}, \end{aligned} \quad (3.23)$$

where index  $w$  refers to water (for references on the absorption and scattering properties of water *per se* see the discussion in Pozdnyakov and Grassl, 2003).

Since  $R(\lambda) \approx b_b(\lambda)/a(\lambda)$  in the first approximation, one can write (Aguirre-Gomez *et al.* 2001b):

$$\frac{dR(\lambda)}{d(\lambda)} \approx \frac{b_b(\lambda)}{a(\lambda)^2} \left[ \frac{da_w}{d\lambda} + \frac{da_{php}}{d\lambda} + \frac{da_{sm}}{d\lambda} + \frac{da_{doc}}{d\lambda} \right] + \frac{1}{a(\lambda)} \left[ \frac{db_{b_w}}{d\lambda} + \frac{db_{b_{php}}}{d\lambda} + \frac{db_{b_{sm}}}{d\lambda} \right] \quad (3.24)$$

High-order derivatives can be calculated iteratively. The presence of phytoplankton pigments, suspended inorganic matter, and dissolved organics can be estimated by considering the reflectance spectrum components as mutually independent (the fundamental attribute of case II waters).

Aguirre-Gomez *et al.* (2001b) applied this approach to their field measurements in the English Channel at stations near Plymouth. In order to locate and identify peaks in the reflectance spectra, derivative curves were generated using a three-point central difference numerical technique that estimates the derivative of a function at both end-points and in the mid-point of any three points, as long as the points are contiguous and evenly spaced. Reflectance spectra were interpreted through the data provided by absorption spectra of natural populations. Figure 3.14 illustrates the absorption by phytoplankton and second derivative spectra ( $\times 10$ ). Local minima show pigment absorption peaks (dashed line). Table 3.4 (culled from Table 1 in Aguirre-Gomez *et al.*, 2001b) indicates the correspondence between the observed peaks and their interpretation.

Importantly, when processing water reflectance data in *marine* waters, derivative

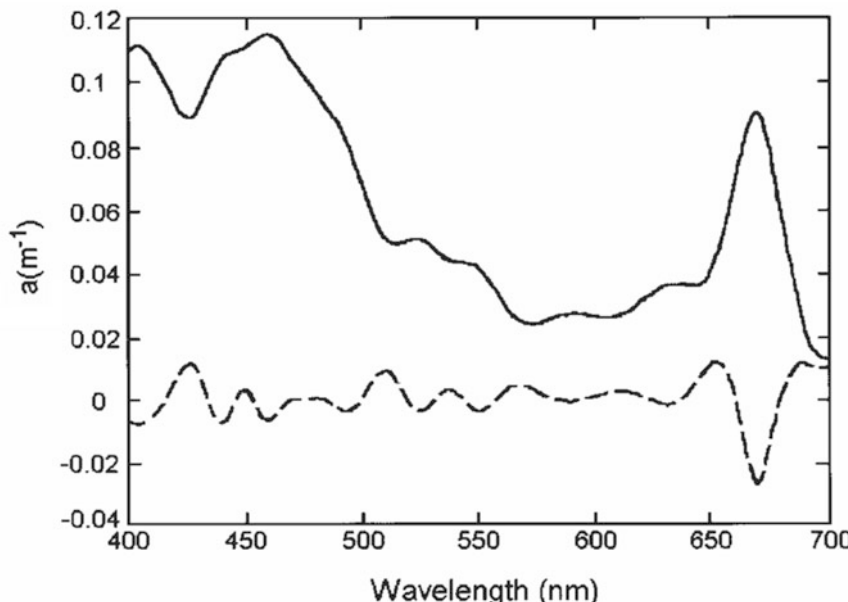


**Figure 3.14.** Absorption by phytoplankton (solid line), and second-derivative spectra (dashed line) ( $\times 10$ ). Local minima show pigment absorption peaks (dashed line) (Aguirre-Gomez *et al.*, 2001a).

**Table 3.4.** Absorption peak locations and their interpretation in terms of associated pigments (data from June 14, 1995) for subsurface waters of the English Channel (Aguirre-Gomez *et al.*, 2001b).

Band	Peak location, nm	Pigment
1	426	Chlorophyll- <i>a</i>
2	442	Chlorophyll- <i>c</i>
3	460	Fucoxanthin
4	476	Carotenes
5	494	Carotenes
6	540	Carotenes
7	568	Protein complex
8	594	Chlorophyll- <i>c</i>
9	626	Chlorophyll- <i>c</i>
10	676	Chlorophyll- <i>a</i>

$R(-0, \lambda)$  spectra should be free of peaks associated with *doc*, *sm*, or bubble optical contributions due to their monotonic spectral variations both in adsorption and scattering (see Sections 3.5.5.1–3.5.5.3). Generally speaking, the backscattering spectra of phytoplankton do not vary monotonically (see Section 3.5.2) due to depressions at the wavelengths of maximum absorption. But phytoplankton are known to scatter the light only weakly, and the aforementioned depressions can be expected as inconsequential. In case II waters particularly rich in *doc* (when the colloidal fraction can be present), the absorption and backscattering spectra of *sm* can also bear some spectral irregularities due to the “coating” effect (see Section 3.5.5.1). Therefore, for such cases appropriate provisions should be made. Also, for certain CPA concentration vectors, the fluorescence spectral manifestations of pigments and *doc* are shown (Pozdnyakov and Grassl, 2003) to affect water column reflectance spectra. Therefore, this effect should be closely considered when applying the derivative approach to spectra obtained under natural water conditions.

Figure 3.15 illustrates the reflectance spectrum measured by Aguirre-Gomez *et al.* (2001b) on June 14, 1995 (upper panel) and the fourth-derivative spectrum (dashed line, lower panel). The data in Table 3.4 and in Figure 3.15 compare reasonably well and, hence, they have the common interpretation of bands discussed above. The long-wavelength band at about 688 nm in Figure 3.15, which is not listed in Table 3.4, is believed to be due to *chl-a* fluorescence (see Section 3.5.3). Thus, the discussed results explicitly indicate that the derivative analysis of reflectance spectra

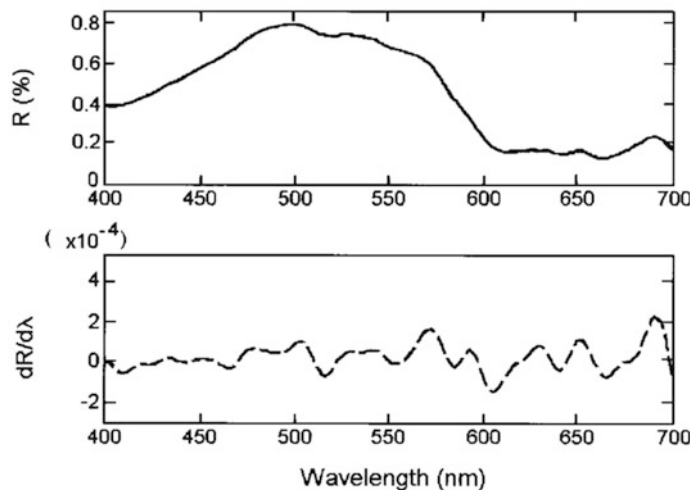


**Figure 3.15.** Reflectance spectrum measured on June 14, 1995 (upper panel) and the fourth-derivative spectrum (dashed line, lower panel). Absorption peaks are apparent as local minima (Aguirre-Gomez *et al.*, 2001a).

of natural waters can fundamentally be an efficient tool to identify the presence of different pigments present in a natural *monospecific* phytoplankton population.

Hunter *et al.* (2008) studied the first-derivative reflection spectra of six phytoplankton species: *Cylindrospermopsis*, *Synechococcus* (blue-green), *Synechococcus* (red) (all three are Cyanophyta), *Scenedesmus*, *Selenastrum* (both are Chlorophyta), and *Diatom* (Bacillariophyta) grown in a controlled tank mesocosm environment. The  $\partial R/\partial\lambda$  spectra of both the Cyanophyta and diatom peaks and troughs (specifically in the 500–600 nm region) are absent in the respective Chlorophyta spectrum and, thus, are easily identifiable. In the case of the Cyanophyta spectra these  $\partial R/\partial\lambda$  features indicate the position of the absorption maxima associated with phycocyanin and phycoerythrin. It is noteworthy that the  $\partial R/\partial\lambda$  spectra from the same color groups (two Cyanophyta species and two green Chlorophyta species) have nearly identical  $\partial R/\partial\lambda$  signatures. Increases in the concentration of the brown diatom result in proportional increases in reflectance across the entire spectrum, whereas increases in the concentration of the green Chlorophyta do not yield appreciable growth of reflectance, rather the reflectance can be seen to decrease in the blue and green regions where carotenoid and chlorophyllous pigments absorb strongly and also in the red region where *chl-a* dominate absorption. In the case of Cyanophyta, reflectance increases in proportion to the concentration of *chl-a*, but it is apparent that, as the concentration enhances, the absorption features due to phycocyanin and *chl-a* become more prominent. Similar effects are observed in the spectra of red Cyanophyta, but reflectance decreases at  $\lambda \leq 600$  nm with increasing algal content, in particular in proximity to the phycoerythrin absorption maximum; however, reflectance grows with greater *chl-a* at  $\lambda$  beyond 600 nm. Although these observations are to be expected, they are very useful for interpreta-

tion of satellite high-resolution spectra from the perspective of monospecific HAB identification.

Stæhr and Cullen (2003) used fourth-derivative absorption spectra to differentiate *Karenia mikimotoi* (a toxic gyroxanthin diester-carrying dinoflagellate) from another toxic dinoflagellate *Prorocentrum minimum*, which does not contain this pigment. A comparison has been made of the efficiency of the two methods: a spectral similarity index (*SI*) and a multivariate partial least squares (PLS) regression technique. Spectral absorption (380–800 nm) signatures recorded with a 0.5 nm resolution were obtained for pure and mixed cultures grown under a variety of light illumination and nitrogen availability conditions.

The *SI* (varying between zero and one) was computed as an angle between the vectors  $\mathbf{A}$  comprising the fourth-derivative spectra of the standard sample with 100% *K. mikimotoi* (=std) and the unknown mixed sample (=unk):  $[(\mathbf{A}_{\text{std}} \cdot \mathbf{A}_{\text{unk}})/[\|\mathbf{A}_{\text{std}}\| \times \mathbf{A}_{\text{unk}}]]$ . Arc-cosine transformation and division by  $\pi/2$  were applied in order to convert the non-linear relationship between *SI* and the percent biomass of the gyroxanthin-carrying species into a linear relationship between zero and one (Millie *et al.*, 1997).

The multivariate regression technique uses a PLS regression model for predicting one or several  $Y$ -dependent variables on the basis of several independent  $X$ -variables (phytoplankton absorption spectra), by relating the two data matrices,  $X$  and  $Y$ . Thus, the model is a regression relationship between linear combinations  $\mathbf{t} = \mathbf{Xw}$  of  $X$  and  $\mathbf{u} = \mathbf{Yc}$ , where  $w$  and  $c$  are eigenvectors maximizing the covariance between  $\mathbf{t}$  and  $\mathbf{u}$  (Esbensen *et al.*, 1994).

Both approaches proved able to differentiate not only between the two species grown under standard conditions, but also when they are grown subject to varying light and nutrient supply levels. However, the *SI* technique may be less robust to photo-acclimation and phytoplankton assemblage structure and does not yield reliable estimates of absolute pigment or cell concentrations, whereas the PLS determinations are not susceptible to such shortcomings. One drawback of the PLS approach is that it initially requires a large number of confidently calibrated and validated samples.

Understandably, the spectral decomposition/derivative analysis technique discussed above can only be efficient if the input spectrum of water reflectance is obtained (i) with the lowest possible spectral distortions (due to instrumental and, when measured from aircraft and satellites, atmospheric effects), and sufficiently high spectral resolution (ideally, 1–2 nm across the visible spectral range).

The prerequisite that the spectral decomposition/derivative analysis technique should only be applied to monospecific phytoplankton populations is not limiting for remote detection of HABs, which can be considered, at least in the first approximation, as a single-species event (Section 3.1).

Bracher *et al.* (2009) have explicitly shown the feasibility of a satellite sensor with high spectral resolution, initially developed for atmospheric studies. As such, Bracher *et al.* used SCIAMACHY (Scanning Imaging Absorption Spectrometer for Atmospheric Chartography) mounted on ENVISAT. The instrument measures transmitted, scattered, and reflected light from the Earth's atmosphere and surface,

observing in nadir and limb-viewing geometries spanning from the UV to the near IR at the spectral resolution (from UV to VIS) 0.26–0.44 nm. Phytoplankton groups (diatoms and cyanobacteria) were identified by means of the differential optical absorption spectroscopy (DOAS) method (Vountas *et al.*, 2007). Performing least squares fit, DOAS exploits the sharp spectral features in backscattered solar spectra that are caused by molecular absorption by atmospheric constituents, by spectral re-distribution features as induced by the Ring effect (inelastic scattering by atmospheric N<sub>2</sub> and O<sub>2</sub> molecules), by inelastic vibrational Raman scattering (VRS) in ocean water, and by the absorption of marine phytoplankton. Absorption cross-sections of relevant atmospheric absorbers have been measured in the laboratory and cross-sections for absorption by certain phytoplankton groups have been measured from natural samples. Pseudo-absorbers such as Ring and VRS have been modeled. The DOAS technique permits the separation and, hence, retrieval of the higher frequency absorption features from broad-band spectra (this contribution is subtracted as a low-order polynomial  $\sum_{k=0}^n a_k \lambda^k$ , with typically  $n \leq 4$ ).

Depending on the targeted absorber (i.e., phytoplankton absorption and VRS), an optimal wavelength window is selected and all the relevant radiative contributions within this window are considered. The DOAS fit was applied to the global data set within the 429.0–495.0 nm spectral range. For fitting phytoplankton absorption, reference spectra specific to cyanobacteria and diatom absorption obtained from water sample absorption measurements were used. To convert the extracted SCIA-MACHY fit factor for diatoms or cyanobacteria into concentrations, information on the light penetration depth was employed (from the VRS fit via conversion of the wavelength window 349.0–382.0 nm to the phytoplankton DOAS fit: 429.0–495.0 nm).

### **3.5.1.2 Use of spectral expressions of the fluorescence of phytoplankton pigments**

Phytoplankton fluorescence has been considered by some workers as an important process in determining the spectral distribution of volume reflectance and upwelling radiance in the red part of the visible spectrum. The fluorescence peak of chlorophyll at 680–685 nm was suggested as a means of remotely retrieving the content of phytoplankton or, rather, chlorophyllous pigments as their proxy in case I waters (Gower and Borstad, 1977, 1990, 1993; Neville and Gower, 1977; Doerffer, 1981; Gower *et al.*, 1999, and some others; for references see also Kondratyev *et al.*, 1999). The Medium Resolution Imaging Spectrometer (MERIS), which was launched by the European Space Agency on ENVISAT, has a band at 681.25 nm for *chl* fluorescence (rather than at 685 nm because of the presence of O<sub>2</sub> absorption at 687 nm). Gower *et al.* (1999) suggest using five bands in the spectral range 620–754 nm for inferring  $C_{chl}$  and interpreting features of  $L_u(\lambda, +0)$ . The algorithm proposed for estimating the *chl* fluorescence signal, called Fluorescence Line Height (FLH), involves subtraction of an interpolated baseline designed to represent the spectrum of  $L_u(\lambda, +0)$  in the absence of fluorescence. In the simplest case this interpolation is

linear, and the *FLH* retrieval algorithm may be written in the form:

$$FLH = L_u(\lambda_2, +0) - L_u(\lambda_1, +0) - (L_u(\lambda_3, +0) - L_u(\lambda_1, +0)) \frac{(\lambda_2 - \lambda_1)}{(\lambda_3 - \lambda_1)} \quad (3.25)$$

where  $\lambda_2$  is the MERIS band centered on the *chl* fluorescence, while bands  $\lambda_1$  and  $\lambda_2$  determine the baseline. Numerical and field experiments indicated that the optimal combination of  $\lambda_2$ ,  $\lambda_1$ , and  $\lambda_3$  is 682, 665, and 705 nm, respectively.

The relationship between *FLH* and  $C_{chl}$  obtained by Gower *et al.* (1999) on the coast of British Columbia and in the Baltic Sea appears to be linear, but very different in slope depending on the location. Generally, this linearity only holds around  $C_{chl} = 1 \mu\text{g/L}$  and strongly departs at  $C_{chl}$  close to  $0.1 \mu\text{g/L}$  and at  $C_{chl} > 10 \mu\text{g/L}$  (at  $C_{chl} \geq 30 \mu\text{g/L}$  the slope even changes sign).

Extending the *FLH* algorithm to waters containing an enhanced amount of suspended matter, Gower *et al.* (1999) found that, although suspended matter strongly reduces the *chl* fluorescence peak, the value of *FLH* remains, however, approximately stable. Importantly, as was shown by Hoge *et al.* (2003) the *FLH* approach is also robust in non-case I waters containing appreciable amounts of *doc*. This statement is however questionable, because increased absorption by *doc* is bound to lead to a decrease in the light absorbed by algal cells and, therefore, in phytoplankton fluorescence (see Sathyendranath *et al.*, 2004b).

However, the issue of *retrieval accuracy* remains open under a significantly reduced *absolute* value of the *chl* fluorescence peak in case of enhanced suspended and dissolved organic matter. In addition, as will be emphasized below, the absorption by water *per se* becomes strong in the red part of the spectrum (Pope and Fry, 1997). In situations with a vertically inhomogeneous *chl* distribution (e.g., submerged maximum), the *chl* fluorescence peak will be drastically reduced. Remote-sensing estimates via *chl* fluorescence in such waters will underestimate productivity.

Recently, Gower and Borstad (2004) investigated the feasibility of MODIS and MERIS for imaging chlorophyll fluorescence in the world's oceans. Sensitivity to fluorescence is a function of the signal-to-noise ratio of bands 667 and 678 nm (with a smaller contribution from the band at 748 nm) for MODIS and at 665, 681, and 709 for MERIS. The estimated lowest detectable *chl* concentrations are  $0.07 \text{ mg m}^{-3}$  for MODIS and  $0.10 \text{ mg m}^{-3}$  for MERIS. To apply the *FLH* approach, the 667 and 748 nm bands are to be used to define a linear baseline giving a reference level at 678 nm in the case of MODIS. For MERIS the peak near 700 nm can be detected using the baseline bands at 681, 709, and 754 nm.

The *FLH* approach thus cannot discriminate between different algal species and, as such, is unable to detect a harmful algal bloom *per se*. However, this assumption has recently been called into question by Wynne *et al.* (2008) who claimed that, due to relatively enhanced backscattering properties, cyanobacteria *can* be detected via the *FLH* approach. They seemingly found that the spectral shape around 681 nm was not a positive quantity, as scattering due to cyanobacteria (at concentrations in excess of  $5 \mu\text{g/L}$ ) overwhelm the fluorescence signal, thus rendering the *FLH* value negative. However, Wynne *et al.* admit that this assertion needs further substantia-

tion. Indeed, there are other algae whose backscattering efficiency is comparable to cyanobacteria (e.g., the green alga *Dunaliella bioculata* or the coccolithophore alga *Isochrysis galbana*, etc.; Ahn *et al.*, 1992). Moreover, the presence of coccoliths or mineral suspended matter (even in small amounts) can result in a similar negative *FLH*.

A more discriminative approach was reported by Vincent *et al.* (2004) for the detection of the cyanobacterium *Microcystis* in Lake Erie. Using fluorometer-derived *in situ* data on the ratio of *in vivo* phycocyanin and *chl* fluorescence peaks (termed PC = relative phycocyanin content), the following relationship was found for relating PC and LANDSAT 7 spectral bands:

$$PC = 0.78 - 0.0539(B1) + 0.176(B2) - 0.21(B5) + 0.117(B7), \quad (3.26)$$

where *B1*, *B3*, *B5*, and *B7* stand for dark object-subtracted digital numbers of LANDSAT TM band 1, band 3, band 5, and band 7, respectively.

Since PC values are bound to be proportional to absolute phycocyanin content,  $C_{\text{phycocyanin}}$  ( $\mu\text{g/L}$ ), the expression (3.26) was further transformed to directly relate the satellite data to  $C_{\text{phycocyanin}}$ :

$$\begin{aligned} C_{\text{phycocyanin}} = & 47.7 - 9.21(R31) + 29.7(R41) - 118(R43) - 6.81(R53) + 41.9(R73) \\ & - 14.7(R74), \end{aligned} \quad (3.27)$$

where *R* = the ratio of signals in respective channels.

Using eq. (3.27), Vincent *et al.* (2004) retrieved the concentrations of phycocyanin in Lake Erie on several occasions from both LANDSAT 7 and LANDSAT 5 data, and found that  $C_{\text{phycocyanin}}$  varied between  $\sim 5$  and  $12 \mu\text{g/L}$  (with the assessed standard error of  $0.6 \mu\text{g/L}$ ).

Detection and monitoring of the toxic dinoflagellate, *Karenia brevis*, is suggested by Craig *et al.* (2006). The inversion of  $R_{rs}(\lambda)$  spectra to  $a_{\text{php}}^{rs}(\lambda)$  is followed by comparison of the fourth derivatives of the  $a_{\text{php}}^{rs}(\lambda)$  spectra with the fourth derivative of the reference *K. brevis* absorption spectrum obtained from spectrometric measurements of filter-padded samples. The comparison is performed by means of the aforementioned similarity index (*SI*) analysis but applied to remote-sensing reflectance (Kirkpatrick *et al.*, 2000):

$$SI = \frac{A_{\text{ref}} A_{R_{rs}}}{|A_{\text{ref}}| \times |A_{R_{rs}}|}, \quad (3.28)$$

where  $A_{\text{ref}}$  and  $A_{R_{rs}}$  are the vectors that comprise the fourth derivatives of the *K. brevis* reference filter pad absorption spectrum and the reflectance-derived phytoplankton absorption spectrum, respectively. The *SI* calculation yields a number from 0–1, with the value of 1 corresponding to absolute similarity between the reference and derived spectra. This approach is not efficient at very low phytoplankton cell counts and has problems in the presence of high CDOM concentrations.

The retrieval of  $a_{\text{php}}^{rs}(\lambda)$  from  $R_{rs}(\lambda)$  can be performed using a variety of algorithms (such as neural network, linear matrix inversion, MODIS semi-analytical,

quasi-analytical, GSM semi-analytical algorithms), whose characterization and references to detailed descriptions are available in IOCCG (2006) (see also Section 3.5.2.1).

Babichenko *et al.* (1993) used a shipborne tunable KLS-10 lidar based on a dye laser for detecting chlorophyllous pigments at the excitation band of 445 nm. The emitted light was captured at  $\sim 680$  nm. To diagnose phytoplankton biliproteins (i.e., phycoerythrin and phycocyanin), the excitation bands were chosen at 550 and 630 nm, respectively. Fluorescence by phycoerythrin was registered at  $\sim 575$  nm and that of phycocyanin at 645 nm (which is in full conformity with the data we discussed in Section 3.3).

To assess the *concentration* of phytoplankton fluorophores, emission intensities were normalized by the intensity of the maximum of water *Raman* inelastic scattering. The major incentive of normalization resides in the fact that in the overwhelming number of cases of natural waters loaded with *chl*, *sm*, and *doc*, the intensity of water Raman scattering remains unaffected by other water constituents at the first approximation (Kondratyev *et al.*, 1999). Raman scattering is a type of scattering of electromagnetic radiation in which light changes its frequency (as well as its phase) as it passes through a medium. Hence, it is called *inelastic* scattering as opposed to *elastic* scattering of light occurring in gaseous and liquid media without a wavelength or frequency shift.

This change in scattered light frequency or wavelength is due to the interaction of light with the vibrational modes of the molecules constituting the medium. In water the dominant Raman line is generated due to modulation of the amplitude of the propagating light wave/vibration by the fundamental O–H stretching mode of the H<sub>2</sub>O molecule.

The Raman band is relatively broad with a maximum at a wavenumber shift of 3,330 cm<sup>-1</sup> (Waters, 1995). Because the differential Raman scattering cross-section of water molecules  $(d\sigma_{\text{H}_2\text{O}}/d\Omega)_{90^\circ} = 8.3 \times 10^{-30} \text{ cm}^2 \text{ molecule}^{-1} \text{ sr}^{-1}$  for the exiting wavelength  $\lambda_{\text{ex}} = 488$  nm in a direction perpendicular to the polarization plane of the incoming light beam, when integrated over the Raman emission linewidth.

Integration of the differential Raman cross-section of water over the full solid angle ( $4\pi$  steradians), using eq. (3.29):

$$d\sigma_{\text{H}_2\text{O}}/d\Omega = (d\sigma_{\text{H}_2\text{O}}/d\Omega)_{90^\circ} \frac{[\rho + (1 - \rho) \sin^2 \alpha]}{(1 + \rho)} \quad (3.29)$$

(where  $\alpha$  = the scattering angle, and  $\rho$  = the depolarization ratio of water) results in a volume scattering coefficient,  $b_r$ , due to inelastic scattering

$$b_r(\delta\nu_r) = N \int_{4\pi} \left( \frac{d\sigma_{\text{H}_2\text{O}}}{d\Omega} \right) d\Omega, \quad (3.30)$$

where  $\delta\nu_r$  = the Raman frequency shift,  $N$  = number of water molecules per cm<sup>-3</sup> (at normal sea level pressure  $N \cong 3.3 \times 10^{22} \text{ cm}^{-3}$ ; Fadeev *et al.*, 1982).

The integration of eq. (3.28) over  $4\pi$  and further integration over the Raman frequency shift distribution  $\delta\nu_r$  results in  $b_r = 2.6 \cdot 10^{-4} \text{ m}^{-1}$  at  $\lambda_{\text{ex}} = 488$  nm.

The wavelength dependence of the Raman band and, thus,  $b_r$  is very strong and is proportional to  $\lambda_{em}^{-5}$ , whereby  $\lambda_{em}$  is the wavelength of inelastically scattered light (Sugihara *et al.*, 1984). Consequently, in order to calculate  $b_r$  at wavelengths other than 488 nm, a simple relationship can be used:

$$(d\sigma_{H_2O}/d\Omega)_{\lambda_i} = (d\sigma_{H_2O}/d\Omega)_{\lambda=488\text{ nm}} \left( \frac{\nu_i - \overline{\delta\nu_r}}{\nu_{488} - \overline{\delta\nu_r}} \right)^5, \quad (3.31)$$

where  $\nu_i = 1/\lambda_i$ , and  $\overline{\delta\nu_r}$  is the mean Raman frequency shift.

Sugihara *et al.* (1984) report an expression for the maximum wavelength of the Raman band,  $\lambda_{em_{max}}$  (nm), as a function of the exiting wavelength ( $\lambda_{ex}$ , nm):

$$\lambda_{em_{max}}(\lambda_{ex}) = \frac{\lambda_{ex}}{-3.357 \cdot 10^{-4} \lambda_{ex} + 1}. \quad (3.32)$$

The Raman scattering phase function  $\beta_r(\theta)$  can be approximated via (Porto, 1966):

$$\beta_r(\theta) = \frac{3}{16\pi} \frac{1+3\rho}{1+2\rho} \left( 1 + \frac{1-\rho}{1+3\rho} \cos^2 \theta \right), \quad (3.33)$$

where  $\rho$  = the depolarization ratio of water ( $\rho = 0.17$  at  $\overline{\delta\nu_r} = 3,400\text{ cm}^{-1}$  (Ge *et al.*, 1995)).

The value of  $b_r(\lambda)$  has been determined by many workers (for references see Kondratyev *et al.*, 1999). It lies in the range  $2.7 (\pm 0.2) \times 10^{-4}\text{ m}^{-1}$  for  $\lambda = 488\text{ nm}$ . Introducing  $b_{b_r}(\lambda)$  (the Raman coefficient for backscattering) and  $b_{b_r}(\lambda) = B_r b_r(\lambda)$  ( $B_r$  = the inelastic backscattering probability), it is possible to assume from eq. (3.33) that  $B_r \approx 0.5$ . The intensity of inelastically backscattered light (i.e., the light emerging from beneath the water surface) is proportional to  $b_{b_r}(\lambda)$  and the intensity of laser light.

In turn, the intensity of pigment fluorescence is proportional to the fluorescence cross-section (see Section 3.5.3) and the intensity of excitation light. Thus, the concentration of a fluorescent pigment,  $C_{pigm}$ , can be found through an empirical equation relating  $C_{pigm}$  to the ratio of respective fluorescence at the wavelength of maximum emission to the maximum of water Raman scattering at the wavelength determined by eq. (3.32). Through adjusting the coefficient of proportionality between the normalized fluorescent signal and  $C_{pigm}$ , the latter can be obtained in absolute units ( $\text{mg} \cdot \text{m}^{-3}$ ). Such relationships are seemingly area specific (primarily due to specific indigenous algae) and are to be established for each targeted water body (Kondratyev *et al.*, 1998, 1999). In the case of waters of high trophy, the Raman normalization procedure for water needs to be supplemented by subtracting the possible contribution of chromophoric *doc* fluorescence (Section 3.5.5.2). Chromophoric *doc* emission is most significant at short wavelengths and is expected to affect substantially the amplitude of signals of Raman normalization for water and biliprotein fluorescence, with the *chl* fluorescence peak remaining only marginally influenced. This subtraction procedure could be performed provided the envelope parameters of *doc* emission and the *doc* fluorescence cross-section (for

the wavelength of excitation) are known. For further discussion and relevant parameters, see Kondratyev *et al.* (1999) and Pozdnyakov and Grassl (2003).

### 3.5.2 Detection of massive HABs through remote estimation of *chl-a* concentration/phytoplankton biomass levels

Although the detection of *chl-a* *per se* in water cannot be considered an unequivocal indication of HAB, the concentration of *chl-a* may qualify as such because collected evidence (Franks, 1997a, b; Barlow *et al.*, 2002; Bianchi *et al.*, 2002; Anonymous, 2003a, b; Doney *et al.*, 2003) points to frequently high *chl* in HAB events. Mesoscale ocean circulation features such as eddies occur often and may be critical for phytoplankton dynamics such as bloom initiation, retention, and transport. Other features are also important. The convergence of fronts associated with upwelling or with river plumes may increase plankton density. Frontal jets may increase the alongshore transport of harmful blooms and cause inshore blooms or be diverted offshore due to prominent coastal headlands. Tidal fronts, formed at the abutment of stratified offshore water and tidally mixed inshore waters, have been shown to be sites of dense accumulations (Anonymous, 2003b). There may also be biological reasons for highly enhanced cell density in harmful algal blooms (e.g., due to drastically reduced grazing rates because some harmful species are inedible for zooplankton).

In addition, remote-sensing assessments of *chl* spatial distributions are efficient in delineating/mapping the blooms and surveying their temporal dynamics (Bricaud *et al.*, 2002).

As described in Section 3.4, the world's natural waters fall into two major categories in terms of their composition and optical properties: case I and case II waters (Morel and Prieur, 1977). For pristine/offshore oceanic waters qualifying as case I waters, it was long believed that considerable simplifications are possible resulting in a combination of statistical and semi-analytical universally applicable relationships between the ratios of either upwelling radiance  $L_u(\lambda, +0)$ <sup>1</sup> or remote-sensing reflectance  $R_{rs}(\lambda, +0)$  at two or several wavelengths and the desired parameter: the concentration of chlorophyll-*a*.

A revision of operational band ratio algorithms was suggested at the SeaWiFS Bio-optical Algorithm Mini-Workshop (SeaBAM) (January 1997). While the ocean chlorophyll algorithm 2 (OC2)—a modified cubic polynomial function that uses the ratio  $R_{rs}(490, +0)/R_{rs}(555, +0)$  and simulates well the sigmoidal pattern revealed between log-transformed radiance ratios and *chl*—was chosen as the pre-launch SeaWiFS operational *chl-a* algorithm (for OC2, OC2v2, OC2v3 parameters see Smyth *et al.*, 2002a), improved performance was obtained using the ocean chlorophyll algorithm 4 (OC4), a four-band (443, 490, 510, 555 nm), maximum band ratio

<sup>1</sup> Radiance,  $L$ , in a specified direction at a point in the radiation field is defined as the radiant flux  $\Phi$  at that point per unit solid angle  $d\Omega$  per unit area  $dA$  at right angles to photon propagation. The standard unit of radiance is  $\text{W m}^{-2} \text{sr}^{-1}$ .

formulation (O'Reilly *et al.*, 1998):

$$C_{chl} = 10^{(a_0 + a_1 \xi + a_2 \xi^2 + a_3 \xi^3)} + a_4, \quad (3.34)$$

where  $\xi$  is the greatest log-ratio among  $R_{rs}(443)/R_{rs}(555)$ ,  $R_{rs}(490)/R_{rs}(555)$ , and  $R_{rs}(510)/R_{rs}(555)$ ;  $a_0 = 0.4708$ ;  $a_1 = -3.8469$ ;  $a_2 = 4.5338$ ;  $a_3 = -2.4434$ ;  $a_4 = -0.0414$ .

With the increasing accuracy of satellite sensors and more demanding user requirements with respect to the quality/precision of remote-sensing retrievals, the case I water community is presently searching for new algorithms capable of meeting the above challenges. To achieve these goals, many workers resort to area-specific algorithms. For instance, Gohin *et al.* (2002) suggested using the OC4 algorithm as an input parameter for a regression area-specific algorithm OC5 of the form  $OC5 = OC4 - A_1(OC4 - 0.55)^{A_2}$ , where  $A_1$  and  $A_2$  are empirically estimated at 0.18 and 2.0, respectively.

It is noteworthy that the OC4 algorithm has recently been shown to be used for discrimination of the main algal groups in case I waters, based on ample and homogeneous shipborne spectro-fluorometric and HPLC data collected during nine cruises from Le Havre (France) to Nouméa (New Caledonia) across the North Atlantic, along the eastern coast of the U.S., through the Caribbean Sea to Panama, and across the equatorial and tropical South Pacific to New Zealand and eventually New California. In the framework of the GeP&CO (Geochemistry, Phytoplankton, and Color of the Ocean) monitoring program, Alvain *et al.* (2005) found that coincident normalized SeaWiFS data on the normalized spectral water-leaving radiance  $nL_w(\lambda)$  between 412 and 555 nm varied significantly with *in situ* pigment composition, so that four major phytoplankton groups can be distinguished. Seven pigments have been taken as indicators of algal groups: *chl-a* (all algae except *Prochlorococcus*), divinyl *chl-a* (*Prochlorococcus*), pheophytin-*a* (degraded algae), fucoxanthin (diatoms), peridinin (dinoflagellates), 19'-hexanoyloxyfucoxanthin (Prymnesiophyta), and zeaxanthin (*Synechococcus*-like cyanobacteria or SLC and *Prochlorococcus*).

To isolate second-order variation from total  $nL_w(\lambda)$  variability, a specific water-leaving radiance,  $nL_w^*$ , was employed:

$$nL_w^*(\lambda) = nL_w(\lambda)/nL_w^{ref}(\lambda, chl-a), \quad (3.35)$$

where  $nL_w^{ref}$  is a simple model of  $nL_w$  that accounts only for the SeaWiFS standard *chl-a*.  $nL_w^*$  was defined empirically from a large dataset of SeaWiFS *chl-a* and  $nL_w$ , and a lookup table of  $nL_w^{ref}(\lambda, chl-a)$  has been generated.

Although there is general agreement on the taxonomic indication of each biomarker (e.g., divinyl *chl-a* as a biomarker of *Prochlorococcus*), the relative concentrations/pigment ratios differ in literature reports. To overcome this difficulty, thresholds were set up to associate relative pigment concentration to a specific algal group. Dinoflagellates were left out of the group identification scheme as they were present in the GeP&CO data as a minor component.

Combined concurrent shipborne and SeaWiFS data explicitly indicated that

there should be a relationship between both the spectral shape and the amplitude of the satellite signal and the dominant phytoplankton group. Indeed,  $nL_w^*$  is: (a) low at all wavelengths for haptophytes with a pronounced drop at 412 and 443 nm; (b) neutral and slightly below unity; (c) slightly larger at 412 nm and, generally, above unity; and (d) high values and a steep spectrum decreasing from 412 to 510 nm. From this rationale, a characteristic range of  $nL_w^*$  was derived and laid down as the basis of algorithms for algal group discrimination.

Miller *et al.* (2006) suggested a multivariate classification approach as a means to discriminate HAB and non-HAB algal development areas. Three linear discriminant analysis classifiers were individually trained to recognize the toxic red tide bloom-producing dinoflagellate alga *Karenia mikimotoi* (*Gymnodinium nagaesakiense*), mucilage-releasing *Chattonella verruculosa* (Raphidophyceae), and toxic cyanobacteria.

The procedure starts by retrieving spectral variations of water absorption and backscattering from satellite data (normalized water-leaving-radiance,  $L_{wn}(\lambda)$ ) making use of the model based on the analyses of spectral curvature slope (Smith *et al.*, 2006, 2007). The model is applicable to case I and case II waters. Used for multivariate discrimination, Fisher ( $F$ ) statistics deals with the ratio of between-class variance to within-class variance—that is, high  $F$  values ( $\gg 1$ ) indicate significant differences between classes, and hence their enhanced differentiability. To maximize the  $F$  value, the optimal linear combination of variables (i.e.,  $L_{wn}(\lambda)$ ,  $a(\lambda)$ , and  $b_b(\lambda)$ ) are identified via linear discriminant analysis (Flury and Riedwyl, 1988) and further employed as classifiers (Miller *et al.*, 2006).

For SeaWiFS spectral bands, the strongest identifiers for cyanobacteria proved to be  $L_{wn}(510)$  and  $L_{wn}(490)$ , although  $a(510)$ ,  $b_b(490)$ , and  $L_{wn}(670)$  also appeared fairly consequential. For *Chattonella* these are  $a(443)$ ,  $a(490)$ , and  $a(510)$ , whereas for *Karenia* they are  $L_{wn}(670)$ ,  $a(443)$ , and, to a somewhat lesser degree,  $L_{wn}(443)$  and  $L_{wn}(553)$ .

To enhance the discriminative power of the procedure, subtraction of the time-averaged median background values of  $L_{wn}(\lambda)$  and *chl-a* levels is performed to further generate difference maps for  $\Delta chl-a$  and  $\Delta L_{wn}(\lambda)$ . This removes the effects of the sediment spectral impact on  $L_{wn}(\lambda)$  and associated anomalies; pixels with  $\Delta chl-a$  and  $\Delta L_{wn}(\lambda)$  ( $\lambda = 490$  and 555 nm) simultaneously being above zero are to be discarded.

The identification power of the classification scheme can be enhanced if area-specific information is used for weighting classifier outputs according to the historical probability of occurrence of sought-for harmful species. The use of MERIS (whose number of spectral channels and their placements are more appropriate for such purposes and allow including *chl-a* fluorescence as an additional classifier) and data on SST can further strengthen this approach.

Sathyendranath *et al.* (2004b) suggested an area-specific algorithm based on SeaWiFS data for discrimination of diatoms from other phytoplankton in case I waters. The approach is based on the finding that variations in the proportion of the pigment fucoxanthin (a pigment common to diatoms) to *chl-a* change the blue-green ratio of phytoplankton absorption by a factor of up to 6 and, hence, affects

**Table 3.5.** Spectral values of the parameters  $U(\text{m}^{-1})$ ,  $S[\text{m}^3(\text{mg chl-}a)^{-1}]$ , and  $a_2^*[\text{m}^2(\text{mg chl-}a \cdot \text{g})^{-1}]$  for mixed and diatom-dominated phytoplankton populations for the SeaWiFS wavelengths and their corresponding Raman wavelength (upper wavelength and corresponding number) (Sathyendranath *et al.*, 2004b).

$\lambda$ , nm	Mixed phytoplankton			Diatom phytoplankton		
	$U$	$a_2^*$	$S$	$U$	$a_2^*$	$S$
362	0.0624	0.0273	0.541	0.0254	0.0234	8.72
412	0.0376	0.0269	1.01	0.103	0.00950	0.234
386	0.0424	0.0236	0.753	0.0277	0.0161	2.43
443	0.0281	0.0310	1.80	0.0747	0.0118	0.270
421	0.0340	0.0285	1.23	0.0939	0.0102	0.252
490	0.0248	0.0146	1.68	0.0122	0.00981	4.68
435	0.0306	0.0316	1.65	0.0897	0.0113	0.248
510	0.0178	0.00979	1.41	0.00786	0.00810	4.77
468	0.0236	0.0249	2.12	0.0177	0.0128	2.95
555	0.00386	0.00554	2.13	0.00302	0.00443	2.35
547	0.00542	0.00644	1.93	0.00349	0.00522	3.12
670	0.00586	0.0169	2.29	0.0110	0.0104	1.51

the spectral distribution of  $R_{rs}(\lambda)$ . Total reflectance is assumed to be the sum of contributions due to elastic and Raman scattering.

The absorption coefficients of diatoms and the mixed populations ( $a_{ph}$ ) at each of the SeaWiFS wavelengths and their corresponding Raman source wavelengths were parameterized as non-linear functions:

$$a_{ph} = U(\lambda)\{1 - \exp[-S(\lambda)C]\} + Ca_2^*(\lambda), \quad (3.36)$$

where  $U(\text{m}^{-1})$ ,  $S[\text{m}^3(\text{mg chl-}a)^{-1}]$ , and  $a_2^*[\text{m}^2(\text{mg chl-}a \cdot \text{g})^{-1}]$  are parameters fitted as a function of  $\lambda$  and the *chl* concentration,  $C_{chl}$  ( $\text{mg chl-}a \cdot \text{m}^{-3}$ ); their determined values are given in [Table 3.5](#).

Based on the data in [Table 3.5](#), lookup tables for the predicted ratios of remote-sensing reflectance,  $R_{rs}$ , at 510 and 555 nm for diatoms and mixed populations can be calculated for the expected range of *chl-a* concentrations. This criterion is employed to differentiate between diatom and mixed population pixels.

This may facilitate improving the retrieval accuracy of *chl-a* concentrations, the logic being that if a pixel is identified as being dominated by diatoms, then the bio-

optical model for diatoms is to be used and a mixed population model can be employed for the remaining pixels.

Through numerical simulations, Stramska and Stramski (2005) showed that the relative error in  $R_{rs}$  ( $350 < \lambda < 700$  nm) may reach 70% due to the non-uniformity of oceans where surface *chl* is low (i.e., very clear off coastal waters) and the depth of the *chl* maximum is shallower than the penetration depth. In this light, OC standard algorithms for case I waters can be further improved to account for the non-uniform vertical profiles of *chl* concentration. Xiu *et al.* (2007) suggested modifying the empirical SeaWiFS OC2V4 (O'Reilly *et al.*, 1998, 2000):

$$C_{chl} = a_4 + 10^{a_0+a_1R+a_2R^2+a_3R^3}, \quad (3.37)$$

where  $R = \log_{10}(\tilde{R}_{rs})$ ;  $\tilde{R}_{rs} = R_{rs}(490)/R_{rs}(555)$ ;  $a_0 = 0.39$ ,  $a_1 = -2.336$ ,  $a_3 = -0.135$ ,  $a_4 = -0.071$  as follows:

$$C_{chl} = 10^{b_0+b_1P+b_2P^2+b_3P^3}, \quad (3.38)$$

where  $b_0 = -0.139$ ,  $b_1 = 8.17$ ,  $b_2 = -35.8$ ,  $b_3 = 76.0$ ;  $P = \log_{10} \dot{R}$ ,  $\dot{R} = R \left( \frac{R_{rs}(\lambda_0)}{R_{rs}(\lambda_1)} \right)^a$ ,  $\lambda_1 = 360$  nm,  $a = 1.2$ ,  $\lambda_0$  is a function of  $C_{chl}$  and is to be taken from a lookup table (Xiu *et al.*, 2007).

Analysis of the spectral curvature of  $R_{rs}(\lambda)$  has been shown to be instrumental in the identification of coccolithophores, golden-brown algae of the class Prymnesiophyceae that possess external calcareous plates called coccoliths. Like diatoms, they constitute an abundant and widely distributed component of marine plankton. An example of a globally significant coccolithophore is *Emiliania huxleyi*. *E. huxleyi* blooms can be detected in visible satellite imagery by their specific spectral signature. They appear milky white to turquoise in color due to their *high volume reflectance* and, hence, high values of  $R_{rs}(\lambda)$ . The latter exhibits a very strong maximum at about 490 nm or at longer wavelengths if co-existing with other phytoplankton (Brown and Podesta, 1997). This spectral property is used to flag coccolithophore blooms in SeaWiFS, MODIS, and MERIS images.

The global algorithms for case I waters may require modifications for oceanic provinces rich in coccolithophores. Coccoliths increase radiance upwelling from beneath the water surface both in the blue and green, thus producing respective changes in  $R(\lambda)$  and  $R_{rs}(\lambda)$ . “Flattening” of the reflectance spectrum in coccolithophore blooms implies that the standard ratio pigment algorithms will not provide correct pigment retrievals within such blooms. To overcome this problem, Balch *et al.* (2005) suggested a two-band ratio algorithm for SeaWiFS data relating  $L_w(443)_N/L_w(550)_N$  to  $C_{chl}$ , accounting for the coccolith concentration/count number. Based on the semi-analytical model by Gordon *et al.* (1988), respective lookup tables were calculated, providing not only more accurate pigment retrieval, but also restoring the concentration of coccoliths. Note that this approach is applicable solely to case I waters.

Although, by definition, in case I waters the concentrations of other CPAs are strictly proportional to  $C_{chl}$  and changes in the latter determine water color varia-

tions, increasingly numerous reports from different provinces of the world's oceans indicate that this is not necessarily the case (Sathyendranath, 2000).

In an attempt to decouple phytoplankton chlorophyll concentration from the concentrations of other substances co-existing in Case I waters, Garver and Siegel (1997) developed a model for case I waters in which the optical impact of combined *doc* and detrital material was assumed *independent* of  $C_{chl}$ . *Cross-sections* of the chosen CPAs were used and a *non-linear* least squares inversion procedure was employed.

Chomko *et al.* (2003) applied to case I waters a spectral optimization procedure consisting in minimizing at each wavelength the squared difference between modeled and actually measured normalized water reflectance. The procedure results in assessment of the abundance of *chl*, colored dissolved organic matter, detrital particles, and particles of other kinds.

The above tendency in the case I water "community" to go over from simplistic algorithms to more sophisticated ones was actually prompted by the development of water quality retrieval approaches for case II waters (Bukata *et al.*, 1995). Due to the optical complexity of case II waters (Section 3.1), simplistic algorithms proved to be untenable, and this triggered extensive searches for procedures that would be able to cope with the major challenge of case II waters: uncorrelated and not infrequently simultaneously high contents of *chl*, *sm*, and *doc*.

Along with statistical regularization, simplex optimization, and maximum likelihood methods (for references see Kondratyev *et al.* 1999), a multivariate optimization procedure and neural networks were suggested to grapple with this task, as described below.

### 3.5.2.1 Multivariate optimization procedure

The subsurface remote-sensing reflectance,  $R_{rsw}(\lambda, \mathbf{C}, a, b_b)$ —which by definition is the upwelling spectral radiance just beneath the water-air interface,  $L(-0, \lambda)$ , normalized by the downwelling spectral irradiance,  $E(-0, \lambda)$ , at the same level (Jerome *et al.*, 1996)—depends on both  $\mathbf{C} = \sum_i C_i$ , the concentration vector encompassing all the major CPAs and the specific absorption  $a^*$  and backscattering  $b_b^*$  coefficients of co-existing water constituents. If  $S_j$  is the measured/retrieved subsurface remote-sensing reflectance at wavelength  $\lambda_j$ , then the residual between  $S_j$  and  $R_{rsw_j}$  can be computed in one of the following ways:

$$g_j = [S_j - R_{rsw_j}] / S_j; \quad (3.39)$$

$$g_j = [S_j - R_{rsw_j}] / R_{rsw_j}; \quad (3.40)$$

$$g_j = [S_j - R_{rsw_j}]. \quad (3.41)$$

The multidimensional least-squares solution that uses every wavelength is found by minimizing the squares of the residuals:

$$f(\mathbf{C}) = \sum_j g_j^2(\mathbf{C}). \quad (3.42)$$

The absolute minimum of  $f(\mathbf{C})$  can be found with the Levenberg–Marquardt finite difference algorithm (Levenberg, 1944; Marquardt, 1963), which assures rapid convergence of the iterative procedure. The following iterative expression is used to this goal:

$$\mathbf{C}_{k+1} = \mathbf{C}_k + \zeta_k (F'_k F_k + \mu_k D_k)^{-1} F'_k \left( 1 - \frac{R_{rsw}(\mathbf{C}_k)}{\{S_k\}} \right), \quad (3.43)$$

where  $k$  = the iteration step,  $D_k = \text{diag}(F'_k F_k)$  = the diagonal matrix consisting of the elements  $F'_k F_k$ , with  $F(\mathbf{C}) = \left| \frac{\partial R_{rsw}}{\partial \mathbf{C}_j} \right|$  = a matrix composed of  $n \times m$  elements ( $n$  = the number of wavelengths, at which measurements/retrievals  $S_i$  have been conducted,  $m$  = the dimension of the concentration vector  $\mathbf{C}$ ),  $F'(\mathbf{C})$  = the transposed matrix,  $\mu_k$  = the direction of minimization, and  $\zeta_k$  = the length of the minimization step.

The actual length  $\zeta_k$  can be chosen easily and effectively through applying the method of reduction, which consists in the following: in a certain iteration step  $k$  a deliberately high value of  $\zeta_k$  is chosen (e.g., 50). From eq. (3.43) a new concentration vector  $\mathbf{C}_{k+1}$  is determined, for which the inequality  $f(\mathbf{C}_{k+1}) < f(\mathbf{C}_k)$  is tested. If it is not satisfied,  $\zeta_k$  is reduced by a factor of 2, and a new round of searches is initiated. This iterative procedure is continued until the above inequality is satisfied: until the newly determined concentration vector proves to be closer to the minimum of the function of residuals  $f(\mathbf{C})$  as compared to the concentration vector established in the previous iteration step.

In the course of the iterative descent to the global minimum of the function of residuals, the above procedure could end in a *local* minimum. If the determined  $\mathbf{C}_k$  happens to be going downhill and the length of the iteration step  $\zeta$  is sufficiently high, then the next concentration vector  $\mathbf{C}_{k+1}$  might also go downhill toward a deeper minimum. In this case the search process will move to a new point provided the inequality  $f(\mathbf{C}_{k+1}) < f(\mathbf{C}_k)$  is satisfied. Thus, a search with a variable length  $\zeta$  can, under favorable conditions, evade a local *minor* minimum and end either in a *deeper* or even in the *global* minimum.

However, equally possible is the situation that the concentration vector  $\mathbf{C}_{k+1}$  is *uphill* of a certain local minimum of  $f(\mathbf{C})$ . In this case, the search ends in this local minimum, which corresponds to an inadequate solution of the inverse problem. Naturally, the probability for the latter option increases with measurement/retrieval errors.

To avoid the above difficulty, it is advisable to initiate the iteration procedure for an array of initial guess values,  $\mathbf{C}_0$ . Afterwards the deepest minimum of  $f(\mathbf{C})$  is selected. The number  $N$  of the initial vectors  $\mathbf{C}_0$  should not be excessively high because the computation time for the inverse problem solution increases proportionally with  $N$ .

Nevertheless, the use of an array of initial vectors  $\mathbf{C}_0$  does not guarantee that the iterative procedure converges or/and the eventually established concentration vector  $\mathbf{C}$  is realistic. To overcome this problem, *a priori* limits can be imposed on each of

CPA concentrations,  $C_i$ :

$$C_{i_{\min}} \leq C_i \leq C_{i_{\max}}, \quad (3.44)$$

where  $i$  is the  $i$ th constituent of the aquatic medium.

### 3.5.2.2 Neural network approach

There are many different types of neural networks (NNs) but one of the most commonly used neural networks in remote sensing is the multi-layer perceptron (MLP; Atkinson and Tatnall, 1997). The MLP generally consists of three layers: input layer neurons are the elements of a vector, which might consist of radiances at certain wavelengths; the second layer is the internal or “hidden” layer; in the third layer, the number of neurons equals the number of parameters to be determined. Each neuron in the network is connected to all neurons in both the preceding and subsequent layer with an associated weight.

Input signals are transferred to the neurons in the next layer in a feed-forward manner. As the signal propagates from neuron to neuron, it is modified by the appropriate connection weight. The receiving neuron sums the weighted signals from all neurons in the previous layer. The total input that a single neuron receives is weighted in the following way:

$$net_j = \sum \omega_{ji} o_i, \quad (3.45)$$

where  $\omega_{ji}$  is the connection weight between neuron  $i$  of the preceding layer and neuron  $j$  in the receiving layer, and  $o_i$  is the output from neuron  $i$  of the preceding layer. The output from a given neuron  $j$  is then obtained from:

$$o_j = f(net_j). \quad (3.46)$$

The function  $f$  is usually a non-linear sigmoid function. It is applied to the weighted sum of inputs before the signal reaches the next layer. When the signal reaches the output layer, network output is produced. The created network should be trained so that it can generalize and predict outputs from inputs that it has not processed before. A training pattern is fed into the neural network and the signals are forwarded. After that, network output is compared to true output, the error is computed and back-propagated through the network. As a result, the connection weights are modified following the generalized rule:

$$\Delta \omega_{ji}(n+1) = \eta(\delta_j o_i) + \alpha \Delta \omega_{ji}(n), \quad (3.47)$$

where  $\eta$  is the learning rate parameter,  $\delta_j$  is an index of the error change rate, and  $\alpha$  is the momentum parameter.

Training carries on until the output error reaches a desired level. The trained neural network is then tested against some verification data to assess the network performance.

The important advantage of the discussed optimization and NN approaches resides in their robustness (within certain limits) to input data noise (up to 15%, Pozdnyakov *et al.*, 2004), whereas the band ratio algorithms such as OC2, OC2v2, OC2v3, OC4 (eq. 3.32) and others are unable to extrapolate.

As seen, both minimization-based and NN approaches require use of the hydro-optical model (which gives spectral values of the absorption and backscattering cross-sections of major CPAs) as well as confidently established equations relating to water column reflectance and bulk water IOPs (Section 3.4). Under certain hydro-optical conditions, water Raman scattering and *chl* and *doc* fluorescence can interfere and consequently corrupt the results of retrieval of *chl* (Sections 3.5.3 and 3.5.5) as well as other CPA concentrations (Gordon, 1999; Pozdnyakov and Grassl, 2003). Moreover, mucilage, surfactants, and air bubbles (Section 3.5.4) can affect the retrieval results.

The aforementioned methodologies of *chl* inference from remote-sensing data are very sensitive to input error produced by, for example, incomplete adequacy of the applied hydro-optical model, inaccurate subtraction of the optical impact originating in the atmospheric layer intervening between the water surface and the remote sensor, or sensitivity degradation in different spectral channels of the remote-sensing ocean color sensor. Accurate assessment of the atmospheric impact or path radiance (Section 3.1) is also important when applying the method of differential spectroscopy (Section 3.6.1.1). The impact of the above factors on the light signal registered by a remote-sensing sensor can lead to significant alterations of the spectral curvature of the quantity (e.g.,  $R_{rs}$ ) to be processed and, hence, result in somewhat inaccurate interpretations of derivative spectra.

None of these reservations necessarily rules out the possibility of HAB bloom detection by remote sensing, but their judicial consideration is nevertheless required when the above methodologies are applied to specific water bodies/water masses.

Removal of atmospheric influence (i.e., atmospheric correction) is especially challenging (e.g., Siegel *et al.*, 2000; Yan *et al.*, 2002b; Gordon, 2003, Stamnes *et al.*, 2003). The major difficulty resides in the optical properties of atmospheric suspended particles termed “aerosol”. Atmospheric aerosol is a very complex and variable in time and space ensemble of particulate matter, especially in the lower troposphere over land and strand areas. The atmospheric aerosol over case I waters is generally homogeneous spatially and chemically both in the upper and lower troposphere. It consists of mostly marine particulate matter, and its influence on light transfer is largely by scattering. Its optical properties are fairly well established and, hence, are generally adequately assessed in atmospheric correction procedures.

In the atmosphere over case II waters, however, aerosol composition originates from a number of distributed and point sources, often anthropogenic. This results in pronounced spatial and compositional inhomogeneity of the aerosol. In addition, aerosol over such areas is no longer purely scattering but also absorbing. That is why atmospheric correction over case II waters presents a very serious problem (for references see Pozdnyakov *et al.*, 2000a, b).

Initially, atmospheric correction procedures were decoupled from the retrieval procedures for *chl* or more generally CPAs (e.g., Ruddick *et al.*, 2000; Sturm and Zibordi, 2002; Vermote *et al.*, 2002; Li, 2003; Stamnes *et al.*, 2003). Frequently, a decoupled atmospheric correction procedure result in errors that nearly linearly increase with  $\lambda^{-1}$ , which is due to the extrapolation approach that forms their basis: the aerosol optical impact is first assessed in the infrared and then extrapolated

to the blue part of the spectrum. As a result, the input error can reach 15% at short wavelengths of the visible spectrum. Pozdnyakov *et al.* (2004) found through numerical simulations that the  $\lambda$ -dependent input error presents the hardest case for the retrievals of CPAs with acceptable accuracy.

Later on, a variety of optimization-based procedures and NNs were employed to simultaneously retrieve both CPA concentrations and atmospheric aerosol optical characteristics (Fischer and Doerffer, 1987; Doerffer and Fischer, 1994; Schroeder *et al.* 2002; Chomko *et al.*, 2003). The latter approach seems more promising—at least, in terms of the expected independence of the error from  $\lambda$ —although its vulnerability increases, because not only is an adequate hydro-optical model required but embedded options of the optical models of atmospheric aerosol also need to be appropriate to the area amenable to remote sensing.

The other problem relating to the optical impact of the atmosphere is the contamination of multispectral satellite images by spatially varying, semi-transparent cloud and aerosol layers frequently referred to as haze (Zhang *et al.*, 2002). Haze can arise from a variety of atmospheric constituents including water droplets, ice crystals, or fog/smog particles, as well as contrails.

Therefore, there is a pressing need for a robust image-based capability to accurately detect and flag/mask spatially varying forms of haze. This is especially relevant for water surface monitoring, over which such phenomena are fairly frequent. The task of isolation of coccolith blooms in the presence of haze is also a challenge since both are efficient reflectors of sun/sky light. For terrestrial applications, a few procedures such as HOT (haze optimization transformation) and TC (tasseled cap transformation) (Richter, 1996; Zhang *et al.*, 2002) have been proposed. In the case of natural water tracts, flags and masks act as a means of insuring special quality by discarding pixels with haze and by detecting the contours of coccolithophore blooms (Pozdnyakov *et al.*, 2004).

### **3.5.2.3 Combination of multivariate optimization and NN approaches: the BOREALI algorithm**

The authors of this book have developed a combined approach that culminated in the BOREALI algorithm (e.g., Korosov *et al.*, 2009). The BOREALI algorithm's principal architecture is illustrated in Figure 3.16. Having been subjected to preliminary processing and atmospheric correction, the satellite image is further treated by calculating for each pixel the corresponding subsurface remote-sensing reflectance spectrum  $R_{rsw}(\lambda)$  (Pozdnyakov *et al.*, 2003). First, the normalized upwelling radiance,  $nL_w(\lambda)$  is achieved on the basis of ancillary data: namely, instantaneous extraterrestrial solar flux  $F_0(\lambda)$  and Sun zenith angle  $\theta_0$ . For each pixel,  $R_{rsw}(\lambda)$  serves as input to the broad-band (B-B) neural network procedure (NN-1 in Figure 3.16). If the concentration of one of the CPAs (i.e., *chl*, *sm*, and *doc*), as determined by NN-1, falls in the CPA range concentration 0–5 (in respective units), a corresponding narrow-band NN (NN-2, 3, 4 in Figure 3.16) is initiated.

In the next step, the CPA concentration vector  $C$  (*chl*, *sm*, *doc*) thus determined is used to ascertain an array of initial concentrations,  $C_0$ . From this pool of initial

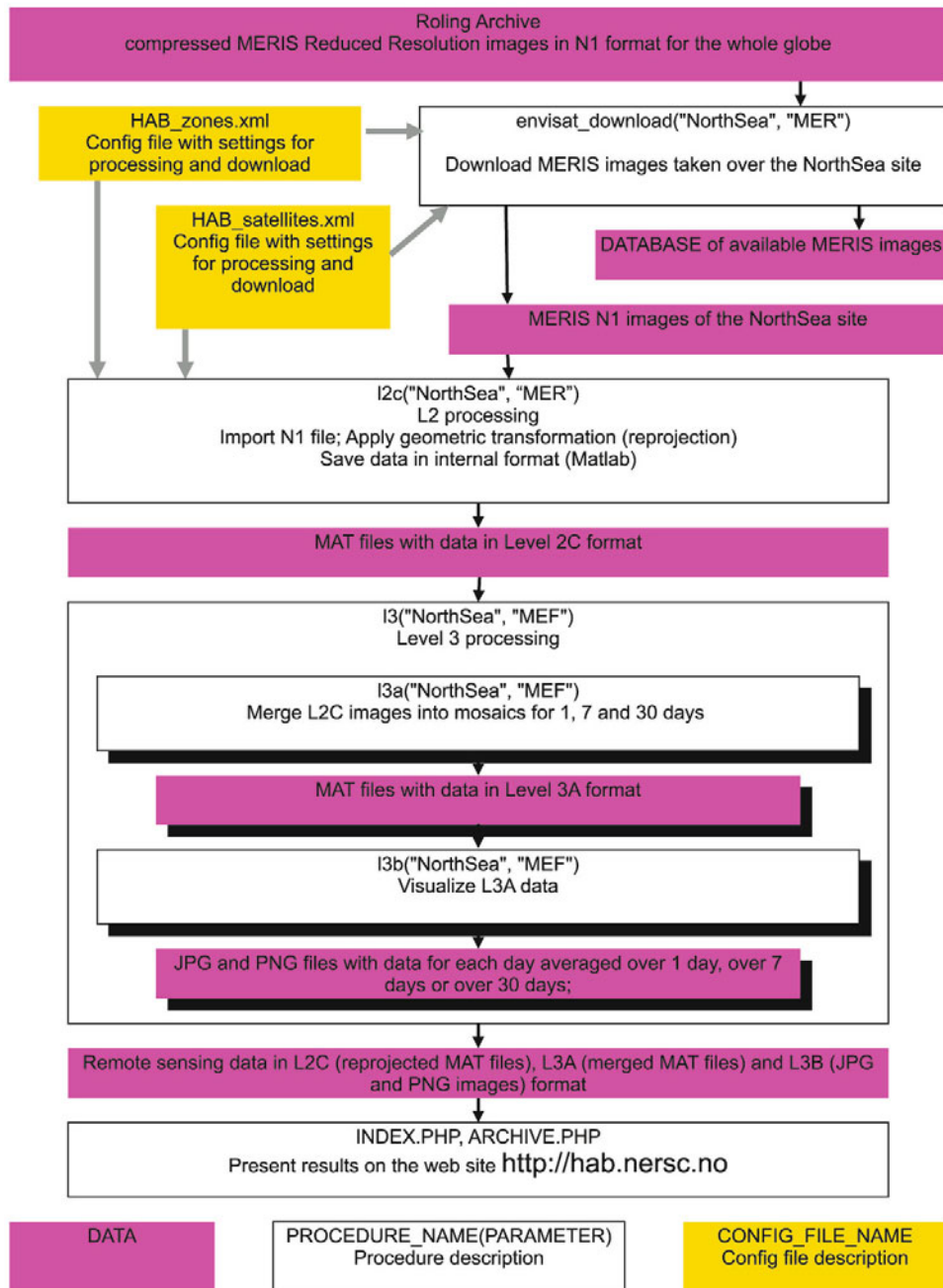


**Figure 3.16.** Flow diagram of the Nansen Centers' Bio Optical Retrieval Algorithm (BOREALI). Pink blocks indicate data, white blocks indicate operations, and yellow blocks indicate configuration files. *Courtesy: A. Korosov.*

concentrations, starting concentrations  $C_i$  for each CPA are randomly taken as input to the Levenberg–Marquardt (L–M) procedure to complete the retrieval process.

On exiting the coupled NN → L–M sequence, the final concentration values of  $chl$ ,  $sm$ , and  $doc$  emerge. Understandably, this algorithm requires (i) a hydro-optical model appropriate to the water body and (ii) a parametric relationship (e.g., eq. 3.6) relating  $R_{rsw}(\lambda)$  and the water bulk absorption and backscattering coefficients  $a$  and  $b_b$  (Section 3.4).

This algorithm has two quality assessment units. The first eliminates pixels that suffer from imprecise atmospheric correction. It manifests itself in (a) negative values of  $R_{rsw}(\lambda)$  at short wavelengths (400–450 nm) due to overestimation of path radiance, and (b) enhanced values of  $R_{rsw}(\lambda)$  in the blue part of the spectrum (channels 1 and 2 in the case of SeaWiFS) followed by a dip/trough in either the second or third channel due to underestimation of path radiance.

Compared with case I waters, case II waters are generally loaded with appreciable amounts of  $sm$  and, thus, present a serious challenge to distinguish the  $chl$  signal correctly. This algorithm allows unambiguous differentiation of areas with low and high  $sm$  and can retrieve  $chl$  even in the presence of ample amounts of  $sm$  and  $doc$ . At the same time, the algorithm operates equally well in case I waters. Identification of case I and case II waters is performed by jointly analyzing both the envelope of  $R_{rsw}(\lambda)$  spectra and their mean spectral value. The latter is known (e.g., Bukata *et al.*, 1985) to be distinctly different for clear and turbid waters, and a corresponding threshold is imposed.

The second quality assurance (mask) is intended to detect pixels corresponding those areas of the studied water body whose hydro-optical properties significantly differ from those covered by the applied hydro-optical model. This might be, *inter alia*, due to the presence of some particular algal species (e.g., red tide or monospecific blooms like those of cyanobacteria), which go beyond the scope of the applied hydro-optical model.

This second mask/flag operates as follows: the CPA vector yielded in the second step of the retrieval procedure (i.e., by the L–M technique) is further used for reconstruction of the corresponding  $R_{rsw}(\lambda)$  spectrum using the embedded hydro-optical model and the parametric relationship  $R_{rsw} = f(\mathbf{a}, \mathbf{b}_b)$  employed. The reconstructed  $R_{rsw}(\lambda)$  spectrum ( $R_{rsw(r)}$  in Figure 3.16) is then compared with the  $R_{rsw}(\lambda)$  spectrum initially retrieved from the satellite data ( $R_{rsw}$  in Figure 3.16). If the mean spectral value of  $R_{rsw}(\lambda)$  is significantly higher than that of  $R_{rsw(r)}$ , then the pixel can either be discarded or attributed to a coccolith expression. Coccoliths are known (e.g., Smyth *et al.*, 2002b) to appear on or just below the water surface as whitish relatively bright spots surrounded on all sides by dark water. Therefore, the coccolith option is activated provided the retrieved  $R_{rsw}(\lambda)$  spectrum, in addition to its high values across the visible wavelengths, also exhibits only weak spectral variance ( $\lambda^{-\zeta}$ ,  $1 < \zeta < 1.35$ , see Smyth *et al.*, 2002b). The appropriate limits for departures of  $R_{rsw}(\lambda)$  from its mean value are duly imposed.

The application of both quality assurance stages helps eliminate from the retrieved spatial distributions of CPA those pixels/areas with erroneous concentrations of either  $chl$ ,  $sm$ , or  $doc$ . This inevitably results in the appearance of lacunas in

the CPA distributions retrieved. However, application of the standard SURFER CODE (SURFER Brochure, 2004) facilitates the visual interpretation of such images by presenting them as a sequence of color-scaled areas, whose borders correspond to the concentration isolines of the relevant CPA.

So, given a hydro-optical model for the specific HAB species which is generally known either from the literature (if this is a recurring phenomenon in the study area) or from dedicated shipborne sampling analyses (if this is an unusual event), the above algorithm is capable not only of delineating the area of high algal biomass, but also of yielding a quantitative assessment of the surface content of thriving algae unless foam has formed on the sea surface (a complication that can arise with cyanobacterial blooms under calm weather conditions, as discussed earlier).

### 3.6 SYNERGISTIC APPROACHES FOR HAB DETECTION AND MONITORING

As emphasized in Chapter 2 and mentioned in Section 3.1, increasing evidence indicates that the distribution of HAB species is changing significantly throughout the world's oceans. Some species are expanding their geographical range; in other instances, new toxic species are being identified that were previously considered harmless. Alien species have been introduced to new ecosystems where conditions are favorable for them (e.g., where there are few natural predators). New and strict international legislation and regulations about the discharge of ballast water may limit the future spread of alien algae species between different marine ecosystems; however, some damage has already occurred in this respect. Moreover, the same species can sometimes have widely different impacts in different aquatic environments—the same species can be toxic in one location and non-toxic in another. On many occasions, genetic analyses are needed to differentiate between morphologically similar algae, whose environmental impact proves to be so strikingly different.

On the other hand, genetic variations can be driven by changes in water chemistry, light (especially UV radiation) regime, water temperature, salinity, and inter-species food web and sexual interactions. Some of these factors are explicitly driven by climate variations. Indeed, the latter can be expected to result in changes in species composition, trophic structure, and function of aquatic ecosystems. Some quasi-periodic atmosphere–ocean phenomena, such as the Southern Oscillation (ENSO), the North Atlantic Oscillation (NAO), or the Pacific Decadal Oscillation (PDO) are thought to be important in this context.

The complexity of both the HAB phenomenon *per se* and causative mechanisms naturally implies the necessity of a synergistic approach to studying and monitoring HABs. *In situ* observations, chemical and biological models coupled with 3D thermohydrodynamic ocean models at different spatial scales and time resolutions, climate models, and remote-sensing methods are among the facilities that need to be exploited in a concerted manner to successfully cope with this ubiquitous ecological

challenge. Increased human activities in the marine ecosystem also emphasize the need for monitoring and management in order to be prepared for and able to implement mitigation actions.

As seen from the previous sections, remote-sensing methods can identify HABs, using hyperspectral or lidar sensors. Presently, there is no such spaceborne instrumentation, although in the not-too-distant future such facilities may become operational. Presently available satellite-based multispectral remote sensors (such as SeaWiFS, MODIS, and MERIS) are only really appropriate for the detection of algal biomass abundance and spatial distribution, with a few exceptions for HAB identification as discussed above.

Fast buoy-based and laboratory analyses of bloom cells and, if applicable, the identification of harmful species, followed or accompanied by remote-sensing data would be the best way for early detection and surveillance of HABs. The utility of such an approach is further favored by the above discussion about the formal affiliation of an alga to a species that can be innocuous or harmful dependent on the water conditions. Presently, only very sophisticated (although fast) laboratory analysis can confidently qualify the bloom as harmful or innocuous. If qualified as harmful, the HAB can then be monitored by remote sensing and its density and contours determined through delineating the spatial distribution of the *chl* concentration.

The aforementioned synergistic approach implies not only bringing together observational, modeling, and remote-sensing data. Within the remote-sensing option *per se*, it can be equally instrumental: by concatenating simultaneously or quasi-simultaneously the data obtained from satellite sensors operating in the visible, infrared, and microwave spectral regions mutually enriched data on the phenomenon under consideration can be offered.

Being vulnerable to cloudy/heavy haze conditions, optical remote surveillance can, under unfavorable weather and light conditions, be prevented from providing information for long time periods. Meanwhile, due to biological and hydrodynamic mechanisms, the remotely detected bloom may undergo significant changes (e.g., Letelier *et al.*, 1993) and drift far from its initial location (for references see Anonymous, 2003b). Such gaps in monitoring data are often highly detrimental for early warning and forecasting of a specific bloom event.

In contrast, microwave radar radiation is not hindered by clouds or lack of daylight, and a radar signal does not penetrate the water significantly. Instead, it reflects from the water surface and returns information to the radar's receiving unit about water surface conditions including data on the geometry of the water surface (wave and ripples) and material present on the water surface such as phytoplankton, oil pollution, and other waste (e.g., Espedal, 2001; Zhang and Hallikainen, 2002).

The most commonly observed biological effects in SAR images are elongated streaks of low radar return thought to be due to the Bragg wave dampening properties of accumulated biological surfactants. Indeed, the Bragg wave dampening effects of biological surfactants are known to produce low radar return patterns in SAR images when surface winds are below  $\sim 7 \text{ m s}^{-1}$  (e.g., Johannessen *et al.*, 1996).

Above this threshold, the local surface flow field is able to strongly affect the actual locations and shapes of surfactant effects.

Because biologically driven dampening appears similar to SAR manifestations of surface oil slicks, grease ice, wave-current shear interactions, and localized atmospheric boundary layer effects, the capability to positively identify biological features needs to be experimentally proven. In order to relate plankton distributions to the occurrence of low-backscatter patterns in ERS-1 Synthetic Aperture Radar imagery, Svejkovsky and Shandley (2001) concurrently used AVHRR data to simultaneously retrieve *chl* spatial distributions. In addition, the AVHRR data were used to determine sea surface temperature (SST) patterns in the target area. Within the area of Svejkovsky and Shandley's research, the most dense accumulations of phytoplankton proved to be restricted to surface manifestations on *cold* marine waters, which originated due to upwelling events and, hence, the enhanced availability of nutrients brought up from the depths. At the same time, the inherent convergence and divergence patterns in surface flow can enhance the dispersion of surfactants, thus affecting their spatial distribution. These effects may, in turn, decouple the actual film distribution from the underlying plankton distribution. Notwithstanding these complications, SAR as a complimentary technique can be used as an additional source of information for tracing the dynamics of already identified algal blooms under cloudy conditions, when optical sensors are ruled out. This was recently demonstrated by Zhang *et al.* (2002) who successfully used SAR (ERS-2) backscatter as one of the input data sources for developing an empirical neural network as a tool for the estimation of *chl-a* and some other water quality parameters. Zhang *et al.* have convincingly shown that the inclusion of the SAR channel into the array of input neurons has significantly improved the accuracy of *chl* and other CPA retrievals (for more details see Chapter 4).

Under cloud-free conditions, the synergistic coupling of visible and near-infrared imageries for concerted analysis can also provide better insight into the nature and dynamics of algal blooms. For instance, both types of satellite sensors were used in order to better understand the patterns, persistence, and inter-relationship between ocean color and thermal features (Arnone, 1987; Solanki *et al.*, 2001), as well as for a better estimate of algal primary production (Bricaud *et al.*, 2002). Based on the data from AVHRR, Solanki *et al.* (2001) found that chlorophyll frontal zone positions coincide with temperature boundaries at some locations, which demonstrates that the physical and biochemical processes are closely coupled at these locations. At the same time, horizontal displacement between *chl* and SST features was detected in some other locations, along with distinct differences in the fine morphology of these features. Cross-frontal diffusion, the time lag that ensues from phytoplankton growth variable rates (as a result of nutrient budget and light availability), can explain the above displacements of algal biomass and SST fields. In spite of the possible spatial displacements of these two kinds of fields, expressions of many phenomena have been shown to be confidently identified due to the concerted use of color and thermal channels. Mesoscale eddies; rings; tongue, mushroom, and anchor-shaped formations; coastal jets; meanders; and fringe fronts are among them. These data are highly valuable for qualitative and numerical model

analyses and data assimilation of bloom dynamics and spatial displacements for prediction and early warning.

### 3.7 CLOSING REMARKS

Whatever the reasons, coastal regions throughout the world are now subject to an unprecedented variety and increased frequency of HAB events. These events are associated with two general types of causative organisms: toxin producers and the high-biomass producers. Some of the algal species are invariably toxic; some others are only toxic at specific locations or under specific weather/climate/anthropogenic forcing conditions. Frequently, only rather sophisticated *in situ*/laboratory analysis is able to confidently qualify the toxicological status of algal cells initiating the bloom.

Notwithstanding this challenging uncertainty and innate intricacy of the phenomenon, remote-sensing methods are potentially instrumental in detecting and monitoring HABs. Derivative spectroscopy analyses (DSAs) and lidar techniques (LTs) are generally capable of confidently determining the presence of algal pigments characteristic of harmful algae. However, for the practical implementation of DSAs, very high spectral resolution of the satellite-received signal is required and very powerful lasers need to be placed in orbit. Presently, neither (non-commercial) hyperspectral sensors nor lidars are available on satellite platforms. This makes the aforementioned assets associated with these two approaches more potential than practical.

The presently operating spaceborne multispectral/multiband sensors for studying the color of the world's oceans (such as SeaWiFS, MODIS, MERIS) do not have sufficiently high spectral or spatial resolutions. This precludes use of their data from DSA processing, and leaves only limited opportunities for identification of the algal type by revealing the biliprotein fluorescence signal in pristine oceanic waters.

At the same time, the present ocean color sensors are suited for inferring *chl* concentrations from both offshore oceanic (case I) and coastal and inland (case II) waters, although significantly different methodological approaches need to be applied to the two distinctly different aquatic environments. *Chl*, as a proxy of algal biomass, can be used to assess bloom density and to contour its spatial distribution. Given favorable weather conditions (i.e., cloudless skies and the absence of haze), spaceborne optical sensors can provide valuable data on the temporal dynamics of algal concentrations and bloom progression from the location of its initiation. The major challenge facing qualitative assessment of algal cell concentrations resides in case II waters, whose optical complexity makes the *chl* retrieval procedure much more onerous and cumbersome. This is due to light absorption and scattering by *sm* and *doc* as well as the *doc* fluorescence that intervenes in light photon interactions with the aquatic medium. More area-specific and vegetation season-specific hydro-optical models need to be developed and validated to include not only the spectral absorption and backscattering cross-sections of

major CPAs, and *chl* and *doc* fluorescence yields, but also account for the succession of algal species across the annual algal vegetation period.

Successful performance of the retrieval procedures of *chl* and other CPAs largely depends on the accuracy of atmospheric correction. This equally applies to both future satellite hyperspectral sensors suitable for the implementation of derivative analyses and spaceborne lidar systems detecting the fluorescence of algal pigments. Again, the most serious problems here are associated with case II waters, the atmospheres over which are generally highly inhomogeneous in terms of particulate matter composition and spatial distribution. Present in the atmospheres over land and strand areas, anthropogenic aerosol that is not only scattering but also absorbing, frequently corrupts the accuracy of atmospheric correction. Some further breakthrough studies are required here in order to improve the use of ocean color data for the mapping of aquatic phytoplankton.

A comprehensive synergistic approach to monitoring HABs should be strongly encouraged. The term “synergy” implies here not only concerted use of *in situ*, laboratory, modeling, and remote-sensing facilities, but also bringing together simultaneously or quasi-simultaneously obtained data from different satellite sensors operating in the visible, infrared, and microwave spectral regions. Jointly analyzed and concatenated data from the above set of sensors are able to offer mutually enriching information on the phenomenon under consideration (e.g., Pettersson *et al.*, 2003).

# 4

## Monitoring harmful algal blooms from space

In Chapter 2, we discussed the various factors and processes that are conducive to the initiation, development, and growth of harmful algal blooms (HABs) in marine and coastal waters. The lifetime of HAB events is typically some weeks, but can be shorter or longer being a function of the concurrence of required favorable conditions, including light and nutrient availability, other biogeochemical ocean state variables, and the algae genus and species involved. In some aquatic environments, HABs exhibit a regular annual cycle, whereas in other regions of the world's oceans, HAB outbreaks are rather sporadic, with an observed tendency to be more frequent and affecting the ecosystem of new marine shelf zones (Anderson *et al.*, 2002). The early detection of arising HAB events and monitoring of both their development, peak occurrence, and decay, as well as their pathways of displacement driven either by advection or other biogeophysical factors which have been discussed earlier. Integrated monitoring and assessment of potential HAB events are needed and justified in order to effectively and safely utilize marine waters. The European contribution to GEOSS (the Global Earth Observation System of Systems), the GMES (Global Monitoring for Environment and Security) initiative includes marine core specialized services related to regular monitoring and forecasting of HABs and water quality conditions in European waters, among other services exploiting satellite Earth observations and *in situ* data as well as modeling and predictions. These services are developed and tailored to specific public or private user needs regionally or nationally, covering applications such as aquaculture, fisheries, recreation, and tourism, to mention a few.

Clearly, an integrated monitoring approach exploiting the presently available means and technologies should be employed. These include *in situ* measurements from buoys, stations, and ships, numerical ocean modeling, and satellite and air-borne Earth observation (EO) remote sensing. Satellite EO, being able to observe large areas of the ocean surface at medium spatial and ideally high temporal resolution (e.g., daily) can be especially useful for monitoring coastal and marine waters.

Indeed, optical and indirectly thermal infrared remote-sensing information can be used for early detection of algal blooms and timely decisions on planning of further field sampling in an emerging bloom that can potentially become a HAB event. This is of great importance, because only biochemical laboratory analyses of water samples can definitively identify the bloom as a harmful one. Regular in-water monitoring using automated ship-mounted FerryBox systems (see, e.g., <http://www.ferrybox.org/>) provide information to further identify and quantify a bloom observed from space and *vice versa*. Indications of potential HAB events observed in satellite EO data can be used to initiate and plan further investigations by other observations of higher precision. On the other hand, spaceborne remote-sensing information can be used as both input for biogeochemical numerical ocean modeling and validation data as well as for assimilation of satellite-based information into marine ecosystem models (Natvik and Evensen, 2003a; Simon and Bertino, 2009), but also as a means of revealing large-scale environmental changes in marine environments (e.g., Kahru, 1997). From this perspective, there is the potential of remote sensing for early warning of the development and advection of HAB events. However, in order to implement remote-sensing monitoring, dedicated methodologies need to be developed and validated based on knowledge of the capabilities and limitations of the available potential sources of information. The latter can only be based, in turn, on knowledge of the optical properties of harmful algae (i.e., the properties that determine the distinguishing spectral features of the light signal coming out from the water surface and eventually captured by the satellite sensor at an altitude of several hundred kilometers. Based on this knowledge of algal optical attributes, a variety of bio-optical retrieval algorithms have been developed (as discussed in Chapter 3), primarily quantifying the concentrations of Chlorophyll-*a* and a few of these are species specific.

This chapter (i.e., Chapter 4) presents a discussion of practical utilization of satellite optical remote sensing applied to HAB monitoring. Section 4.1 presents a range of reported studies of separate algal blooms/events and then provides examples of regular use of remote-sensing data as a key component of the HAB monitoring services developed and established (in Norway, in particular). This basic research and its development was triggered by the major *Chrysochromulina polylepis* bloom in 1988 in Norwegian coastal waters (Johannessen, O. M. *et al.*, 1988, 1989; Dundas *et al.*, 1989) and HAB monitoring from space became operational after the launch of the U.S. SeaWiFS ocean color sensor 10 years later in 1998 (see Preface). Section 4.2 discusses the role of multiple satellite EO data synergies in HAB monitoring. Some examples of regular near-real-time monitoring of HABs are presented in Section 4.3. We will also address some remaining research challenges that are pending for efficient exploitation of different information sources in the context of operational monitoring of HAB events.

## 4.1 SOME CASE STUDIES OF BLOOM EVENTS IN THE WORLD'S OCEANS

As indicated in the previous chapter (Section 3.6.2), band ratio bio-optical algorithms—primarily applicable to open ocean waters (case I waters)—are based

essentially upon the absorption features of chlorophyll-*a* (*chl-a*) (i.e., the pigment universally present in all autotrophic algae, including harmful ones). From this point of view, such algorithms are not discriminative in terms of algal taxa. In other words, they can detect an algal bloom (not necessarily being able to assess accurately the *chl-a* concentration), but certainly unable to identify the single or multiple species responsible for a specific algal bloom.

The same limitation is inherent in the Fluorescence Line Height (*FLH*) approach (Section 3.6.1.2). Because it is also based on the *chl-a* optical property (namely the *chl-a* fluorescence in the red part of the visible spectrum), this technique can only provide evidence of increased concentrations of phytoplankton, but not their floristic nature (Neville and Gower, 1977; Gower and Borstad, 1993; Gower *et al.*, 1999; Huot *et al.*, 2005, 2007).

The retrieval algorithms developed for case II waters (typically coastal waters under terrestrial influence) necessarily incorporate a hydro-optical model determining the IOPs of major CPAs (see e.g., Korosov *et al.*, 2009), including phytoplankton (see Chapter 3). Therefore, without *a priori* information on the predominant blooming algal species, state-of-the-art algorithms are neither able to identify whether a bloom is harmful or not. However, with some modifications, such algorithms can develop capabilities toward that direction (as discussed below).

Thus, the above types of algorithms can only be employed for detecting the early initiation of algal bloom events, including potential HABs, delineating their spatial distribution and monitoring both algal abundance proliferation and bloom displacement (due to the hydrodynamic and biological processes discussed in Chapter 2).

With the advent of satellite Earth observation sensors outfitted with sensitivity in spectral bands in the visible and near infrared, such as LANDSAT, AVHRR, CZCS, three decades ago, a broad community of researchers began using band ratio and *FLH* algorithms investigating the facility of satellite sensors in flagging and monitoring the dynamics of HABs (e.g., Steidinger and Haddad, 1981; Haddad, 1982; Vargo *et al.*, 1987; Stumpf and Tyler, 1988; Johannessen, O. M. *et al.*, 1988, 1989; Dundas *et al.*, 1989; Tester *et al.*, 1991; Keafer and Anderson, 1993; for more references for that period see, e.g., Cullen *et al.*, 1997).

The new generation of these so-called ocean color satellite Earth observation sensors started in 1998 with the launch of the U.S. SeaWiFS sensor (later comprising sensors such as OCTS, OCM, MODIS, the European Medium Resolution Imaging Spectrometer MERIS, to mention a few) with more numerous and better optimized and justified placement of spectral bands which provided new capabilities and revived the interest of scientists and operational stakeholders in employing such data to investigate the marine ecosystem, plankton blooms—including (H)AB events—and marine primary production. Although space agencies aim to provide homogeneous ocean parameters from different sensors, both the algorithms used and the technical specifications of each sensor generate differences in the actual data products delivered (Figure 4.1). Initiatives to harmonize data from different sensors have been done (e.g., through the ESA GlobColour project).

This section presents this research and its applications, giving examples from a variety of marine/aquatic environments throughout the world oceans in order to better illustrate our discussion in Chapters 1–3.

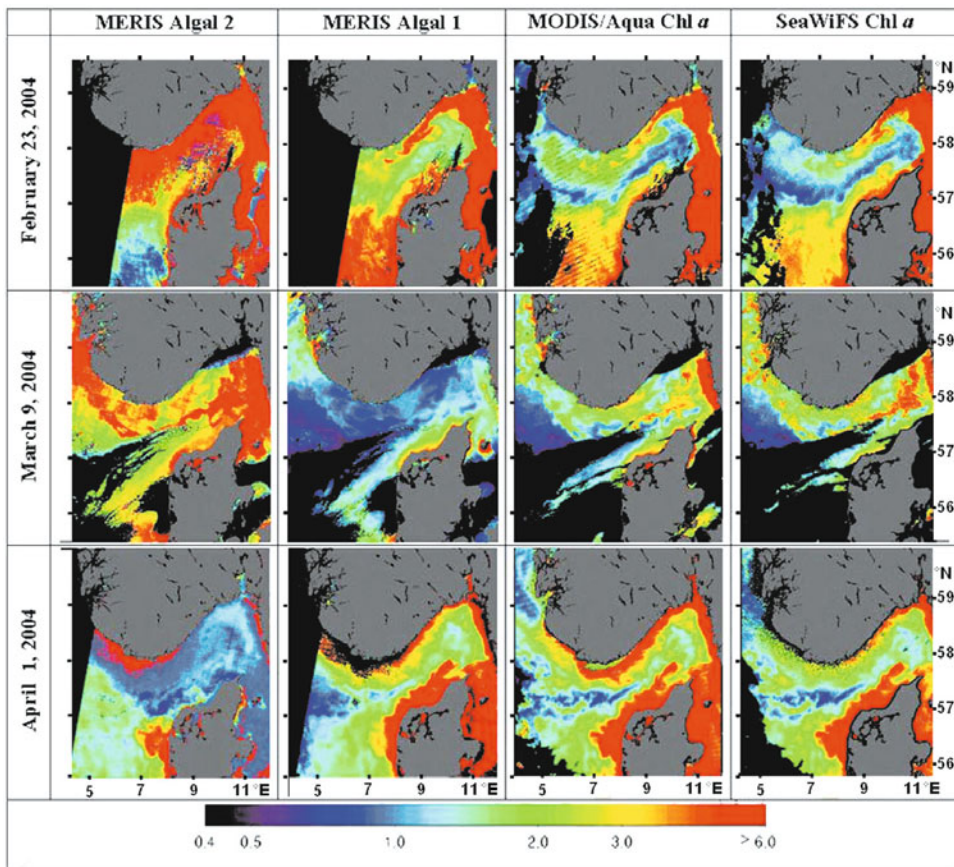


**Figure 4.1.** Chlorophyll distribution in North Sea and Skagerrak region as retrieved by the MERIS (Algol-2 and Algol-1 algorithm), MODIS/Aqua, and SeaWiFS (from left to right) for February 23, March 9, and April 1, 2004 (from top to bottom). Black areas indicate unprocessed pixels (clouds, corrupt atmospheric correction, or out-of-swath areas). Data are plotted with the same logarithmic color scale, as indicated by the color bar. The unit is  $\text{mg m}^{-3}$ . Copyrights: ESA/NASA/Orbimage. Courtesy: Folkestad *et al.* (2007).

#### 4.1.1 The North and Baltic Seas

The multivariate classification approach used in Miller *et al.* (2006) to discriminate HAB and non-HAB algal development areas was discussed in the preceding chapter. Miller *et al.* applied this method to SeaWiFS images to identify toxic red tide blooms of the dinoflagellate *Karenia mikimotoi* (*Gymnodinium nagasakiense*), mucilage-releasing *Chattonella verruculosa* (later reclassified correctly as *Pseudochattonella*, see Section 4.1.9), and toxic cyanobacteria in several marine waters: the U.K. southwest approaches, the Celtic Sea (south of Ireland), the North Sea, and the Baltic Sea. An example of such a HAB likelihood map is shown in Figure 4.2. Classification

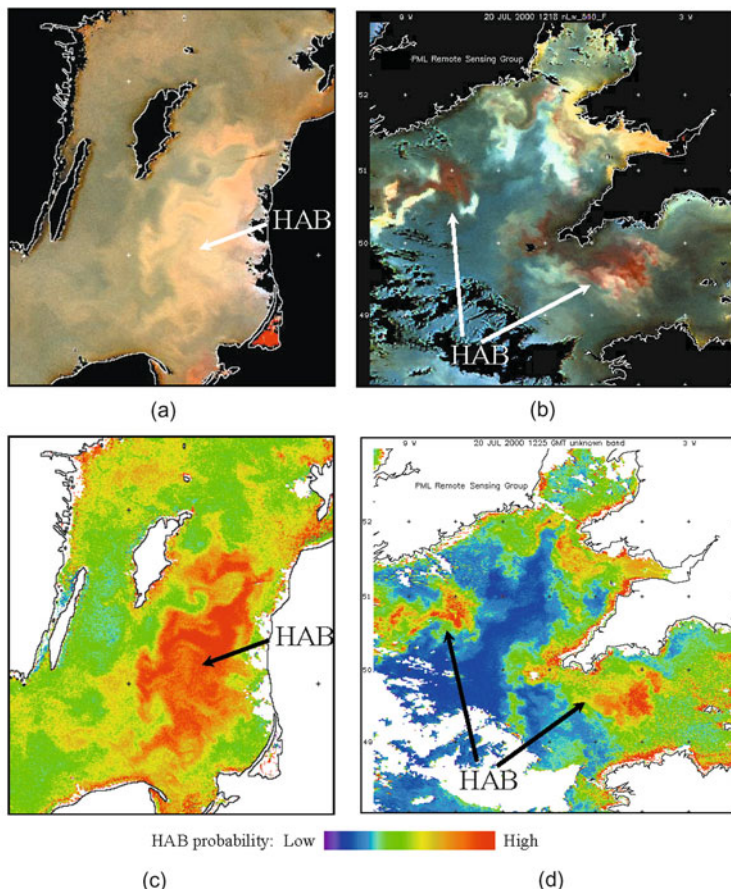


**Figure 4.2.** Example SeaWiFS contrast-enhanced false-color composites (555, 510, and 443 nm) of HABs: (a) Baltic Sea, June 5, 2002, 11:28 UTC, with cyanobacteria bloom; (b) U.K. SW approaches, July 20, 2000, 12:25 UTC, showing two *Karenia* blooms; (c), (d) corresponding HAB likelihood maps. Courtesy: Miller (2006).

accuracy proved to be very good, ranging from 83 to 98% in terms of explained variance.

This approach was further used to study the initiation and evolution of HABs of the aforementioned algal species. Starting from a date (June 24, 2002) prior to the formation of the *Karenia* bloom in the English Channel, Miller *et al.* obtained a sequence of HAB likelihood maps spanning the initiation of the bloom on July 3, its development through July 14–20, peaking on July 28, and rapid decay by August 3. On the same day (August 3), a new *Karenia* bloom event was observed to the southeast of the first bloom; the second bloom faded rapidly and had disappeared by August 24.

During the same summer, Miller *et al.* observed the evolution of the notorious cyanobacteria blooms in the Baltic Sea. The bloom began rapidly developing on

July 9, peaked on July 16, only to significantly decay by July 30 (although some bloom remnants continued to persist at the entrance to the Gulf of Finland).

In the North Sea, vast areas of *Chattonella* blooms were detected on May 13, 2000 within the western coastal waters of western Denmark (Jutland). Importantly, in close vicinity to this bloom (along the southern Norwegian coast) there was a coexisting area in which harmless algae had strongly developed, and the applied multivariate classification procedure successfully diagnosed and delineated both regions.

In all three of these case studies, independent shipborne observations were performed that confirmed the classification results of the remote-sensing data, thereby supporting the efficiency of the Miller *et al.* statistical methodology for the identification of HAB bloom events.

#### 4.1.2 The Korean Southeast and East China Seas

*Cochlodinium polykrikoides* is a planktonic dinoflagellate known to produce red tides in Korean coastal waters, particularly during summer and fall. Ahn *et al.* (2006) analyzed spatial and temporal variations in *chl-a* concentration from SeaWiFS for the period 1998–2002 in the enclosed and semi-enclosed bays of the Korean Southeast Sea.

In the absorption spectra of red tide waters, there are two distinct peaks centered respectively at 430 and ~665 nm and a less pronounced peak at 630 nm. The spectra of  $R_{rs}$  showed two maxima at 575–580 and 685–690 nm with an inflexion at 635 nm. The NASA OC4 bio-optical algorithm (Section 3.6.2) available in the SeaDAS software was employed to process Level 1A SeaWiFS data for Korean waters. Atmospheric correction was performed with the spectral shape-matching method developed by Ahn and Shamugam (2004). NOAA AVHRR data were used to retrieve sea surface temperature (SST) using the standard so-called “split-window” SST dual-channel algorithm (e.g., Wan and Dozier, 1996).

The obtained remote-sensing information proved to be able to demarcate the locality, spatial extent, and distribution of the blooms; however, in agreement with our discussion above, unique identification of *C. polykrikoides* in these sediment-dominated bay waters remained unsuccessful using satellite data alone.

SeaWiFS-derived concentration of *chl-a*,  $C_{chl}$ , in August 1998 varied from 3 to 54 mg/m<sup>3</sup> inside the targeted bay (Jin Bay) and from 0.6 to 14 mg/m<sup>3</sup> outside the bay—a region subject to coastal upwelling. According to analysis of the SeaWiFS time series, the bloom event lasted about 2 months in the bay, but only 1–2 weeks in the upwelling zone.

In September 1999, a *C. polykrikoides* bloom emerged farther to the north off Jin Bay. It is assumed that this bloom was triggered by anthropogenic nutrients discharged through the Yagil River. The northward extension of this bloom is believed to be associated with an episodic anticyclonic meso-scale eddy circulation feature with sufficient energy to pump up an essential amount of nutrients into the euphotic zone.

In September 2000, *C. polykrikoides* bloomed extensively and discolored the waters all along the southeastern Korean coast. In the immediate vicinity of the coast, in relatively cold and low-salinity waters, the bloom was initiated by monsoon rains, while the offshore extension of the *C. polykrikoides* bloom was sustained by the warm water currents.

Thus the areas with high  $C_{chl}$  concentrations were initially identified using SeaWiFS data. Then, in conjunction with physical oceanographic and hydrobiological information as well as spaceborne SST data, the observed bloom events were classified as harmful and the mechanisms for their initiation and development were elucidated.

However, in their studies of *C. polykrikoides* bloom events, Ahn *et al.* (2006) were unable to always confidently discriminate between turbid dissolved organic-rich and bloom-laden waters (i.e., the three main in-water constituents determining the optical ocean signal in coastal waters, as addressed earlier in this book). This may be because of their use of the standard NASA OC4 bio-optical retrieval algorithm, and not an algorithm tuned to case II waters. Nevertheless, they obtained generalized statistically robust data on the spectral distributions of water-leaving radiance and, based on these data, produced a rough classification of the targeted waters.

This was done by following the basic concepts suggested by Pasterkamp *et al.* (2002) and Danaher and Omongain (1992). However, Ahn *et al.* (2006) used forward principal component analysis (FPCA) and the method of minimum spectral distance (MSD). This enabled them to identify red tide areas, mixed areas (algae plus suspended mater), and areas loaded solely with suspended mater.

Earlier Huang and Lou (2003) exemplified the possibility of avoiding the problem of mixed areas encountered by Ahn *et al.* (2006) through employing the *neural network* statistical approach for the detection of HABs in case II/coastal waters. They trained their neural network—consisting of three layers, with the neurons in the first layer receiving AVHRR data from bands 1 and 2, then the SST values retrieved from bands 4 and 5, and then the output layer with only two neurons (“non-red tide”/“red tide”)—to detect red tides that occurred in Bohai Bay in July 1999. Comparison of the results of red tide delineation by the neural network algorithm and simultaneous aerial photography and shipborne monitoring indicated that this relatively simple approach proved to provide satisfactory results.

#### 4.1.3 The Pearl River Estuary, China

Using AVHRR and SeaWiFS data, Tang *et al.* (2003) investigated the HAB (dinoflagellate *Gymnodinium cf. catenatum* Graham) that occurred in the Pearl River estuary in late autumn, 1998. A multi-parameter environmental mapping system was used to obtain real-time measurements of water quality properties and surface wind data across the HAB area and beyond.

This red tide bloom was evident as a sequence of red parallel stripes that were 100–300 m long and 10–30 m wide over a total area of about 20–30 km<sup>2</sup>. *G. cf. catenatum* belongs to the group of dinoflagellates that are capable of diurnal vertical migration, and accordingly are able to exploit nutrient-rich water below the euphotic

zone, particularly when nutrients in the upper water column are depleted. The brackish water column within the HAB area was stratified, the water temperature was 24–25°C, and salinity was in the range 18–20 psu. Oxygen saturation on the surface reached 130% and the prevailing northern wind over the area was rather low ( $3\text{--}4 \text{ m s}^{-1}$ ).

SeaWiFS images processed with a standard algorithm (OC4) have shown high values of  $C_{chl}$  within the HAB area, although they are not able to discriminate between different algal classes. High concentrations of dissolved organic matter in the area have clearly led to overestimation of  $C_{chl}$ , but helped to delineate the HAB area. The combination of SeaWiFS  $C_{chl}$  data and AVHRR SST data (processed with an MCSST-based algorithm; McClain *et al.*, 1985) indicated that the HAB took place along the front between cooler lower salinity river water and warmer higher salinity South China Sea water.

#### 4.1.4 The Yellow Sea/Bohai Sea, China

A similar study was conducted by Tang *et al.* (2003) in China's Bohai Sea. In the autumn of 1998, SeaWiFS provided evidence of major HAB (dinoflagellate *Ceratium furca*) events in this sea. The HABs affected an area of up to 8,000 km<sup>2</sup> and caused the largest recorded economic loss in fisheries by killing fish and devastating aquaculture. The Bohai Sea is relatively shallow with an average depth of 20 m; the deepest part is in the Bohai Strait where the depth reaches 70 m. Four large rivers carry industrial and domestic wastewater from several large cities in China into the Bohai Sea.

Bohai coastal waters are reported to be subjected to moderate eutrophication throughout the year, but in the northern part of the sea waters prove to be more eutrophied during summer, the season when HABs mostly occur there. Seasonal water stratification begins in April and breaks down at the end of September. Ocean circulation in the Bohai Sea is controlled by tide, wind, and baroclinity forcing factors that are subject to temporal and spatial variations.

SeaWiFS images were processed with the OC4 algorithm and complemented with AVHRR and QuikScat data to map SST and wind vector variations, respectively. The multi-sensor satellite data jointly with hydrographic observations revealed that stable and high SSTs in combination with strong stratification is one of the driving mechanisms of HAB initiation in this area, because the high level of nutrients are predominantly available there throughout the phytoplankton growth season.

SeaWiFS data showed that the algal bloom occupied a large area extending from the west to the east coast of the Bohai Sea and lasted more than one month. SST and hydrographic data strongly indicate that the frontal zone between the Yellow River discharge and oceanic water provides suitable conditions for HAB events. Because coastal waters in the Bohai Sea are discolored not only by algae, but also significantly by the suspended matter and dissolved organics brought in with waters from the Yellow River and other rivers, confident identification of *chl*-rich/HAB areas in

the coastal zone is often very difficult, but becomes easier as the HAB occurs further offshore.

#### 4.1.5 Vietnam coastal waters

Under some particularly favorable hydro-optically conditions, the mixed colored agent problem does not interfere even when using case I water algorithms (as exemplified by Tang *et al.*, 2004). Based on SeaWiFS data processed with the four-band ocean color algorithm ([Table 3.4](#)), Tang and co-workers investigated an extensive HAB off southern Vietnam during June to July 2002, which is believed to be the most extensive and serious HAB event recorded in Vietnam to that date—it affected up to 90% of marine ecosystem conditions at the time.

Although highly nutrient-rich Southern Vietnamese waters are transported by currents to the western South China Sea, where the algal bloom occurred, coastal nutrients become rapidly diluted there and it is unlikely that they could cause such an event. Hydrographic studies have shown that the HAB (dominated by the flagellate haptophyte *Phaeocystis* cf. *globosa*) was induced and supported by offshore upwelling that brings nutrients from the deep ocean to the surface.

To support their study, Tang *et al.* also exploited contemporaneous data from AVHRR (to retrieve SST) and QuikScat (to retrieve surface wind speed and direction), as well as *in situ* ship observations. The HAB was flagged and evaluated through the retrieved *chl* concentrations based on ocean color data. Starting their remote-sensing survey in May ( $C_{chl}$  were less than  $0.1 \text{ mg/m}^3$ ), Tang *et al.* detected the initiation of the HAB in early June ( $C_{chl}$  were  $>4.5 \text{ mg/m}^3$ ) about 200 km northwest of the Mekong River mouth. The bloom appeared as a belt measuring 50 km in width by 200 km in length. The bloom area continued to expand in late July lasting nearly six weeks before its decay in September.

One of the reasons for successful application of SeaWiFS data processed with a standard case I algorithm in coastal waters resides in the fact that the study area featured a steep near-coastal continental shelf facing the open ocean where the influence of suspended matter and dissolved organics was relatively limited.

#### 4.1.6 Moreton Bay, Australia

In Australia, large-scale blooms of a toxic filamentous cyanobacteria *Lyngbya majuscula* have become common since 1997 (e.g., Roelfsema *et al.*, 2006). Interestingly, *L. majuscula* is normally found attached to seagrass, algae, and corals, but can rise to the surface by the accumulation of gas bubbles (Albert *et al.*, 2005). Roelfsema *et al.* (2006) investigated *L. majuscula* blooms in Moreton Bay waters (south-east Queensland) making use of Landsat 7 ETM+ data.

Extensive ship-based field survey data were acquired to provide the basis for a supervised classification of the ETM+ image data to map *L. majuscula* occurrence. The satellite-based mapping provided a total areal coverage with 58% accuracy, in contrast to the ship-based survey covering only 0.5% of the area albeit with much higher measurement accuracy of the limited number of taken samples. In most cases,

the bloom areas were not exclusively *L. majuscula* and consisted of up to 1 m thick patches.

A library of spectral signatures of *L. majuscula* and non-*L. majuscula* (seagrass, coral, mud, sand) substrate species has been developed, and a radiative transfer model (Hydrolight 4.1) was used to account for the effects of a water column of variable depth.

Based on field spectrometer analysis results, the blue, green, and red spectral bands of the Landsat 7 ETM+ image were used to classify the image and to generate the substrate cover maps.

The determined spectral signatures of *L. majuscula* proved to be only slightly different from seagrass *Halophila spinulosa* and *Hydroclathrus clathratus* for the blue band and from *H. spinulosa* in the green and red bands. Understandably, with increasing bottom depth, the discriminating ability of this approach rapidly worsens, becoming the source of the inaccuracies specified above.

As seen, this type of approach is rather an assessment of *potential* areas of HAB rather than mapping the actual bloom event. Its application is restricted to coastal zones with highly clear waters, in which the light signal coming out from beneath the water-air interface carries information about bottom spectral reflectivity features.

As indicated in Section 3.3, phycocyanin is the pigment that is primarily present in cyanobacteria. Dekker (1993) has shown that it is possible to estimate the concentration of this pigment in water using remote-sensing methods. Unlike *in vitro*, the absorption peak of this accessory pigment *in vivo* lies at about 630 nm (as found for Dutch lakes studied by Dekker).

If the concentration of cyanobacteria is sufficiently high (i.e., the concentration of  $C_{chl}$  is at least 8–10 mg/m<sup>3</sup>), then the phycocyanin absorption feature in the reflectance spectra near 630 nm and a small peak near 650 nm can be used to recognize the predominance of cyanobacteria in the targeted water. The MODIS bands do not provide the required information from this spectral region ([Table 4.1](#)).

#### 4.1.7 The Gulf of Finland

A more discriminative approach for detection of cyanobacteria is suggested by Kutser and Vahtmäe (2006) using MERIS, whose band configuration is more appropriate for turbid waters (e.g., waters with strong blooms) and bands 615–625 and 660–670 nm can be used for identification of cyanobacteria.

In addition, because cyanobacteria are capable of regulating their buoyancy and under calm weather conditions tend to form subsurface accumulations and surface scum instead of being uniformly mixed in the upper water column (Section 3.2), MERIS bands around 681.3 and 705 nm can be very useful for discrimination of cyanobacteria. Indeed, under calm weather conditions, cyanobacteria impart to the water surface the reflection features characteristic of green vegetation with a strong reflectance in the red part of the spectrum (Pozdnyakov and Grassl, 2003; Kutser, 2004; Gower *et al.*, 2005; Kutser *et al.*, 2006). In this case, however, no light with a wavelength beyond 750 nm comes up from beneath the water surface. Therefore, the

**Table 4.1.** Comparison of the spectral band locations of the MODIS and MERIS sensors in the visible and near-infrared spectral ranges, including an indication of their primary applications.

<i>Wavelength (nm)</i>		<i>Primary application</i>
<i>MODIS</i>	<i>MERIS</i>	
405–420	407.5–417.5	Yellow substance and detrital pigments
438–448	437.5–447.5	Chlorophyll absorption maximum
459–479		Land/Clouds/Aerosols properties
483–493	485–495	Chlorophyll and other pigments
	505–515	Turbidity, suspended sediment, red tides
526–536		Biogeochemistry
545–565 546–556	555–565	Land/Clouds/Aerosols Chlorophyll absorption, suspended sediment
	615–625	Suspended sediment
620–670 662–672	660–670	Land/Clouds/Aerosols boundaries Chlorophyll absorption, fluorescence reference
673–683	678–684.5	Chlorophyll fluorescence peak
	703.75–713.75	Atmospheric correction, red edge, fluorescence reference
743–753	750–757.5	Oxygen absorption reference, cloud, vegetation
	758.75–762.5	Oxygen absorption R-branch
	771.25–786.25	Aerosols, vegetation
862–877	855–875	Aerosols corrections over ocean
890–920	875–895 890–910	Atmospheric water vapor absorption reference, vegetation Water vapor
931–941		Atmospheric water vapor
915–965		Atmospheric water vapor

reflectance data from MERIS bands 620 nm and 665 nm, or 681.3 nm and 705 nm can be used to identify the cyanobacteria bloom.

Utilizing the spectral bands in the red part of the spectrum is of particular importance. Cyanobacteria infrequently form scum on water surfaces under calm weather conditions. Scum is conducive to high reflectance in the red and near

infrared. That is why none of the standard atmospheric correction procedures of satellite optical data from all contemporary sensors are optimal or adequate. However, application of the red band does at least allow the scum areas to be flagged, which is important information in its own right. This issue will be returned to in Section 4.1.10.

This approach has been exploited by Kutser and Vahtmäe (2006) in processing MERIS images over the Gulf of Finland, known for its typically case II waters. Since the application of the MERIS standard (case I) bio-optical algorithm failed to produce reasonable results for such optically complex waters, Kutser and Vahtmäe used their analytical algorithm based on the above considerations. Although the developed algorithm is not appropriate for determination of cyanobacteria concentration, it provides a practical tool of discrimination between cyanobacterial and non-cyanobacterial algal communities in the Baltic Sea (i.e., for classification purposes and delineation of the HAB extension area).

The applied approach resulted in a complex and visually incoherent mosaic pattern of pixels ascribed by the algorithm to areas accommodating cyanobacteria. The reason for such a complex pattern evidently resides in the fact that the algal composition in the targeted area was mixed. Although the cyanobacterium *Nodularia spumigena* was the predominant species, it coexisted along with other summertime species whose share varied across the Gulf of Finland. Through analysis of the time series of images, the uncertainties in the algorithm applied for each image seem to be reduced and the spatial extent of the cyanobacteria bloom was more precisely delimited.

#### 4.1.8 Lake Erie, U.S.A./Canada

The Laurentian Great Lakes have experienced HABs of the cyanobacterium *Microcystis* somewhat regularly over recent decades. Phosphorus reduction strategies initiated as part of the Great Lakes Water Quality Agreement have been largely successful in the reduction of algal biomass and restoring lake water transparency. Notwithstanding these improvements, blooms of *Microcystis* have returned to Lake Erie, recurring each summer since 1995 (Raikow *et al.*, 2004). The return of *Microcystis* is thought to be caused by the spread of invasive zebra mussels throughout Lake Erie that selectively filter other algae but reject *Microcystis* sp.

A massive HAB event in Lake Erie in 1995 resulted in a variety of water quality problems. During September 1995 the bloom resembled a thick slick of grass-green “paint” that extended over the entire surface of the western basin. Vincent *et al.* (2004) employed LANDSAT TM (bands 450–520 nm, 520–600 nm, 630–690 nm, 760–900 nm, 1,550–1,750 nm, 2,080–2,350 nm) to develop a set of band ratio algorithms to specifically detect cyanobacterial blooms in Lake Erie based on the spectral signature produced by phycocyanin absorption at about 620 nm—see Section 3.6.1.2 and eqs. (3.26) and (3.27). The main thrust of the study was to assess the capability of LANDSAT TM data with six visible/reflective infrared spectral bands with about 30-meter spatial resolution to detect the early stage formation of cyanobacterial

blooms. LANDSAT TM data were processed and dark object subtraction (Vincent, 1997) was applied to each band to reduce the effects of atmospheric haze.

Importantly, the algorithms of Vincent and co-workers employ not only short-wavelength bands, but also bands in the red and infrared spectral regions, rendering the algorithm robust at detecting situations when HABs are present as scum areas. At the same time, the algorithm is only suited to detect cyanobacterial HABs and assess their density, but does not provide quantitative information on phytoplankton concentrations, although some indirect indication of this parameter (algal biomass) can be assessed to some extent from the water turbidity values (in nephelometric turbidity units, NTU) retrievable with the regression algorithm suggested by the same authors.

Thus, summarizing the experience gained from the above eight case studies, it is worth emphasizing that the use of satellite-derived  $C_{chl}$  abnormally high values as indices of potential HABs (see also Stumpf *et al.*, 2003 and the discussion in Section 4.3) is a species-nondiscriminative approach. The studies based upon standard bio-optical algorithms such as OC4 for SeaWiFS data are prone to large uncertainties due to the residual (unknown) optical impact of the atmosphere (i.e., residual errors in the atmospheric correction) and other than phytoplankton color-producing agents (suspended matter, dissolved organics, detritus, etc.) as well as bottom reflectivity in shallow waters. Moreover, this approach “overlooks” several types of HABs of high toxicity but of moderate to low  $C_{chl}$  concentrations. New approaches have been proposed based on *in situ* data to use backscattering/ $C_{chl}$  ratio or fluorescence/ $C_{chl}$  ratio to differentiate HABs from other blooms (see Hu *et al.*, 2005); however, operational application of these algorithms using satellite data still requires further research since most results are based on “case studies” with limited validity and number of algal species. Further, we consider several studies that were conducted through employing integrated HAB monitoring services (see Section 4.3).

#### 4.1.9 Norwegian coastal waters

In 1988 the Nansen Environmental and Remote Center in Bergen, Norway introduced the use of remote-sensing technologies in the monitoring and studies of HAB events in Norwegian coastal waters and Nordic Seas (Johannessen *et al.*, 1988). An integrated approach combining the applications of satellite monitoring, airborne surveillance, and numerical ocean model simulations, conjointly with shipborne *in situ* observations, were suggested in order to investigate a major HAB event that occurred in May–June 1988 (Dundas *et al.*, 1989; Johannessen *et al.*, 1989a, b). The alga *Chrysochromulina polylepis* (class Haptophyta) had a massive bloom during May–June starting in the Skagerrak–Kattegat area, causing significant public attention (see Preface), due to its devastating effect on coastal aquaculture and the killing of caged fish. Unexpected and unpredicted, this bloom started after the normal annual spring bloom of diatoms in the Skagerrak. Later, the *C. polylepis* bloom spread northwards with the Norwegian Coastal Current (NCC) along the western coast of Norway to about 60°N, causing damage in major parts of the ocean and coastal waters. This hemolytic and ichthyotoxic species caused the death of both wild

and caged aquaculture fish through clogging up their gills. It brought an approximately

U.S.\$5 million loss to the aquaculture industry along the southern and southwestern coast of Norway before precautions were taken and the bloom decayed naturally. *Ad hoc* monitoring and forecasting actions (e.g., Dundas *et al.*, 1989) were initiated and the development of the bloom was daily reported in all major news media and carefully monitored by the fisheries in order to guide and impose regulations on the aquaculture industry.

In spite of its high cell concentrations (up to 100 million cells per liter), the bloom was not easily observable at the surface because it had in many places a submerged maximum. The satellite observations regularly available in 1988 (i.e., the NOAA AVHRR data) combined with ship and airborne information indicated early that there was a close correlation between the algal front and the surface warm-water fronts resolved in the sea surface temperature (SST) distribution ([Figure 4.3](#)). The SST images were accordingly a valuable source of information to delineate the extension and meso-scale meanders in the Norwegian Coastal Current or the boundary between the coastal and off-shore oceanic waters. The spread and advection of the algal bloom was thus indirectly monitored using satellite thermal infrared (TIR) SST data and visually observed from airborne reconnaissance. To forecast the daily proliferation and development of the bloom ([Figure 4.4](#)), numerical model simulations by a two-layer quasi-geostrophic ocean circulation model with a grid scale of 5 km (Ikeda *et al.*, 1989) was exploited and assessed ([Figure 4.5](#)). Based on the forecasts, on the west coast of Norway some 200 aquaculture farms, containing fish with a value of approximately U.S.\$200 million, were evacuated prior to the bloom invasion at their locations. Thus, such a loss was avoided by towing the cages with fish (see the book cover photo) into brackish water where the bloom did not develop and no fish died.

The lessons learned from this pioneering *ad hoc* integrated monitoring and forecasting activities, triggered by a really massive HAB event, have further led to the development of an international, interdisciplinary and inter-institutional research strategy for the development of an integrated monitoring and forecasting system exploiting satellite remote sensing, *in situ* (ship and shore-based) observations, and numerical ocean modeling to be used for early detection and monitoring of HAB events in coastal (Norwegian and Nordic) waters. The Nansen Center has pursued and developed this research approach in cooperation with national and international research partners since the late 1980s.

Since 1998, when ocean color satellite data became regularly available, the Nansen Center has regularly performed Earth observation (EO) monitoring for research and application purposes of the North Sea, Skagerrak, and southern Norwegian coastal waters making these publicly available through <http://HAB.nersc.no/> The geographical areas of interest have gradually been extended to include geographical areas outside the Norwegian sphere of influence as well.

Research activity is aimed at developing methods to improve the capability to detect at an early stage and classify potential harmful algal blooms along with their

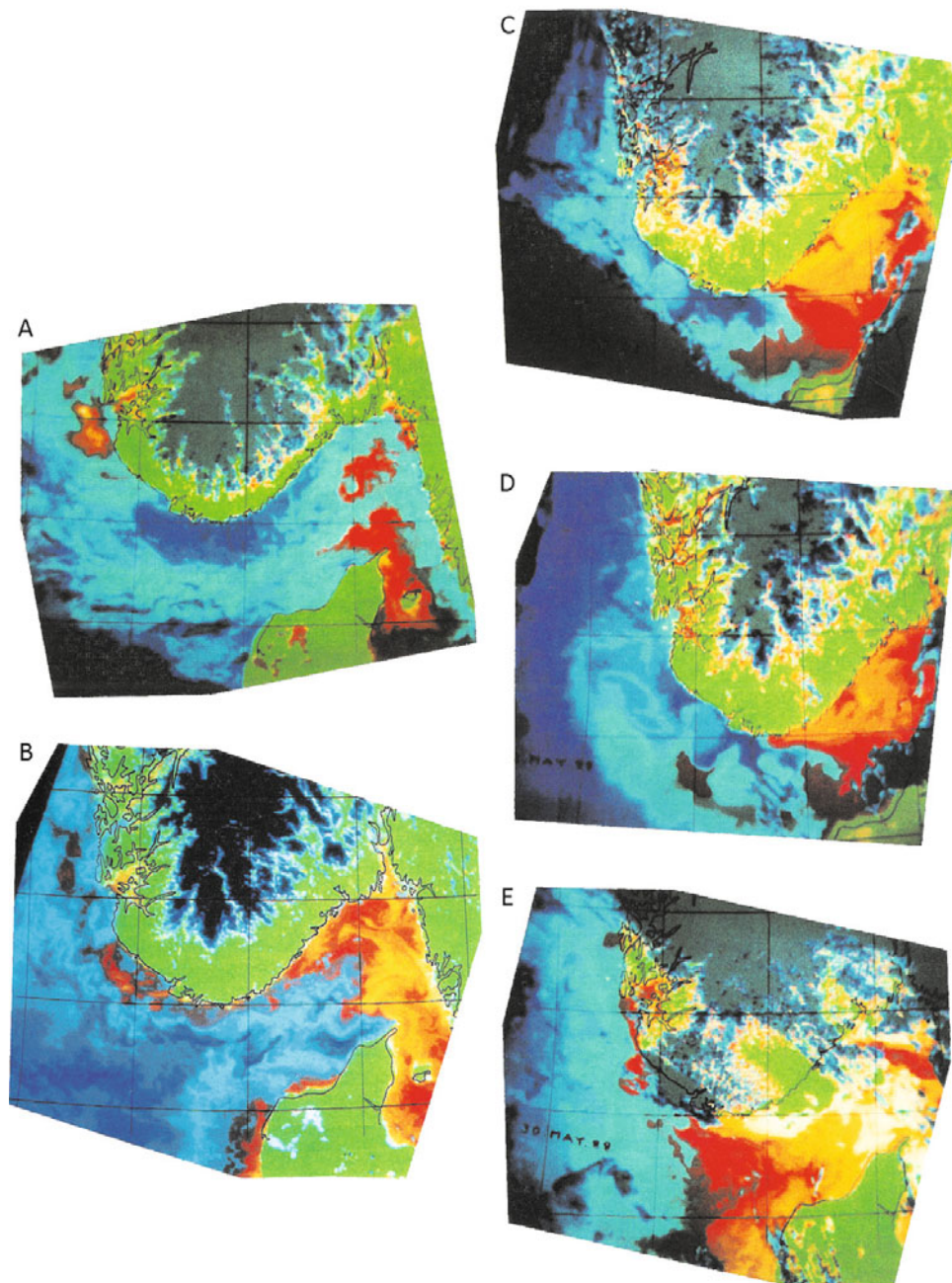


**Figure 4.3.** Evolution of sea surface temperature fields (color-coded, red = warm and blue = cold) for the North Sea based on NOAA AVHRR data from April 28 (A), May 15 (B), May 21 (C), May 22 (D), and May 30 (E), 1988 during an extensive *Chrysochromulina* bloom. Courtesy: Johannessen *et al.* (1989).

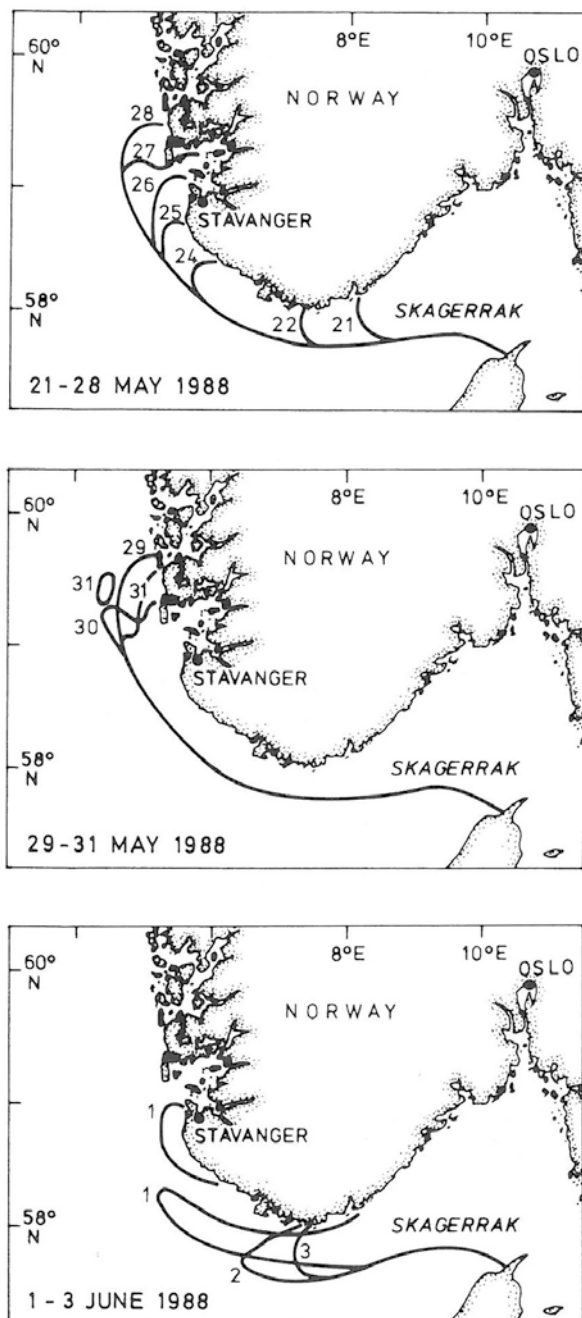


**Figure 4.4.** Summary of the observed algal front location during the *Chrysochromulina* bloom during its advance-and-retreat period (May 21 to June 3, 1988) in the Norwegian Coastal Current. Courtesy: Johannessen *et al.* (1989).

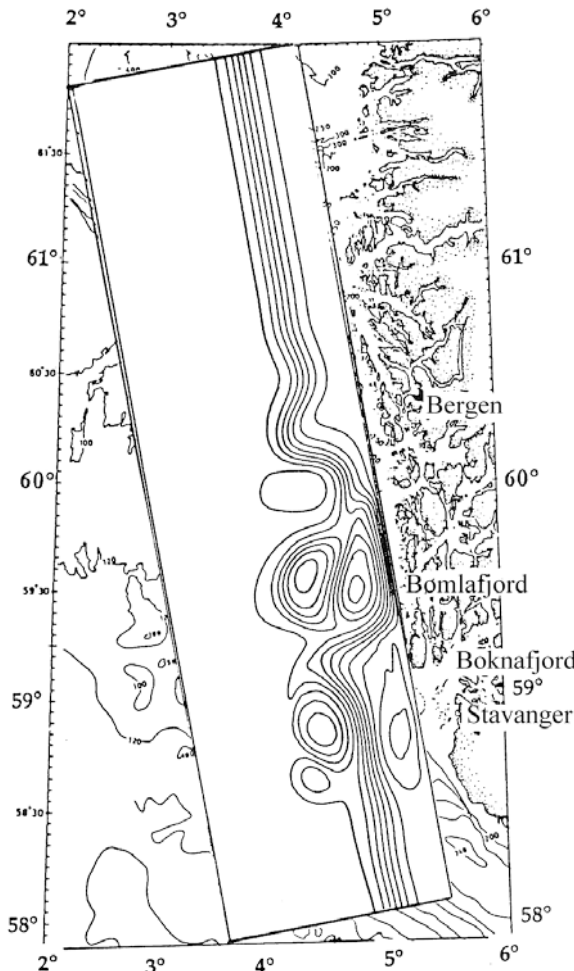


**Figure 4.5.** Modeled stream function in the upper layer predicted for June 1 during the *Chrysochromulina* bloom in 1988. Courtesy: Dundas *et al.* (1989).

concentration, distribution, further evolution, and decay. A major part of routine monitoring activity involves characterizing the dominant ocean circulation pattern and currents, such as frontal convergence and divergence, eddy development and rotation, occurrences of jet-like filaments, and influx of cold water from, for example, the Kattegat. While the advantage of synergistic use of ocean color and remotely sensed SST data for HAB monitoring has already been well documented within this activity (Section 4.2), the potential additional benefit of using satellite microwave radar (SAR) has hitherto not been systematically explored and documented for algal bloom monitoring (Pettersson *et al.*, 2000, 2001; Durand *et al.*, 2002). The research-based service has over the years provided information to

fishery and aquaculture authorities, industry, the general public, and the research community.

The Nansen Center furthered this research through implementation of a number of large-scale oceanographic and coastal experiments such as the NORCSEX'88 and '91 experiments (Johannessen *et al.*, 1991) and the COASTWATCH'95 experiments (Johannessen *et al.*, 1997; Haugan *et al.*, 1991), which exploited the integrated use of ship, satellite, and numerical ocean modeling for coastal ocean studies. During the NORSMAP'89 experiment (Pettersson, 1990; Pettersson *et al.*, 1991) the first use of airborne spectrometry in Norwegian waters was made, "paving" the way for the use of ocean color remote sensing. The area of research studies and regular monitoring extends beyond Norwegian territorial waters since outlying areas may exert an indirect impact on the Norwegian Coastal Current (NCC) though the prevailing ocean currents in the region—from the "upstream" North Sea and continental Europe to the "downstream" Barents Sea. The research-driven service concept can now be found in several other locations worldwide; there is one that covers Central American waters and another for the Venetian Lagoon, to mention a couple (Figure 4.6 and see <http://HAB.nerc.no>).

#### 4.1.9.1 *Pseudochattonella* blooms in Norwegian coastal waters

Throughout Section 4.1 we discuss the feasibility of using satellite information from sensors operating in different spectral regions with the emphasis on ocean color data, while the exploitation of synergy between different EO sensors is specifically addressed in Section 4.2.

Seasonal phytoplankton bloom cycles are monitored daily in order to identify potentially massive or harmful blooms. The data provide a useful tool to study the natural seasonal bloom cycles of major phytoplankton genera and their inter-annual temporal and spatial variations, however the primary focus has been the early identification and monitoring of extreme bloom events causing damage to the aquaculture industry (i.e., the duration of the extensive blooms of various alga species). Between early and late spring the bloom-forming ichthyotoxic *Pseudochattonella* sp. forms such massive blooms in northern European waters (see Section 2.4).

Initially, the first massive *Pseudochattonella* sp. bloom that occurred in North European waters in 1998 and in some subsequent years was falsely classified as *Chattonella* sp. (Hara *et al.*, 1994), due to difficulties in species identification using a light microscope. Riisberg and Edvardsen (2008) determined through genetic and DNA studies that the correct classification should be *Pseudochattonella verruculosa* and that the population had been homogeneous and stable in the Skagerrak waters during several years. Throughout this book we have accordingly used *Pseudochattonella* sp. although the original studies used *Chattonella* sp.

Five cases of massive blooms of *Pseudochattonella verruculosa* (Table 4.2) are addressed below, the bloom situations varying in both time of observations as well as oceanographic and meteorological conditions. Days/areas in which there were cloud-free conditions over the bloom areas have been identified in SeaWiFS and AVHRR satellite EO data. Since cloudiness is the major limiting factor for using ocean color

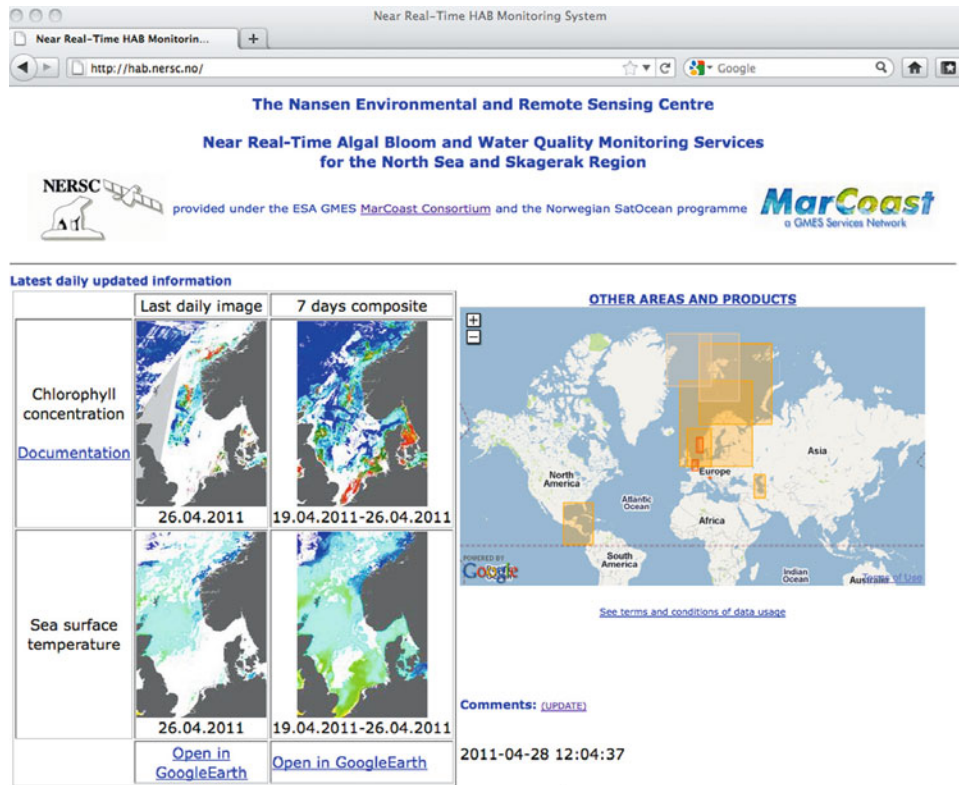


**Figure 4.6.** The web page of the NERSC service providing near-real time access to satellite-based EO data products for monitoring of HAB events (<http://HAB.nerc.no>). The service is developed for Norwegian and North Sea waters and implemented for other geographical regions worldwide.

and infrared EO data for surface monitoring (Figure 4.7), composites of seven consecutive days have been generated. These temporally binned data may blur some of the peak bloom abundance information, but provide a more holistic view of the situation during blooms (Figure 4.8). To exploit possible synergies between various satellite EO data, ERS-2 SAR and RADARSAT ScanSAR (limited by the number of synoptic overlapping data that are available) have been investigated in an attempt to identify overlapping SAR mapping of high algal bloom areas and using them to investigate the potential capabilities of using different EO sensors to map high-biomass phytoplankton blooms. However, wind conditions during the acquisition of SAR images must be sufficiently calm (<10 m/s) to resolve ocean circulation-induced features accurately, so that current-induced surface roughness is not obscured by the wind-generated capillary waves at the surface. For wind speeds above 10 m/s, the wind-generated roughness fully dominates the ocean surface and the backscatter signature in the SAR data. The number of such synoptic matches of

**Table 4.2.** Overviews of HAB events (mainly *Pseudochattonella* sp. blooms) in and around the North Sea where multiple EO satellite sensor data have been studied to assess the algal bloom situation. Dates, acquisition time, and EO sensors available are indicated for each case. Each case is discussed below and illustrated in the respective figure.

Case #	Date	Time (UTC)	EO sensor (data type)	Figure #
I	May 13, 1998	05:51	RSAT ScanSAR	4.13
		12:41	SeaWiFS	4.10, 4.13
	May 14, 1998	11:48	SeaWiFS	4.10, 4.13
I B	May 15, 1998	12:32 12:30 10:33	SeaWiFS AVHRR SST ERS-2 SAR (5*PRI)	4.10–4.13 4.10, 4.13 4.12b, 4.13
II	May 3, 2000	—	ERS-2 SAR (LRI)	Not shown
	May 4, 2000	05:54	AVHRR SST	4.14, 4.15
		12:19	SeaWiFS	4.14, 4.15
		21:30	ERS-2 SAR (LRI)	4.14, 4.15
	May 5, 2000	04:42	AVHRR SST	4.15
II B	May 12, 2000	06:00 11:34 14:55	RSAT ScanSAR SeaWiFS AVHRR SST	4.18 4.18 4.18
III	March 27, 2001	11:43 10:27	SeaWiFS ERS-2 SAR (4*PRI)	4.19, 4.20 4.19, 4.20
IV	May 8, 2001	21:33	ERS-2 SAR (5*PRI)	4.22
	May 9, 2001	06:18	AVHRR SST	4.22
		12:51	SeaWiFS	4.22
IV B	May 15, 2001	12:13 21:13	SeaWiFS ERS-2 SAR (PRI)	Not shown Not shown

data is very limited; some of the high-quality data are summarized in [Table 4.2](#) and will be discussed further below.

Routines to automatically download and process different EO data have been implemented in order to facilitate access to and evaluation of the applicability of satellite EO data for the identification and monitoring of algal blooms in coastal and offshore waters. In summary, such useful, high-quality, and overlapping near synoptic EO data during major algal bloom events (mainly requiring less than  $\pm 12$ -hour time difference between observations, which is very long for phenomena sensitive to wind variations) have been gathered for one to four days each year during the major bloom events in the 4-year period from 1998 to 2001 (Pettersson *et al.*, 2007).

Algal bloom events were regularly identified and monitored in processed *chl* concentration images based on SeaWiFS data, using standard processing tools and researcher-tailored regional algorithms (Korosov *et al.*, 2009). The *chl* concentration was estimated from the amount of algal pigments in the upper layer of the

## Early signs of the 2006 spring bloom—daily

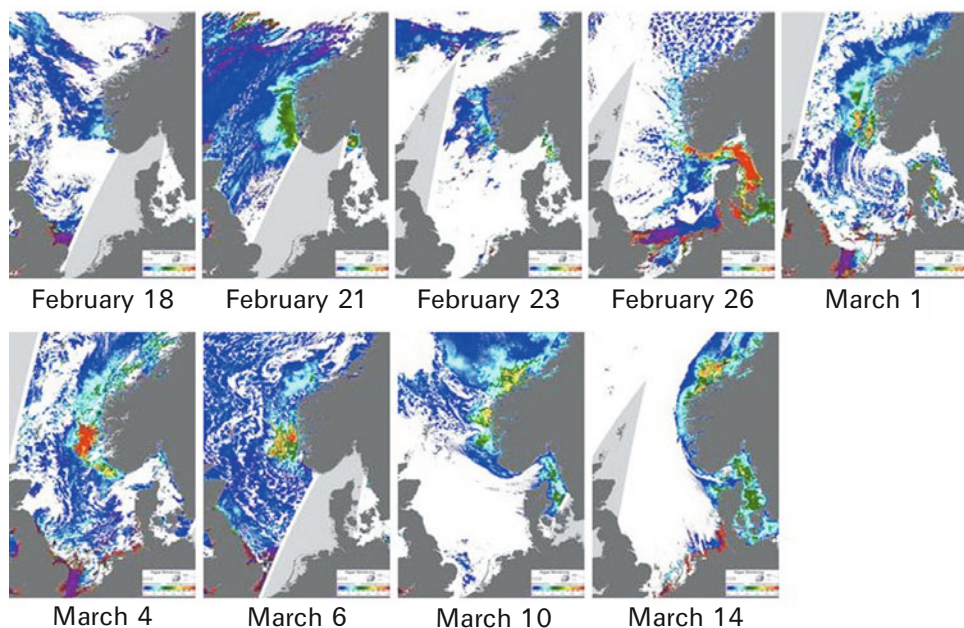


**Figure 4.7.** Daily images of the  $C_{chl}$  concentrations during the early spring bloom in 2006 in the North Sea and Norwegian Coastal Current. Source: <http://HAB.nerc.no>

## Early signs of the 2006 spring bloom—7 days

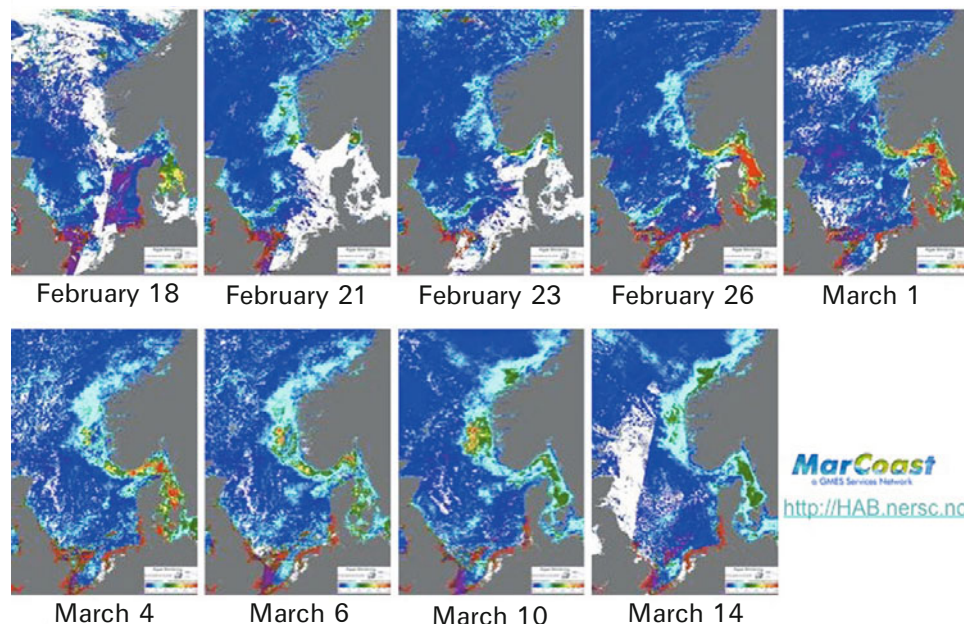


**Figure 4.8.** Seven-day composites of the  $C_{chl}$  concentrations during the early spring bloom in 2006 in the North Sea and Norwegian Coastal Current. Source: <http://HAB.nerc.no>

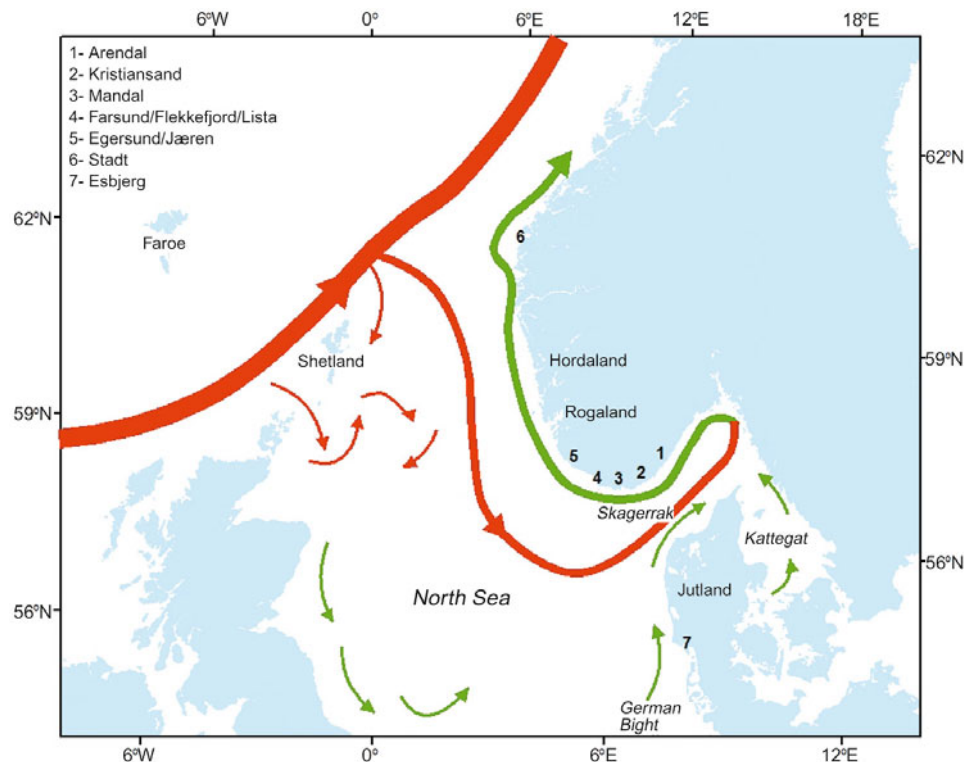
water column (depending on the transparency of the water). Hence, algal blooms with a high biomass near the surface are more visible or prominent in ocean color EO data than those with a subsurface peak concentration. Surface wind conditions, as discussed in the previous section, must also be taken into consideration in synergistic analysis of the environmental conditions, through using satellite radar (SAR) data to map the surface expression of, for example, biological films or surfactants on the ocean surface (see also Section 4.2 which addresses some case studies of synergetic use).

True-color composite images were generated and used to characterize the spectral water reflection (i.e., red–green–blue [RGB] composites of the reflectance at respectively 555, 490 and 412 nm). These data were used to improve the interpretation of the causes and variability in algal pigment concentration ( $C_{chl}$ ) products. In order to confirm and identify the algal bloom species, *in situ* sampling and observations were used, primarily made available through shore and shipborne observations performed by the Norwegian Institute of Marine Research (IMR) and the Norwegian Directorate of Fisheries (FD). Later, FerryBox ship measurements also became available from the Norwegian Institute for Water Research (NIVA)—<http://www.niva.no/> Despite uncertainty about the absolute accuracy of satellite EO data derived parameters, these data have shown themselves capable of providing useful information on the early detection of the initiation, development, locations, and gradients in algal bloom parameters. Accordingly, satellite EO-based information products have been made publicly available and distributed to aquaculture and fisheries authorities and industry in order to be used in combination with other information sources to detect and monitor algal bloom events in Norwegian coastal waters (<http://HAB.nerc.no>).

Simultaneously, SST data from NOAA AVHRR and MODIS sensors are used to characterize the physical (SST) properties of the water masses as well as current extent, meso-scale eddies, and gradients in the coastal current and further offshore, utilizing the fact that water masses of different origin have different surface temperature characteristics, depending on geographical location and season of the year. Through analysis of the difference between SST and the air temperature, the stability of the atmospheric boundary layer can be assessed.

By means of case studies, below we will illustrate the applications and interpretations of various EO data for studies of the marine phytoplankton distribution during specific HAB events in the North Sea and coastal Norwegian waters. In order to facilitate the use of place names, a map showing the locations mentioned is provided in [Figure 4.9](#). The information content in the various EO data sources will be discussed, compared, and assessed in conjunction with observations and, to some extent, marine ecosystem modeling (see Chapter 5).

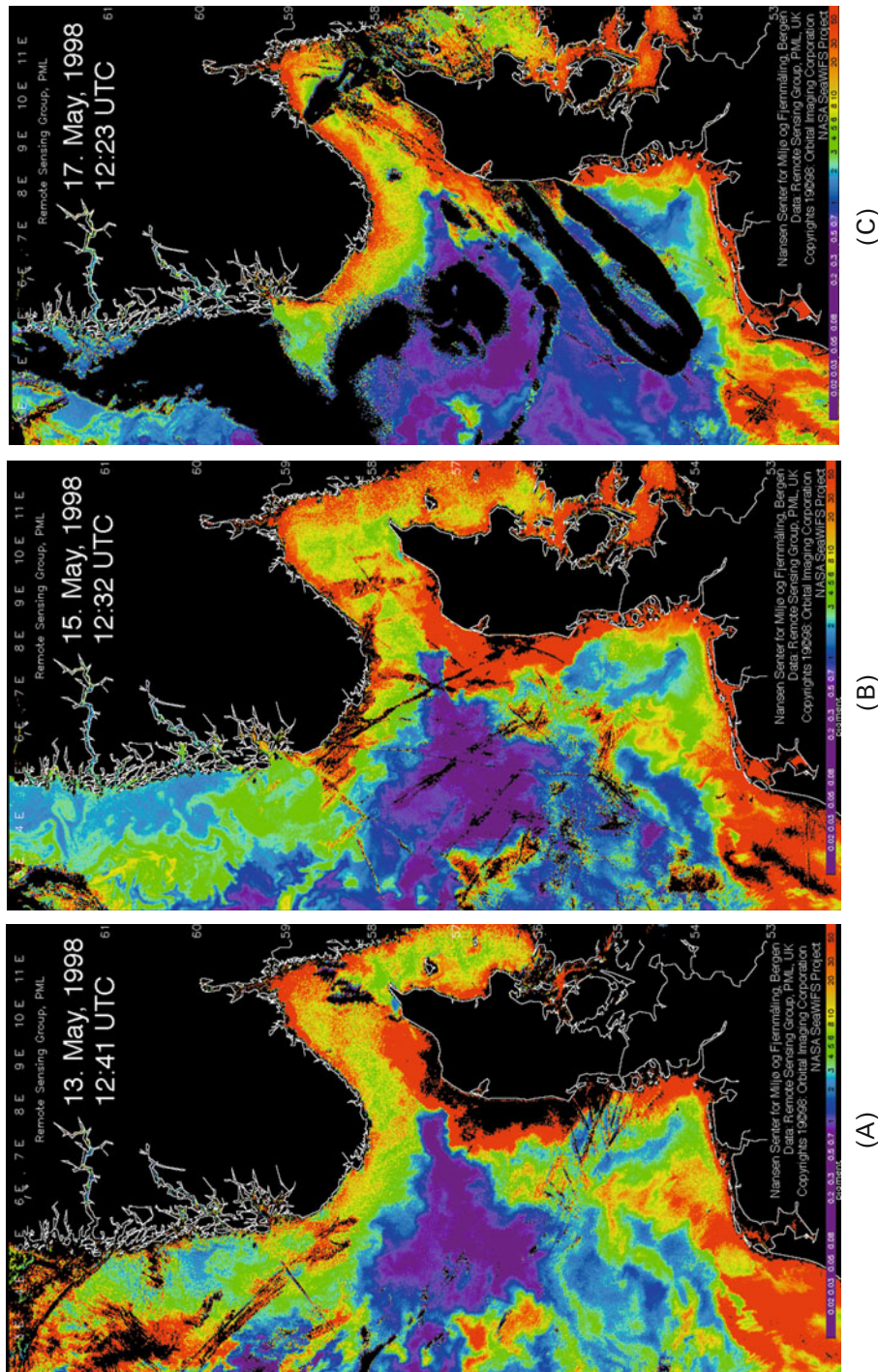
**Case I.** *Pseudochattonella* sp. bloom west of Jutland in May 1998. In early May 1998, a large HAB dominated by the flagellate *Pseudochattonella* aff. *verruculosa* caused mass mortality of fish, killing about 350 tons, representing a value of about €1 million, in numerous fish farms within the Farsund and Flekkefjord areas in southern Norway (Aure *et al.*, 2001). This was the first time a massive bloom of



**Figure 4.9.** Map of the key current circulation features in the North Sea (based on map from IMR). Water of Atlantic origin in red and coastal water in green. Names of the locations mentioned and discussed in this book are indicated.

*Pseudochattonella* was reported in European waters in such high concentrations. Most likely the species was introduced to these waters through ballast water. This flagellate species was later observed off the western coast of Sweden and later on, this HAB affected the entire water area of the Skagerrak (Figure 4.10), and finally high algal concentrations were reported along the west and northern coasts of Jutland causing large-scale death of wild species such as garfish, herring, and sand eel. High concentrations of *Pseudochattonella* in the Skagerrak waters and along the western coast of Jutland were found in the areas, which proved to be unusually enriched in nutrients during this time of the year. Together with favorable sunlight conditions, high levels of anthropogenic nitrate arriving from the southern part of the North Sea stimulated the observed extreme growth of the algal bloom.

The bloom had its maximum extension during mid May and culminated towards the last week of the month. Throughout this period, several high-quality SeaWiFS ocean color images were available for thorough analyses together with contemporaneous SAR and SST data from ERS and AVHRR. The Institute of Marine Research conducted their dedicated field investigations in Danish waters in this period with



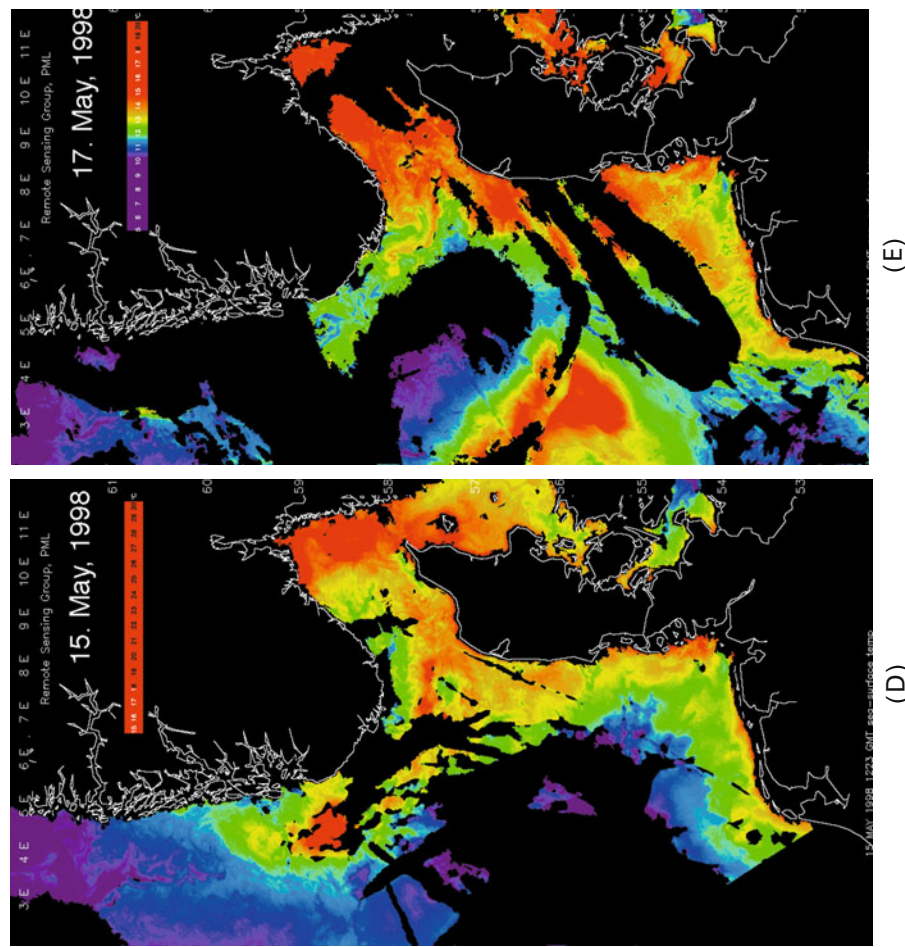
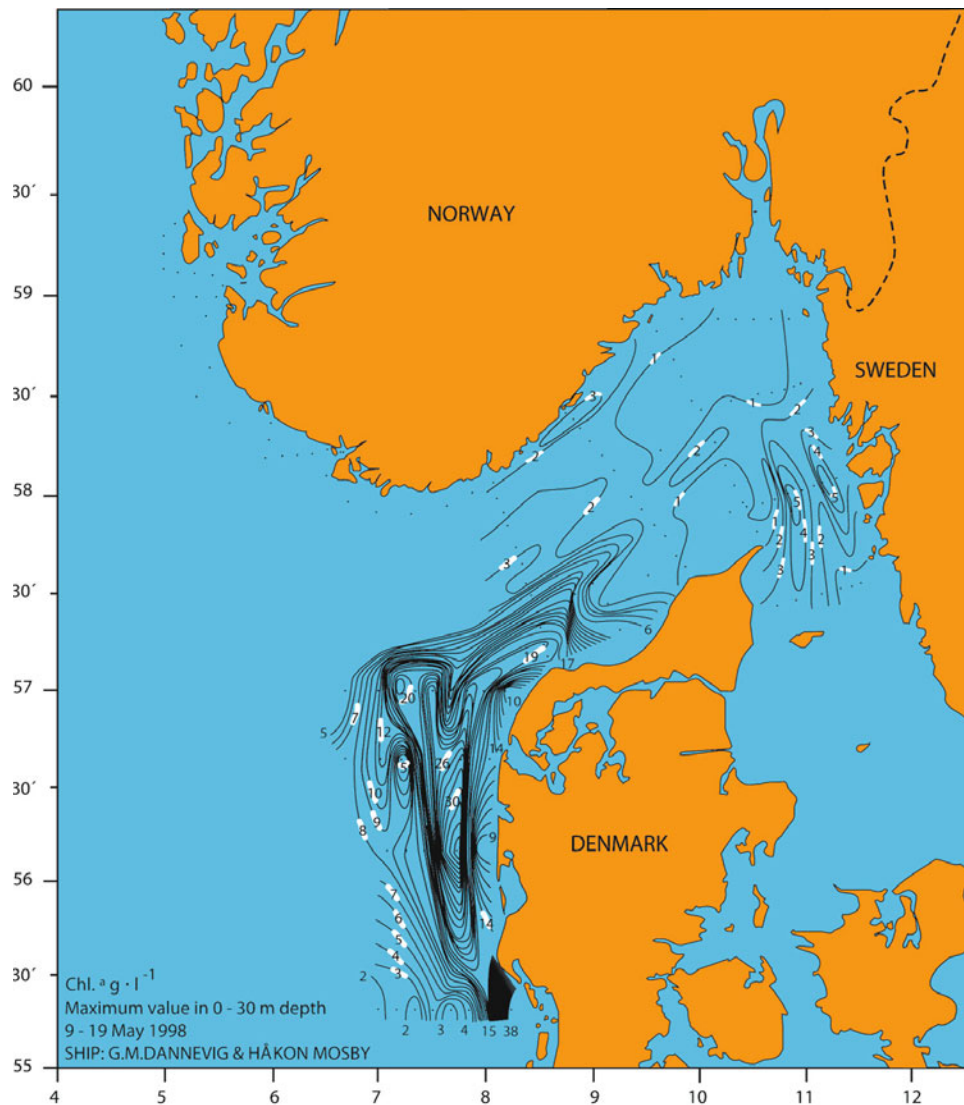


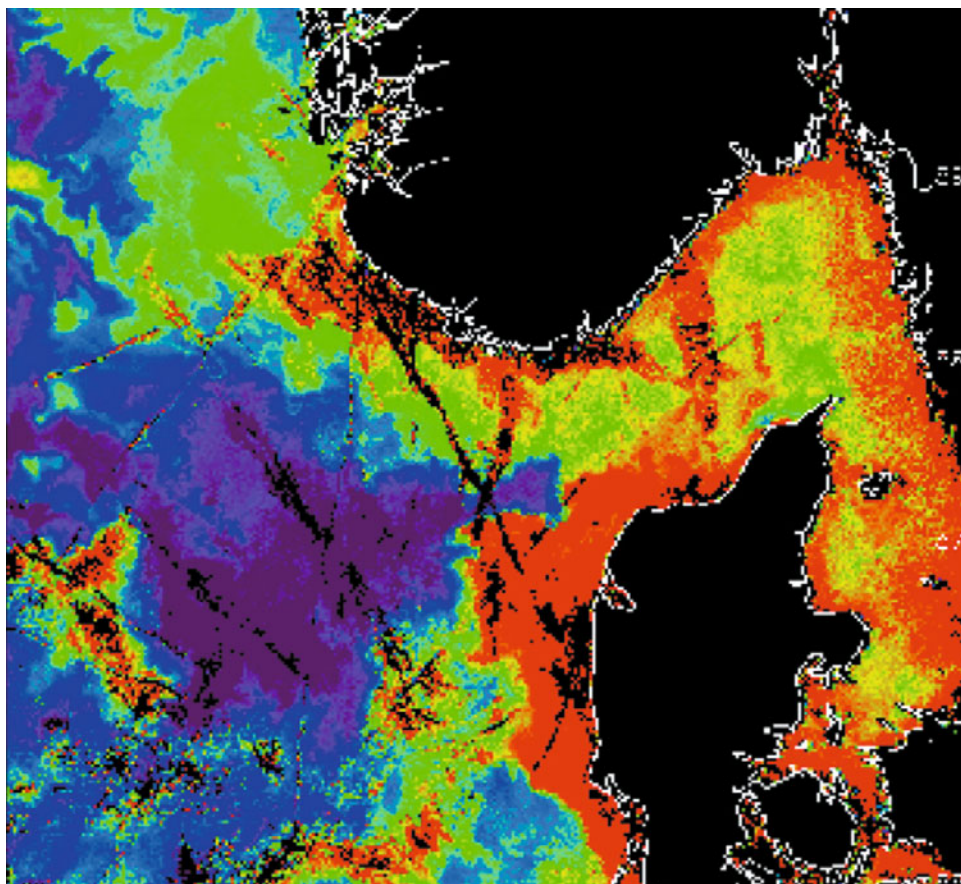
Figure 4.10. Sequence of three SeaWiFS images resolving *chl-a* concentration (A)–(C) and two sea surface temperature (SST) images (D), (E) during the *Pseudothettonella* bloom in May 1998. Courtesy: Steve Groom, PMEL.



**Figure 4.11.** (This page) Contour plot of the maximum *chl-a* values in 0 to 30-meter depth, based on data collected by R/V *Dannevig* and *Håkon Mosby* during the period May 9 to 19, 1998. Courtesy: IMR. (Facing page) Subsection of the SeaWiFS *chl-a* concentration image from May 15 (Figure 4.10B) resolving the instantaneous phytoplankton distribution in the same areas as mapped during 10 days by ship measurements.

two research vessels, and measurements of the hydrography and phytoplankton community were obtained in the period May 9 to 19 (Figure 4.11).

The AVHRR SST image of May 15 in the western Skagerrak was partly contaminated by clouds and aircraft contrails that obscured some of the surface



May 15, 1998

signal and gradients in the SST. For this specific HAB event, some additional ERS and Radarsat SAR data were employed in a synergistic analysis together with meteorological boundary layer information from ECMWF (Figures 4.12 and 4.13). Examination of the synoptic data obtained on May 17 supports the following interpretation.

The coastal water in the NCC was colder than the offshore Skagerrak water in the area south of Kristiansand. A tongue of warm water broke out through the central part of Skagerrak and extended west/northwestward up along the west coast of Jæren. The temperature of these water masses was close to that of the surface water in the central Skagerrak gyre. SeaWiFS ocean color data revealed an offshore decreasing gradient in *chl-a* concentrations (offshore *chl* concentrations constituted 20–50% of the respective coastal values). In the central Skagerrak, there was an inflow of colder and significantly less chlorophyll-rich water of Atlantic origin passing through the North Sea. The propagation of waters of Atlantic

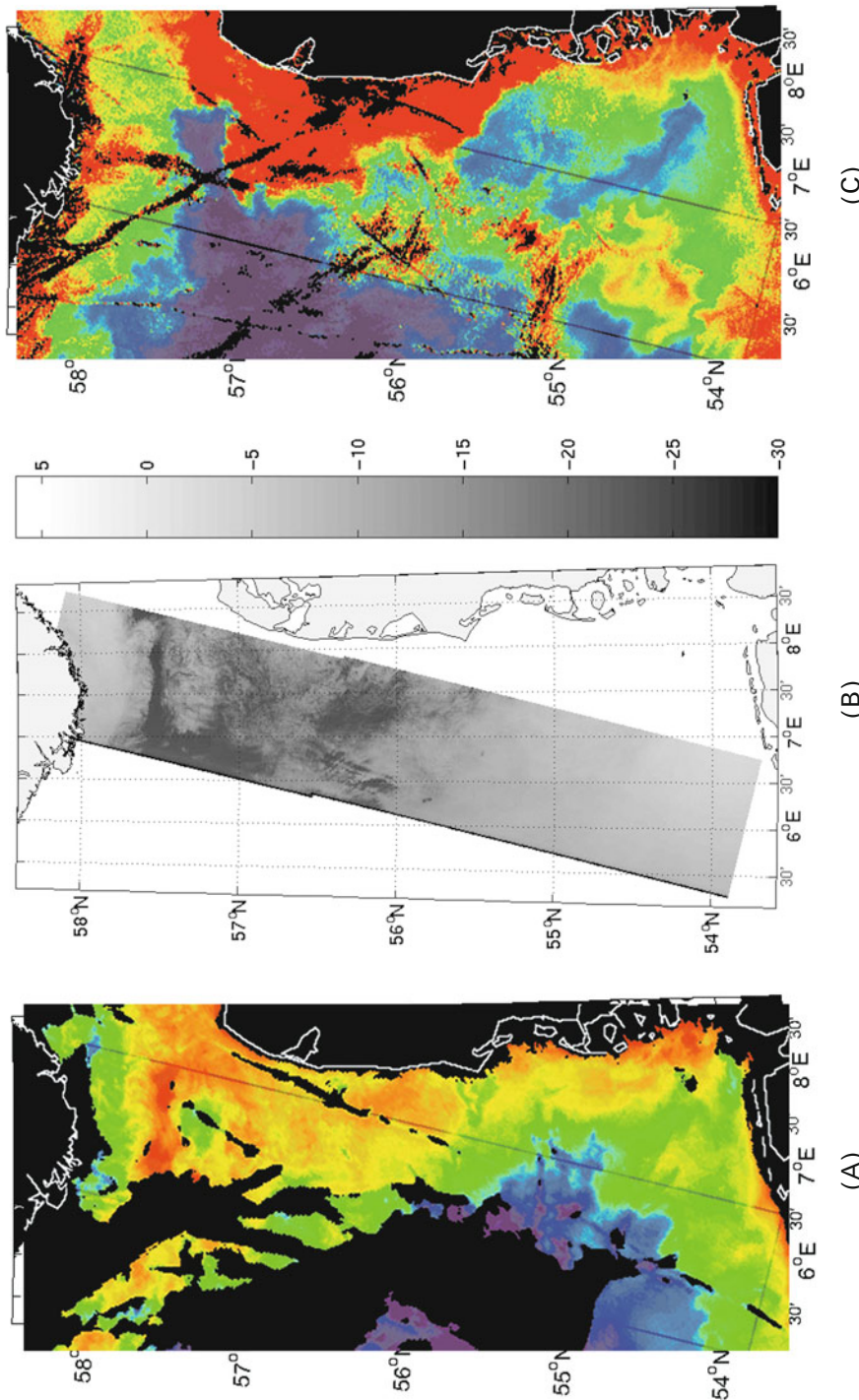
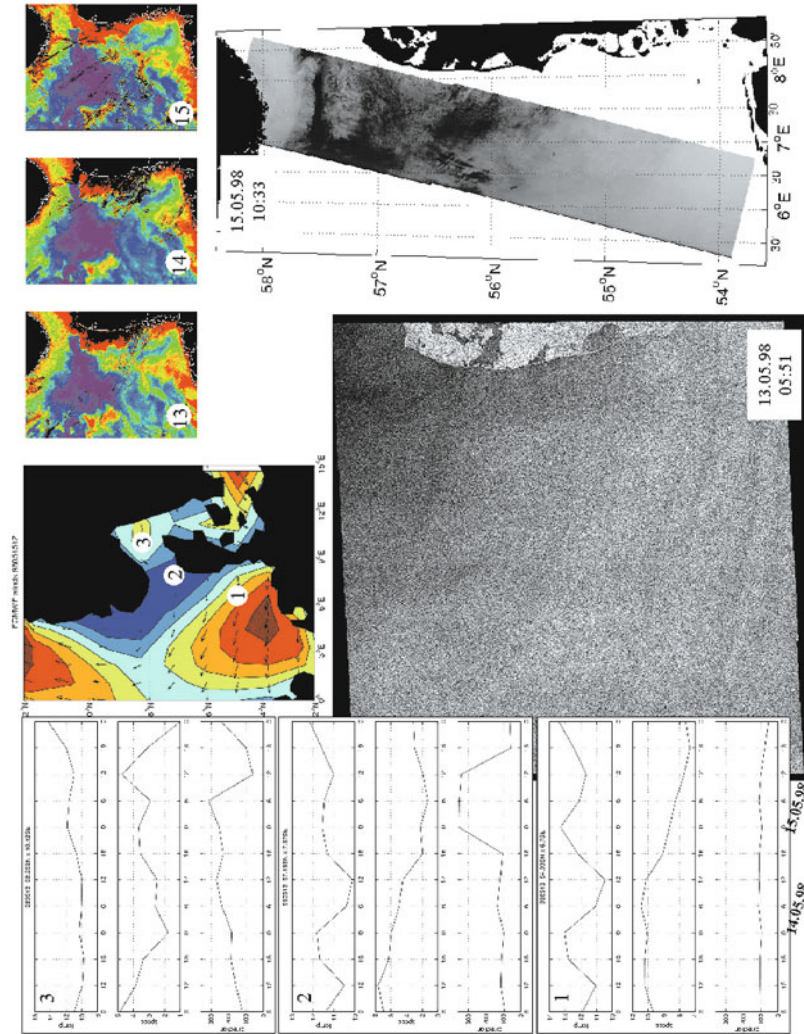


Figure 4.12. Near-synoptic coverage of the (A) AVHRR SST, (B) ERS SAR image, and (C) SeaWiFS *chl-a* distribution covering the western Skagerrak and Jutland Current on May 15, 1998.



**Figure 4.13.** (Upper right) SeaWiFS *chl-a* pigment data for May 13, 14, and 15 (same as shown in Figure 4.8), 1998. (Upper middle) Surface wind (from ECMWF) speed and direction are plotted for May 15 at noon. (Left) Plots of temperature, wind speed, and wind direction are obtained at locations 1–3 indicated in the contour plot of the wind field. The wind speed in this figure ranges from 0 to 7 m/s. Due to higher wind on May 13 (lower middle: the date of the Radarsat overflight) than on May 15 (the date of the ERS-2 overflight), more backscatter contrast is observed in the ERS-2 image (lower right).

origin through the North Sea was to a very large extent steered by the topographic features of the deep Norwegian Trench. Synergetic analyses indicate that SST and *chl* satellite-based data provide similar and complementary information on water mass distribution and their biological and geophysical conditions including the aforementioned ocean circulation pattern. The expression of this ocean circulation pattern is observable through significant contrasts in both *chl* concentrations and SST gradients inherent in the NCC.

On May 15, the air temperature (from ECMWF reanalysis data, [Figure 4.13](#)) was about 11°C in this area and the SST data from AVHRR proved to be about 1°C warmer ([Figure 4.10](#), two lower panels). The wind speed and atmospheric boundary layer stability (i.e., the temperature difference between the water surface and the air temperature) should therefore cause a rougher ocean surface that will result in higher radar backscatter along the Norwegian coast than that for the colder water mass present farther offshore. This supposition was expected as a result of turbulence created by less stable near-surface conditions and complies well with the surface signatures resolved in the ERS SAR image data of May 15. The current system in the area off Lista as mapped in the SST data of May 17 proved to be well confirmed by the model simulations for both May 15 and 17 using the Nansen Center HYCOM ocean circulation model, with an even more pronounced SST signature for May 17.

**Case II.** *Pseudochattonella bloom west of Esbjerg, Denmark, April–May 2000.* On April 18, 2000, a significant increase in *chl* concentration was detected in SeaWiFS imagery along the southwestern coast of Jutland (Pettersson *et al.*, 2000). The high concentration of algae observed from space was further confirmed two days later by measurements in the same region conducted by IMR from the R/V *G.M. Dannevig*. Most of the algal biomass in the region was due to phytoplankton of the class Raphidophyceae. In this class of algae, several harmful species are known (e.g., *Pseudochattonella*, *Fibrocapsa*, and *Heterosigma*; Section 3.2).

Very high concentrations of *Pseudochattonella* aff. *verruculosa* were observed west of Esbjerg on April 20. The further development and subsequent decay of the bloom were efficiently monitored using combined EO and *in situ* data. Due to the extent and rapid development of the algal bloom, the monitoring operation went into an alert mode, in accordance with the national contingency plan implemented by the Norwegian Directorate of Fisheries (FD).

During this period, satellite data were also used to initiate and update (using a simple scheme of data assimilation/re-initialization) respective model predictions of the bloom development, using the IMR research forecasting algae model (NORWECOM) (see Chapter 5). The clear benefits of using EO data were identified with respect to planning monitoring operations, the *in situ* data-sampling strategy, and to assessing model predictions of the algal bloom dynamics. Similar algal blooms of *Pseudochattonella* sp. and *Heterosigma* were observed in 1998 (Case I, discussed above) within the Jutland current, but also in Norwegian coastal waters (near Farsund and Flekkefjord).

Later during early May an intrusion of a narrow tongue of water with an enhanced *chl* concentration from the Jutland current into the central and northern

parts of Skagerrak was evident ([Figure 4.14](#)). These waters most likely accommodated *Pseudochattonella* species and could possibly be advected farther into Norwegian coastal waters. Some dedicated field investigations were initiated in order to evaluate this observation and analysis of these field data confirmed the above interpretation of the SeaWiFS satellite image. Fortunately, the bloom did not reach Norwegian coastal waters to become a threat to the numerous sites of fish farms along the coast.

On May 4, three EO data sources were acquired throughout the day ([Table 4.2](#)): SST data at 05:54 UTC (as well as at 04:42 the following morning—not shown here), SeaWiFS *chl* mapping at 12:19 UTC, and ERS SAR at 21:30 UTC ([Figure 4.14](#)). This implies that the spaceborne observations were not synoptic and the environmental conditions most likely changed during the time intervals between acquisitions of the different satellite sensors—underlining the practical challenges in synergetic applications of multiple satellite EO data. However, some distinct similarities in the oceanographic features and phenomenon revealed by different EO data sources have been established for the areas not covered by clouds.

In the German Bight and offshore southern Jutland, very high *chl* concentrations were observed in the SeaWiFS image and were further confirmed by *in situ* observations. In some areas, the SeaWiFS standard bio-optical algorithm yielded data saturation, which was interpreted as confirmation of exceedingly high *chl* concentrations in the study area ([Figures 4.14](#) and [4.15](#)), and also as deficiencies in the applied atmospheric correction method. The wind pattern ([Figure 4.16](#)) in this region changed significantly during the day. In the morning, the wind speed was 8 m/s whereas in the evening, during the ERS SAR overpass, the wind over the entire swath area was homogeneous and low (2–3 m/s). In some (but not all) of the *chl*-enhanced locations, a low radar backscatter signal in the ERS SAR image was also recorded. One possible explanation is that the reduced backscatter observed in the SAR image was due to a very high algal biomass generating surfactants in surface waters that damped out surface capillary waves ([Figure 4.17](#), areas C and D).

In the central part of SAR images (around 56°30'N, [Figure 4.15](#)), the radar backscatter roughness is more homogeneous and seems to be dominated by the wind blowing from Skagerrak (i.e., in the northeast direction). The wind signature in the SAR image over this region indicates somewhat higher winds than those reported in the ECMWF data.

In the northern part of the SAR image (57–58°N), closer to the Norwegian coast ([Figure 4.15](#)) the extension and meandering of the front of the NCC around Lista is identified in the SST images. The enhanced concentrations of *chl* (slightly less contrasting, but still clearly detectable) as well as a spatially coincident feature in the ERS SAR backscatter pattern together indicate the occurrence of current shear in that area (i.e., the offshore extension of the NCC).

Farther offshore, beyond the extent of the NCC and in a larger region across the SAR image covering central Skagerrak between Denmark and Norway ( $\approx$ 57°15'N), there are two areas of low-scatter SAR signals. These regions of low SAR signals/surface slicks did not correspond exactly with the areas of the highest *chl* concentration. One area of a low-backscatter signature in the SAR image proved to be co-

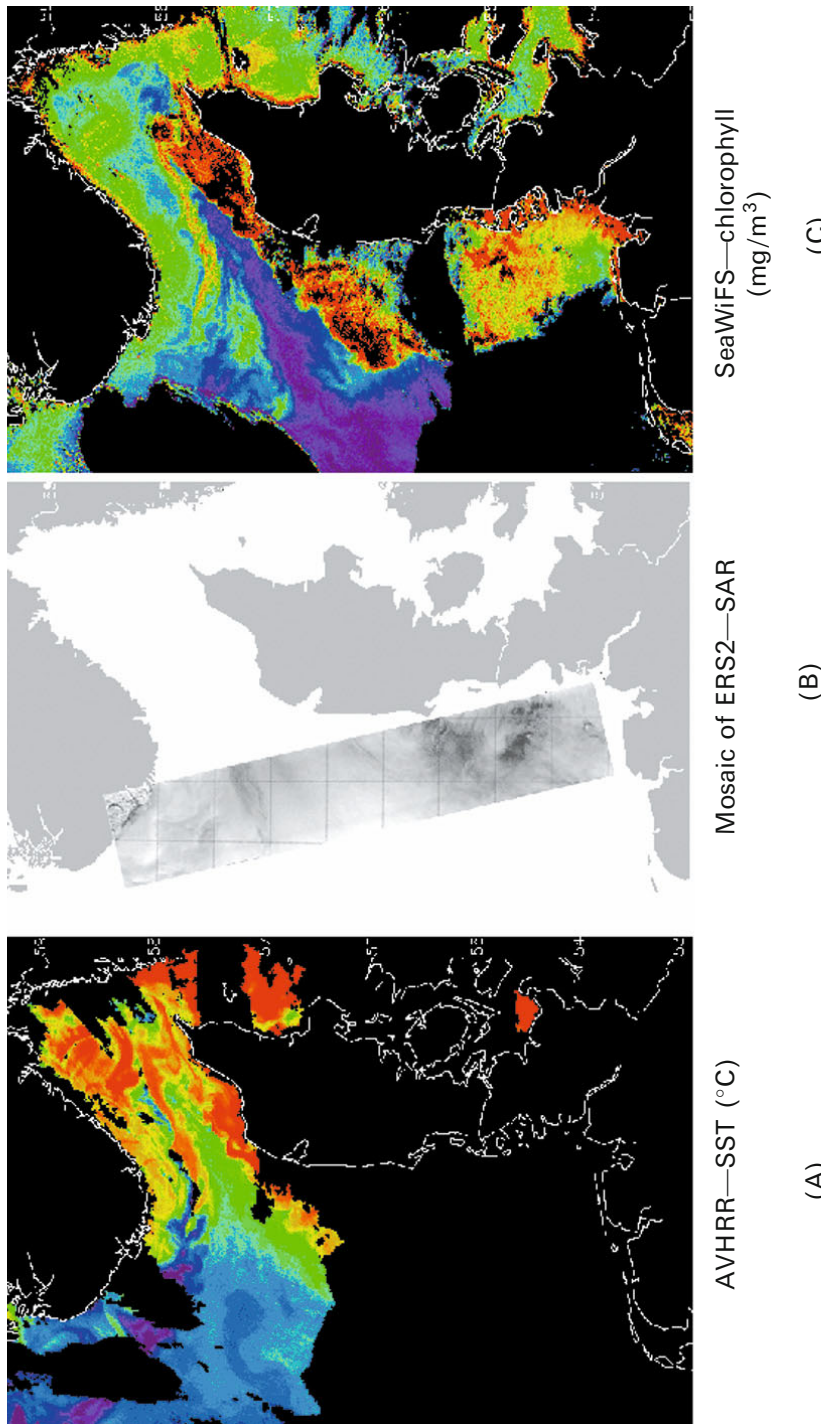
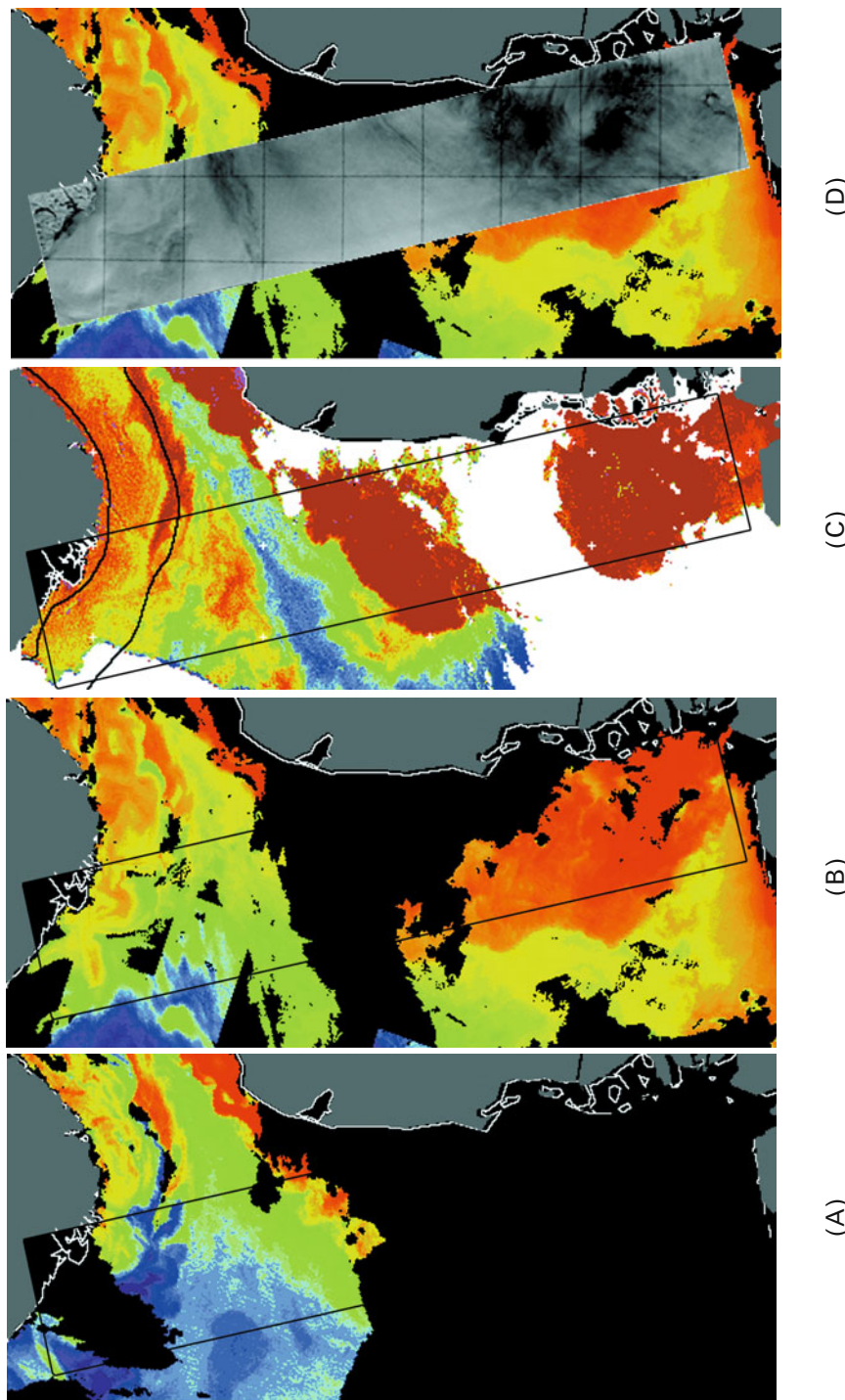
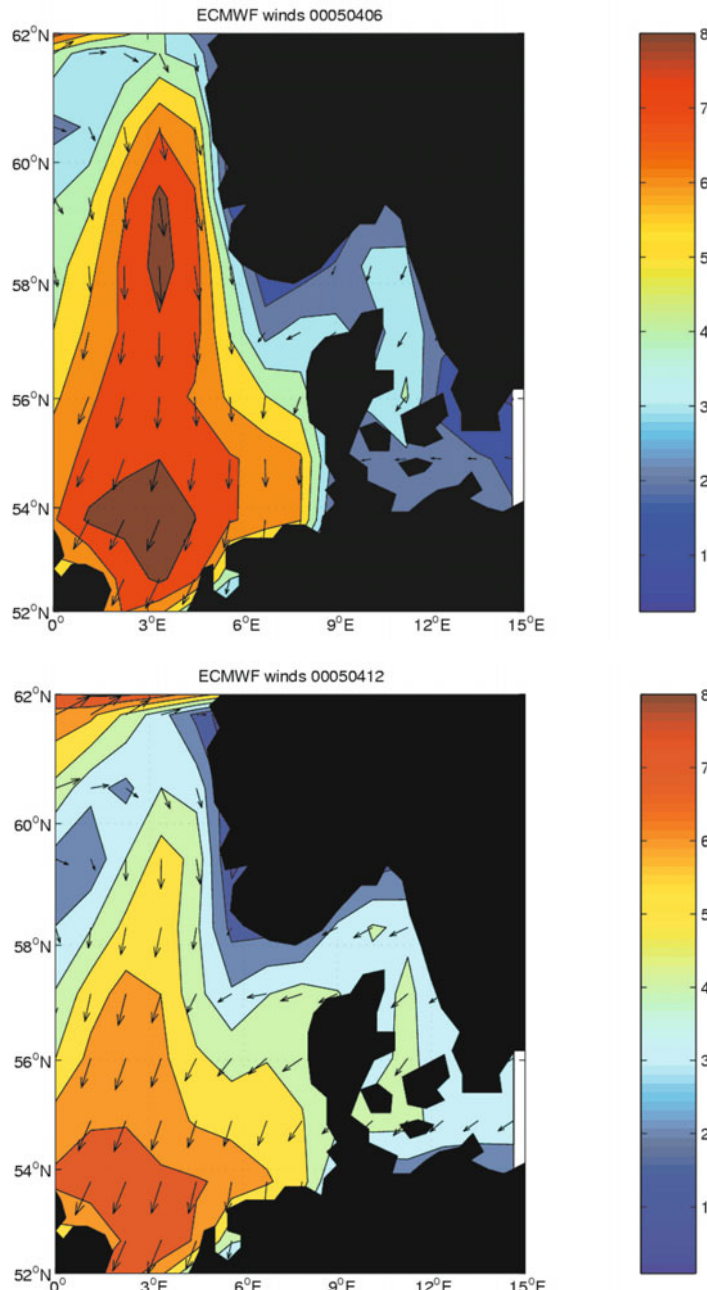


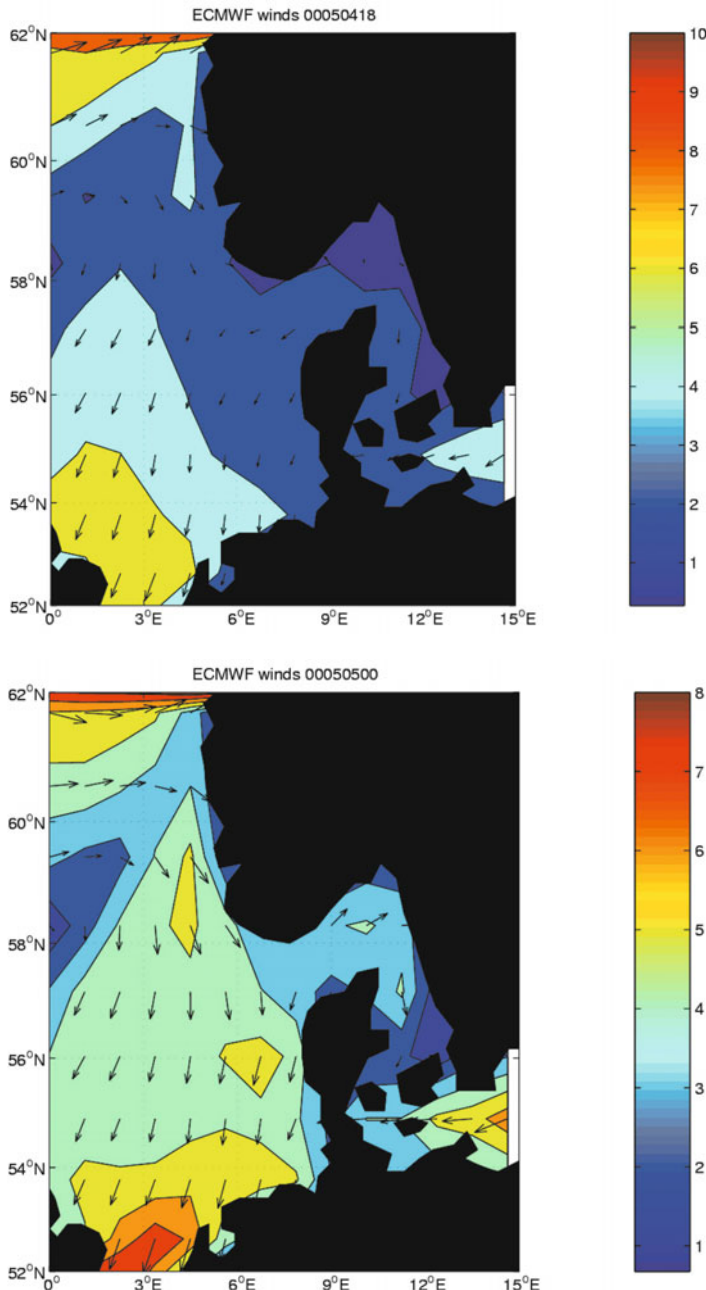
Figure 4.14. Near-synoptic coverage of (A) AVHRR SST ( $^{\circ}\text{C}$ ), (B) ERS-2 SAR backscatter, and (C) SeaWiFS *chl-a* concentration ( $\text{mg}/\text{m}^3$ ) on May 4, 2000 covering the Skagerrak region. The scales are the same as in Figure 4.10.



**Figure 4.15.** Extract from [Figure 4.12](#) focusing on the West Jutland current, showing the AVHRR SST ( $^{\circ}\text{C}$ ) at (A) 05:54 UTC, (B) 04:42 UTC, (C) SeaWiFS *chl-a* concentration ( $\text{mg}/\text{m}^3$ ) at 12:19 UTC, and (D) ERS-2 SAR backscatter at 21:30 UTC on May 5, 2000.



**Figure 4.16.** Reanalysis wind fields (from ECMWF) during May 4, 2000 at, respectively, 06:00, 12:00, 18:00, 24:00 UTC (notice the different color scales for the wind speed). The data resolve the large diurnal variation in the surface winds, imposing strict requirements on simultaneous observations.



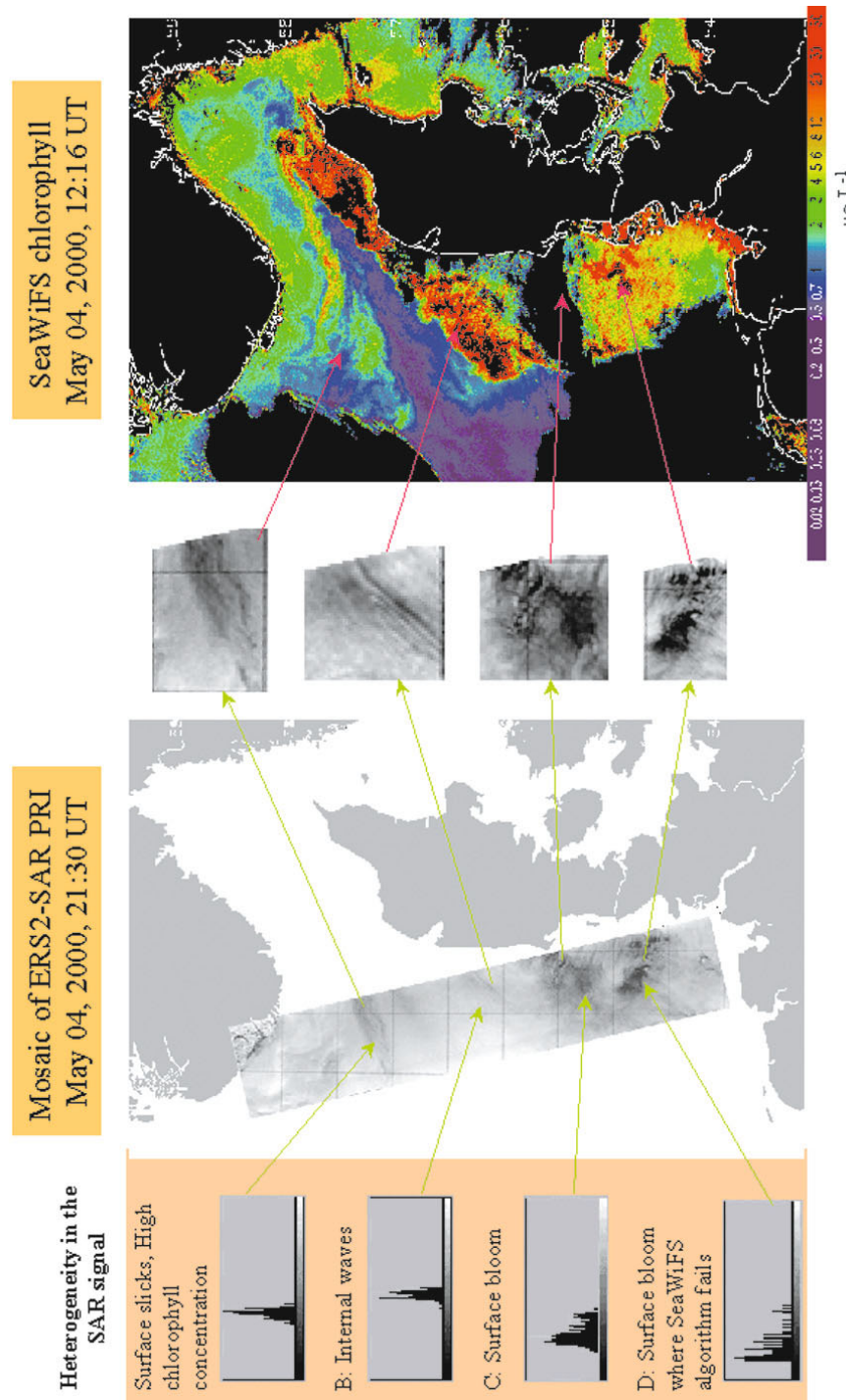


Figure 4.17. Example of various sea surface features and phenomenon resolved in SAR radar and SeaWiFS *chl-a* data taken 9 hours apart on May 4, 2000. The radar backscatter intensity and distribution for each area is indicated on the left.

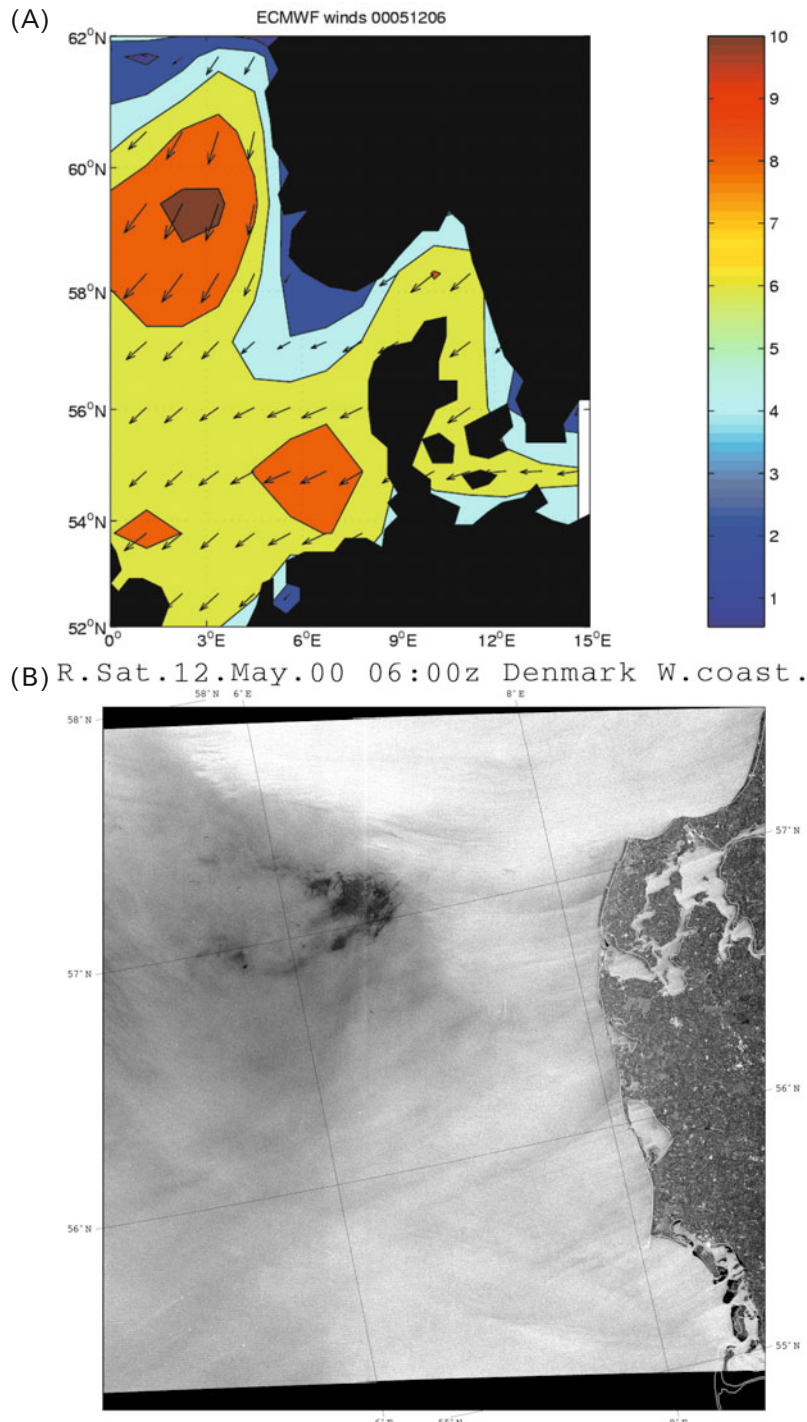
located with the frontal boundary between the waters of the Skagerrak origin and inflow of Atlantic (North Sea) water. The ocean circulation pattern proved to be characterized by (1) an inflow of colder and less chlorophyll-rich water and (2) an outflow of warmer and more chlorophyll-rich coastal water from the Skagerrak. Current shear causing convergence was expected in the area, which may have caused the observed low-backscatter SAR signature in the region (Johannessen *et al.*, 1996).

According to the Radarsat image of May 12 taken at 06:00 UTC, the surface wind speed in the region was higher in the near shore and particularly in the northern (upper) parts of the image (Figure 4.18), which is not exactly consistent with the ECMWF weather map of the surface wind field. However, the area of the lowest wind speeds revealed in the NW area of the image complies well with the ECMWF data. The area of damped SAR backscatter seems to be confined close to the western boundary of the high-biomass extension west of Jutland, again being co-located with the boundary between the warmer coastal and colder offshore water masses. Assuming a homogeneous air temperature distribution in the region, the air masses over offshore waters could be expected to be more stable than those in the coastal areas. Accordingly, it is possible to conclude that the synergies in the image signatures found in the region of low wind speed are most likely triggered by SST impact on the stability of the atmosphere–ocean boundary layer.

**Case III.** *Pseudochattonella* algal bloom along “Sørlandet”, March 2001. Earlier than seasonally expected, a massive bloom of *Pseudochattonella* occurred in Norwegian coastal waters along the coast of Sørlandet westward of Egersund (see Figure 4.9) in late March 2001, killing about 1,100 tons of farmed salmon, representing a value of about €3.8 million. The first high concentration of *Pseudochattonella* was reported in Flødevigen (Arendal) on March 16. Simultaneously, enhanced *chl* concentrations were deduced from analysis of SeaWiFS images over central Skagerrak, and also along large areas off the coast of Sørlandet. On March 17 and 18, a significant loss (650 tons) of farmed fish was reported and very high cell concentrations of *Pseudochattonella* (in excess of  $16 \cdot 10^6$  cells/L) were reported nearby this location on March 26.

Northeasterly winds prevented this bloom from being advected farther northwestward up along the coast of Jæren and farther into the region of the major Norwegian aquaculture industry (i.e., Rogaland and Hordaland counties). Confirmed by *in situ* observations, the SeaWiFS data explicitly indicated that the major part of the bloom front was trapped in two eddies located south of Kristiansand–Mandal and offshore the Lista–Flekkefjord areas (Figure 4.19).

No synoptic ERS SAR data were available for this area. However, the area located farther east in central Skagerrak was covered by an ERS-2 SAR overpass on March 27. Although the bloom in this region during this period was in a decaying stage, the algal concentration remained still sufficiently high to cause the low-backscatter signatures in the SAR image due to generation of surfactants at the ocean surface. The sequence of *chl* distributions retrieved from SeaWiFS imagery over the period March 25–27 (Figure 4.19) indicates a clear decay in algal bloom



(C)

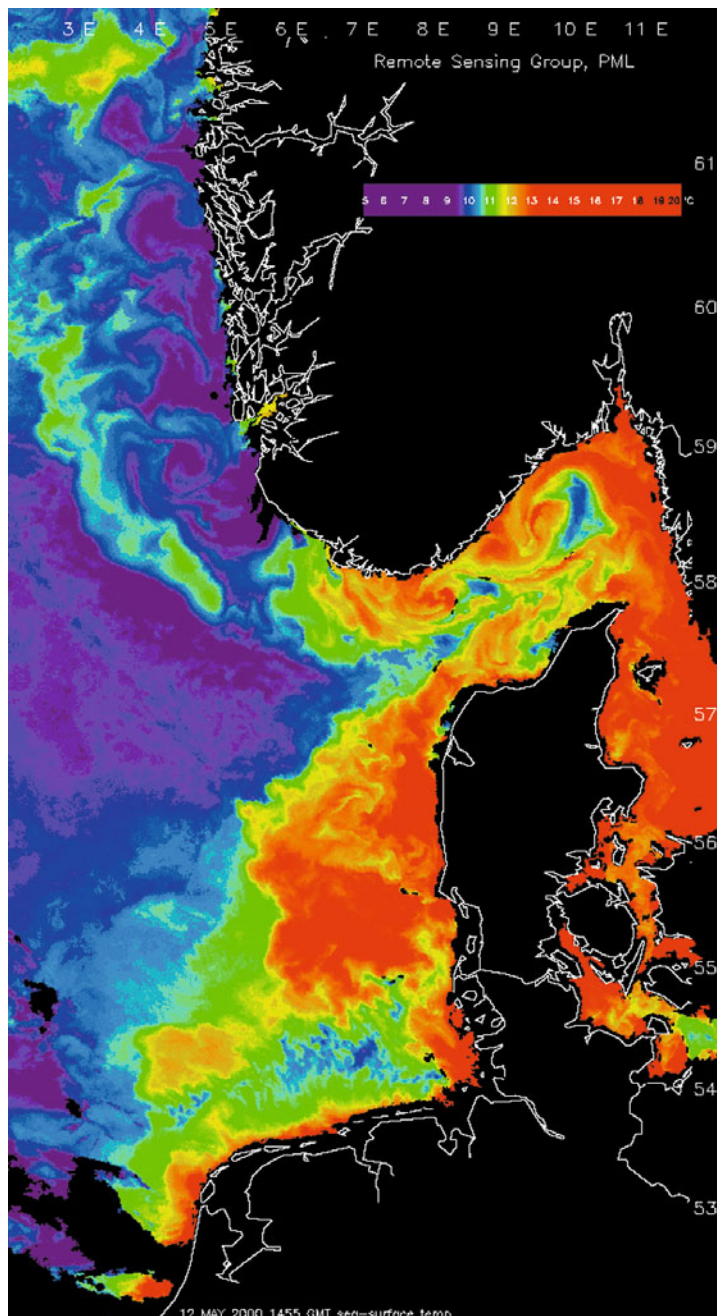
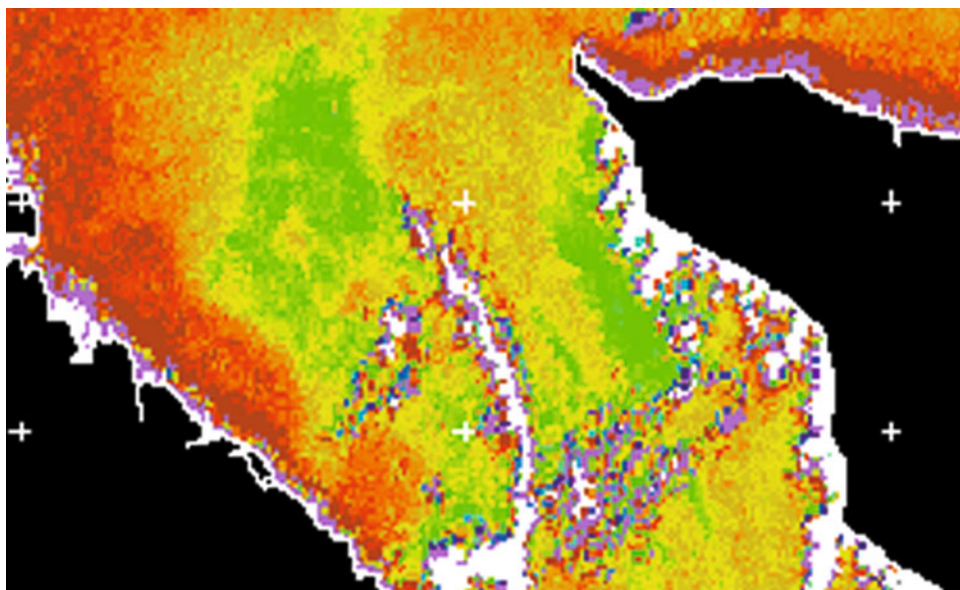
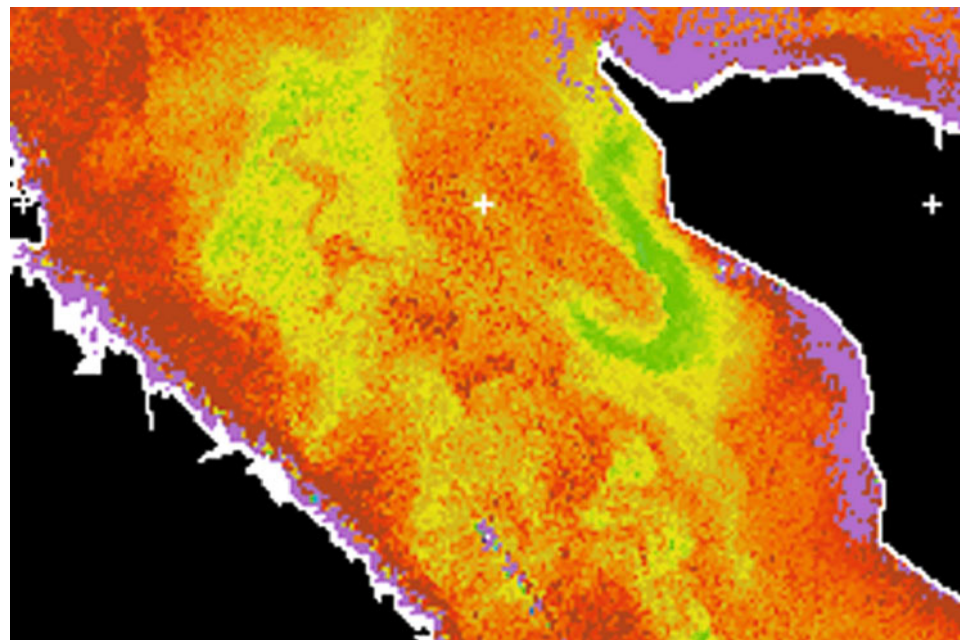


**Figure 4.18.** (A, opposite page) ECMWF wind field for the eastern North Sea at 06:00 UTC on May 12, 2000. (B, opposite page) Radarsat ScanSAR image (at 06:00 UTC) and the corresponding (C) AVHRR SST image (at 14:55 UTC).



(B)



(A)

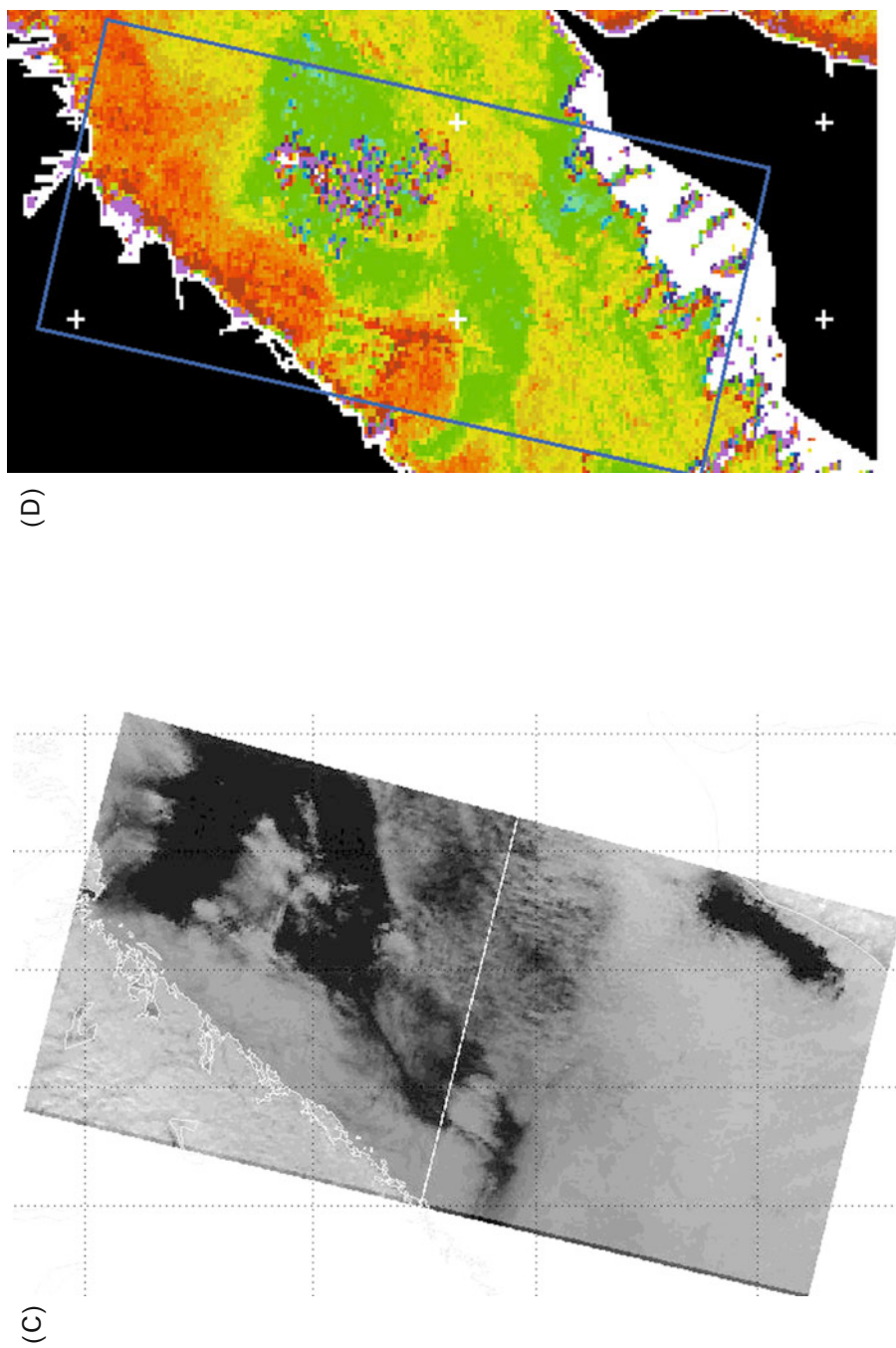


Figure 4.19. SeaWiFS  $chl-a$  concentrations for, respectively, March 25 (A), March 26 (B), and March 27 (C), 2001, and a mosaic of the two ERS-2 SAR scenes (D).

activity. Analysis of the wind field obtained from ECMWF as well as from the SAR derived wind field revealed a significant latitudinal gradient in the wind speed from 1–2 m/s in northern Skagerrak to above 10 m/s in southern Jutland waters (Figure 4.20). Accordingly, the wind effect dominated the SAR image signatures and no oceanographic influence was detectable in the SAR image in the high-wind region. Interestingly, in the northern part of the sequential ERS-2 SAR images, there were no low radar backscatter signals, although the winds were low in this area (Figure 4.21).

Analysis of the location of surface areas with high contrasts in respectively the SAR and SeaWiFS images over the Skagerrak area revealed some consistency between the area of gradient contrasts in *chl* distribution and the area of low backscatter in the SAR images (Figures 4.19 and 4.21). However, this match seems related not to algal-produced surfactants, but rather to local atmospheric and other hydrodynamic effects on sea surface roughness.

**Case IV. Late spring bloom in the Eastern North Sea and Skagerrak, May 2001.** A typical late spring algal bloom situation occurred in the Eastern North Sea and Skagerrak region during May 2001. High levels of  $C_{chl}$  reside in the coastal zone of continental Europe (from the Netherlands to Denmark, Figure 4.22, upper left panel), indicating that the bloom was initiated in the central North Sea and was accordingly advected towards the western Skagerrak waters. There, the bloom formed a front delineating the water area of lower *chl* concentration in central Skagerrak and the North Sea that extended towards the NCC region.

SeaWiFS and AVHRR data were acquired for May 9, whereas the SAR data were acquired one day before (Figure 4.22). The temporal mismatch was caused by both the unavailability of SeaWiFS and AVHRR imagery due to cloudy conditions on May 8 and the absence of SAR data coverage for May 9. Therefore, there was no exact temporal and spatial match between the data, and their interpretation was accordingly hampered.

The areas with the lowest SAR backscatter values were confined to the areas of the highest gradients, as observed in the SeaWiFS-derived  $C_{chl}$  (i.e., in the southern parts of the region). Farther north, the lowest backscatter areas matched high  $C_{chl}$  areas including the maximum gradient areas. In the northern part of the sequence of SAR images, low backscatter occurs in areas of relatively cold waters with lower  $C_{chl}$  concentrations. No exact interpretation can be given; however, the time difference (and hence the effect of advection) as well as temporal changes in the environmental conditions prone to changes during those few hours may explain the low level of commonality in the environmental phenomenon observed in different EO images.

*Pseudochattonella verruculosa* has been persistent northward of the German Bight, in the Danish Coastal, Skagerrak, Kattegat, and Norwegian coastal waters since 1998 and, from year to year, massive blooms have been reported as described above. Due to these events *Pseudochattonella* became a major species in the regular Norwegian *in situ* monitoring program for HABs (Figure 4.23) as well as in the marine ecosystem run for the North Sea (Section 5.3.1). These blooms have occurred late in the spring, typically April to May, when the water temperature is up to 18°C,

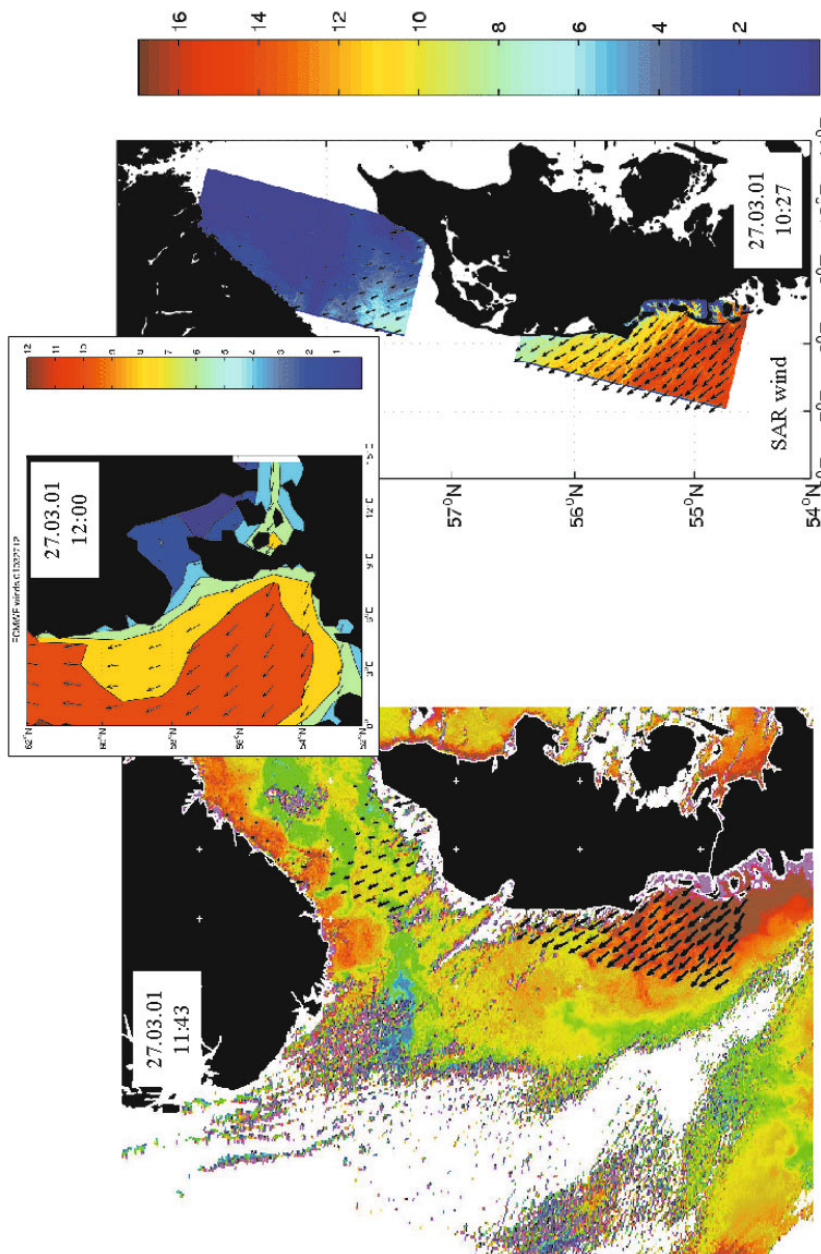
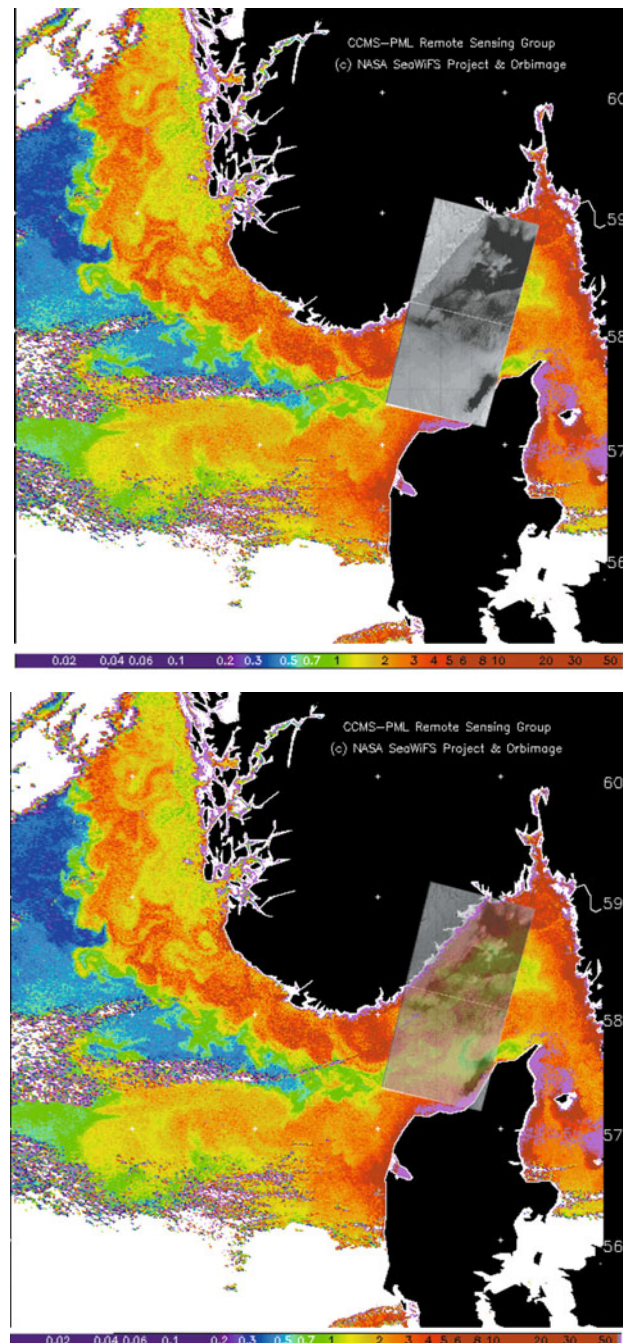


Figure 4.20. (Right) Wind field as retrieved from ERS-2 SAR using the CMOD-IFR2 algorithm and wind direction from the image spectra. (Left) Wind vectors overlaid on the SeaWiFS *chl-a* image, for comparison with the ECMWF wind field (middle panel).



**Figure 4.21.** ERS-2 SAR images overlaid on the SeaWiFS *chl-a* concentration distribution for March 27, 2001, shown with different opacity of the SAR image.

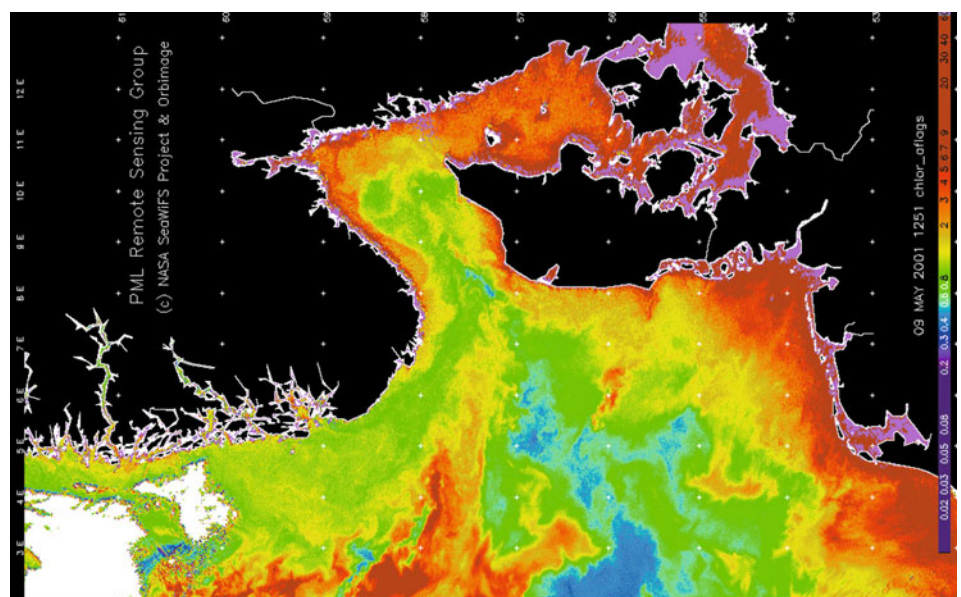
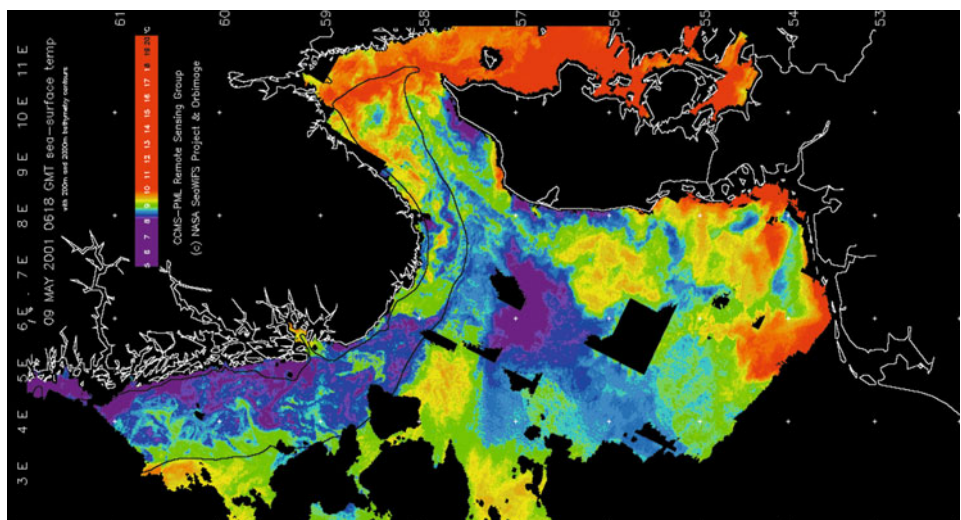
as was the case in 1998, 2000, 2002, and 2004. In 2001, 2006, and 2007 the *Pseudochattonella* blooms occurred earlier in the year (between January and March) when the water temperatures were significantly colder (2–5°C). From 2008 *Pseudochattonella* spp. have also been reported during the entire winter period (from December) in Skagerrak waters (see Chapter 2). Also, in April 2009 a *Pseudochattonella farcima* bloom was reported in West Jutland coastal waters. An early indication of the bloom was reported based on the analysis of the MERIS data from April 17 ([Figure 4.24-A](#)) and later confirmed by coastal and the routine annual ship investigations by the institute of Marine Research during April 24 and 25 ([Figure 4.24-B](#)). To some extent this bloom was also confirmed in NORWECOM marine ecosystem model simulations performed by IMR ([Figure 4.24-C](#) and see also Chapter 5).

#### 4.1.9.2 Blooms in the ocean frontal zones west of Shetland

The SeaWiFS-based true color (RGB) images taken over the North Sea and Baltic Sea ([Figure 4.25A](#)) invariably resolve the highly heterogeneous patterns of ocean color variations, which are a reflection of the diversity of ecological conditions in these aquatic environments. Indeed, the phytoplankton *chl* spatial distribution patterns derived from ocean color data reveal information on the state of regional ecosystems, their seasonal variations and, in some instances, the causal mechanisms involved. Thus, in [Figure 4.25B](#) the enhanced abundance of *chl* westward of the Shetland archipelago is most certainly driven by the North Atlantic Current bringing warm and nutrient-rich waters with an ongoing red tide algae bloom event into the Norwegian and North Seas. Restricted to the coastal waters of the U.K., Belgium, the Netherlands, Germany, Denmark, and southern Norway, the areas of increased  $C_{chl}$  are the consequence of coastal shelf waters (shallow, nutrient rich, and relatively warm waters) and, predominantly, by shallow-water re-suspension as well as land and river runoff supply of nutrients. The expansion of eutrophic waters within the coastal zone of southern Norway north into the Norwegian Sea is certainly a result of their entrainment by the NCC. The most *chl*-abundant areas in the North Sea are the coastal waters of Belgium, the Netherlands, Germany and the U.K., which are also influenced by other color-producing agents in the water. The central pelagic area of the North Sea is relatively unaffected by the terrestrial influence, with significantly less phytoplankton abundance. The mapped oceanographic situations are not unique and similar phenomena are observed in [Figure 4.27](#).

#### 4.1.9.3 The North Sea marine “ecosystem”

Cloud-free conditions over almost the entire North Sea enabled detailed mapping of the major ocean circulation features resolved in both the SeaWiFS  $C_{chl}$  concentrations and in the NOAA AVHRR sea surface temperature (SST) data from May 1999. [Figure 4.26](#) (upper panels) provided high-quality EO data with the SST (AVHRR data taken at 06:46 UTC) and phytoplankton distribution ( $C_{chl}$ ) (SeaWiFS data taken at 12:12 UTC). Joint analysis of these EO data provides valuable information on different water masses in the region, including the inflow of



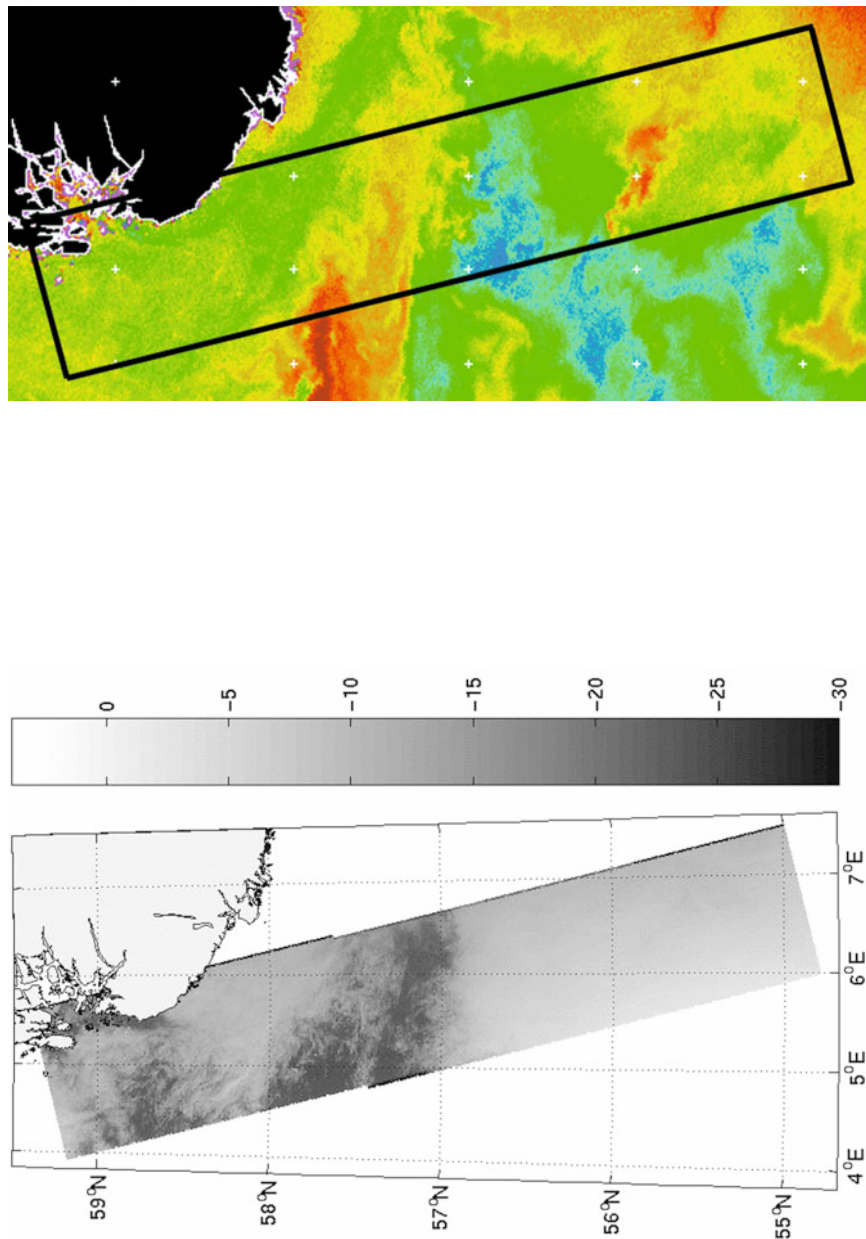
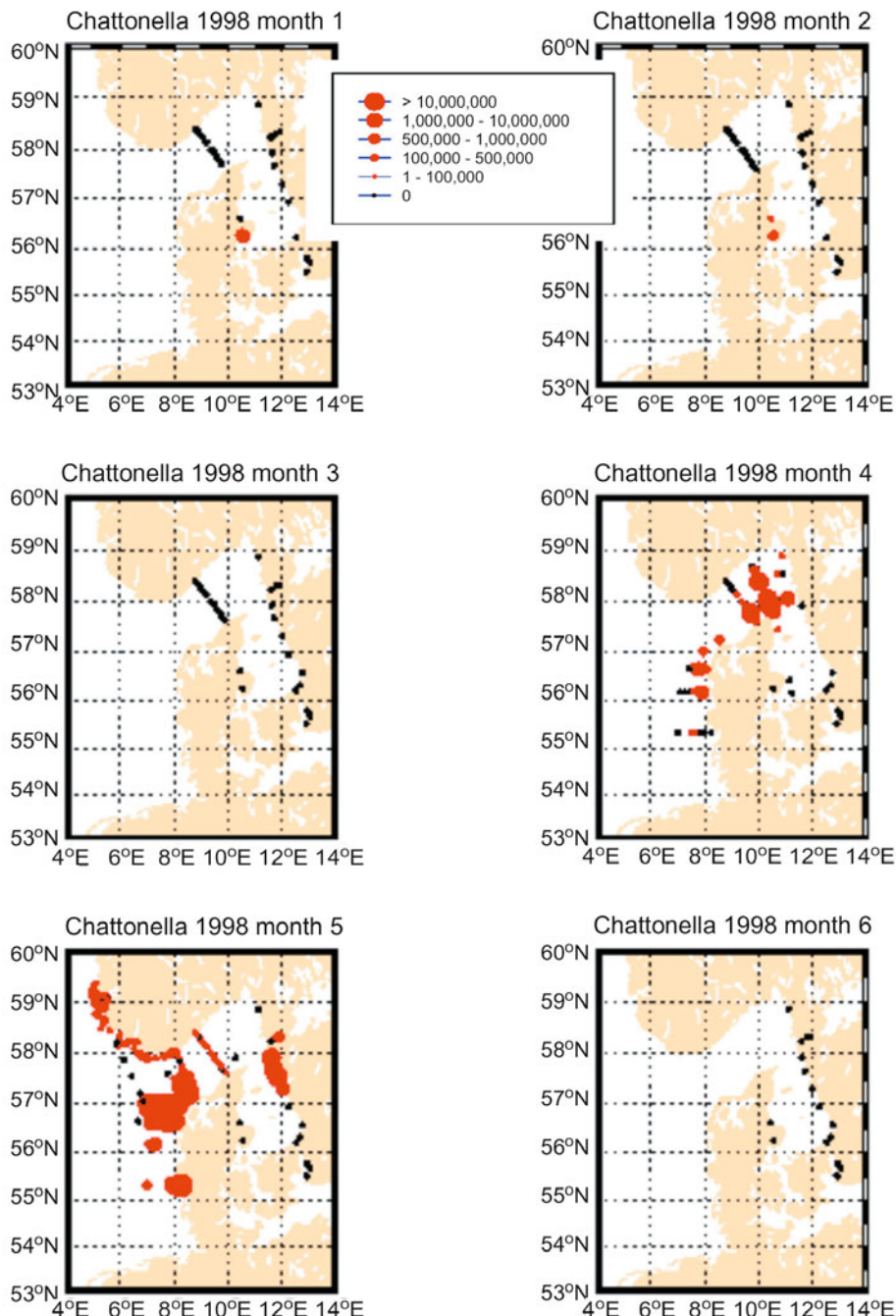
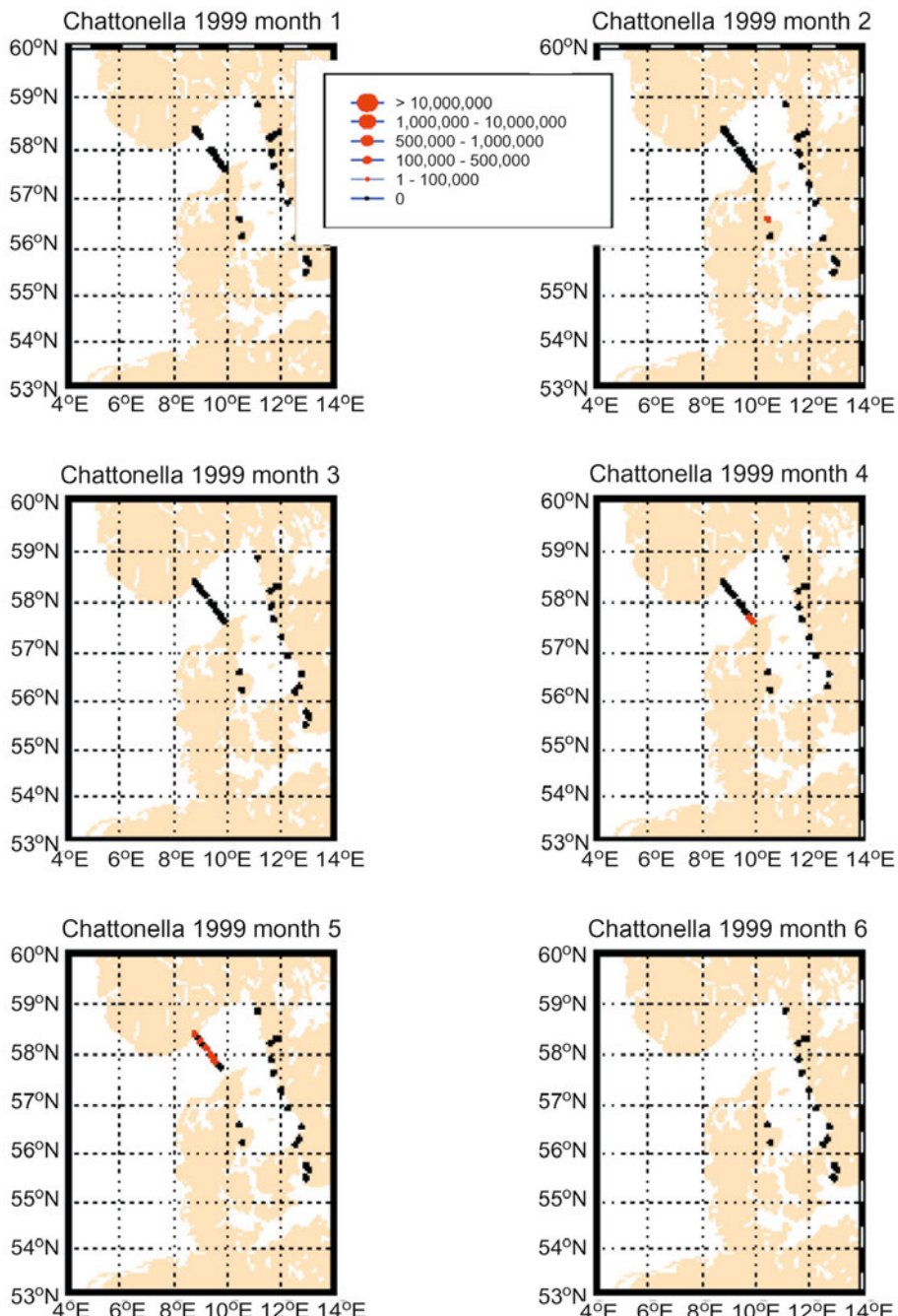
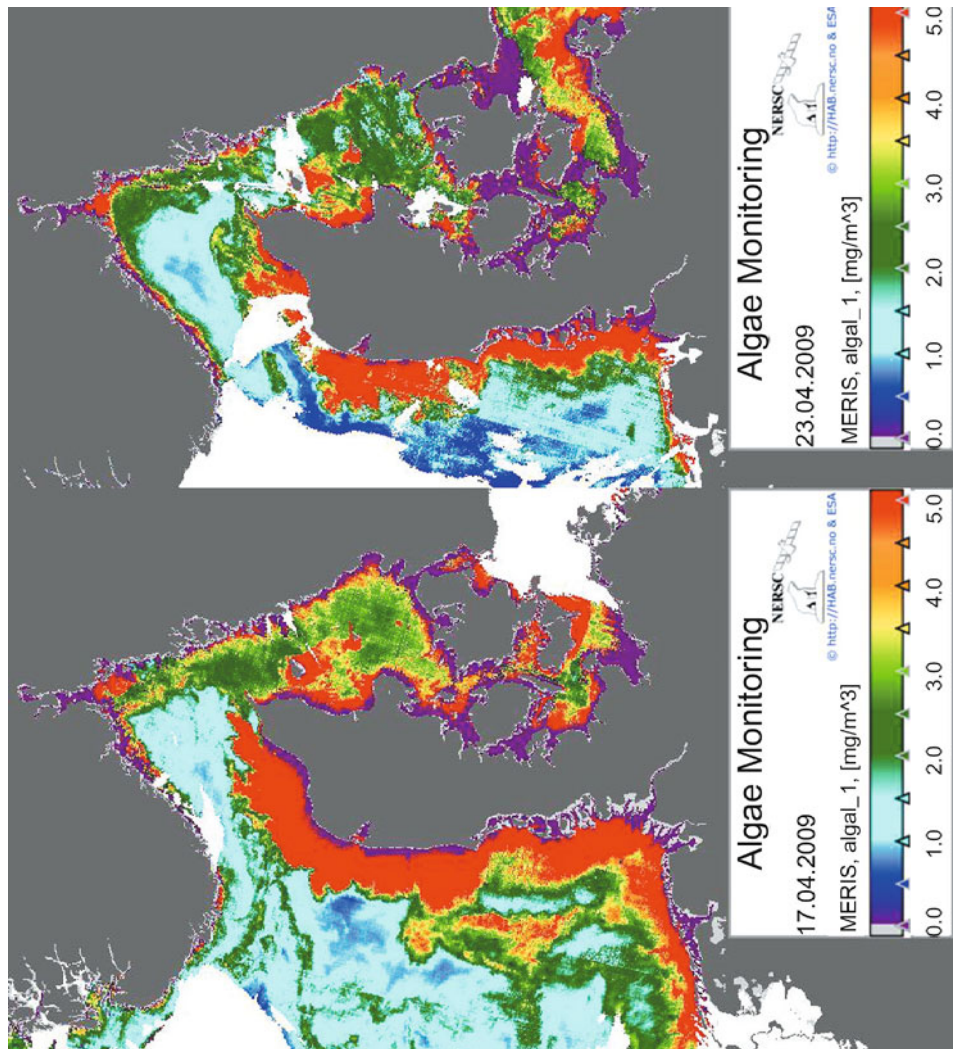


Figure 4.22. Satellite EO data for May 8 and 9, 2001, comparing *chl-a*, SST, and radar backscatter. (Upper left) SeaWiFS-derived *chl-a* concentration for the North Sea region. (Upper right) Sub-image of the AVHRR SST coverage. (Lower right) ERS SAR swath strip. (Lower left) Sub-image of the SeaWiFS *chl-a* concentration extracted from the upper left panel.



**Figure 4.23.** Monthly summary of *in situ* cell counts of the abundance of *Pseudochattonella* during the period January to June in 1998 (this page) and 1999 (opposite page). Courtesy: L.-J. Naustvoll, IMR.





(A)

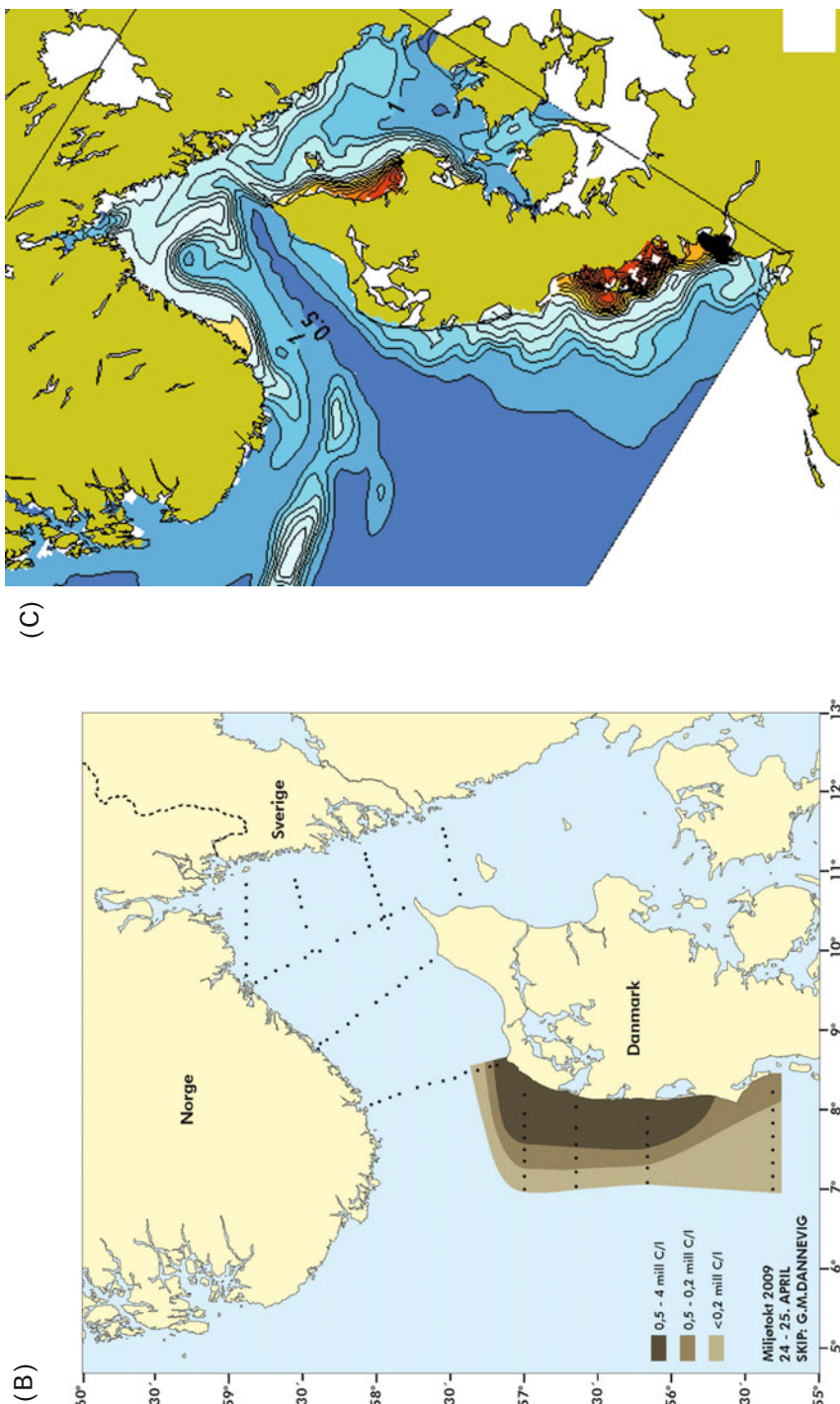
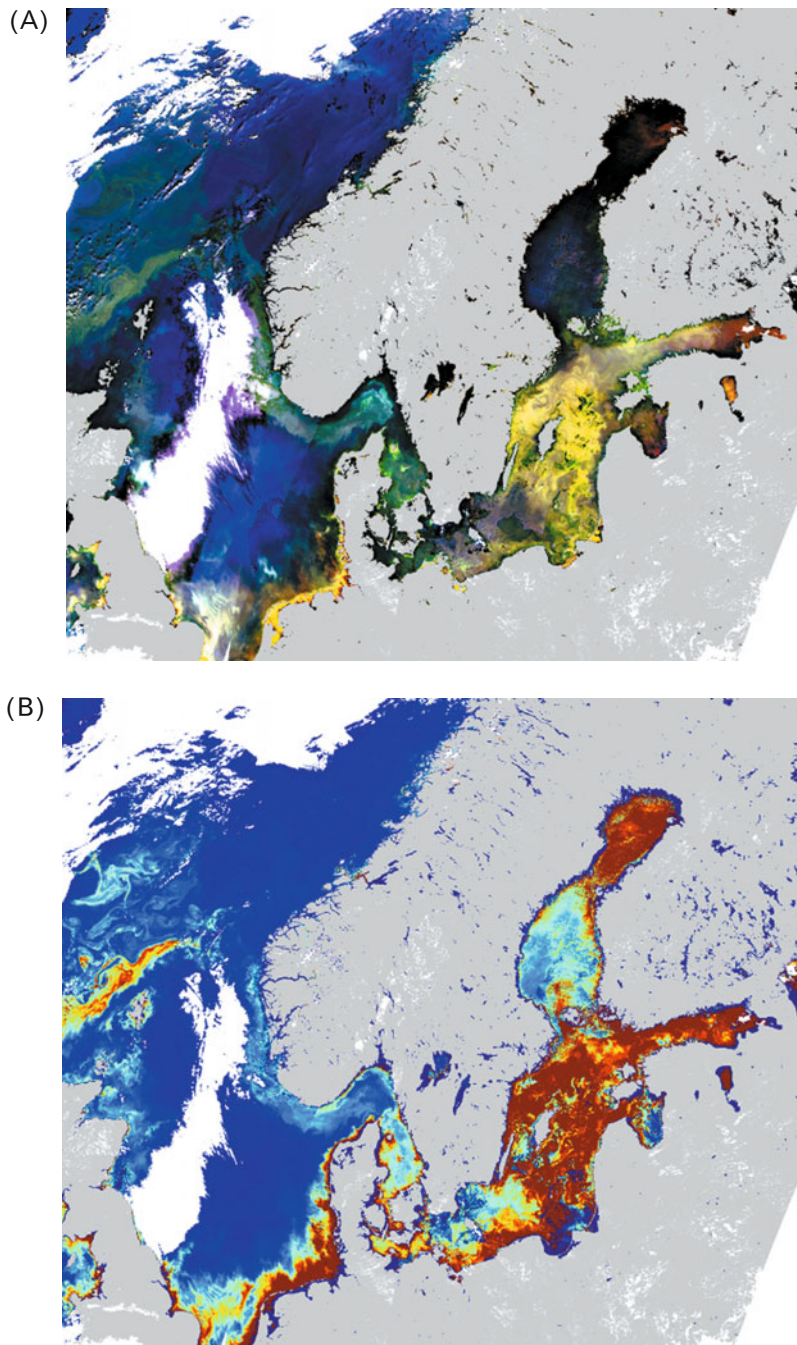


Figure 4.24. Monitoring of west Jutland Danish waters in April 2009 during the *Pseudocharonella* bloom. (A) MERIS based *chl-a* concentrations from April 17 and 23. (B) Algae cell counts from the R/V Damnevig annual field survey on April 24 and 25. (C) 4 km resolution NORWECOM modeling of surface layer phytoplankton concentrations on April 23. Courtesy for (B) and (C): M. Skogen, IMR.



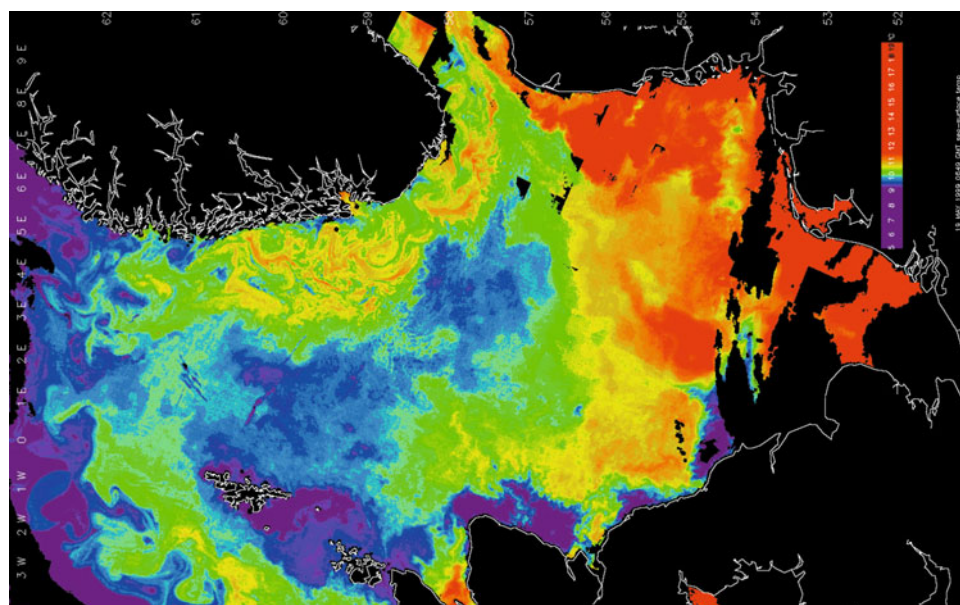
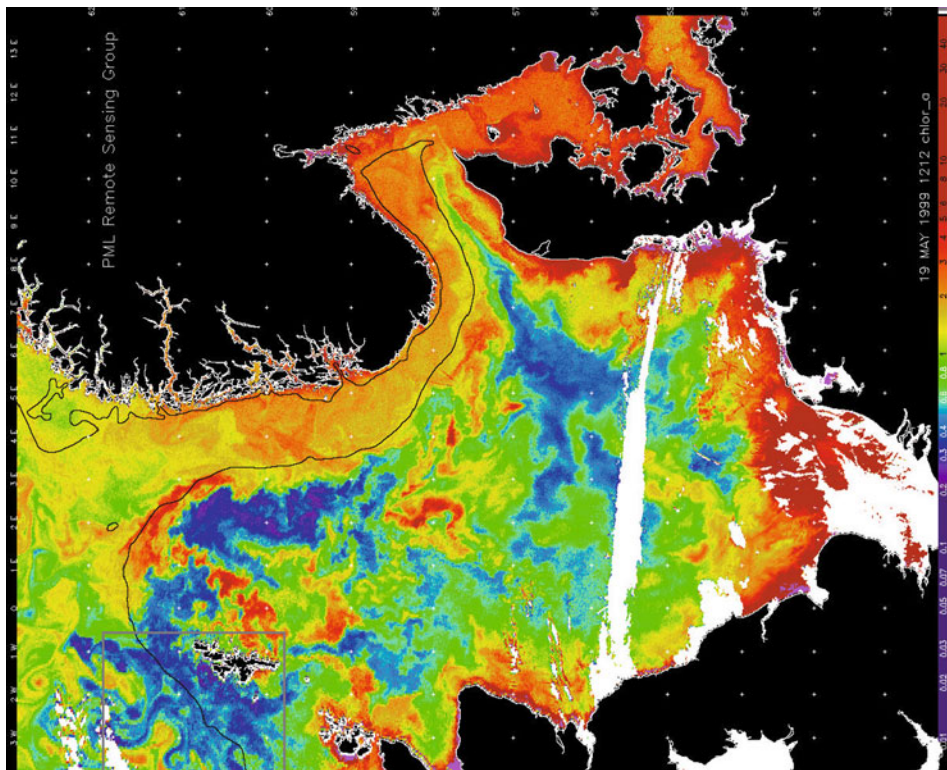
**Figure 4.25.** (A) A MERIS RGB image during cloud-free conditions over the Baltic and North Seas and (B) spatial distribution of the *chl-a* concentration derived from the same satellite data.

Atlantic waters to the northwest of Shetland, the central North Sea circulation, and the coastal currents extensions from continental Europe to the NCC along the western coast of southern Norway. The meso-scale nature of the major currents is well pronounced in the various EO data and the frontal boundaries consistently mapped.

In the area located between Shetland and the Faeroe Islands, the inflow of warm Atlantic waters (the North Atlantic Current) is typically 1°C warmer than the shelf water near the Faeroe Islands. This is seen in SST distributions derived from AVHRR data ([Figure 4.26](#), upper left panel). Similarly the gradients in the  $C_{chl}$  are resolved in the ocean color data. The same water masses of Atlantic origin exhibited moderate biological activity ([Figure 4.26](#), upper right panel), with the typical algal  $chl$  concentration varying within the range between 0.3 and 0.5 mg/m<sup>3</sup>, which was significantly lower than that farther westward on the shores around the Faeroe Islands, where it was assessed at above 2.0 mg/m<sup>3</sup>.

A high degree of correlation between the spatial patterns resolved in the SST and  $C_{chl}$  distributions was established, albeit there were inverse gradients in the two parameters and some spatial displacement, the latter probably being due to the 6-hour time difference in data acquisition. The absolute difference (contrasts) in biological phytoplankton bloom activity is larger than the contrast in the SST on spatial scales typically ranging from 5 to 15 nautical miles. The Shetland eddy circulation feature was characterized by opposite spatial gradients in the SST and  $chl$  distributions. The same day, but ten hours later (overpass time 22:03 UTC) an ERS SAR image ([Figure 4.26](#), lower panel) covered both the area of the above eddy circulation feature and the current boundary between the warmer and less productive Atlantic water and the colder and algae-rich areas closer to the Faeroe shelf. The SAR image also clearly revealed the gradient zone as well as the eddy circulation feature generated at the boundary between these two different water masses (i.e., the North Atlantic Current and the Faeroe Island Shelf waters).

In another SeaWiFS image from July 16, 2003 the entire North Sea is almost cloud free ([Figure 4.27](#)). Moreover, these data confirm a similar situation with respect to information on the state of the North Sea marine ecosystem. Starting from the northwest, the images resolve the inflow of Atlantic water through the Faroe–Shetland channel, which is high in chlorophyll-*a* concentration and even “discoloring” the water changing it to a reddish color, indicating that a red tide algal bloom is present. Algal blooms of various groups, species, and concentrations are observed in the coastal waters of the U.K., Denmark, Norway, and the rest of Europe in general. In the central North Sea generally low chlorophyll-*a* concentrations are observed; however, there are several very bright areas associated with cocolithophorid blooms. In the NCC, the concentrations of phytoplankton are higher and the color of coastal waters turns “bright brownish” indicating blooms of diatoms. The pronounced meso-scale structures of water circulation, including meso-scale eddies, are observed in most parts of the North Sea region and, in particular, in the inflow of Atlantic water and in the NCC. The offshore topographic steering of the NCC due to the shallow Møre Plateau is observed as is a complex circulation pattern in the area where the Atlantic and coastal waters interact.



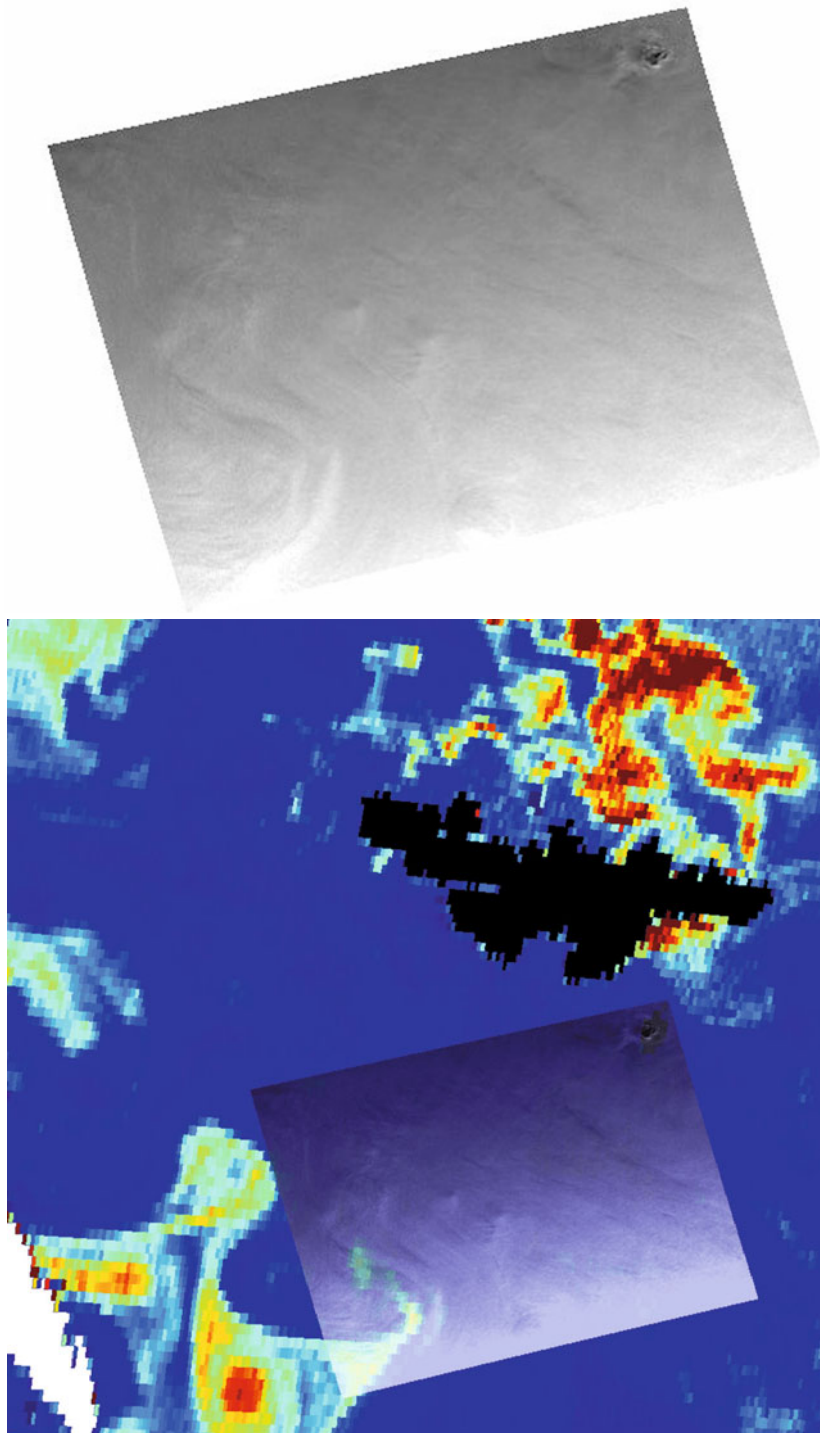


**Figure 4.26.** Cloud-free conditions over major parts of the North Sea on May 19, 1999. (Upper left) AVHRR sea surface temperature. (Upper right) SeaWiFS *chl-a* distribution. (Lower images) ERS SAR image respectively superimposed on the *chl-a* image (different color scale from upper right panel) and radar image separate (lower left). Both satellite images resolve the ocean front area of the inflow of North Atlantic water between the Faroe and Shetland Islands (the blown-up sub-area is indicated on the upper right panel).

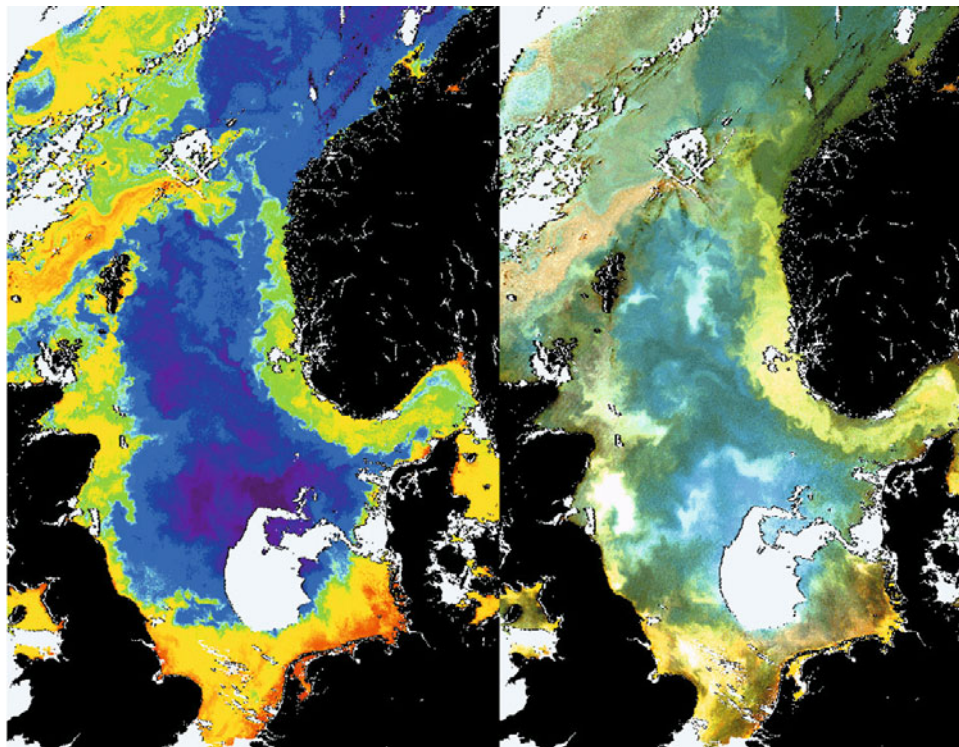


**Figure 4.27.** SeaWiFS ocean color image from July 16, 2003 covering major parts of the North Sea. (Left) Derived  $chl\text{-}a$  concentrations. (Right) True-color composite (RGB) resolving the “visual” color differences of the ocean and coastal water masses and circulation features.

#### 4.1.9.4 Norwegian Coastal Current

In the EO data from May 1999 (Figure 4.26) a typical late-spring situation in the NCC is observed, with generally higher  $C_{chl}$  concentrations in the coastal waters and generally lower biological activity in offshore regions (waters of Atlantic/North Sea origin). The acquired AVHRR SST data reveal generally warmer waters in the NCC than those farther offshore, but, as seen in the SST data, the western boundary of the NCC was less pronounced than that observed in the pattern of SeaWiFS-derived  $chl$  spatial distribution. This is due to diurnal variation in solar heating, which masks some of the surface characteristics of the SST (during summer daytime) in the NCC and Atlantic waters, while the phytoplankton growth in the NCC water is not affected to the same extent by diurnal variation in solar heating.

Detailed investigations reveal several areas within the NCC that have a very high *positive* correlation between gradients and features in the SST and  $chl$  spatial distributions; however, revealed mismatches between the two types of EO data may

be explained by the temporal difference between the two observations. Clear topographic steering of the westward extension of the NCC by the Norwegian Trench is seen in the distribution of *chl* (Figure 4.26, upper right area of the image with the superimposed 200-meter depth contour).

Thus, optical (*chl*) and thermal infrared (SST) spaceborne data often reveal a close correlation between the physical and biological properties of the ocean since both are related to ocean circulation patterns and their origin to different water masses. Under some conditions (depending on areas and season) the relationship between high algal biomass and SST (as was the case in some parts of the NCC) is direct whereas under other conditions the relation is reversed (as was found in the area west of Shetland and in the high bloom areas of the Central North Sea). The concurrence between spatial distribution patterns observed in the SST and  $C_{chl}$  is largely determined by both the seasonality (time) and regional characteristics of the water masses as well as the stage of bloom development. Typically, SST-determined features within the NCC are more strongly expressed than those of  $C_{chl}$  during wintertime and conversely in late spring, when the SST is more influenced by diurnal solar heating.

In summary, the research results presented in this section support the fact that satellite-based ocean color data are efficient for (H)AB identification, monitoring, analyses, and interpretation, provided they are used in conjunction with *in situ* data. The spatial coverage of EO data makes them well suited for analysis of coupled physical–biogeochemical processes related to algal blooms by providing complementary information about the various water masses and ocean circulation patterns resolved in the ocean color and thermal infrared EO data. It should be emphasized that confident interpretation of biological activity, based exclusively on SAR data without relevant *in situ* or other EO data, is still an evolving research task that is not fully ready for use in general monitoring. Indeed, the very high sensitivity of radar backscatter to local wind conditions (known to vary on short timescales and spatial scales) makes the radar mapping of the ocean features much more sensitive to other environmental (oceanographic and meteorological) conditions rather than to the ocean features mapped in SST and ocean color images. The temporal changes in surface wind speed that dominate the SAR signal impose very strict requirements on synoptic observations.

Furthermore, the spatial coverage of EO data makes them well suited for analysis and assessment of coupled physical–biogeochemical processes related to algal blooms by providing complementary information about the various water masses and ocean circulation patterns.

The above results are indicative of the work undertaken by the Nansen Center in Bergen together with its European partners including the Plymouth Marine Laboratory (PML), the Institute of Marine Research, the Norwegian Directorate of Fisheries (FD), and others. Comprehensive studies into monitoring the development and decay of algal blooms have been carried out by these institutions using daily-updated satellite images, regular, dedicated, and even haphazard *in situ* measurements as well as the prognostic results of numerical marine ecosystem modeling (see Chapter 5).

#### 4.1.10 Applications of FLH data products for HAB monitoring

The Fluorescence Line Height (*FLH*) method has been thoroughly presented and discussed in Chapter 3. In the past decade it was exploited not only for determination of phytoplankton  $C_{chl}$  *per se*, but also for detecting, delineating, and monitoring the dynamics of HABs.

Applying fluorescence signals from phytoplankton pigments to the study of HABs has received increasing interest from the remote-sensing community (e.g. Maritorena *et al.*, 2000). Below some case studies are discussed.

Gower *et al.* (2005) studied a red tide case (*Heterosigma akashiwo* accompanied by the marginal presence of *Gymnodinium sanguineum* and *Cochlodinium polykrikoides*) through employing the 709 nm spectral band (at 300 m resolution—FR data) of the MERIS imaging spectrometer. Targeting an area located within the coastal zone of Vancouver Island at the site of a fish farm where bloom conditions were confirmed by surface observations and measurements, Gower *et al.* (2005) developed a new detection method that provides a more specific algal bloom response. The authors use non-atmospherically corrected at-satellite altitude radiances (level-1 data) in the belief that level-2 product computations rely on water having optical properties that do not in general apply to intense plankton blooms, and therefore results tend to be erroneous or even missing in their waters of interest. Also, since the aim of the work is to design an approach that can detect bloom events in nearly real time, use of raw level-1 data has a significant advantage in not depending on pre-processing of an atmospheric correction algorithm.

Here the basic algorithm is *FLH* (Section 3.6.1.2), where the *FLH* is calculated as the radiance at 681 nm (Table 4.1) above the baseline formed by linear interpolation between the radiances at 709 nm and 753 nm. The *FLH* obtained through this combination of bands is coined by Gower *et al.* as the Maximum Chlorophyll Index (MCI). The sign of MCI is positive for either high phytoplankton *chl* concentrations or benthic vegetation close to the water surface or for floating macrophytes, and negative for low *chl* concentrations.

This means that without good knowledge of the bathymetry, positive MCI can give a “false alarm” for bloom detection. This uncertainty can be avoided if a threshold for radiance at 865 nm is established: a lower threshold level can dismiss vegetation areas, although in this case more areas of thin cloud would be masked, and in other scenes larger areas of haze and sun glint would also be missed (Pozdnyakov *et al.*, 2000a, b).

Hu *et al.* (2005) developed a regression algorithm relating  $C_{chl}$  with *FLH* to detect and monitor red tide blooms in the southwest Florida shelf. Red tide blooms occur every year on the U.S. west Florida shelf, mainly between late fall and early spring but also occasionally at other times of the year. Caused by *Karenia brevis* (alias *Gymnodinium breve*), these HABs are toxic, producing brevetoxins that accumulate in shellfish (e.g., oysters and clams) and cause mortalities of fishes, birds, marine mammals, and can cause inflammation of the eyes and respiratory malfunctions in animals and humans (see Chapter 1). There are indications that red tides typically initiate offshore in nutrient-poor waters and then advect toward the shore

under favorable wind and current conditions. Near the coast, HAB development may be stimulated by additional nutrients from land/river runoff, or upwelling where algal mass accumulation may be driven by convergent water movements along ocean fronts. However, the *exact* mechanisms causing *K. brevis* blooms remain unclear to date. Hu *et al.* (2005) developed a non-linear regression algorithm relating  $C_{chl}$  with  $FLH$ :

$$C_{chl}(\text{mg/m}^3) = 1.255(10 \cdot FLH)^{0.86} \quad (4.1)$$

This relationship (4.1) was developed for MODIS data, processed using the atmospheric correction approach by Stumpf *et al.* (2003) for turbid coastal waters to obtain the water-leaving radiance, which was then used in the OC4 algorithm. A baseline subtraction algorithm (Letelier and Abbot, 1996) was used to determine  $FLH$ . The  $FLH$  matched *in situ*  $C_{chl}$  variations well ( $r^2 = 0.92$ ;  $n = 777$ ) across a large range of values and environmental conditions, from a pure marine environment (salinity in excess of 36 psu) to coastal runoff-affected conditions (salinity less than 35 psu); however, the MODIS  $C_{chl}$  showed a bias of factors between 3–15 times *in situ*  $C_{chl}$  and lower correlation with *in situ* data, particularly at high values. The authors attributed this problem to enhanced chromophoric dissolved organic components in coastal waters, but also the influence of bottom reflectance in shallow areas (water depths typically less than 10 m).

A comparison of the retrieval results obtained with the use of eq. (4.1) and the standard products from MODIS and SeaWiFS indicate that the mean relative error in the  $FLH$  predicted  $C_{chl}$  to be about 76% compared with 124% in the MODIS and SeaWiFS band ratio OC4 algorithm regardless of water type. The same refers to establishing *synoptic* patterns.

Further research has been undertaken at the Nansen Center (Folkestad *et al.*, 2006) aimed at improving the EO component of the HAB-monitoring system in Norway. The main source for determination of the phytoplankton distribution used in regular services is based on band ratio algorithms, while the  $FLH$  information is regarded as complementary.

Even though the  $FLH$  product has been applied and validated for other regions (see Section 4.1 and Gower and King, 2003; Gower *et al.*, 2003, 2005; Gower and Borstad, 2004), documentation of the  $FLH$  product efficiency in European waters such as the North Sea is very limited. At the same time, it was well worth comparing the  $FLH$  product with  $chl$  measured *in vitro*, and endeavor establishing the relationship between the two quantities with regard to a variety of atmospheric and hydrographic conditions based on the ample shipborne data that were available.

Moreover, the study by Folkestad *et al.* (2006) assessed the quality of atmospherically corrected MERIS L2 products. MERIS Reduced Resolution Level 2 (RR-L2) data were analyzed for a total of eight days in 2003 and 2004 (Table 4.3). The days were selected according to cloud-free conditions along all or major parts of the FerryBox data from the NIVA (<http://niva.no>) daytime transect in Skagerrak stretching from Oslo (Norway) to Hirtshals (Denmark).

The  $FLH$  product was generated from L2 spectral surface reflectance data using the BEAM  $FLH$  processor (<http://www.brockmann-consult.de/cms/web/beam/>). From

**Table 4.3.** Dates of synoptic acquisition of the MERIS RR and NIVA FerryBox data.

Year	
2003	2004
March 28	February 24
May 22	March 9
June 6	March 16
June 20	June 29

the eight MERIS images, the values of all L2 products—including case 1 water *chl* (*Algal 1*), case 2 water *chl* (*Algal 2*), *FLH*, *FLH* slope, and the value (0/1) of all 24 L2 flags—were extracted along the *in situ* measurement transect.

Continuous transect measurements of water temperature, salinity, *in vivo* fluorescence, and turbidity as well as photosynthetically active radiation (PAR) above the sea surface were provided by the NIVA's Ferrybox system [<http://www.niva.no>]. The maximum time difference between shipborne measurements and the EO data used in the analyses was four hours. The *in vitro* sample for *chl* by the Ferrybox system had previously been found to correlate better with nighttime *in vivo* fluorescence than with daytime *in vivo* fluorescence (Sørensen, pers. commun.). Therefore, in addition to the data extracted along the daytime transects, *in vivo* nighttime fluorescence data for the daytime transects were used to serve as a quality check of *in vitro chl*.

The spatial distributions of the MERIS *FLH* product in Skagerrak were generated (Figure 4.28) exhibiting a wide range of *FHL* values (0–0.0015 str<sup>-1</sup>). The respective MERIS L2 *chl* products (*Algal 1* and *Algal 2*) were visually compared with the *FLH* maps. The validity of the *Algal 1* and *Algal 2* products was checked for all pixels in each image making use of the value of the L2 confidence flag (PCD 15 and PCD 17 for case I and case II, respectively).

The results of comparison of the MERIS *FLH*, *Algal 1*, and *Algal 2* products with both *in situ chl* concentration and *in vivo* fluorescence levels measured along daytime transects (remember, phytoplankton fluorescence was assessed for nighttime but for the same transect, see above) are illustrated in Figure 4.29. The *FLH* product is given in units of reflectance (str). Therefore, the *FLH* product is not directly comparable to  $C_{chl}$  measured *in situ* or retrieved with other algorithms from ocean color data.

To investigate the relationship between *FLH* and *chl* concentration levels in the study region, the *FLH* data in Figure 4.26 were scaled to fit the measured *chl* range. However, the scaling factor (i.e., the *FLH:chl* ratio) is generally liable to daily variations due to changes in incident radiation, aquatic environmental and phytoplankton physiological conditions, etc. Therefore, more ample statistical data were required to attain the above goal.

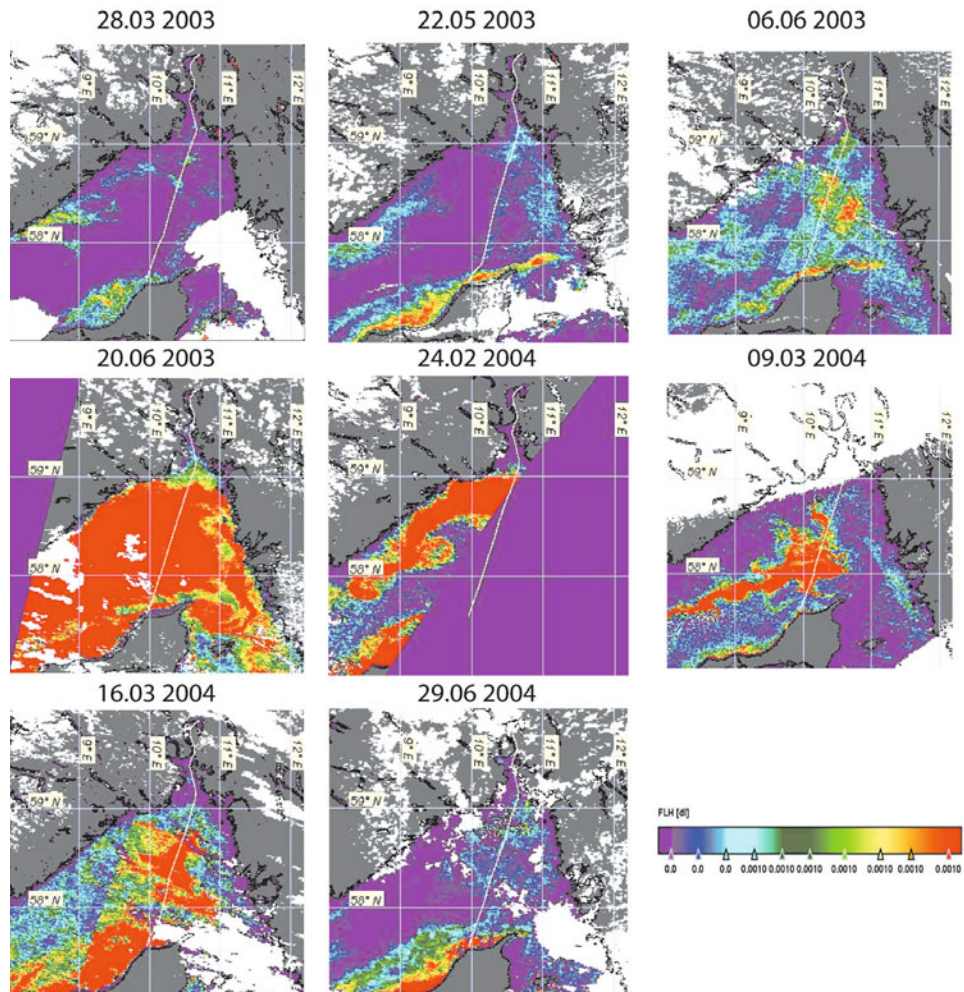


**Figure 4.28.** MERIS-based  $FLH$  values (lower right scale in reflectance,  $str^{-1}$ ) in Skagerrak for the eight dates in 2003 and 2004. The white lines indicate the NIVA FerryBox transect data. Cloud cover, land, and unreliable/unprocessed MERIS data are colored white, gray, and purple, respectively. *Courtesy:* Yunfei Wang.

Along the ship transect, the correlation between  $FLH$  and  $chl$  levels was investigated with due regard to the MERIS L2 product confidence and scene flags that could influence the validity of the generated  $FLH$  product according to Table 4.4 (Pellegrini, 2003).

As discussed in Section 3.6.1.2, Gower *et al.* (1999) found a linear relationship between  $FLH$  and  $chl$  levels that had been established for waters in British Columbia.

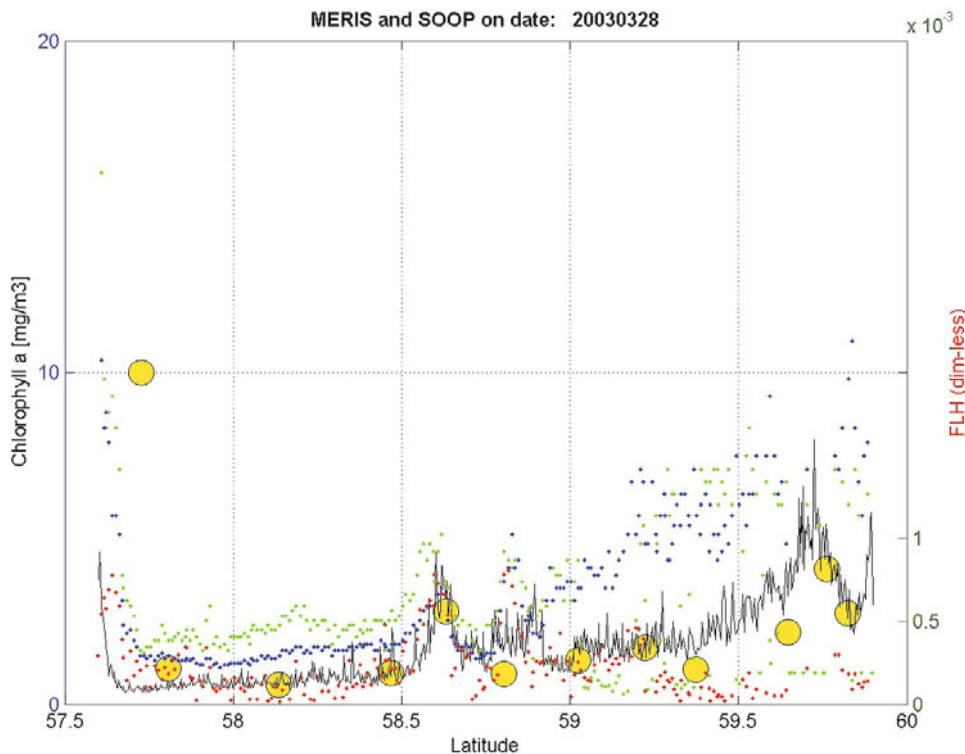


**Figure 4.29.** Spatial pattern of the MERIS  $FLH$  product (reflectance,  $\text{str}^{-1}$ ) in Skagerrak for the eight dates specified in Table 4.3. The white lines stand for the transect specific for each day. White, gray, and purple areas refer, respectively, to cloud-screened, land, and unreliable/unprocessed spaceborne data. Courtesy: Yunfei Wang.

The slope of the function was reported to vary between datasets obtained under different weather and hydrological conditions.

However, using  $FLH$  values generated from MERIS Level 1 data (i.e., TOA radiance, see Section 4.1) Gower and King (2003) later suggested a non-linear relationship:

$$FLH = \zeta + a \cdot C_{chl} (1 + 0.2C_{chl})^{-1}, \quad (4.2)$$

where  $\zeta$  is the offset, and  $a$  is a factor depending on the sun elevation angle (season), fluorescence efficiency and vertical distribution of the phytoplankton in the water column, and the sensor's bandwidth.  $C_{chl}$  is the near-surface concentration (although a linear relationship between  $FLH$  and  $chl$  may be assumed for  $C_{chl}$  under  $\sim 8 \text{ mg} \cdot \text{m}^{-3}$ ).

In Section 4.1, it was indicated that Hu *et al.* (2005) also found a slightly non-linear relationship between  $FLH$  and  $chl$  levels in south Florida shelf waters (eq. 4.1).

**Table 4.4.** Flag designations used in MERIS products.

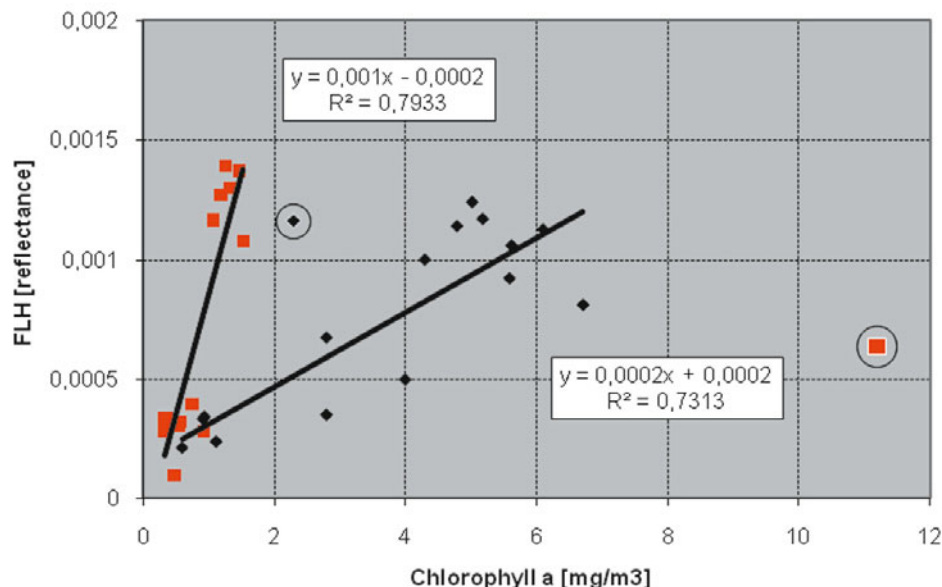
<i>Pixel classification</i>	<i>Description</i>
LAND	Land
CLOUD	Clouds
WATER	Water
<i>Product confidence flags</i>	
PCD_1_13	Reflectances in spectral bands
PCD_15	Algal 1
PCD_17	Algal 2
<i>Science flags</i>	
CASE2_S	Case 2 water
CASE2_ANOM	Anomalous scattering
CASE2_Y	Yellow substance loaded water
ICE_HAZE	Ice or haze
MEDIUM_GLINT	Glint correction turned on
HIGH_GLINT	Uncorrectable glint

Figure 4.30 illustrates the relationship found between  $FLH$  and  $chl$  values for the eight dates studied by Folkestad *et al.* (2006). Different clustering of data for each individual date is evident, which is indicative of wide variability in mutual dependences between the  $FLH$  and phytoplankton  $C_{chl}$ .

In order to reveal the effect of seasonality in  $FLH$  product variations, the dataset was divided in two parts: springtime (February and March) (black diamonds in Figure 4.30) and summertime (May and June) (red squares). Using this seasonal grouping, a linear regression analysis between  $FLH$  and  $chl$  levels was performed. It is worth mentioning that the dataset for the May–June period characterized by high  $FLH$  levels ( $>0.001 \text{ str}^{-1}$ ) and higher  $FLH:chl$  ratios are heavily influenced by the data including the *Coccolithophore* bloom observed on June 20, 2003.

The data of statistical regression for satellite  $FLH$  levels obtained under similar conditions (the same season of the year, the same water temperature, close PAR values) explain about 73–75% of the observed variance in the  $FLH:chl$  ratio. The slope of the linear relationship between  $FLH$  and  $chl$  varies by a factor of 5 from springtime ( $2.0 \times 10^{-4}$ ) to summertime ( $1.0 \times 10^{-3}$ ).

The dependence of the  $FLH:chl$  ratio on water temperature and PAR is illustrated in Figure 4.31. Even though a positive correlation is observed between  $FLH:chl$  and water temperature, PAR may be the most important factor affecting the  $FLH:chl$  ratio. Indeed, the correlation between  $FLH:chl$  and water temperature may simply be due to the fact that water surface temperature strongly correlates with PAR, due to seasonal variation in solar heating. Although not specifically studied, seasonal variations in the phytoplankton community composition certainly influence algal cell fluorescence efficiency and hence the  $FLH:chl$  ratio.



**Figure 4.30.** Based on the data in [Figure 4.25](#), FLH values (averaged over 5 pixels along each ship transect) are plotted versus NIVA FerryBox *in situ*  $C_{chl}$ . Red squares stand for data obtained during summer (May–June), while black diamonds refer to data collected during spring (February–March). Data points with a white edge were disregarded in statistical analysis because of high measurement uncertainty. *Courtesy:* Yunfei Wang and *in situ* data from Kai Sørensen, NIVA.

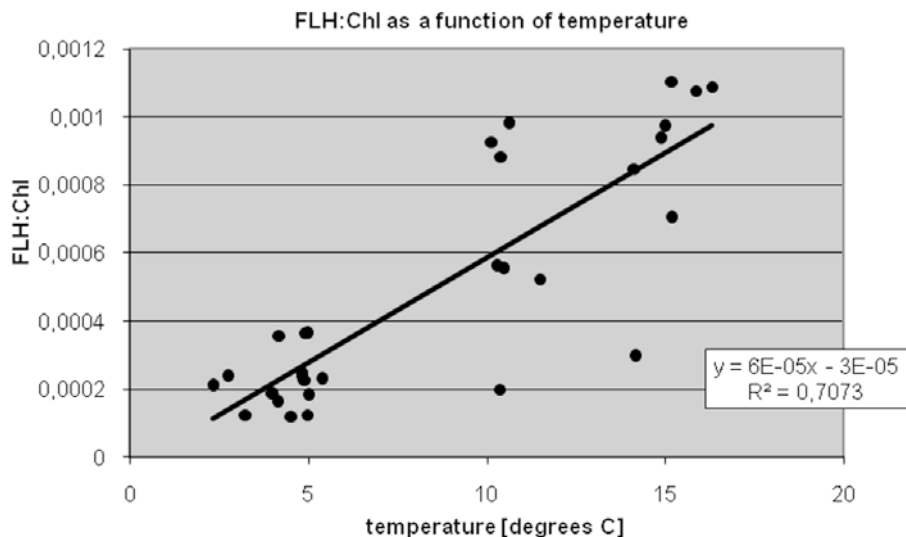


**Figure 4.31.** Statistical regression of the  $FLH:chl$  ratio as a function of (A) temperature and (B) photosynthetically available radiation (PAR) for the data set in [Figure 4.27](#). *Courtesy:* Yunfei Wang and *in situ* data from Kai Sørensen, NIVA.

Thus, although the above results are not exhaustive and further investigations are warranted, the conducted study provides strong evidence of the high potential of *FLH* data in a quantitative interpretation of algal blooms. However, quantitative use of *FLH* algorithms will be based on regional applications and validation during different periods of the phytoplankton vegetation season. Folkestad *et al.* (2006) conclude that the use of *FLH* data together with other complementary data, both spaceborne and *in situ*, can actually help reduce the number of “false” alarms of phytoplankton blooms that might arise from erroneously high *chl* levels indicated by standard ocean color algorithms.

However, as discussed in Section 3.5.3 and in more detail in Pozdnyakov and Grassl (2003), *FLH* data should be interpreted with caution, since phytoplankton fluorescence varies significantly (up to one order of magnitude) both spatially and temporally due to taxonomy, nutrient and light availability (also controlled by wind mixing conditions), grazing, and, as indicated above, water temperature, as well as other biogeophysical factors.

## 4.2 ROLE PLAYED BY SYNERGIES BETWEEN SATELLITE EO DATA IN HAB MONITORING

The discussion above demonstrates that combined use of optical satellite data using different retrieval algorithms with satellite-derived data on SST and surface winds proves to be instrumental at providing better information on the state of the aquatic environment including the circulation and wind speed impact on marine and coastal phytoplankton blooms. Needless to say, detection and monitoring of HABs will strongly benefit from a dense network of *in situ* observations, as these are crucial in definitively identifying any particular HAB event.

Such a synergistic approach has been developed further by combining the above spaceborne optical sensor data with satellite microwave SAR image interpretation (e.g., Pettersson *et al.*, 2007). This addition is motivated by at least two considerations. First, satellite SAR data provide information on water surface roughness (and, hence, wind mixing/water column mixing depth, and ultimately on the state of stratification conditions), but they can also provide complementary information on the presence and location of ocean and atmospheric fronts of various nature/zones of convergence, eddies and other hydrodynamic features, which, as discussed in Section 2.1, are important mechanisms in the context of algal bloom initiation and development. Second, practically unaffected by the presence of clouds and lack of daylight, SAR data have been examined as a tool for detection of algal blooms under cloudy conditions through the capacity of algae to produce accumulated biological surfactants that dampen surface roughness (e.g., Vesecky and Stewart, 1982; Johannessen *et al.*, 1996; Seuront *et al.*, 2006).

The important advantage of synergy between data from different satellite sensors is that limitations of one data type can be compensated for by the strengths of another, as indicated in the right column in [Table 4.5](#). This applies to sampling

**Table 4.5.** Detection capabilities and deficiencies using sensor synergy combining SAR, IR radiometry, passive microwaves, spectrometry, and altimetry for monitoring meso-scale dynamics and variability (Pettersson *et al.*, 2008).

Sensor type	Detection capability	Major deficiency
SAR radar cross-section	Expressions of fronts, filaments, and eddies are frequently seen at wind regimes below 10–12 m/s. Resolution of features can be finer than 1 km.	Difficult to make quantitative interpretations as the relationship between the NRCS and the surface current is not fully understood.
SAR Doppler velocity	The line-of-sight velocity of the moving ocean surface can be estimated from a Doppler centroid frequency shift, consistently extracted within the ASAR scenes.	The Doppler centroid shift results from the combined action of near surface wind on shorter waves, longer wave motion, wave breaking, and surface current. Validation of the surface current is highly needed.
AVHRR/AATSR Thermal infrared	Thermal gradients associated with meso-scale features are well captured at a resolution of about 1 km.	No imaging in presence of clouds. Often difficult to obtain regular cloud-free time series.
AMSR-E Passive microwaves	Thermal gradients are obtained at a low-resolution scale of about 25 km. Useful in areas with strong signals such as in the Gulf Stream and the Agulhas current. Impact of cloud cover is limited.	Resolution may sometimes be too coarse to resolve features at the 1–5 km scale of Rossby radius of deformation. Also less sensitive to SST in cold water.
MERIS/MODIS Spectrometers	Spatial distribution of surface chlorophyll, often connected with the advective and convective properties of meso-scale features are detected under cloud-free conditions.	No imaging in presence of clouds. Often difficult to obtain regular cloud-free time series. Case 2 water implies extra care in corrections for suspended matter. Light dependent—does not work under winter darkness.
Altimetry	Sea level anomalies related to surface slopes are used to compute surface geostrophic currents.	Bands of strong convergence and divergence can be difficult to detect.

parameters like spatial resolution, sensitivity to clouds and atmospheric boundary layer processes, and sensitivity to the physical properties of the ocean.

The benefits of the synergistic use of satellite data for studies of ocean productivity and mesoscale ocean circulation features can be demonstrated (e.g.,

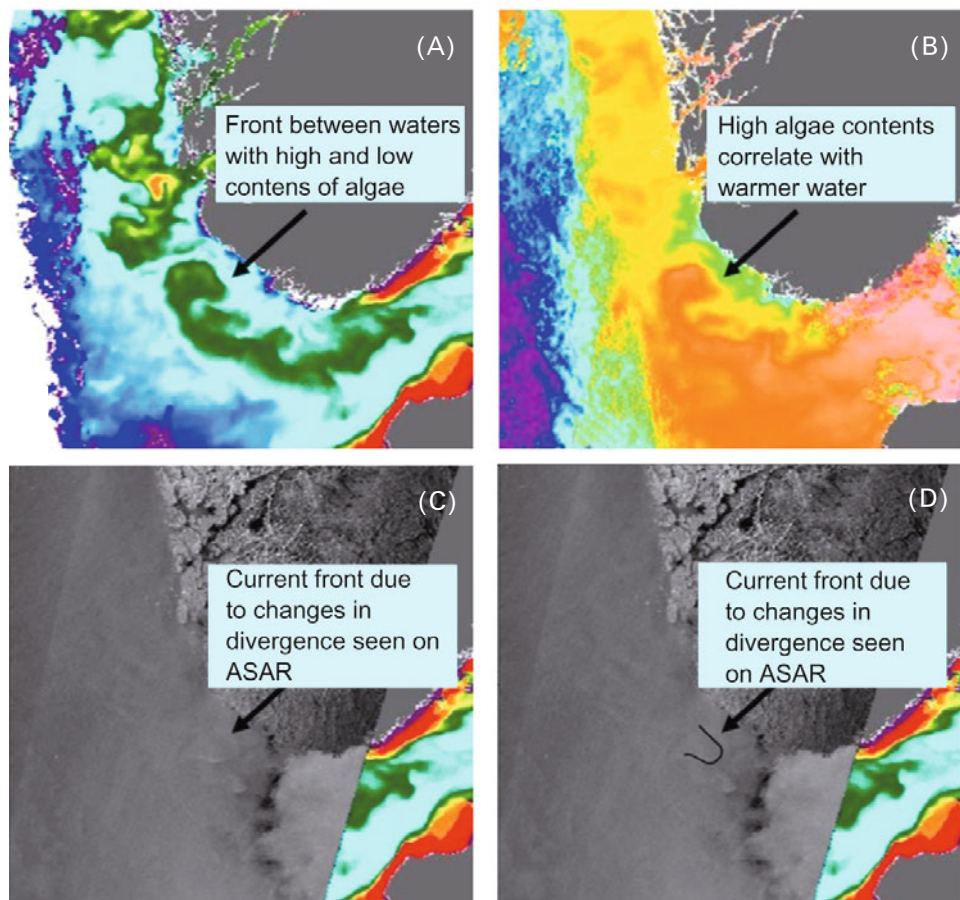


**Figure 4.32.** Sensor synergies illustrated with EO images from June 5, 2006 illustrating the co-location of the ocean fronts in the Norwegian Coastal Current expressed in the gradients in (A)  $C_{chl}$ , (B) sea surface temperature, and (C), (D) ASAR radar backscatter, respectively.

in the above case studies for the North Sea, Skagerrak, Kattegat, southern and south-western Norwegian waters). Figure 4.32 illustrates that mutually supplementing synoptic satellite EO images in the visible, IR, and microwave reveal the interrelationships between such features as ocean fronts, current shear, and convergence zones, including coastal current extension and boundaries, eddy circulation patterns, and biological film/high-biomass surface algal blooms.

The potential of the synergistic use of remote-sensing data—in the visible, IR, and microwave spectral regions, as well as spaceborne radar altimetry data—to enhance data interpretation can be further illustrated through a number of dedicated studies. Svelkovsky and Shandley (2001) employed a combination of AVHRR (channel 1: 580–700 nm, channel 2: 720–1,000 nm; spatial resolution: 1.1 km at

nadir) and ERS-1 SAR image data for the detection of plankton blooms in sediment-free oceanic waters along the U.S. west coast. Occurring in spring and summer, upwelling events there provide extremely favorable study conditions, since they give rise to intense, offshore-reaching algal blooms in waters largely devoid of suspended terrestrial matter.

Svelkovsky and Shandley (2001) used the atmospheric correction approach suggested by Stumpf and Pennock (1989) for moderately turbid estuaries. A very simple color ratio index suggested by Stumpf and Tyler (1988) was used as a proxy for  $C_{chl}$ . The actual  $chl$  concentrations measured across the study area varied between 1 and 12 mg/m<sup>3</sup>.

The Bragg wave dampening effects of biological surfactants are known to produce low radar return patterns in SAR images when surface winds are below 7 m/s (Ochadlick *et al.*, 1992; Johannessen *et al.*, 1996). The important issue in this regard is the variety of phenomena that can result in wave dampening. Indeed, not only biological surfactants, but also wave-current interactions, marine atmospheric boundary layer variability/formation of cool water surface films due to boundary layer stratification, upwelling, and natural oil spills can be at the origin of low SAR response signals.

In the area studied by Svelkovsky and Shandley (2001), low wind conditions (wind speeds mostly <2 m/s) persisted during the period of high-quality spaceborne data. Relatively broad as well as narrow elongated patterns of low backscatter were visible in SAR images. These areas generally correspond to the locations of high reflection, as determined from AVHRR visible data. Because the wide area of enhanced  $C_{chl}$  was situated within a well-defined upwelling area (distinctly expressed in respective thermal AVHRR data), the SAR patterns also showed accordance with the surface thermal structure. However, important differences between SAR features and thermal and plankton spatial distributions were also apparent from respective comparisons.

However, a number of environmental conditions (such as wind, waves, currents, eddies, slicks, surfactants other than of phytoplanktonic nature, sea ice, etc.) affect the ocean surface in such a way that the biogeophysical interpretation of the radar backscatter might become ambiguous.

The importance of wind action on SAR patterns generated by phytoplankton was evidenced (e.g., in our study of HAB blooms in the Baltic Sea). In the summer of 2005, there was the largest cyanobacterial bloom in the Baltic Sea seen in recent years. MODIS and MERIS images over the bloom-affected area were processed by us making use of the operational algorithm developed for clear and turbid natural waters described in Chapter 3 (Pozdnyakov *et al.*, 2005; Korosov *et al.*, 2009). In the hydro-optical model embedded in the algorithm, the phytoplankton component corresponded to the cyanobacteria cross-sections of absorption and backscattering (Siegel *et al.*, 2005).

Figures 4.33 and 4.34 compare the  $chl$  spatial distributions obtained using standard MODIS and MERIS retrieval algorithms with the corresponding mosaics obtained when the BOREALI cyanobacteria-specific algorithm is applied. First and foremost, the standard products produced by MODIS and MERIS (Plate a

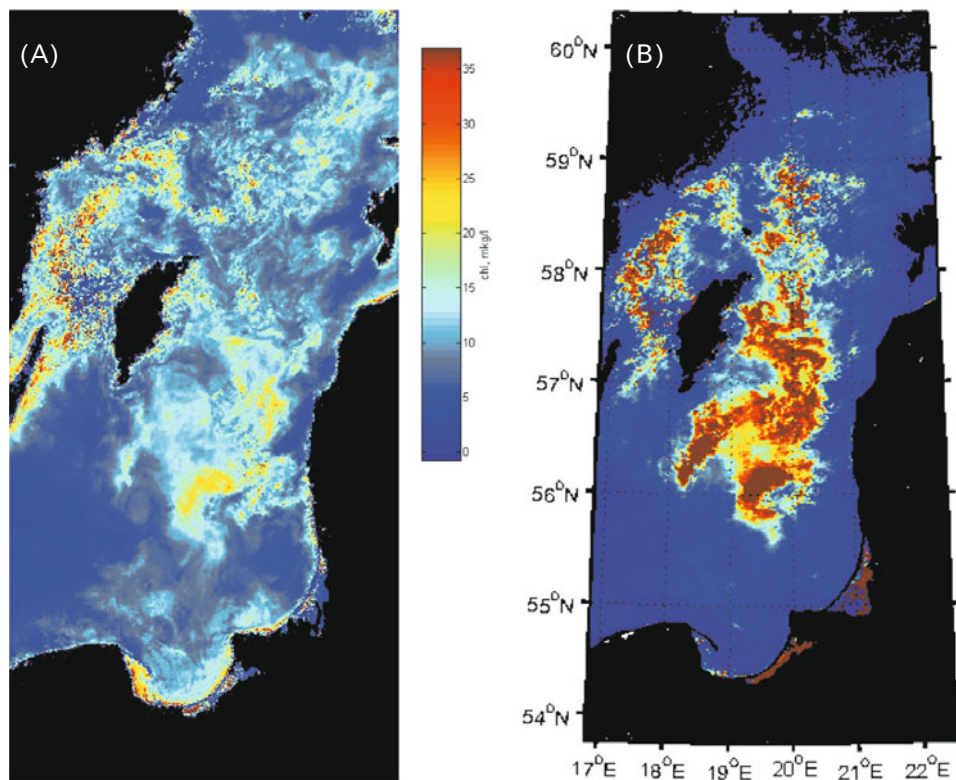


**Figure 4.33.** An example of a cyanobacterial bloom in the Baltic Sea on July 25, 2005: (A) resolved with standard processing of NASA MODIS data. (B) Same data processed with the NIERSC cyanobacteria-specific bio-optical retrieval algorithm.

in both figures) differ very significantly not only in terms of *chl* concentrations, but also spatial patterns retrieved.

At the same time, the spatial patterns emerging from the application of the BOREALI bio-optical algorithm to both the MODIS and MERIS satellite *raw* (i.e.,  $R_{rsw}(\lambda)$ ) data resolves very similar features when comparing Figures 4.33 and 4.34. However, though similar, both *chl* distributions are, first, not completely identical in gradients and, second, they differ very essentially in terms of the absolute values of retrieved  $C_{chl}$ .

These comparisons indicate that not only do both standard algorithms work differently, but the radiation fluxes (and, consequently,  $R_{rsw}(\lambda)$ ) measured by both satellites are also in disagreement with each other—the issue that we discuss below.

To examine the feasibility of the synergistic use of ocean color (MODIS, MERIS), active microwave sounding data, ASAR (ENVISAT), and IR (MODIS) images were obtained for this area synoptically. The combined data distinctly reflect some salient features observable on the Baltic Sea water surface, such as a meso-scale

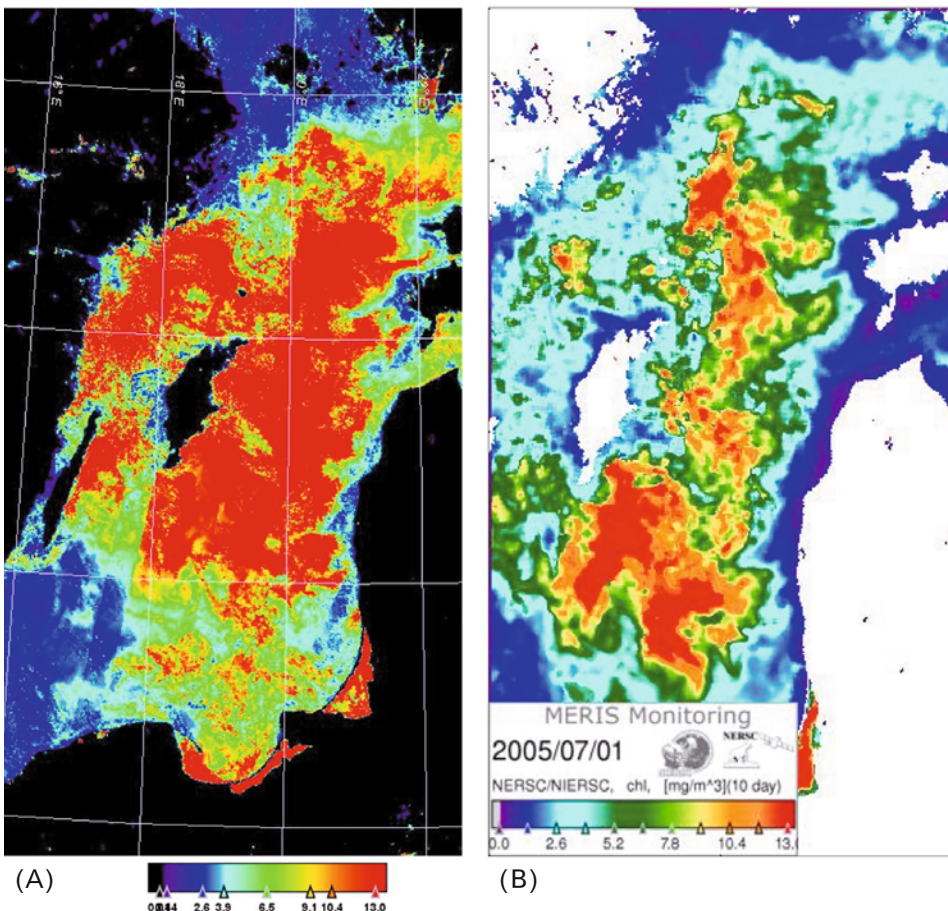


**Figure 4.34.** Another example of a cyanobacterial bloom in the Baltic Sea on July 1, 2005: (A) resolved with standard processing of ESA MERIS RR ( $1.2 \times 1.2$  km resolution) data. (B) Same data processed with the NIERSC cyanobacteria-specific bio-optical retrieval algorithm.

eddy to the south of Gotland (Figure 4.35), and a front caused by the coastal current in the southernmost area of the Baltic Sea (Figure 4.36 and Figure 4.37, lower part).

However, apart from the hydrodynamic features revealed above, joint analysis of the ASAR data (Figure 4.37B) and the SST (Figure 4.37A) failed to co-register the surface expression of the major HAB area provided by ocean color data (Figures 4.33 and 4.34). This conclusion disregards the fact that the algal concentrations were very high, indicating that the surface algal biomass should be sufficient to damp out the capillary surface roughness resolved in the radar backscatter. This emphasizes the fact that environmental mechanisms and forcing influencing radar backscatter are multifaceted and originate as a result of physical oceanic, atmospheric, and actual biochemical conditions.

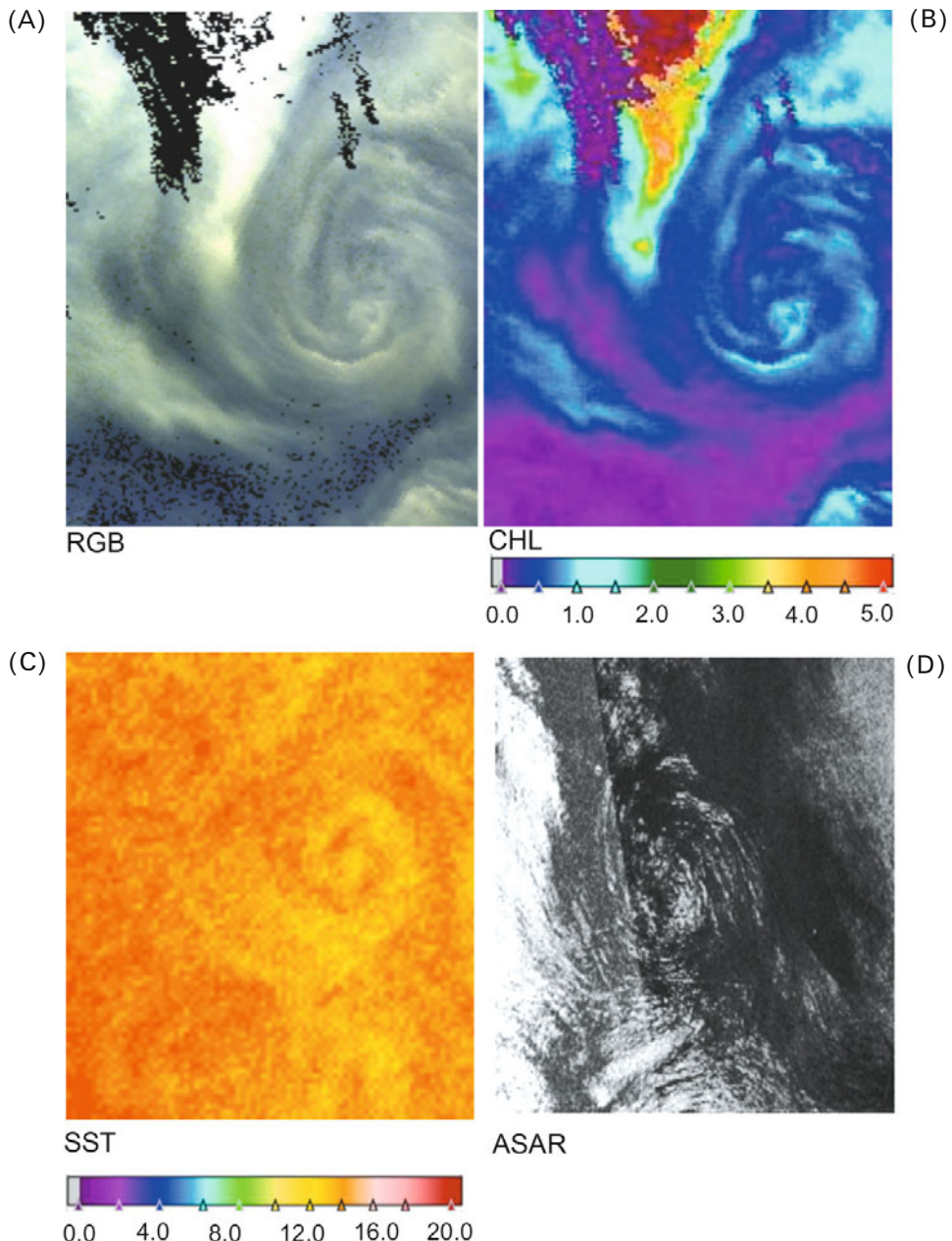


**Figure 4.35.** A meso-scale eddy during a cyanobacteria bloom in the Baltic Sea as revealed in (A) visible (RGB from MERIS, full resolution, 300 m), (B) IR (SST from MODIS), (C) microwave (surface roughness from ASAR), and (D) the *chl-a* concentration (MERIS). RGB = a composite image from MERIS channels in the red, green, and blue parts of the spectrum.

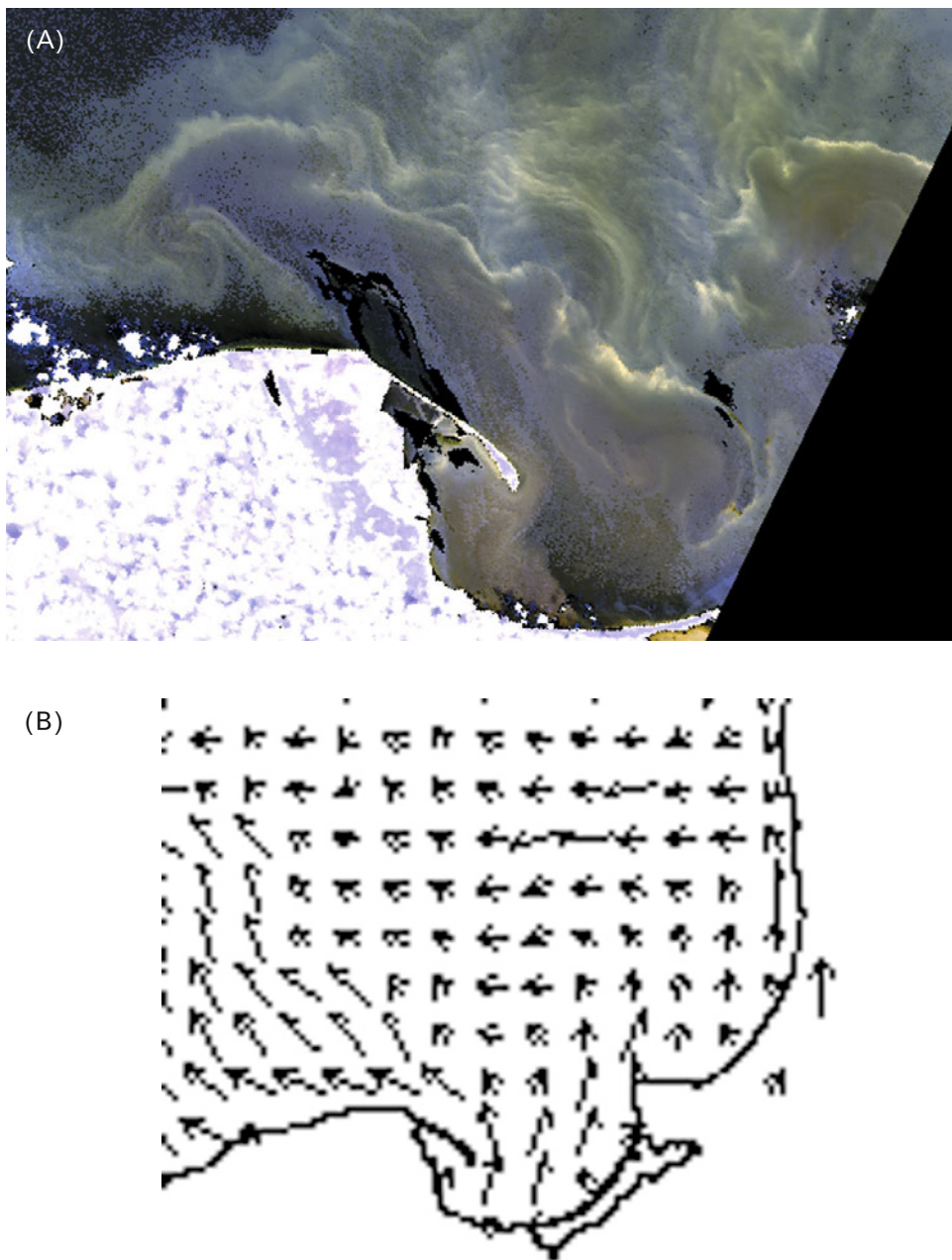
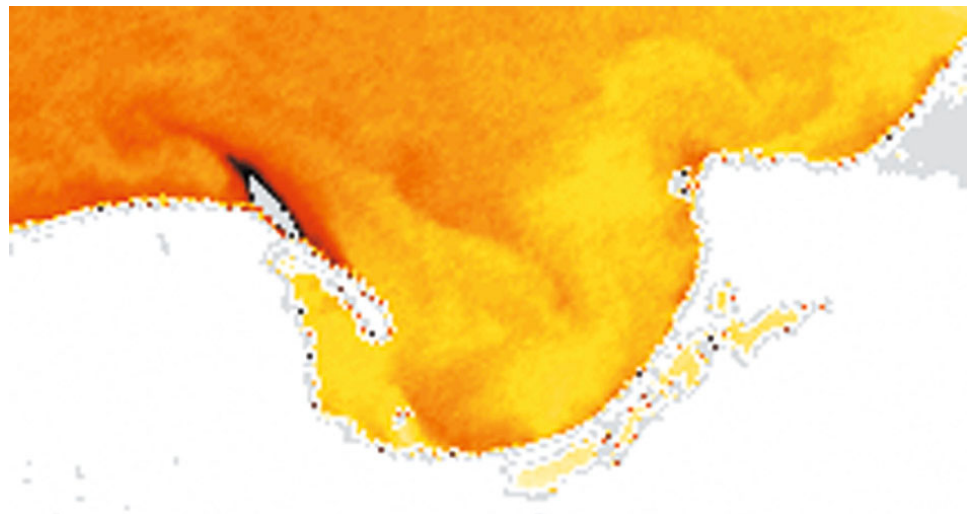
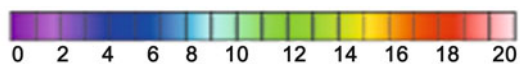
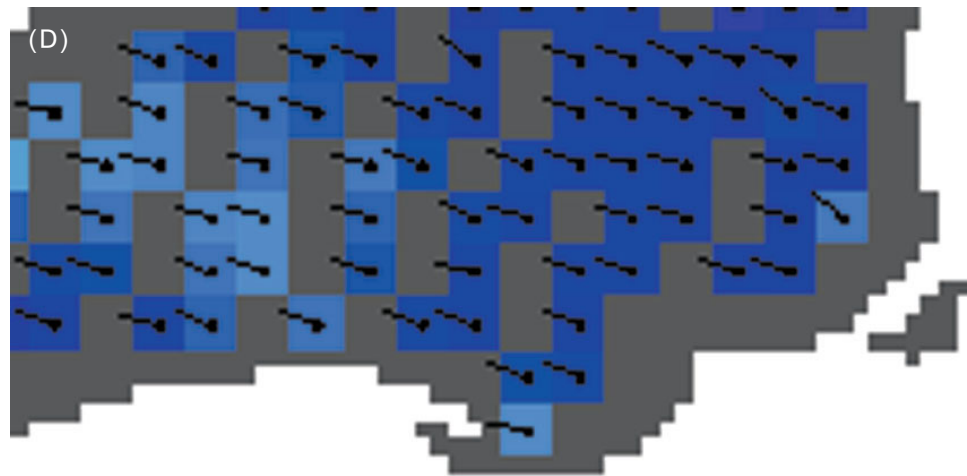


**Figure 4.36.** A coastal front in the southernmost part of the Baltic Sea revealed in (A) the visible (RGB from MERIS, full resolution, 300 m), (B) thermal IR (SST from MODIS), (C, opposite page) surface winds from QuickScat), and (D, opposite page) modeled ocean currents (from the GFAMNH model). RGB = composite image from MERIS channels in the red, green, and blue parts of the spectrum.

(C)



(D)



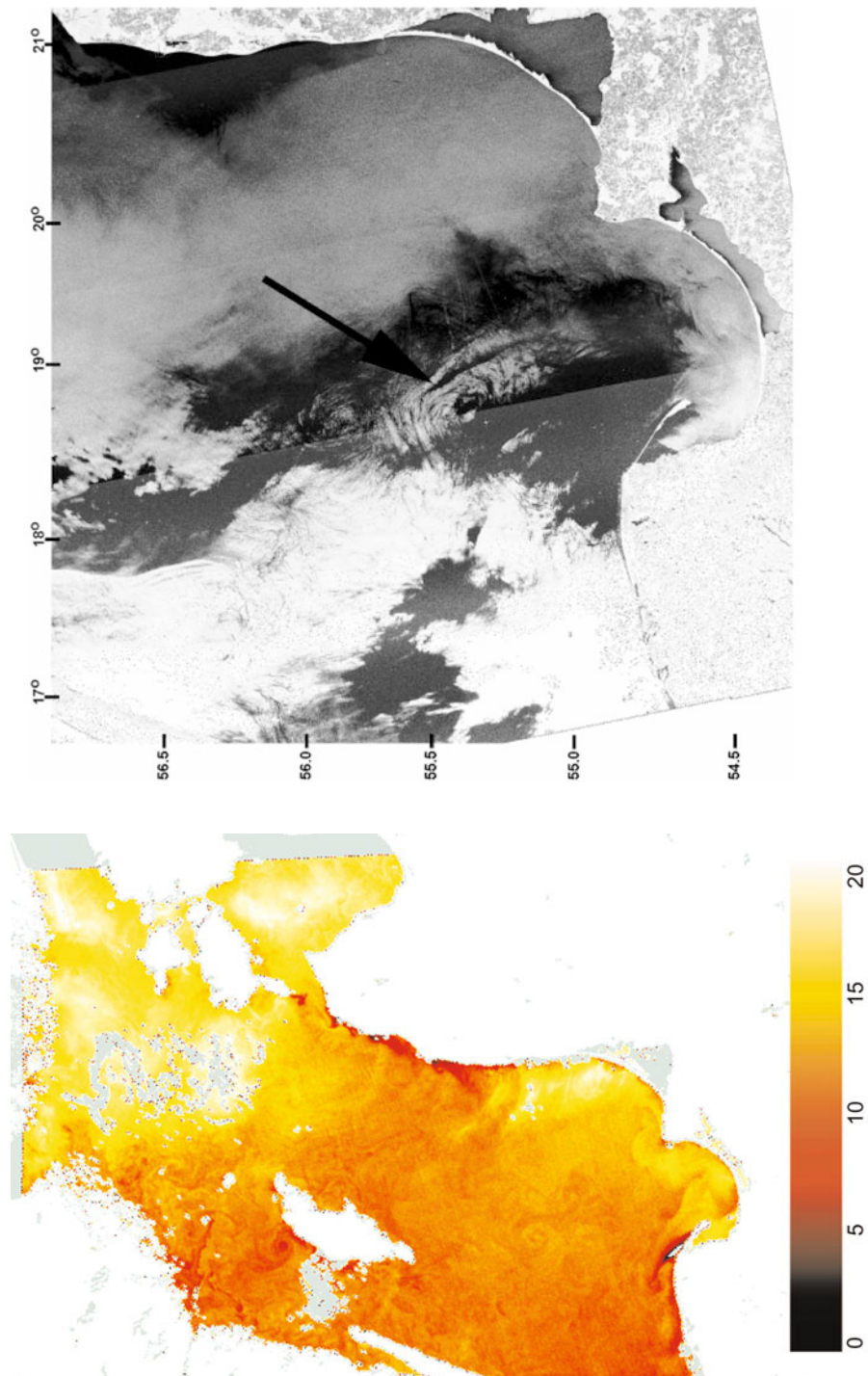
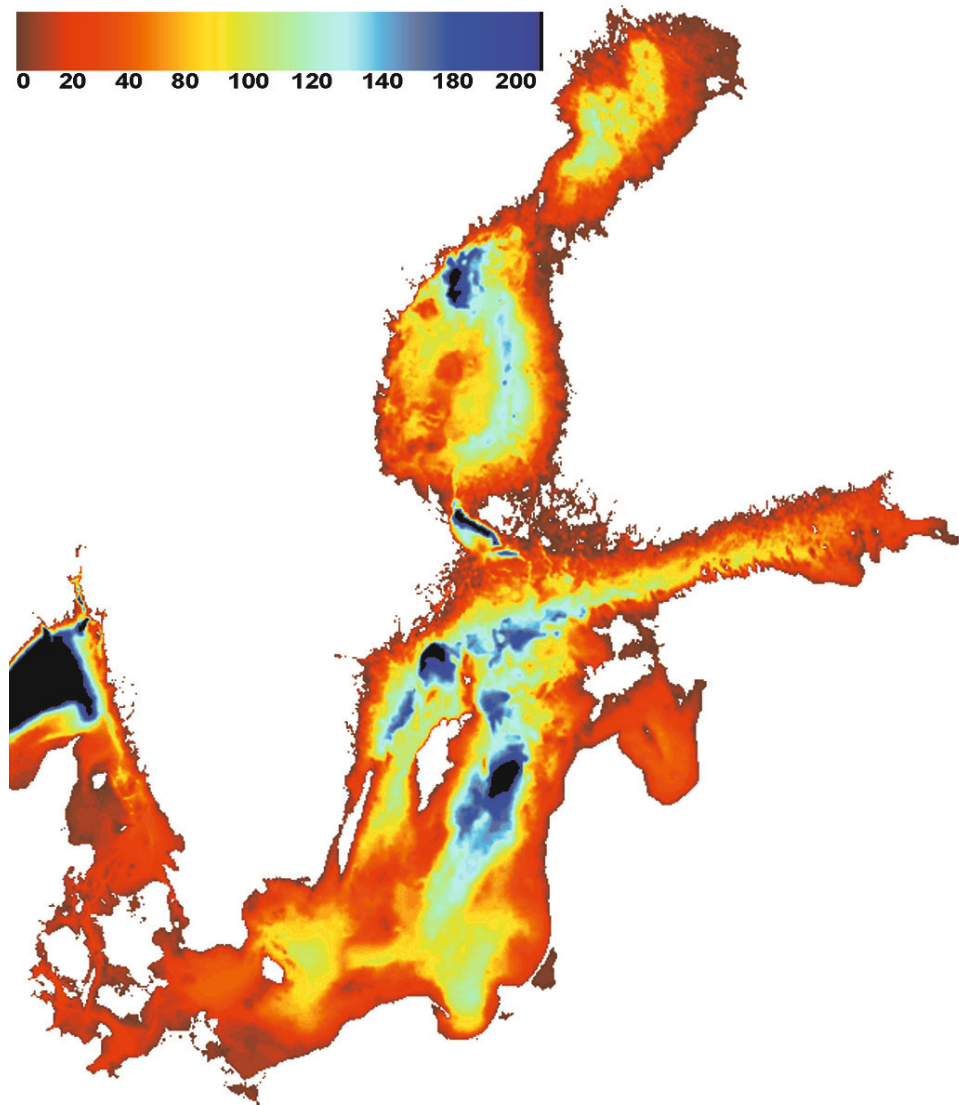


Figure 4.37. A meso-scale eddy in the Baltic Sea revealed in (A) sea surface temperature (SST in °C) derived from the MODIS data and (B) revealed in the surface roughness as resolved by Envisat ASAR.

Our analyses have shown that although the conditions for formation of algal surfactants were generally favorable because of the occurrence of a major bloom in the deepest parts of the Baltic Sea ([Figure 4.38](#)) and surface water currents were slow ( $2.5 \text{ cm s}^{-1}$ ), fairly high winds (about  $10 \text{ m s}^{-1}$ ) masked out the impact of biological surfactants at the water surface. Obviously, high winds modulated the slick produced by the algae, and the cyanobacteria, inconvenienced by wind-induced turbulent



**Figure 4.38.** Bathymetry of the Baltic Sea  
(<http://www.google.ru/imglanding?q=Baltic%20Sea%20Bathymetry>).

mixing, moved downward to reach more comfortable conditions. Accordingly, there was no high algal biomass available at the surface to dampen the capillary waves enough to influence the radar backscatter signal.

So, these case studies explicitly indicate that—under favorable conditions—first and foremost, low surface winds ( $>8\text{--}10\text{ m s}^{-1}$ ), zones of convergence and divergence due to current shear and eddies, ocean fronts, current speed gradients and circulation features inherent in ocean dynamics are revealed in SAR images. SAR data can then be used to identify areas of wave dampening by surface films of biological or chemical (natural or anthropogenic) origin. However, due to ambiguities in the bio-geophysical mechanisms and processes of origin, SAR should be exploited with caution, because definitive interpretation of slick features arising from algal blooms is plagued by uncertainties arising from a number of non-biological processes, which can, however, result in ocean surface conditions causing similar patterns in SAR images. Interpretation of SAR images without synoptically optical and/or IR data are accordingly very difficult since the environmental mechanisms dampening surface capillary waves are complex. Notwithstanding these limitations, in many instances the synergy of ocean color, infrared, and SAR satellite data in algal bloom monitoring is useful in research and can be used to supplement HAB detection, delineation, and monitoring.

### 4.3 NEAR-REAL TIME SURVEILLANCE OF HABs

Due to the spatial and temporal variability of HABs, it is important for monitoring services exploiting the use of satellite EO data to have at their disposal a *near-real-time processing system* (Johannessen, O. M. *et al.*, 1989a). Some national monitoring systems will be described below, including components of the downstream services of the European Global Monitoring for Environment and Security (GMES) initiative.

#### 4.3.1 Norwegian HAB-monitoring services

The Nansen Center has made HAB monitoring and forecasting one of its strategic research foci since the 1980s (Johannessen *et al.*, 1989). A near-real-time HAB-monitoring system was developed (Pettersson *et al.*, 2006) as soon as ocean color satellite EO data became regularly available in 1998. This system was further supplied with additional research components provided under the EC HABILE project (Harmful Algal Bloom Initiation and Prediction in Large European Marine Ecosystems—EVK3-CT2001-00063) in cooperation with several European partners. It was further improved by embedding an autonomous system for near-real-time processing and dissemination of MERIS images and their interpretations (Pettersson *et al.*, 2006). Using state-of-the-art web map technology (WMS and WFS), satellite and shipborne data and model predictions can be integrated and distributed by means of a web portal (see <http://HAB.nersc.no/> and Figure 4.39). The system has been implemented and applied to ocean waters outside the Norwegian sphere of influence, such as Central America and the Venetian Lagoon.

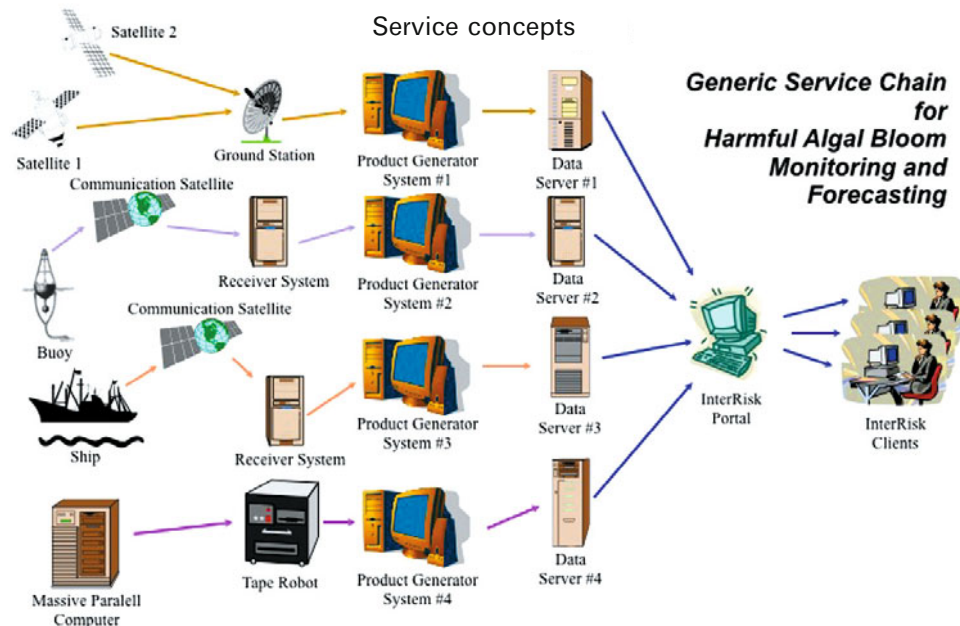


**Figure 4.39.** The generic chain for delivery of HAB monitoring and forecasting services developed at NERSC. The delivery of information can be distributed between several service providers, but integrated in the user front end. *Courtesy: Torill Hamre, NERSC.*

Monitoring HABs that affect Norwegian coastal waters is a major national concern due to the severe impact HABs have on the important and growing aquaculture industry. Accordingly, the fishery authorities and industry have implemented monitoring services based on *in situ* observations from some 40+ coastal stations. Weekly reports (Figure 4.40) on the algal bloom situation in coastal and inshore waters are published on <http://algeinfo.imr.no>. Furthermore, the food and nutrition authority provides recommendations related to safety issues in consuming seafood. In cooperation with commercial shipping NIVA has implemented automatic FerryBox systems providing automatic ship measurements along the Norwegian coast and in the Skagerrak and Kattegat waters (Figure 4.41) of the key biophysical ocean parameters related to the HAB situation (see <http://www.niva.no>).

The satellite EO-based service production chain for information generation is based on near-real-time access to the ESA on-line MERIS rolling archive and MODIS data from NASA. Currently, EO data are gathered from the GMES core services node in Europe. Both MERIS RR and FR data at, respectively, 1.2 km and 350 m resolution are acquired and processed and then tailored to the application or to individual user needs. The rolling archive is automatically checked daily for new relevant EO data updates within the geographic area of operation(s) of the service concerned and subsequently new MERIS data are downloaded at a given time interval (every afternoon). These standard MERIS Level-2 data are locally stored

**Algeinfo**

<http://algeinfo.imr.no/>

**Algeinfo**  
- En ukentlig informasjon om algesituasjonen langs norskekysten

SINTEF NIVA FISKERIDIREKTORATET

Hjem Tidligere algeinfo Algedatabase Stasjonsoversikt Nyttige lenker språk:

Dato: 11.07.2011 - Neste algeinfo 18.07.2011

Algeinfo er en ukentlig informasjon som utgis av Havforskningsinstituttet i samarbeide med SINTEF, Fiskeridirektoratet og NIVA. Ønsker du informasjon om hvorvidt blåskjell er spiselige eller ikke, anbefales Mattilsynet sin website eller blåskjelletelefonene 820 33 333.

Vi kan kontaktes på [e-mail](#)

**Området Finnmark-Vikna (1-2)**  
Det ble registrert høy algebiomasse i Øst-Finnmark, der *Skeletonema* dominerte, men også betydelig forekomst av *Heterocapsa triquetra*. Middels høy algebiomasse i Vest-Finnmark og Troms der dinoflagellater dominerte algeforekomstene. I Alta var algebiomassen dominert av *Dinophysis norvegica*, *Heterocapsa triquetra* og *Scrippsiella trochoidea*. I Tromsø-området dominerte *Protoperidinium* pellucidum og i Sør-Trøms var *Ceratium* dominerende med C. tripos som den mest framtredende arten. *Alexandrium* registreres i hele området, med forekomst av A. tamarensis over *faregrensen* i Alta og opp mot *faregrensen* i Tromsø-området. I Nordland er det artsrike algesamfunn med innslag av både kiselalger *Skeletonema*, *Chaetoceros*, *Leptocylindrus*, *Dactyliosolen*, *Pseudonitzschia* og dinoflagellater *Ceratium*, *Protoperidinium*, *Scrippsiella*, *Heterocapsa*, *Ensiculifera*). I Nordfjorden er det en oppblomstring av kiselalger dominert av *Skeletonema*, ellers er det små totalbestander/svake blomstringer av kiselalger i prøver fra Nordland denne uken. Både *Alexandrium* og *Dinophysis* påvises i spormengder flere steder i området.

**Området Vikna-Stad (3-3)**  
Det er varierende algemengder i Midt-Norge med små totalbestander av kiselalger og/eller dinoflagellater til kiselalgedominerte oppblomstringer. De viktigste kiselalgene i dette området denne uken er *Pseudonitzschia*, *Skeletonema*, *Leptocylindrus* og *Dactyliosolen*. Det er også et høyt innslag av dinoflagellater i håvtrekkprøver hvor *Ceratium*, *Protoperidinium*, *Gonyaulax*, *Amyxylum*, *Heterocapsa* og *Scrippsiella* er vanlige. Det er også spormengder av kalkflagellater i området, spesielt i Møre og Romsdal. Og ved Ålesund er det påvist sporebestander av både *Spatulodinium pseud Noctiluca* (dinoflagellat) og *Acanthocystis quattropisina* (kalkflagellat) den uken. *Dinophysis* er vanlig i hele området, og forekommer i mengder over *faregrensen* i Trondheimsfjorden. *Alexandrium* påvises i mengder under *faregrensen* ved Molde, i Trondheimsfjorden og på Fosen.

**Stad-Flekkefjord (3-4)**  
Ingen prøver fra Nordfjord og fortsatt lave algeforekomster i Dalsfjorden. Ytterst i Sognefjorden, i Gulen, er algebiomassen fortsatt høy og dominert av *Chaetoceros curvisetus*, men også en del *Skeletonema*. Også høy algebiomasse i Hjeltefjorden der *Skeletonema* dominerer. Moderate algeforekomster i Osterfjorden der *Dinophysis norvegica* er mest framtredende med forekomst over *faregrensen*. I Sunnhordland er algebiomassen generelt høy. I ytre strok registreres et blandingsplankton der kiselalger er den mest framtredende gruppen med *Chaetoceros curvisetus* som den mest framtredende arten. Sterk dominans av C. curvisetus i ytre deler av Hardangerfjorden. Fortsatt registreres *Alexandrium* flere steder i området men i lavt antall. Økende algeforekomster ved Svelø, det er hovedsakelig kiselalgen *Chaetoceros socialis* som dominerer algesamfunnet her med 8 mill celler/L. Lave til moderate totalbestander i Midt-Rogaland. Kalkflagellaten *Emiliania huxleyi* fremdeles fremtredende i dette området, spesielt ved Tyssvær hvor det ble registrert forekomster på 1 mill celle/L. Kiselalgen *Proboscia alata* er også denne uken vanlig i dette området. Moderate algeforekomster ved Egersund, artsrik algesamfunn dominert av kiselalgen *Proboscia alata* og *Chaetoceros*.

**Området Flekkefjord-Hvaler (4-5)**  
Økende algebiomasse lengst sør i området. Det er dinoflagellatene som bidrar mest til biomassen. *Ceratium fusus* er dominerende sammen med slekten *Dinophysis* og *Scrippsiella*. Det registeres økende kiselalgeforekomster (1,7 mill celle/L) ved Risør. Lave algeforekomster i Indre Oslofjord. Moderate kiselalgeforekomster ved Tønsberg og Hvaler. *Dinophysis norvegica* og *Dinophysis acuminata* er vanlig i hele området, og *Dinophysis acuminata* ble registrert i mengder over *faregrensen* ved Arendal og Risør. De høyeste forekomstene av *Dinophysis norvegica* ble registrert ved Moss (2520 celle/L).

**Ønsker du å motta en e-post når vi publisere ny algeinfo?**

E-post:  Meld på

Copyright © 2011, Havforskningsinstituttet.

Find: Q cha Next Previous Highlight all Match case

The map shows the coastline of Norway with various sampling stations marked by red dots. A legend titled 'TEGN/PORKLARING' (Legend) provides the following information:

- Large red dot: Store algeforekomster (Large algal blooms)
- Medium red dot: Moderate algeforekomster (Moderate algal blooms)
- Small red dot: Små algeforekomster (Small algal blooms)
- Red cross: Mye alger, skadelig for fisk (Many algae, harmful for fish)
- Red cross with 'A': Alexandrium sp. Alger som kan forårsake DSP (Paralytic shellfish poisoning)
- Red cross with 'D': Dinoflagellat sp. Alger som kan forårsake DSP (Diarrhetic shellfish poisoning)

Numbered locations on the map correspond to specific sampling areas:

- 1: Northernmost point (likely Finnmark)
- 2: North coast (likely Tromsø area)
- 3: Central coast (likely Sunnhordland)
- 4: Southern coast (likely Rogaland)
- 5: Southernmost point (likely Flekkefjord/Hvaler area)

**Figure 4.40.** An example of the weekly AlgeInfo bulletin assessing the state of algae populations along the coasts of Norway. The bulletin is published weekly during the algae growth season, typically from March until October. Source: <http://algeinfo.imr.no>

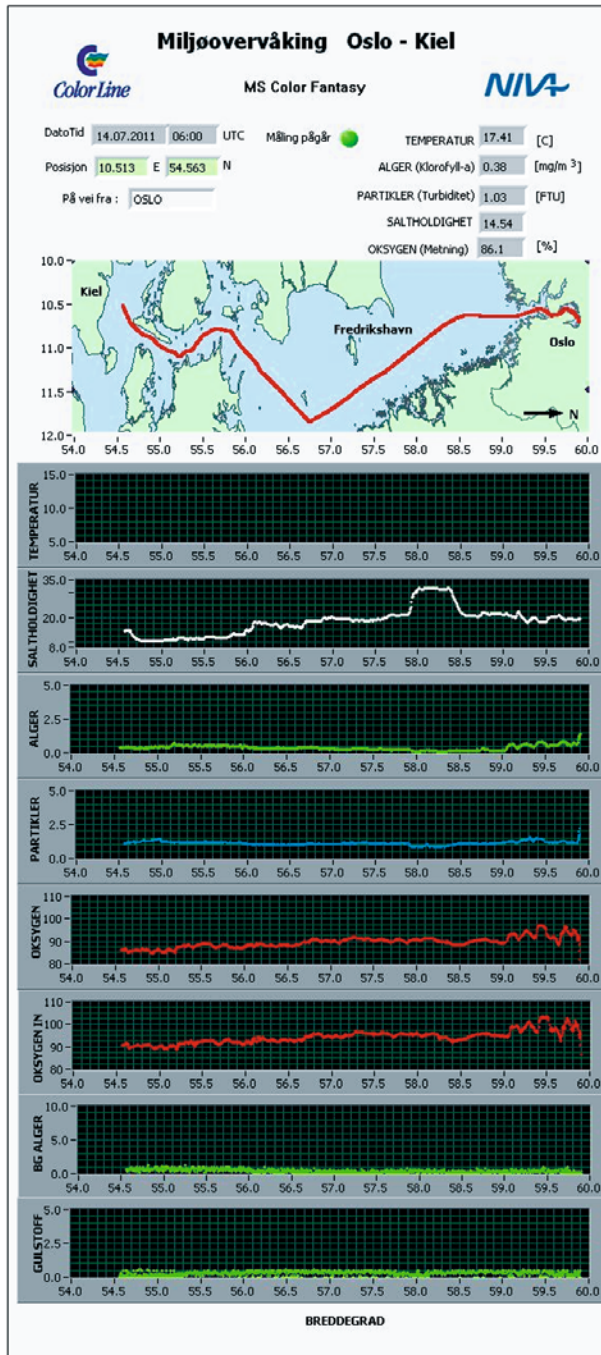


**Figure 4.41.** An example of NIVA FerryBox observations acquired from several ships of opportunity in Norwegian coastal and off-shore waters. Source: <http://www.niva.no>

at NERSC for further processing and generation of a range of service products. The software routines for processing and hardware storage capacities are regularly improved in order to make the service performance more robust and routine processing more efficient with less human interaction in case of irregularities. A modular-based solution has been developed, with a structure that makes it re-usable for new geographical areas and for the introduction of new products.

Commonly, satellite Earth Observation data are organized at no fewer than three levels, due to their level of processing and aggregation: Level 1 is the sensor-based engineering unit; Level 2 is geophysical retrieval of the parameter to be mapped; and Level 3 is time and space binning of geophysical quantities.

A production line for EO data acquisition, processing, product generation, and dissemination (web map server) for each study area is implemented, where level-2 data are used to generate higher level information for users. Satellite-based water quality information is being ingested into the service in near real time on a daily basis by accessing data sources made available by the space agencies (e.g., the ESA ground segment for MERIS and other satellite EO data). The products are generated according to the NERSC-specific processing chain illustrated in [Figure 4.42](#), which includes three major tasks:

- Task 1: Access to and acquisition of EO Level-1 and 2 data products
- Task 2: Production Processing Line and Statistical Binning of EO data products
- Task 3: Data Integration, Analysis, and Assessment/Visualization

**Task 1. Access to EO Data (Level-1/2).** Access to satellite EO data is established through the near-real-time archives of the space agencies for supply of Level-1B or Level-2 satellite EO data. In the context of GMES such data is available through the FP7 Marine Core Services for European waters. The rolling archive option is currently in operation and a script to download MERIS data is initiated within fewer than 12 hours (i.e., on the following evening after the morning satellite overpass).

**Task 2. Production Line for EO Product Processing (Level 2) and Statistical Binning (Level 3).** The production line for the geographical sub-sampling and presentation of EO data products is based on daily generation of merged 7-day binned products as well as monthly binning of regional data once per calendar month for all derived parameters. The generated products are based on ESA MERIS RR (1.2 km) and FR (350 m) data. These products are the concentrations of *chl*, total suspended matter (*tsm*), dissolved organic matter (*dom*), mean square error (difference between measured and reconstructed spectra of subsurface remote-sensing reflectance—an error estimate), *FLH*-based *chl* concentration, an RGB image, and SST. Both in-house developed (BOREALI) and public domain (e.g., BEAM and SeaDAS) software are used for the processing and generation of Level 2 and 3 products. The BOREALI processing algorithm ([Figure 3.16](#), Pozdnyakov *et al.*, 2003) is unique in that it simultaneously retrieves the concentrations of *chl*, *tsm*, and the yellow substance

Level	Steps	Data format
Download	MERIS, MODIS, AATSR on FTP (ESA rolling archive, NASA FTP subscription)	N1, HDF
	Data download	
	MERIS, MODIS, AATSR on NERSC server	N1, HDF
L2C	Reading N1; Reprojection; Calculating additional products; Application of advanced algorithms; Saving;	
	L2C data (algal_1, algal_2, total_susp, yellow_subs, kd490, sst_aqu, lmchl, lmtsm, lmdoc, lmmse)	MAT
L3	Binning input data into 1, 7 and 30 day averages	
	L3A data (averaged products)	MAT
	Visualization of averaged products	
	L3B data visualized maps with concentration distributions	JPG, PNG
Dissemination	WEB-visualization	
	Data on the screen and web-map for end users	HTML, KML

**Figure 4.42.** Schematic of the various levels of data processing implemented in the near-real time processing of satellite EO data at the Nansen Center for use in monitoring of HAB events in coastal waters as well as other applications.

(YS) absorption coefficient as well as the mean square error (MSE) and produces flags for delineating areas of inaccurate atmospheric correction.

Further, the median data values from the last seven days are daily calculated for each pixel. Median values are also calculated for each calendar month, which is done on the first day in every month ([Figure 4.43](#) and [Figure 4.44](#)). They are used for trend change analysis such as in the context of climate change impact on marine environments.

EO data products are generated as image files for web display (GeoTIFF), in KML format for use in GoogleEarth, and as data files (e.g., MatLab) for further processing and generation of derived products. Data products from daily, weekly, and monthly averaged data files are visualized and accessible via the internet at <http://HAB.nerc.no/>

**Task 3. Data Integration, Analysis and Assessment.** Finally, the information products generated are ingested in a web map service to be merged and integrated

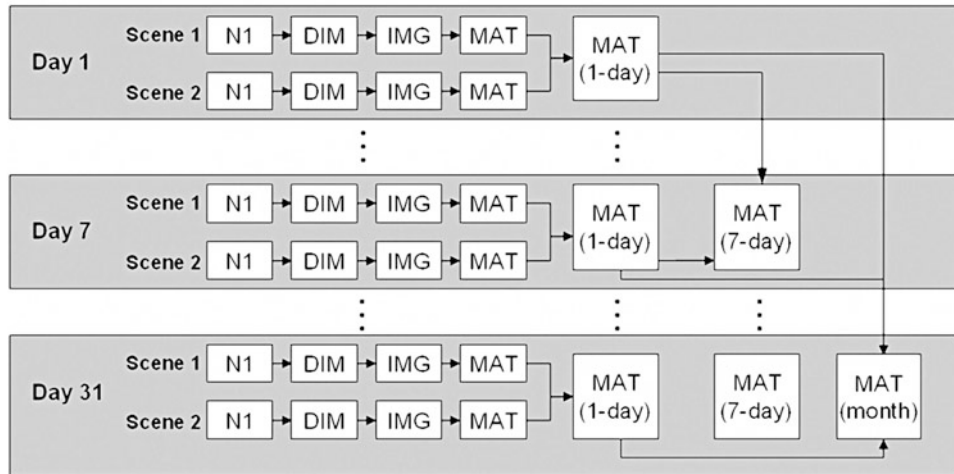


**Figure 4.43.** The sequence of data files generated for the time-averaging (binning) of MERIS data in the near-real time satellite Earth observation processing system in operation at the Nansen Center.

with the environmental information provided by satellite EO, *in situ*, and modeling information sources.

At the Nansen Center an OGC Web Map Service (WMS) system (OGCv) is implemented that has distributed data nodes, each providing an OGC WMS interface, and a portal that communicates with the nodes and provides various client applications such as a map viewer, profiler, and metadata catalogue. The system uses Java and XML technologies, with the Open Source University of Minnesota (UMN) MapServer, running as a CGI application under the Apache web server that provides the core web GIS client and OGC WMS (both client and server) functionality. The main components of this system (based on DISPRO-2) are the catalogue, the profiler, and the web GIS. In brief, the catalogue keeps track of all products available through the providers' data nodes, the profiler allows users to tailor the system to deliver specific types of products for their area of interest, and the web GIS allows the user to view the map layers in the particular geographic bounding box and map projection previously selected using the profiler form. The web GIS browser client interface provides basic functions such as selection/de-selection of layers, drag select zoom box, panning, zooming and centering, and reference map area and scale bar. It consists of four main areas: the map area, the layer list, the map controls, and the information panel.

As discussed in detail above, the NERSC system of satellite HAB monitoring is not confined only to ocean color data, it also includes complementary SST data and SAR-derived water surface roughness data (Figure 4.45) and is being developed towards integration with marine ecosystem modeling (see also Chapter 5).

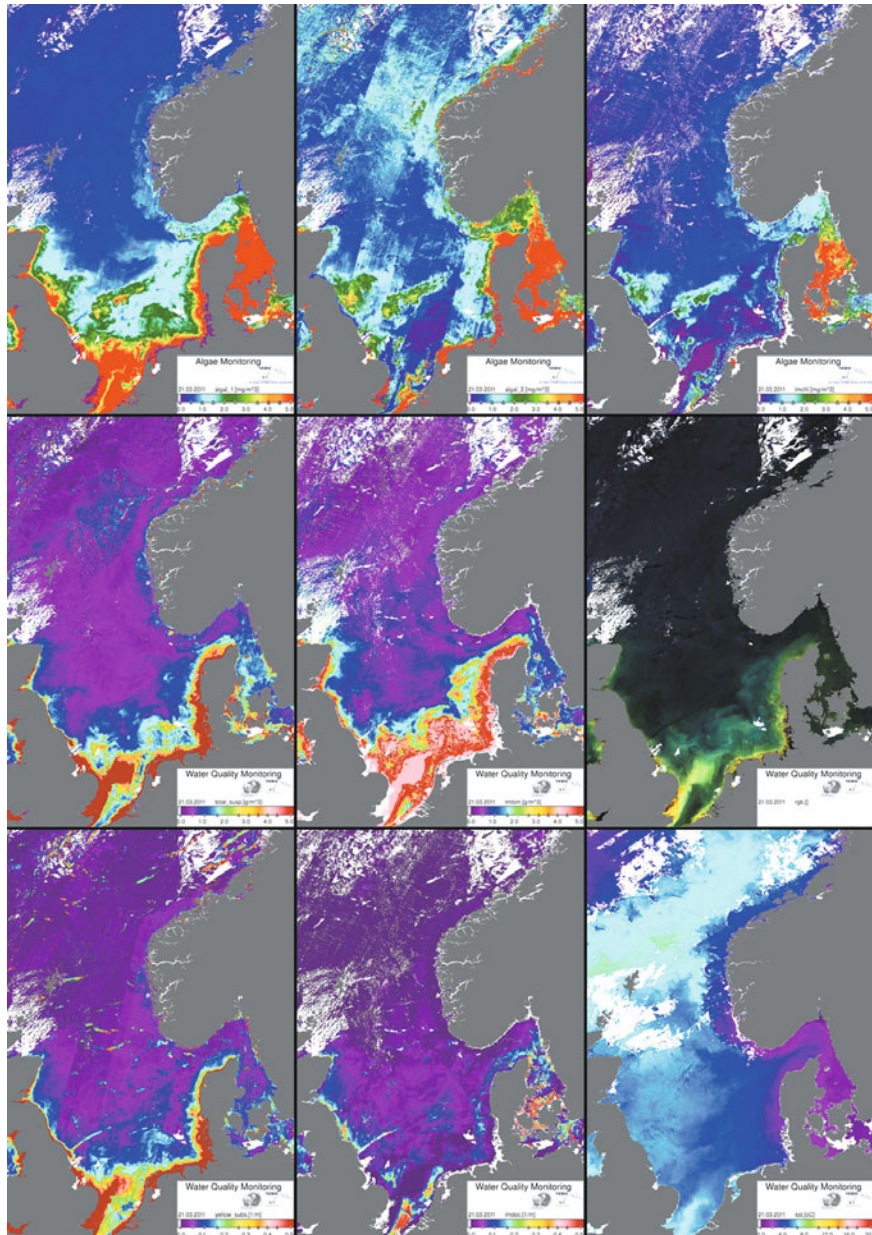


**Figure 4.44.** The suite of near-real time EO-based products available at <http://hab.nersc.no> on a daily basis. (a) ESA case I *chl-a*, (b) ESA case II *chl-a*, (c) NERSC BOREALI case II *chl-a*, (d) ESA total suspended matter, (e) NERSC BOREALI total suspended matter, (f) true color RGB composite, (g) ESA yellow substance absorption, (h) NERSC BOREALI yellow substance absorption, and (i) NASA MODIS sea surface temperature (SST). Source: <http://HAB.nersc.no>

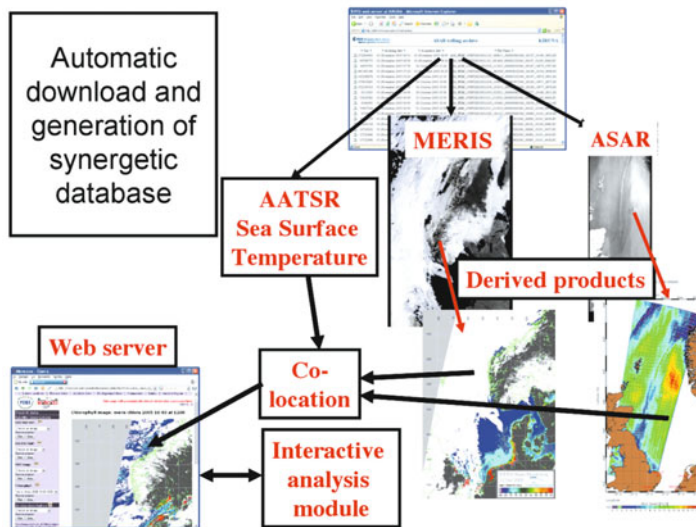


**Figure 4.45.** Schematic view of synergies between different satellite EO data products exploited through combining products from various sensors and production chains in a common processing and analysis infrastructure. *Source:* <http://sat.nerc.no/saris/>

An efficient information system must also be able to provide seamless access to a variety of ancillary data such as weather forecasts, wave forecasts, as well as sea level, current speed, bottom topography, etc. Furthermore, the inclusion of background information including climatological and re-analysis data, bathymetry, seabed characteristics, and key site locations is necessary from the perspective of building up a synoptic view of the state of the marine environment and the impact or influence of human activities.

The Web Map Service (WMS) approach (Figure 4.46) designed at NERSC for the dissemination of information products in a flexible manner has proved to be efficient in many fields. Several commercial GIS applications meet the need for flexible and functional treatment and integration of the available information; however, most users need direct access to the key information vital for the decisions to be taken about their daily operations. The screenshot in Figure 4.46 shows the WMS page displaying the spatial distribution of *chl* overlaying surface current vectors; common capabilities such as zooming, panning, etc. are activated by using the system toolbar. Available data and background layers listed in the menu at the left are regularly updated as new data arrive at the data server. WMS has a notable advantage of facilitating the exchange of graphical renderings—not data—between collaborating servers, thereby opening new avenues for special user-defined integrated information products.

Thus, the satellite EO component of the Norwegian HAB monitoring service developed by the Nansen Center meets the main objectives associated with this activity:

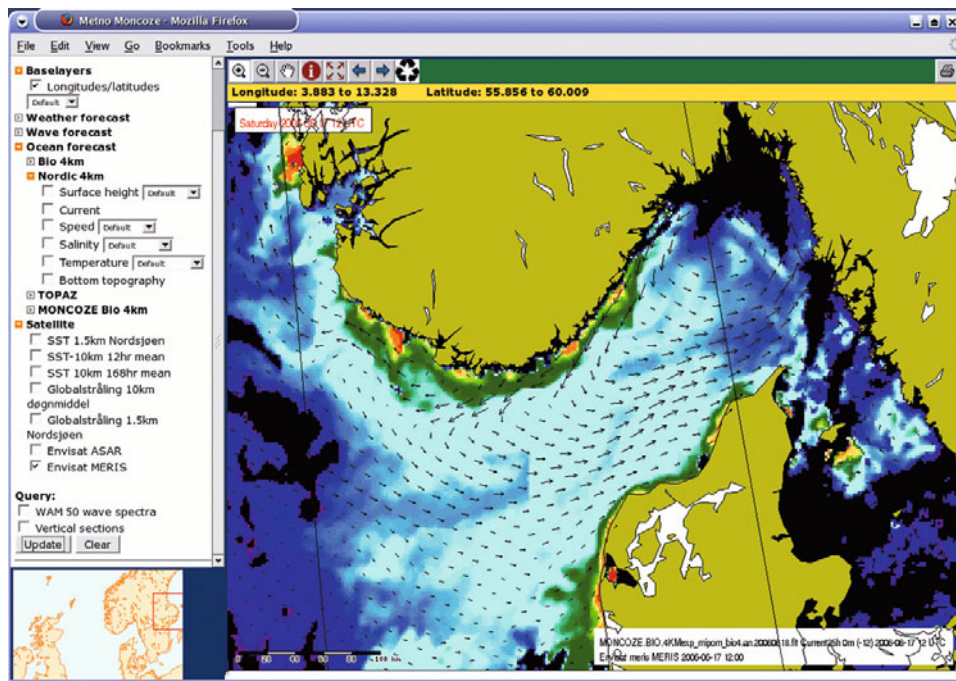


**Figure 4.46.** Data from various distributed sources and services are integrated in a Web Map Service (WMS), in order to facilitate user access and interpretations, here illustrated with an example from the MONCOZE project coordinated by the Nansen Center. *Courtesy: met.no.*

- *early warning* of potential bloom developments;
- geo-positioning of *ocean fronts* (in pigment concentrations and thermal structures) and *advection of water masses* of different origin;
- *EO data assimilation* for improved marine ecosystem modeling and forecasting of HAB situations (see Chapter 5);
- mapping *interannual variability* on the occurrence, extent, life time, etc. of blooms in Norwegian and adjacent waters.

Together with other national HAB-monitoring activities, the EO-based service component contributes to the early management of algae-induced hazards in Norwegian and adjacent coastal waters.

#### 4.3.2 British EO Data Acquisition and Analysis Service (NEODAAS)

Back in the 1970s, the Dundee Satellite Receiving Station (DSRS) began receiving and archiving direct broadcast satellite data from sensors in polar and geostationary orbits. In 1995 the Plymouth Marine Laboratory established their Remote Sensing Data Analysis Service (RSDAS). In September 2006, a new service named the British

NERC (Natural Environment Research Council) Earth Observation Data Acquisition and Analysis Service (NEODAAS) (<http://www.neodaas.ac.uk>) was launched to combine the assets of these two leading British institutions in the area of remote sensing.

At NEODAAS, data are received routinely from AVHRR (1978 to the present day), MODIS (2000 to the present day), CZCS (1979 to 1986), SeaWiFS (1997 to 2004, and from December 2004 to the present day but data-encrypted). A 30-day rolling archive of images is also available from other geostationary satellites covering the Indian and Pacific Oceans and the American continents.

Apart from spaceborne data, images over water from the NERC airborne Compact Airborne Spectrographic Imager (CASI) are available at NEODAAS for research and monitoring applications.

One of the thrusts of the British National Observatory is to process satellite marine data for their regions of interest (ROI). The most demanded ROI is the northwest continental shelf region encompassing the U.K., Ireland, and coastal regions of the North Sea and English Channel. The routine availability of satellite data in the infrared and in the visible allows the end-user to explore the potential of synergistic studies of marine processes.

The NEODAAS data on SST and *chl* are also used to validate outputs from a physical ecosystem model run by the U.K. Meteorological Office for the National Centre for Ocean Forecasting (NCOF). Coupled with data assimilation to initialize or update models, model validation is becoming increasingly important for NEODAAS.

Merged data products from a combination of ocean color products from MODIS, MERIS, and SeaWiFS data are generated. NEODAAS also delivers global ENVISAT ASAR products made available from the ESA ground segment.

In Section 4.1 we discussed the application of the Miller *et al.* (2006) methodology for identification of HABs and demarcation of the areas of intense development of three harmful algal species, viz. the toxic red tide bloom producing dinoflagellate *Karenia mikimotoi* (*Gymnodinium nagasakiense*), the mucilage-releasing *Pseudochattonella verruculosa*, and toxic cyanobacteria in several marine locations: the U.K. southwest approaches, the Celtic Sea (south of Ireland), the North Sea, and the Baltic Sea. The British National Observatory also envisages using this methodology in their routine processing.

Shutler *et al.* (2005) report on PML's development of an automatic system to process MODIS data. This system was formed within the NASA DAAC code. Located at Dundee, the satellite receiving station acquires raw data (level 0) to further process them using NASA level 0 to level 1b software, each minute granule taking around 15 minutes to complete. The geolocated and calibrated data (level 1b) are then processed by the ocean color software developed at the University of Miami, this stage taking 20 minutes to process five minute granules. The processing results of each granule are then stitched and mapped. Importantly, the system allows continuity with the PLM SeaWiFS archive and it can process a multitude of MODIS overflight data simultaneously. Past overflight data can also be processed simultaneously without any loss in processing speed. The system also

accommodates ancillary data that can be important for image interpretation and thematic analysis. The availability of MODIS Terra and MODIS Aqua data ensures higher frequency of measurement and, hence, higher temporal resolution and partially compensates for the cloudiness limitation of optical satellite EO data.

#### 4.3.3 U.S. HAB monitoring system for the Gulf of Mexico

Finalizing Section 4.3, we provide a brief description of the HAB bloom monitoring tool developed in the U.S.A. for the Gulf of Mexico (Stumpf *et al.*, 2003). The reason for selecting this service for our discussion resides, first and foremost, in the methodology of HAB discrimination developed by Stumpf *et al.* (2000).

HABs of *Karenia brevis*, a toxic dinoflagellate, are a recurrent red tide problem in the Gulf of Mexico, with nearly annual occurrences on the Florida southwest coast, and less frequent occurrences on the northwest Florida and Texas coasts. Typically, *K. brevis* blooms start in late summer and continue until mid winter, although the duration varies considerably.

Beginning in 1999, NASA has been issuing Gulf of Mexico HAB Bulletins to support state monitoring and management efforts. These bulletins involve analyses of satellite imagery with field and meteorological station data. The analyses are aimed at (i) tracing an algal bloom that has been identified as a HAB (Type 1), (ii) detection of new blooms as HAB or non-HAB (Type 2), (iii) forecasting the displacement of the HAB identified (Type 3), and (iv) predicting the conditions that can be favorable for a HAB to occur within the area of monitoring (Type 4).

Types 1 and 2 understandably rely upon routine satellite remote sensing, whereas Types 3 and 4 employ interpretive and numerical modeling. Satellite data are obtained from SeaWiFS by using *coastal-specific* bio-optical retrieval algorithms (Stumpf *et al.*, 2002), and wind data are provided by coastal and offshore buoys. Field observations are performed by state agencies, and forecasts are generated by the U.S. National Weather Service.

There are a couple of options for optical discrimination of *K. brevis*. One is the relatively low backscatter by this species (Cannizzaro *et al.*, 2002). The other is a climatological approach, given the late-summer dominance of *K. brevis*. Although during late summer or autumn there is another bloom-forming organism, *Trichodesmium* sp., that can be abundant in the Gulf of Mexico, this alga is highly reflective. As emphasized in Chapter 3, HABs are generally monospecific and, hence, the bloom areas here should either be high reflective or low reflective.

An anomaly that flags up *K. brevis* is the difference in *chl* concentration between a single image and the mean over 2 months (up to 2 weeks prior to acquisition of the image): the 2-week lag reduces the probability that a persistent and stationary bloom will bias the mean. The 2-month term was chosen because it is long enough to collect a sufficient number of images to characterize the seasonal pattern and at the same time it is short enough to remain within a single season. A  $C_{chl}$  anomaly  $\geq 1 \text{ mg m}^{-3}$  is taken as an indicator of the occurrence of *K. brevis* (eastern Gulf of Mexico waters are oligotrophic with background *chl* levels less than  $1 \text{ mg m}^{-3}$ ). The satellite-derived data on *chl* level anomalies are combined with local expertise and hydrobiological

and hydrographical knowledge of the study area in the monitoring system: together, the combined information can be used to guide monitoring efforts to investigate suspect blooms.

Tracing the displacement of HABs (Type 3) is important not only from the perspective of forecasting future locations of blooms, but also for visualizing the surface expression of the current location. Such an analysis is performed in the monitoring system using wind data. Culver *et al.* (2000) have found that red tide blooms are advected westward along the northern Gulf of Mexico at about 7% of the alongshore wind speed. Southerly winds indicate that the bloom is advected northward at the coast, whereas northerly winds cause southerly HAB transport. In the westward direction, red tide blooms are advected with the prevailing coastal currents during each season of the year.

The Type 4 function of any HAB-monitoring system is crucially important for marine management agencies. In the Gulf of Mexico, *K. brevis* blooms frequently occur at the west coast of Florida with upwelling winds. This observation is the basis for the prediction of bloom appearance at the coast. An important prerequisite for application of this approach is that wind-induced upwelling occurs after the bloom has developed offshore (for southwest Florida, these winds should be easterly to northerly).

As is clear, the HAB-monitoring system for the Gulf of Mexico relies upon good knowledge of atmospheric and oceanographic conditions in the study area, rather than on hydrodynamic and biogeochemical modeling (like the NERSC system discussed above). This simplistic approach has its limitations, which are addressed in the next chapter.

#### 4.4 CLOSING REMARKS

In summary, the use of satellite optical and partly infrared EO data has a crucial role to play in the early detection of potential algal blooms in waters that might not be surveyed by other means. Specifically, for the identification of HAB events EO data has a complementary role in most systems for early identification and monitoring of HABs—other means of observations and modeling are needed to provide integrated and needed information. However, the above discussion indicates that until recently the identification of HABs by means of satellite remote sensing has been based on identifying just those areas of algal blooms with a high  $C_{chl}$  concentration. Further qualification of the detected bloom as a HAB is performed by other means encompassing water sampling and laboratory analyses, historical data and experience on the incidence of HABs in the targeted area, hydrological and meteorological data, etc. This implies that the feasibility of remote sensing as an analytical tool remains largely potential and not fully realized.

There are several reasons for the present state of the art in this area. First, satellite sensor feasibility: the number of bands, their positioning, and spectral resolution are insufficient to detect the fine signatures of species-specific pigments other than *chl*. Second, this problem is further aggravated by limitations inherent in

contemporary atmospheric correction techniques/algorithms. As a result, the practical applications of derivative methodologies (which can reveal some spectral signatures characteristic of species-defining pigments, see Section 3.5) or of the fluorescence approach (see Section 3.5.1.2) are hampered, even though the fundamentals of such approaches are well developed and their practical implementation is underway, especially the use of algae fluorescence as a species-discriminative tool.

The other aspect of this challenge resides in the intrinsic properties of algae *per se*: as repeatedly mentioned in this and previous chapters, it still remains unclear why some algal species generally known as harmful turn out to be harmless in some situations and, *vice versa*, generally non-harmful algae on closer inspection prove to be harmful. This is under research by the marine biology community (e.g., Roy *et al.*, 2011). It implies that mere identification of the species forming a bloom is not enough to reach a conclusion about its harmfulness.

In practical monitoring, SAR data have very limited applications with respect to direct mapping of the biological signal from HABs; however, they have proven their usefulness for other marine applications justifying their role as a part of an integrated ocean monitoring system.

Moreover, it should not be overlooked that the main principle of detection of HABs from space resides in the assumption that the  $C_{chl}$  concentration in the revealed area of discolored waters should necessarily be high, which is the case for many flagellate and diatom species. However, this criterion cannot be universally applicable: sometimes the toxicity of algae can be so high that they present a real environmental danger even at relatively low concentrations. Monitoring in this case will depend significantly on *in situ* sampling and analysis.

Therefore, the scheme adopted by some monitoring services that include satellite remote sensing as one of the key components with other sources of information from *in situ* sampling seems well justified. However, this comprehensive approach can be further strengthened and enriched with a prognostic function if complemented with ecological numerical modeling—the issue discussed in the next chapter.

# 5

## Integrated modeling and satellite monitoring of algal blooms

This chapter presents the capabilities and prospects for combining numerical ocean modeling and satellite remote-sensing techniques for monitoring algal blooms. Section 5.1 first describes the nature, capabilities, and limitations of ecosystem modeling of marine environments. Section 5.2 presents some specific features of regional to global model simulations, highlighting applications from the Equatorial Pacific, tropical, and subtropical waters including the Southern Benguela upwelling system, the Mediterranean Sea, and European continental shelf waters. Section 5.3 describes key aspects of modeling HABs as an element of integrated marine monitoring, featuring applications in the North Sea and Skagerrak waters, the Baltic Sea, and elsewhere in coastal and off-shore waters. Section 5.4 provides some concluding remarks.

### 5.1 MARINE/SHELF SEA ECOSYSTEM MODELING: NATURE, CAPABILITIES, AND LIMITATIONS

#### 5.1.1 General characterization of marine ecosystem models

Ecosystem modeling (EM) of marine environments constitutes an important component of comprehensive HAB detection and monitoring schemes. In this context, EM comprises the physical ocean dynamics model and the ecosystem model that simulates the biological interactions in the lower levels of the marine food web, (i.e., primarily phytoplankton, zooplankton, and bacteria). Within the foci of this book, the primary function of EM is to deepen the understanding of how different basic aquatic organisms interact with each other and their surrounding environment. This is vitally important not only for elucidating the nature of the HAB phenomenon, but also for confident forecasting of the location and time evolution of the emergence of a particular HAB event and the spatial and temporal

dynamics under given physical environmental conditions. EM simulations of HAB events are tools with applicability to near-real-time predictions, hindcast simulations for study purposes, increase knowledge of HAB variability and occurrence, and simulation studies of the impact of future changes as a result of changing infrastructure, anthropogenic load, and long-term climate change processes.

EM is considered an indispensable component of any integrated operational HAB-monitoring system, generally encapsulating satellite monitoring and *in situ* measurement data. However, the coupling between and integration of physical and biological observation data and marine ecosystem models, essential for a successful operational monitoring and forecasting system, is still under scientific development. The other relevant aspect that will be discussed later in this chapter is the assimilation of satellite data for efficient initiation, updates, and validation of EM predictions. Efficient tools for data assimilation of physical state variables in ocean models are today operational (Bertino *et al.*, 2003). The assimilation of biological data is still under development (Natvik and Evensen, 2003a); however, there has been significant recent progress towards operational use (Simon and Bertino, 2009, 2011).

The core element of numerical EM incorporates a number of ecological constituents whose interactions are determined by mathematical equations expressing the initiation, growth, and decay of algal blooms as well as prey–predator relationships. The degree of EM complexity depends on the number and type of principal variables used to simulate the functioning of the marine ecological system, the nature of the governing equations, and the involvement of external forcing parameters. In specific situations, water column-associated biota may also be simulated in conjunction with such processes as sedimentation, resuspension, and sediment transport that incorporate the indigenous benthic biota (Moll and Radach, 2003).

Ideally, the more complex the EM, the more realistically it reflects the totality/complexity of trophic levels, as well as the physical and chemical interactions inherent in the aquatic environment's status and dynamics. Moreover, higher spatial resolution EM means more adequate simulation results can be expected since recent research demonstrates that EM is highly sensitive to both the grid resolution of the coupled model ([Figure 5.1](#)) and its capabilities to resolve meso-scale processes (Hansen and Samuelsen, 2009).

However, such (over)sophisticated models require an insurmountable number of empirical—and often area-specific—parameters; moreover, they are difficult to operate and adequately validate. Such models thus possess many degrees of freedom and simulation results must be interpreted with caution. Therefore, the concrete level of EM complexity must be determined by the specific problem that is being addressed. Often, the focus is on the specific HAB species of regional concern and their prey and predators.

The simplest ecosystem models are called Nutrient–Phytoplankton–Zooplankton–Detritus (NPZD) models because the state variables simply represent the partitioning of an element, typically nitrogen, between nutrient, phytoplankton, zooplankton, and detritus. NPZD models (also called growth models, see

Dippner, 2006) are quite well developed and thoroughly validated, both in coastal and pelagic aquatic systems. They can simulate the concentration of both phytoplankton and nutrients reasonably well. However, such models are insufficient for adequately simulating the functioning of coastal ecosystems that are affected not only by HAB events, but also by eutrophication and/or aquaculture. Losa *et al.* (2006) and Hansen (2008) have reported examples of NPZD model applications to the North Atlantic.

To meet the challenges inherent in modeling the functioning of shelf sea ecosystems, an EM with a higher degree of complexity is required:

- (a) Multi-size class models (so-called allometric models, see Dippner, 2006), in which the phytoplankton and zooplankton are divided into two or more size classes; these models can also include several types of nutrients. In such models (e.g., NORWECOM; Skogen and Søiland, 1998; Skogen and Moll, 2000; Søiland and Skogen, 2000; Samuelsen *et al.*, 2009) the largest phytoplankton group is typically diatoms and, thus, the realm of application of this class of models is pelagic waters.
- (b) Multi-species models that operate with a number of phytoplankton groups (including HAB species) that are thought to be dominant in the targeted ecosystem; the level of complexity in such models can be high and, in addition to phytoplankton, can incorporate higher trophic levels such as zooplankton (filtrators, predators, and symbiotic species) and also some species of fish (e.g., European Regional Seas Ecosystem Model—ERSEM; Allen *et al.*, 2001).
- (c) Ecosystem models focused on one or two specific species (e.g., migrating fish or zooplankton, or HAB species, or algae interacting with mussels).

Because a single-box model (or compartment model, see Dipper, 2006) describes the ecosystem development over time assuming that each variable is homogeneously distributed within the area and depth-integrated box, a realistic simulation of interactions between such boxes requires that they are closely linked to a 3-D ocean circulation model that defines all the physical variables required by the ecosystem model. Therefore, the complexity and spatiotemporal resolution of the employed 3-D physical/thermo-hydrodynamic model needs to be harmonized with overall model system complexity in order to achieve the degree of realism required by the application. 3-D models are frequently run with simpler ecosystem models because of the added computational load that comes from models with numerous ecosystem state variables. The increased efficiency and reduced cost of supercomputers are increasing the opportunities to run more complex ecosystem models at higher resolution.

Models used to study algal blooms, in general, and HABs, in particular, can be considered a subset of those conceived to examine more general planktonic processes. Frequently, such models are heuristic, examining the likelihood of certain processes generating a HAB. Such models are less used and have gradually been replaced by ones closely coupled to and assimilating field data and providing insights into the dynamics underlying the observations. In this capacity, the new vintage of HAB models is akin to general ecosystem models.

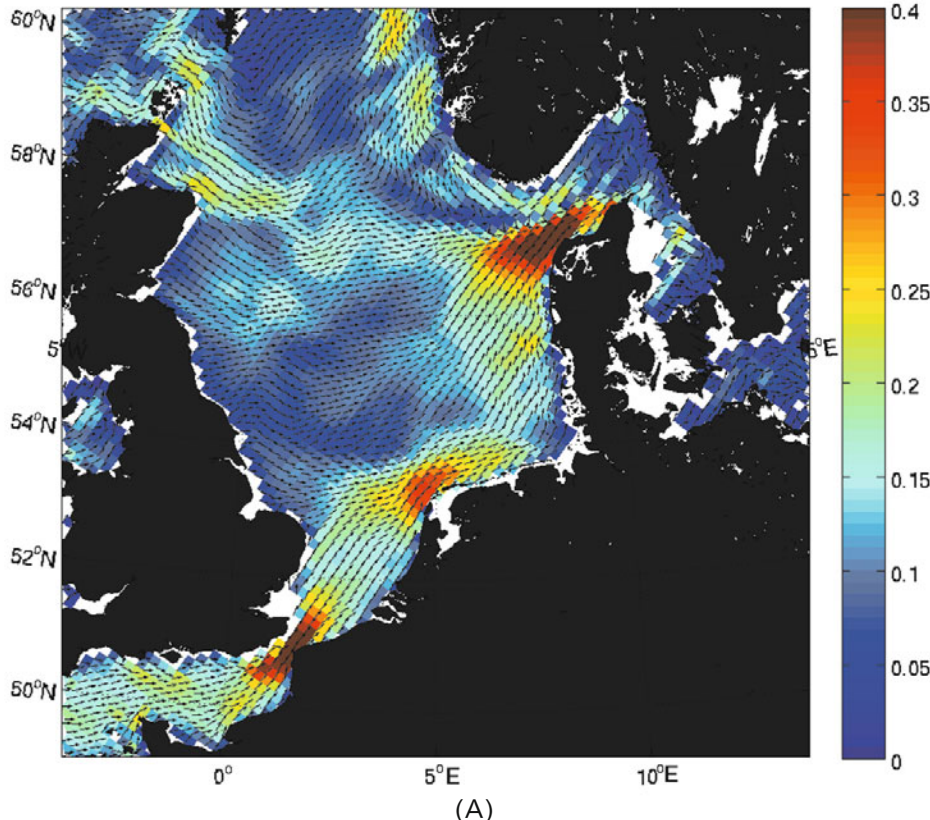
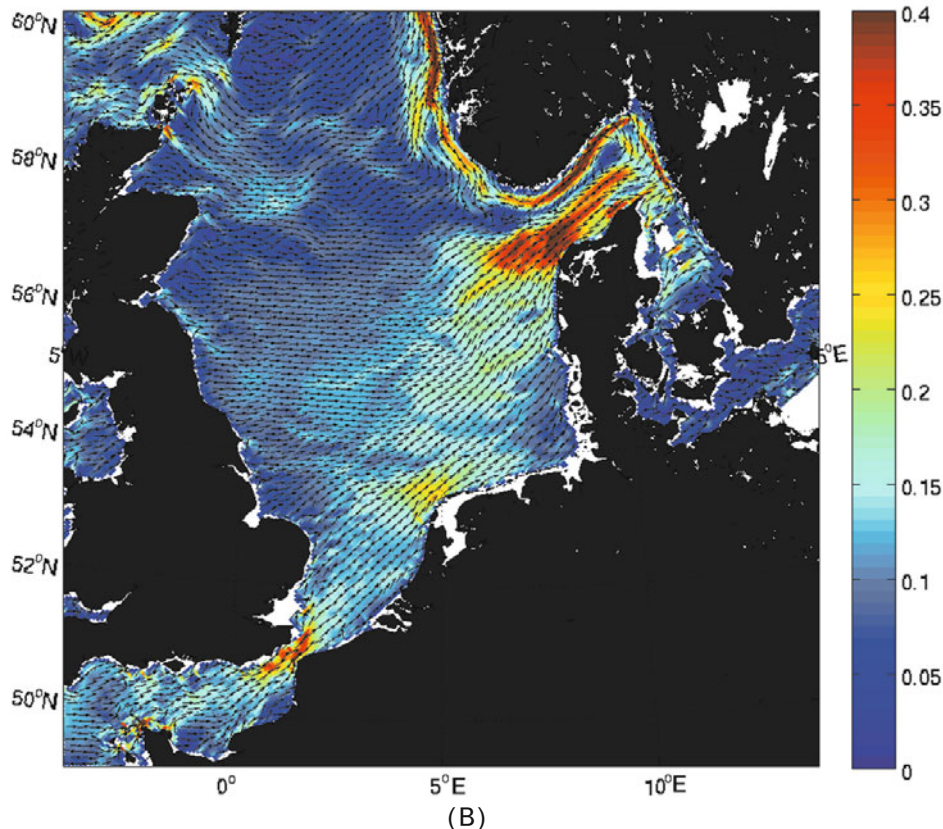


**Figure 5.1.** Monthly average sea surface current vectors and current speed (m/s) from the NERSC ToPAZ model system (<http://topaz.nersc.no>) for January 2008. Every third vector is plotted. (A) The ToPAZ Nordic Seas model at  $\approx 15$  km grid cells and (B, opposite page) the TOPAZ North Sea model at  $\approx 5$  km grid cells. The characteristics of the mesoscale dynamics of the NCC is not resolved in the coarse scale model. *Courtesy: I. Keghouche, NERSC.*

Indeed, although the fundamental feature of HABs is obvious—that is, HABs generally consist of a single species (see Chapter 3) that grows toxic or extremely dense, or else possesses some other environment impairing properties)—the description of exact mechanisms/pathways of how a HAB interacts with other biota is essential for understanding the overall dynamics of the ecosystem under investigation. Running a few steps forward, it should be acknowledged that highly ramified HAB interactions with the indigenous ecosystem often remain more poorly determined rather than confidently established and parameterized.

### 5.1.2 Types of marine ecosystem models simulating algal blooms

Franks (1997b) summarized the major examples of HAB models developed until 1995 (Table 5.1).



Aggregated models simulate the reduction of grazing pressure as the concentration of cells increases due to swimming (allowing algal cells to grow relatively unchecked). This certainly is applicable to calm conditions. Such models generally discriminate between non-swimming and swimming phytoplankton with their characteristic growth rates and the grazing rate. Thus, in such models a red tide can occur if the grazing pressure is reduced to the point that the growth rate allows net growth of the cells present.

Such models can be designed to be vertically resolved (Kishi and Ikeda, 1986). The red tide forms when phytoplankton migrate vertically out of phase with zooplankton. Truscott (1995) improved this type of model by introducing a variable that accounts for the proportion of grazed phytoplankton that become the new zooplankton biomass and the zooplankton death rate. The forcing parameter here is the dynamics of available light. The situation leading to a bloom is conditioned by an exponential growth with time of the algal growth rate. The model also allowed growth rate changes to be driven by changes in physical processes (e.g., in the mixed layer). Although the Truscott model analysis was limited to the case of a changing algal growth rate, it could easily be extended to incorporate the impact of changing nutrient conditions or grazing stress.

**Table 5.1.** Examples of marine ecosystem models for the prediction of HABs developed before 1995 (Franks, 1994).

HAB model type	Author(s)	Year
Aggregated models	Kishi and Ikeda Truscott Wyatt and Horwood	1986 1995 1973
Multispecies models	Ebenhoh Kemp and Mitsch Kishimoto Montealegre <i>et al.</i>	1987 1979 1990 1995
Models with simple physics (e.g., swimming or diffusion)	Franks Kamykowski Kierstead and Slobodkin Kishi and Suzuki Kishi and Ikeda Levandowsky Stommel Tett Wroblewski <i>et al.</i>	1997b 1974, 1979, 1981a, b 1953 1978 1986 1979 1949 1987 1975
Models with detailed physics	Kishi and Ikeda Yanagi <i>et al.</i>	1986 1995

*Multispecies* models. Within this paradigm, a HAB phenomenon is a special event in natural plankton succession. Therefore, in order to unravel the mechanisms, the environmental factors controlling the type of species and population number in time and space should be identified, quantitatively assessed, and further used to elucidate the interaction between both the key environmental variables: the mechanism causing the selection of a species to thrive and become dominant, or else become toxic and eventually generate a HAB. This type of model is based on the “paradox of the phytoplankton” (Hutchinson, 1961) phenomenon explaining that an unlimited number of competing algal species (with slightly different nutrient uptake) can coexist in an unstable and inhomogeneous/fluctuating nutrient-accommodating environment (Ebenhoh, 1987). Changes in mortality rates allow both periodic and chaotic fluctuations of species abundances and, hence, an occasional occurrence of dominance by a single species. This justifies the development of ecosystem models incorporating a judiciously defined variety of indigenous and co-existent plankton species.

Anderson (2005) emphasizes, however, that incorporating extra complexity beyond simple NPZD models is “fraught with difficulties”, particularly when introducing specific plankton functional types (PFTs) in global biogeochemical models (see below). There should be a tradeoff between complexity and generality in global models. However, the challenge seems to be more surmountable in the case of

regional ecosystem models, due to a better region-specific understanding of how to aggregate the diversity within PFTs into meaningful state variables and constants, and the known sensitivity of output to the parameterizations employed. Moreover, confident knowledge of area-specific forcing of the physical and chemical environment is extremely helpful in this regard.

However, HAB models must consider not only grazing pressure and competition for nutrients and light, but also the physical environment as an agent controlling competition (Hansen and Samuelsen, 2009). Interestingly, the dinoflagellate growth rate, for example, is more strongly depressed than that of diatoms in response to small-scale turbulence (Tynan, 1993) due to the inherent inhibition of dinoflagellate cell division. Notwithstanding this fact, it is found that—even in the case of diatoms—small-scale turbulence affects the growth of diatoms of different size (Peters *et al.*, 2006): laboratory experiments and modeling have been performed for phosphorus-limited cultures, *Thalassiosira pseudonana* (6 µm in diameter) and *Coscinodiscus* sp. (*ca.* 109 µm in diameter), under still water and turbulent conditions. Unlike *T. pseudonana*, *Coscinodiscus* sp. exhibited enhanced (by 1.7 times) growth due to turbulence, which was tentatively attributed to the higher size-dependent need for phosphorus in still cultures.

*Models with simple ocean physics.* Models linking biological and physical dynamics are based upon various versions of the flux divergence equation:

$$\frac{\partial P}{\partial t} + \frac{\partial P u(x, y, z, t)}{\partial x} + \frac{\partial P v(x, y, z, t)}{\partial y} + \frac{\partial P w(x, y, z, t)}{\partial z} = \text{biological dynamics}, \quad (5.1)$$

where  $P$  = the phytoplankton concentration field driven in time ( $t$ ) by horizontal ( $x, y$ ) and vertical ( $z$ ) velocities ( $u, v, w$ ), the latter being generally determinable from measurements or versions of momentum equations.

Small-scale motions (which are unresolved at the model scale) are generally lumped into diffusion terms:

$$\frac{\partial P}{\partial t} + \frac{\partial}{\partial x} P u + \frac{\partial}{\partial y} P v + \frac{\partial}{\partial z} P w = k_h \left( \frac{\partial^2 P}{\partial x^2} + \frac{\partial^2 P}{\partial y^2} \right) + k_v \frac{\partial^2 P}{\partial z^2} + \text{biological dynamics}, \quad (5.2)$$

where  $k_h$  and  $k_v$  are horizontal and vertical *eddy* diffusion coefficients. Understandably, the difficulty immediately arising is obtaining the situation-relevant values for the velocity components  $u, v, w$ , eddy diffusion coefficients  $k_h, k_v$ , and the biological dynamics.

The early model by Kierstead and Slobodkin (1953) proved to be the first and simplest coupled physical–biological model, in which algal growth was forced by biological diffusion in maintaining large patches of phytoplankton (smaller patches become diffused faster than they can grow). Kishi and Suzuki (1978) improved the model by introducing an arbitrary function,  $f$ , which could be a Michaelis–Menten source or sink term or a logistic-type density dependence of growth. Horizontal velocities  $u$  and  $v$  may be spatially dependent, but do not vary *in time*—an important assumption.

Subsequently, Levandowsky (1979) added a few other parameters—maximal grazing rate,  $\gamma$ ; grazing efficiency,  $\lambda$ ; and a threshold concentration of phytoplankton,  $P_0$ , below which grazing is zero—to get logistic growth:

$$\frac{\partial P}{\partial t} = k \frac{\partial^2 P}{\partial x^2} + rP \left(1 - \frac{P}{K}\right) - \gamma \{1 - \exp[-\lambda(P - P_0)]\}, \quad (5.3)$$

where  $r$  is the growth rate of phytoplankton,  $K$  is the zooplankton carrying capacity,  $k$  is the coefficient of horizontal diffusion. The model reveals that the smallest patches must be, say, 10 km in extent, rather than 1 km or less. Applications of this model support the theory that red tides can develop in fairly isolated patches whose size is governed by horizontal salinity gradients.

The issue of small-scale (10 m–10 km) patch formation in dense algal blooms is both important and can be tackled to a certain degree with simple models. This is because when patches are small enough, the local growth processes are generally less important than the interactions of behavioral responses (swimming, sinking, and floating) with the physical dynamics at these scales. The streaks formed by Langmuir circulation and bands generated by internal waves are examples of such interactions (e.g., Kamykowski, 1974, 1979, 1981a,b). Further investigations (Tett, 1987; Truscott, 1995) indicated the importance of nutrient-dependent algal vertical migration followed by a floating phase in the generation of blooms in excess of 100 mg chl m<sup>-3</sup>.

Models with detailed ocean physics. Such models differ in the degree of complexity ranging from two-layered media forced by steady winds to models with continuous stratification and detailed sub-models accommodating transient wind and tidal forcing. Notwithstanding the increased complexity, these types of models are still based on eq. (5.2), with the differences residing in how  $u$ ,  $v$ , and  $w$  are specified.

Kishi and Ikeda (1986) developed both an idealized 2-D and realistic topography 3-D models of red tides in the Seto Inland Sea of Japan. One important result of the 2-D model is that a balance between physical dispersal and biological growth must be maintained for a red tide bloom.

The 2-D model contained seven compartments: *Chattonella antiqua* (the red tide forming species), diatoms, zooplankton, phosphorus detritus, nitrogen detritus, dissolved organic phosphorus, and dissolved organic nitrogen. The model was forced by diurnal light variations, spatially variable steady wind, and tides. A very similar model by Yanagi *et al.* (1995) developed to simulate *Gymnodinium mikimotoi* in the same sea differs only in that it has three levels in the vertical. Both nitrate and ammonium were included as nutrient sources with only ammonium being taken up at night in the middle layer. No zooplankton dynamics were included. Interestingly, rather than simulating the biological dynamics (see eqs. 5.1 and 5.2) as a Eulerian field, a Lagrangian approach was employed to follow temporal variations in the patch size of phytoplankton.

Thus, the HAB models discussed above differ in the choice of biological compartments, processes linking compartments, parameterization of processes,

and choice of physical forcing, the importance of which is emphasized by many workers (see, e.g., Skogen and Moll, 2005). In a sense, HAB models can be considered specific cases of more general multi-compartment physical–biological models.

In retrospect, it is interesting to assess what basic premises and features of vintage models proved to be useful enough to be employed in recent developments of marine ecosystem and, specifically, HAB models. We will proceed through several specific examples that are discussed below in an order that reflects the geographical location of aquatic environments moving from south to north. We start, nevertheless, with the issue of a global-scale marine ecosystem model.

## 5.2 GLOBAL TO REGIONAL MODEL SIMULATIONS: SPECIFIC FEATURES

### 5.2.1 General considerations

The issue of incorporating biogeochemical functional groups (i.e., groups of organisms that mediate specific chemical reactions in the ocean through catalyzing phase state transitions from either gas to solute/solid or from solute to solid/gas phases) into ecosystem models is central in terms of both the model's portability/applicability on basin-wide or global scales and their ability to predict how biogeochemical cycles in the ocean would respond to environmental and climate changes.

The aforementioned chemical reactions incorporate: (a) conversion of gaseous CO<sub>2</sub> through autotrophic carbon fixation to a wide variety of organic carbon-bearing molecules (which are mostly solid or dissolved solids at physiological temperatures) and *vice versa* (through respiration); (b) denitrification/nitrogen fixation leading to the reduction of, respectively, nitrate-N to N<sub>2</sub> and N<sub>2</sub> to ammonium-N and further on to organic compounds and *vice versa* (through oxidation of ammonium-N to nitrate-N); (c) calcification and silification resulting in the conversion of, respectively, inorganic carbon and Ca to solid phase calcite and aragonite, and soluble silicic acid to solid hydrated amorphous opal. The reactions (a) to (c) are brought about through specific metabolic sequences.

As far as the notion of functional groups implies no phylogenetic meaning, any functional group encompasses all hydrobiota entities with one and the same biochemical functions, irrespective of their evolutionary origins.

This means that for an adequate simulation of the abovementioned and other reactions, models generally need to consider the entire suite of respective organisms (see [Figure 5.4](#), p. 240). For instance, not only phytoplankton (coccolithophores) species must be included as calcifiers but also such zooplankters as foraminifera and pteropods as well as reef-building species. Silification involves not solely a variety of diatoms, but also silicoflagellates and radiolarian species. Nitrogen fixation should be presented by cyanobacteria such as *Trichodesmium* and also symbiotic diazotrophs.

The task outlined above seems intractable. In each specific case/marine environment/physical forcing it is important to identify those players that can either be ignored or aggregated with others. In global change studies, it is critical to keep in the functional group those entities that are most responsive to climate-driven changes in their physical and chemical environment. Moreover, the evolution issue should not be overlooked.

In some cases, simplified models yield results that are no worse (in terms of minimization of the difference between model estimates and available observations) than those from models with a larger number of state variables. Does this mean that such simplified models are always preferable? Perhaps not; this is because sophisticated interactions and, hence, modeling play a very important role in ocean sciences as they can be used to test and improve our knowledge of processes, using simplified models/empirical approaches. Moreover, sophisticated models are more prone to fine-tuning than simple models given the respective independent datasets. At the same time, using traditional multispecies ecosystem modeling approaches to incorporate “exhaustively” complete functional groups to generate more sophisticated models may not result in higher predictive skills.

Hood *et al.* (2006) reviewed the state of the art and major challenges associated with the incorporation of specific biogeochemical groups into mostly pelagic oceanic biogeochemical models that can be used to predict how oceanic ecosystems might be affected by large-scale forcings (e.g., global change, eutrophication, cross-breeding/ alien species massive intrusion/proliferation, etc).

The review by Hood *et al.* seems to be largely supportive of the ideas expressed above. It highlighted not only the necessity of including a wider spectrum of entities in each functional group, but also emphasized the importance of considering/simulating the influences exerted on the above (a) to (c) reactions by nutrient cycling. Thus, nitrogen fixation ( $N_2$ ) is affected not only by iron (Fe) limitation, but also by phosphorus limitation, stratification, and mixing. This co-limitation impact is evidenced, for example, for Atlantic environments (Dyhrman *et al.*, 2002; Coles *et al.*, 2004). ENSO and NAO oscillations are perhaps underlying the significant interannual variability in ocean pelagic  $N_2$  fixation (Bates and Hansell, 2004). Although the revealed discrepancies between direct  $N_2$  fixation rate estimates and higher geochemical estimates point to a bigger role played by microbial diazotrophs (as they grow in open oceans like *Trichodesmium*), too little is yet known about them in order to include this entity into models (Capone, 2005).

Importantly, if  $N_2$  fixation is included in long-term simulations, denitrification and (ammonia) oxidation need to be simulated as well. Developing in marine sediments and oxygen-impoverished water zones, denitrification goes through the sequence of reduction reactions [ $NO_3 \rightarrow NO_2 \rightarrow NO \rightarrow$  gaseous  $N_2$ ] that are produced by numerous benthic bacterial organisms subsumable under the category of facultative anaerobes, which are capable to respiring not only in the presence of oxygen, but also in the presence of alternative electron acceptors like nitrate or nitrite (King, 2005). Importantly, in many open coastal zones and semi-enclosed seas (e.g., the Baltic Sea) nitrification is stimulated by ongoing eutrophication

processes. Thus, the problem of handling nitrification–denitrification linkages remains hitherto a standing challenge.

Regarding silica producers and diatoms, in particular, the role of silicoflagellates (small golden-brown Chrysophyceae with silica skeletons) and radiolarians (amoeboid protozoans that produce intricate skeletons) should not be overlooked. The oceanic cycle of silicate (Si) is rather simple: dissolved Si in the form of silicic acid  $[\text{Si}(\text{OH})_4]$  is partially dissociated to  $\text{SiO}(\text{OH})_3$  (about or less than 0.5% of the total). Uptake of  $\text{Si}(\text{OH})_4$  by diatoms follows Michaelis–Menten kinetics. Detrital  $\text{SiO}_2$  and  $\text{SiO}_2$  in cell walls dissolve in seawater as the latter is significantly undersaturated in terms of  $\text{SiO}_2$ . Mortality due to grazing converts some cellular silica into detrital silica and, upon dissolution, both of them regenerate into  $\text{Si}(\text{OH})_4$ . Importantly, the rate of dissolution of detrital  $\text{SiO}_2$  is much faster than that of cell wall-originated  $\text{SiO}_2$ , and this needs to be taken into account in modeling. The sinking of cellular and detrital  $\text{SiO}_2$  generates opal deep-sea sediments that are one of the three main constituents of bottom deposits along with calcite and terrestrial soil erosion/weathering.

Iron (Fe) limitation strongly affects the Si:C and Si:N ratios in diatoms. Tracking the changes in these cellular ratios and in the Fe:C ratio is important and can be used as proxies for cellular C, N, Si, and Fe content. The very fact that  $\text{NO}_3^-$ ,  $\text{NH}_4^+$ , and  $\text{Si}(\text{OH})_4$  uptake is not significantly dependent on light (which also occurs at night, although at reduced rates) should be accounted for in models, and the frequent practice of shutting down diatom Si uptake needs to be rectified (Hood *et al.*, 2006).

As mentioned above, calcifying organisms within pelagic waters are coccolithophores, planktonic foraminifera (a large group of amoeboid protists), and pteropods—also called sea butterflies, small marine gastropods of the subclass Opisthobranchia having a pair of winglike flaps (parapodia) that are used for swimming. Precipitation of calcium carbonate ( $\text{CaCO}_3$ ) affects the inorganic carbon equilibrium and water alkalinity by depleting surface  $\text{CO}_3^{2-}$  and increasing  $p\text{CO}_2$ , which potentially reduces  $\text{CO}_2$  influx into the surface ocean (Thierstein and Young, 2004). Within the euphotic zone, overlooking the production of  $\text{CaCO}_3$  by foraminifera and pteropods (which are heterotrophic) can lead to underestimation of calcification if based on strictly photosynthetic organisms (i.e., coccolithophores, primarily *Emiliania huxleyi*). The latter species is of particular importance in terms of global climate change as it can be a significant source of dimethyl sulfide. Except for extreme polar regions, *E. huxleyi* is omnipresent in ocean and coastal surface waters worldwide (see Figure 4.27, example for the North Sea). Model incorporation of this function of *E. huxleyi* (i.e., producing dimethyl sulfide) is one of the goals to be pursued in future modeling. The ecology of *E. huxleyi* is relatively well studied as opposed to the ecological interactions controlling heterotrophic calcification: very little is known in this regard, although both foraminifera groups and pteropods can be highly abundant in ocean surface water.

Calcification has been simulated in several ways ranging from assuming a fixed calcification:total photosynthesis ratio to detailed representations of coccolithophore growth,  $\text{CaCO}_3$  production, and export. The first approach is prone to serious

inaccuracies because the proportion of calcifying species in the phytoplankton changes dramatically both spatially and temporally. Although light inhibition of calcification is not inherent in coccolithophores, but due to the presence of trace metals, there might be a significant decoupling of calcification and photosynthesis under high-light conditions. This mechanism is still poorly understood, as is the utilization of dissolved organic nitrogen and ammonium by coccolithophores (Lessard *et al.*, 2005).

Although impressive, the blooms of *E. huxleyi* may play a subordinate role in total global calcification and production of calcite: non-bloom forming coccolithophores as well as foraminifera and pteropods are believed to account for the major amount of calcium carbonate generation (Sarmiento *et al.*, 2002). Thus, Hood *et al.* (2006) insist upon the strict necessity of including heterotrophic calcifiers and non-bloom forming coccolithophores into modeling.

Elucidating the role of higher trophic levels is another issue that is also presently topical. Indeed, biogeochemical functional groups in the ocean span multiple trophic levels, and top-down regulatory interactions most probably significantly control the ecology of such groups. However, contemporary models are usually confined to grazing and mortality mechanisms at the phytoplankton–zooplankton level, leaving higher level trophic interactions and regulatory mechanisms beyond consideration.

Heterotrophic bacteria play a pivotal role in driving marine biogeochemical processes and providing the important link for cycling of dissolved organic matter (DOM) and detritus. Importantly, they compete with phytoplankton for nutrients and are involved in nitrification and denitrification cycling. Lastly, they control the export of biogenic carbon to surface waters and downwards. This raises the question of whether these two players need to be explicitly included in biogeochemical modeling? Obviously, the answer must be affirmative, but to date most large-scale biogeochemical models do not include bacteria (at least not explicitly). Implicitly, some models account for bacterial workings through their inclusion in the detritus pool assuming that bacterial biomass and activity co-vary with primary production (bacterial production is believed to be ~30% of primary production) and organic matter concentration. However, there are reports stating that this percentage can vary between 2 and 120% (Ducklow, 1999) and, hence, a constant relationship between bacterioplankton, phytoplankton, and detritus might be unsuitable for universal/global applications, but suitable for regional coastal ecosystem modeling. Many of these arguments apply to DOM as well. However, there are as yet numerous uncertainties in formalizing the DOM composition (different constituents), roles of phytoplankton and zooplankton in producing DOM, partitioning of fractions of different liability, and DOM cycling. Most large-scale biogeochemical models do not include DOM, though some do (e.g., Popova and Anderson, 2002), and advocate that the inclusion does not produce any significant effect on simulation results. However, the model of Pahlow and Vezina (2003) reveals that there is a negative relationship between DOM accrual and water temperature. This can lead to a strong positive feedback between water temperature and CO<sub>2</sub> release from DOM (Hood *et al.*, 2006). Therefore, there is no general agreement on whether bacteria and DOM

should be included, although the arguments seem to be rather convincing in favor of their inclusion.

Thus, on the one hand, there is a need to incorporate more details and functional groups in models to adequately reflect the actual complexity of marine biogeochemistry (especially if a model is intended to simulate seasonal/interannual variability at a specific regional location). On the other hand, adding complexity and increasing the number of parameters that cannot be defined/substantiated by the available observation data can result in an effect opposite to the one expected (i.e., a decrease in the predictive capacity of sophisticated models).

Friedrichs *et al.* (2007) addressed the issue of model complexity specifically. Twelve ecosystem models with complexity varying from four—phytoplankton, zooplankton, dissolved inorganic nitrogen (DIN) and detritus—to twenty-four components—multiple limiting nutrients (N, P, Si, and Fe), multiple phytoplankton functional groups (picoplankton/nanoplankton, diatoms, diazotrophs), a single-size adaptable zooplankton pool, and two detritus pools—were applied to two distinct regions: the Equatorial Pacific and the Arabian Sea. Time series of photosynthetically active radiation (PAR), water temperature, vertical diffusivity, and vertical velocity were used to run the ecosystem models in the one-dimensional testbed framework.

The application of a formal parameter optimization scheme allows determination of whether disparities among cross-examined model simulations result from differences in model composition or from differences in fine-tuning of various unconstrained parameters (Friedrichs *et al.*, 2006). By avoiding the parameter optimization procedure, the more complex models (with multiple phytoplankton functional groups and multiple limiting nutrients) produce lower model–data misfits than simpler models. However, if a diverse group of models are all objectively and equally optimized, the simpler models produce least squares fits to the data from individual locations just as well as the more complex models.

At the same time, Friedrichs *et al.* (2007) advocate that a high level of model–data fit is not necessarily associated with the higher predictive capacity of the model (the model becomes “over-tuned” in much the same way as occurs with over-trained neural networks—they lose their generalization ability). Reducing the number of optimized parameters slightly degrades the model–data fit for individual locations but greatly improves the model’s ability to reproduce an unassimilated independent data set.

Thus, when just a few biogeochemical parameters are optimized, the models with greater phytoplankton compartment complexity are generally more *portable* than simple models. Conversely, models with enhanced complexity of the zooplankton compartment do not necessarily outperform models with single zooplankton compartments, even when zooplankton biomass data are assimilated. This cross-validation experiment explicitly indicates the importance of the availability of more comprehensive data sets that would uniquely constrain the different element flow pathways through which models producing similar least squares model–data misfits operate. It is believed that this rather unexpected result is perhaps due to either an inappropriate constraint for the modeled

zooplankton or/and some misrepresentation of zooplankton dynamics in the models.

Moore *et al.* (2002) report an example of an intermediate complexity marine ecosystem model (EM) for the global ocean domain. This EM is developed for incorporation into the National Center for Atmospheric Research (NCAR) 3-D ocean circulation model (Bryan and Lewis, 1979). The ecosystem model includes multiple potentially limiting nutrients (mainly, nitrate, ammonium, phosphate, iron, and silicate) and factors (light levels), three phytoplankton groups (diatoms, atmospheric nitrogen-fixing bacteria, and *diazotrophs*, which are cyanobacteria inclusive), a generic small phytoplankton class, one zooplankton class that grazes the above three phytoplankton groups, and a small and a large detrital pools. The large detrital pool is allowed to sink out of the mixed layer, but there is a smaller non-sinking detrital pool that is composed of dissolved organics (but also the colloidal fraction of dissolved organics) and suspended tiny particulate matter. Remineralization of detrital pools is parameterized with a temperature-dependent function.

The small phytoplankton size group encompasses nano and pico-sized algae. Algal growth rates are simulated with a modified growth model by Geider *et al.* (1998). Relative uptake rates of Fe, P, and Si were modeled using Michaelis–Menten kinetics. Photoadaptation was modeled according to Geider *et al.* (1998). Chlorophyll synthesis was assumed to be proportional to nitrogen uptake, reflecting the need for the synthesis of proteins used in light-harvesting complexes and elsewhere in the photosynthetic system. The maximum *chl*/N ratio, as one of the input parameters to the model, was taken equal to 3.0 mg *chl*/mmol N.

The non-grazing mortality, which includes respiration, was set at 15% per day for the bacteria compared to 10% per day for other phytoplankton groups. The iron requirement for *diazotrophs* was assumed to be eight times that of eukaryotic phytoplankton, which is substantiated by laboratory data.

Parameterization of calcification rates by phytoplankton was performed following the field results by Milliman (1993): rates are low at the highest latitudes (lowest sea surface temperature), and also lower in mid-ocean gyres, but they are higher in both waters at temperate latitudes and in coastal upwelling areas. Thus, this rate is parameterized as a function of the minimum nutrient quota squared, sea surface temperature, and the phytoplankton group (e.g., the calcification/photosynthesis ratio was allowed to grow for small phytoplankton class blooms). This is justified because coccolithophores are frequently a dominant component of non-diatom phytoplankton blooms.

The single zooplankton compartment that encompasses the actions of both microzooplankton and larger zooplankton is included in the ecosystem model in highly parameterized form. Maximum growth rates for the zooplankton were allowed to vary with the food source (i.e., set higher for the small phytoplankton group than for diatoms, large detritus, or *diazotrophs*). Thus, under optimum growing conditions, the diatoms are able to escape grazing control and bloom until nutrients become limiting.

The grazing equations contain a term enforcing grazing rates to decline at low prey densities/biomass. Lessard and Murrell (1998) found evidence for such a thresh-

old effect on grazing. The grazing threshold for diatoms and large detritus was set lower than for small phytoplankton and diazotrophs: this is justified by the fact that large zooplankton (capable of mobility and actively filtering the water in search of prey) feed on diatoms and large detrital particles. Zooplankton incorporate 30% of grazed matter into new zooplankton biomass; the remaining 70% of the grazed material is lost due to sloppy feeding, remineralization within the gut, excretion, or fecal pellets.

There are three types of phytoplankton mortality/loss in the model: (1) grazing losses, (2) losses due to non-grazing mortality (viral lysis, internal respiration/degradation), and (3) losses due to aggregation/sinking. The former is set at 10% per day for diatoms and small phytoplankton and at 15% per day for diazotrophs.

Zooplankton mortality closes the ecosystem model at the upper end of the food chain. It consists of a linear (6% per day) and quadratic-dependent mortality loss. These loss terms effectively set a strong cap on zooplankton biomass and, when phytoplankton escape grazing control, large blooms occur if there is sufficient light and nutrients available. In the model, most of the effectively larger zooplankton enter the sinking pool upon death, while a smaller fraction of microzooplankton grazing is passed up the food chain and enters the sinking detrital pool.

Moore *et al.*'s model has been validated by ample shipborne data collected as part of the international Joint Global Ocean Flux Study (JGOFS) program and by some historical time series stations (Moore *et al.*, 2002). Overall, this global marine ecosystem model reproduces very well the patterns observed in the field data from nine diverse oceanic locations. At the same time, at some locations (e.g., the Equatorial Pacific), modeled primary production and phytoplankton biomass tended to be lower than observed. However, this is a first step towards creation of a model suitable for use across diverse world ocean ecosystems.

As seen, the above model is not explicitly specialized to simulate HABs *per se*, but the inclusion of generally bloom-forming algae such as nitrogen-fixing species (e.g., *Trichodesmium* spp.) and calcifying algae makes it instrumental in this respect as well.

It is noteworthy that the universality of the Moore *et al.* model resides in the scope of biogeochemical options/marine ecosystem components covered by it. This capacity seems even more enhanced in the model developed by Follows *et al.* (2007). Nearly 80 types of potentially viable phytoplankton determined stochastically can be initialized (with identical distributions of biomass) in each simulation, each type distinguished by its role in ecosystem functioning and by the parameters controlling the rates and sensitivity of metabolic processes. Phytoplankton types were classified in four broad functional groups according to the specificity of their physiology: (i) diatom analogs; (ii) large eukaryotes (except for diatoms); (iii) small cyanobacteria analogs; and (iv) other small photo-autotrophs. The model allows initialized organisms to interact with one another and their environment, eventually evolving into a sustainable ecosystem (after an initial adjustment, the biomass of some phytoplankton types fell below the threshold of numerical noise, and these types were assumed to have gone "extinct"). Thus, the phytoplankton community

structure in this model “emerges” from a wider set of possibilities in the course of model running given specific physical forcing and the processes of natural selection are mimicked. This allows avoiding subjective/arbitrary selection of functional groups and renders the system flexible, capable of adapting to changing physical/climatological forcing where some radical shifts in the community structure might occur.

As seen, the ideology behind this model is innovative for marine ecosystem models, although this approach has already been used to simulate terrestrial ecosystems (e.g., Kleidon and Mooney, 2000).

A global ocean circulation model constrained by observation data is used in Kleidon and Mooney (2000) to define flow fields and mixing coefficients which together determine the transport of biological and chemical entities. As a result, global patterns of open ocean biomass (i.e., the broad-scale patterns of productivity and nutrients) proved to be highly consistent with *in situ* and remote sensing (SeaWiFS) observations.

However, to attain more accurate results there is a clear need for fine-tuning of the specific coefficients and reaction rate parameters in the overall 164 equations simulating marine ecosystem functioning. This feature brings global models closer to regional/area-specific ones.

### 5.2.2 Equatorial Pacific Ocean

Salihoglu and Hofmann (2007) developed a one-dimensional multi-component lower trophic level ecosystem model that includes detailed algal physiology. The model is focused on accurate assessment of carbon fluxes. In spite of upwelling that provides nutrients to upper water layers, the Equatorial Pacific is characterized by fairly low chlorophyll concentrations and low rates of primary production of about, respectively, 0.2–0.3 µg/L and 75 mmol C m<sup>-2</sup> day<sup>-1</sup>. This high-nutrient, but low-*chl* environment has been attributed to low iron concentration: the deficiency in iron keeps phytoplankton growth rates below their physical potentials and affects the composition of the phytoplankton community by promoting smaller cells. The grazer community (represented by two groups: microzooplankton and mesozooplankton), particularly microzooplankton, contribute to reducing the chlorophyll content. Interestingly, low iron concentrations promote high nitrate conditions because in iron-stressed areas the indigenous phytoplankton preferentially uptake ammonium rather than nitrate.

The autotrophic compartment is represented by five algal groups, which have light and nutrient consumption parameters of low light-adapted *Prochlorococcus*, high light-adapted *Prochlorococcus*, *Synechococcus*, autotrophic eukaryotes, and large diatoms. The simulated distributions and rates were validated against shipborne data in the Equatorial Pacific collected during the 1992 U.S. JGOFS experiment. The model is focused on accurate assessment of carbon fluxes, in the formation of which recycled iron is an important factor because, as mentioned above, sustained growth of algal groups depends on remineralized iron that accounts

for 40% of the annual primary production in the Cold Tongue Region ( $0^{\circ}\text{N}$ ,  $140^{\circ}\text{W}$ ) of the Equatorial Pacific.

The detrital component is divided into two detritus groups (one small and one large) according to their unique sinking and remineralization rates. Cumulative detrital remineralization replenishes the content of ammonium and iron. Dissolution of silicate in the large detritus compartment provides a source for this nutrient.

The effects of the physical environment are included in the ecosystem using the advective velocity and temperature time series from the mooring data collected within the framework of the Tropical Atmosphere–Ocean experiment (TAO). Forcing by the physical environment is reduced to vertical advection, vertical diffusion, and mixing. The time-varying mixed layer depth is also obtained from TAO mooring measurements, and the theoretically derived vertical diffusion coefficients are input into the ecosystem model.

The phytoplankton model is coupled to a module simulating the spectral underwater light field that drives phytoplankton primary production via a bio-optical model given in detail in Salihoglu (2005).

The reference simulation was one year, 1992, for the Cold Tongue Region substantiated by the aforementioned U.S. JGOFS Equatorial Pacific cruises. The year of 1992 covered both an El Niño event and the transition to non-El Niño (normal) conditions. The results of the simulations proved to be in full agreement with generally accepted explanations for ecosystem processes in the Equatorial Pacific Region. Simulation results were indicative of the need, when focusing on carbon cycling, to get a broad spectrum of algal groups involved because a few key groups (such as low light-adapted *Prochlorococcus*, high light-adapted *Prochlorococcus* and *Synechococcus*) might be sufficient to simulate primary production and export variability in tropical Pacific waters.

Importantly, the results from the modeling by Salihoglu and Hofmann suggest that the net effect of increased stratification and water temperature conditions would promote the remineralization rates of nutrients (including iron), which is bound to enhance carbon production and export. Thus, the inclusion of iron dynamics may be needed to fully reflect the effect of climate variability on Equatorial Pacific conditions (as the principal site of the El Niño–Southern Oscillation, which is known as the primary cause of interannual variability in the tropical oceans).

Once embedded into a comprehensive 3-D thermohydrodynamic model, this ecosystem model can also be considered as not only a basin-scale but also a global scale tool for simulating the onset and spatiotemporal variations of algal fields in oceanic waters (optical Case I water). However, the serious difficulty remains as to how to validate such basin and global scale models, given the present facility of relevant satellite observations (mainly, spatiotemporal resolution, discrimination of phytoplankton groups, etc.).

Unlike the previously discussed model, the ecosystem model developed by Villanoy *et al.* (2006) for Manila Bay in the Philippines (see Section 5.2.3.2) is explicitly intended to simulate the bloom dynamics of *Pyrodinium*, a tropical toxic dinoflagellate.

### 5.2.3 Subtropical and tropical waters

#### 5.2.3.1 Southern Benguela upwelling system (*Southern Africa*)

Kone *et al.* (2005) have reported on the development of a 3-D primitive equation model, the Regional Ocean Modeling System (ROMS) coupled to two biogeochemical models/compartments. The model was designed to study the dynamics of the first trophic levels of the pelagic food web in the southern Benguela upwelling system, which is one of the four major current systems existing at the eastern boundaries of the world oceans (Carr and Kearns, 2003). These eastern boundary systems are characterized by upwelling along the coast of cold nutrient-rich waters. The coastal upwelling area of the Benguela ecosystem extends from southern Angola ( $\sim 17^{\circ}$ S) along the west coast of Namibia and South Africa around the southernmost part of the continent. This system is unique in that it is bordered at both its northern and southern boundaries by two warm water systems, the Angola Current and the Agulhas Current, respectively. Interestingly, along the southern Benguela shore, equatorward wind induces numerous upwelling cells along the coast rendering the aquatic environment highly heterogeneous in space and time (Backeberg *et al.*, 2009).

The ROMS model (Shchepetkin and McWilliams, 2005) solves the free surface primitive equations in an Earth-centered rotating environment, based on the Boussinesq approximation and hydrostatic vertical momentum balance. ROMS is discretized for coastal and terrain regions following curvilinear coordinates. The horizontal resolution ranges from 18 km at the coast to 31 km offshore and, on the vertical, there are 20 levels whose density increases near the surface to better resolve upper-level variability. The model was forced using the atmospheric forcing fields based on monthly climatologies derived from the Comprehensive Ocean–Atmosphere Data Set (COADS) (Da Silva *et al.*, 1994). Momentum forcing was given by the longitudinal and latitudinal components of wind stress.

The first biogeochemical model contains four state variables: dissolved inorganic nitrogen or nitrate ( $\text{NO}_3^-$ ), phytoplankton, zooplankton, and detritus. The second biogeochemical model used  $\text{NH}_4^+$ , nitrate, small phytoplankton, large phytoplankton, small zooplankton, large zooplankton, small detritus, and large detritus as state variables. Differentiation between flagellates/diatoms and ciliates/copepods is relevant with regard to *a priori* knowledge of the main plankton and zooplankton groups present in the study area.

All prognostic variables are expressed in nitrogen units ( $\text{mmol N m}^{-3}$ ),  $\text{chl-}a$  in  $\text{mg} \cdot \text{m}^{-3}$  is derived from the phytoplankton concentration using a constant carbon/ $\text{chl}$  ratio of 50 (Tian, 2000). Phytoplankton growth was forced by PAR, water temperature, and dissolved nitrogen ( $\text{NO}_3^-$ ). PAR was calculated at each step by linearly interpolating monthly climatological values. Phytoplankton growth was computed as the product of all limitation terms.

The Michaelis–Menten expression was used to describe zooplankton ingestion as a function of phytoplankton concentration. Detritus was assumed to be a mixture of zooplankton fecal pellets, dead organisms (zooplankton and phytoplankton, the mortality rate of which was set the same for algae and zooplankton). Large zoo-

plankton (copepods) were allowed to consume small and large phytoplankton and small zooplankton with different filtration efficiency (e.g., copepods filter the diatoms with more efficiency than flagellates). Small zooplankton also feed on small and large phytoplankton with different filtration efficiency.

Small detritus were a mixture of small zooplankton fecal pellets, dead organisms of small zooplankton, and small and large phytoplankton. Large detritus were mainly composed of large zooplankton fecal pellets and dead bodies. The remineralization rate of detritus into nitrate was assumed constant. The algorithm for assessing the vertical sinking rate of both phytoplankton and detritus was based on the piecewise parabolic method by Colella and Woodward (1984).

Pilot simulations using the Kone *et al.* (2005) biogeochemical models coupled to the ROMS ocean model indicate that both models reproduce the spatiotemporal distributions of *chl-a* and zooplankton in the Southern Benguela upwelling system relatively realistically. However, unlike the first model, the second biogeochemical model distinctly reveals the seasonality of small and large zooplankton distributions, which is highly consequential for assessing the food continuum for fish larvae.

### 5.2.3.2 Manila Bay, the Philippines

Villanoy *et al.* (2006) conducted a model study of the bloom dynamics of *Pyrodinium bahamense* var. *compressum*, the major causal organism of toxic blooms in Manila Bay since 1987 as well as in several areas in the tropical world.

The complex life cycle of *Pyrodinium* includes the formation of cysts that settle onto sediments, which can serve as the inoculum for the next bloom. This suggests that sediments may be important pathways in the encystment–excystment cycle: resuspension of sediments by physical forcing may be a precursor to *Pyrodinium* blooms. Sediments affect the algal composition as well as inter-species and algal–zooplankton trophic interactions by controlling the PAR light availability. Hydrodynamically, *Pyrodinium* cysts behave like clay particulates and, hence, are affected by the physiochemical environment in a similar way.

Villanoy *et al.* (2006) employed the 3-D Princeton Ocean Model (POM) adjusted to the thermohydrodynamic conditions in Manila Bay, whose area is about 2,000 km<sup>2</sup>. Forced by both horizontally uniform wind and tidal motions, the resulting model is a primitive equation model realized in a  $\sigma$ -coordinate system with an embedded turbulence closure unit. The model grid has a 900 × 900 m resolution with 18 levels in the vertical. Wave generation, propagation, and dissipation in Manila Bay was simulated using a shallow-water wave model called SWAN (Simulating WAves Nearshore)—a non-stationary wave model based on the discrete spectral action balance equation (Ris and Holthuijsen, 1997). The transport of *Pyrodinium* cells was simulated using a 3-D Lagrangian particle dispersal model. Each particle was transported by advection and diffusion (similar to the model of Yanagi *et al.*, 1995).

Because HAB events in the study area occur during the southwest monsoon season, simulations were performed with the respective physical environment forcing conditions.

After resuspension, cysts were assumed to germinate to form vegetative cells with the further reproduction time of  $\sim 3$  days, which is then followed by encystment and settling back to the sediment. Accordingly, the growth function is simulated as follows:

$$\frac{\partial P}{\partial t} = (r - r_d - r_s)P, \quad (5.4)$$

where  $r$ ,  $r_d$ , and  $r_s$  are the phytoplankton growth rate, death rate, and respiration rate, respectively. In the model it was assumed that  $r_d + r_s = 0.1 \text{ day}^{-1}$ . The model also takes into account buoyancy forces acting on *Pyrodinium* cells given by Stokes law.

Simulations of the *Pyrodinium* bloom have shown that the direction of advection was almost invariably along the wind direction, and the dispersal distances increase if *Pyrodinium* cells are located higher in the water column. Simulated locations of cyst formation after a bloom are fairly consistent with available *in situ* data. Simulations indicate the existence of two systems for bloom formation: one is fed by cyst beds in the west and advected along the west–northeast coast, while the other is fed by southeast cyst beds and dominates in the east–southeast area.

Importantly, although this model is not an ecosystem model in the proper sense, but a simplified cyst-based model, it proved to be capable of providing new insight into *Pyrodinium* bloom temporal and spatial dynamics and its causal mechanisms in the study area.

#### 5.2.4 Barcelona Harbor, the Mediterranean Sea

Addressing the HAB problem in the Mediterranean, Sole *et al.* (2006) focused their simulations on examining the influence of allelopathic and trophic interactions causing feeding avoidance by predators on the formation of HABs under environmental scenarios typical of Barcelona Harbor. They applied a modified version of ERSEM to study this process.

Although models of allelopathy have been proposed by several authors (e.g., An *et al.*, 2003), they have not dealt with HAB implications. A zero-dimensional version of the ERSEM (European Regional Seas Ecosystem Model) is described by, among others, Baretta and Baretta-Bekker (1997).

The ERSEM ecosystem model is composed of a set of interlinked modules describing biological and chemical processes in a coupled water column–benthos system. The full ecosystem model incorporates a pelagic submodel with functional groups of bacteria, phytoplankton, micro and mesozooplankton, and, as mentioned above, a benthic submodel with bacteria and several types of predators (Allen *et al.*, 2008). The rate of change of each functional group is described in terms of physiological processes (ingestion, respiration, excretion, etc.) and trophic interactions, which are defined in a food web matrix: each element of the matrix varies between 0 and 1 and indicates the relative availability of each functional group of food source for predators. The nutrients were presented as phosphate, nitrate, ammonia, and silicate.

The primary production module used by Sole *et al.* is based on that developed by Ebenhoh *et al.* (1997; see Section 5.1) with a modification to introduce the functional group of toxic algal species. Four functional groups of primary producers were included in the model: (1) picoalgae eaten by heterotrophic nanoflagellates; (2) diatoms eaten by micro and mesozooplankton; (3) non-toxic autotrophic flagellates eaten by micro and mesozooplankton; and (4) toxic autotrophic flagellates eaten by micro and mesozooplankton. The introduction of flagellates (instead of typical toxin-producing dinoflagellates, see Chapter 4) is performed to avoid excessive complication.

To simulate a realistic situation, Sole *et al.* used a time series of physical (irradiance, water temperature, wind mixing of the water column, and meteorological variables) and chemical (major nutrients) parameters as environmental forcing. Although ERSEM can be coupled with a hydrodynamical flow model, advection and dispersion processes were not included in the Sole *et al.* simulations with the only exception of a term accounting for biomass losses due to advection of water through the harbor mouth regardless of the obvious importance of this physical forcing (Martin *et al.*, 2005).

The effect of toxicity (allelopathy) on non-toxic flagellates is formulated as:

$$\frac{\partial P}{\partial y} \Big|_{all} = \eta P_1^2 P_2^2 \quad (5.5)$$

where  $\eta$  is the allelopathic parameter,  $P_1$  and  $P_2$  are concentrations on non-toxic and toxic groups, respectively, and  $P$  is the net concentration of primary producers.

The aforementioned food matrix was used to parameterize prey-shifting behavior by two types of zooplankton due to prey toxicity.

A regular blooming species in Barcelona Harbor between 1996 and 1999 was the PSP-producing *Alexandrium catenella*. However, between 2000 and 2002, this species was replaced by other dinoflagellates: namely, *Prorocentrum minimum*, *P. triestinum*, *Scrippsiella* spp., *Gyrodinium impudicum*, and to a far lesser degree by *Dinophysis*. Conversions from population densities measured in cell/L to biomasses in mg C/m<sup>3</sup> were effected as in Verity *et al.* (1992). Toxic and non-toxic algal cell initial concentrations were allowed to vary between 1.25 and 200 mg C/m<sup>3</sup> in both groups. The initial nutrient concentrations (mmol/m<sup>3</sup>) were set at 1.20 (phosphate), 5.68 (nitrate), 6.50 (ammonium), 3.01 (silicate). The consumer initial biomass (mg C/m<sup>3</sup>) was low for microzooplankton (only 0.15) and up to 8 for the remaining predators.

The Sole *et al.* model verification lacked actual data on the degree of horizontal heterogeneity. The evolution of nutrient concentrations and blooming onset timings were in close compliance with the available observation data: the model reproduced the time distribution of *chl-a* correctly indicating winter, late summer, and autumn peaks. However, the exact timing and intensity of the peaks, and the flagellate content did not match well, evidently because the Sole *et al.* simulations did not include a coupled hydrodynamic ocean model, which is needed for the proper simulation of ecosystem dynamics, and no allelopathic or otherwise toxic species were

found in the harbor samples during the study period. At the same time, sensitivity analysis indicated that perhaps the allelopathic factor was not significant for the area—at least, not in the outset stage of algal biomass accrual—and did not introduce appreciable modifications in the long-term evolution of the system. This is in conflict with the results of laboratory investigations (see, e.g., Hansen, 2002) and may be because toxic cell counts exceeded 1,000 cells/mL in the laboratory experiments, much higher than those found in pre-bloom phases of natural populations (Guisande *et al.*, 2002). Thus, it is more likely that allelopathic impacts can be highly consequential not only in well-developed blooms, but also in the immediately pre-bloom phase (the algal growth rate is high enough to yield appreciable cell concentrations). Albeit not conclusive, the study by Sole *et al.* implies the potential importance of allelopathic and prey-shifting interactions for the development of HABs.

The issue of predator–prey interactions was also investigated by Armstrong (2003) without, however, attempting to include the allelopathic aspect. Generally, model formulations allow extending ecosystem state variables in order to comply with the specific features of the study area. The model was tested against *in situ* data from the IronEx II experiment (Landry *et al.*, 2000) in the eastern Equatorial Pacific. Only phytoplankton and zooplankton are explicitly included in the model, along with the associated nutrient dynamics. Bacteria are implicitly included as phytoplankton of an appropriate size range.

Unlike models considering zooplankton as omnivores, the Armstrong model did not explicitly include zooplankton–zooplankton interactions. The basic assumption adopted in this model is that all zooplankton are carnivorous unless herbivory is imposed by the presence of phytoplankton—that is, when enough phytoplankton are present, some omnivorous zooplankton species will switch their dietary preference to phytoplankton.

The strength of the predator–prey interaction between phytoplankton of size  $x$  and zooplankton of size  $y$  is accounted for by a function having the Gaussian curve:

$$\varphi(y, x) = \exp[-(y - x)^2 / 2\sigma_\zeta^2], \quad (5.6)$$

where the variance  $\sigma_\zeta^2$  characterizes the degree to which herbivores of size  $y$  specialize in phytoplankton prey of size  $x$ . Evidently, the function  $\varphi(y, x)$  takes the value of 1 when  $(y - x) = 0$ .

The Armstrong model—unlike the “add-a-box” strategy, where state variables are added on an *ad hoc* basis—clearly generates new state variables within the framework of a size spectrum. This is important because multi-phytoplankton–multi-zooplankton ecosystems can be very vulnerable in the sense that small changes in the model structure can entail significant alterations to model behavior.

In its fit to data from IronEx II, the model proved to be able to represent maintenance of a diverse community of small phytoplankton, while allowing large phytoplankton to bloom. The model does not address the issue of how to represent zooplankton idiosyncrasy, nor does it consider mixotrophy. However, even in its

present state it can be included as a module in more comprehensive marine ecosystem models.

## 5.2.5 European continental shelf waters

### 5.2.5.1 North European continental waters

Allen *et al.* (2001) outlined an approach to complex spatiotemporal marine ecosystem modeling as applied to the northwestern European continental shelf. The model combines a high-resolution hydrodynamic ocean model—the POL-3DB baroclinic model (a 3-D finite difference primitive equation model formulated in spherical polar coordinates) on a 12 km horizontal grid (Holt and James, 2001)—in combination with ERSEM (see Section 5.1). The coupling is unidirectional; that is, ERSEM takes input describing the physical forcing (water temperature, salinity, and diffusivity) from the hydrodynamic ocean model, but there is no feedback from ERSEM to the hydrodynamics.

This integration of models describes a wealth of processes including benthic–pelagic coupling, the dynamics of zooplankton, and carbon, nitrogen, phosphorus, and silicate cycling—the processes that are thought to be indispensable for attaining adequate simulation results. The integrated thermo-hydrodynamic and biogeochemical model system was employed to illustrate how spatial and temporal variations in physical forcing (especially spatial gradients in coastal regions) impact the onset of the spring bloom in the North Sea.

In addition to the brief description of ERSEM in Section 5.2.3, it is noteworthy that the *pelagic* food web in this version of ERSEM considers a pool of three types of algae based on size and trophic position (picoplankton, 0.2–2 µm; autotrophic flagellates, 2–20 µm; and diatoms, 20–200 µm), three types of zooplankton (heterotrophs, microplankton, and mesozooplankton), bacteria (consuming dissolved organics, decomposing detritus, and competing for inorganic nutrients with algae), detritus, dissolved organics, Si, NO<sub>3</sub>, NH<sub>4</sub>, PO<sub>4</sub>, and CO<sub>2</sub> cycling.

Nutrient uptake was made dependent on both the levels of intercellular storage and ambient nutrient concentrations. All three zooplankton groups are cannibalistic. Microzooplankton consume diatoms, autotrophic and heterotrophic flagellates, picoplankton, and bacteria. Mesozooplankton consume microzooplankton, diatoms, and both types of flagellates.

The *benthic* food web of ERSEM describes nutrient and carbon cycling via both aerobic and anaerobic bacterial pathways, the zoobenthic food web, bioturbation/bioaggregation, and vertical transport in the sediment of particulate matter due to the activity of benthic biota.

Suspended particulate matter is considered by ERSEM as silt with a typical settling velocity of 0.0001 m s<sup>-1</sup>.

The baroclinic ocean model (POL-3DB), with 20 levels in the vertical and allowing the spacing of  $\sigma$ -levels to vary horizontally, permits a similar resolution in the upper ocean beyond the shelf break to that of the continental shelf and simulates a seasonal thermocline in deep-water regions. To describe the horizontal

advection of both physical and biogeochemical variables adequately, as well as to minimize numerical diffusion and preserve front properties, the “piecewise parabolic method” (PPM) was employed (James, 1996). Calculation of horizontal pressure gradients by interpolation onto horizontal planes essentially reduced the numerical inaccuracy commonly found in  $\sigma$ -coordinate modeling over steep topography.

The computational area encompasses the shelf seas surrounding the U.K. ( $12^{\circ}\text{W}$ – $13^{\circ}\text{E}$  and  $48^{\circ}\text{N}$ – $63^{\circ}\text{N}$ ), whose depth is within the 20–200 m range with the exception of the western extremity where depths increase rapidly to around 2,000 m.

Simulations performed with this coupled model (POL-3DB/ERSEM) indicate that the model is capable of reproducing regional variations in phytoplankton biomass and nutrient cycling and appears to simulate unstratified waters better than seasonally stratified ones. The performance of the higher trophic levels in the model is poorer, thought to be due to insufficiently adequate parameterizations, particularly with respect to overwintering mesozooplankton. Moreover, the spatial resolution of the model is still unable to resolve meso-scale features such as estuarine plumes, near-shore distributions of particulate suspended matter, frontal zones, and benthic inhomogeneity. The significance of these effects remains unassessed.

Allen *et al.* (2008) analyzed the capacity of the coupled POLCOMS–ERSEM model to forecast high-biomass bloom events in eutrophic coastal areas, such as the Irish Sea, southern North Sea, and the English Channel. There are a number of HAB species found regularly in these northern European waters, representing all of the major phytoplankton classes. Based on statistical methods, Allen *et al.* found that the model is capable of predicting high-biomass blooms at the mean discrimination threshold, but not at the higher ( $>50\%$  mean) threshold, although significant errors were observed in the timing of the spring bloom and there was high bias in frontal regions. These model inaccuracies are thought to be due to underestimation of the intensity of turbulent mixing (e.g., Hansen and Samuelsen, 2009) and inadequate model representation of hydro-optical conditions.

Proctor *et al.* (2003) specifically addressed the significance of nutrient fluxes and budgets in light of increased eutrophication over the previous three decades due to enhanced riverine nutrient discharge. Simulations showed that advection generally provides less than 10% of the nutrients and river discharge is only important close to the continental shelf. Simulations also revealed the net flux onto the shelf from the Atlantic Ocean for all nutrients (N, P, Si). Simulated fluxes and budgets have been compared, where possible, with other flux estimations presented in the literature, and proved to be invariably lower (especially, for  $\text{NO}_3^-$ ). Since the annual fluxes assessed by Proctor *et al.* were derived from instantaneous values, not from a combination of averaged flows and averaged (or interpolated) concentrations (as performed in comparable reports), the results obtained are believed to be more accurate.

### 5.2.5.2 Danish coastal waters

Within the framework of our description of marine ecosystem models, it is interesting to compare the ERSEM–POL-3DB tool with the Danish hydrodynamic ecosystem model named DHI MIKE 3 as applied to Danish coastal waters covering

the Baltic Sea through the inner Danish straits and extending out to the North Sea (Edelvang *et al.*, 2005).

The commercially available software DHI MIKE 3 is characterized as a means of fast, inexpensive, and efficient assessment of the state of phytoplankton with appropriate scaling of resolution. DHI MIKE 3 is considered to be an indispensable element of an operational monitoring system that also incorporates shipborne observations and satellite EO-monitoring data.

DHI MIKE 3 comprises (i) a 3-D hydrodynamic module for describing water level/tidal motions, currents, salinity, and temperature; (ii) an advection-dispersion (AD) module (based on the Quickest–Sharp scheme; Vested *et al.*, 1992) for simulating transport and concentrations; and (iii) an ecological/eutrophication unit for modeling the rates at which processes transform in the system of considered eco-parameters (detritus, zooplankton, inorganic carbon, sediments, benthic vegetation) with special consideration given to phytoplankton primary production. The DHI MIKE 3 system offers a choice of turbulence models. To increase the resolution in the horizontal (important for the narrow Danish straits), an interactive two-way nesting technique is used, which solves the hydrodynamic equations simultaneously in grids of different horizontal resolution.

In order to simulate phytoplankton primary production rates, the ecological/eutrophication unit of DHI MIKE 3 (DHI, 2000; Erichen and Rasch, 2001) describes the processes of sedimentation, grazing, algal and zooplankton extinction, zooplankton respiration and excretion, detritus sedimentation and mineralization, sediment mineralization and accumulation, benthic vegetation production and extinction, and exchanges with the ambient medium. Thus, the model does not include secondary products at levels higher than zooplankton, whose abundance dynamics is simulated by applying a high death rate. A model covering a larger geographical area is used to generate the oceanographic boundary conditions.

The results of the DHI MIKE 3 Danish Sea model have been validated using SeaWiFS and *in situ* measurement data on *chl*. Generally, with all caveats taken into account, good agreement between modeled and observation data is reported, although the exact timing of the spring bloom was described with appreciable uncertainties.

### 5.2.5.3 North Sea–Baltic Sea

Burchard *et al.* (2006) developed another ecosystem model for the marine area encompassing the North Sea and the Central Baltic Sea (Gotland Sea). The physical basis of this model is the public domain water column model, the General Ocean Turbulence Model (GOTM; <http://www.gotm.net/>). The biogeochemical models for the northern North Sea (Kuhn and Radach, 1997) and for the central Baltic Sea (Neumann *et al.*, 2002) coupled to GOTM are Eulerian in type: all state variables are expressed as concentrations no matter whether they are dissolved chemicals (such as nutrients) or particulate organic or inorganic matter. The Kuhn and Radach model operates with seven state variables—phytoplankton, zooplankton, bacteria, particulate organic matter/detritus, dissolved organics, and nutrients (nitrate and

ammonium). The Neumann *et al.* model consists of 10 state variables. The nutrient state variables are ammonium, nitrate, and phosphate. Phytoplankton are represented by three functional groups: diatoms, flagellates, and cyanobacteria—the latter being a nitrogen source for the system and generating very high-biomass HAB blooms in the Baltic Sea (see Section 4.2, Figures 4.33 and 4.34). Physical forcing was introduced via vertical mixing, water temperature and salinity, light availability, and a number of other mechanisms.

The hydrodynamic ocean model is based on Reynolds-averaged Navier–Stokes equations with the Boussinesq approximation in a rotating reference frame as well as on Reynolds-averaged versions of the transport equations of water temperature and salinity. For shallow-water areas, both turbulent transport and horizontal advection were assumed negligible, and the corresponding equations were reduced to their boundary layer forms.

The numerical experiment conducted with this coupled marine ecosystem model indicated that the observations of physical and biogeochemical parameters were reasonably well reproduced in simulations.

#### 5.2.5.4 Scottish Western Highland

In some applications (such as ecosystem modeling of fjord environments) simple coupled models remain useful and appropriate for the purpose of providing insights into linked physical and biological processes. For instance, a three-box model addressing the eutrophication problem in fjords due to the influx of nutrients from fish farms has been suggested by Laurent *et al.* (2006) for Loch Creran (Scottish Western Highlands). The list of state variables used in the model consisted of (i) phytoplankton *chl*; (ii) dissolved inorganic nitrogen; and (iii) dissolved inorganic phosphorus. The physical forcing parameters include mean solar irradiance and freshwater inflow. The nutrient-controlled growth rate for phytoplankton was also a state parameter.

To simulate the physical environment, two physical processes were parameterized: the first process is total terrestrial freshwater inflow, the second involves the exchange between the model domain and the adjacent sea. Since the studied loch shows characteristic salinity layering, the model domain was divided into two layers—the “upper” and “lower”. Being very strong, tidal circulation was implicitly included in the model as well via the water exchange rate.

Intended to assess the capacity of the fjord system to assimilate nutrients of exogenous/anthropogenic nature, the biological model uses a parameterized phytoplankton–nutrient link as a ratio,  $q$ , of the formed *chl-a* to the assimilated nutrient. The value of  $q$  was adopted from Gowen *et al.* (1992) who estimated  $q$  empirically from observations in Scottish fjords and coastal waters.

Simulations conducted with Laurent *et al.*’s model described immediately above showed good agreement between modeled and observed values of all three state variables in winter and spring with the amplitude of peaks and falls as well as their phase. However, for *chl* the simulated concentrations in summer and autumn

(unlike in winter) differed somewhat from the corresponding observational data. Simulated nutrient concentrations are in better agreement with observations.

#### 5.2.5.5 Five 3-D marine ecosystem models for the European continental shelf

Although European shelf waters and, particularly, the North Sea shelf region have been the subject of extensive numerical modeling, the examples given above are far from being exhaustive. Moll and Radach (2003) reviewed (along with the aforementioned ERSEM and POL-3DB–ERSEM models) another five 3-D marine ecosystem models: NORWECOM, GHER, ECOHAM, ELISE, COHERENS, POL-3DB–ERSEM (for references see Moll and Radach, 2003, and explanations below). All of these models except COHERENS, NORWECOM, and ELISE cover at least the whole North Sea area. COHERENS resolves the southern North Sea only, while the ELISE model only simulates the English Channel. NORWECOM focuses on the Skagerrak and Norwegian Coastal Current waters. The spatial resolutions are 7 km (COHERENS), 12 km (POL-3DB–ERSEM), 18–20 km (GHER, ECOHAM, and NORWECOM), and 1° (ERSEM). Except for ERSEM, all models resolve the diurnal cycle. The temporal resolution for the reviewed models is 15–20 min (except for ERSEM), which is sufficient to resolve major water motions except for temporally short waves and small-scale turbulence. The biological timescales of the population dynamics of algae and bacterioplankton are also resolved. The spatial resolution of the models can be as coarse as 44 km such that medium to small-scale patchiness features are accordingly not resolved, meaning that these EMs cannot resolve small to medium-scale physical processes properly (Hansen and Samuelsen, 2009).

(A) *NORWECOM* The Norwegian Ecological Model System (NORWECOM) was implemented by the IMR (Skogen, 1993), further developed by Skogen and Søiland (1998), and extended to include oxygen, silicate shells, and suspended particulate matter (Søiland and Skogen, 2000). Largely based on the approach suggested by Aksnes and Lie (1990), NORWECOM describes two functional groups in phytoplankton—diatoms and flagellates—which entails the inclusion of silicate as a nutrient along with phosphate and inorganic nitrogen. A zooplankton component (both in the water column and benthos) is missing but its role in phytoplankton density regulation is accounted for by the algal mortality fraction. All nutrients are generated from detritus residing both in the water column and benthic sediments; benthic regeneration is consequently modeled. Heavy metals and polychlorinated biphenyls (PCBs) are included as pollutants. Thus, NORWECOM simulates phytoplankton succession, algal blooms, and nutrient limitations (but only partially, as only two algal groups are described).

The NORWECOM biological module is nested inside the Princeton Ocean Model (POM) (Blumberg and Mellor, 1987) at the IMR. Its physical forcing factors are atmospheric wind and pressure, tides, freshwater runoff, surface heat fluxes, and inflows and outflows at the open boundaries. The prognostic variables are three components of the velocity fields, water temperature and salinity, turbulent

kinetic energy, macro-scale turbulence, and water level. The governing equations are the horizontal momentum equations, hydrostatic approximation, the continuity equation, the conservation equations for water temperature and salinity, and a turbulence closure model. In the vertical, a  $\sigma$ -coordinate representation is used, and the horizontal grid uses the Cartesian coordinate system. The model can provide a horizontal resolution of  $20 \times 20$  km; in the vertical, 12 bottom-following  $\sigma$ -layers are used (currently it is nested to a 4 km resolution).

(B) *ECOHAM-1* Developed for estimating annual primary production in the North Sea, the ECOlogical North Sea Model, HAMBurg, v. 1 (ECOHAM-1) (Moll, 2000; Moll and Radach, 2003) 3-D model is a spatial extension of the 1-D water column model by Radach and Moll (1993). ECOHAM simulates phytoplankton biomass, phosphate concentration, and sediment detritus during the annual cycle. Presented by one state variable, phytoplankton production is assumed to be limited by phosphorus or dissolved inorganic nitrogen (DIN). Nutrient regeneration is simulated as immediate regeneration of a certain part of suspended detritus and by a linear process of detritus regeneration at the bottom. Grazing of phytoplankton by zooplankton is treated by employing the Michaelis–Menten formulation, including a threshold value below which the phytoplankton grazing process ceases. Underwater light is calculated by a diagnostic differential equation that includes shading due to phytoplankton.

(C) *GHER* The Geo-Hydrodynamics and Environment Research model (GHER) is a 3-D model coupling a meso-scale circulation model (with a resolution of one sixth of a degree in both horizontal directions) with an ecosystem model. The ecosystem accommodates as state variables nitrogen-containing nutrients (nine compartments), small and large phytoplankton, heterotrophic flagellates, zooplankton, bacteria, detritus, and dissolved organics (Delhez, 1998). Heterotrophic flagellates and mesozooplankton graze on small and large phytoplankton separately. As is the case with ERSEM, bacteria compete with phytoplankton for nutrients. In all compartments of the food web the carbon-to-nitrate (C/N) ratios are allowed to vary. GHER provides a spatial resolution of 18 km and very high temporal resolution. The biological module is embedded in the 3-D hydrodynamical ocean model described by Delhez (1996).

(D) *ELISE* The Ecological Modeling Software for interactive modeling (ELISE) was first driven by a realistic fine-mesh flow field of two-dimensional tidal residual currents in the English Channel. Later, it was set into a quasi 3-D model based on a fine grid with a mesh size of two nautical miles. Essentially, this version is a vertical 1-D model embedded in a 2-D depth-integrated advection–dispersion ocean model. The biological model operates with eight state variables accounting for dissolved organic nitrogen and silicate as nutrients. Zooplankton and higher trophic levels are not included as either prognostic or diagnostic state variables. Microbial biomass is not explicitly simulated and the decomposition processes are expressed via temperature-dependent rates.

(E) *COHERENS* The Coupled Hydrodynamic Ecological Model for Regional Northwest European Shelf Seas (COHERENS) is a 3-D “multipurpose” ocean model that allows setting up a model system from basic modules describing the general circulation of the shelf sea, biology dynamics, sedimentation, contamination transport/dispersal. The biological module (Tett and Walne, 1995) operates with eight state variables (microplankton carbon and nitrogen, detrital carbon and nitrogen, nitrate, ammonium, oxygen, and zooplankton nitrogen) and does not involve benthic state variables. It was embedded in the 3-D hydrodynamic ocean model described by Luyten (1996).

Comparison of the feasibility of the above models was conducted by Moll and Radach (2003) along the following lines: phytoplankton system (algal blooms and primary production, succession, annual cycles, limitation by nutrients and by light, eutrophication), benthic system, cycling of matter, ecosystem dynamics under external forcing (role of hydrodynamic forcing, role of solar radiation forcing, role of riverine and atmospheric inputs, role of exchanges with the Atlantic and the Baltic Sea), and the variability of ecosystem dynamics.

Within the framework of this chapter, we confine the results of this comparison to the ecosystem modeling of phytoplankton and, more specifically, to algal blooms and production. All models reproduce the main regional features of the annual total general characteristics for the North Sea similarly: they yield high production in coastal regions ( $>200 \text{ g C m}^{-2} \text{ yr}^{-1}$ ) and a minimum in the central area (less than  $100 \text{ g C m}^{-2} \text{ yr}^{-1}$ ). ERSEM assesses mean annual water column net production for the study region at  $100\text{--}175 \text{ g C m}^{-2} \text{ yr}^{-1}$  during 1984–1995. NORWECOM and ECOHAM yield a mean value of 134 and  $124 \text{ g C m}^{-2} \text{ yr}^{-1}$  for the same years, respectively. GHER’s result for only one year (1989) is 150, while COHERENS and POL-3DB-ERSEM does not quantify annual net production.

More importantly, primary production for specific algal groups was assessed by the GHER model by separating large and small species, by the NORWECOM model for diatoms and flagellates, by the POL-3DB-ERSEM model for three groups of phytoplankton (picophytoplankton, diatoms, and flagellates), and by ERSEM by considering three algal groups plus large *Phaeocystis* colonies (inedible).

To study eutrophication, the model ecosystem must include several state variables of nutrients and algae, and also involve the microbial loop. Only NORWECOM, ERSEM, and POL-3DB-ERSEM comply with such requirements (although, as seen from Section 5.2.5.4, for local conditions, a rather simplistic model for a fjord environment by Laurent *et al.*, 2006 also proved to be efficient).

Summing up their review, Moll and Radach (2003) emphasize that a variety of simulations performed with the above models have given new insights regarding the functioning of the North Sea ecosystem, such as the temporal and spatial generation and distribution of primary production, its limitations, mechanisms of nutrient regeneration, the effect of coastal eutrophication, and the budgets of phosphorus, nitrogen, and silicon.

At the same time, obvious deficiencies were revealed: the models consider a very limited scope of processes and algal species. Only one model (NORWECOM) incorporates simulation of specific contaminant dynamics. Sediment chemistry and benthic biology is not represented enough. Higher trophic level ecosystem models, including fish, is a recommendation for better representation of the role played by prey and predator chains in net production regulatory mechanisms (Miller *et al.*, 2006). Moll and Radach assume that the complexity of ecosystem models should be increased to attain at least the level of ERSEM. The hydrodynamic models employed should meet the complexity of water dynamics at the meso-scale in the study area (Skogen and Moll, 2005). Basin scale circulation models for the North Atlantic to precisely simulate boundary conditions need to be employed. Altogether, this should enhance the predictive capability of marine ecosystem models. Such large-scale physical boundary conditions for major ocean state variables are now routinely available for the global oceans through the GMES Marine Core service provided by the EC MyOcean project.

Since the comparison by Moll and Radach (2003) the NORWECOM model has been developed to also incorporate a module for *Chattonella* algae (see Section 4.1.9.1). It has also been extended with options to include detritus phosphorus and two size classes of zooplankton. As an alternative to the Eulerian approach to modeling zooplankton, NORWECOM has also been coupled to an individual-based model (IBM) for the copepod *Calanus finmarchicus* (Samuelson *et al.*, 2009) and is in the process of being coupled to IBMs of key species of krill and fish in order to represent all trophic levels of the ecosystem in Norwegian waters (NORWECOM.E2E).

NORWECOM has also been coupled to the TOPAZ (HYCOM–NORWECOM) system at NERSC and has been used in several studies of the North Atlantic (Hansen and Samuelson, 2009; Samuelson *et al.*, 2009; Hansen *et al.*, 2010). While the biological module is exactly the same, the physical model is different. The fact that HYCOM–NORWECOM is run for real-time forecasts and, thus, forced by instantaneous rather than temporally averaged physics makes the two-model system hard to compare. In agreement with the results of Skogen and Moll (2005), the model is quite sensitive to the choice of hydrodynamic circulation model. NERSC has included recent developments in NORWECOM but, since the focus is on lower trophic levels, have not extended the model to include IBMs for zooplankton and fish. Great efforts have also been made to develop data assimilation methods of remotely sensed chlorophyll-*a* using the Ensemble Kalman Filter (EnKF) (Simon and Bertino, 2009, 2012). Currently, EnKF is being applied for parameter estimation in a 1-D version of the model.

#### 5.2.5.6 Model validation using satellite EO data

The predictive capability of marine ecosystem modeling is of direct application to the topic discussed in this book. Prediction, in general, can be divided into the categories of deterministic and statistic predictions. The former describes the precise value of state variables at a given time in the future, while the latter yields the probability of a

particular realization. Various recent investigations in different regions of the world's oceans indicate that a major part of inter-annual and inter-decadal biological variability can indeed be attributed to changes in the physical climate and to anthropogenic impacts. Dippner (2006) assumes that tackling such issues as controlling factors of the time-varying biogeochemical state of the ocean system (mainly, its food webs) and its response to global change, and the rate of carbon cycles (its accumulation and release) will be the future directions for marine ecosystem modeling.

The variety of spatial and temporal scales at which the models yield their simulation results renders their validation a challenging task. Only since the launch of SeaWiFS in 1997 have satellite data become available to be used for this purpose. For example, Fouest *et al.* (2006) have applied SeaWiFS and AVHRR data for meso-scale and regional validation of a 3-D high-resolution physical–biological model of the Gulf of St. Lawrence (Canada). Although the applied SeaWiFS/OC4 algorithm failed to reproduce simulated *chl-a* data in the gulf because of freshwater-associated turbidity, the striking agreement between SeaWiFS-derived ocean color data and the contours of turbid water masses allowed the regional estuarine circulation and associated mesoscale variability to be validated.

An example of another application of SeaWiFS and AVHRR imagery for model validation has been reported for the White Sea (Pozdnyakov *et al.*, 2007) where an operational algorithm for simultaneous retrieval of *chl-a*, suspended minerals, and dissolved organics was applied (Pozdnyakov *et al.*, 2005b, see also Chapters 3 and 4). There was good correspondence between spaceborne *chl* and simulated phytoplankton biomass ([Figure 5.2](#)) for a haphazardly chosen year (2002). In addition, the location of riverine fronts and their temporal dynamics in the mouths of White Sea bays and tide-driven upwellings predicted by a 3-D physical–biological model (Neelov, 2005) proved to be distinctly expressed in SeaWiFS and AVHRR images available for the respective time periods.

Another recent example of a physical–biological model being validated by satellite images is reported by Edelvang *et al.* (2005). The results of the DHI MIKE 3 Danish Sea model have been compared with those obtained from SeaWiFS images and the measurement of water samples. Two stations in Skagerrak and one station in Kattegat were chosen to this end. As a result of satellite data lacunas caused by cloud cover interference, some of the important phases of phytoplankton development could not be monitored by SeaWiFS, but data for clear sky periods proved to be in good compliance with model nowcasts. At the same time, SeaWiFS/OC4 data nearly invariably yielded lower values of *chl-a* during the spring bloom compared to model simulations, but there was good agreement with measured values.

Satellite EO data validation is intimately related to the issue of ground truth data. Data assimilation is the incorporation of observations to readjust and optimize model predictions (reducing model error functions), thus obviating the effects of inaccurate initial conditions and reducing drifting model predictions (Franks, 1997; Natvik and Evensen, 2003a, b; Werner *et al.*, 2004; Evensen, 2006). Importantly, data assimilation can also be very useful for providing poorly known model

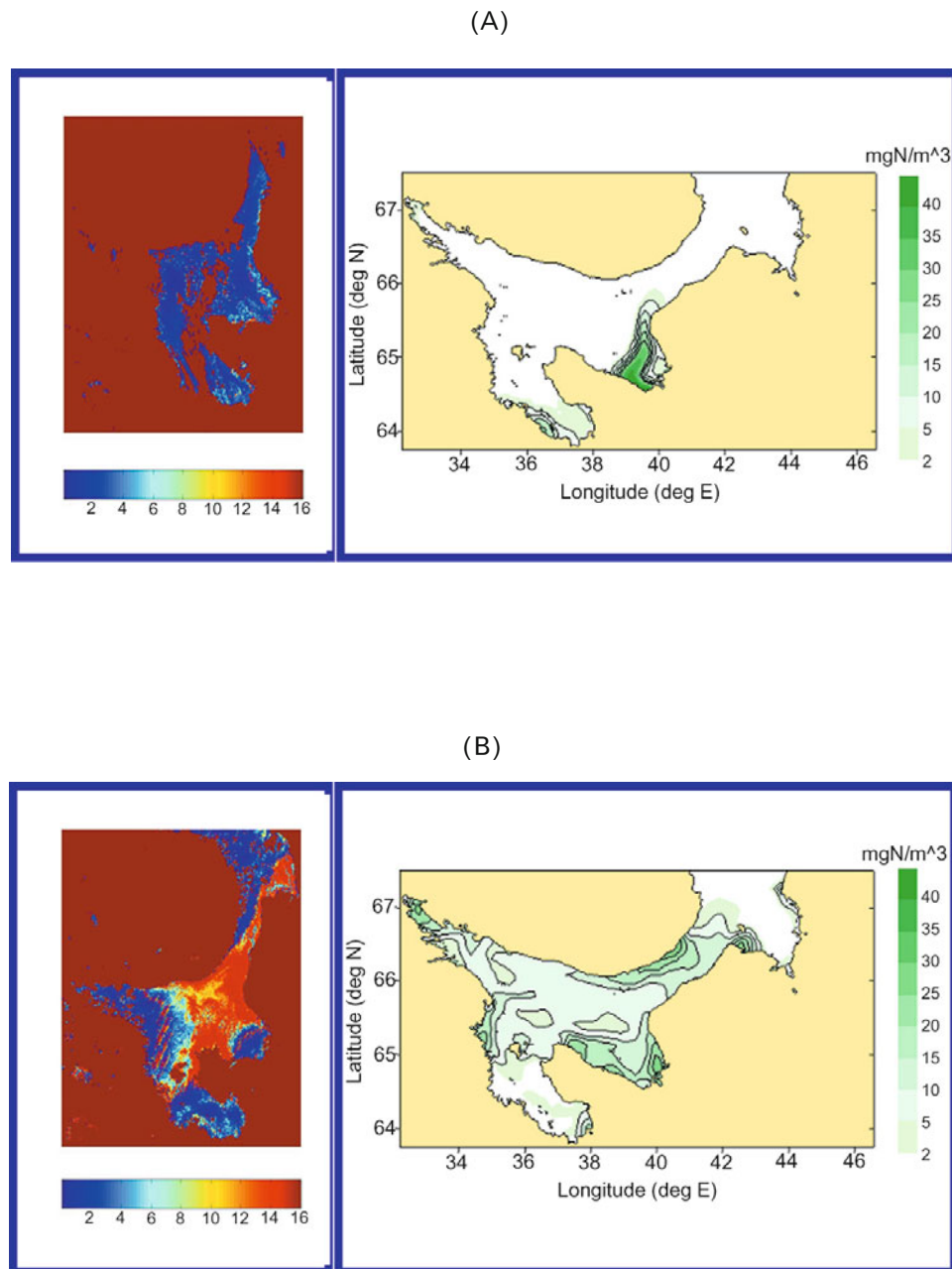
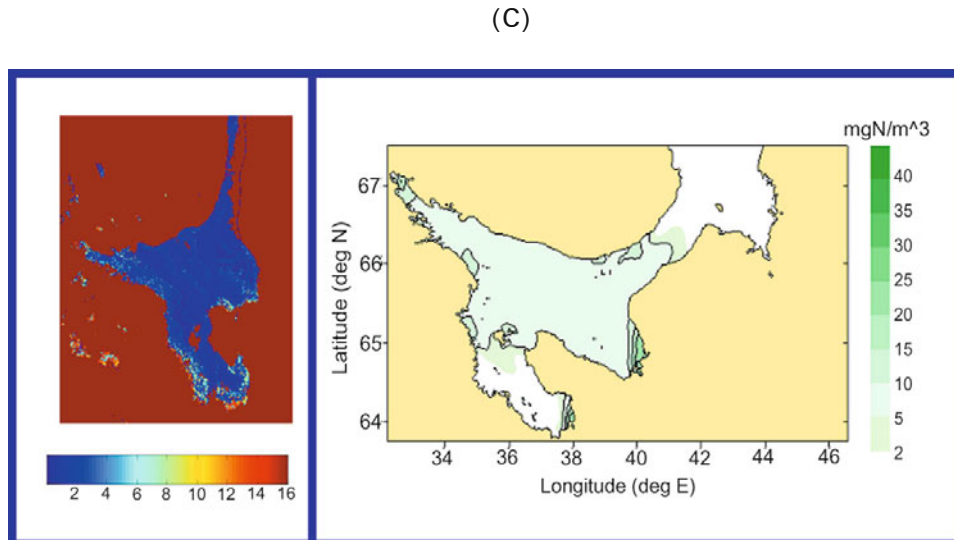


**Figure 5.2.** Qualitative comparison between the spatial distributions of *chl-a* concentration ( $\mu\text{g/L}$ ) obtained from a SeaWiFS image taken over the White Sea in late May (A), June (B), and October (C, opposite page), 2001 (left panels) and the modeled phytoplankton biomass ( $\text{mg N/m}^3$ ) for the same time periods and year (right panel). Courtesy: Filatov *et al.*, 2005.



parameters (Lawson *et al.*, 1995). The advantage of data assimilation over conventional numerical modeling is that it provides an *improved* presentation of variables, where the errors and deficiencies of both models and data are reduced in a complementary fashion (Gregg *et al.*, 2009).

There are several techniques used for inserting observation data into models (for references see Franks, 1997b; Gregg, 2008; Evensen, 2009). These techniques can be classified into two global groups: variational (inverse) methods and forward (sequential) methods (Anderson, L. A. *et al.*, 2000). The process of data assimilation proceeds through a gentle “nudging” of model solutions toward the observed data without causing unrealistic oscillations in the model. Use of the Ensemble Kalman Filter (EnKF) (Evensen, 2006, 2009) has proven to be efficient for several applications including ocean modeling. However, assimilation of biological observation data presents serious challenges as it deals with a highly non-linear system and a community of different species composition, different physiological states, sophisticated and highly ramified feedback interactions. Therefore, in the case of marine biology, different forcing factors may behave quite differently and unexpectedly.

However, sea surface pigment concentration from satellite observations may be a good candidate. New algorithms are being developed (see Chapters 3 and 4 for references, but also Alvain *et al.*, 2005, and Folkestad *et al.* 2007), and models should be developed to incorporate/assimilate such data.

Direct comparison of observed and simulated pigment concentration is challenging: the respective value inferred from satellite *chl* data is expressed in units  $\mu\text{g/L}$  or  $\text{mg/m}^{-3}$ , whereas biological models are typically designed with nitrogen as the measure of phytoplankton biomass. Conversion of the nitrogen content of phytoplankton into the pigment content is neither constant nor obvious. The other

challenging issues are: (i) conservation of mass (How can non-assimilated compartments be readjusted to accommodate the changes in mass driven by the assimilation of data into one compartment?); and (ii) data compatibility (How do observed field data relate to the simulated spatial distribution?).

One of the first coupled physical–biological models to use spaceborne data assimilation was that developed by Ishizaka (1990). He simply replaced phytoplankton fields in the model with CZCS estimates of sea surface pigment. The remaining biological fields were updated in several ways, one of which was assumption of a constant ratio of dissolved *nitrogen:zooplankton:detritus* and conservation of mass. Later, Armstrong *et al.* (1995) used satellite data to adjust phytoplankton concentrations by adding a fraction,  $\varepsilon$ , of the difference between modeled and observed phytoplankton at each time step,  $\Delta t$ . Thus,  $\varepsilon$  determines the rate at which the model is dragged toward the observation data; slow rates of change are called “nudging” (see above). The other model components were allowed to readjust without any special treatment and nitrogen was not conserved.

Bertino *et al.* (2003), Natvik and Evensen (2003a, b), and Simon and Bertino (2009) have all reported advances in data assimilation in marine ecosystem modeling. Although rather simplified, these techniques resulted in a substantial improvement of the predictive ability of the marine ecosystem model. At the same time, in some specific cases relating to ecosystems with intimately interrelated state variables, data assimilation leads to a worse result. Indeed, whereas data assimilation for simpler ocean models is well understood, the extension of methods to non-linear dynamics is non-trivial. As Natvik and Evensen (2003b) have shown, a data assimilation problem might become extremely complicated for strongly non-linear problems, statistical moments of any order may develop from Gaussian initial conditions during non-linear evolution, and important information might be discarded by calculating an estimate based only on the Gaussian part of the full probability distribution.

However, algal blooms (ABs), which often behave quite independently of the larger ecosystem, may be excellent testbeds to explore the utility of data assimilation methodologies and their ability to generate accurate predictions of algal bloom dynamics.

### 5.3 MODELING HABs AS AN ELEMENT OF INTEGRATED MARINE MONITORING

The EC FP5 HABILE (Harmful Algal Bloom Initiation and Prediction in Large European Ecosystems; Pettersson *et al.*, 2005)—coordinated by the Nansen Environmental and Remote Sensing Centre in Bergen, Norway—reflects further progress in European research into the modeling and prediction of HABs. These scientific developments have (along with other activities) been brought further into operational service through the ESA MarCoast Project (<http://gmes-marcoast.com>) implemented under the European Global Monitoring for Environmental Security (GMES) program.

In the previous chapters, we discussed some of the results of satellite monitoring case studies conducted *inter alia* over the waters in the North Sea/Skagerrak, the Baltic Sea, and some other locations (Sections 4.1 and 4.3). Conjointly with remote-sensing studies, extensive ecological modeling investigations have also been conducted within HABILE not only for the above but also for the Galician Rías (Iberian Peninsula).

### 5.3.1 HAB modeling for the North Sea and Skagerrak waters

Implemented by the IMR (Skogen, 1993), ocean ecosystem modeling was carried out by means of the NORWECOM model in conjunction with satellite remote sensing and *in situ* observations for monitoring and forecasting of HAB events in the North Sea and Skagerrak/Kattegat waters. NORWECOM provides prognostics of physical state variables such as sea surface height, current direction and speed, salinity, and temperature. The biological state variables are inorganic nitrogen (DIN), phosphorus (PHO), and silicate (SI); two different types of phytoplankton (diatoms and flagellates); detritus (dead organic matter); diatom skeletals (biogenic silica); inorganic suspended particulate matter (ISPM); oxygen; and light. As a result of the massive *Pseudochattonella* bloom in 1998, a dedicated phytoplankton parameterization of “*Chattonella*” was developed and implemented in NORWECOM (including growth rates in [Figure 5.5](#)). Remote-sensing data were mainly provided by NERSC, in cooperation with Plymouth Marine Laboratory (PML) in the U.K.

For general purposes, NORWECOM has been set up and used to cover the entire North Sea with a horizontal grid resolution of  $20 \times 20$  km ([Figure 5.3A](#)). This resolution is too coarse to properly model the meso-scale ocean processes within the Norwegian Coastal Current and Skagerrak, and for that purpose a nested version of the model is used in this region. In the nested model, boundary conditions from the coarse North Sea model are used as input to a fine-grid ( $4 \times 4$  km) model for the eastern North Sea, Skagerrak, and Kattegat ([Figure 5.3B](#)).

The main features of NORWECOM were described in Section 5.2 and its application is illustrated in [Figure 5.3](#). This model discriminates between two groups of phytoplankton—diatoms (DIA in [Figure 5.4](#)) and flagellates (FLA)—and their growth is affected by nutrient concentrations, light intensity, and temperature. The nutrients are represented by inorganic nitrogen (NIT) such as nitrate and ammonia, inorganic phosphorus (PHO, phosphate) and inorganic silicon (SIL) (silicate). The main difference between diatoms and flagellates is that silicate is not limiting for the production of flagellates. Nutrients are added to the system through river runoff and from the atmosphere. Further nitrogen and phosphorus are regenerated from dead algae (DET) and silicate from biogenic silica (SIS) at a constant rate. Oxygen (OXY) is released during primary production and is consumed in respiration and when detrital matter is regenerated. Oxygen is assumed to be saturated at the surface. For both dead and living algae, the sinking rate, which may depend on the nutrient concentration, is included. In the model, there are no zooplanktons eating the algae. Instead, a constant death rate, which is also assumed to include grazing, is included. Thus, in this context, zooplankton grazing is also

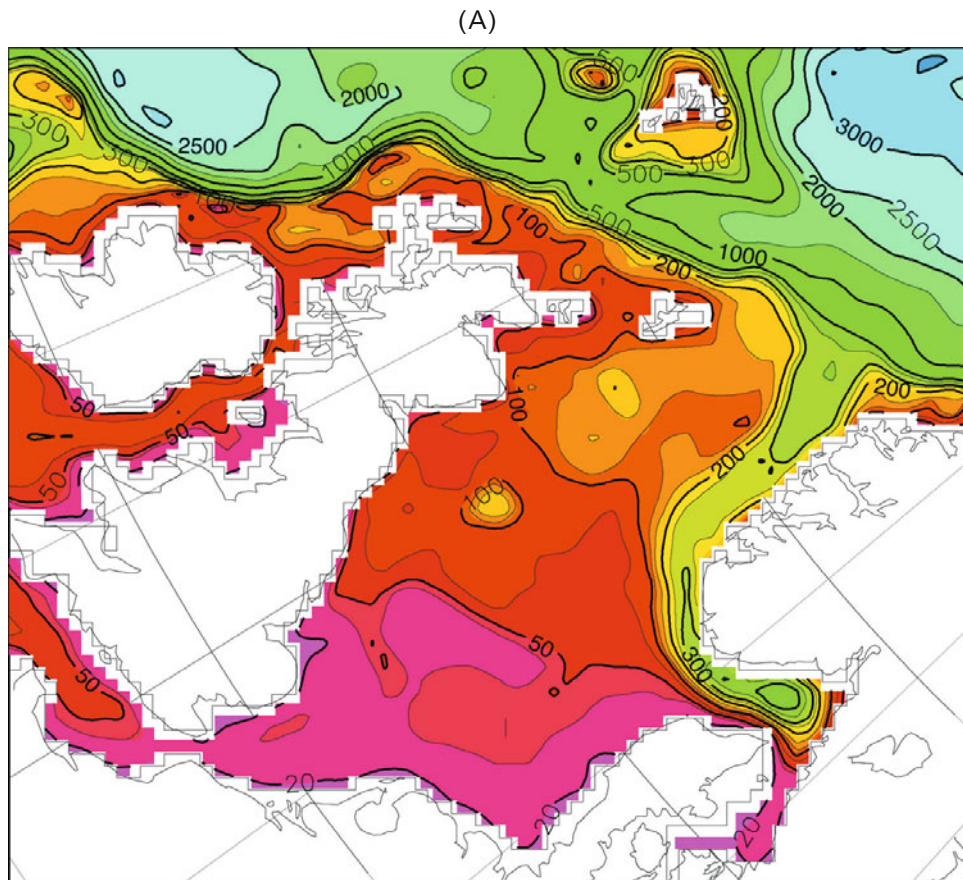


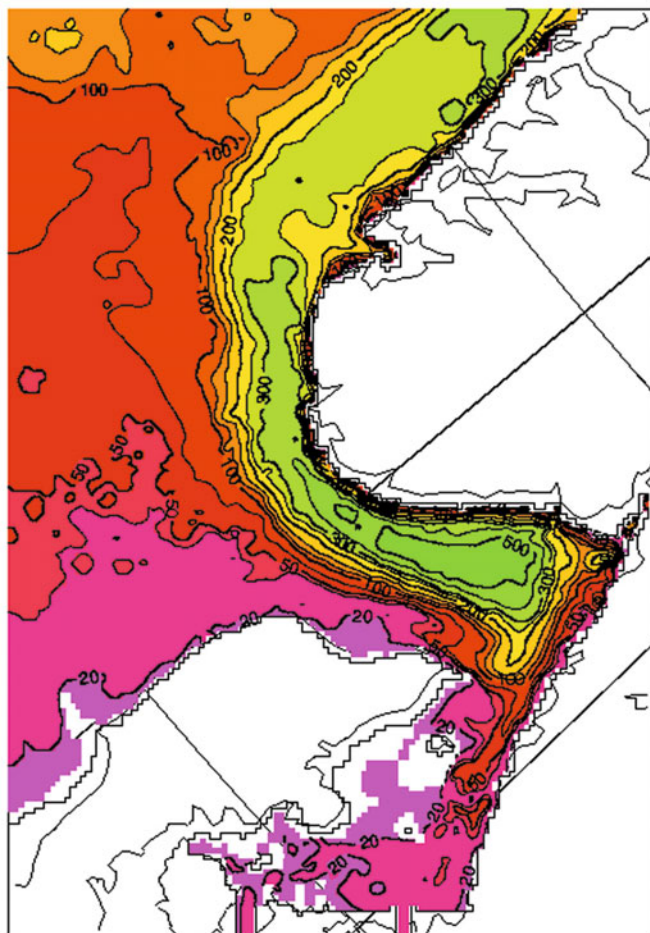
**Figure 5.3.** An illustration of the physical impact of the model grid size illustrated by the bottom topography maps for the coarse grid resolution NORWECOM model (20 km, A) and fine (4 km, B, opposite page) grid resolution. *Courtesy: M. Skogen, IMR (see also Figure 5.1).*

included as a forcing variable. In addition to the eight prognostic variables already mentioned (DIA, FLA, NIT, PHO, SIL, DET, SIS, and OXY), light in the water column (RAD), and an inorganic suspended particulate matter variable (ISPM) are included.

The sedimentation/re-suspension of ISPM and DET is determined by the critical values of bottom stress determined by modeled bottom currents and/or effects from surface waves. Hindcast surface wave fields provided by the Norwegian Meteorological Institute were used to simulate wave forcing.

The description of NORWECOM in Section 5.2 implied that the model did not have a particular harmful algae species as a state variable, just diatoms and flagellates as the two phytoplankton functional groups. Within HABILE, the HAB-modeling capability of NORWECOM has been enhanced by introducing a third

(B)



functional plankton group representing HABs by *Chattonella* spp. (i.e., *Pseudochattonella*, as outlined in Section 4.1.9.1). *Pseudochattonella* spp. have accordingly been implemented with a specially developed HAB module in NORWECOM and its appearance is accordingly predicted. At every time step, the concentration of *Pseudochattonella* is updated according to:

$$\frac{\partial chl-a}{\partial t} + \text{adv}(chl-a) = \text{diff}(chl-a) + P_{chl-a} - R_{chl-a} - D_{chl-a} + \phi(chl-a). \quad (5.7)$$

where  $\text{adv}$  = advection,  $\text{diff}$  = diffusion,  $P$  = production,  $R$  = respiration,  $D$  = death, and  $\phi$  = sink and source terms describing sedimentation/resuspension and sinking (vertical migration) of *Pseudochattonella* spp. The advection, diffusion, and respiration terms are identical to those used for other phytoplankton, while the other terms

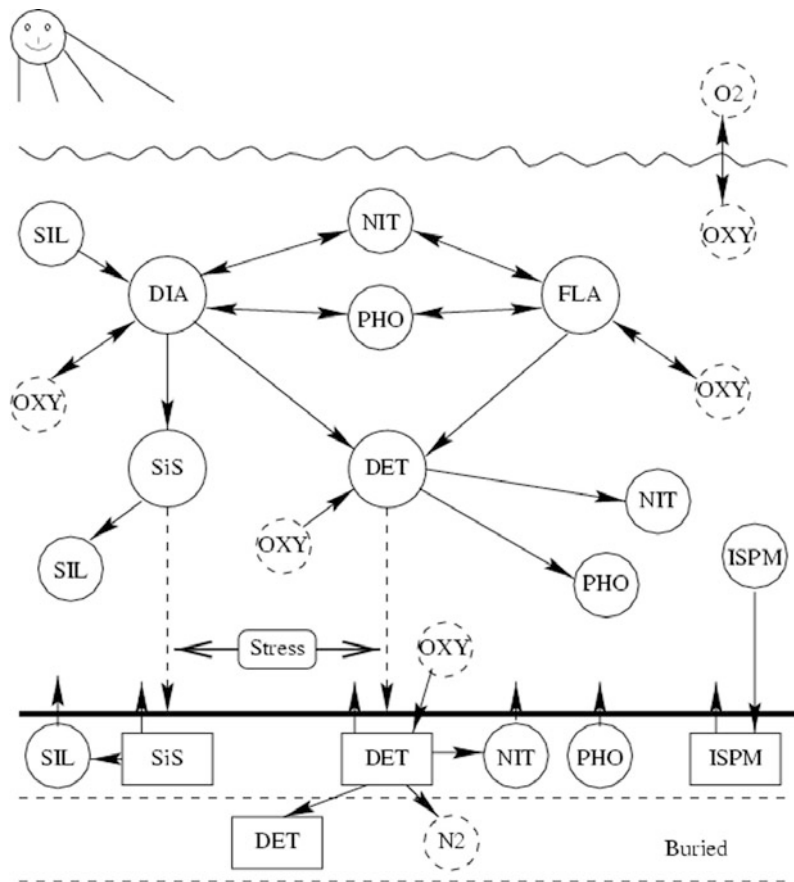
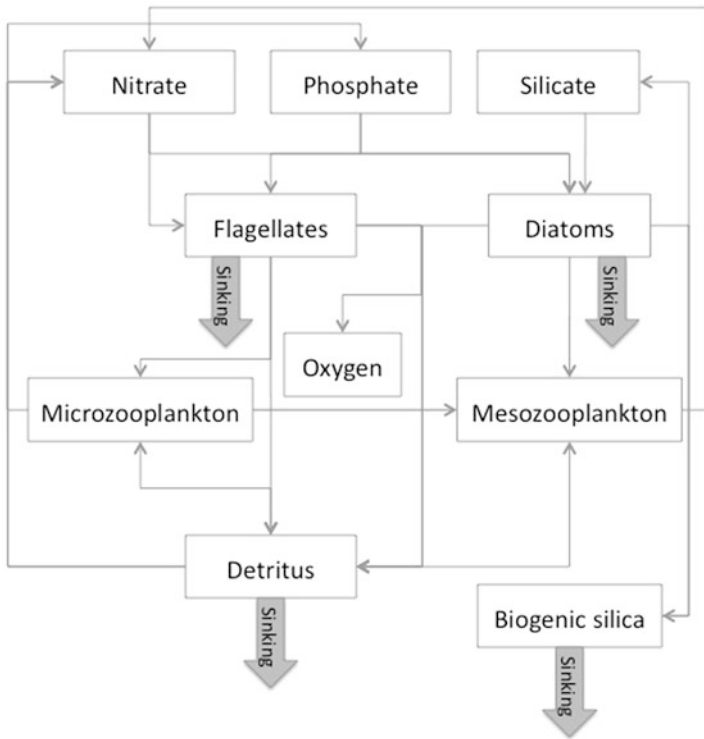


**Figure 5.4.** Schematics of the main biochemical compartments and processes in the NORWECOM marine ecosystem model used at IMR. Courtesy: M. Skogen, IMR. (Opposite page) The main compartments of the NORWECOM model version implemented at the Nansen Center. Courtesy: A. Samuelsen.

are based on *in situ* and laboratory findings. In the HAB module, the maximum production rate,  $F$ , is set to  $1.6 \cdot F(S, T)$ , where  $F(S, T)$  is a third-order polynomial interpolation for the estimated growth rates as a function of water salinity ( $S$ ) and temperature ( $T$ ).

Ocean color satellite data were invariably used to fine-tune model initiation and verify model predictions. Salient bloom features were frequently revealed in optical satellite images, as presented in Section 4.1.9.1. In turn, this stimulated the search for relevant *in situ* data as well as initiating adequate monitoring or emergency actions at the appropriate level.

As discussed in Chapter 3, at present there are no “standard” (e.g., from NASA or ESA) bio-optical algorithms available for harmful algae discrimination or quantitative assessment of their concentration from satellite EO data. However,



when significant amounts of a harmful algae (i.e., high biomass) are detected, a best possible evaluation from satellite, *in situ*, and modeled data is made to assess both the HAB-covered area and the actual algae concentrations. In HABILE, modeled fields of flagellates were re-initialized interactively in the marine ecosystem using thus-assessed algae (*chl*) concentration maps from satellite EO data. Accordingly, the model continued predicting HAB development, displacement/advection, and subsequent bloom decay although the timing of the initiation of the bloom was not accurately predicted in the model. This method seems to work well for high-biomass algae like *Chattonella* as it is “similar” to the NORWECOM “average” flagellate. Repeated observations of the bloom for validation and re-initialization were only employed if model predictions proved to drift away from observed values.

### 5.3.1.1 Modeling the advection and decay of the *Pseudochattonella* bloom in 2001

As described in Section 4.1.9.1, a *Pseudochattonella* bloom caused damage to the southern coast of Norway at the end of March 2001. The bloom turned out to be limited to the waters along the coast of Sørlandet (11-4 in [Figure 4.9](#)). Analysis of the NORWECOM-based prediction for a 7-day period starting on March 21, 2001 ([Figure 5.6](#)) indicated the threat that HAB development during the following week

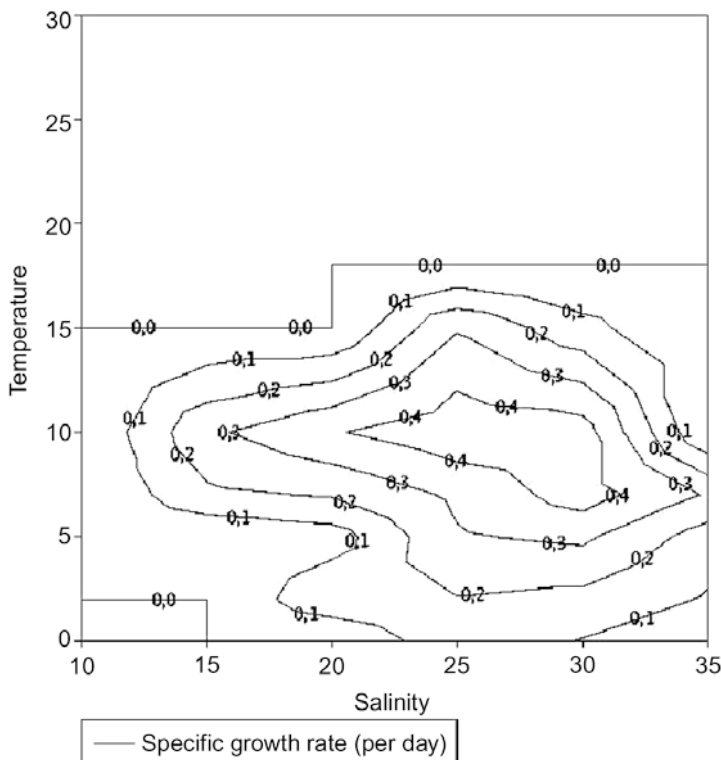


**Figure 5.5.** Specific growth rate ( $\text{day}^{-1}$ ) for *Chattonella* as a function of water salinity and temperature as parameterized in the NORWECOM model. Courtesy: L.-J. Naustvoll, IMR.

could become hazardous to fish farms in western Norway. The first predictions by NORWECOM up to March 28 (Figure 5.6A) showed that northeastward currents would persist along the coast of Norway, keeping the harmful algae from being transported around the southern part of Norway (Lista) and then northward along the western coast. In addition, the simulations also indicated that the algae had moved somewhat farther offshore along Sørlandet. At the same time the *Chattonella* algae population reported just off the Danish coasts appeared to be stationary. *In situ* observations from several places at the southwest and western coasts revealed little or no *Pseudochattonella* (or other potential harmful species). After March 26 cloud cover dominated the region and, hence, limited the availability of high-quality satellite EO information.

The next model prediction for a 7-day period was done on March 29. The circulation pattern extended northeastward along the Norwegian coast, while the algal bloom located along the west coast of Denmark gradually encroached on the southern Skagerrak area. During this forecasting period up to April 5, the model showed a significant decrease in flagellate concentrations (Figure 5.7) due to (modeled) nutrient limitations all over the Skagerrak area. New *in situ* observations

from several locations along the southwest and western coasts showed little or no *Pseudochattonella* (or for that matter, other potential harmful species), and observations from the southeastern coast indicated significantly reduced concentrations of *Pseudochattonella*. Based on these data which showed clear indications of the *Pseudochattonella* bloom coming to an end and expert assessments, the prediction for the following week was that there was little threat of harmful algae occurring along the western coastline of Norway and harming fish farms; however, the *Pseudochattonella* problem remained along Sørlandet in south/southeastern Norway.

Thus, for the predictions during both time periods the prognosis proved to be correct convincingly demonstrating the ability of the employed approach (mainly, NORWECOM) to simulate the development and decay of a HAB event based on high-quality initial conditions.

On the larger scale NORWECOM data are also used to simulate the onset and peak of the ecologically important *diatom spring bloom* and its interannual spatiotemporal variations ([Figure 5.8](#)).

A challenge for predictions of phytoplankton in NORWECOM is the ability to actually match the timing of the onset of bloom events. Simulation results might run either ahead or behind the actual pace at which bloom events unfold. As discussed above, this could clearly be improved by proper assimilation of the *Chl-a* distribution for satellite EO data. In order to provide accurate *Chl-a* concentrations from satellite EO data in these waters, standard Case I algorithms are inappropriate. Regionally tuned bio-optical retrieval algorithms are needed (see Chapter 2) as well as a means of coping with other limitations of EO monitoring such as spatial coverage, cloud cover, lack of vertical information, etc.

### 5.3.1.2 Simulations of interannual variability of *Pseudochattonella*

Simulations of the interannual variability of *Pseudochattonella* in North Sea waters were undertaken for 1999–2001 using the NORWECOM “*Chattonella*” module. For all three years, the model predicts bloom onset to be in mid March (i.e., around day 100, more specifically between day 85 and 125) and bloom duration to be around one month, but with significant inter-annual variations in the absolute values and spatial distribution of integrated *Chattonella* production ([Figures 5.9](#) and [5.10](#)).

Comparing these multi-year model simulations with observations of *Pseudochattonella* made during these years highlights some limitations. The first is that the model indicates an extensive bloom in 1999, when no *Chattonella* bloom was observed (see [Table 2.1](#)). It is believed that the turbulence-dependent death rate and the relatively strong winds in 1999 (see [Figure 5.11](#)) should have been sufficient to prevent the onset of the bloom in the model, but this was not the case. In NORWECOM the bloom starts during a relatively calm (but short in duration) period on day 105, and later its intensity dynamics primarily followed wind stress variations. Indeed, the strong decline of the modeled bloom coincided with very strong wind around day 120. This indicates that the mortality rate set in the

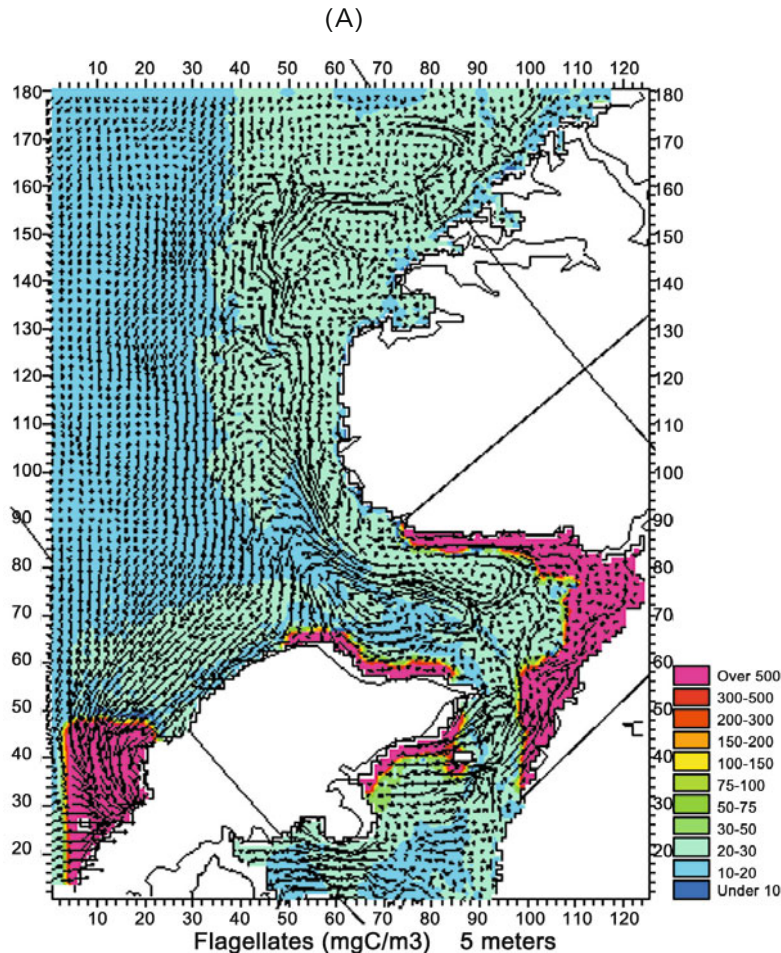
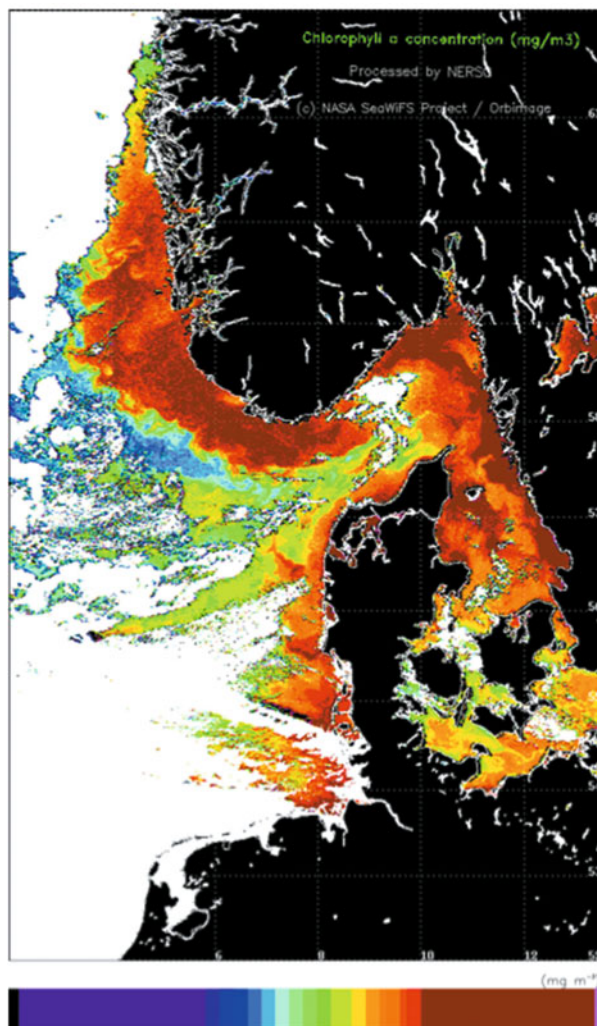


**Figure 5.6.** NORWECOM model simulations of (A, this page) surface currents (arrows) and flagellate concentrations on March 21, 2001 and (B, opposite page) the satellite image from the same day. Note that color scales are not comparable because the model assessment is in carbon-based units, whereas the satellite data are in *chl-a* units. Courtesy: M. Skogen, IMR.

model was probably too weak to reduce the growth rate of *Chattonella* in the NORWECOM model.

Observations indicated that the *Pseudochattonella* bloom in 1998 actually emerged about three weeks later than the one in 2000 (Table 2.1). This is also consistent with observed records of wind stress in the region (Figure 5.11) which indicated a long calm period in 2000 from around day 100. Model simulations for 2000 estimated the first production maximum to be around day 105, followed by a decline before a new maximum emerged around day 120 (Figure 5.10C). In 1998, peak production occurred around day 115 (Figure 5.10A), after a few days of almost no wind (Figure 5.11A).

(B)



This set of *Pseudochattonella* bloom simulations analyzed together with observational physical and biological data highlighted the importance of accurate assessment of the balance between the maximum growth rate and the death rate in the modeling of phytoplankton in marine ecosystem models. Laboratory experiments are strongly indicative of nearly complete depletion of *Pseudochattonella* as turbulence grows (Aure *et al.*, 2001). Therefore, strong winds will cause almost immediate removal of algae in the surface layer, and those algae that were only produced during a few days of calm weather would not be sufficient to generate a massive bloom.

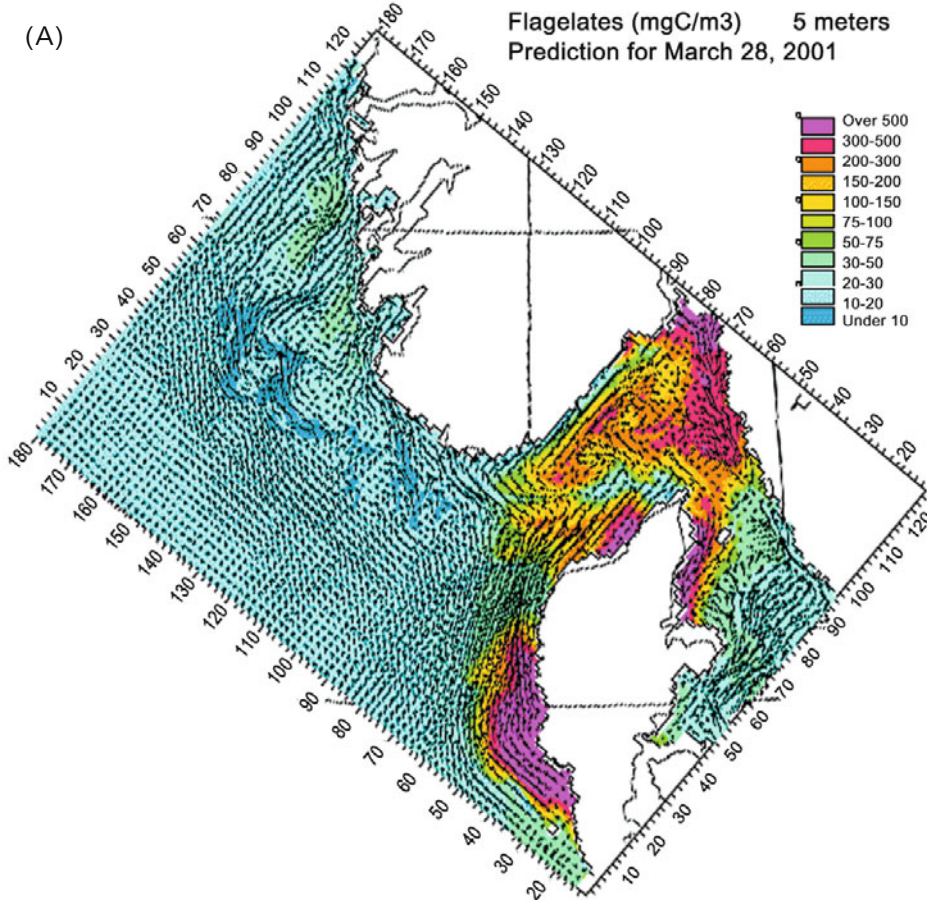
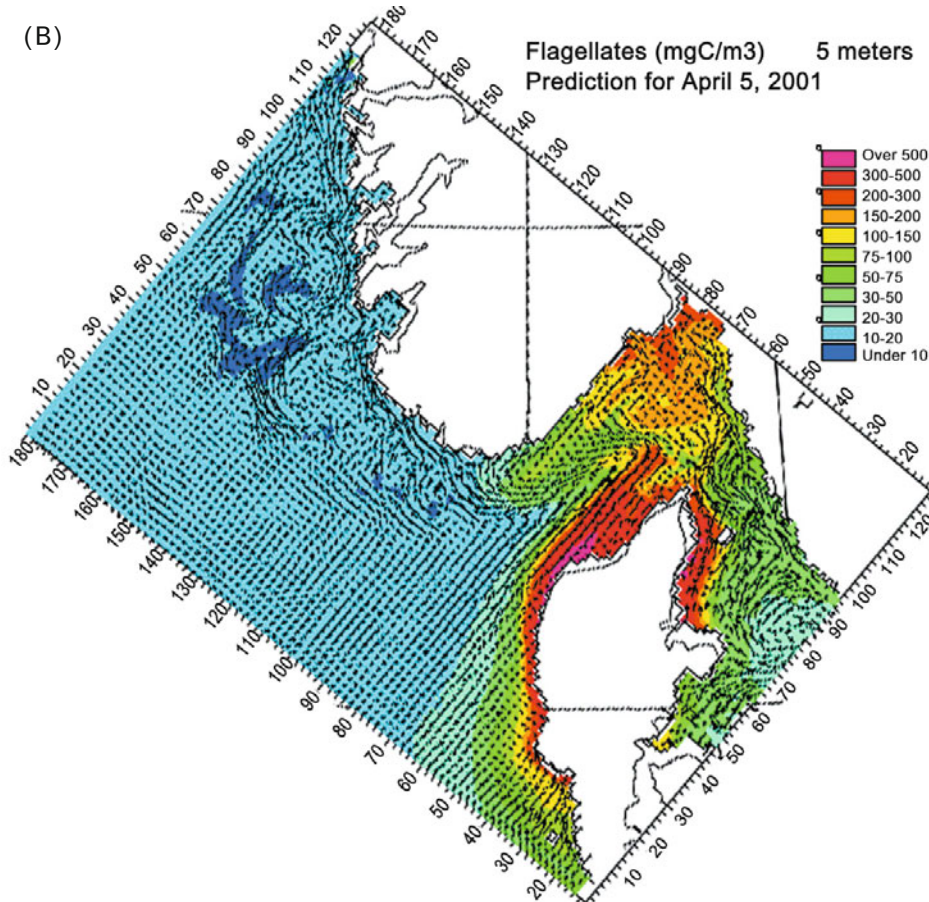


**Figure 5.7.** NORWECOM model simulations of surface circulation (5 m depth) and flagellate concentrations on March 29 (A, this page) and April 5, 2001 (B, opposite page), respectively, based on the assimilation of satellite observations from March 21 (see [Figure 5.4B](#)). Courtesy: M. Skogen, IMR.

Observed *Pseudochattonella* blooms lasted for approximately one month, indicating that there should be some sort of death rate-based mechanism that prevents the development of a *Pseudochattonella* bloom unless there are periods of several weeks of relatively calm weather. Thus, it can be concluded that the temporal behavior of the death rate should be exponential, and the maximum growth rate should be accordingly adjusted vs. formulation of the death rate. Indeed, this is a challenging task remembering that the growth rate is a function of many environmental parameters, including physical parameters such as water salinity and temperature (see [Figure 5.5](#)). This is supported by observations of minimum salinity in the Norwegian Coastal Current occurring as a result of spring snow and ice melt discharge through river flooding between March and May, apparently implying that



the model is not capable of simulating the occurrence of blooms in May. Also, the depletion of nutrients, as a result of month-long ongoing blooming during April, influences the decay and timing of the end of the *Chattonella* bloom as simulated in NORWECOM. Later in summer, water temperature possibly becomes an efficient limitation factor preventing/supressing a second *Chattonella* bloom from occurring in the model.

### 5.3.2 HAB modeling for the Baltic Sea

Cyanobacteria blooms (exemplified in Figures 4.33–4.34) have a dramatic impact on marine ecosystems and are considered to be a natural annual bloom phenomenon for the Baltic Sea. The Baltic Sea is one of the biggest brackish water seas with salinity ranging from almost freshwater in the Bay of Bothnia to 15 psu in the Danish Belt

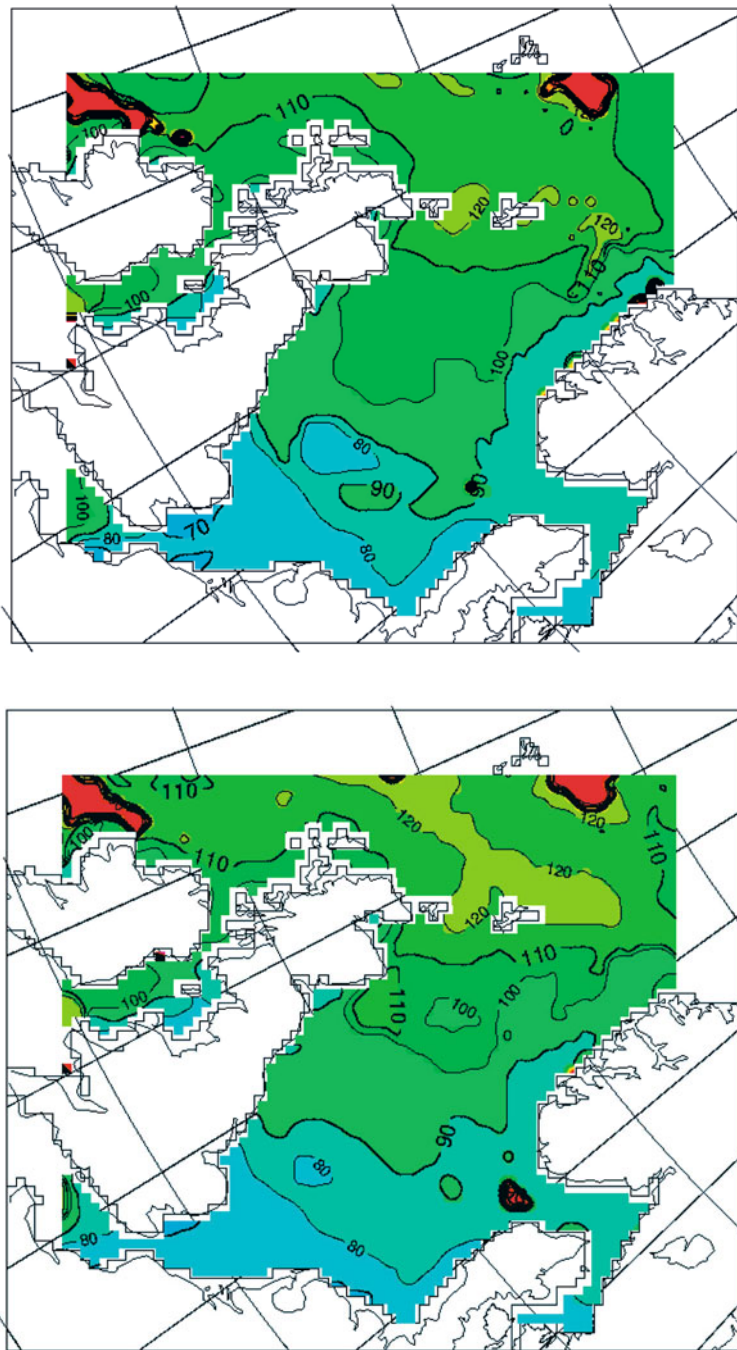
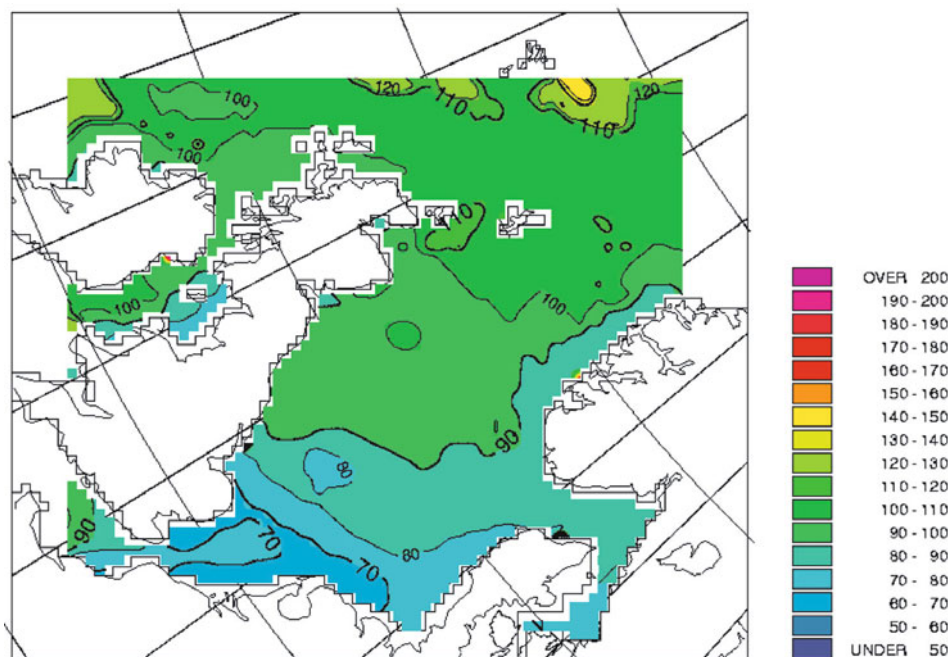


**Figure 5.8.** NORWECOM model simulations of peak production of diatoms in 2000 (top), 2001 (bottom), and 2002 (opposite page). Courtesy: M. Skogen, IMR.



area between Denmark and Sweden and has pronounced vertical stratification. Salinity and temperature stratification (especially during summer) prevents the vertical mixing and input of inorganic nutrients from lower layers to the surface (Leppäranta and Myrberg, 2009).

Nutrient load has increased several fold for nitrogen and even more so for phosphorus since 1900 (Larsson *et al.*, 1985). Alterations of nutrient ratios seem to be the key factor in generating cyanobacteria blooms in the Baltic Sea, although there is still not common agreement on the limiting nutrient in the Baltic Sea, albeit some preference is given to nitrogen.

The most common species constituting cyanobacteria blooms in the Baltic Sea are *Nodularia spumigena* Mertens and *Aphanizomenon flos-aquae* Ralfs (further on referred to as *Nodularia* and *Aphanizomenon*). Accordingly, countries around the Baltic Sea have paid considerable attention to the monitoring and forecasting of the occurrence of these species.

The physical processes that trigger HABs differ significantly within the semi-enclosed Baltic Sea, but riverine freshwater inflow (rich in phosphorus) and short-term wind-driven upwelling/downwelling events are among the most important physical processes (Kaitala *et al.*, 2004). Water temperature and salinity level are also determining factors: whereas *Aphanizomenon* grows best in water temperatures of about 12–17°C and salinity  $S \leq 10$  psu, *Nodularia* has its optimum temperature for growth at 12–25°C and  $3 \text{ psu} \leq S < 30 \text{ psu}$  (the upper limit is not found in the Baltic Sea).

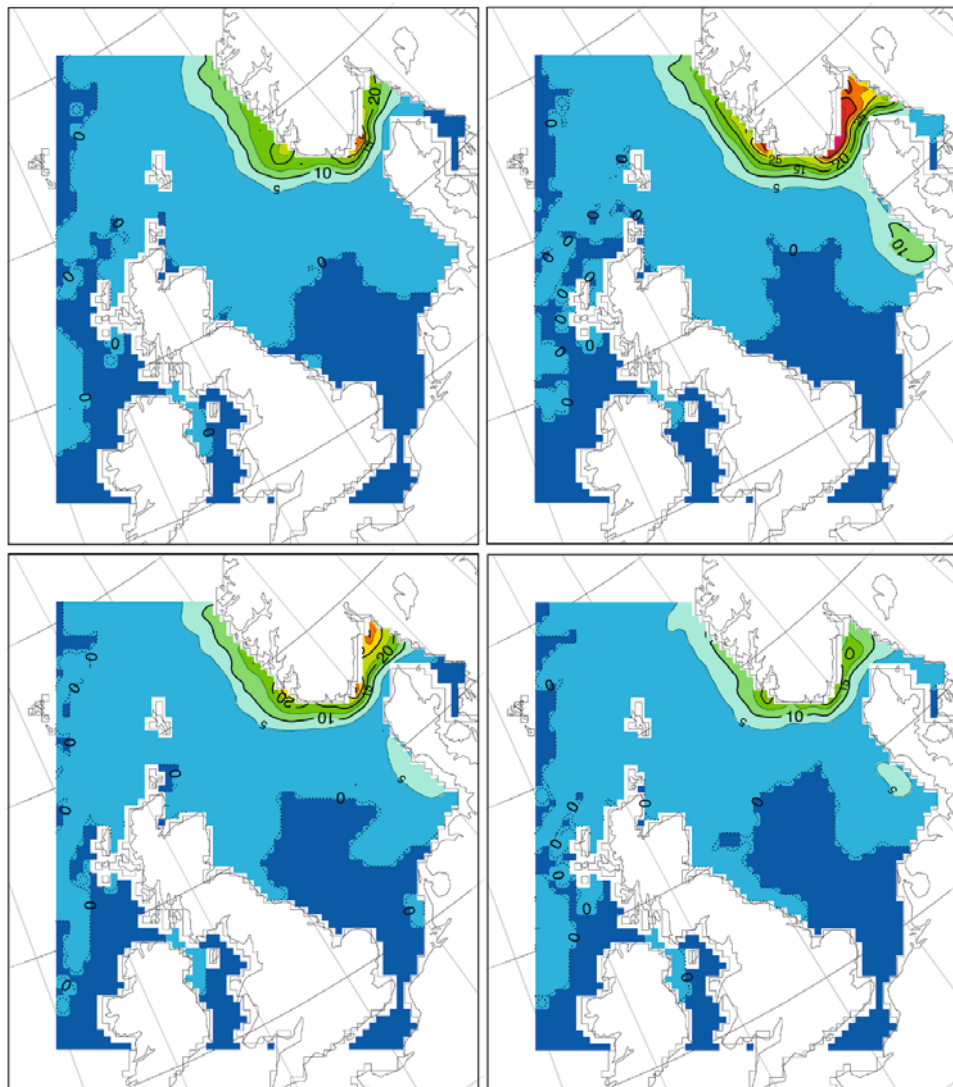


**Figure 5.9.** NORWECOM model simulations of annual depth-integrated production of *Chattonella* for 1998 (upper left), 1999 (upper right), 2000 (lower left), and 2001 (lower right). Courtesy: M. Skogen, IMR.

To model the Baltic Sea ecosystem, the Finnish Institute for Marine Research (FIMR) HAB (cyanobacteria) model (Stipa, 2002) has been applied. It is nested inside the non-hydrostatic ocean model developed by Marshall *et al.* (1997) and has been configured for the Baltic Sea on a spherical polar grid with approximate  $11 \times 11\text{ km}$  horizontal resolution and 21 vertical layers with increasing thickness with depth.

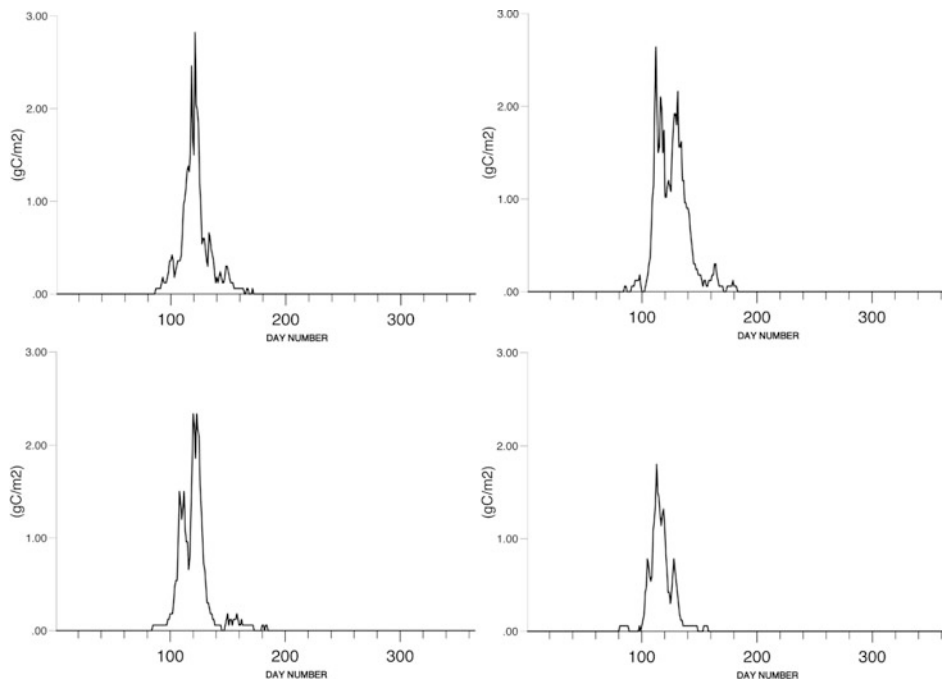


**Figure 5.10.** NORWECOM model simulations of the time series of *Chattonella* production ( $\text{gC}/\text{m}^2/\text{day}$ ) at a location outside Lista for the years 1998 (upper left), 1999 (upper right), 2000 (lower left), and 2001 (lower right). Courtesy: M. Skogen, IMR.

For all tracers, including HABs, a positive definite non-linear flux-limited advection scheme is used. The sub-grid scale vertical turbulent transport of both oceanographic and biological tracers in the presented configuration is parameterized using the non-local K-profile parameterization (KPP) closure (Large *et al.*, 1994).

The marine ecosystem model employed is a modified version of the biological model developed by Aksnes *et al.* (1995) and also used in NORWECOM. The model comprises the following compartments: phosphates, dissolved inorganic nitrogen and silicate, and three algal groups—diatoms, flagellates, and cyanobacteria (*Nodularia* and *Aphanizomenon*). Fluxes between the algal and nutrient (nitrogen) compartments are expressed in nitrogen units ( $\text{mm N m}^{-3}$ ). The model also includes a prognostic silicate and phosphate compartment. Biochemical changes in the concentrations of primary producers are controlled by growth rates, metabolic losses, and mortality, which includes natural mortality as well as grazing by zooplankton. A fixed N/P ratio for the uptake and metabolic losses of primary producers was assumed whereas, for diatoms, a fixed Si/N ratio for the relevant uptake and growth was set.

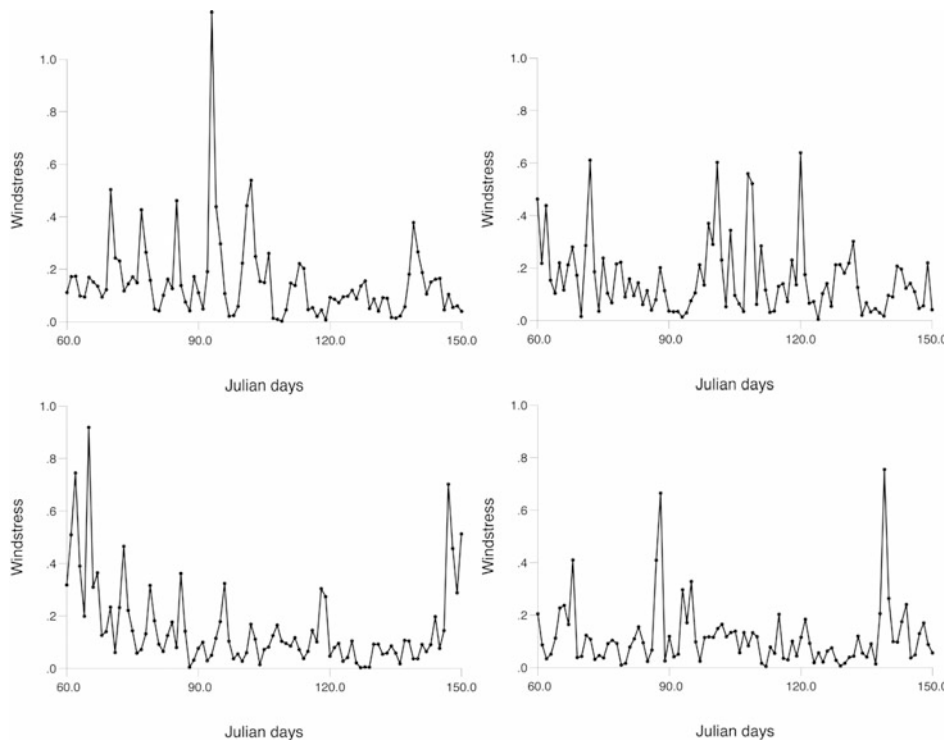


**Figure 5.11.** NORWECOM model simulations of the daily mean wind stress ( $\text{m}^2 \text{ s}^{-2}$ ) for a location outside Lista in the years 1998 (upper left), 1999 (upper right), 2000 (lower left), and 2001 (lower right) for the period March–May. *Courtesy: M. Skogen, IMR.*

### 5.3.2.1 Model hindcasts of cyanobacteria blooms in the Baltic Sea

The results of forecasting simulations indicated that the FIMR HAB model described the nutrient concentrations in spring well: they were high enough to support the growth of phytoplankton. Simulated phytoplankton growth generally starts between March and April in the Baltic Sea, which is consistent with the data provided by Alg@line (Ruokanen *et al.*, 2003): typically, the spring bloom propagates from south to north and from west to east in the Baltic Sea.

The simulated spring algal bloom was followed by depletion of dissolved inorganic nitrogen, whereas phosphate concentrations remained high. Although it has been proposed that cyanobacteria take up phosphate that has been left over, simulation experiments have shown that the maximum of cyanobacteria biomass may occur about 60 days later than the minimum N/P ratio, which is consistent with available observations (Figure 5.12).

The model, however, overestimated the increase of the N/P ratio during the period of cyanobacteria growth. This can be attributed either to total neglect of remineralization processes or else to the ability of cyanobacteria to take up dissolved inorganic phosphorus, neither of which was included in the ecosystem model.

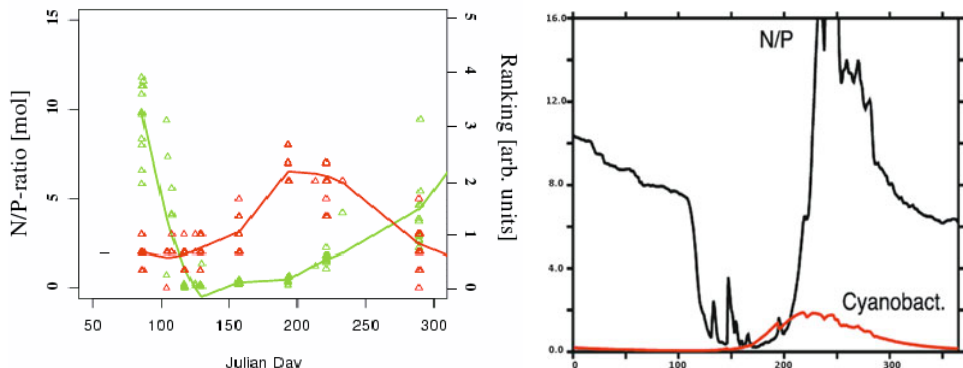


**Figure 5.12.** Temporal variability of the N/P ratio (green) and cyanobacterial biomass (red) derived from observations (left) and from model simulations (right). Courtesy: S. Kaitala, FIMR.

However, the simulated time of cyanobacterial biomass maximum and maximal water temperature coincided ([Figure 5.13](#)).

Analysis of cyanobacteria growth dynamics indicates that cyanobacterial blooms emerge almost instantaneously throughout the Baltic Sea. As *Aphanizomenon* prefers a lower temperature than *Nodularia*, its maximum biomass is reached approximately 20 days earlier. *Aphanizomenon* can build up extensive blooms with a higher biomass than *Nodularia*, as happened in 2000. The highest concentrations of *Aphanizomenon* occurred mainly in the vicinity of the Swedish coast and at the mouth of the Gulf of Finland. Low concentrations of *Nodularia* in summer can be attributed to low surface water temperatures. Simulations explicitly indicate ([Figure 5.14](#)) that in the case of upwelling of cold water below the pycnocline, the growth rates of *Nodularia* decline significantly. At the same time, the growth rate of this alga increases if surface water was previously well heated before descending.

Interestingly, whereas low water surface temperatures favored the growth of *Aphanizomenon* in 2000 and slowed down the growth of *Nodularia*, a year before the situation was opposite. Simulations have yielded lower concentrations of *Aphanizomenon* in 1999 compared to those in 2000 and also lower biomass compared to *Nodularia*. High concentrations of *Nodularia* in 1999 were correctly hindcast in the southern and central Baltic Sea as well as in the mouth of the Gulf of Finland. In both years, the simulated biomass of *Aphanizomenon* was high mainly along the Swedish coast and in the southern vicinity of the mouth of the Gulf of Finland.

Simulations yielded strikingly low concentrations of *Nodularia* and *Aphanizomenon* in the Gulf of Bothnia, which could be attributed to the low phosphate concentrations revealed by modeling.

The salinity effect simulated by the FIMR model is highly compatible with available observations: low salinity in the Gulf of Finland due to river inflow prevented *Nodularia* from building up a high biomass, whereas high salinity in Skagerrak proved to be unfavorable for the growth of both cyanobacteria species.

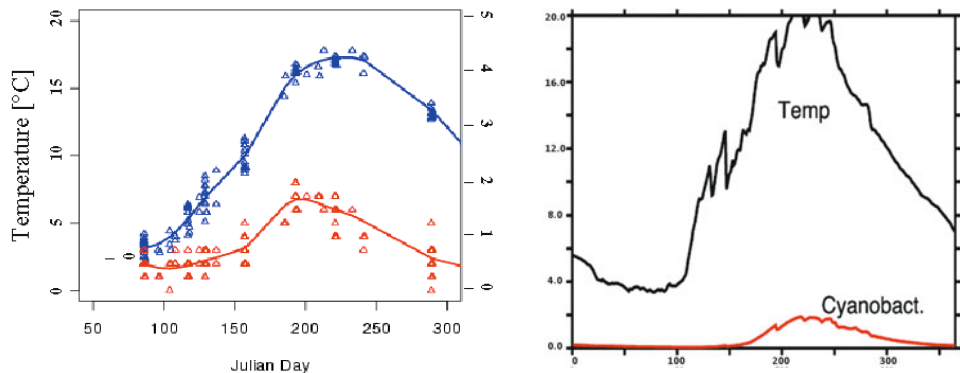


**Figure 5.13.** Temporal variability of water temperature (blue) and cyanobacterial biomass (red) derived from observations (left) and from model simulations (right). *Courtesy:* S. Kaitala, FIMR.

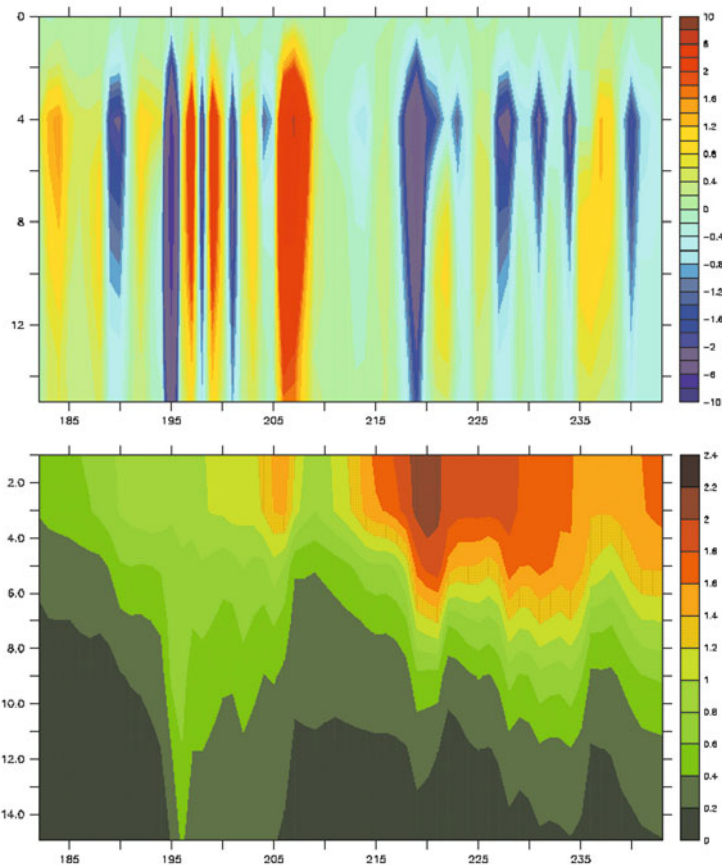


**Figure 5.14.** Temporal variability of *Nodularia* biomass and vertical velocity in the water column. *Courtesy:* S. Kaitala, FIMR.

### 5.3.2.2 Model forecasts of cyanobacteria blooms across the entire Baltic Sea

Employing the above monitoring data as initial conditions for prognostic runs of the ecosystem model, two scenarios for the growth of cyanobacteria during summer 2004 were developed with due consideration of the knowledge built up by the Alg@line forecasters at FIMR.

Two scenarios for the development of cyanobacteria in the summer of 2004 were derived. Simulations were initiated with the actual weather conditions during February 2004. The monitoring results that were used to derive the indicators of the cyanobacteria bloom were used as initial conditions for the ecosystem model. Integration was performed with synoptic atmospheric forcing for years 2000 and 2002 representing weather patterns during a typically cold summer (2000) and a warm summer (2002). Mean cyanobacterial biomass in the top 10 meters was forecast for the summer season, July–August ([Figure 5.15](#)).

Both scenarios yielded a high biomass for cyanobacteria in the Gulf of Finland. This was attributed to high levels of phosphate. The interannual variations (cold or warm summer) in cyanobacteria spatial distribution revealed in the simulated data were interpreted as a manifestation of variations in Baltic Sea mean circulation patterns.

Unlike somewhat lower cyanobacterial biomasses in the northern Baltic governed by the lower temperature scenario, simulated cyanobacterial biomass in the southwestern Baltic proved to be higher in the case of the “cold” 2000 conditions than in the case of the “warm” 2002 conditions. This appears to be an indication that the annual development of cyanobacterial blooms is determined more by actual weather conditions than by the initial environmental conditions employed (i.e., wintertime nutrient concentrations).

Model predictions of the Baltic Sea ecological system state in the summer of 2004 were compared to the results of intense monitoring of cyanobacterial abundance performed by the Alg@line system. The correspondence between monitoring and research results, on the one hand, and model results, on the other hand, were assessed several times per week, and general consistency was found to be satisfactory in terms of the onset and duration of bloom initiation as well as its growth dynamics (peak, decay, and termination).

Throughout the summer of 2004, which turned out to be cooler than 2002, most of the cyanobacterial biomass observed by Alg@line was due to *Aphanizomenon*, which, as pointed out above, prefers lower temperatures. In daily model predictions, the *Aphanizomenon* biomass was indeed consistently higher than that of *Nodularia*, and this held up throughout the entire summer. Thus, the model correctly predicted this situation. However, as the observed abundance of cyanobacteria was estimated via cell counts that should be compared with the cellular concentration of nitrogen as predicted by the model, direct quantitative comparison was not possible.

### 5.3.3 HAB modeling in the Galician Rías

In Section 2.4.3, we discussed the specific features of blooms of dinoflagellates, often harmful and relatively frequent in the Rías Baixas of Galicia (Spain), in four bays

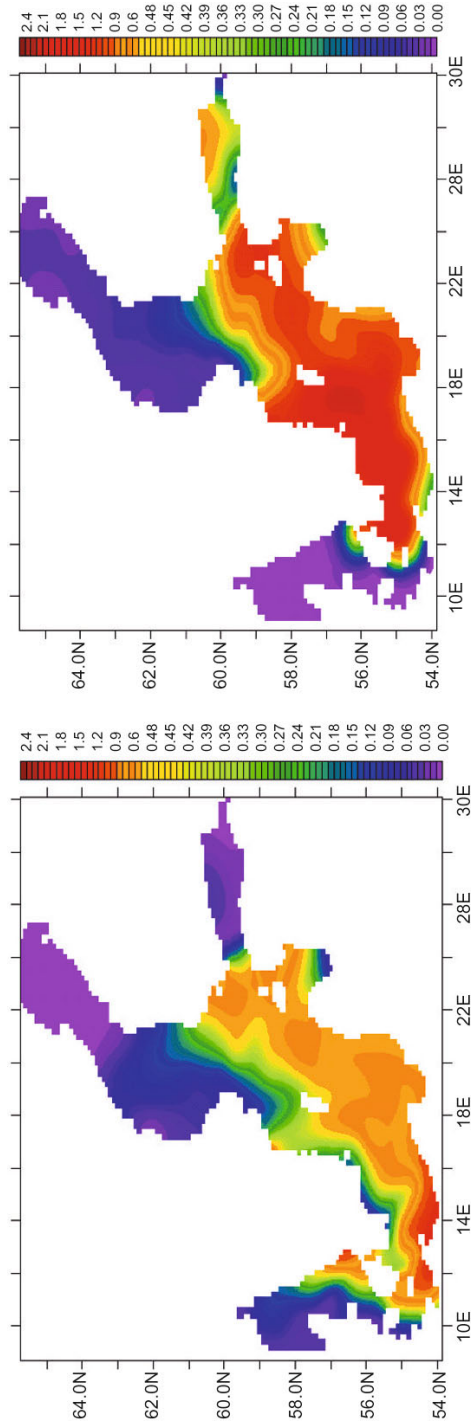


**Figure 5.15.** Simulated summer distribution of *Nodularia* (left), *Aphanizomenon* (right) for the Baltic Sea during summer. Courtesy: T. Stipa, FIMR.

(*rías*) on the NW Iberian peninsula where seasonal upwelling/downwelling is one of the main oceanographic features determining ocean circulation and algal bloom conditions (Figueiras *et al.*, 2002).

We reiterate only very briefly here the main processes initiating and controlling the HAB events in these *rías*, and for illustrative purposes we refer back to the respective figures in Section 2.4.3 ([Figures 2.11–2.14](#)).

Seasonal upwelling on the NW Iberian shelf occurs on average from March to September when northerly winds are dominant, whereas downwelling prevails during the rest of the year owing to the predominance of southerly and westerly winds. Coastal upwelling and downwelling greatly influence circulation in the *rías* ([Figure 2.10](#)) and, therefore, the exchange processes between *rías* and the adjacent shelf. Upwelling forces two-layer density-induced positive circulation in the *rías*, characterized by the outflow of surface waters and the compensating inflow of upwelled water at the bottom.

The transition to seasonal downwelling, which coincides with the rapid change to southerly winds, establishes a reversal circulation during which surface coastal water enters the *rías* to develop a downwelling front at the location where it meets inner waters with higher continental influence. During this reversal circulation, the outflow towards the ocean in the outer circulation cell ([Figure 2.10b](#)) takes place at the bottom layer.

Reversal circulation modifies the distribution of microplankton assemblages along the *rías* and in the nearest shelf which, under upwelling conditions, is characterized by the dominance of diatoms in the inner waters and the higher importance of dinoflagellates towards the shelf.

Downwelling causes the advection of dinoflagellates to the interior of the *rías* and promotes their accumulation in the downwelling front (Fermín *et al.*, 1996). This is predominantly due to the vertical swimming capability of dinoflagellates, which allows them to compensate for convergence-driven downward velocity. Diatoms, unable to withstand downward movement, are pushed down in the water column only to be then exported towards the shelf by the bottom outflow current ([Figure 2.11](#)). This type of HAB initiation was also documented through analysis of a one-year time series of weekly sampled data from a station on the shelf ([Figure 2.12](#)).

The 3-D coupled hydrodynamic–ecosystem model POLCOMS–ERSEM was employed for the Ría de Vigo by PML and IIM. The ERSEM model was employed as the ecosystem model (see Section 5.2.3). The hydrodynamic component was the 3-D baroclinic B-grid model described by Holt and James (2001). As already discussed (Section 5.2.4), this is a primitive equation finite difference model that has a sophisticated advection scheme to minimize numerical diffusion and ensure the preservation of features even on coarse grids under oscillatory flows. Horizontal pressure gradients are calculated by interpolation onto horizontal planes. Turbulent viscosities and diffusivities are calculated using a Mellor–Yamada level-2.5 turbulence closure, but with an algebraically specified mixing length.

Forced by six hourly European Centre for Medium-Range Weather Forecasting (ECMWF) meteorological variables, the ecosystem model was set up with a

resolution of  $750 \times 550\text{m}$ , with 16 vertical levels for the Ría de Vigo. ECMWF winds were applied only over the shelf domain while *in situ* wind measurements, freshwater inputs, and cloud cover were applied to the domain inside the Ría de Vigo. No nutrient loading was included in the freshwater input under the assumption that the ría's ecosystem dynamics is mostly driven by upwelling/downwelling and the main nutrient source is bottom water from the shelf.

The boundary conditions of 15 tidal harmonics were used to drive the model, while sea surface temperature (SST) and salinity data were interpolated from the Atlantic Shelf Wide 12 km grid model run operationally by the U.K. Met Office (<http://www.met-office.gov.uk/index.html>).

No boundary conditions were used for ERSEM, which means it was run as a 1-D model at the domain's boundaries. ERSEM was initialized from winter conditions and spun up for two years. The parameter set used for ERSEM is identical to the generic parameter set used in Blackford *et al.* (2004).

Analyses of simulation results indicate that the model reproduces the hydrodynamics of the ría system well. The ría system is characterized by the predominance of downwelling events in winter, with northward shelf flow and enhanced stratification inside the ría due to high freshwater inflow.

During the summer period (May–September), low river inflow proved to be coupled with high solar insolation and upwelling winds, which maintained stratification inside the ría due to advection of more saline colder waters from the shelf to the bottom layer.

The coupled model reproduced both episodes of upwelling and downwelling well. During periods of upwelling and southward circulation on the shelf, surface outflow takes place predominantly through the southern mouth (as exemplified in [Figure 5.16A](#)). Conversely, during downwelling and northward shelf flow, ría outflow is mostly through the northern mouth ([Figure 5.16B](#)) and freshwater outflow is advected northward close to the coast. The model also reproduced coastal upwelling in response to northerly winds well. The two-layer circulation of the ría (outflow at the surface and inflow at the bottom, [Figure 2.10](#)) proved to be realistically reproduced. Moreover, the aforementioned episodes of reversal circulation were reproduced under enforced conditions of strong downwelling.

The model proved to be capable of accurately describing the seasonal patterns of nutrient concentrations in the ría, with the exception of silicate, which turned out to be 30% lower than expected. This might suggest that river discharge can be an additional silicate source that is not included in the model setup.

The variability revealed by simulations in nutrient fields and attributed to wind forcing (on short and seasonal timescales) proved to be further reflected in phytoplankton biomass levels. Modeling indicated that vernal and autumnal diatom blooms were superimposed onto shorter timescale wind-driven dynamics.

Simulations showed that during upwelling episodes, nutrient-rich bottom shelf water was transported inshore ([Figure 5.17A](#)), fueling algal production inside the ría ([Figure 5.17B](#)). The reverse situation occurred during downwelling episodes; the two-layer circulation weakened and in time reversed. Nutrient-poor surface waters

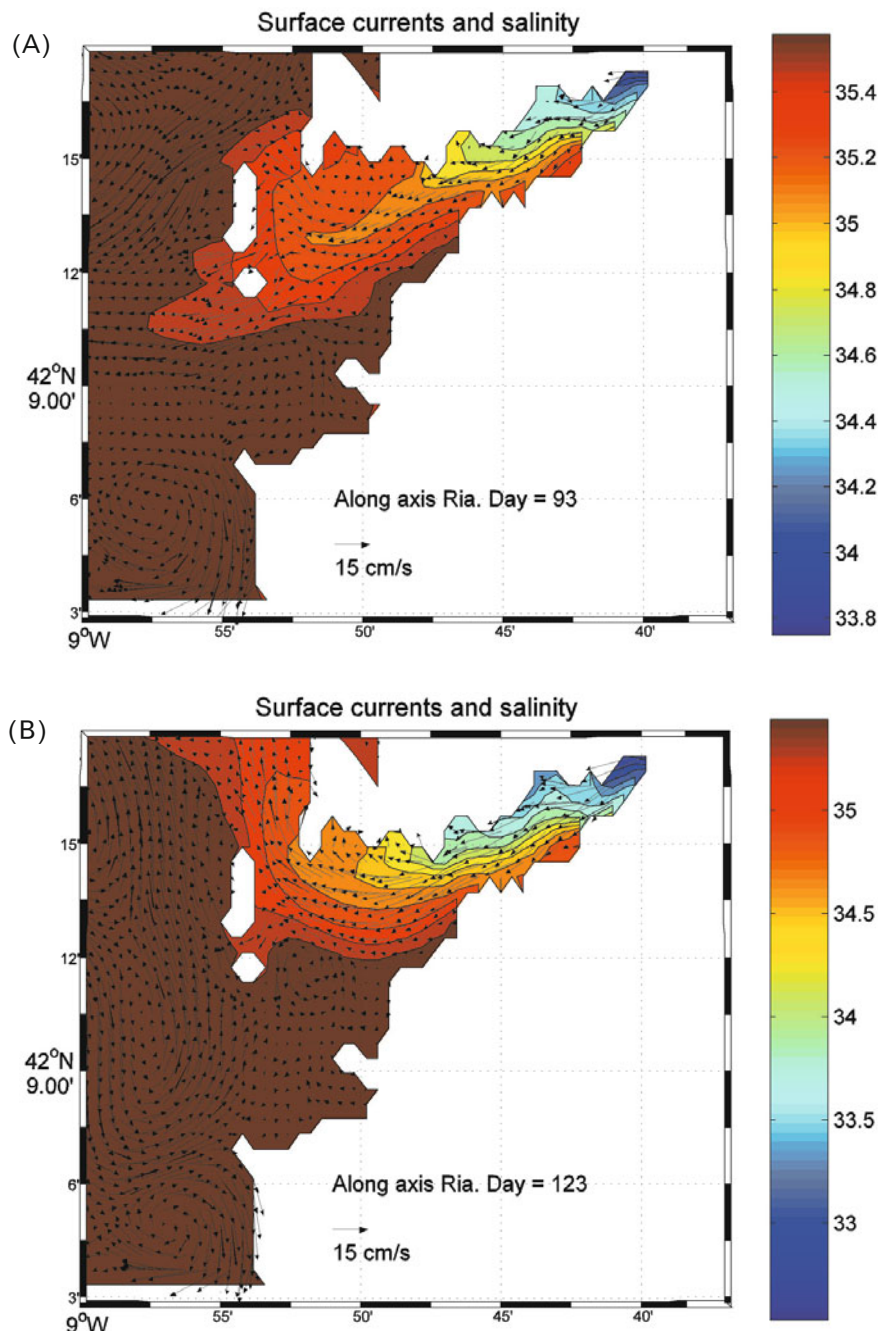


**Figure 5.16.** Surface currents and salinity distribution during (A) the upwelling episode on April 3, 2003 and (B) the pronounced downwelling event on May 3, 2003 in the Galician Rías. Courtesy: F. G. Figueiras, IIM.

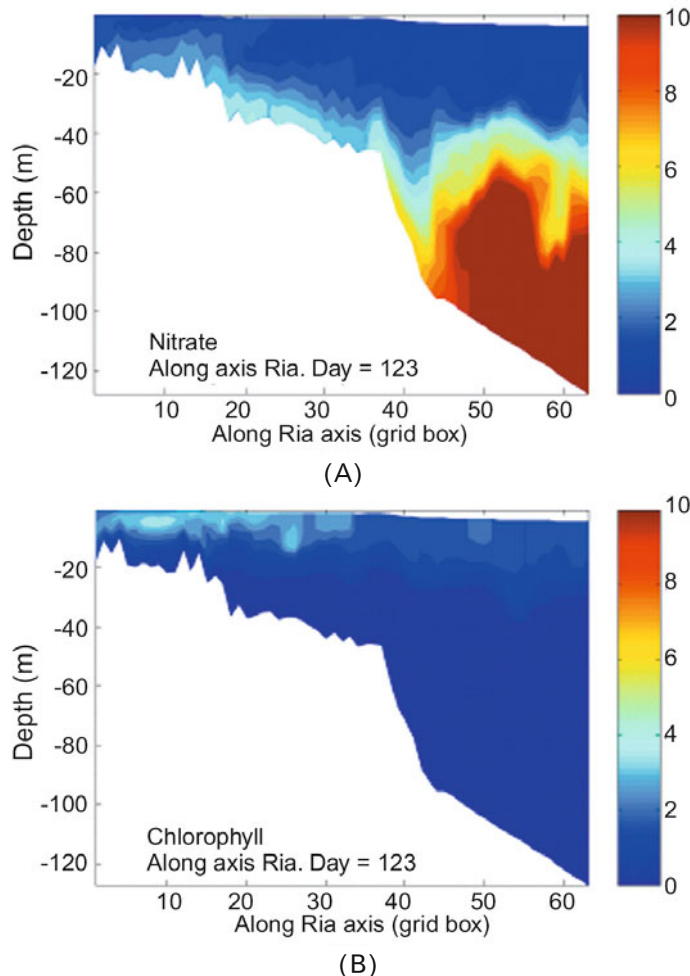


**Figure 5.17.** Transect along the ría's axis during the 2003 upwelling episode for (A) nitrate ( $\text{mmol N/m}^3$ ) and (B) total chlorophyll ( $\text{mg/m}^3$ ). Courtesy: F. G. Figueiras, IIM.

were advected onshore (e.g., nitrate in Figure 5.18A), in turn reducing productivity (e.g., total chlorophyll in Figure 5.18B).

Model simulations allowed net water flux throughout 2003 to be quantified, showing alternations between net export onto the shelf and net import into the ría, which turned out to be in contrast with the general net import of nitrate into the inner ría.

Modeling revealed that the phytoplankton biomass was generally exported from the ría and only strong downwelling events (e.g., in February) resulted in net biomass import. This suggests that a large proportion of primary productivity inside the ría is evidently generated locally.

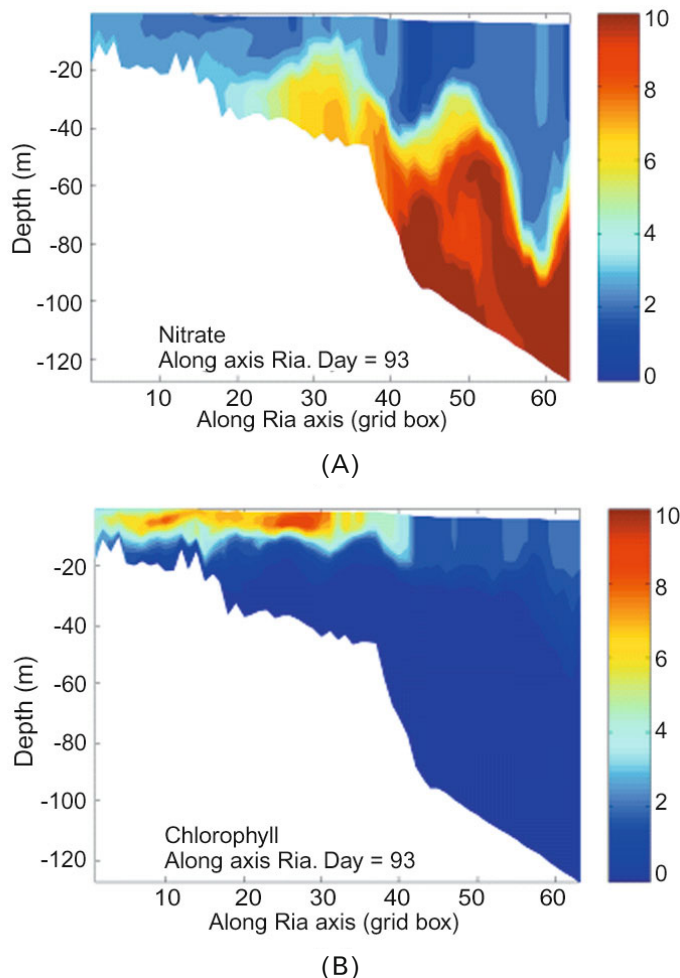


**Figure 5.18.** Transect along the ría's axis during the pronounced downwelling event for (A) nitrate ( $\text{mmol N/m}^3$ ) and (B) total chlorophyll ( $\text{mg/m}^3$ ). *Courtesy: F. G. Figueiras, IIM.*

## 5.4 CLOSING REMARKS

The extensive but far from exhaustive suite of examples of marine ecosystem models discussed above clearly indicate that there is a significant variety of approaches that differ conceptually and in their complexity.

In each specific case, the choice of model type is determined by the study goals and by the distinguishing features of the water body and ecosystem being simulated. In some cases, local hydrodynamic conditions and the indigenous ecosystem allow simplifications without compromising the simulation results of the model.

Nevertheless, in general, when tackling extensive ecosystems nested inside even larger marine environments that determine complex boundary conditions, modelers need to design tools that are able to accommodate a wide spectrum of state variables, functional groups, and trophic interactions, as well as a variety of physical forcing mechanisms and options. To be used predictively, such sophisticated models need to be appropriately sensitive to global change and anthropogenic loading impacts (Edwards *et al.*, 2006), as well as capable of resolving the impact of natural changes in the marine ecosystem. This can only be attained if biogeochemical models are suitably nested inside 3-D hydrodynamic models that have sufficiently flexible temporal and spatial resolutions to be able to accurately describe marine phenomena and processes on a variety of time and space scales.

In some of the cases discussed above, we presented the capabilities, advantages, and limitations of using satellite EO data for validation of model predictability of ocean state variables at the sea surface. Combined use of *in situ* and satellite EO-derived parameters have still unexploited potential for model validation.

Closely related to this, satellite data assimilation is another important potential application for the further development of marine ecosystem modeling. For several physical ocean state variables (e.g., SST, sea surface height, sea ice, as well as *in situ* temperature and salinity profiles), this is routinely applied in near-real-time forecasting. However, data assimilation of biological parameters in marine ecosystem modeling is still at the scientific research stage and not ready for practical/routine applications, although some models have demonstrated their potential for routine operational use.

Finally, although sensitivity analyses of responsiveness to global change and anthropogenic loading have been performed for many models, there is still no definitive elucidation of the reasons behind the increasing HAB occurrence in our coastal and marine waters. This query still needs further investigation.

## Afterword

The increasing occurrence of harmful algal bloom (HAB) events in coastal and marine waters has posed many challenges—both scientific and societal—that need to be faced. However, new knowledge and technology have contributed greatly to our assessment and knowledge of the state of the oceans including HABs. This book elaborates the advantages and limitations of incorporating satellite Earth observation (EO) data as an important and integral part of HAB monitoring; its focus is on coastal European waters that have been identified by the European Science foundation as an urgent research topic (e.g., Robinson *et al.*, 2008).

An assessment of the current state of the environment in Europe is provided in the *European Environment, State and Outlook 2010* (SOER, 2010; Anonymous, 2010). SOER (2010) gives a comprehensive list of subjects that need to be studied: climate change impact, mitigation, and adaptation; biodiversity; land use efficiency; marine and coastal environments; water resources; freshwater quality; air pollution; the urban environment; among many others.

The state of marine and coastal environments as well as assessments of the respective ecosystems, habitats, and species under SOER (2010) are part and parcel of the European Union's Marine Strategy Framework Directive, which is considered the environmental pillar of the EU's Integrated Maritime Policy. Special emphasis is placed on the hydro-geochemical status of European seas, since the pollution of coastal and marine waters in many cases directly affects the lower levels of the trophic system first.

As the anthropogenic input of nitrogen oxides and phosphates (acting as nutrients) spurs on the processes of eutrophication and excessive growth of phytoplankton (including such harmful algae as cyanobacteria in the Baltic Sea), SOER 2010 collates data on the spatial patterns of the concentration and distribution of nutrients and phytoplankton *chl-a*, which is of importance in assessing the impact on and changes to the marine environment and in planning for mitigation measures.

This book has highlighted the need for an integrated approach to exploring satellite EO, *in situ* data, and ocean modeling tools to facilitate the monitoring and assessment of HAB events in coastal and marine waters. The concentration of *chl-a* is suitable for assessing the eutrophic state of coastal waters. In SOER 2010, some near coastal observations of *chl-a* from northern Europe (in stark contrast with very few data from the Mediterranean and Black Seas) are used to illustrate the eutrophic state of the ocean.

[Figure A.1](#) illustrates the applicability of satellite ocean color for use in the assessment of the eutrophic state through collocation of *in situ* data on *chl-a* in European seas for 2008 and satellite EO *chl-a* data averaged over the summer period. The benefits of satellite EO will improve dramatically when the approaches to HAB identification, extent, and quantification discussed in this book become routine as a result of the advent of new generations of ocean color sensors. It is from this perspective that the European Global Monitoring for Environment and Security (GMES) initiative has fully incorporated satellite EO in its development and implementation of marine monitoring and forecasting in Europe.

Scientific efforts aimed at discovering what lies behind the escalation of both HAB emergence and proliferation across the world's oceans are presently multi-faceted, but can be partitioned into three major groups: *in situ/laboratory* investigations, numerical ecosystem modeling, and further sophistication of satellite EO algorithms for the detection and surveillance of HAB events.

Although the diversity of satellite sensors is greater than ever before, there is still a lack of truly suitable sensors. Indeed, SeaWiFS, MODIS, and MERIS sensors are presently the most easily accessible working tools for the remote sensing of natural water quality, but they do not meet all the requirements for the early detection and surveillance of HABs.

Limited spectral bands and resolution stand out among the limitations of the above sensors. As discussed in Chapters 3 and 4, to be able to discriminate major algal groups reasonably confidently and, hence, to identify harmful species requires application of sophisticated procedures such as differentiation of the spectral envelope of remote-sensing reflectance,  $R_{rs}(+0, \lambda)$ . However, the spectral resolution of  $R_{rs}(+0, \lambda)$  retrievable from SeaWiFS, MODIS and MERIS is inadequate for this purpose.

In addition to shortcomings with limited spectral resolution, there are challenges aggravated by still-inadequate processing algorithms. This applies to the entire chain of sequential steps in aquatic optical remote sensing, starting with atmospheric correction and extending to color-producing agent (CPA) retrieval algorithms. These shortcomings are particularly pronounced for the remote sensing of coastal and inland waters, generally case II waters, where the impacts of HABs on humans are most pronounced.

For the remote sensing of case II waters, the following list of priorities is given (no attempt has been made to rank them in order of importance).

Physical models simulating the interaction of aquatic media with electromagnetic radiation in the visible and near infrared need to be improved. Such

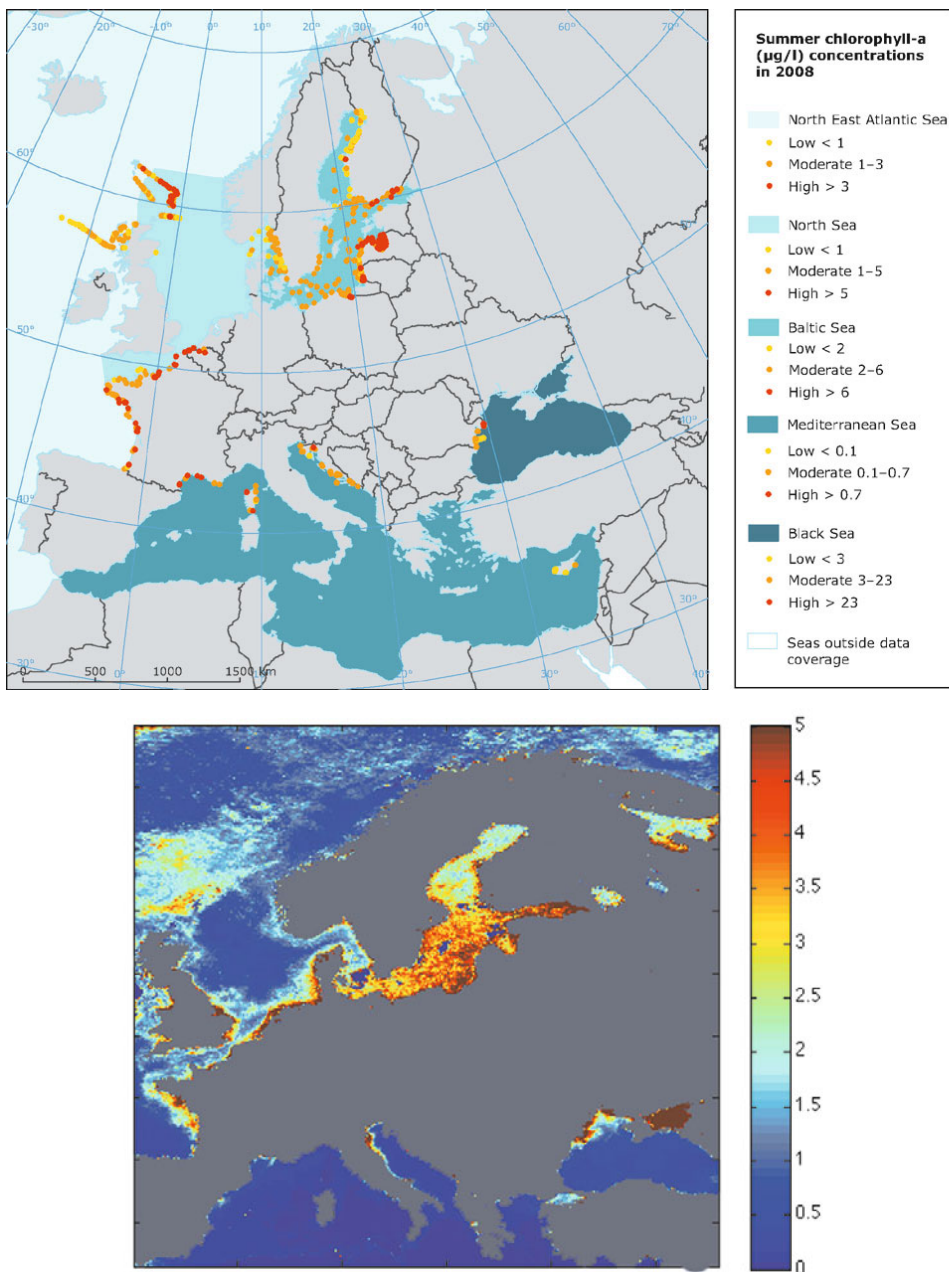


**Figure A.1.** Concentrations of *chl-a* ( $\mu\text{g/L}$ ) in coastal European waters during 2008 summer reported from (top) *in situ* measurements and (bottom) retrieved from satellite data (summertime-averaged GlobColour data, processed according to Maritorena *et al.*, 2002). Courtesy: EEA, <http://www.eea.europa.eu/soer> and GlobColor, <http://www.globcolour.info/>, processed by D. Petrenko.

models should be based on as extensive an amount of data obtained both *in situ* and in the laboratory as possible. These models have to be supplemented, first, by the fluorescence quantum yields of natural fluorophores (such as algal pigments and dissolved organics) and, second, by the fluorescence band characteristic half-width and the wavelength of maximum emission. Moreover, the fluorescent fraction of *doc* has to be known as well.

Clearly, next-generation hydro-optical models should be specific to the water area/body and vegetation season. An international program aimed at producing an atlas of the specific inherent properties of CPAs for a variety of marine water bodies, at least for the main vegetation seasons, will contribute to this. Such an atlas should also include information on bottom types and their spectral albedo along with the available bathymetric data, predominant currents, and average spatial distribution of water temperature and salinity (for marine waters). Such atlases should be specific to the main algal groups, their combinations, and monospecific algae (HAB) populations.

Equally important is the development of adequate hydro-optical models to improve the accuracy of assessment of light penetration into the water column, and thus render light-driven physical forcing more realistic.

Retrieval algorithms are far from being adequate. Improved retrieval algorithms are likely to be based on new mathematical foundations, exploiting the potential, for example, of the L–M multivariate optimization technique, self-organizing neural networks, matrix operator methods, and look-up tables (to mention a few).

As mentioned above, atmospheric correction is one of the most serious challenges facing the remote sensing of coastal waters. Appropriate techniques should adequately account for atmospheric aerosols and their absorption properties.

Continued attention should be given to validation campaigns that gather *in situ* data on concentrations of CPAs and CPA retrieval results (e.g., the compatibility of spatial scales, the spatial integration problem, statistical analyses) for marine and coastal reference sites. Both dedicated research cruise investigations and utilization of ships of opportunity are needed in this respect. Hence, the calibration and validation of bio-optical and other forward and inverse models must be done regularly at carefully chosen reference sites.

In physics, equations can sometimes claim precision; however, biology, biochemistry and environmental sciences are often governed more by statistics. Such statistical analyses, however, depend on sampling schemes and the statistical accuracy of environmental models. In addition, they are geographically and temporally site specific. Hence, remote sensing should not be expected to provide data that are more reliable than those acquired by ground/ship-based monitoring stations. However, remote-sensing monitoring will contribute to attaining better spatiotemporal coverage and, thus, providing data for use in marine ecosystem models.

The extensive number of case studies discussed in this book unequivocally indicate that the coupling of general/regional circulation models of the atmosphere–ocean/land system with hydro-optical and phytoplankton population (ecosystem) models for algal bloom simulation is very promising in terms of hind-

casting, nowcasting, and short-term prediction and biomass production estimates in marginal seas and large inland water bodies.

Nevertheless, to achieve the above goals, marine ecosystem modeling requires significant improvements. This is especially so when addressing large water bodies: they need to be more sophisticated to describe the much wider spectrum of aquatic organisms and their trophic interactions, as well as biogeochemical interactions with the dynamic ambience. The latter encompasses a variety of nutrients, pollutants, and dissolved and particulate organic matter in the water column, as well as the benthic community that are involved in the complex, yet insufficiently quantified dynamic processes of bottomwater–column exchanges between matter and energy. This will make ecosystem models more complex and may be unachievable. Tailored models for a specific ecosystem and a specific HAB species may be a strategy that develops complex marine ecosystem models.

For the efficient and quantitative use of available data, data assimilation techniques in marine ecosystem modeling need to be strengthened. This requires ecological models to be designed to harmonically include satellite data, thereby limiting the conflicts between compartments (i.e., individual sub-models constituting the entire all-encompassing model) that are readjusted due to the assimilation of satellite data and compartments directly unaffected by assimilation-driven alterations.

Another important aspect closely related to data assimilation is the validation of ecological modeling using satellite retrieval results. Although very desirable, satellite-based validation is not yet common practice, mostly because it is deemed unnecessary as a result of a high level of confidence in these data.

Beyond short-term operational forecasting, marine ecosystem modeling should ultimately also be developed so that it can be integrated in coupled Earth system models for climate change prediction.

Current achievements toward combined use of 3-D marine ecosystem models, satellite EO remote sensing, field surveillance, and monitoring services in European shelf seas (Norway, in particular) will improve as a result of targeted efforts from a multi-disciplinary marine scientific community and stakeholders in the user community in years to come.

## References

- Ackleson, S. G., Balch, W. M., and Holligan, P. M. (1994) Response of water-leaving radiance of particulate calcite and chlorophyll *a* concentrations: A model for Gulf of Maine coccolithophore blooms. *Journal of Geophysical Research* **99**(C4), 7483–7499.
- Aguirre-Gomez, R., Boxall, S. R., and Weeks, A. R. (2001a) Detecting photosynthetic algal pigments in natural populations using a high-spectral-resolution spectroradiometer. *International Journal of Remote Sensing* **22**(15), 28675–2884.
- Aguirre-Gomez, R., Weeks, A. R., and Boxall, S. R. (2001b) The identification of phytoplankton pigments from absorption spectra. *International Journal of Remote Sensing* **22**(2/3), 315–338.
- Ahn, Y-H. and Shanmugam, P. (2004) New methods for correcting the atmospheric effects in Landsat imagery over turbid (Case-2) waters. *Korean Journal of Remote Sensing* **20**(5), 289–305.
- Ahn Yu-Hwan, Bricaud, A., and Morel, A. (1992) Light backscattering efficiency and related properties of some phytoplanktoners. *Deep-Sea Research* **39**(11/12), 1835–1855.
- Ahn, Y-H., Shanmugam, P., Ryu, J-H., and Jeong, J-C. (2006) Satellite detection of harmful algal bloom occurrences in Korean waters. *Harmful Algae* **5**, 213–231.
- Aksnes, D. L. and Lie, U. (1990) A coupled physical–biological pelagic model of a shallow Sill Fjord. *Estuarine, Coastal and Shelf Science* **3**, 459–486.
- Aksnes, D. L., Ulvestad, K. B., Balino, B., Berntsen, J., Egge, J., and Svendsen, E. (1995) Ecological modelling in coastal waters: Towards predictive physical–chemical–biological simulation models. *Ophelia* **41**, 5–36.
- Albert, S., O’Neil, J. M., Udy, J. W., Ahern, K. S., O’Sullivan, C. M., and Dennison, W. C. (2005) Blooms of the cyanobacterium *Lyngbya majuscula* in coastal Queensland, Australia: Disparate sites, common actors. *Maine Pollution Bulletin* **55**, 428–437.
- Allali, K., Bricaud, A., and Herve, K. (1997) Spatial variations in the chlorophyll-specific absorption coefficients of phytoplankton and photosynthetically active pigments in the equatorial Pacific. *Journal of Geophysical Research* **102**(C6), 12413–12423.
- Allard, B. H., Boren, C., Pettersson, C., and Zhang, G. (1994) Degradation of humic substances by UV irradiation. *Environmental Interactions* **20**, 97–101.

- Allen, J. I., Blackford, J., Holt, J., Proctor, R., Ashworth, M., and Siddom, J. (2001) A highly spatially resolved ecosystem model for the North West European Continental Shelf. *Sarsia* **86**(6), 423–440.
- Allen, J. I., Smyth, T. J., Siddorn, J. R., and Holt, M. (2008) How well can we forecast high biomass algal bloom events in a eutrophic coastal sea? *Harmful Algae* **8**, 7–76.
- Alvain, S., Moulin, C., Dandonneau, Y., and Breon, F. M. (2005) Remote sensing of phytoplankton groups in case I waters from global SeaWiFS imagery. *Deep-Sea Research I* **52**, 1989–2004.
- Álvarez-Salgado, X. A., Gago, J., Míguez, B. M., Gilcoto, M., and Pérez, F. F. (2000) Surface waters of the NW Iberian margin: Upwelling on the shelf versus outwelling of upwelled waters from the Rías Baixas. *Estuarine, Coastal and Shelf Science* **51**, 821–837.
- An, M., Liu, D., Johnson, I. and Lovett, J. (2003) Mathematical modeling of allelopathy, II: The dynamics of allelochemicals from living plants in the environment. *Ecological Modeling* **161**, 53–66.
- Andersen, J. H., Schueter, L. and Ærtenbjerg, G. (2006) Coastal eutrophication: Recent developments in definitions and implications for monitoring strategies. *Journal of Plankton Research* **27**(7), 621–628.
- Anderson, D. M., Hoagland, P., Kaoru, Y., and White A. W. (2000) *Estimated Annual Economic Impacts from Harmful Algal Blooms (HABs) in the United States* (WHOI-2000-II). Woods Hole Oceanographic Institution, 196 pp.
- Anderson, D. M., Andersen, P., Bricelj, V. M., Cullen, J. J., and Rensel, J. E. (2001) *Monitoring and Management Strategies for Harmful Algal Blooms in Coastal Waters* (APEC #201-MR-01.1/IOC Technical Series. No. 59). Asia Pacific Economic Program, Singapore/Intergovernmental Oceanographic Commission, Paris, 261 pp.
- Anderson, D. M., Glibert, P. M., and Burkholder, J. M. (2002) Harmful algal blooms and eutrophication: Nutrient sources, composition, and consequences. *Estuaries* **25**, 704–726.
- Anderson, L. A., Robinson, A. R., and Lozano, C. J. (2000) Physical and biological modeling in the Gulf Stream, I: Data assimilation methodology. *Deep-Sea Research. Part I. Oceanic Research Papers*, 1887–1827.
- Anderson, T. S. (2005) Plankton functional type modeling: Running before we can walk? *Journal of Plankton Research* **27**(11), 1073–1081.
- Andrefouet, S., Costello, M. J., Rast, M., and Sathyendranath, S. (2008) Earth observations for marine and coastal biodiversity and ecosystems. *Remote Sensing of Environment* **112**(8), 3297–3299.
- Anonymous (1981) *Physiological Bases of Plankton Ecology* (Bulletin 210, edited by T. Platt). Department of Fisheries & Oceans, Ottawa, 43 pp.
- Anonymous (1992) *Lake Ladoga*. Nauka, St. Petersburg, 325 pp.
- Anonymous (1995) *Manual on Harmful Marine Microalgae* (IOC Manuals and Guides No. 33, edited by G. M. Hallegraeff, D. M. Anderson, and A. D. Cembella). UNESCO, Paris, 430 pp.
- Anonymous (1997) *Phytoplankton Pigments in Oceanography: Guidelines to Modern Methods* (edited by S. W. Jeffrey, R. F. C. Mantoura, and S. W. Wright). UNESCO, Paris, 615 pp.
- Anonymous (2003a) *Report of the ICES-IOC Working Group on Harmful Algal Bloom Dynamics*. International Council of the Exploration of the Sea, Copenhagen, Denmark, 37 pp.
- Anonymous (2003b) The EU-US scientific initiative on harmful algal blooms. *Workshop Jointly Funded by the European Commission-Environment and Sustainable Development Programme and the U.S. National Science Foundation, September 5–8, 2002, Trieste, Italy*, 57 pp.

- Anonymous (2003c) *Complex Environmental Systems: Synthesis for Earth, Life, and Society in the 21st Century*. NSF Advisory Committee, Washington, D.C., 178 pp.
- Anonymous (2003d) *LIFEHAB: Life Histories of Microalgal Species Causing Harmful Blooms* (Research in Enclosed Seas Series No. 12, edited by E. Garces, A. Zingone, M. Montresor, B. Reguera, and B. Dale). Publisher, Location. 200 pp.
- Anonymous (2003e) *Harmful Algal Blooms Observing System* (Workshop Report on the Design and Implementation Plan for a Pilot Project for the Coastal Component of the U.S. Integrated Ocean Observing System: Detection and Prediction of Harmful Algal Events in the Northern Gulf of Mexico (Pensacola Beach, Florida), November 27–December 1, 2000. Available at <http://www.Habrc.noaa.gov>
- Anonymous (2005a) <http://www.ifremer.fr/envlit/documentation/dossiers/ciem/aindex.htm>
- Anonymous (2005b) <http://www.whoi.edu/redtide/HABdistribution/HABmap.html>
- Anonymous (2008) In-depth review of ongoing work on alien species that threaten ecosystems, habitats or species. *Proceedings of the Ninth Conference of the Parties to the Convention on Biological Diversity, Bonn, May 19–30, 2008*. United Nations Environment Program, Zurich, Switzerland, 18 pp.
- Anonymous (2010) *The European Environment, State and Outlook 2010: Marine and Coastal Environment* (SOER, 2010). EEA, Copenhagen, 55 pp. Available at <http://www.eea.europa.eu/soer>.
- Antoine, D. and Morel, A. (2000) *Atmospheric Correction over the Ocean (Case 1 Waters)* (MERIS ATBD 2.7). Laboratoire de Physique et Chimie Marines, France, 165 pp.
- Aponasenko, A. D., Shchur, L. A., Filimonov, V. S., and Lopatin, V. N. (1997) Structural studies of aquatic ecosystems based on the concept of phase boundaries on the surface of suspended matter. *Journal of Aquatic Ecology* **1**(2), 13–25.
- Armstrong, R. A. (2003) A hybrid spectral representation of phytoplankton growth and zooplankton response: The “control rod” model of plankton interaction. *Deep-Sea Research II* **50**, 2895–2916.
- Armstrong, R. A., Sarmiento, J. L., and Slater, R. D. (1995) *Monitoring Ocean Productivity by Assimilating Satellite Chlorophyll into Ecosystem Models* (Ecological Time Series, edited by J. Steele and T. Powell). Chapman & Hall, pp. 371–390.
- Arnone, R. A. (1987) Satellite-derived color–temperature relationship in the Alboran Sea. *Remote Sensing of Environment* **23**, 417–437.
- Atkinson, P. M. and Tatnall, A. R. (1997) Neural networks in remote sensing. *International Journal of Remote Sensing* **18**(4), 699–709.
- Aure, J., Danielsen, D. S., Skogen, M., Svendsen, E., Soiland, H. and Pettersson, L. H. (2001) Environmental conditions during the *Chattonella* bloom in the North Sea and Skagerrak in May 1998. *Proceedings of the Ninth Conference on Harmful Algae (HAB2000), Hobart, Tasmania, Australia, February 7–11, 2000*, pp. 123–127.
- Babichenko, S., Poryvkina, L., Arikese, V., Kaitala, S., and Kuosa, H. (1993) Remote sensing of phytoplankton using laser-induced fluorescence. *Remote Sensing of Environment* **45**, 43–50.
- Babichenko, S., Kaitala, S., Leeben, A., Poryvkina, L., and Seppala, J. (1999) Phytoplankton pigments and dissolved organic matter distribution in the Gulf of Riga. *Journal of Marine Research* **23**(1/3), 69–82.
- Babichenko, S., Leeben, A., Poryvkina, L., Shalapyonok, A., and Seppala, J. (2001) Variability of *Chlorella* sp. fluorescence in response to different nitrogen conditions. *International Journal of Remote Sensing* **22**(2/3), 403–414.
- Babin, M. and Stramski, D. (2002) Light absorption by aquatic particles in the near-infrared spectral region. *Limnology and Oceanography* **47**(3), 911–915.

- Backeberg, B. C., Bertino, L., and Johannessen, J. A. (2009) Evaluating two numerical advection schemes in HYCOM for eddy-resolving modeling of the Agulhas Current. *Ocean Science* **5**, 173–190.
- Balch, W. M., Kilpatrick, K. A., Holligan, P., Harbour, D., and Fernandez, E. (1996) The 1991 coccolithophore bloom in the central north Atlantic, 2: Relating optics to coccolith concentration. *Limnology and Oceanography* **41**(8), 1684–1696.
- Balch, W. M., Drapeau, D. T., Cucci, T. L., Vaillancourt, R. D., Kilpatrick, K. A., and Fritz, J. J. (1999) Optical backscattering of calcifying algae: Separating the contribution of particulate inorganic and organic carbon fractions. *Journal of Geophysical Research* **104**(C1), 1541–1558.
- Balch, W. M., Gordon, H. R., Bowler, B. C., Drapeau, D. T., and Booth, E. S. (2005) Calcium carbonate measurements in the surface global ocean based on Moderate-Resolution Imaging Spectroradiometer data. *Journal of Geophysical Research* **110**(C07001), doi: 10.1029/2004JC002560.
- Barbini, R., Colao, C., Fantoni, R. M., Ferrari, G. M., Lai, A., and Palucci, A. (2003) Application of a lidar fluorosensor system to the continuous and remote monitoring of the Southern Ocean and Antarctic Ross Sea: Results collected during XIII and XV Italian oceanographic campaigns. *International Journal of Remote Sensing* **24**(16), 3191–3204.
- Baretta, J. and Baretta-Bekker, J. (1997) Special issue: European regional seas ecosystem model: A complex marine ecosystem model. *Netherlands Journal of Sea Research* **33**, 233–246.
- Barlow, R. G., Aiken, J., Holligan, P. M., Cummins, D. G., Maritorena, S., and Hooker, S. (2002) Phytoplankton pigment and absorption characteristics along meridional transects in the Atlantic Ocean. *Deep Sea Research I* **49**(4), 637–660.
- Bates, N. R. and Hansell, D. A. (2003) Temporal variability of excess nitrate in the subtropical mode water of the North Atlantic Ocean. *Marine Chemistry* **84**, 225–241.
- Bernhardt, H. (2005) Über die Entfernung von *Oscillatoria rubescens* aus einem Talsperrenwasser durch Flockung und Filtration. *Archiv für Hydrobiologie* **101**(3), 311–327.
- Berthon, J-F., Zibordi, G., and Hooker, S. B. (2000) Marine optical measurements of a mucilage event in the northern Adriatic Sea. *Limnology and Oceanography* **45**, 322–327.
- Bertilsson, S. and Travnik, L. J. (2000) Photochemical transformation of dissolved organic matter in lakes. *Limnology and Oceanography* **45**(4), 753–762.
- Bertino, L., Evensen, G., and Wackernagel, H. (2003) Sequential data assimilation techniques in oceanography. *International Statistical Review* **71**, 223–241.
- Bianchi, T. S., Rolff, C., Widbom, B., and Elmgren, R. (2002) Phytoplankton pigments in the Baltic Sea seston and sediments: Seasonal variability, fluxes, and transformations. *Estuarine, Coastal and Shelf Science* **55**(3), 369–383.
- Bidigare, R. R. and Ondrusek, M. O. (1990) *In vivo* absorption properties of algal pigments. *Ocean Optics X. SPIE* **1302**, 290–302.
- Bidigare, R. R., Morrow, J. H., and Kiefer, D. A. (1989) Derivative analysis of spectral absorption by photosynthetic pigments in the western Sargasso Sea. *Journal of Marine Research* **47**, 323–341.
- Blackford, J. C., Allen, J. I., and Gilbert, F. J. (2004) Ecosystem dynamics at six contrasting sites: A generic modelling study. *Journal of Marine Research* **52**(1/4), 191–215.
- Blough, N. V. and Green, S. A. (1995) Spectroscopic characterization and remote sensing on non-living organic matter. *The Dahlem Workshop on the Role of Non-living Organic Matter in the Earth's Carbon Cycle, Berlin, 1993* (edited by R. G. Zepp and C. Sonntag). John Wiley & Sons, New York, pp. 23–45.

- Blumberg, A. F. and Mellor, G. L. (1987) A description of a three-dimensional coastal ocean circulation model. In: *Three-dimensional Coastal Ocean Models* (AGU #4, edited by N. Heaps). American Geophysical Union, Washington, D.C., pp. 87–105.
- Bowers, D. G., Harker, G. E. L., and Stepan, B. (1996) Absorption spectra of inorganic particles in the Irish Sea and their relevance to remote sensing of chlorophyll. *International Journal of Remote Sensing* **17**(12), 2449–2460.
- Bracher, A., Vountas, M., Dinter, T., Burrows, J. P., Rottgers, R., and Peeken, I. (2009) Quantitative observation of cyanobacteria and diatoms from space using PhytoDOAS on SCHIAMACHY data. *Biogeosciences* **6**, 751–764.
- Bratbak, G., Jacquet, S., Larsen, A., Pettersson, L. H., Sazhin, A. F., and Thyrhaug, R (2011) The plankton community in Norwegian coastal waters: Abundance, composition, spatial distribution and diel variation. *Continental Shelf Research*, accepted, doi: 10.1016/j.csr.2011.06.014, 2011.
- Bricaud, A., Morel, A., and Prieur, L. (1983) Optical efficiency factors of some phytoplankters. *Limnology and Oceanography* **28**, 816–832.
- Bricaud, A., Babin, M., Morel, A. and Claustre, H. (1995) Variability in the chlorophyll-specific absorption coefficients of natural phytoplankton: Analysis and parameterization. *Journal of Geophysical Research* **100**(C7), 13321–13332.
- Bricaud, A., Bosc, E., and Antoine, D. (2002) Algal biomass and sea surface temperature in the Mediterranean Basin: Intercomparison of data from various satellite sensors, and implications for primary production estimates. *Remote Sensing of Environment* **81**, 163–178.
- Brown, C. W. and Podesta, G. P. (1997) Remote sensing of coccolithophore blooms in the western south Atlantic Ocean. *Remote Sensing of Environment* **60**, 83–91.
- Bryan, K. and Lewis, L. J. (1979) A water mass model of the world ocean. *Journal Geophysical Research* **84**, 2503–2517.
- Bukata, R. P., Jerome, J. H., Kondratyev, K. Ya., and Pozdnyakov, D. V. (1991) Estimation of organic and inorganic matter in inland waters: Optical cross sections of Lakes Ontario and Ladoga. *Journal of Great Lakes Research* **17**, 461–469.
- Bukata, R. P., Jerome J. H., and Bruton, J. E. (1985) *Application of Direct Measurements of Optical Parameters to the Estimation of Lake Water Quality Indicators* (Environment of Canada Inland Waters Directorate Scientific Series No. 140), 35 pp.
- Bukata, R. P., Jerome, J. H., Kondratyev, K. Ya., and Pozdnyakov, D. V. (1995) *Optical Properties and Remote Sensing of Inland and Coastal Waters*. CRC Press, Boca Raton, FL, 362 pp.
- Burchard, H., Bolding, K., Kuhn, W., Meister, A., Neumann, T., and Umlauf, L. (2006) Description of a flexible and extandable physical–biogeochemical model system for the water column. *Journal of Marine Systems* **61**, 180–211.
- Butler, W. L. and Hopkins, D. W. (1970) Higher derivative analysis of complex absorption spectra. *Photochemistry and Photobiology* **12**, 816–832.
- Cannizzaro, J. P., Carder, K. L., Chen, F. R., Walsh, J. J., Lee, Z. P., Heil, C., and Villareal, T. (2002) A novel optical classification technique for detection of red tides in the Gulf of Mexico: Application to the 2001–2002 bloom event. In: *Proceedings of the 10th International Conference on Harmful Algae, St. Petersburg Beach, FL, October 21–25, 2002*, pp. 43–48.
- Capone, D. G., Burns, J. A., Montoya, J. P., Subramaniam, A., Mahaffey, C., Gunderson, T., Michaels, A. F., and Carpenter, E. J. (2005) Nitrogen fixation by *Trichodesmium* spp.: An important source of new nitrogen to the tropical and subtropical North Atlantic Ocean. *Global Biogeochemical Cycles* **19**(GB2024), doi: 1029/2004GB002331.266.

- Carder, K. L., Chen, F. R., Lee, Z. P., Hawes, S. K., and Kamykowski, D. (1999) Semianalytic moderate-resolution imaging spectrometer algorithm for chlorophyll *a* backscattering and absorption within bio-optical domains based on nitrate-depletion temperatures. *Journal of Geophysical Research* **104**(C3), 5403–5421.
- Carr, M.-E. and Kearns, E. J. (2003) Production regimes in four Eastern Boundary Current systems. *Deep-Sea Research II* **50**(22/26), 3199–3221.
- Chai, F., Lindley, S. T., and Barber, R. T. (1996) Origin and maintenance of a high NO<sub>3</sub> condition in the equatorial Pacific. *Deep-Sea Research II* **43**, 1031–1064.
- Chomko, R. M., Gordon, H. R., Maritorena, S., and Siegel, D. (2003) Simultaneous retrieval of oceanic and atmospheric parameters for ocean color imagery by spectral optimization: A validation. *Remote Sensing of Environment* **84**, 208–220.
- Church, M. J., Ducklow, H. W., and Korl, D. M. (2002) Multiyear increases in dissolved organic matter inventories at Station ALONA in the Northern Pacific Subtropical Gyre. *Limnology and Oceanography* **47**(1), 1–10.
- Ciollari, A. M., Lewis, M. R., and Cullen, J. J. (2002) Assessment of the relationships between dominant cell size in natural phytoplankton communities and the spectral shape of the absorption coefficient. *Limnology and Oceanography* **47**(2), 404–417.
- Ciotti, A. M. and Bricaud, A. (2006) Retrieval of a size parameter for phytoplankton and spectral light absorption by colored detrital matter from water leaving radiance at SeaWiFS channels in a continental shelf region of Brazil. *Limnology and Oceanography Methods* **4**, 237–253.
- Coble, P. G. (1994) Investigation of the geochemistry of dissolved organic matter in coastal waters using optical properties. *Ocean Optics XII, Proc. SPIE* **1302**, 291–302.
- Coles, V. J. and Hood, R. R. (2004) Modeling the impact of *Trichodesmium* and nitrogen fixation in the Atlantic Ocean. *Journal of Geophysical Research* **109**(C06007), doi: 10.1029/2002JC001754, 266 [in Norwegian].
- Colella, P. and Woodward, P. R. (1984) The piecewise parabolic method (PPM) for gas-dynamical simulations. *Journal of Computational Physics* **54**, 174–201.
- Craig, S. E., Lohrenz, S. E., Lee, Z., Mahoney, K. L., Kirkpatrick, G. J., Schofield, O. M., and Steward, G. S. (2006) Use of hyperspectral remote sensing reflectance for detection and assessment of the harmful alga, *Karenia brevis*. *Applied Optics* **45**, 5414–5425.
- Cullen, J. J., Ciotti, A. M., Davis, R. F., and Lewis, M. R. (1997) Optical detection and assessment of algal blooms. *Limnology and Oceanography* **42**(5), 1223–1239.
- Culver, M. E., Soracco, M., Stumpf, R. P., Change, P. S., and Steidinger, K. A. (2000) Integrating wind data to determine the influence on movement of a harmful algal bloom along the northwest coast of Florida. In: *Proceedings of the Sixth International Conference on Remote Sensing for Marine and Coastal Environments*, Ann Arbor, MI. Veridian ERIM International Publishing, pp. 31–33.
- Dahl, E. T., Aune, K., and Tangen K. (1999) *Giftalger og algegifter I norske farvann. Havets Miljø 1999*. Havforskningsinstituttet, Universitetet i Bergen, 78 pp. [in Norwegian].
- Danaher, S. and Omongain, E. (1992) Singular value decomposition in multispectral radiometry. *International Journal of Remote Sensing* **19**, 1771–1777.
- Da Silva, A. M., Young, C. C., and Levitus, S. (1994) *Atlas of Surface Marine Data 1994, Vol. 1: Algorithms and Procedures* (NOAA Atlas NESDIS #6). National Oceanic and Atmospheric Administration, Silver Springs, MD, 74 pp.
- Dekker, A., G. (1993) Detection of optical water quality parameters for eutrophic waters by high resolution remote sensing. Ph.D. thesis, Vrije Universiteit, Amsterdam, 239 pp.
- Delhez, E. J. M. (1996) On the residual advection of passive constituents. *Journal of Marine Systems* **8**(3/4), 147–169.

- Delhez, E. J. M. (1998) Macroscale ecohydrodynamic modeling on the northwest European Continental Shelf. *Journal of Marine Systems* **16**, 171–190.
- Devred, E., Sathyendranath, S., Stuard, V., Maass, H., Ulloa, O., and Platt, T. (2006) A two-component model of phytoplankton absorption in the open ocean: Theory and applications. *Journal of Geophysical Research* **111**, CO3011, doi: 10.1029/2005JC002880.
- DHI (2000) MIKE 3: Environmental hydraulics. *DHI Software User Guide: Documentation and Reference Manual*. DHI Water & Environment Publishing, Horsholm, Denmark, 81 pp.
- Dippner, J. W. (2006) Future aspects in marine ecosystem modeling. *Journal of Marine Systems* **61**, 246–267.
- Doerffer, R. (1981) Factor analysis in ocean colour interpretation. In: *Marine Science, 13: Oceanography from Space* (edited by J. F. R. Gower). Plenum, New York, pp. 339–345.
- Doerffer, R. (1992) Imaging Spectroscopy for detection of chlorophyll and suspended matter. In: *Imaging Spectroscopy: Fundamentals and Prospective Applications* (edited by F. Toselli and J. Bodechtel). ECSC, EEC, and EAEC Publishing, Brussels and Luxemburg, pp. 215–257.
- Doerffer, R. and Fischer, J. (1994) Concentrations of chlorophyll, suspended matter, and gelbstoff in Case II waters derived from satellite coastal zone scanner data with inverse modeling methods. *Journal of Geophysical Research* **99**(C4), 7457–7466.
- Doney, S. C., Glover, D. M., McCue, S. J., and Fuentes, M. (2003) Mesoscale variability of Sea-viewing Wide Field-of-view Sensor (SeaWiFS) satellite ocean color: Global patterns and spatial scales. *Journal of Geophysical Research* **108**(C2) 3024–3029.
- Ducklow, H. W. (1999) The bacterial component of the oceanic euphotic zone. *FEMS Microbiology Ecology* **5**, 231–255.
- Dugan, N. R. and Williams, D. J. (2006) Cyanobacteria passage through drinking water filters during perturbation episodes as a function of cell morphology, coagulant and initial filter loading rate. *Harmful Algae* **5**, 26–35.
- Dundas, I., Johannessen, O. M., Berge, G., and Heimdal, B. (1989) Toxic algal bloom in Scandinavian waters, May–June 1989. *Oceanography* **2**(1), 9–14.
- Durand, D., Pettersson, L. H., Johannessen, O. M., Svendsen, E., Søiland, H., and Skogen, M. (2002) Satellite observation and model prediction of toxic algae bloom. In: *Operational Oceanography: Implementation at the European and Regional Scales* (Elsevier Oceanography Series #66; Editor-in-Chief: N. C. Flemming). Elsevier, The Netherlands, pp. 505–515.
- Duysens, L. M. (1956) The flattening effect of the absorption spectra of suspensions as compared to that of solution. *Biochemistry and Biophysical Acta* **19**, 1–12.
- Dyhrman, S. T., Webb, E. A., Anderson, D. M., Moffett, J. W., and Waterbury J. B. (2002) Cell-specific detection of phosphorus stress in *Trichodesmium* from the western North Atlantic. *Limnology and Oceanography* **47**(6), 1832–1836.
- Ebenhoh, W. (1987) Coexistence of an unlimited number of algal species in a model system. *Theoretical Population Biology* **34**, 130–144.
- Ebenhoh, W. (1997) Coexistence of an unlimited number of algal species in a model system. *Theoretical Population Biology* **34**, 130–144.
- Edelvang, K., Kaas, H., Erichsen, A. C., Alvarez-Berastegui, D., Bundgaard, K., and Jorgensen, P. V. (2005) Numerical modeling of phytoplankton biomass in coastal waters. *Journal of Marine Systems* **57**, 13–29.
- Edwards, M., Johns, D. G., Leterme, S. C., Svendsen, E., and Richardsen, A. J. (2006) Regional climate change and harmful algal blooms in the northeastern Atlantic. *Limnology Oceanography* **51**(2), 820–829.

- Elbrächter, M. and Schnepf, E. (1996) *Gymnodinium chlorophorum*, a new, green bloom forming dinoflagellate (Gymnodiniales, Dinophyceae) with a vestigial prasinophyte endosymbiont. *Phycologia* **35**, 381–393.
- Ericken, A. C. and Rasch, P. S. (2001) Two- and three-dimensional model system predicting the water quality of tomorrow. In: *Proceedings of the Seventh International Conference on Estuarine and Coastal Modeling* (edited by M L. Spauling). American Society of Civil Engineers, Boston, pp. 89–95.
- Esbensen, K. H., Midtgård, T., and Schönkpf, S. (1994) *Multivariate Analysis in Practice*. Wennberg Press, Trondheim, Norway, 345 pp.
- Espedal, H. A. and Johannessen, O. M. (2000) Detection of oil spills near offshore installations using synthetic aperture radars (SAR). *International Journal of Remote Sensing* **21**, 2141–2144.
- Evensen, G. (2006) *Data Assimilation: The Ensemble Kalman Filter*. Springer-Verlag, 279 pp. Available at <http://www.nerc.no/biblio/author/2030>
- Evensen, G. (2009) *Data Assimilation: The Ensemble Kalman Filter* (Second Edition). Springer-Verlag, 320 pp. Available at <http://www.nerc.no/pub/data-assimilation-ensemble-kalman-filter-0>
- Fadeev, V. V., Chekaliuk, A. M., and Choubarov, V. V. (1982) Nonlinear laser fluorometry of organic substances. *Proceedings of the Russian Academy of Sciences* **262**(2), 338–342 [in Russian].
- Falconer, I. R. (2005) *Cyanobacterial Toxins of Drinking Water Supplies: Cylindrospermopsins and Microcystins*. CRC Press, Boca Raton, FL, 237 pp.
- Fermín, E. G., Figueiras, F. G., Arbones, B., and Villarino, M. L. (1996) Short-time evolution of a *Gymnodinium catenatum* population in the Ría de Vigo. *Journal of Phycology* **32**, 212–221.
- Figueiras, F. G., Labarta, M. J., and Reiriz, F. (2002) Coastal upwelling, primary production and mussel growth in the Rías Baixas of Galicia. *Hydrobiologia* **484**, 121–131.
- Filatov, N. N., Pozdnyakov, D., Johannessen, O. M., Pettersson, L. H., and Bobylev, L. P. (2005) *The White Sea: Its Marine Environment and Ecosystem Dynamics Influenced by Global Change* (Nansen Center Polar Series No. 3). Springer/Praxis, Heidelberg, Germany/Chichester, U.K., 472 pp.
- Fischer, J. and Doerffer, R. (1987) An inverse technique for remote detection of suspended matter, phytoplankton and yellow substances from CZCS measurements. *Advancement in Space Research* **7**(2), 21–26.
- Flury, B., and Riedwyl, H. (1988) *Multivariate Statistics: A Practical Approach*. Chapman & Hall, London, 320 pp.
- Folkestad, A. (2006) Satellite monitoring of algal blooms in Norwegian coastal waters. PhD thesis, Geophysical Institute, University of Bergen, 74 pp. ISBN 82-308-0117-7.
- Folkestad, A., Pettersson, L. H., and Høkedal, J. (2006) *Quality Assessment of MERIS Chlorophyll Fluorescence Line Height (FLH) Product for the Skagerrak Region* (Technical Report No. 20). NERSC, Bergen, Norway, 42 pp.
- Folkestad, A., Pettersson, L. H., and Durand, D. D. (2007) Intercomparison of ocean colour data during algal blooms in Skagerrak. *International Journal of Remote Sensing* **28**(3/4), 569–592, doi: 10.1080/01431160600821044.
- Follows, M. J., Dutkiewicz, S., Grant, S., and Chisholm, S. W. (2007) Emergent biogeography of microbial communities in a model ocean, *Science* **315**, 1843–1846.
- Fouest Le, V., Zakardjian, B., Soucier, F. J., and Cizmel, S. A. (2006) Application of SeaWiFS- and AVHRR-derived data for mesoscale and regional validation of a 3-D

- high-resolution physical–biological model of the Gulf of St. Lawrence (Canada). *Journal of Marine Research* **60**, 30–50.
- Fraga, S. and Bakun, A. (1993) Global climate change and harmful algal blooms: The example of *Gymnodinium catenatum* on the Galician Coast. In: *Toxic Phytoplankton Blooms in the Sea* (edited by T. M. Smayda and J. Shimizu). Elsevier, New York, pp. 59–65.
- Franks, P. J. (1997a) Spatial patterns in dense algal blooms. *Limnology and Oceanography* **42**(5), 1297–1305.
- Franks, P. J. S. (1997b) Models of harmful blooms. *Limnology and Oceanography* **45**(5), 1273–1282.
- Franks, P. J. S. and Anderson, D. M. (1992) Alongshore transport of a toxic phytoplankton bloom in a buoyancy current: *Alexandrium tamarensis* in the Gulf of Maine. *Marine Biology* **116**, 153–164.
- Friedrichs, M. A. M., Hood, R. R., and Wiggert, J. D. (2006) Ecosystem model complexity versus physical forcing: Quantification of their relative impact with assimilated Arabian Sea data. *Deep Sea Research Part I: Tropical Studies in Oceanography* **53**(5/7), 576–600.
- Gallie, E. A. and Murtha, P. A. (1992) Specific absorption and backscattering spectra for suspended minerals and chlorophyll *a* in Chilko Lake, British Columbia. *Remote Sensing of Environment* **39**, 103–118.
- Garver, S. A. and Siegel, D. A. (1997) Inherent optical property inversion of ocean color spectra and its biogeochemical interpretation, I: Time series from the Sargasso Sea. *Journal of Geophysical Research* **102** 18607–18625.
- Ge, Y., Voss, K. J., and Gordon, H. R. (1995) *In situ* measurements of inelastic light scattering in Monterey Bay using solar Fraunhofer lines. *Journal of Geophysical Research* **100**(C7), 13227–13236.
- Gege, P. (1998) Characterization of the phytoplankton in Lake Constance for classification by remote sensing (*Archiv für Hydrobiologie* special issues). *Advancement in Limnology* **53**, 179–193.
- Gege, P., Heege, T., Albert, A., and Thiemann, S. (2001) Determination of water constituents in Lake Constance, Germany. *Proceedings of the Workshop on Remote Sensing and Resource Management in Nearshore and Inland Waters, October 23, 2001, Wolfville, Canada*, pp. 78–79.
- Geider, R. J., MacIntyre, H., and Kana, T. M. (1998) A dynamic regulatory model of phytoplankton acclimation to light, nutrients, and temperature. *Limnology and Oceanography* **43**, 1287–1306.
- Glibert, P. M., R. Magnien, M. W. Lomas, J. Alexander, C. Fan, E. Haramoto, M. Trice, and T. M. Kana (2001) Harmful algal blooms in the Chesapeake and coastal bays of Maryland, USA: Comparison of 1997, 1998, and 1999 events. *Estuary* **24**, 875–883.
- Gohin, F., Druon, J. N., and Lampert, L. (2002) A five channel chlorophyll concentration algorithm applied to SeaWiFS data processed by SeaDAS in coastal waters. *International Journal of Remote Sensing* **23**(8), 1639–1661.
- Gordon, H. R. (1999) Contribution of Raman scattering to water-leaving radiance: A reexamination. *Applied Optics* **38**(15), 3166–3174.
- Gordon, H. R. (2002) Inverse methods in hydrologic optics. *Oceanologia* **44**(1), 9–58.
- Gordon, H. R. (2003) Pitfalls in the atmospheric correction of ocean colour imagery: How should aerosol optical properties be computed? (Reply to Comment). *Applied Optics* **42**, 542–544.
- Gordon, H. R. and Morel, A. Y. (1983) *Remote Assessment of Ocean Colour for Interpretation of Satellite Imagery*. Springer-Verlag, New York, 115 pp.

- Gordon, H. R., Brown, O. B., Evans, R. H., Brown, J. W., Smith, R. C., Baker, K. S., and Clark, D. K. (1988) A semi-analytic radiance model of ocean color. *Journal of Geophysical Research* **93**, 10909–10924.
- Gordon, H. R., Boynton, G. C., Balch, W. M., Groom, S. B., Harbour, D. S., and Smyth, T. J. (2001) Retrieval of coccolithophore calcite concentration from SeaWiFS imagery. *Geophysical Research Letters* **28**(8), 1587–1590.
- Gorlenko, V. M., Dubinina, G. A., and Kuznetsov, S. I. (1974) *Ecology of Aquatic Microorganisms*. Nauka, Moscow, 289 pp. [in Russian].
- Gowen, R. J., Tett, P., and Jones, K. J. (1992) Predicting marine eutrophication: The yield of chlorophyll from nitrogen in Scottish coastal phytoplankton. *Marine Ecology Progress Series* **85**, 153–161.
- Gower, J. F. R. and Borstad, G. A. (1990) Mapping of phytoplankton by solar-stimulated fluorescence using an imaging spectrometer. *International Journal of Remote Sensing* **11**, 313–320.
- Gower, J. F. R. and Borstad, G. A. (1977) Use of imaging spectroscopy to map solar-stimulated chlorophyll fluorescence, red tides and submerged vegetation. In: *Proceedings 16th Canadian Symposium on Remote Sensing Ottawa*. Canada Remote Sensing Soc., pp. 95–98.
- Gower, J. F. R. and Borstad, G. A. (1993) Use of imaging spectroscopy to map solar-stimulated chlorophyll fluorescence, red tides and submerged vegetation. In: *Proceedings 16th Canadian Symposium on Remote Sensing Ottawa*, Canada Remote Sensing Society, pp. 95–98.
- Gower, J. and Borstad, G. (2004). On the potential of MODIS and MERIS for imaging chlorophyll fluorescence from space. *International Journal of Remote Sensing* **25**(7/8), 1459–1464.
- Gower, J. and King, S. (2003) Validation of chlorophyll fluorescence derived from MERIS on the west coast of Canada. In: *Proceedings of ENVISAT Validation Workshop: MAVT 2003, Frascati, Italy*, pp. 45–49.
- Gower, J. F. R., Doerffer, R., and Borstad, G. A. (1999) Interpretation of the 685 nm peak in water leaving radiance spectra in terms of fluorescence, absorption and scattering, and its observation by MERIS. *International Journal of Remote Sensing* **20**(9), 1771–1786.
- Gower, J., King, S., Yan, W., Borstad, G. and Brown, L. (2003) Use of the 709 nm band of MERIS to detect intense plankton blooms and other conditions in coastal waters. In: *Proceedings of ENVISAT Validation Workshop: MAVT 2003, Frascati, Italy*, pp. 57–61.
- Gower, J., King, S., Borstad, G., and Brown, L. (2005) Detection of intense plankton blooms using the 709 nm band of the MERIS imaging spectrometer. *International Journal of Remote Sensing* **26**(9), 2005–2012.
- Graneli, E., Paasche, E., and Maestrini, S. Y. (1993) Three years after the *Chrysochromulina polylepis* bloom in Scandinavian waters in 1988: Some conclusions of recent research and monitoring. In: *Toxic Phytoplankton Blooms in the Sea* (edited by T. M. Smayda and Y. Shimizu). Elsevier, New York, pp. 23–32.
- Green, S. and Blough, N. V. (1994) Optical absorption and fluorescence properties of chromophoric dissolved organic matter in natural waters. *Limnology and Oceanography* **39**, 1903–1916.
- Gregg, W. W. (2008) Assimilation of SeaWiFS ocean chlorophyll data into a three-dimensional global ocean model. *Journal of Marine Systems* **69**, 205–225.
- Gregg, W. W., Chen, F. C., and Mezaache, A. L. (1993) *The Simulated SeaWiFS Data Set, Version 1* (SeaWiFS Technical Report Series #9, edited by S. B. Hooker, NASA

- Technical Memo. 1999-20692). NASA Goddard Space Flight Center, Greenbelt, MD, pp. 1–17.
- Gregg, W. W., Friedrichs, M. A. M., Robinson, A. R., Rose, K. A., Schlitzer, R., Thompson, K. R., and Doney, S. C. (2009) Skill assessment in biological data assimilation. *Journal of Marine Systems* **76**, 16–33.
- Guisande, C., Frangopoulos, M., Maneiro, I., Vergara, A. R., and Riveiro, I. (2002) Ecological advantages of toxin production by the dinoflagellate *Alexandrium minutum* under phosphorous limitation. *Marine Ecology Progress Series* **225**, 169–176.
- Haddad, K. D. (1982) Hydrographic factors associated with west Florida toxic red tide blooms: An assessment for satellite prediction and monitoring. M.Sc. thesis, Univ. South Florida, St. Petersburg, 118 pp.
- Hallegraeff, G. M. (2003) Harmful algal blooms: A global overview. In: *Manual on Harmful Marine Algae* (edited by G. M. Hallegraeff, D. M. Anderson, and A. D. Cembella). UNESCO, pp. 25–49.
- Hansen, C. (2008) Simulated primary production in the Norwegian Sea: Interannual variability and impact of mesoscale activity. NERSC thesis No. 77, 56 pp.
- Hansen, C. and Samuelsen, A. (2009) Influence of horizontal model grid resolution on the simulated primary production in an embedded primary production model in the Norwegian Sea. *Journal of Marine Systems* **75**(1/2), 236–244.
- Hansen, G., Botes, L., and De Sallas, M. (2007) Ultrastructure and large subunit rDNA sequences of *Lepidodinium viride* reveal a close relationship to *Lepidodinium chlorophorum* comb. nov. (= *Gymnodinium chlorophorum*). *Phycological Research* **55**(1), 25–41.
- Hansen, C., Kvaleberg, E., and Samuelsen, A. (2010) Anticyclonic eddies in the Norwegian Sea: Their generation, evolution and impact on primary production. *Deep Sea Research Part I: Oceanographic Research Papers* **57**(9), 1079–1091.
- Hansen, P. (2002) Effect of high pH on the growth and survival of marine phytoplankton: Implications for species succession. *Aquatic Microbial Ecology* **28**, 279–288.
- Hara, Y., Doi, K., and Chihara, M. (1994) Four new species of *Chattonella* (Raphidophyceae, Chromophyta) from Japan. *Japanese Journal of Phycology* **42**, 407–402.
- Haugan, P. M., Evensen, G. Johannessen, J. A. Johannessen, O. M., and L. H. Pettersson (1991) Modeled and observed mesoscale circulation and wave-current refraction during the 1988 Norwegian Continental Shelf Experiment. *Journal of Geophysics Research* **96**(C6), 10487–10506, June 15, 1991.
- Henriksen, P., Riemann, B., Kaas, H., Sorensen, H. M., and Sorensen, H. L. (2002) Effects of nutrient-limitation and irradiance on marine phytoplankton pigments. *Journal of Plankton Research* **24**(9), 835–858.
- Hernes, P. J. and Benner, R. (2003) Photochemical and microbial degradation of dissolved lignin phenols: Implications for the fate of terrigenous dissolved organic matter in marine environments. *Journal of Geophysical Research* **108**(C9), 3291–3300.
- Hessen, D. O., Carroll, J., Kjeldstad, B., Korosov, A. A., Pettersson, L. H., Pozdnyakov, D. V. and Sirensen, K. (2010) Input of organic carbon as determinanant of nutrient fluxes, light climate and productivity in the Ob and Yenisey estuaries. *Estuarine, Coastal and Shelf Science* **88**, 53–62, doi: 10.1016/j.ecss.2010.03.006.
- Hirata, T., Aiken, J., Hardman-Mountford, N., Smith, T. J., and Barlow, R G. (2008) An absorption model to determine phytoplankton size classes from satellite ocean colour. *Remote Sensing of Environment* **112**, 3153–3159.
- Hoeger, S. J., Shaw, G., Hitzfeld, B. C., and Dietrich, D. R. (2004) Occurrence and elimination of cyanobacterial toxins in two Australian drinking water treatment plants. *Toxicon* **43**, 639–649.

- Hoepffner, N. and Sathyendranath, S. (1992) Bio-optical characteristics of coastal waters: Absorption spectra of phytoplankton and pigment distribution in the western Atlantic. *Limnology and Oceanography* **37**(8), 1660–1679.
- Hoepffner, N. and Sathyendranath, S. (1993) Determination of the major groups of phytoplankton pigments from the absorption spectra of total particulate matter. *Journal of Geophysical Research* **98**(C12), 22789–22803.
- Hoge, F. E., Lyon, P. E., Swift, R. N., Yungel, J. K., Abbott, M. R., Letelier, R. M., and Essaias, W. E. (2003) Validation of Terra-MODIS phytoplankton chlorophyll fluorescence line height, I: Initial airborne lidar results. *Applied Optics* **42**(15), 2767–2771.
- Holligan, P. M. (1979) Dinoflagellate blooms associated with tidal fronts around the British Isles. In: *Toxic Dinoflagellate Blooms* (edited by D. L. Taylor and H. H. Seliger). Elsevier, New York, pp. 249–256.
- Holligan, P. M., Viollier, M., Harbour, D. S., Camus, P., and Champagne-Phillipe, M. (1983) Satellite and ship studies of coccolithophore production along a continental shelf edge. *Nature* **304**, 339–342.
- Holmedal, L. E. and Utne, T. (2006) Physical–biological interactions and their effect on phytoplankton blooms in fjords and near-coastal waters. *Journal of Marine Research* **64**(1), 97–122.
- Holt, J. T. and James, I. D. (2001) An s-coordinate density evolving model of the northwest European continental shelf, Part 1: Model description and density structure. *Journal of Geophysical Research—Oceans* **106**, 14015–14034.
- Hood, R. R., Laws, E. A., Armstrong, R. A., Bates, N. R., Brown, C. W., Carlson, C. A., Chai, F., Doney, S. C., Falkowski, P. G., and Feely, R. A. (2006) Pelagic functional group modeling: Progress, challenges and prospects. *Deep-Sea Research Part II* **53**, 459–512.
- Hu, C., Muller-Karger, F. E., Taylor, C., Carder, K., Kelble, C., Johns, E., and Heil, C. A. (2005) Red tide detection and tracing using MODIS fluorescence data: A regional example in SW Florida coastal waters. *Remote Sensing of Environment* **97**, 311–321.
- Huang, W. G. and Lou, X. L. (2003) AVHRR detection of red tides with neural networks. *International Journal of Remote Sensing* **24**(10), 1991–1996.
- Hunter, P. D., Tyler, A. N., Presing, M., Kovacs, A. W., and Preston, T. (2008) Spectral discrimination of phytoplankton colour groups: The effect of suspended particulate matter and sensor spectral resolution. *Remote Sensing of Environment* **112**, 1527–1544.
- Huot, Y., Brown, C. A., and Cullen, J. J. (2005) New algorithms for MODIS sun-induced chlorophyll fluorescence and a comparison with present data products. *Limnology and Oceanography: Methods* **3**, 108–130.
- Huot, Y., Brown, C. A., and Cullen, J. J. (2007) Retrieval of phytoplankton biomass from simultaneous inversion of reflectance, the diffuse attenuation coefficient, and Sun-induced fluorescence in coastal waters. *Journal of Geophysical Research* **112**(C06013), doi: 10.1029/2006JC003794.
- Hutchinson, G. E. (1961) The paradox of the plankton. *The American Naturalist* **45**, 137–145.
- Ikeda, M., Johannessen, J. A., Lygre, K., and Sandven, S. (1989) A process study of mesoscale meanders and eddies in the Norwegian Coastal Current. *Journal of Physical Oceanography* **19**, 20–35.
- IOCCG (2006) *Remote Sensing of Inherent Optical Properties: Fundamentals, Tests of Algorithms, and Applications* (edited by Z.-P. Lee, Reports of the IOCCG #5). International Ocean-Colour Coordinating Group, Dartmouth, Canada, 126 pp.

- Ishizaka, J. (1990) Coupling of coastal zone color scanner data to a physical–biological model of the southeastern U.S. continental shelf system, 3: Nutrient and phytoplankton fluxes and CZCS data assimilation. *Journal of Geophysical Research* **95**, 20201–20212.
- James, I. D. (1996) Advection schemes for shelf sea models. *Journal of Marine Systems* **8**, 237–254.
- Jerlov, N. G. and Nielsen, S. E. (1974) *Optical Aspects of Oceanography*. Academic Press, London, 389 pp.
- Jerome, J. H., Bukata, R. P., and Miller, J. R. (1996) Remote sensing reflectance and its relationship to optical properties of natural water. *International Journal of Remote Sensing* **17**(1), 43–52.
- Johannessen, J. A., Johannessen, O. M., and Haugan, P. M. (1989a) Remote sensing and model simulation studies of the Norwegian coastal current during the algal bloom in May 1988. *International Journal of Remote Sensing* **10**(12), 1893–1906.
- Johannessen, J. A., Johannessen, O. M., and Haugan, P. M. (1989b) *Remote Sensing and Model Simulation Studies of the Norwegian Coastal Current during the Algal Bloom in May 1988* (Technical Report No. 16). Nansen Environmental and Remote Sensing Center, Bergen, Norway, 16 pp.
- Johannessen, J. A., Røed, L. P., Johannessen, O. M., Evensen, G., Hackett, B., Pettersson, L. H., Haugan, P. M. Sandven, S., Schuchman, R. A. (1993) Monitoring and modeling of the marine coastal environment. *Photogrammetric Engineering and Remote Sensing* **59**(3), March, 351–361.
- Johannessen, J. A., Schuchman, R. A., Digranes, G., Lyzenga, D. R., Wackerman, C., Johannessen, O. M., and Vachon, P. W. (1996) Coastal ocean fronts and eddies imaged with ERS-1 Synthetic Aperture Radar. *Journal of Geophysical Research* **101**, 6651–6667.
- Johannessen, J. A., Vachon, P. W., and Johannessen, O. M. (1997) ERS-1 SAR imaging of marine boundary layer. *Earth Observations and Remote Sensing* **14**(3), 449–462.
- Johannessen, J. A., Pettersson, L. H., Eldevik, T., Durand, D., Evensen, G., Winther, N., and Breivik, Ø. (2006). Coastal physical and biochemical processes. In: *The Manual of Remote Sensing, Third Edition, Vol. 6: Remote Sensing of the Marine Environment* (edited by J. F. R. Gower). American Society of Photogrammetry and Remote Sensing, Bethesda, MD, 360 pp.
- Johannessen, J. A., Hackett, B., Svendsen, E., Søiland, H., Røed, L. P., Winther, N., Albretsen, J., Danielssen, D., Pettersson, L. H., Skogen, M., and Bertino, L. (2007) Operational oceanography: Challenges and potential. In: *The Norwegian Coastal Current: Oceanography and Climate* (edited by R. Sætre). Tapir Academic Press, Trondheim, Norway.
- Johannessen, O. M. and Pettersson, L. H. (1988) *The Operational Ocean Monitoring and Forecasting System (HOV)* (NERSC Conference Report No. 1, February, 1988). Nansen Environmental and Remote Sensing Center, Bergen, Norway, 26 pp. [in Norwegian].
- Johannessen, O. M., Olaussen, T. I., Pettersson, L. H., Johannessen, J. A., Haugan, P. M., Kloster, K., Sandven, S., Hansen, L., and Geiger, C. (1988) *The Toxic Algal Bloom in May 1988: Recommendations for Future Application of Remote Sensing* (NRSC Special Report No. 1). Norwegian Space Center.
- Johannessen, O. M., Olaussen, T. I., Pettersson, L. H., Johannessen, J. A., Haugan, P. M., Kloster, K., Sandven, S., Hansen, L., and Geiger, C. (1989) *The Toxic Algal Bloom in May 1988, with Recommendations for Future Application of Remote Sensing* (NERSC Special

- Report #1 for the Norwegian Space Center). Nansen Environmental and Remote Sensing Center, Bergen, Norway, 35 pp.
- Johannessen, O. M., Pettersson, L. H., Bjørge, E., Espedal, H., Evensen, G., Hamre, T., Jenkins, A., Korsbakken, E., Samuel, P., and Sandven, S. (1997) A review of the possible applications of earth observation data within EuroGOOS. In: J. Stel, H. W. A. Behrens, J. C. Borst, L. J. Doppert, and J. P. van der Meulen (Eds.), *Operational Oceanography: The Challenge for European Co-operation: Proceedings First International Conference on EuroGOOS*. Elsevier Science, ISBN 0 444 82892 3, pp. 192–205.
- Johannessen, O. M., Bengtsson, L., Miles, M. W., Kuzmina, S. I., Semenov, V., Alekseev, G. V., Nagurny, A. P., Zakharov, V. F., Bobylev, L. P., Pettersson, L. H. et al. (2004) Arctic climate change: Observed and modelled temperature and sea ice. *Tellus, Dynamic Meteorology and Oceanography, Series A* **56A**(3), 1–18, May.
- Johannessen, S. C., Miller, W. L., and Cullen, J. J. (2003) Calculation of UV attenuation and coloured dissolved organic matter absorption spectra from measurements of ocean colour. *Journal of Geophysical Research* **108**(C9), 3301–3314.
- Johnsen, G., Volent, Z., Sakshaug, E., Sigernes, F. and Pettersson, L. H. (2009) Remote sensing in the Barents Sea. In: *Ecosystem of the Barents Sea* (edited by E. Sakshaug, G. Johnsen, and K. Kovacs). Tapir Academic Press, Trondheim, Norway, pp. 139–166.
- Johnsen, G., Moline, M. A., Pettersson, L. H., Pinckney, J., Pozdnyakov, D. V., Egeland, E. S., and Schofield, O. M. (2011) Optical monitoring of phytoplankton bloom pigment signatures. Chapter 14 in: *Phytoplankton Pigments: Updates on Characterization, Chemotaxonomy and Applications in Oceanography* (edited by S. Roy, E. S. Egeland, C. Llewellyn, and G. Johnsen). Cambridge University Press, pp. 538–581.
- Kahru, M. (1997) Using satellites to monitor large-scale environmental change in the Baltic Sea. In: *Monitoring Algal Blooms: New Techniques for Detecting Large-scale Environmental Change* (edited by M. Kahru and C. W. Brown). Springer-Verlag, pp. 43–61.
- Kaitala, S., Anderssen, P., Naustvoll, L., Karlsson, B., Hense, I., Fleming, V., Laamanen, M., Stipa, T., Pettersson, L. H., Durand, D. et al. (2004) *Regional Studies of HAB Events in European Waters* (HABILE Progress Report). Nansen Environmental and Remote Sensing Center, Bergen, Norway, 103 pp.
- Kamykowski, D. (1974) Possible interactions between phytoplankton and semidiurnal internal tides. *Journal of Marine Research* **32**, 67–89.
- Kamykowski, D. (1979) The growth response of a model *Gymnodinium splendens* in stationary and wavy water columns. *Journal of Marine Research* **50**, 289–303.
- Kamykowski, D. (1981a) Laboratory experiments on the diurnal vertical migration of marine dinoflagellates through temperature gradients. *Journal of Marine Research* **62**, 57–64.
- Kamykowski, D. (1981b) The simulation of a southern California red tide using characteristics of a simultaneously measured internal wave field. *Journal of Marine Research* **12**, 253–265.
- Karabyshev, G. S. (1998) Concentration dependence of chlorophyll fluorescence in oceanic waters of diverse trophicity. *Marine Biology* **38**(3), 381–386.
- Karr, M.-E. and Kearns, E. J. (2003) Production regimes in four Eastern Boundary Current systems. *Deep-Sea Research II* **50**, 3199–3221.
- Keafer, B. A. and Anderson, D. M. (1993) Use of remotely-sensed sea surface temperature in studies of *Alexandrium tamarense* bloom dynamics. In: *Toxic Phytoplankton Blooms in the Sea: Proceedings of the Fifth International Conference on Toxic Marine Phytoplankton, Newport, RI, October 20–November 1, 1991* (edited by T. M. Smayda and Y. Shimizu). Elsevier Science, New York, pp. 763–768.

- Kemp, W. M. and Mitsch, W. J. (1979) Turbulence and phytoplankton diversity: A general model of the “paradox of the plankton”. *Ecological Modeling* **7**, 2001–222.
- Kierstead, H. and Slobodkin, L. B. (1953) The size of water masses containing plankton blooms. *Journal of Marine Research* **12**, 141–147.
- Kim, D-L., Matsuyama, Y., Nagasoe, S., Yamagushi, M., Yoon, Y-H., Oshima, Y., Imada, N., and Hojo, T. (2004) Effects of temperature, salinity and irradiance on the growth of the harmful red tide *Cochlodinium polykriodes* Margalef (Dinophyceae). *Journal of Plankton Research* **26**(1), 61–66.
- Kirk, J. T. O. (1983) *Light and Photosynthesis in Aquatic Ecosystems*. Cambridge University Press, London, 320 pp.
- Kirkpatrick, G. J., Schofield, O. M., Millie, D. F., and Moline, M. (2000) Optical discrimination of a phytoplankton species in natural mixed populations. *Limnology and Oceanography* **45**, 467–471.
- Kirkpatrick, G. J., Orroco, C., Moline, M. A., Oliver, M., and Schofield, O. M. (2003) Continuous hyperspectral absorption measurements of coloured dissolved organic material in aquatic systems. *Applied Optics* **42**(33), 6564–6568.
- Kishi, M. and Ikeda, S. (1986) Population dynamics of “red tide” organisms in eutrophicated coastal waters: Numerical experiment of phytoplankton bloom in the east Seto Inland Sea, Japan. *Ecological Modeling* **31**, 145–174.
- Kishi, M. and Suzuki, H. (1978) Criterion for stability of phytoplankton patchiness using a Liapunov method. *Journal of Oceanographic Society of Japan* **34**, 149–158.
- Kishimoto, K. (1990). Coexistence of any number of species in the Lotka–Volterra competitive system over two patches. *Theoretical Population Biology* **38**, 149–158.
- Kleidon, A. and Mooney, H. (2000) A global distribution of biodiversity inferred from climatic constants: Results from a process-based modeling study. *Global Change Biology* **6**(5), 507–523.
- Knappe, D. U., Belk, C., Briley, D. S, Ganday, S. R., Rastogi, N., Rike, A. H., Glasgow, H., Hannon, E., Frazier, W. D., Kohl, P., and Pugsley, S. (2004) *Algae Detection and Removal Strategies for Drinking Water Treatment Plants*. American Water Works Association Research Foundation, Denver, CO, 197 pp.
- Kondratyev, K. Ya., Moscalenko, N. K., and Pozdnyakov, D. V. (1983) *Atmospheric Aerosol*. Gidrometeoizdat, Leningrad, 230 pp. [in Russian].
- Kondratyev, K. Ya., Pozdnyakov, D. V., and Isakov, V. Yu. (1990) *Radiation and Hydrooptical Experiments on Lakes*. Nauka, Leningrad, 115 pp. [in Russian].
- Kondratyev, K. Ya., Pozdnyakov, D. V., and Pettersson, L. H. (1998) Water quality remote sensing in the visible. *International Journal of Remote Sensing* **19**(5), 957–979.
- Kondratyev, K. Ya., Filatov, N. N., Johannessen, O. M., Melentyev, V. V., Pozdnyakov, D. V., Ryazhin, S. V., Shalina, E. V., and Tikhomirov, A. I. (1999) *Limnology and Remote Sensing: A Contemporary Approach* (edited by K. Ya. Kondratyev and N. N. Filatov). Springer/Praxis, Heidelberg, Germany/Chichester, U.K., 408 pp.
- Kone, V., Machu, E., Penven, P., Andersen, V., Garcon, V., Freon, P., and Demarcq, H. (2005) Modeling the primary and secondary productions of the southern Benguela upwelling system: A comparative study through two biogeochemocal models. *Global Biogeochemical Cycles* **19**, GB4021, doi: 10.1029/2004GB002427.
- Korosov, A. A., Pozdnyakov, D. V., Pettersson, L. H., and Grassl, H. (2007) Satellite data based study of seasonal and spatial variations of some ecoparameters in Lake Ladoga. *Journal of Applied Remote Sensing on Aquatic Remote Sensing Applications in Environmental Monitoring and Management* **1**, 011508.

- Korosov, A. A., Morozov, Eu. A., Pozdnyakov, D. V., Pettersson, L. H., and Grassl, H. (2009a) Spaceborne identification and mapping of coccolithophore blooms in the Bay of Biscay. *Earth Observations and Remote Sensing* **3**, 67–78 [in Russian].
- Korosov, A. A., Pozdnyakov, D. V., Folkestad, A., Pettersson, L. H., Sorensen, K., and Shuchman, R. (2009b) Semi-empirical algorithm for the retrieval of ecology-relevant water constituents in various aquatic environments. *Algorithms* **2**, 470–497, doi: 10.3390/a2010470.
- Kudela, R. M., Cochlan, W., and Roberts, A. (2002) Spatial and temporal patterns of *Pseudo-nitzschia* spp. in central California related to regional oceanography. In: *Proceedings of 10th International Conference on Harmful Algae, St. Petersburg Beach, FL, October 21–25, 2002*, pp. 157–165.
- Kuhn, W. and Radach, G. (1997) A one-dimensional physical-biological model study of the pelagic nitrogen cycling during the spring bloom in the northern North Sea (FLEX'76). *Journal of Marine Research* **55**, 687–734.
- Kutser, T. (2004) Quantitative detection of chlorophyll in cyanobacteria blooms by satellite remote sensing. *Limnology and Oceanography* **49**(6), 2179–2189.
- Kutser, T. (2009) Passive optical remote sensing of cyanobacteria and other intense phytoplankton blooms in coastal and inland waters. *International Journal of Remote Sensing* **30**(17), 4401–4425.
- Kutser, T. and Vahtmäe, E. (2006) Detection of cyanobacteria bloom from MERIS images over the Gulf of Finland. *Harmful Algae* **6**, 389–398.
- Kutser, T., Metsamaa, L., Strömbeck, N., and Vahtmäe, E. (2006) Monitoring cyanobacterial blooms by satellite remote sensing. *Estuarine, Coastal and Shelf Science* **67**, 303–312.
- Laamanen, M. J., Gugger, M. F., Lehtimaki J. M., Haukka, K., and Sivonen, K. (2001) Diversity of toxic and non-toxic *Nodularia* isolates (cyanobacteria) and filaments from the Baltic Sea. *Applied Environmental Microbiology* **67**(10), 4638–4647.
- Lalli, C. M. and Parsons, T. R. (1995) *Biological Oceanography: An Introduction*. BPC Wheatons, Exeter, U.K., 230 pp.
- Lampert, L., Queguiner, B., Labasque, T., Pichon, A., and Lebreton, N. (2002) Spatial variability of phytoplankton composition and biomass on the eastern continental shelf of the Bay of Biscay (north-east Atlantic Ocean): Evidence for a bloom of *Emiliania huxleyi* (Prymnesiophyceae) in spring 1998. *Continental Shelf Research* **22**, 1225–1247.
- Landry, M. R., Ondrusek, M. E., and Tanner, S. J. (2000) Biological response to iron fertilization in the eastern equatorial Pacific (IronEx II), I: Microplankton community abundances and biomass. *Marine Ecology Progress Series* **201**, 27–42.
- Large, W. G., McWilliams, C., and Doney, S. C. (1994) Oceanic vertical mixing: A review and a model with a nonlocal boundary layer parameterization. *Reviews of Geophysics* **32**, 363–403.
- Larsson, U., Elmgren, R., and Wulff, F. (1985) Eutrophication and the Baltic Sea: Causes and consequences. *Ambio* **14**, 9–14.
- Laurent, C., Tett, P., Fernandes, T., Gilpin, L., and Jones, K. (2006) A dynamic CSTT model for the effects of added nutrients in Loch Creran, a shallow fjord. *Journal of Marine Research* **61**, 149–164.
- Lavender, S. J., Raitsos, D. E., and Pradhan, Y. (2008) Variations in the phytoplankton of the North-Eastern Atlantic Ocean: From the Irish Sea to the Bay of Biscay. In: *Remote Sensing of the European Seas* (edited by V. Barale and M. Gade). Springer Science + Business Media, pp. 67–90.

- Lawson, L. M., Pitz, E. E., Hofmann, E. E., and Long, R. B. (1995) A data assimilation technique applied to a predator-prey model. *Bulletin of Mathematical Biology* **57**, 593–617.
- Leppäranta, M. and Myrberg, K. (2009) *Physical Oceanography of the Baltic Sea*. Springer/Praxis, Heidelberg, Germany/Chichester, U.K., 300 pp.
- Lessard, E. J. and Murrell M. C. (1998) Microzooplankton herbivory and phytoplankton growth in the northwestern Sargasso Sea. *Aquatic Microbial Ecology* **16**, 173–188.
- Lessard, E. J., Merico, A., and Tyrrell, T. (2005) Nitrate:phosphate ratios and *Emiliania huxleyi* blooms. *Limnology and Oceanography* **50**, 1020–1024.
- Letelier, R. M. and Abbot, M. R. (1996) An analysis of chlorophyll fluorescence algorithms for the Moderate Resolution Imaging Spectrometer (MODIS). *Remote Sensing of Environment* **58**, 215–223.
- Letelier, R. M., Bidigare, R. R., Hebel, D. V., Ondrussek, M., Winn, C. D., and Karl, D. M. (1993) Temporal variability of phytoplankton community structure based on pigment analysis. *Limnology and Oceanography* **38**(7), 1420–1437.
- Levandowsky, M. (1979) On a class of mathematical models for *Gymnodinium breve* red tides. In: *Biochemistry and Physiology of Protozoa* (edited by M. Levandowsky and S. H. Hutner). Academic Press, pp. 394–402.
- Levenberg, K. (1944) A method for the solution of certain non-linear problems in least squares. *Quantitative and Applied Mathematics* **2**, 164–168.
- Li, Y. (2003) Atmospheric correction of SeaWiFS imagery for turbid coastal and inland waters: Comment. *Applied Optics* **42**(6), 893–895.
- Lohrentz, S. E., Weidemann, A. D., and Tuel, M. (2003) Phytoplankton spectral absorption as influenced by community size structure and pigment composition. *Journal of Plankton Research* **25**(1), 35–61.
- Lorentzen, T. and Pettersson, L. H. (2005) *How to Estimate Costs from Harmful Algal Blooms: Economic Impacts on Wild Fisheries, Aquaculture and Commercial Tourism*. Institute for Research in Economics and Business Administration, Bergen, Norway, 49 pp.
- Losa, S. N., Vezina, A., Wright, D., Lu, U., Thompson, K., and Dowd, M. (2006) 3D ecosystem modeling in the North Atlantic: Relative impacts of physical and biological parametrizations. *Journal of Marine Systems* **61**, 230–245.
- Lutz, V., Sathyendranath, S., Head, E. J. H., and Li, W. K. W. (1998) Differences between *in vivo* absorption and fluorescence excitation spectra in natural samples of phytoplankton. *Journal of Phycology* **34**, 214–227.
- Luyten, P. J. (1996) An analytical and numerical study of surface and bottom boundary layers with variable forcing and application to the North Sea. *Journal of Marine Systems* **8**(3/4), 171–189.
- Malinverno, E., Ziveri, P., and Corselli, C. (2003) Coccolithophorid distribution in the Ionian Sea, and its relationship to eastern Mediterranean circulation during late fall to early winter 1997. *Journal of Geophysical Research* **108**(C9), 8115–8131.
- Marcailou, C. P., Gentien, P., Lunven, M. et al. (2000) Dinophysis accumulation vertical distribution and specific toxin content in relation to mussel contamination. *Proceedings of IX HAB International Conference, June 17–22, Marseilles, 2000*, pp. 35–36.
- Maritorena, S., Morel, A., and Gentili, B. (2000) Determination of the fluorescence quantum yield by oceanic phytoplankton in their natural habitat. *Applied Optics* **39**(36), 6725–6737.
- Maritorena, S., Siegel, D. A., and Peterson, A. R. (2002) Optimization of a semianalytical ocean color model for global applications. *Applied Optics* **41**(15), 2705–2714.
- Marquardt, D. W. (1963) An algorithm for least-squares estimation of non-linear parameters. *Journal of the International Society of Applied Mathematics* **11**(2), 36–48.

- Marshall, J., Adcroft, A., Hill, C., and Heisey, C. (1997) A finite-volume, incompressible Navier–Stokes model for studies of the ocean on parallel computers. *Journal of Geophysical Research* **102**(C3), 5753–5766.
- Martin, A. P., Zubkov, M. V., Burkill, P. H., and Holland, R. J. (2005) Extreme spatial variability in marine picoplankton and its consequences for interpreting Eulerian time series. *Biological Letters* **1**, 366–369.
- McClain, E. P., Pichel, W. G., and Walton, C. C. (1985) Comparative performance of AVHRR based multi-channel sea surface temperatures. *Journal of Geophysical Research* **90**, 11587–11601.
- Metsamaa, L., Kutser, T., and Strombeck, N. (2006) Recognizing cyanobacterial blooms based on their optical signature: A modeling study. *Boreal Environmental Research* **11**, 493–506.
- Miller, D. C. M., Moloney, C. L., van der Lingen, C. D., Lett, C., Mullon, C., and Field, J. G. (2006) Modelling the effects of physical–biological interactions and spatial variability in spawning and nursery areas on transport and retention of sardine *Sardinops sagax* eggs and larvae in the southern Benguela ecosystem. *Journal of Marine Systems* **61**, 212–229.
- Miller, P., Groom, S., Shutler, J., Neumann, A., Ebert, K., Kaitala, S., Pettersson, L. H., and Folkestad, A. (2004) *Assessment of Future Possibility of Earth Observation Data for HAB Monitoring* (HABILE Progress Report). Nansen Environmental and Remote Sensing Center, Bergen, Norway, 40 pp.
- Miller, P. I., Shutler, J. D., Moore, G. F., and Groom, S. B. (2006) SeaWiFS discrimination of harmful algal bloom evolution. *International Journal of Remote Sensing* **27**(11), 2287–2301.
- Millie, D. F., Schofield, O. M., Kirkpatrick, G. J., Johnsen, G., Tester, P. A., and Vinyard, B. T. (1997) Detection of harmful algal blooms using photopigments and absorption signatures: A case study of the Florida red tide dinoflagellate, *Gymnodinium breve*. *Limnology and Oceanography* **42**, 1240–1251.
- Milliman, J. D. (1993) Production and accumulation of calcium carbonate in the ocean: Budget of a non-steady state. *Global Biogeochemical Cycles* **7**, 927–957.
- Moisander, P. H., Rantajärvi, E., Huttunen, M., and Kononen, K. (1997) Phytoplankton community in relation to salinity fronts at the entrance to the Gulf of Finland, Baltic Sea. *Ophelia* **46**, 187–203.
- Moll, A. (2000) Assessment of three-dimensional physical–biological ECOHAM1 simulations by quantified validation for the North Sea with ICES and ERSEM data. *ICES Journal of Marine Science: Journal du Conseil* **57**(4), 1060–1068, doi: 10.1006/jmsc.2000.0590.
- Moll, A. and Radach, G. (2003) Review of three-dimensional ecological modeling related to the North Sea Shelf System. *Progress in Oceanography* **57**, 175–217.
- Montealegre, R. J., Verreth, J., Steenbergen, K., Møed, J., and Machiels, M. (1995) A dynamic model for the blooming of *Oscillatoria agardhii* in a monomictic lake. *Ecological Modeling* **78**, 17–24.
- Moore, J. K., Doney, S. C., Kleypas, J. A., Glover, D. M., and Fung, I. Y. (2002) An intermediate complexity marine ecosystem model for the global domain. *Deep-Sea Research II* **49**, 403–462.
- Morel, A. (1990) Optics of marine particles. In: *Particle Analysis in Oceanography* (edited by S. Demers). Springer-Verlag, Berlin, pp. 145–175.
- Morel, A. and Bricaud, A. (1981) Theoretical results concerning light absorption in a discrete medium, and application to specific absorption of phytoplankton. *Deep Sea Research, Part A: Oceanographic Research Papers* **28**(11), 1375–1393.

- Morel, A. and Maritorena, S. (2001) Bio-optical properties of oceanic waters: A reappraisal. *Journal of Geophysical Research* **106**(C4), 7163–7180.
- Morel, A. and Prieur, L. (1977) Analysis of variations in ocean colour. *Limnology and Oceanography* **22**, 709–722.
- Morel, A., Antoine, D., and Gentili, B. (2002) Bidirectional reflectance of oceanic waters: Accounting for Raman emission and varying particle scattering function. *Applied Optics* **41**(30), 6289–6306.
- Morozov, Eu. A., Aniskina, O. B., Pozdnyakov, D. V., Pettersson, L. H., Cychov, V. I., and Grassl, H. (2010a) Automated identification and mapping of *Lepidodinium chlorophorum* blooms from MODIS Aqua data. *Earth Observations and Remote Sensing* **5**, 56–68.
- Morozov, E., Korosov, A., Pozdnyakov, D. V., Pettersson, L. H., and Sychev, V. (2010b) A new area-specific bio-optical algorithm for the Bay of Biscay and assessment of its potential for SeaWiFS and MODIS/Aqua data merging. *International Journal of Remote Sensing* **31**(24), 6541–6565, doi: 10.1080/01431161.2010.508802.
- Nair, A., Sathyendranath, S., Platt, T., Morales, J., Stuart, V., Forget, M-H., Devred, E., and Bouman, H. (2008) Remote sensing of phytoplankton functional groups. *Remote Sensing of Environment* **112**, 3366–3375.
- Natvik, L-J. and Evensen, G. (2003a) Assimilation of ocean colour data into a biochemical model of the North Atlantic, Part I: Data assimilation experiments. *Journal of Marine Systems* **40/41**, 127–153.
- Natvik, L-J. and Evensen, G. (2003b) Assimilation of ocean colour data into a biochemical model of the North Atlantic, Part II: Statistical analysis. *Journal of Marine Systems* **40/41**, 155–169.
- Navrud, S. (1992) *Pricing the European Environment*. Scandinavian University Press, Oslo, 190 pp.
- Neelov, V. A. (2005) A comprehensive physical and biogeochemical model for the ecosystem of the White Sea. In: *The White Sea: Its Marine Environment and Ecosystem Dynamics Influenced by Global Change*. Springer/Praxis, Heidelberg, Germany/Chichester, U.K., pp. 253–292.
- Neumann, T. and Schernewski, A. (2004) An ecological model evaluation of two nutrient abatement strategies for the Baltic Sea. *Journal of Marine Research* **56**(1/2), 195–206.
- Neumann, T., Fennel, W., and Kremp, C. (2002) Experimental simulations with an ecosystem model of the Baltic Sea: A nutrient load reduction experiment. *Global Biogeochemical Cycles* **16**, 450, doi: 10.1029/2001GB0001.
- Neville, R. A. and Gower, J. F. R. (1977) Passive remote sensing of phytoplankton via chlorophyll-a fluorescence. *Journal of Geophysical Research* **83**, 3487–3493.
- Ochadlick, A. R., Aho, P., and Evans-Morgis, J. (1992) Synthetic Aperture Radar observations of currents collocated with slicks. *Journal of Geophysical Research* **97**, 5325–5330.
- O'Reilly, J. E., Maritorena, S., Mitchell, B. G., Siegel, D. A., Carder, K. L., Garver, S. A., Kahru, M., and McClain, C. (1998) Ocean color chlorophyll algorithms for SeaWiFS. *Journal of Geophysical Research* **103**(C11), 2493–2495.
- O'Reilly, J. E., Mitchell, B. G., Kahru, M., Chavez, F. P., Strutton, P., Cota, G. F., Hooker, S. B., McClain, C. R., Carder, K. L., and Muller-Karger, F. (2000) Ocean color chlorophyll a algorithms for SeaWiFS, OC2 and OC4: Version 4. In: *SeaWiFS Postlaunch Calibration and Validation Analyses* (Part 3, Chapter 2, NASA Publ. 22). NASA, Washington, D.C.
- Pahlow, M and Vezina, A. F. (2003) Adaptive model of DOM dynamics in the surface ocean. *Journal of Marine Research* **61**(11), 127–146.

- Pasterkamp, R., Peters, S. W. M., Woerd, W. D., and Hoogenboom, H. J. (2002) Detection of algal blooms in the North Sea using supervised classification of SeaWiFS reflectance imagery. In: *Proceedings of the International Conference on Remote Sensing in Marine and Coastal Environments, Florida, May 20–22, 2002*, pp. 56–58.
- Pellegrini, A. (2003) *Envisat-1 Products Specification, Volume 11: MERIS Products Specifications* (PO-RS-MDA-GS-2009). European Space Agency, Noordwijk, The Netherlands, 128 pp.
- Peters, F., Arin, L., Marrase, C., Berdalet, E., and Sala, M. M. (2006) Effects of small-scale turbulence on the growth of two diatoms of different size in a phosphorus-limited medium. *Journal of Marine Systems* **61**, 134–148.
- Petrova, N. A. (1990) *Phytoplankton Successions with the Anthropogenic Eutrophication of Large Lakes*. Nauka, Leningrad, 200 pp. [in Russian].
- Pettersson, L. H. (1989) *Applications of Remote Sensing to Fisheries, Vol. 2* (NRSC Special Report #4, published in the JRC Report No. S.P.I. 89.21). EEC Joint Research Centre, Ispra, Italy.
- Pettersson, L. H. (1990) Application of remote sensing to fisheries. In: C. N. Murray (Ed.), *Application of Remote Sensing to Fisheries*, Vol. 1 (EUR 12867 EN, Commission of the European Community Directorate-General Science, Research and Development, Luxembourg). JRC, Ispra, Italy.
- Pettersson, L. H., Frette, Ø., Johannessen, O. M., Sørensen, K., Borstad, G., Kerr, R., and Gower, J. F. R. (1990) Norwegian Remote Sensing Spectroscopy for Mapping and Monitoring of Algal Blooms and Pollution: NORSMAP '89 Project Report and Recommendations (NRSC Technical Report No. 28, February).
- Pettersson, L. H., Johannessen, O. M., Sørensen, K., Borstad, G. A., Gower, J. F. R., and Frette, Ø. (1991) Airborne imaging spectroscopy for mapping of chlorophyll a and pollution distribution in the Skagerrak region. *EARSeL Advances in Remote Sensing: Imaging Spectroscopy* **1**(1), 93–100, February.
- Pettersson, L. H., Durand, D. D., Svendsen, E., and Søiland, H. (2000) *DeciDe for Near Real-time Use of Ocean Colour Data in Management of Harmful Algae Blooms: Satellite EO Monitoring of the Harmful Algae Bloom of Chattonella in the North Sea in April–May 2000* (NERSC Technical Report No. 123). Nansen Environmental and Remote Sensing Center, Bergen, Norway, 59 pp.
- Pettersson, L. H., Durand, D., Johannessen, O. M., Noji, T., Søiland, H., Svendsen, E., Groom, S., and Regner, P. (2001) Monitoring and model predictions of harmful algae blooms in Norwegian Waters. In: *Proceedings from IGARSS'01, Sydney, Australia, July*, pp. 251–263.
- Pettersson, L. H., Furevik, B. R., Durand, D., and Johannessen, J. A. (2003) *Synergies in Marine Applications of Ocean Colour, Infrared and SAR Satellite EO Data* (NERSC Technical Report No. 242). Nansen Environmental and Remote Sensing Center, Bergen, Norway, 33 pp.
- Pettersson, L. H., Allan, J. I., Andersen, P. et al. (2005) *Harmful Algal Bloom Initiation and Prediction in Large European Marine Ecosystems* (HABILE Final Scientific Report, Fifth Framework Program). Nansen International Environmental and Remote Sensing Centre, St. Petersburg, 59 pp.
- Pettersson, L. H., Folkestad, A., Korosov, A. and Dagestad, K-F. (2006) *An Autonomous System for Near-real time MERIS Processing* (NERSC Technical Report No. 265). Nansen Environmental and Remote Sensing Center, Bergen, Norway, 14 pp.

- Pettersson, L. H., Babiker, M., Sandven, S., Pozdnyakov, D., and Hamre, T. (2007) *Satellite Remote Sensing of Water Quality* (WARMER Project FP6-034472, Deliverable D. 11). Nansen Environmental and Remote Sensing Center, Bergen, Norway.
- Pettersson, L. H., Dagestad, K.-F., Johannessen, J. A., Korosov, A., Kudryavtsev, V., and Miassoedov, A. (2008) *Sensor Synergies Exploiting ENVISAT for Coastal and Ocean Monitoring* (Special Report No. 85, PRODEX No. C90221). European Space Agency/Norwegian Space Center.
- Pingree, R. D., Pugh, P. R., Holligan, P. M., and Foster, G. R. (1975) Summer phytoplankton blooms and red tides along the tidal fronts in the approaches to the English Channel. *Nature* **258**, 672–677.
- Pope, R. M. and Fry, E. S. (1997) Absorption spectrum (380–700 nm) of pure water, II: Integrating cavity measurements. *Applied Optics* **36**(33), 871–873.
- Popova, E. and Anderson, T. (2002) Impact of including dissolved organic matter in a global ocean boxmodel on simulated distributions and fluxes of carbon and nitrogen. *Geophysical Research Letters* **29**(9), 17–21.
- Porto, S. (1966). Angular dependence and depolarization ratio of the Raman effect. *Journal of the Optical Society of America* **56**, 1585–1589.
- Poutenen, E-L. and Nikkilä, K. (2001) Carotenoid pigments as tracers of cyanobacterial blooms in recent and post-glacial sediments of the Baltic Sea. *Ambio* **30**, 179–183.
- Pozdnyakov, D. and Grassl, H. (2003) *Colour of inland and coastal waters: A methodology for Its Interpretation*. Springer/Praxis, Heidelberg, Germany/Chichester, U.K., 170 pp.
- Pozdnyakov, D. V., Kondrayev, K. Ya., and Pettersson, L. H. (1998) Remote sensing assessment of phytoplankton primary productivity: Methodological aspects. *Earth Observation and Remote Sensing (Russian Academy of Sciences, Moscow)* **4**, 56–73 [in Russian and English].
- Pozdnyakov, D., Bakan, S., and Grassl, H. (2000a) *Atmospheric Correction of Colour Images of Case I Waters: A Review* (Report No. 308). Max-Planck Institute for Meteorology, Hamburg, Germany, 33 pp.
- Pozdnyakov, D., Bakan, S., and Grassl, H. (2000b) *Atmospheric Correction of Colour Images of Case II Waters: A Review* (Report No. 308). Max-Planck Institute for Meteorology, Hamburg, Germany, 53 pp.
- Pozdnyakov, D. V., Lyskovsky, A. A., Grassl, H., and Pettersson, L. H. (2002a) Numerical modelling of transpectral processes in natural waters: Implications for remote sensing. *International Journal of Remote Sensing* **23**(8), 1581–1607.
- Pozdnyakov, D. V., Lyskovsky, A. A., Grassl, H., and Pettersson, L. H. (2002b) Numerical modelling of water colour formation in coastal waters. *Earth Observation and Remote Sensing* **2**, 24–37.
- Pozdnyakov, D. V., Pettersson, L. H., Johannessen, O. M., Lyskovsky, A. A., Filatov, N. N., and Bobylev, L. P. (2003) Cover: SeaWiFS maps water quality parameters in the White Sea. *International Journal of Remote Sensing* **24**(21), 4065–4071.
- Pozdnyakov, D. V., Korosov, A. A., Pettersson, L. H., and Johannessen, O. M. (2005a) MODIS evidences the river runoff impact on the Kara Sea trophy. *International Journal of Remote Sensing* **26**(17), 3641–3648.
- Pozdnyakov, D. V., Korosov, A. A., Grassl, H., and Pettersson, L. H. (2005b) An advanced algorithm for operational retrieval of water quality from satellite data in the visible. *International Journal of Remote Sensing* **26**(12), 2669–2687, doi: 10.1080/01431160500044697.
- Pozdnyakov, D. V., Johannessen, O. M., Korosov, A. A., Pettersson, L. H., Grassl, H., and Miles, M. W. (2007) Satellite evidence of ecosystem changes in the White Sea: A semi-

- enclosed Arctic marginal shelf sea. *Geophysical Research Letters* **34**, L08604, doi: 10.1029/2006GL028947.
- Pozdnyakov, D. V., Korosov, A. A., and Pettersson, L. (2008) Visible and infrared remote sensing of the White Sea bio geo-chemistry and hydrology. In: *Remote Sensing of European Seas* (edited by V. Barale and M. Gade). Springer Science + Business Media, pp. 129–140.
- Prezelin, B. B. and Boczar, A. A. (1986) Molecular bases of cell absorption and fluorescence in phytoplankton: Potential applications to studies in optical oceanography. In: *Progress in Phycological Research, Vol. 4* (edited by F. F. Round and D. J. Chapman). Biopress, Bristol, U.K., pp. 349–464.
- Prieur, L. and Sathyendranath, S. (1981). An optical classification of coastal and oceanic waters based on the specific spectral absorption curves of phytoplankton pigments, dissolved organic matter, and other particulate materials. *Limnology and Oceanography* **26**, 671–689.
- Proctor, R., Holt, J., Allen, J. I., and Blackford, J. (2003) Nutrient fluxes and budgets for the north west European shelf from a 3-D model. *Science of the Total Environment* **314/316**, 769–785.
- Radach, G. and Moll, A. (1993) Estimation of the variability of production by simulating annual cycles of phytoplankton in the central North Sea. *Progress in Oceanography* **31**(4), 339–419.
- Raikow, D. F., Sarnelle, O., Wilson, A. E., and Hamilton, S. K. (2004) Dominance of the noxious cyanobacterium *Microcystis aeruginosa* in low-nutrient lakes is associated with exotic zebra mussels. *Limnology and Oceanography* **49**(2), 482–487.
- Randolph, K., Wilson, J., Tedesco, L., Li, L., Pascual, D., and Soyeux, E. (2008) Hyperspectral remote sensing of cyanobacteria in turbid productive water using optically active pigments, chlorophyll *a* and phycocyanin. *Remote Sensing of Environment* **112**, 4009–4019.
- Rhodes, L., Mackenzie, A. L., Kaspar, H. F., and Todd, K. E. (2001) Harmful algae and mariculture in New Zealand. *ICES Journal of Marine Science* **58**, 398–403.
- Richter, R. (1996) A spatially adaptive fast atmospheric correction algorithm. *International Journal of Remote Sensing* **17**, 1201–1214.
- Riisberg, I. and Edvardsen, B. (2008) Genetic variation in bloom-forming ichthyotoxic *Pseudochattionella* species (Dictyochophyceae, Heterokonta) using nuclear, mitochondrial and plastid DNA sequence data. *European Journal of Phycology*, **43**(4), 413–422.
- Ris, R. C. and Holthuijsen, L. H. (1997) Modeling of current induced wave-blocking in a spectral wave model. In: *Eighth International Biennial Conference on Physics of Estuaries and Coastal Seas, The Hague, Netherlands* (edited by J. Dronkers and M. B. A. M. Scheffers), pp. 139–144.
- Risovic, D. (2002) Effect of suspended particulate-size distribution on the backscattering ratio in the remote sensing of seawater. *Applied Optics* **41**(33), 7092–7099.
- Robinson, I. S., Antoine, D., Darecki, M., Gorrige, P., Pettersson, L. H., Ruddick, K., Santolieri, R., Siegel, H., Vincent, P., Wernand, M. R. et al. (2008) *Remote Sensing of Shelf Sea Ecosystems: State of the Art and Perspectives* (Marine Science Board Position Paper No. 12). European Science Foundation, Strasbourg, France.
- Roelfsema, C. M., Phinn, S. R., Dennison, W. C., Dekker, A. G., and Brando, V. E. (2006) Monitoring toxic cyanobacteria *Lyngbya majuscula* (Gomont) in Moreton Bay, Australia by integrating satellite image data and field mapping. *Harmful Algae* **5**, 45–46.

- Roesler, C. S. and Perry, M. (1995) *In situ* phytoplankton absorption, fluorescence emission, and particulate backscattering spectra determined from reflectance. *Journal of Geophysical Research* **100**(C7), 13279–13294.
- Romankevich, E. A. (1977) *Geochemistry of Organic Matter in the Sea*. Nauka, Moscow, 908 pp. [in Russian].
- Rönneberg, C. and Bonsdorff, E. (2004) Baltic Sea eutrophication: Area-specific ecological consequences. *Hydrobiologia* **514**, 227–241.
- Roy, S., Egeland, E. S., Lewellyn, C., and Johnsen, G (2011, in press) *Phytoplankton Pigments: Updates on Characterization, Chemotaxonomy and Applications in Oceanography*. Cambridge University Press, Cambridge, U.K. ISBN: 9781107000667.
- Ruddick, K. G., Ovidio, F., and Rijkeboer, M. (2000) Atmospheric correction of SeaWiFS imagery for turbid coastal and inland waters. *Applied Optics* **39**(6), 897–912.
- Ruiz-Verdu, A., Dominguez-Gomez, J.-A., and Pena-Martinez, R. (2005, still in press) Use of CHRIS for monitoring water quality in Rosario reservoir. In: *Proceedings of the Third ESA CHRIS/Proba Workshop, March 21–23, 2005, Frascati, Italy*. ESA European Space Research Institute (ESRIN), Frascati, Italy.
- Rukanen, L., Kaitala, S., Fleming, V., and Maunula, P. (2003) Alg@line: Joint operational unattended phytoplankton monitoring system in the Baltic Sea. In: *Building the European Capacity in Operational Oceanography: Proceedings of the Third International Conference on EuroGOOS* (edited by H. Dahlin *et al.*), pp. 519–522.
- Salihoglu, B. (2005) Modeling the effects of physical and biogeochemical processes on phytoplankton species and carbon production in the equatorial Pacific Ocean. Ph.D. thesis, Old Dominion University.
- Salihoglu, B. and Hofmann, E. E. (2007) Simulations of phytoplankton species and carbon production in the equatorial Pacific Ocean, 1: Model configuration and ecosystem dynamics. *Journal of Marine Research* **65**(2), 219–273.
- Samuelson, A., Bertino, L., and Hansen, C. (2009) Impact of data assimilation of physical variables on the spring bloom from TOPAZ operational runs in the North Atlantic. *Ocean. Sci.* **5**(13), 635–647. European Geoscience Union, doi: 10.5194/os-5-635-2009.
- Sarmiento, J. L., Dunne, J., Gnanadesikan, A., Key, R. M., Matsumoto, K., and Slater, R. (2002) A new estimate of the  $\text{CaCO}_3$  to organic carbon export ratio. *Global Biogeochemical Cycles* **16**(4), 1107, doi: 10.1029/2002GB001919.283.
- Sathyendranath, S. (2000) General introduction. In: *Remote Sensing of Ocean Colour in Coastal and Other Optically Complex Waters* (edited by S. Sathyendranath, IOCCG Report No. 3). International Ocean-Colour Coordinating Group, Dartmouth, Canada, pp. 5–21.
- Sathyendranath, S. and Platt, T. (1997) Analytic model of ocean color. *Applied Optics* **36**(12), 2620–2629.
- Sathyendranath, S., Lazzara, S. L., and Prieur, L. (1987) Variations in the spectral values of specific absorption of phytoplankton. *Limnology and Oceanography* **32**, 403–415.
- Sathyendranath, S., Prieur, L., and Morel, A. (1989) A three-component model of ocean colour and its application to remote sensing of phytoplankton pigments in coastal waters. *International Journal of Remote Sensing* **10**(8), 1373–1394.
- Sathyendranath, S., Stuart, V., Irwin, B. D., Maass, H., Savidge, G., Gilpin, L., and Platt, T. (1999) Seasonal variations in bio-optical properties of phytoplankton in the Arabian Sea. *Deep-Sea Research II* **46**, 633–653.
- Sathyendranath, S., Cota, G., Stuart, V., Maas, H., and Platt, T. (2001) Remote sensing of phytoplankton pigments: A comparison of empirical and theoretical approaches. *International Journal of Remote Sensing* **22**(2/3), 249–273.

- Sathyendranath, S., Platt, T., Irwin, B., Horne, E., Borstard, G., Stuart, V., Payzant, L., Maass, H., Kepkay, P., Li, W. K. W. *et al.* (2004a) A multispectral remote sensing study of coastal waters off Vancouver Island. *International Journal of Remote Sensing* **25**(5), 893–919.
- Sathyendranath, S., Watts, L., Devred, E., Platt, T., Caverhill, C., and Maass, H. (2004b) Discrimination of diatoms from other phytoplankton using ocean-colour data. *Marine Ecology Progress Series* **72**, 59–68.
- Scatasta, J., Stolte, S. W., Graneli, E., Weikard, H. P., and Ireland, E. van. (2004) *Harmful Algal Blooms in European Marine Waters: Socio-economic Analysis of Selected Case Studies*. Kalmar University, Sweden, 189 pp.
- Schroeder, T., Schale, M., Fell, F., and Fischer, J. (2002) Atmospheric correction algorithm for satellite data over case-I waters. In: *Proceedings of the Seventh International Conference on Remote Sensing for Marine and Coastal Environments, Miami, FL, May 20–22, 2002*, pp. 123–127.
- Sellner, K. G., Lacouture, R. V., Cibik, S. J., Brindley, A., and Brownlee, S. G. (1991) Importance of a winter dinoflagellate-microflagellate bloom in the Patuxent River estuary. *Estuarine, Coastal and Shelf Science* **32**, 27–42.
- Sellner, K. G., Doucette, G. J., and Kirkpatrick, G. J. (2003) Harmful algal blooms: Causes, impacts and detection. *Journal of Industrial Microbiology and Biotechnology* **30**, 383–406.
- Seuront, L., Vincent, D., and Michell, J. G. (2006) Biologically induced modification of seawater viscosity in the Eastern English Channel during a *Phaeocystis globosa* spring bloom. *Journal of Marine Systems* **61**, 118–133.
- Sharples, J., Ross, O. N., Scott, B. E., Greenstreet, S. P. R., and Fraser, H. (2006) Interannual variability in the timing of stratification and the spring bloom in the northwestern North Sea. *Continental Shelf Research* **26**, 733–751.
- Shchepetkin, A. F. and McWilliams, J. C. (2005) The Regional Ocean Model System (ROMS): A split-explicit, free-surface, topography-following coordinate oceanic model. *Ocean Modeling* **9**, 347–404.
- Shutler, J. D., Smyth, T. J., Land, P. E., and Groom, S. B. (2005) A near-real time automatic MODIS data processing system. *International Journal of Remote Sensing* **26**(5), 1049–1055.
- Siegel, H., Gerth, M., Neumann, T., and Doerffer, R. (1999) Case studies of phytoplankton blooms in coastal and open waters of the Baltic Sea using Coastal Zone Color Scanner data. *International Journal of Remote Sensing* **20**(7), 1249–1264.
- Siegel, D. A., Wang, M., Maritorena, S., and Robinson, W. (2000) Atmospheric correction of satellite ocean color imagery: The black pixel assumption. *Applied Optics* **39**, 3582–3591.
- Siegel, H., Gerth, M., and Heene, T. (2005) Ocean colour remote sensing relevant water constituents and optical properties of the Baltic Sea. *International Journal of Remote Sensing* **26**(2), 315–330.
- Simis, S. G. H., Peters, S. W. M., and Gons, H. J. (2005) Remote sensing of the cyanobacterial pigment phycocyanin in turbid inland water. *Limnology and Oceanography* **50**, 237–245.
- Simis, S. G. H., Ruiz-Verdu, A., Domingues-Gomez, J. A., Pena-Martinez, R., Peters, S. W. M., and Gons, H. J. (2007) Influence of phytoplankton pigment composition on remote sensing of cyanobacteria biomass. *Remote Sensing of Environment* **106**, 414–427.
- Simon, E. and Bertino, L. (2009) Application of the Gaussian anamorphosis to assimilation in a 3-D coupled physical-ecosystem model of the North Atlantic with the EnKF: A twin experiment. *Ocean Science* **5**, 495–510.
- Simon, E. and Bertino, L. (2012) Gaussian anamorphosis extension of the DEnKF for combined state parameter estimation: Application to a 1D ocean ecosystem model.

- Journal of Marine Systems* **89**(1), January, 1–18, ISSN 0924-7963, 10.1016/j.jmarsys.2011.07.007 (<http://www.sciencedirect.com/science/article/pii/S0924796311001576>).
- Sinha, R. P., Klisch, M., Groeniger, A., and Haeder, D.-P. (1998) Ultraviolet-absorbing screening substances in cyanobacteria, phytoplankton and macroalgae. *Journal of Photochemistry and Photobiology B: Biology* **47**(2/3), 83–94.
- Skogen, M. D. (1993) *A User's Guide to NORWECOM: The NORWegian ECOlogical Model System* (Technical Report #6). Institute of Marine Research, Bergen, Norway, pp. 1–23.
- Skogen, M. D. and Moll, A. (2000) Interannual variability of North Sea primary production: A comparison from two model studies. *Continental Shelf Research* **20**(2), 129–151.
- Skogen, M. and Moll, A. (2005) Importance of ocean circulation in ecological modeling: An example from the North Sea. *Journal of Marine Systems* **57**, 289–300.
- Skogen, M. and Søiland, H. (1998) A user's guide to NORWECOM Version 2: The Norwegian Ecological Modeling System. *Fiskeri og Havet* **18**, 42.
- Smyth, T. J., Groom, S. B., Cummings, D. G., and Llewellyn, C. A. (2002a) Comparison of SeaWiFS bio-optical chlorophyll-a algorithms with the OMEX II programme. *International Journal of Remote Sensing* **23**(11), 2321–2326.
- Smyth, T. J., Moore, G. F., Groom, S. B., Land, P. E., and Tyrrell, T. (2002b) Optical modeling and measurements of a coccolithophore bloom. *Applied Optics* **41**(36), 7679–7688.
- Smyth, T. J., Moore, G. F., Hirata, T., and Aiken, J. (2006) Semianalytical model for the derivation of ocean color inherent optical properties: Description, implementation, and performance assessment. *Applied Optics* **45**(31), 1–16.
- Smyth, T. J., Moore, G., Hirata, T., and Aiken, J. (2007) A semi-analytical model for the derivation of ocean color inherent optical properties: Description, implementation and performance assessment (Erratum). *Applied Optics* **46**, 429–430.
- SOER (2010) *The European Environment, State and Outlook 2010: Marine and Coastal Environment*. EEA, Copenhagen, 55 pp. Available at <http://www.eea.europa.eu/soer>.
- Søiland, H. and Skogen, M. D. (2000) Validation of a three-dimensional biophysical model using nutrient observations in the North Sea. *ICES Journal of Marine Science* **57**, 816–823.
- Solanki, H. U., Dwivedi, R. M., and Navak, S. R. (2001) Synergistic analysis of SeaWiFs chlorophyll concentration and NOAA-AVHRR SST features for exploring marine living resources. *International Journal of Remote Sensing* **22**(1), 3877–3882.
- Sole, J., Estrada, M., and Garcia-Ladona, E. (2006) Biological control of harmful algal blooms: A modeling study. *Journal of Marine Systems* **61**, 165–179.
- Soohoo, J. B., Kiefer, D. A., Collins, D. J., and McDermid, I. S. (1986) *In vivo* fluorescence excitation and absorption spectra of marine phytoplankton, I: Taxonomic characteristics and responses to photoadaptation. *Journal of Plankton Research* **8**(1), 197–214.
- Sosik, H. M. and Mitchell, B. G. (1995) Light absorption by phytoplankton, photosynthetic pigments and detritus in the California Current System. *Deep-Sea Research* **42**(10), 1717–1728.
- Sournia, A. (1978) *Phytoplankton Manual* (UNESCO Monographs on Oceanographic Methodology #6). UNESCO, Paris, pp. 1–337.
- Stæhr, P. A. and Cullen, J. J. (2003) Detection of *Karenia mikimotoi* by spectral absorption signatures. *Journal of Plankton Research* **25**(10), 1237–1249.
- Stamnes, K., Yan, B., Li, W., Stamnes, J. J., and Tsay, S.-C. (2003) Pitfalls in the atmospheric correction of ocean colour imagery: How should aerosol optical properties be computed? (Reply to Comment). *Applied Optics* **42**(3), 545–549.

- Steidinger, K. A. and Haddad, K. D. (1981) Biologic and hydrographic aspects of red tides. *Bioscience* **31**, 814–819.
- Stiansen, J. E., Loeng, H., Svendsen, E., Pettersson, L., Johannessen, J., Furevik, T., Handegard, N. O., and Fredo, O. (2002) *Climate–Fish Relations in Norwegian Waters* (No. 12). Fiskeri og havet, Institute of Marine Research, Bergen, Norway.
- Stommel, H. (1949) Trajectories of small bodies sinking slowly through convection cells. *Journal of Marine Research* **8**, 25–29.
- Stramska, M. and Stramski, D. (2005) Effects of uniform vertical profile of chlorophyll concentration on remote sensing reflectance of the ocean. *Applied Optics* **44**, 1735–1747.
- Stramski, D. (1994) Gas microbubbles: An assessment of their significance to light scattering in quiescent seas. In: *Ocean Optics XII* (edited by J. S. Jaffe, Proceedings of the SPIE, Vol. 2258), pp. 704–710.
- Stramski, D., Bricaud, A., and Morel, A. (2001) Modeling the inherent optical properties of the ocean based on the detailed composition of the planktonic community. *Applied Optics* **40**(18), 2929–2945.
- Stramski, D., Sciandra, A., and Clausure, H. (2002) Effects of temperature, nitrogen and light limitation on the optical properties of the marine diatom *Thalassiosira pseudonana*. *Limnology and Oceanography* **47**(2), 392–403.
- Strand, J. (2007) Valuing benefits of recreational fishing in Norway: The Gaula case. In: *Proceedings of the UNESCO Symposium on Decision Making in Water Resource Planning, May 5–7, 1986, Oslo*, pp. 245–278.
- Stipa, T. (2002) Freshwater, density gradients and biological processes in cold, brackish seas: Aspects of the biogeophysical fluid dynamics characterising the Baltic Sea. Doctoral dissertation 2002-06-14, Department of Meteorology, Stockholm University, 42 pp.
- Stumpf, R. P. and Pennock, J. R. (1989) Calibration of a general optical equation for remote sensing of suspended sediments in a moderately turbid estuary. *Journal of Geophysical Research* **94**, 14363–14371.
- Stumpf, R. P. and Tyler, M. A. (1988) Satellite detection of bloom and pigment distribution in estuaries. *Remote Sensing of Environment* **24**, 385–404.
- Stumpf, R. P., Arnone, R. A., Could, R. W., Martinolich, P., Ransibrahmanakul, V., Tester, P. A., Steward, R. G., Subramaniam, A., Culver, M. E., and Pennock, J. R. (2000) SeaWiFS ocean colour data for the US Southeast coastal waters. In: *Proceedings of the Sixth International Conference on Remote Sensing for Marine and Coastal Environments, Ann Arbor, MI*. Veridian ERIM International Publishing, pp. 25–27.
- Stumpf, R. P., Arnone, R. A., Gould, Jr., R. W., Martinolich, P., and Ransibrahmanakul, V. (2002) A partially-coupled ocean–atmosphere model for retrieval of water-leaving radiance from SeaWiFS in coastal waters. In: S. B. Hooker and E. R. Firestone (Eds.), *Algorithm Updates for the Fourth SeaWiFS Data Reprocessing*, Vol. 22 (NASA Tech. Memo. 2002-206892). NASA Goddard Space Flight Center, Greenbelt, MD.
- Stumpf, R. P., Culver, M. E., Tester, P. A., Tomlinson, M., Kirkpatrick, G. J., Pederson, B. A., Truby, E., Ransibrahmanakul, V., and Soracco, M. (2003) Monitoring *Karenia brevis* blooms in the Gulf of Mexico using satellite ocean colour imagery and other data. *Harmful Algae* **2**, 147–160.
- Sturm, B. and Zibordi, G. (2002) SeaWiFS atmospheric correction by an approximate model and vicarious calibration. *International Journal of Remote Sensing* **23**(3), 489–501.
- Subramanian, A., Carpenter, E. J., and Falkowski, P. G. (1999) Bio-optical properties of the marine diazotrophic cyanobacteria *Trichodesmium* spp. II: A reflectance model for remote sensing. *Limnology and Oceanography* **44**(3), 618–627.

- Subramanian, A., Brown, C. W., Hood, R. R., Carpenter, E. J., and Capone, D. G. (2002) Detecting *Trichodesmium* blooms in SeaWiFS imagery. *Deep-Sea Research II* **49**, 107–121.
- Sugihara, S., Kishino, M., and Okami, N. (1984) Contribution of Raman scattering to upward irradiance in the sea. *Journal of Oceanographical Society of Japan* **40**, 397–404.
- SURFER Brochure. (2004) [ftp://goldensoftwareftp-dl:go;den@goldensoftwareftp.com/S8\\_Brochure.pdf](ftp://goldensoftwareftp-dl:go;den@goldensoftwareftp.com/S8_Brochure.pdf)
- Svejkovsky, J. and Shandley, J. (2001) Detection of offshore plankton blooms with AVHRR and SAR imagery. *International Journal of Remote Sensing* **22**(2/3), 471–485.
- Takishita, K., Kawachi, M., Noel, M-H., Matsumoto, T., Kakizoe, N., Watanabe, M., Inouye, I., Ishira, K-I., Hashimoto, T., and Inagaki, Y. (2008) Origins of plastids and glyceraldehyde-3-phosphate dehydrogenase genes in the green-colored dinoflagellate *Lepidodinium chlorophorum*. *Gene* **410**(1), 26–36.
- Tang, D., Kester, D. R., Ni, I-H., Qi, Y-Z., and Kawamura, H. (2003) In situ and satellite observations of a harmful algal bloom and water conditions at the Pearl River estuary in late autumn, 1998. *Harmful Algae* **2**, 89–99.
- Tang, D. L., Kawamura, H., Doan Nhu, H., and Takahashi, W. (2004) Remote sensing oceanography of a harmful algal bloom off the coast of southern Vietnam. *Journal of Geophysical Research* **109**(C03014), doi: 10.1029/2003JC002045.
- Tassan, S. (1993) An algorithm for the detection of the white-tide (“mucilage”) phenomenon in the Adriatic Sea using AVHRR data. *Remote Sensing of Environment* **45**, 29–42.
- Tassan, S. and Ferrari, G. M. (2003) Variability of light absorption by aquatic particles in the near-infrared spectral region. *Applied Optics* **42**(24), 4802–4810.
- Tester, P. A., Stumpf, R. P., Vukovich, F. M., Fowler, P. K., and Turner, J. T. (1991) An expatriate red bloom: Transport, distribution and persistence. *Limnology and Oceanography* **36**(5), 1053–1061.
- Tett, P. (1987) The ecophysiology of exceptional blooms. *Rapports et Procès-Verbaux des Réunions du Conseil International pour l'Exploration de la Mer* **187**, 47–60.
- Tett, P. B. and Walne, A. (1995) Observations and simulations of hydrography, nutrients and plankton in the southern North Sea. *Ophelia* **42**, 371–416.
- Thierstein, H. R. and Young, J. R. (2004) *Coccolithophores: From Molecular Processes to Global Impact*. Springer-Verlag, Berlin, 565 pp.
- Tian, R. C. (2000) Effects of pelagic food-web interactions and nutrient remineralization on the biogeochemical cycling of carbon: A modeling approach. *Deep-Sea Research II* **47**, 637–662.
- Tilstone, G. H., Figueiras, F. G., and Fraga, F. (1994) Upwelling–downwelling sequences in the generation of red tides in a coastal upwelling system. *Marine Ecology Progress Series* **112**, 241–253.
- Tilstone, G. H., Míguez, B. M., Figueiras, F. G., and Fermín, E. G. (2000) Diatom dynamics in a coastal ecosystem affected by upwelling: Coupling between species succession, circulation and biogeochemical processes. *Marine Ecology Progress Series* **205**, 23–41.
- Trees, C. C., Clark, D. K., Bidigare, R. R., Ondrusek, M. E., and Mueller, J. L. (2000) Accessory pigments versus chlorophyll *a* concentrations within the euphotic zone: A ubiquitous relationship. *Limnology and Oceanography* **45**, 1130–1143.
- Truscott, J. E. (1995) Environmental forcing of simple plankton models. *Journal of Plankton Research* **17**, 2207–2232.
- Twardowski, M. S. and Donaghay, P. C. (2002) Photobleaching of aquatic materials: Absorption removal, spectral alteration, and their interrelationship. *Journal of Geophysical Research* **107**(C8), 3091–3115.

- Tynan, C. T. (1993) The effects of small-scale turbulence on dinoflagellates. Ph.D. thesis, Univ. California, San Diego, 227 pp.
- Tyrrell, S., Holligan, P. M., and Mobley, C. D. (1999) Optical impacts of oceanic coccolithophore blooms. *Journal of Geophysical Research* **104**(C2), 3223–3241.
- Vachon, P. W., Johannessen, O. M., and Johannessen, J. A. (1994) Analysis of atmospheric lee waves near Hopen. *Journal of Geophysical Research* **9**(C111), 24345–24357.
- Vargo, G. A., Carder, K. L., Gregg, W., Shanley, E., Heil, C., Steidinger, K. A., and Haddad, K. D. (1987) The potential contribution of primary production by red tides to the west Florida shelf ecosystem. *Limnology and Oceanography* **32**, 762–767.
- Verity, P., Robertson, C., Tronzo, C., Andrews, M., Nelson, J., and Sieracki, M. (1992) Relationships between cell volume and the carbon and nitrogen content in marine photosynthetic nanoplankton. *Limnology and Oceanography* **37**, 1434–1446.
- Vermote, E. F., Saleous, N. E., and Justice, C. O. (2002) Atmospheric correction of MODIS data in the visible to middle infrared: First results. *Remote Sensing of Environment* **83**, 97–110.
- Vesecky, J. F. and Stewart, R. H. (1982) Observation of ocean surface phenomena using imagery from the sea-set synthetic aperture radar: An assessment. *Journal of Geophysical Research* **87**, 3397–3430.
- Vested, H. J., Justesen, P., and Ekebjaerg, L. C. (1992) Advection-dispersion modeling in three dimensions. *Applied Mathematical Modeling* **16**, 234–249.
- Villanoy, C. L., Azanza, R. V., Altemerano, A., and Casil, A. L. (2006). Attempts to model the bloom dynamics of *Pyrodinium*, a tropical toxic dinoflagellate. *Harmful Algae* **5**, 156–183.
- Vincent, R. K. (1997) *Fundamentals of Geological and Environmental Remote Sensing*. Prentice Hall, Upper Saddle River, NJ, pp. 102–108.
- Vincent, R. K., Qin, X., McKay, R. M., Miner, J., Czajkowski, K., Savino, J., and Bridgeman, T. (2004) Phycocyanin detection from LANDSAT TM data for mapping cyanobacterial blooms in Lake Erie. *Remote Sensing of Environment* **89**, 381–392.
- Voss, K. J., Balch, W. M., and Kilpatrick, A. (1998) Scattering and attenuation properties of *Emiliania huxleyi* cells and their detached coccoliths. *Limnology and Oceanography* **43**, 870–876.
- Vountas, M., Dinter, T., Bracher, A., Burrows, J. P., and Sierk, B. (2007) Spectral studies of ocean water with space-borne sensor SCIAMACHY using Differential Optical Absorption Spectroscopy (DOAS). *Ocean Science* **3**, 429–440.
- Wan, Z. and Dozier, J. (1996) A generalized split-window algorithm for retrieving surface temperature from space. *Geoscience and Remote Sensing, IEEE Transactions* **34**(4), 892–905.
- Waters, K. J. (1995) Effects of Raman scattering on water-leaving radiance. *Journal of Geophysical Research* **100**(C7), 13151–13161.
- Werner, F. E., Aretxabaleta, A., and Edwards, K. P. (2004) Modeling marine ecosystems and their environmental forcing. In: *Marine Ecosystems and Climate Variation* (edited by N. C. Stenseth, G. Ottersen, J. W. Hurrell, and A. Belgrano). Oxford University Press, London, pp. 33–46.
- Westerberry, T. K., Siegel, D. A., and Subramanian, A. (2005) An improved bio-optical model for the remote sensing of *Trichodesmium* spp. blooms. *Journal of Geophysical Research* **110**(C06012), doi: 10.1029/2004JC002517.
- Whitehead, R. F., Mora, S., Demers, S., and Gosselin, M. (2000) Interactions of ultraviolet-B radiation, mixing, and biological activity on photobleaching of natural chromophoric dissolved organic matter: A mesocosm study. *Limnology and Oceanography* **45**(2), 278–291.

- Whitlock, C. H., Poole, L. R., and Ursy, J. W. (1981) Comparison of reflectance with backscatter for turbid waters. *Applied Optics* **20**, 517–522.
- Whitte, W. G., Whitlock, C. H., and Harriss, R. C. (1982) Influence of dissolved organic materials on turbid water optical properties and remote sensing reflectance. *Journal of Geophysical Research* **87**, 441–446.
- Wroblewski, J. S., O'Brien, J. J., and Platt, T. (1975) On the physical and biological scales of phytoplankton patchiness in the ocean. *Mémoires Société Royale des Sciences de Liège* **6**(7), 43–57.
- Wu, J. (1988) Bubbles in the near-surface ocean: A general description. *Journal of Geophysical Research* **93**, 587–590.
- Wyatt, T. and Horwood, C. (1973) Model which generates red tides. *Nature* **244**, 238–240.
- Wynne, T. T., Tomlinson, M. C., Warner, R. A., Tester, P. A., Dyble, J., and Fahnstiel, G. L. (2008) Relating spectral shape to cyanobacterial blooms in the Laurentian Great Lakes. *Int. J. Remote Sens.* **29**, 3665–3672, doi: 10.1080/01431160802007640.
- Xiu, P., Liu, Y., and Tang, J. (2007) Variations of ocean colour parameters with nonuniform vertical profiles of chlorophyll concentration. *International Journal of Remote Sensing* **29**, 831–849.
- Yan, B., Chen, B., and Stamnes K. (2002a) Role of oceanic air bubbles in atmospheric correction of ocean color imagery. *Applied Optics* **41**(12), 2202–2212.
- Yan, B., Stamnes, K., Li, W., Chen, B., Stamnes, J. J., and Tsay, S.-C. (2002b) Pitfalls in the atmospheric correction of ocean color imagery: How should aerosol optical properties be computed? *Applied Optics* **41**(2), 412–423.
- Yanagi, T., Yamamoto, T., Koizumi, Y., Ikeda, T., Kamizono, M., and Tamori, H. (1995) A numerical simulation of red tide formation. *Journal of Marine Systems* **6**, 269–285.
- Yentsch, C. S. and Phinney, D. A. (1985) Spectral fluorescence: An ataxonomic tool for studying the structure of phytoplankton populations. *Journal of Plankton Research* **7**, 617–632.
- Zepp, R. G. and Schlotzhauer, P. F. (1981) Comparison of photochemical behavior of various humic substances in water, III: Spectroscopic properties of humic substances. *Chemosphere* **10**, 479–486.
- Zhang, X., Lewis, M., and Johnson, B. (1998) Influence of bubbles on scattering of light in the ocean. *Applied Optics* **37**(27), 6525–6536.
- Zhang, Y. and Hallikainen, M. (2002) Application of an empirical neural network to surface water quality estimation in the Gulf of Finland using combined optical data and microwave data. *Remote Sensing of Environment* **82**, 327–336.
- Zhang, Y., Guidon, B., and Cihlar, J. (2002) An image transform to characterize and compensate for spatial variations in thin cloud contamination of LANDSAT images. *Remote Sensing of Environment* **82**, 173–187.

# Index

- absorption
- coefficient 14, 17, 18, 20, 21, 25, 29, 30, 36, 50
  - cross-section 17–20, 26, 28, 33, 65, 67, 74, 75
  - specific (*see also* cross-section) 14, 16–18, 20, 21, 29, 34, 36, 52, 69, 73
  - spectra 1, 5, 6, 8, 36–38, 41, 49, 53, 54, 56–60, 74, 84, 85, 90, 118
- acids
- fulvic 77
  - humic 77
- accuracy of retrieval 33, 43, 50, 61
- advection 219–223, 226–228, 230, 239, 241, 251, 257, 259
- aerosol 15, 123
- Agulhas Current 178, 220
- air bubbles 79, 80, 85, 103
- albedo 82
- algae
- blue–green (*see also* Cyanobacteria) 50, 55, 61, 81, 88, 97
  - diatom 4, 11, 13, 14, 30, 31, 37, 38, 41, 47, 51, 65, 66, 72, 82, 83, 88, 90, 96–100, 125, 165, 201, 205, 209–211, 213, 215, 216–218, 220, 223, 225, 226, 228, 230, 231, 237, 238, 243, 248, 351, 252, 257, 258
  - green 50, 52, 83, 88, 92, 99, 253
- algal
- bloom 1–4, 6, 8, 10, 12, 14–16, 18, 20–22, 24, 37–43, 46, 47, 80–86, 88, 90, 92, 95–100, 103–110, 114–137, 139, 141–145, 147, 149, 151, 154, 155, 157, 159, 161, 163, 165, 167, 169, 170–201, 243–250, 252–266
  - harmful 1–4, 6, 15, 21, 26, 29, 91, 95, 114, 130, 188, 236, 263
- pigments
- biliproteins 53, 55, 61, 64, 65, 68, 72, 93
  - carotenes 53, 54, 64, 65, 87
  - chlorophylls 52, 53, 64, 68, 69, 72, 85
  - xanthophylls 53, 54, 55, 64, 65
- simulations 32, 125, 126, 142, 157, 215, 231, 233, 244, 246, 248, 251, 253, 261
- species
- Alexandrium* 14, 27, 31, 51, 223
  - Amphidinium* 51
  - Anabaena* 9, 14, 51
  - Aphanizomenon* 30, 41–43, 51, 249, 251, 253, 255, 256
  - Bacterastrum* 83
  - Ceratium* 51, 120
  - Chaetoceros* 13, 14, 51, 83
  - Chattonella* 14, 15, 22, 26, 32–40, 52, 97, 117, 118, 130, 210, 232, 237, 239, 241–244, 250, 251
  - Chrysochromulina* 14, 15, 30, 31, 51
  - Cochlodinium* 51, 118, 170

- algal species (*cont.*)  
*Coscinodiscus* 51  
*Cylindrospermopsis* 51, 88  
*Dinophysis* 10, 11, 14, 27, 31, 51, 223  
*Emiliania huxleyi* 51, 70, 71, 81, 82, 99, 213, 214  
*Fibrocaspida* 51  
*Gambierdiscus* 14, 15, 51  
*Gonyaulax* 14, 51  
*Gymnodinium* 14, 15, 31, 34, 46, 47, 51, 54, 116, 119, 170, 198, 211  
*Halophila* 122  
*Hemiaulus* 83  
*Heterocapsa* 29  
*Heterosigma* 14, 15, 22, 38, 52, 142, 170  
*Hydroclathrus* 122  
*Karenia* 45, 89, 92, 97, 116, 117, 170, 198, 199  
*Katagymnemene* 83  
*Lepidodinium chlorophorum* 52, 82, 83  
*Lyngbya* 121  
*Mesodinium* 29, 31  
*Microcystis* 9, 14, 51, 92, 124  
*Noctiluca* 14, 31, 51  
*Nodularia* 14, 30, 41, 42, 43, 50, 51, 124, 249, 251, 253–256  
*Nostoc* 51  
*Olisthodiscus lutes* 52  
*Oscillatoria* 51, 54  
*Osteopsis* 14  
*Pfiesteria* 51  
*Phaeodactylum* 85  
*Phaeocystis* 30, 51, 121, 231  
*Prorocentrum* 10, 14, 29, 39, 51, 89, 223  
*Prymnesium* 14, 15, 51  
*Pseudochattonella* 32, 33, 35, 36, 38–40, 116, 130, 132, 134, 135, 137, 142, 143, 149, 154, 157, 160, 163, 198, 237, 239, 241–246  
*Pseudonitzschia* 12, 14, 51  
*Pyrodinium* 14, 51, 219, 221, 222  
*Rhizosolenia* 83  
*Scenedesmus* 88  
*Scrippsiella* 14, 223  
*Selenastrum* 88  
*Stephanopyxis* 54  
*Synechococcus* 83, 88, 96, 218, 219  
*Thalassiora* 51  
*Trichodesmium* 14, 51, 81, 83  
*AlgeInfo in situ* network 189, 190  
algorithms  
band ratio  
OC2 95, 99, 102  
OC3 102  
OC4 95, 96, 102, 118, 119, 120, 125, 171  
OC5 96  
case II waters  
Levenberg–Marquardt 82, 101, 106  
neural networks 100, 102  
Angola Current 220  
AOP (apparent optical properties) 63  
approach, synergistic 107–111, 171  
aquaculture 3, 13, 15, 20, 22–24, 30, 31, 50, 51, 113, 120, 125, 126, 130, 134, 149, 189, 205  
ASAR (Advanced Synthetic Aperture Radar) 178, 179, 181–183, 186, 198  
Asia 22  
ASP (amnesic shellfish poisoning) 8, 9, 11, 13, 14  
Atlantic Ocean 68, 71, 96, 135, 139, 149, 157, 165, 167, 168, 205, 212, 231, 232, 258  
atmospheric correction 50, 103, 104, 106, 111, 116, 118, 123–125, 143, 170, 171, 180, 193, 201  
attenuation coefficient 62, 63, 73, 80  
AVHRR (Advanced Very High Resolution Radiometer) 73, 80, 109, 121, 126, 127, 130, 132, 134, 135, 138, 151, 154, 157, 159, 165, 167, 168, 178–180, 198  
Bacillariophyta (*see also* diatoms) 51–54, 65, 72, 72, 83, 85, 88  
backscattering 63, 64, 70, 80–82, 91, 92, 94, 97, 125, 180  
coefficient 64, 70, 71, 75, 85, 100, 106  
cross-section 64, 68, 70, 73–76, 103, 111  
probability 64, 76, 94  
specific (*see also* cross section) 70  
spectra 74, 77, 87, 97  
bacteria 2, 3, 9, 10, 15, 52, 61, 67, 70, 73, 203, 212, 214, 216, 222, 224, 225, 227, 230  
bacterioplankton 76, 79, 85, 214, 229  
Baltic Outflow Current 33, 37

- Baltic Sea 28–32, 37, 40–43, 50, 70, 91, 116, 117, 124, 157, 180–198, 203, 212, 227, 228, 231, 237, 247, 249, 250, 252, 253, 255, 256
- band
- Gaussian 67–69, 84, 85
  - Lorentzian 84, 85
  - Soret 52
- Barcelona Harbor 222, 223
- bays
- Bothnia (Scandinavia) 40, 247, 253
  - Biscay (France) 71, 82, 83
  - Jin (Korea) 118
  - Moreton (Australia) 121
  - Manila 119, 221
- beam attenuation coefficient 62
- BEAM code 171, 192
- Benguela 203, 220, 221
- benthic 10, 15, 27, 170, 204, 212, 222, 225–227, 229, 231, 232
- community 6
- benthos 222, 229
- Bergen (Norway) 125, 169, 236
- biliproteins 53, 55, 64, 65, 68, 72, 93
- allophycocyanins 53, 61
  - phycocyanins 53, 61, 93
  - phycoerythrins 53, 61, 93
- biodiversity 6, 263
- biomass
- bacteria 214, 230
  - phytoplankton 3, 4, 80, 89, 95, 107–110, 124, 125, 131, 134, 142, 143, 149, 169, 179, 182, 188, 217, 223, 224, 226, 228, 230, 233, 234, 235, 241, 252, 253–255, 258, 260
  - zooplankton 207, 215–217
- bio-optical model 81, 82, 90, 99, 100, 103, 104, 106, 107, 110, 115, 122, 142, 180
- Black Sea 30, 264
- Bohai
- Bay (China) 119
  - Sea 22, 120
  - Strait 120
- Boknafjord (Norway) 32
- BOREALI 104, 105, 180, 181, 192, 195
- bottom 28, 30, 31, 40, 44, 122, 196, 213, 230, 238, 248, 257, 258
- reflection 122, 171
- sediments 15, 27, 30, 31, 35
- British Columbia 74, 91, 173
- California 66, 96
- Caribbean Sea 96
- carotenoids 55, 65, 67–69, 85
- case I waters 61, 64, 70, 73, 76, 77, 82, 90, 91, 95–97, 99, 100, 103, 106, 114
- case II waters 62, 73, 75, 86, 87, 95, 97, 100, 103, 106, 110, 111, 115, 119, 124
- CASI (Compact Airborne Spectrographic Imager) 198
- Chesapeake Bay 26, 27
- Chilko Lake 76
- Chlorophyceae 68, 70
- chlorophylls 64, 68, 69, 72
- chl-a* 52, 53, 69, 85
  - chl-b* 53, 69
  - chl-c*<sub>1,2,3</sub> 53, 69, 85
- Ciguatera* fish poisoning toxin 10, 14, 15
- circulation 27, 28, 37, 44, 47, 95, 120, 126, 129, 133, 135, 142, 149, 165, 168, 169, 177–179, 188, 205, 210, 216, 228, 230–233, 242, 246, 257, 258
- Langmuir 210
- mesoscale 26, 118
- climate 81, 107, 110, 233
- change 25, 47, 77, 82, 107, 193, 204, 211–213, 219
- COADS *see* Comprehensive Ocean–Atmosphere Data Set)
- coastal 4, 23, 26, 27, 30, 35, 43, 50, 78, 95, 157, 165, 168, 171, 177, 179, 182, 184, 189, 199, 200, 205, 213, 214, 216, 220, 231, 237, 246, 257, 258
- eddies 134
  - jet 29, 109, 129
  - waters 1, 4, 15, 24–26, 30–34, 44, 62, 66, 74, 75, 77, 82, 83, 99, 110, 149, 154, 157, 165, 168, 170, 171, 189, 191, 193, 197, 198, 203, 212, 226, 228, 229, 231, 262,
- COASTWATCH'95 130
- coccolithophores 64, 70, 71, 81, 83, 99, 211, 213, 214, 216
- coccoliths 64, 65, 70, 71, 82, 92, 99, 106
- COHERENS 229, 231

- community 25, 96, 100, 115, 130, 170, 201  
 benthic 6, 170, 204, 212, 225, 227, 229, 231  
 phytoplankton 1, 26, 27, 29, 31, 34, 43, 61,  
   66, 67, 68, 81, 83, 175, 217, 218, 224,  
   235
- Comprehensive Ocean–Atmosphere Data Set (COADS) 220
- Constance Lake (Bodensee) 66
- convergence 101, 109, 257  
   front 26, 44, 95, 129, 149, 177– 179, 188
- corals 121
- Coriolis effect 29
- cost 22, 23, 205  
   economic 20, 21  
   labor 21
- crabs, brown (*Cancer pagurus*) 21
- cross-section  
   absorption 65–68, 74, 75, 81, 90, 100, 103,  
   180  
   backscattering 68, 70, 73, 75, 76, 93, 100,  
   103, 110, 180  
   fluorescence 72, 94
- currents 26–28, 30, 33, 119, 121, 129, 130,  
   165, 178, 180, 184, 187, 200, 227,  
   230, 238, 242, 244, 259  
   offshore 30
- cyanobacteria 3, 9, 12, 14, 28, 30, 31,  
   40–43, 50, 51, 55, 72, 81, 83,  
   90–92, 96, 97, 106, 107, 116, 117,  
   121–125, 180–183, 187, 198, 216,  
   217, 228, 247, 249–255
- countries/continents  
   Australia 9, 11, 13, 24, 121  
   Canada 11, 13, 74, 223  
   Central America 130, 188  
   Chile 11  
   China 22, 24, 118–121  
   Denmark 32, 33, 118, 142, 143, 154, 157,  
   165, 171, 242, 244  
   Europe 5, 7, 8, 11–13, 15, 16, 18, 22–24,  
   29, 32, 66, 90, 113, 130, 135, 154, 165,  
   171, 189, 192, 203, 225, 226, 229, 231  
   France 22, 23, 82, 96  
   Ireland 23, 116, 198  
   Italy 22, 23  
   Japan 11, 13, 26, 210  
   Latin America 24
- Middle East 24
- Namibia 220
- New Zealand 11, 13, 15, 31, 96
- North America 6, 9–11, 13, 16, 18, 66
- Norway 21, 22, 27, 32–34, 38, 114, 125,  
   126, 134, 143, 157, 165, 171, 190, 236,  
   241–243
- Peru 66
- Philippines 220, 221
- Polynesia 24
- Portugal 26
- South Africa 220
- Spain 15, 22, 23, 26, 31, 255
- Sweden 32, 37, 135, 249
- Thailand 11
- The Netherlands 23, 154, 157
- U.S.A. 24, 26, 124, 199
- CPAs (color-producing agents) 62, 64, 65,  
   73, 82, 85, 99, 100, 101, 103, 104,  
   111, 115, 266
- Cryptophyceae 70
- cyanobacterium 14, 43, 92, 124
- data assimilation 110, 114, 142, 197, 198,  
   204, 232, 233, 235, 236, 243, 246,  
   262
- degradation 30, 53, 67, 103, 217  
   bleaching/photodegradation 77, 78  
   microbial 78
- detritus 3, 70, 81, 85, 125, 204, 210,  
   214–217, 219–221, 225, 227–230
- DHI MIKE 3 (Danish hydrodynamic  
   ecosystem model ) 227, 228, 233
- DSP (diarrheic shellfish poisoning ) 7, 10,  
   11, 13, 14, 21
- diatoms 11, 13, 14, 30, 31, 38, 44, 45, 51,  
   66, 72, 82, 83, 90, 96–99, 125, 165,  
   205, 209–221, 225, 228–232, 237,  
   238, 248, 251, 257
- diazotrophs 211, 212, 215–217
- dimension 28, 64, 101, 215, 218, 222, 230  
   socio-economic 24
- Dinophyta (see also Dinoflagellates) 51–54
- Dinoflagellates 10, 14, 15, 31, 43–45, 47,  
   51, 66, 83, 96, 223, 255, 257

- dissolved 6, 38, 55, 57–60, 62, 77, 211, 214, 227
- inorganic carbon
- nitrogen (DIN) 41, 210, 215, 220, 225, 228, 230, 251, 252
  - phosphorus (DIP) 41, 210, 225, 228, 252
  - silicon (Si) 213, 225
- organic carbon (*doc*)
- allochthonic (terrigenous) 73, 77
  - autochthonic 3, 76
  - chromophoric/colored 78, 81, 94, 171
  - matter 4, 64, 65, 73, 76–81, 85, 86, 91, 100, 119–121, 125, 192, 214, 216, 225, 227, 233
- DOAS (differential optical absorption spectroscopy) 90
- DSRS (Dundee Satellite Receiving Station) 197
- economic 20, 22
- aspects 20, 21
  - cost 20, 21
  - impact 3, 22, 23
  - loss 23, 24, 120
- eddies 26, 27, 177, 178, 180, 188
- mesoscale 26, 29, 34, 165
- Egersund 149
- egestions (metabolic exudation) 72, 76
- ENSO (El Niño–Southern Oscillation) 212
- emission 50, 52, 53, 61, 79, 82, 93, 94
- bands 72
- English Channel 26, 86, 87, 117, 198, 226, 229, 230
- environment 4, 21, 22, 24, 25, 27, 41, 50, 72, 88, 107, 119, 143, 154, 169, 180, 182, 188, 193, 194, 201, 204, 206, 208, 209, 217–222, 228, 230, 231, 237
- aquatic 1–4, 20, 26, 50, 52, 76, 107, 110, 113, 116, 157, 172, 177, 204, 220
  - marine 15, 30, 68, 72, 114, 171, 193, 196, 203, 212, 262
  - pelagic 2, 35
- ENVISAT 89, 90, 181, 198
- epidemic 21
- Equatorial Pacific Ocean 218
- Cold Tongue Region 219
- ERS-2 SAR 131, 132, 144, 149, 153–156
- Esbjerg 142
- Eulerian field 210
- Europe 5, 7, 8, 11–13, 15, 16, 18, 22–24, 29, 32, 66, 113, 130, 135, 165, 171, 189, 192, 204, 225, 229
- ECMWF (European Centre for Medium-range Weather Forecasting) 139, 141–143, 146, 149, 151, 154, 155, 257, 258
- ECOHAM (Ecological North Sea Model, Hamburg) 229–231
- ELISE (Ecological Modeling Software for interactive modeling) 229, 230
- ERSEM (European Regional Seas Ecosystem Model) 205, 222, 223, 225, 226, 229–232, 257, 258
- ESA (European Space Agency) 115, 116, 182, 189, 192, 195, 198, 236, 240
- eutrophication 25, 30, 40, 120, 205, 212, 226–228, 231
- eutrophic
- waters 1, 59, 67, 177, 226
  - zone 3, 6
- expression
- semianalytical 70
- Faeroe Islands 165
- Farsund 134, 142
- FD (Norwegian Directorate of Fisheries) 134, 142, 169
- FerryBox 114, 134, 171–173, 176, 189, 191
- FIMR (Finnish Institute of Marine Research) 41, 42, 250, 252–256
- fish 13–15, 20–22, 24, 31, 32, 120, 125, 126, 134, 143, 149, 170, 171, 205, 221, 228, 232, 243
- fishery 20, 130, 189
- commercial 22, 23
- fjord 22, 28, 31, 33, 66, 78, 134, 142, 149, 228, 231
- Flekkfjord 22
- flocculation 78
- Flødevigen 35, 149
- Florida 15, 170, 174, 199, 200

- fluorescence  
*chl* 53, 72, 123  
 cross-section 72, 94  
*doc* 94  
 line height (FLH) 90, 91, 115, 170, 172  
 pigments 90, 94, 110, 111  
 quantum yield  
*chl-a* 90  
*doc* 79  
 fluorophores 50, 55, 93  
 flux, radiative 49, 96, 104  
 foam 4, 10, 51, 52, 107  
 food 1–4, 6, 9, 11, 14, 15, 20, 107, 189  
 safety 9, 11, 13, 15, 17, 19  
 forecast, simulations 252, 255  
 forward scattering coefficient 63  
 front/frontal 26, 28, 29, 44, 45, 47, 120,  
 126, 128, 129, 143, 149, 154, 165,  
 167, 171, 177–179, 182, 184, 188,  
 197, 226, 233, 257  
 function, sigmoidal 95
- Galician Rías (Spain) 32, 43, 47  
 Galway (Ireland) 23  
 Georges Bank 68, 69  
 germination, cyst 36  
 GHER (Geo-Hydrodynamics and Environment Research model )  
 229–231  
 GIS 194, 196  
 GMES (European Global Monitoring for Environment and Security) 113, 188, 189, 192, 264  
 Gotland 182  
 GOTM (General Ocean Turbulence Model)  
 227  
 green algae 83  
 gulfs  
 Finland 2, 19, 118, 122, 124, 253, 255  
 Maine 27  
 Mexico 15, 26, 199  
 St. Lawrence (Canada). 233
- HABs (harmful algal blooms)  
 economic aspects 20, 21, 23  
 health and sanitary aspects 3, 9, 11, 13, 15,  
 17, 19  
 identification *Chapter 3*
- monitoring *Chapter 4*  
 shipborne *Chapter 4*  
 spaceborne/satellite *Chapter 4*  
 occurrence 2, 24  
 populations 31  
 prediction, model-based 204, 208, 232,  
 233, 236, 240–243, 255  
 proliferation 13, 25, 27–29, 31, 32  
 HABILE (Harmful Algal Bloom Initiation and Prediction in Large European Ecosystems) 236–238, 241  
*Haptophytes* (*see also Prymnesiophytes*) 51, 97  
 health, public 22, 23  
 Hirtshals (Denmark) 171  
 Hordaland (Norway) 149  
 HOT (haze optimization transformation)  
 104  
 HPLC (high performance liquid chromatography) 85, 96  
 Hydrolight code 122  
 hydro-optical models 110
- Iberian (Spain)  
 peninsula 43, 44, 47  
 shelf 43, 257  
 images, multispectral 82, 83, 99, 104, 107  
 impact  
 climate change 25, 193, 204, 211, 213  
 ecological, HAB 3, 4, 6, 20, 22, 23  
 IMR (Norwegian Institute of Marine Research) 35–40  
 index, willingness-to-pay (WTP) 21, 22  
 inelastic scattering (*see also Raman scattering*) 49, 90, 93, 94  
 inorganic salts 77  
 interactions, trophic 20, 214, 221, 222, 262  
 inverse problem 101  
 invertebrates 14, 51  
 IOCCG (International Ocean Color Coordination Group) 93  
 IOPs (inherent optical properties) 49,  
 62–64, 67, 107, 115  
 irradiance  
 attenuation coefficient 63  
 downwelling 63, 64  
 upwelling 63  
 iterative procedure 101

- Jæren (Norway) 139, 149  
 JGOFS (Joint Global Ocean Flux Study) 217–219  
 Jutland = Jylland (Denmark) 27, 33, 34  
 Current 33
- Kattegat 26, 30, 32, 33, 35–37, 39, 40, 125, 129, 179, 189  
 Kinetics. Michaelis–Menten 209, 213, 216, 220, 230  
 Kristiansand (Norway) 139, 149  
 Kuroshio (Japan) Stream 26
- lakes  
 Chilko (British Columbia) 66, 74, 76  
 Constance 66  
 Erie (U.S.) 92  
 Ladoga (Russia) 66, 68, 74–76  
 Ontario (U.S.) 66, 68, 74, 76  
 La Pradet 23  
 Latin America 24  
 Laurentian Great Lakes 124  
 lidar 93, 108, 110, 111  
 life cycles, phytoplankton 61  
 Lindesnes (Norway) 37  
 Lista (Norway) 142, 143, 149  
 Loch Creran (Scottish Western Highlands) 228  
 Louisiana (US) 26
- Management 22–24, 197, 200  
 Mandal (Norway) 34, 37  
 marine ecosystem 24, 35, 83, 107, 108, 114, 115, 121, 134, 157, 165, 169, 196, 197, Chp. 5  
 MATLAB 193  
 MCI (Maximum Chlorophyll Index) 170  
 meander 126, 143  
 mechanisms, hydrodynamic 29  
 melanoids 77  
 Mekong (China) River 121  
 mesotrophic, waters 77  
 methods, spectrophotometric 78  
 microalgae/microplankton 1, 3, 4, 10, 52, 66, 67, 80, 225, 231, 257  
 mineralization 216, 217, 219, 221, 227, 252
- minimum  
 global 101  
 local 101  
 mixotrophy 224  
 models  
 aggregated 207, 208, 212  
 allometric 205, 224, 228  
 box 205  
 ecological/biogeochemical 209, 212, 214, 220, 221, 225, 227, 230, 231, 237, 262  
 heuristic 205  
 multispecies 208, 212  
 one-dimensional (1-D) 215, 218  
 physical 203, 205, 209, 211, 232, 233, 236  
 three-dimensional (3-D) 205, 210, 216, 219–221, 225, 227, 229–233, 257, 262  
 monitoring  
 service 114, 125, 188, 189, 196, 201  
 system 171, 188, 200, 201  
 Monte Carlo simulations 64  
 morphology 28, 109  
 mucilage 3, 51, 72, 73, 85, 97, 103, 116, 198  
 multivariate optimization procedure 82, 89, 100, 104
- nanoplankton 52  
 NAO (North Atlantic Oscillation) 31, 47, 212  
 NASA (National Aeronautics and Space Administration) 116, 118, 119, 181, 189, 198, 199  
 DAAC code 198  
 natural water(s) 61, 65, 76, 79, 88, 93, 95, 104, 180  
 NCC (Norwegian Coastal Current) 125, 130, 139, 142, 143, 154, 157, 165, 168, 169, 206  
 NEODAAS (Natural Environment Research Council Earth Observation Data Acquisition and Analysis Service) 197, 198  
 NERSC (Nansen Environmental and Remote Sensing Center, Norway) 127, 130, 133, 134, 188, 189, 192–196, 200, 206, 232, 237  
 neural networks 100, 102, 215

- NIERSC (Nansen International Environmental and Remote Sensing Center, Russia) 181, 182
- nitrate 46, 135, 210, 211, 212, 216, 218, 220–223, 227–231, 260, 261
- nitrification/denitrification 29, 30, 211, 213, 214
- nitrogen 30, 38, 40, 41, 43, 65, 72, 83, 89, 204, 210–212, 214–216, 220, 225, 230, 231, 235–237, 249, 251, 252, 255
- NIVA (Norwegian Institute for Water Research) 22, 171–173, 176, 189, 191
- Noctilucoids 51
- NORCSEX (Norwegian Continental Shelf Experiment) 130
- NORSMAP 130
- North Atlantic 68, 71, 107, 205  
Current 157, 165, 167  
shelf waters 96
- North Central Pacific 66
- Norway 21, 22, 27, 32–34, 38, 114, 125, 126, 134, 143, 157, 165, 171, 190, 236, 241–243
- NORWECOM (Norwegian Ecological Model System) 142, 157, 163, 205, 229, 231, 232, 237–252
- nowcasts, simulations 233
- NPZD (nutrient–phytoplankton–zooplankton–detritus) 204, 205, 208
- NSP (neurotoxic shellfish poisoning) 11–15, 20
- nutrients  
depletion 26, 36, 43, 247, 252  
limitation 40, 61, 65, 212, 229, 231, 242  
regeneration 229, 230, 231  
remineralization 31, 216, 217, 219, 221, 252
- OCTS (Ocean Color and Thermal Scanner) 115
- occurrence of HABs 2, 24, 29, 30, 32, 35, 41–43, 49, 97, 113, 121, 187, 199, 204, 208, 247, 249, 262
- oligotrophic waters 1, 2, 67, 77, 199
- optical properties of water 62, 79, 95, 106
- organic dissolved matter 4, 62, 64, 73, 76, 78, 79, 81, 85, 86, 91, 100, 119, 120, 125, 171, 192
- Oslo (Norway) 171
- oxygen  
depletion 3, 51, 72  
dissolved 6
- PDO (Pacific Decadal Oscillation) 107
- Pearl River (China) 119
- perceptron 102
- pheophytin 67, 96
- phosphorus, inorganic 41, 237, 252
- photodegradation 78
- photooxidation 77, 78
- photosynthesis 1, 55, 76, 213, 214, 216
- photosynthesizing pigments 52, 53, 66, 68, 72
- phytoplankton  
autotrophic 29, 64, 83, 115, 218, 223, 225  
death rate 222, 243, 245, 246  
heterotrophic 29, 64, 67, 213, 214, 223, 230
- picoplankton 52, 66, 215, 225
- pigment  
absorption 86  
chlorophyllous 68, 72, 85, 88, 90, 93  
packaging effect 68
- pigments  
biliproteins 53, 55, 61, 62, 68, 72, 93  
carotenes 53–55, 64, 66, 87  
chlorophylls 64, 68, 69, 72  
xanthophylls 53–55, 64, 65
- PLS (multivariate partial least squares regression technique) 89
- PML (Plymouth Marine Laboratory) 137, 169, 198
- pollutants 229
- Polynesia 24
- POM (Princeton Ocean Model) 221, 229
- Pomeranian Bight 70
- Po River 73
- Portugal 15, 26
- predators 204, 205, 222, 223
- Prego (Spain) 26
- prey 204, 216, 217, 223, 224, 232
- primary production 1, 36, 109, 115, 214, 217–219, 223, 227, 230, 231, 237
- Prorocentroids 51
- protein complex 55, 87

- Prymnesiophytes 14, 15, 51  
 PSP (paralytic shellfish poison) 5, 6,  
   13–15, 47, 223  
 pycnocline 29, 32, 253
- Queensland (Australia) 122  
 QuikScat 120, 121
- radiance 50, 63, 68, 90, 95–97, 99, 100,  
   104, 106, 119, 170, 171, 174  
 Raman scattering 90, 93, 94, 98, 103  
 Raphidophytes 14, 15, 51  
 recreation 4, 10, 21–23  
 remineralization 216, 217, 219, 221, 252  
 remote sensing  
   active 50  
   optical 49, 50  
   passive 50  
   reflectance, subsurface 64, 82, 100, 104  
   synergistic 50, 107–111  
 resuspension 204, 221, 222, 239  
 retrieval algorithms 81, 114, 115, 177, 180,  
   199  
 Riccione (Italy) 23  
 rivers  
   Mekong (China) 121  
   Pearl (China) 119  
   Yellow (China) 120  
   Yogil (Korea) 118  
 Rogaland (Norway) 149  
 ROMS (Regional Ocean Modeling System)  
   220, 221  
 RSDAS (Data Analysis Service) 197  
 runoff  
   land 28, 30, 32  
   river 2, 27, 28, 30, 38, 47, 157, 171, 229,  
   237  
 salmon, farmed 22  
 SAR (Synthetic Aperture Radar) 144, 145,  
   148, 149, 151, 153–156, 159, 165,  
   169, 177–180, 201  
 satellite, sensors  
   AMSR-E 178  
   ASAR 178, 179, 181–183, 186, 198  
   ASTER 80
- AVHRR 73, 80, 109, 121, 126, 127, 130,  
   132, 134, 135, 138, 151, 154, 157, 159,  
   165, 167, 168, 178–180, 198  
 CZCS 71, 80  
 ERS 131, 132  
 LANDSAT 80, 92, 115, 121, 122, 124, 125  
 MERIS 80, 81, 90, 91, 97, 99, 110, 115,  
   116, 122–124, 157, 163, 164,  
   170–175, 178, 180–282, 184, 188,  
   189, 192, 194, 198  
 MODIS 80, 82, 83, 91, 92, 99, 108, 110,  
   115, 116, 122, 123, 134, 171, 178, 180,  
   181, 183, 184, 186, 189, 195, 198, 199  
 RADARSAT 131, 139, 141, 149, 151  
 SCIAMACHY 89, 90  
 SeaWiFS 80, 95–100, 106, 108, 110,  
   114–121, 125, 132, 135, 137–145,  
   148, 149, 153–159, 165, 167, 168,  
   171, 198, 199  
 SPOT 80  
 scattering  
   back 63, 64, 70, 80–82, 91, 92, 94, 97, 125,  
   180  
   elastic 49, 93, 98  
   forward 63, 102  
   inelastic (Raman) 49, 90, 93, 94  
   isotropic 63, 64  
   phase function 63, 94  
 seas  
   Adriatic 73  
   Baltic 28–30, 32, 33, 37, 40, 41, 43, 50, 70,  
   91, 116, 117, 124, 157, 164, 180–183,  
   187, 198, 203, 212, 227, 228, 231, 237,  
   247, 249, 250, 252, 253, 255, 256  
   Barents 130  
   Belt 40  
   Black 30, 116  
   Bohai 120  
   Caribbean 96  
   Gotland 182, 227  
   Ionian 71  
   Irish 74, 226  
   Mediterranean 15, 203, 222  
   North 15, 26, 32–34, 36, 39, 40, 54, 157,  
   159, 164, 165, 167–169, 171, 179,  
   198, 204, 213, 225–227, 229–231,  
   237, 242, 243  
   Sargasso 66  
   South China 120, 121

- seas (*cont.*)  
 Southeast (Korean) 118  
 White 233, 234  
 Yellow 120
- SeaDAS 82, 118, 192
- seagrass 121, 122
- sedimentation 2, 204, 227, 231, 238, 239
- sediments 15, 27, 30, 31, 35, 43, 212, 213, 221, 227, 229
- sensors  
 hyperspectral 50, 108, 110, 111  
 multispectral/multiband 60, 110
- shellfish 3, 4, 10, 11, 14, 15, 20, 21, 31, 82, 170
- Shetland 157, 165, 169
- silica 30, 74, 213, 216, 219, 239
- silicoflagellates 83, 211, 213
- silicon 231  
 inorganic 237
- Skagen 33
- Skagerrak 26, 27, 30, 32–34, 36, 37, 39, 40, 116, 125, 126, 130, 135, 138–140, 143, 144, 149, 154, 157, 171–174, 179, 189, 203, 229, 233, 237, 242, 253
- slick 109, 124, 143, 180, 187
- SOER (*The European Environment, State and Outlook 2010*) 263, 264, 265
- solar radiation 63, 76, 78
- Soret band 52
- spaceborne data 169, 174, 180, 198, 236
- spectral  
 region 50, 68, 75, 76, 79, 81, 90, 111, 122, 123, 125, 130, 179  
 resolution 50, 80, 89, 90, 110, 200
- specific  
 absorption (*see also* cross-section) 62, 64, 65, 66, 68, 69, 78, 82, 84, 100  
 backscattering (*see also* cross-section) 70, 71, 82
- spores 31
- Stokes law 222
- St. Petersburg xv, xvii, xxix
- stratification 27, 29, 30, 43, 120, 177, 180, 210, 212, 219, 249, 258
- insolation-induced 29
- thermal 28, 40, 249
- water density 26
- subpycnocline 29
- subsurface remote-sensing reflectance 64, 82, 100, 104
- surfactant 85, 103, 108, 109, 134, 143, 149, 154, 177, 180, 187
- SURFER 107
- surplus  
 producers' 22  
 consumers' 20, 22
- suspended inorganic matter (*sm*) 75, 86, 227
- system  
 basin-scale 119  
 early warning 32, 114, 197  
 ecological 204, 225, 255
- TAO (Tropical Atmosphere–Ocean experiment) 219
- Texas 26, 199
- thermocline 40, 225
- three-dimensional models (3-D) 205, 210, 216, 219–221, 225, 227, 229–231, 233, 257, 262
- tide 3, 4, 15, 29, 51, 97, 106, 116, 118, 119, 121, 123, 157, 170, 198–200, 207, 210, 229, 233
- TOPAZ model (Towards an Operational Prediction system for the North Atlantic European coastal Zones) 206, 232
- tourism 4, 15, 20, 22, 23  
 sector 22
- toxic algae 21, 27, 28
- toxins/toxic effects  
 ASP 8, 9, 11, 13, 14  
 CFP 14, 15  
*Ciguatera* 10, 14, 15  
 DSP 7, 10, 11, 13, 14, 21  
 NSP 11, 13–15, 20  
 PSP 5, 6, 13–15, 47
- trophic food web interactions 3
- United States (U.S., U.S.A.) 21–24, 26, 96, 114, 115, 124, 126, 170, 180, 199, 218, 219
- universities  
 Bergen x  
 Miami 198  
 St. Petersburg xviii

- upwelling 26, 27, 29–31, 43, 44, 46, 47, 121, 171, 180, 200, 203, 220, 221, 223, 249, 253, 257–259, 260  
coastal 43, 118, 216, 220, 257, 258
- upwelling irradiance 63, 64, 71, 82, 90, 95, 99, 100, 104
- validation 114, 177, 178, 198, 104, 215, 232, 233, 241, 262,
- Vancouver Island 170
- variability 25, 31, 47, 66, 70, 96, 134, 175, 178, 180, 188, 219, 220, 231, 233, 253, 254, 258  
interannual 38, 41, 43, 197, 212, 215, 219, 243
- vegetation 1, 6, 66, 70, 110, 111, 122, 123, 170, 177, 227
- Venetian lagoon 130, 188
- Virginia, rivers 78
- volume, reflectance 63, 64, 71, 79, 80, 85, 90, 93, 99
- water  
column  
light penetration 90  
stratified 26, 41, 95, 120, 226
- discoloration 3, 4, 6
- nitrification 29, 30, 212–214
- optical properties 73, 79
- salinity 30, 31, 36, 39–43, 107, 119, 120, 171, 172, 210, 225, 227–229, 237, 246, 249, 253, 258, 259, 262
- temperature 29–32, 34, 36, 37, 39, 41, 43–45
- waters  
coastal 1, 4, 13, 24, 30, 32, 34, 44, 66, 75, 77, 82, 99, 110, 135, 139, 142, 143, 149, 154, 157, 165, 168, 170, 171, 189, 191, 193, 197, 198, 203, 212, 214, 226, 228, 231, 257, 262
- eutrophic 1, 67, 77, 157, 226
- hypertrophic 1
- mesotrophic 1, 40, 67, 77
- oligotrophic 1, 67, 77, 79, 199
- pelagic (off-coastal; open) 2, 29, 35, 74, 157, 205, 213
- surface 27, 44, 45, 74, 78, 87, 143, 213, 214, 257, 258
- wave, Bragg 180
- wind 1, 27–29, 31, 34, 43, 44, 80, 108, 151, 154, 155, 169, 171, 177, 178, 180, 184, 187, 188, 199, 200, 210, 220–223, 229, 243, 244, 245, 249, 252, 257, 258
- WMS (Web Map Service) 188, 194, 196, 197
- WQPs (water quality properties) 62
- xanthophylls 53–55, 64, 65
- Yellow River (China) 120
- yellow substance 77, 78, 123, 175, 192, 195
- Yogil River (Chad) 118
- zone, euphotic 3, 6, 26, 27, 29, 31, 40, 118, 213
- zooplankton  
grazing rate 95, 207, 210, 216  
large 216, 217, 220, 221  
small 217, 220, 221